ISSN 2434-9488
PRINT ISSN 2434-947X

KURNS Progress Report 2018

KURNS
Institute for Integrated Radiation and Nuclear Science,
Kyoto University

KURNS Progress Report 2018

APRIL 2018 – MARCH 2019

Published by
Institute for Integrated Radiation and Nuclear Science,
Kyoto University,
Kumatori-cho, Sennan-gun, Osaka 590-0494, Japan

PREFACE

It is a great pleasure for us to publish the KURNS Progress Report 2018. This report contains all of the accomplishments of research and related activities at Institute for Integrated Radiation and Nuclear Science, Kyoto University (KURNS) during the fiscal year 2018 from April 2018 to March 2019. As we rename our institute on April 2018, this is the first progress report of KURNS. Though we change the name of our institute, we will continue to play a distinctive role as a Joint Usage/Research Center, promoting an extensive range of studies from fundamental to applied research with research reactors and accelerators.

It is reassuring to note that the number of applications for Joint Research are increasing although the reactors had sustained operations for several years. We are proud since this demonstrates that researchers and students support our activity, which endorses our facilities as indispensable tools in their research activities with quantum beam and radioisotope. In the past fiscal year, KUR was operated for 809 hours and KUCA was for 796 hours. In total, we accepted 4,711 man-day researchers and students for using research facilities and for attending scientific meetings. A large number of research subjects has been enrolled, which covers various fields of nuclear science and technology, material science, radiation life science and radiation medical science. It is noted that 30 patients have been treated in the clinical studies of the boron neutron capture therapy (BNCT) using KUR in this period. The results of these activities are given in this report.

We strive for safe and stable operations for nationwide use, making it our primary mission to provide scientists the opportunity to conduct research and education. We are happy to dedicate our support to enable users conduct significant interdisciplinary research at KURNS.

Kumatori, June 4, 2019
Yuji Kawabata
Director, KURNS

CONTENTS

I. ANNUAL SUMMARY OF EXPERIMENTAL RESEARCH ACTIVITIES

I-1. PROJECT RESEARCHES

Project 1

PR1 Improvement of Characterization Techniques in High-Energy-Particle Irradiation Research

A. Kinomura

Institute for Integrated Radiation and Nuclear Science, Kyoto University

OBJECTIVES: Irradiation facilities of high-energy particles for neutrons (Material Controlled irradiation Facility), ions (e.g., Heavy ion irradiation facility) and electrons (Temperature-controlled irradiation facilities, KUR-LINAC) have been extensively developed at the Institute for Integrated Radiation and Nuclear Science. The developed facilities have been in operation and opened for joint research projects. One of the objectives of this project is to further improve or optimize irradiation facilities for advanced irradiation experiments.

As characterization techniques for irradiated materials, a slow positron-beam system and a focused ion beam system have been developed and introduced, respectively, in addition to previous characterization facilities such as an electron microscope, an electron-spin-resonance spectrometer, a bulk positron annihilation spectrometer and a thermal desorption spectrometer. Another objective is to introduce new techniques or reconsider analytical methods of previously used characterization techniques.

Based on these two objectives, we expect the enhancement of previous studies and the attraction of new users for the joint research program.

The allotted research subject (ARS) and individual co-researchers are listed below. Note that the titles of research subjects are based on individual reports.

ARS-1:
Study on efficient use of positron moderation materials (A. Kinomura *et al.*)

ARS-2:
Temperature dependence of electron-irradiation effects on diffusion coefficient of Cu in Fe studied by atom probe tomography (K. Inoue *et al.*)

ARS-3:
Change in positron annihilation lifetime of vacancies by hydrogen charging in tungsten 2 (K. Sato *et al.*)

ARS-4:
Electron paramagnetic resonance study on gamma-ray irradiated ZnO bulk single crystal (K. Kuriyama *et al.*)

ARS-5:
The first challenging study on corrosion resistance of fusion divertor materials to liquid metal during electron irradiation (M. Akiyoshi *et al.*)

ARS-6:
Positron annihilation study of Fe-Cr binary alloy after electron irradiation (T. Onitsuka *et al.*)

ARS-7:
PAS study on free volume in several diamond-like carbon thin films (K. Kanda *et al.*)

ARS-8
Positron annihilation spectroscopy on diamond-like carbon films (S. Nakao *et al.*)

RESULTS: In ARS-1, the brightness enhancement system of the KUR slow positron system was evaluated with a positron beam. A total enhancement of the brightness was estimated to be approximately 4. The efficiency of the remoderator was measured to be approximately 2%

In ARS-2, Electron-irradiation was performed for Fe-1.0wt.%Cu alloy with an 8 MeV electron beam at 310 - 475 °C. Needle-like samples for atom probe tomography (APT) were fabricated and diffusivity Cu in Fe was successfully determined by APT measurements.

In ARS-3, high purity tungsten irradiated by 8 MeV electrons were characterized by positron lifetime spectroscopy to investigate the effect of hydrogen charging in vacancies. For comparison, first-principle calculations for atomic position and density for valence electrons were carried using the Vienna Ab initio Simulation Package (VASP) code.

In ARS-4, electron paramagnetic resonance (EPR) measurements were performed for single-crystalline ZnO samples by Co-60 gamma-ray irradiation to introduce vacancies. Red light illumination at 77 K significantly changed the EPR spactra showing the change of ionization states by light illumination.

In ARS-5, aluminum rich ferritic steel (Fe-18Cr-3.3Al-0.4Si) NTK04L with 100μm Al_2O_3 oxidization coating was enclosed with tin in a newly developed irradiation container. The validity of ceramic coating under irradiation environment using KURNS-LINAC was verified.

In ARS-6, electron irradiation by KURRI-LINAC for Fe-40Cr alloy samples were performed at elevated temperatures to investigate phase decomposition under irradiation.

In ARS-7, The change of free volume in hydrogenated DLC film by the irradiation of soft x-rays were characterized by positron annihilation spectroscopy using the slow positron beam system (B-1) at KUR. The S value of hydrogenated DLC film was lowered by the soft x-ray irradiation.

In ARS-8, several types of DLC and carbon films deposited by plasma-based ion implantation under different conditions were characterized by Doppler broadening measurements using the KUR slow positron beam system. Resutls suggest that the situation of the defect in the type III-VI films may be similar in the case of as-grown films.

SUMMARY: In addition to developments on the slow positron beamline and a sample holder for electron irradiation, combinations of new materials and different irradiation/characterization techniques were continuously performed in the line of the objectives of this project. Such studies may enhance new concepts and techniques in the future.

PR1-1 **Study on Efficient Use of Positron Moderation Materials**

A. Kinomura, N. Oshima[1], Y. Kuzuya and A. Yabuuchi

Institute for Integrated Radiation and Nuclear Science, Kyoto University
[1]National Institute of Advanced Industrial Science and Technology (AIST)

INTRODUCTION: Positron annihilation spectroscopy is a unique analytical method to detect vacancy-type defects and free volume of materials. Energy-variable mono-energetic positron beams (slow positron beams) are important to perform depth-dependent positron annihilation spectroscopy of thin films or surface layers. Intense positron sources are required to efficiently obtain slow positron beams. In general, positron sources based on pair creation have higher intensity than radioisotope-based positron sources. Therefore, positron sources using pair-creation by gamma-rays from a nuclear reactor have been developed by using Kyoto University research Reactor (KUR). In the case of the KUR, the source size of the KUR slow positron beam is approximately 30 mm in diameter. For typical sample sizes of materials analysis ($\leq$10 mm), it is necessary to reduce beam sizes efficiently while keeping beam intensity as high as possible. For this purpose, brightness enhancement techniques are used. In this study, we have evaluated the brightness enhancement system in the KUR slow positron beam system.

EXPERIMENTS: The brightness enhancement system of the KUR slow positron beam system has been examined using positron beams after the KUR operation was restarted in August 2017. A single-crystalline Ni thin film was used as a remoderator of the brightness enhancement system. The Ni remoderator film was annealed in the quartz tube furnace before installation and cleaned by thermally excited hydrogen atoms after installation.

A series of experiments were performed for the brightness enhancement system: (1) Optimization of bias-voltages and solenoid/Helmholtz coil currents to maximize positron-beam intensities. (2) Adjustment of a focusing lens of the brightness enhancement system with a microchannel plate (MCP). (3) Transport of a brightness-enhanced beam to the downstream direction. (4) Efficiency evaluation of remoderator thin films before and after the brightness enhancement system.

RESULTS: The trajectory and intensity of the beam were optimized by adjusting voltages for the source components and currents for transport and steering coils by observing the phosphor-screen images on the microchannel plates (MCP's). The excitation current of the focusing lens of the brightness enhancement system was optimized by observing the spot images on the microchannel plate positioned at the focal point of the lens. The brightness-enhanced beam was transported to the sample chamber and the final spot sized was evaluated by using the MCP positioned at the sample position. Spot sizes for horizontal and vertical directions were slightly different. A spot area was reduced by a factor of approximately 20 after focusing at the brightness enhancement system. The efficiency of the remoderator was measured to be ~2% by gamma-ray intensities from the MCPs placed before and after the brightness enhancement system. A total ehancement of the brightness was estimated to be approximately 4.

The brightness-enhanced beam was transported through a pulsing system with a transmission-type chopper. Energy distribution of the positron beam can be evaluated by changing chopper bias voltage. Fig. 1 shows the energy distributions measured by using the chopper electrode of the pulsing system. Figs. 1(a) and 1(b) correspond to the energy distribution before and after the brightness enhancement, respectively. In the case of Fig. 1(a), the focusing lens was turned off and the Ni moderator was retracted from the center of the brightness enhancement system. Different extraction voltages were applied to W moderator electrodes at the positron source of the beamline. Two peaks were identified with a width of 10 – 14 eV in Fig. 1(a). In the case of Fig. 1(b) with the brightness enhanced beam, one narrow peak with a width below 3 eV was obtained. Apparently the energy distribution was reduced after the brightness enhancement. It can be an important advantage for beam pulsing.

In summary, the brightness enhancement system of the KUR slow positron system was evaluated with a positron beam during the KUR operation. The energy distribution of the beam was significantly reduced after the brightness enhancement. Further optimization of the system is in progress.

REFERENCE:

[1] Y. Kuzuya *et al.* J. Phys. Conf. Series **791** (2017) 012012.

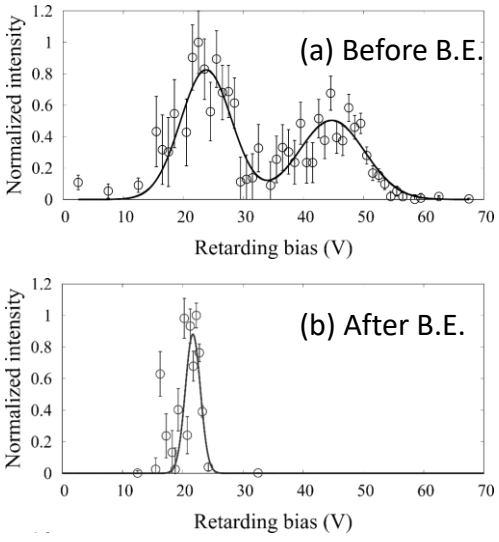

Fig. 1. Energy distribution of the positron beams before and after brightness enhancement (B.E.).

PR1-2 Temperature dependence of electron-irradiation effects on diffusion coefficient of Cu in Fe studied by atom probe tomography

T. Toyama, K. Inoue, Y. Nagai, Y. Shimizu, K. Yoshida, C. Zhao, S. Lan, T. Onitsuka[1], A. Kimomura[2], T. Yoshiie[2], Q. Xu[2], A. Yabuuchi[2]

Institute for Materials Research, Tohoku University

[1]Research Institute of Nuclear Engineering, Fukui University

[2]KURNS, Kyoto University

INTRODUCTION: A reactor pressure vessel (RPV) in a nuclear power plant is thick steel container that holds nuclear fuels, control rods and primary cooling water. The safety of RPV must be guaranteed. Therefore, irradiation-induced embrittlement of RPV steels is vital issue for the safe operation of nuclear power plants. One of the main origins for the irradiation-induced embrittlement of RPV is nano-sized Cu precipitates formed by neutron-irradiation. The diffusion coefficient, *D*, of Cu in Fe is the important basic quantities to understand the kinetics of Cu precipitation [1, 2].

Cu diffusion in Fe occurs by vacancy mechanism and is affected by the concentration of the vacancies in the material. Therefore, Cu diffusivity can be enhanced by irradiation because the vacancies and interstitials are remarkably induced during irradiation. In order to study the electron-irradiation effects on Cu diffusivity in Fe, we employ the electron irradiation at KUR LINAC which can induce simple Frenkel pairs. In the previous study, we investigated Cu diffusion coefficient under electron irradiation at 475℃ in Fe-1.0wt.%Cu alloys via precipitation kinetics using atom probe tomography (APT). The irradiation enhanced Cu diffusivity was clearly observed. In this study, we proceed to investigate Cu diffusion coefficient under electron irradiation in Fe-1.0wt.%Cu alloys at different temperature to reveal the temperature dependency of Cu diffusion coefficient for further understanding of the electron-irradiation effects on Cu diffusion coefficient.

EXPERIMENTS: Fe-1.0wt.%Cu alloy was made from high-purity (5N) Fe and Cu. A plate of 5 mm × 5 mm × 1 mm was fabricated and the surface of the sample was mechanically polished with abrasive papers of #2000. After removal of the machined layer by chemical polishing, the sample was annealed at 825℃ for 4 hours followed by quenching into ice-water.

Electron-irradiation was performed with electron beam with energy of 8 MeV at KUR LINAC. The irradiation dose rates, irradiation temperature, and irradiation time were 4.5 - 6.5×10^{-9} dpa/s, 310 - 475℃, and 1 - 2 hours respectively.

After electron-irradiation, needle-like samples for APT were fabricated with focused-ion beam apparatus. In APT measurement, a voltage pulse mode was employed at temperature of 50 K, pulse fraction of 20%, and a repetition frequency of 200 kHz.

RESULTS: Figure 1 shows atom map of Cu in the electron-irradiated Fe-Cu alloy at various irradiation conditions. Cu precipitates were clearly observed. The number density and the average size of Cu precipitates were analyzed with the standard analysis method. The Cu concentration in Fe matrix was also analyzed. With these parameters, the diffusion coefficient of Cu was estimated by using a formula concerning the diffusion coefficient and precipitation kinetics [3]. Figure 2 shows the Arrhenius plot of the *D* of Cu in Fe in the studied sample together with the *D* under thermal-aged samples [1]. The *D* under electron irradiation obtained in this study was much higher than that in thermal-aged condition. The *D* under electron irradiation was almost constant in the temperature range investigated in this study and was increased with increasing the dose rate. By comparing with estimation of vacancy concentration under irradiation by rate equation model, it is suggested that the observed enhancement of Cu diffusion is quantitatively attributed to the enhancement of vacancy concentration due to electron irradiation.

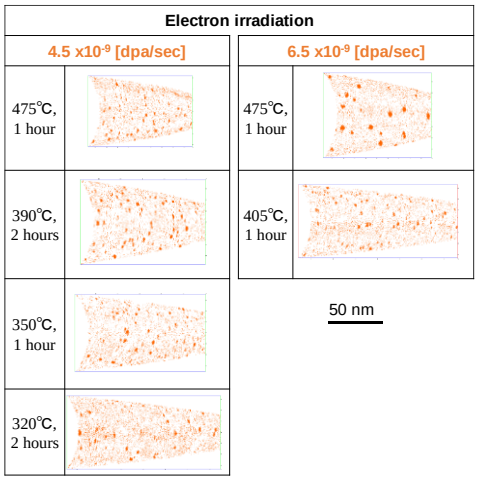

Figure 1: Atom maps of Cu in the electron-irradiated Fe-1.0wt. %Cu alloy at various irradiation conditions.

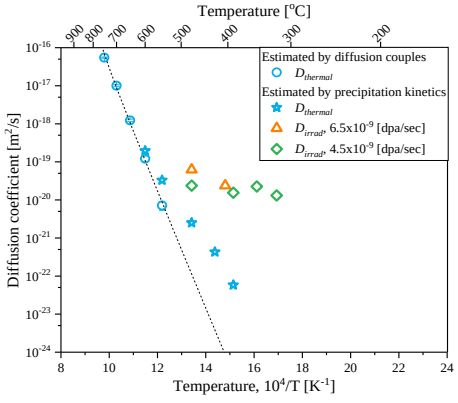

Figure 2: Arrhenius plot of the diffusion coefficient of Cu in Fe.

REFERENCES:

[1] T. Toyama *et al.*, Scrip. Mater., **83** (2014) 5-8.

[2] M. Shimodaira *et al.*, Mater. Trans., **9** (2015) 1513-1516.

[3] M. Koiwa and H. Nakajima, Diffusion in materials (Uchidarokakuho, 2009).

PR1-3 Change in Positron Annihilation Lifetime of Vacancies by Hydrogen Charging in Tungsten 2

K. Sato, Y. Kondo, M. Ota, Q. Xu[1], A. Yabuuchi[1], A. Kinomura[1]

Graduate School of Science and Engineering, Kagoshima University

[1]*KURNS, Kyoto University*

INTRODUCTION: The study of defect-hydrogen isotope complexes is an important issue for the structural materials of fusion reactor. In fusion reactor, neutrons introduce not only a variety of defects but also hydrogen and helium atoms formed by nuclear reaction of (n,p) and (n,α), respectively. In plasma-facing materials (PFMs), hydrogen isotopes penetrate by exposure to fusion plasma. The hydrogen isotopes interact with the irradiation-induced defects, and remain in the materials [1−3]. Retention of hydrogen isotopes leads to a decrease in mechanical properties of materials, e.g. hydrogen embrittlement etc. Tungsten is one of strong candidates for PFMs, which have high melting point, high thermal conductivity, and low sputtering erosion. However, hydrogen solubility is quite low, and interaction between hydrogen atoms and defects is strong [4]. Therefore, to study the interaction between hydrogen and defects is especially important in tungsten. In this study, we calculated the positron annihilation lifetime (PAL) of vacancies containing hydrogen atoms.

EXPERIMENTS: The Schrödinger equation for positron wave function was solved in the method developed by Puska and Nieminen [5]. In this calculation, the potential for a positron, which consisted of a Coulomb potential from nuclei and electrons and a correlation potential between a positron and an electron, must be given. To obtain the Coulomb potential from electrons, electron density was required, which was constructed by superposition of the atomic wave function given by Herman and Skillman [6] for core electrons (1s, 2s, 2p, 3s, 3p, 3d, 4s, 4p, 4d, 4f, 5s, 5p) and was obtained by the first-principle calculation for valence electrons (5d, 6s) (see next paragraph). The correlation potential was given by Boronski and Nieminen [7] based on the local density approximation. The numerical method developed by Kimball and Shortley [8] was used to solve the Schrödinger equation. Enhancement factors arising from the positron-electron correlation effects developed by Boronski and Nieminen [7,9] were used. Atomic position was also determined by the first-principle calculation.

The first-principle calculations for atomic position and density for valence electrons were carried out using the Vienna *Ab initio* Simulation Package (VASP) code [10,11] with projected augment wave (PAW) potentials [12]. The generalized gradient approximation (GGA) developed by Perdew, Burke and Ernzerhof (PBE) [13] was applied for the exchange-correlation energy functional. Lattice cell size was 128 atoms (4 × 4 × 4× 2), and 3 × 3 × 3 **k**-point grid of Monkhorst-Pack scheme [14] were used. The plane-wave energy cutoff was 325 eV. Ionic relaxation was performed until the force acting on every atom became smaller than 0.005 eV/Å. For the PAL calculation, cell shape (cubic) was fixed in this study. Lattice constant of 3.1695 Å was used, which obtained by the cell volume relaxation of perfect lattice.

RESULTS: Positron density heightens at vacancy site, and lowers by the existence of hydrogen atoms. The hydrogen atoms exist on the inner surface of the vacancy, and shifts from Octahedral site as reported by Ohsawa *et al*. [4,15] The simulated PAL of single vacancies containing one, two, three, four, five and six hydrogen atoms was 199 ps, 185 ps, 170 ps, 162 ps, 153 ps, 145 ps and 142 ps, respectively. The PAL of single vacancies containing no hydrogen (199 ps) is almost the same as the previous study (200 ps) [16]. When first hydrogen atom is added to a vacancy, the decrease of the PAL is approximately 15 ps. When second hydrogen atom is added to a vacancy-one hydrogen complex, it is also approximately 15 ps. When third, fourth, and fifth hydrogen atom is added to a vacancy-hydrogens complex, it is approximately 10 ps. When sixth hydrogen atom is added, it is a few pico-seconds. The trend of the change in the PAL is the same as the previous study [16], however, the decrease of the PAL is smaller in this study. This is caused by the location of first hydrogen atom added to single vacancy. The decrease of the PAL after hydrogen charging was approximately 20 ps in experiments. From simulation, when first and second hydrogen atom was added to vacancies, the decrease of the PAL is approximately 15 ps, respectively. It is expected that one vacancy captures one or two hydrogen atoms (on average 1.5 atoms).

REFERENCES:

[1] N. Yoshida, J. Nucl. Mater. **266-269** (1999) 197.
[2] M. Tokitani *et al.*, J. Nucl. Mater. **363** (2007) 443.
[3] V.Kh. Alimov *et al.*, J. Nucl. Mater. **375** (2008) 192.
[4] K. Ohsawa *et al.*, Phys. Rev. B **82** (2010) 184117.
[5] M.J. Puska and R.M. Nieminen, J. Phys. F **13** (1983) 333.
[6] F. Herman and S. Skillman, Atomic Structure Calculations, Prentice Hall, Inc. (1963).
[7] E. Boronski and R.M. Nieminen, Phys. Rev. B **34** (1986) 3829.
[8] G.E. Kimball and G.H. Shortley, Phys. Rev. **45** (1934) 815.
[9] M.J. Puska *et al.*, Phys. Rev. B **52** (1995) 10947.
[10] G. Kresse and J. Hafner, Phys. Rev. B **47** (1993) 558.
[11] G. Kresse and J. Furthmüller, Phys. Rev. B **54** (1996) 11169.
[12] P.E. Blöchl, Phys. Rev. B **50** (1994) 17953.
[13] J.P. Perdew *et al.,* Phys. Rev. Lett. **77** (1996) 3865.
[14] H.J. Monkhorst and J.D. Pack, Phys. Rev. B **13** (1976) 5188.
[15] K. Ohsawa *et al.*, Phys. Rev. B **85** (2012) 094102.
[16] T. Troev *et al.,* Nucl. Inst. Meth. Phys. Res. B **267** (2009) 535.

PR1-4 Electron paramagnetic resonance study on gamma-ray irradiated ZnO bulk single crystal

K. Kuriyama, T. Nishimura, K. Sato, J. Tashiro,
K. Kushida[1], A. Yabuuchi[2], Q. Xu[2] and A. Kinomura[2]

College of Engineering and Research Center of Ion Beam Technology, Hosei University

[1]*Osaka Kyoiku University*

[2] *Institute for Integrated Radiation and Nuclear Science, Kyoto University*

INTRODUCTION: Examining the defects caused by various radiations to ZnO and GaN by assuming the space environment is important. It is expected that the radiation damage is induced by Compton electrons emitted by the high dose gamma-ray irradiation. In our previous study, we reported the modification of the yellow luminescence in GaN bulk single crystal by gamma-ray irradiation [1]. The resistivity varies from 30 Ωcm for an un-irradiated sample to 10^4 Ωcm for gamma-ray irradiated one. The high resistivity was attributed to the carrier compensation due to the deep acceptor level relating to interstitial nitrogen atoms. We also reported that the persistent photoconductivity by electron-irradiated ZnO [2] and a shallow donor level relating to hydrogen interstitial by H-ion implanted ZnO [3]. In the present study, we report the existence of oxygen vacancy in gamma-ray irradiated ZnO by the electron paramagnetic resonance (EPR).

EXPERIMENTS: ZnO bulk single crystals with a thickness of 500 μm were used. The crystals were irradiated at room temperature with gamma-rays of 1.17 and 1.33 MeV from a cobalt-60 source of Institute for Integrated Radiation and Nuclear Science, Kyoto University. Samples were irradiated with an absorp-tion dose rate of 1.771 KGy/h. Total gamma-ray dose was 170 kGy. The resistivity varied from 4.1 x 10^4 Ωcm for an un-irradiated sample to 3.1 x 10^2 Ωcm for gamma-ray irradiated one. The EPR signal was meas-ured at 77 K.

RESULTS: Figure 1 shows EPR spectra in gamma-ray irradiated ZnO. A signal with g =1.996 was assigned to the oxygen vacancy of + charge state (V_O^+) observed in electron-irradiated ZnO [2]. This signal observed under no illumination disappeared after 10-min illumination of a red LED (λ=654 nm; 1.96 eV) at 77 K. The oxygen vacancy of V_O^+ states exists at about 1 eV below the conduction band. By the red LED illumination, electrons excited from the V_O^+ state are captured by V_O^{2+} as the defect localized state [4] in the conduction band. Therefore, V_O^+ states disappear. Since V_O^+ states behave as a deep donor (900~1200 meV), they are not an origin of low resistivity. In analogy with the low resistivity after Al-implanted ZnO [5], the decrease in resistivity after gamma-ray irradiation would be attributed to the shallow donor (30 meV below the conduction band [6]) due to interstitial zinc atoms.

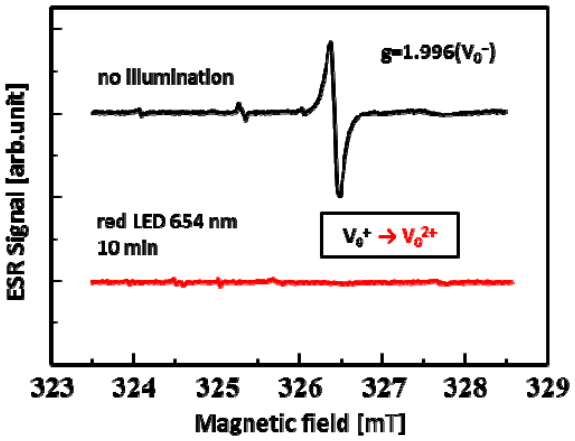

Fig.1 Electron paramagnetic resonance (EPR) spectra at 77 K in gamma-ray irradiated ZnO single crystal. The bottom signal is a spectrum after successive illumination for 10 min with a red LED at 77 K.

Part of this research was presented at 34 th International Conference on Physics of Semiconductors (ICPS2018; Montpellier, France).

REFERENCES:

[1] Y. Torita, N. Nishikata, K. Kuriyama, K. Kushida, A. Kinomura, and Q. Xu, Proceedings of ICPS2016 (Journal of Physics, IOP(UK)) **864** (2017) 012016.

[2] T. Oga, Y. Izawa, K. Kuriyama, K. Kushida, and Q. Xu, Solid State Commun. **151** (2011) 1700.

[3] T. Kaida, K. Kamioka, T. Ida, K. Kuriyama, K. Kushida, and A. Kinomura, Nucl. Instrum, Method Phys. Res. B **332** (2014) 15.

[4] S. Lany and A. Zunger, Phys. Rev. B **72**, 165202 (2007).

[5] T. Oga, Y. Izawa, K. Kuriyama, K. Kushida, and A. Kinomura, J. Appl. Phys. **109** (2011) 123702.

[6] D. C. Look, J. W. Hemsky, and J. R. Sizelove, Phys. Rev. Lett. **82** (1999) 2552.

PR1-5 The first chalenging study on corrosion resistance of fusion divertor materials to liquid metal during electron irradiation

M. Akiyoshi, M. Kondo[1] and A. Kinomura[2]

Radiation Research Center, Osaka Prefecture University
[1]. Lab. for Nucl. Reactors, Tokyo Institute of Technology
[2]Inst. for Integrated Radiation and Nuclear Science, Kyoto University

INTRODUCTION:

Development of divertor material is one of the most important issues for future fusion reactor, where high thermal conductivity in severe neutron irradiation environment, sputtering resistance, and low radioactivity is required. Although development of SiC ceramics, tungsten, and its composite material is furthered, neither has resulted in the solution of this problem.

The liquid divertor is completely different approach from the conventional divertor material development, that is covering a surface of material with coolant liquid metal, and it can expect to moderate damage to the structure material. There is few study on the compatibility of liquid metal and structure material, and furthermore, compatibility study during irradiation is quite limited.

EXPERIMENTS and RESULTS:

Originally, it was planned to perform the corrosion experiment after an electron irradiation, however some corrosion on the surface cannot be prevented by underwater or in air irradiation. Therefore, in this study, tin (Sn) which is a candidate liquid metal coolant was sealed in a small irradiation container (30×34×4mm) created by SUS316L stainless steel, and performed electron irradiation by KURUNS-LINAC that achieved the corrosion action inner side of the container under irradiation environment.

In the irradiation container, aluminum rich ferritic steel (Fe-18Cr-3.3Al-0.4Si) NTK04L with 100μm Al_2O_3 oxidization coating was enclosed with tin, and the validity of ceramic coating under irradiation environment is verified.

In order to perform structure observation out side of the controlled area after the irradiation, irradiation energy was set to 8MeV, and other parameters were set as below; pulse frequency: 100Hz, pulse width: 4μsec, peak current: 250mA, and average current: 100μA. The irradiation experiment was performed during 2.4×10^5 s and achieved 1.1×10^{20} e on the irradiation container and the container was kept in the temperature range of 450 to 550 ℃ using air cooled copper heat sink.

After the irradiation, at the center of container, SUS316L plate had become thin, and a little leakage of tin was observed. It was scheduled to bring out the container for analyze immediately after the irradiation, however the container showed weak radioactivity of 560cpm with GM survey meter. Ge detector showed a transmutation nuclide of Sn-117 (half-life 13.6 days) is generated up to 10kBq. After the cooling period of more than two months, the surface dose showed background level that was checked by a radiological control technician.

In observation by an optical microscope on the cross-section, thinning of stainless container is observed, while Al_2O_3 coated NTK04L specimen showed no thinning. Further analysis is required to clarify the origin of this thinning, that is irradiation induced corrosion or concentration of beam heating or electro migration. Moreover, element distribution analysis by EPMA is advanced now.

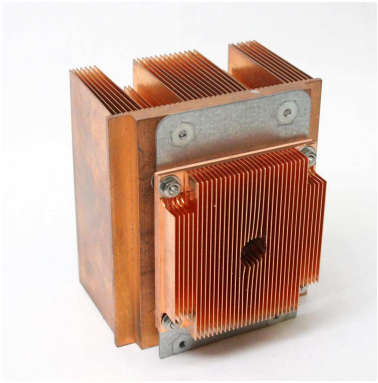

Fig.1 Cu heat sink used for the electron irradiation. The irradiation container was placed between two heat sinks. Pre heat sink was used as aperture (D 20mm).

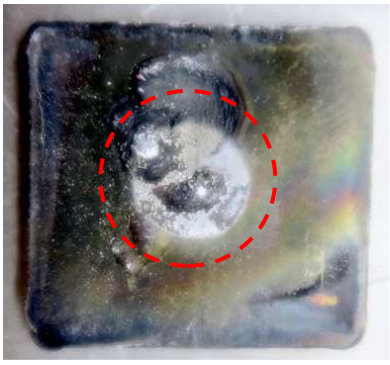

Fig. 2 Red circle shows small leakage of liquid tin from the stainless container. A thinning of the stainless plate was observed by cross-section observation.

PR1-6 Positron Annihilation Study of Fe-Cr binary alloy after Electron Irradiation

T. Onitsuka, K. Sato[1] and Q. Xu[2], J. Kinomura[2] and K. Fukumoto

Research Institute of Nuclear Engineering, Fukui University
[1]Graduate School of Science and Engineering, Kagoshima University
[2]Institute for Integrated Radiation and Nuclear Science, Kyoto University

INTRODUCTION: High-chromium (9-12%Cr) Ferritic/martensitic steels are attractive candidate material for various nuclear energy systems because of their excellent thermal properties, higher swelling resistance and lower activation compared with conventional austenitic stainless steels. The high-chromium steel as also been considered for both in-core and out-of-core applications of fast breeder reactors, and for the first wall and blanket structures of fusion systems, where irradiation induced degradation is expected to be the critical issues for reactor operation [1]. In the present study, the authors focused on a precipitation response for formation of α'-phase in Fe-Cr binary model alloy subjected to electron irradiation, in order to examine fundamental aspects of radiation effects on α'-phase precipitate development in iron-chromium alloys. The positron annihilation measurement technique was used to study the behaviour of microstructural evolution due to irradiation-induced defects and the formation of α'-phase simultaneously.

EXPERIMENTS: Simple binary Fe-40Cr alloy was made by arc melting under argon atmosphere in a water-cooled copper hearth. All the ingots were melted and inverted three times in order to promote chemical homogeneities. The obtained ingot was conducted by solution heat treatment at 1077 ℃ for 2 h followed by water quenching, and then, machined to the dimensions of 10 mm × 10 mm × 0.5 mm. The obtained specimen were irradiated by 9 MeV electrons at KURRI-LINAC. The specimen temperature was fixed at 100 or 475 ℃ during irradiation. The temperature variation was within ±5 ℃ during irradiation. The irradiation time was 88 hours for the batch of 100 ℃ irradiation test and varied from 1 to 10 hours for the batch of 475 ℃ irradiation tests. After the irradiation, all specimens were cooled immediately at the cooling rate of 170 ℃/min, and subsequently mechanically polished and electrolytically polished. Then, positron annihilation lifetime measurement and CDB measurement were performed.

RESULTS: Fig. 1. shows the positron annihilation lifetime measurement results of electron irradiated Fe-40Cr alloy. The longer lifetime components (τ_2) around 150 psec corresponds to vacancy type defects was obtained from a specimen irradiated at 100 ℃. On the other hand, the specimens irradiated at 475 ℃ show almost the same to bulk pure Fe. Fig. 2 shows the CDB ratio curves to bulk pure Cr obtained from positron CDB measurements for the Fe-40Cr alloy. The significant increase of the high-momentum fraction around 20 (P_L, 10^{-3}mc) observed for the specimens irradiated at 475 ℃. This behaviour suggests that the microstructural evolution of the annihilation fraction with electron of Fe due to the phase decomposition into Fe-rich (α) and Cr-rich (α') phases occurred in Fe-Cr alloy. Furthermore, the specimen irradiated at 100 ℃ showed almost similar behaviour in spite of the high concentration of defects.

REFERENCES:

[1] K. Okano *et al.*, Nucl. Instr. and Meth., **186** (1981) 115-120.

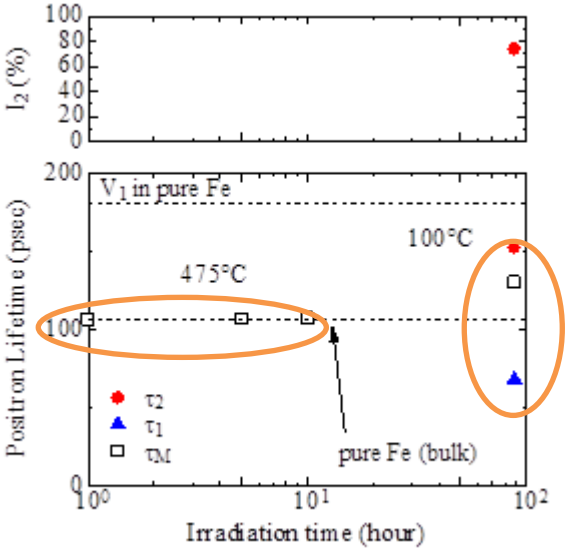

Fig. 1. The positron lifetime results with irradiation time for Fe-40Cr alloy. Bulk and a single vacancy (V_1) of pure Fe are also plotted as a reference.

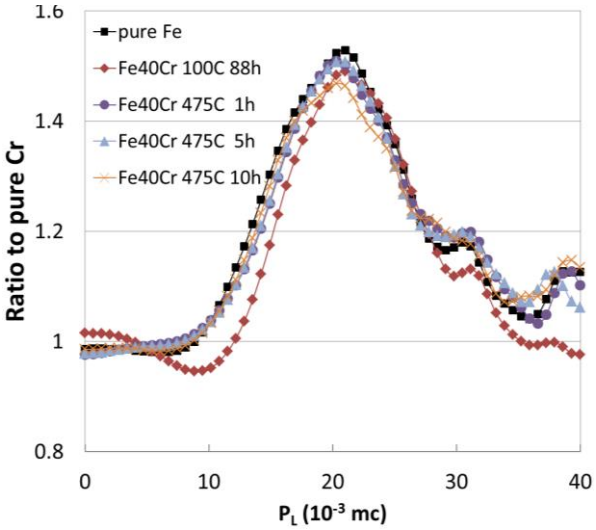

Fig. 2. The CDB ratio curves of irradiated specimens to unirradiated pure Cr. Unirradiated pure Fe is also plotted as a reference.

PR1-7 PAS Study on Free Volume in Several Diamond-like Carbon Thin Films

K. Kanda, F. Hori[1], A. Yabuuchi[2] and A. Kinomura[2]

Laboratory of Advanced Science and Technology for Industry, University of Hyogo
[1]Department of Materials Science, Osaka Prefecture University
[2]Institute for Integrated Radiation and Nuclear Science, Kyoto University

INTRODUCTION: The superlubricity of diamond-like carbon (DLC) film, along with its low friction coefficient, high hardness, chemical inert, and high wear and corrosion resistance, make it one of the most promising coatings for applications such as cutting tools, automobile parts, molds, computer hard disks, optical devices, food containers, and artificial blood vessels [1]. DLC film is amorphous carbon film that contains sp^3 hybridized carbon corresponding to a diamond structure and sp^2 hybridized carbon corresponding to a graphite structure. In addition, DLC film usually contains a certain amount of hydrogen [2].The chemical structure in terms of the coordination of carbon (sp^2 and sp^3 hybridization) and hydrogen atoms are the most important factors governing the quality of DLC films and they are used as classification criteria in ISO20523 published in 2017 [3]. However, DLC film also contains a certain amount of free volume. Free volume was considerable to connect strongly with several important properties of DLC film, such as hardness, Young modulus, and friction coefficient, but it has not been investigated. Positron annihilation spectroscopy (PAS) is a powerful tool for measuring free volume in material. In the present study, several DLC films were analyzed by PAS to evaluate the free volume in DLC films.

EXPERIMENTS: We worked on two kinds of experimental themes as for DLC films. One was the change of free volume in hydrogenated DLC film by the irradiation of soft X-ray. Sample was prepared by the hydrogenated DLC film exposed to synchrotron radiation (SR) at BL06 in the NewSUBARU synchrotron facility of the University of Hyogo [4]. The SR at the BL06 sample stage had a continuous spectrum from the infrared to soft X-ray region and an energy below 1 keV. Another theme was change of free volume by the doping of hetro-atom to DLC film. We deposited DLC films, which include and not include Si atoms, using PE-CVD method.

PAS measurement was performed at the slow positron beam system (B-1). Energy of incident positron, *E*, ranging 0.5 - 30 keV. Doppler broadening profiles of annihilation γ-rays were obtained using a Ge detector for each positron energy. The-low momentum part of spectra was characterized by the *S* parameter, which is defined as the number of annihilation events over the range of 511 ± 0.80 keV.

RESULTS: Figure 1 shows the *S* parameter as a function of incident positron energy *E* for the hydrogenated DLC films before and after irradiation of soft X-ray. The *S* values in the *E* region lower than 2 keV can be considered to attribute to the annihilation of positrons trapped in free volume in the DLC films. The *S* value of hydrogenated DLC film was lowered by the exposure to SR. This decrease was ascribable to the decrement of free volume in the hydrogenated DLC film by desorption of hydrogen from film due to excitation of soft X-rays [5].

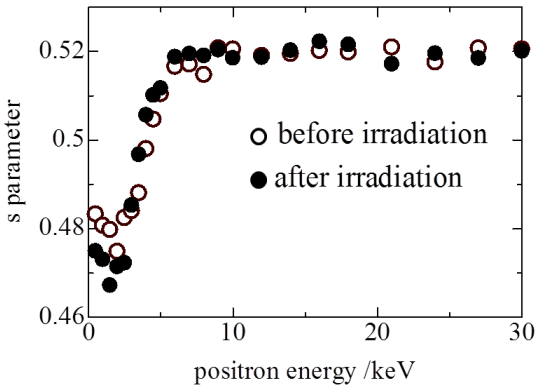

Fig. 1. *S* parameter as a function of positron energy *E* for hydrogenated DLC film before irradiation, ○ and that after irradiation of soft X-ray, ●.

Figure 2 shows the *S* parameter for the DLC films, which include and not include Si atoms. The *S* values of Si-containing DLC film were larger than those of DLC film which did not include Si. This result can be considered that Si atoms enhance the free volume in the DLC film.

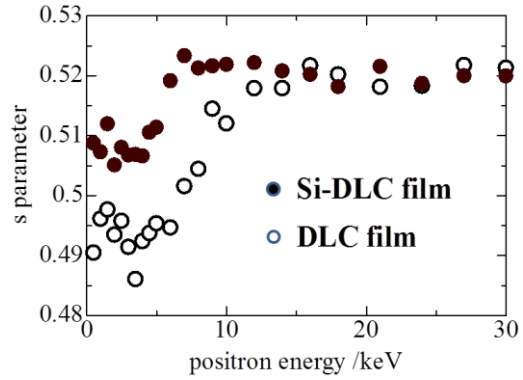

Fig. 2. *S* parameter as a function of positron energy E for DLC film, ○ and Si-DLC film, ●.

REFERENCES:

[1] S. Aisenberg *et al*., J. Appl. Phys. **42** (1971) 3963.
[2] J. Robertson, Surf. Coat. Technol. **50** (1992) 185.
[3] ISO20523, "Carbon based films – Classification and designations".
[4] K. Kanda *et al*., Jpn. J. Appl. Phys. **42** (2003) 3983.
[5] K. Kanda *et al*., Jpn. J. Appl. Phys. **50** (2011) 055801.

PR1-8 Positron annihilation spectroscopy on diamond-like carbon films

S. Nakao, X. Qu[1], A. Yabuuchi[1] and A. Kinomura[1]

Structure Materials Research Institute, National Institute of Advanced Industrial Science and Technology
[1]Institute for Integrated Radiation and Nuclear Science, Kyoto University

INTRODUCTION: Diamond-like carbon (DLC) films have attracted much attention because of their excellent mechanical properties, such as high hardness, high wear resistance and low friction coefficients. However, the properties strongly depend on the microstructure of the films which is varied by the deposition conditions and methods. Recently, DLC or carbon films are categorized from type I to VI, which includes graphite-like carbon (GLC) and polymer-like carbon (PLC).
The thermal stability of the films is of importance for practical applications. However, the thermal stability is not always enough to use it at high temperature. It is considered that the changes of the microstructure at high temperature should be responsible for the degradation of the properties. The structural changes are related to H desorption and behavior of defects at high temperature. Many studies have been carried out on the thermal stability of DLC films. However, the principal phenomena, such as defect behavior, are not always clear. Therefore, to make clear the thermal stability of DLC or carbon films, the examination on the defect behavior is necessary for every type of DLC films (type I to VI) because of different microstructure and hydrogen content. The positron annihilation spectroscopy (PAS) is one of the useful methods to clarify the defect behavior of materials. The aim of this project study is to examine the relationship between the thermal stability and the behavior of defects and bonded hydrogen in several types of DLC films by PAS and thermal desorption (TDS) method.
In a previous report [1,2], the films of type I, III, IV, V and VI were examined by TDS measurement in the range of room temperature (RT) to 800°C and it was found that hydrogen desorption clearly started around 400°C in the case of PLC (type VI) films. On the other hand, ta-C (type I) films did not change significantly until 800°C. It is well known that type I films are stable at high temperature. The result, thus, suggested that defects may be created by hydrogen desorption and the behavior may play important role for the durability of the films. In this study, several types of DLC and carbon films are examined by PAS measurement for the first attempt.

EXPERIMENTS: Samples for PAS measurement were type I, III – VI films. Type I (ta-C) and III (a-C) films were prepared by arc ion plating (AIP) at Nippon ITF Inc. and high-power impulse magnetron sputtering (HiPIMS), respectively. Type IV (a-C:H), V (GLC) and VI (PLC) films were deposited by plasma-based ion implantation (PBII) under the different conditions. The details on the PBII system were reported elsewhere [3]. Si wafer was used as substrate. The PAS spectra of Si substrate and graphite plate were also measured for comparison. The S-parameter was obtained at different positron energies ranging from 0 to 30 keV.

RESULTS: Figure 1 shows the change in S-parameter obtained from the PAS spectra of the samples at different positron energies in the range of 0 – 30 keV. The S-parameters of Si substrate and graphite plate are also indicated for comparison. In Fig. 1(a), the S-parameters of Si and graphite are around 0.51 and 0.47, respectively. On the other hand, the S-parameter of ta-C is a little bit lower than that of graphite, as shown in Fig.1(b). The other samples indicate similar S-parameter around 0.48. These results suggest that the situation of the defect in the type III – VI films may be similar in the case of as grown films. For the next stage, thermal annealing and PAS measurement is underway.

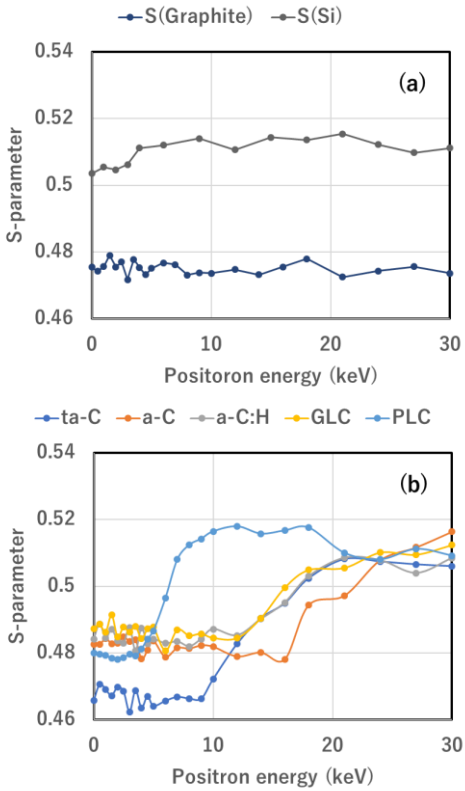

Fig.1. The change in S-parameter of the samples at different positron energies.

REFERENCES:

[1] S. Nakao *et al.*, KURRI Progress Report 2016, 28P12-8 (2016) 57.

[2] S. Nakao *et al.*, KURRI Progress Report 2017, 29P6-8 (2017) 32.

[3] S. Miyagawa *et al.*, Surf. Coat. Technol., **156** (2002) 322-327.

I-1. PROJECT RESEARCHES

Project 2

PR2 Development on Neutron Imaging Application

Y. Saito

Institute for Integrated Radiation and Nuclear Science, Kyoto University

1. Objectives and Allotted Research Subjects

Neutron imaging provides valuable information which cannot be obtained from an optical or X-ray imaging. The purpose of this project is to develop the imaging method itself and also the experimental environment for expanding the application area of the neutron imaging. The allotted research subjects are as follows:

ARS-1 Measurements of Multiphase Dynamics by Neutron Radiography (Y. Saito *et al.*)
ARS-2 Visualization and Measurement of Flow Behavior in Industrial Equipment (H. Asano *et al.*)
ARS-3 Visualization and Measurement of Adsorption/Desorption Process of Ethanol in Activated Carbon Adsorber for Adsorption Heat Pump (N. Asano *et al.*)
ARS-4 Visualization of heavy oil in packed bed reactor by neutron radiography (T. Tsukada *et al.*)
ARS-5 Characteristics of the Void Fraction under Transient Condition (H. Umekawa *et al.*)
ARS-6 Estimation of the Frosting and Defrosting Phenomena by Using Neutron Radiography (R. Matsumoto *et al.*)
ARS-7 Neutron imaging and optics development using simulation of VCAD Systems (Y. Yamagata *et al.*)
ARS-8 Water and Salt Distribution in a Rice Hull Medium under Sodium Chloride Solution Culture (U. Matsushima *et al.*)
ARS-9 Measurement of Water Content in Hardened Cement Paste by Neutron Imaging (T. Numao *et al.*)
ARS-10 In-situ Neutron Radiography Investigation on the Hydraulic Behavior of High Strength Cement Paste under High Temperature (M. Kanematsu *et al.*)
ARS-11 Evaluation of coolant distribution in a flat heat-pipe type heat spreader (K. Mizuta *et al.*)
ARS-12 Visualization of Organic Materials for Development of Industrial Applications (A. Uritani *et al.*)
ARS-13 Visualization of Coolant Flow in a Micro-Structured Wick (Y. Tsuji *et al.*)

2. Main results and the contents of this report

To develop neutron imaging, our imaging system was developed so that high-speed imaging could be performed at thermal neutron flux of 10^7 n/cm^{2}s. Such improved system was shared with all of the project members and valuable results were obtained as follows:

ARS-1 improved the above-mentioned high-speed imaging system at the B4 port. The spatial and temporal resolution of the system was tested. Then, the present system was applied to investigate the effect of motion blur in the observation of rapidly moving object and to visualize air-water two-phase flow structure.

ARS-2 applied to neutron imaging to simultaneous measurements of water distribution in Polymer Electrolyte Fuel Cell (PEFC). From the measurement results, the existing correlations for the protonic conductivity of PEFC overestimates the measured values. This results indicate that change in the protonic conductivity with respect to the water content becomes small in low range of water content.

ARS-3 applied neutron imaging to measurements of distribution of adsorbed refrigerant in adsorbent particle layer. The dynamic behavior of the refrigerant during the adsorption was clearly visualized.

ARS-4 applied neutron imaging to the flow visualization of heavy oil in packed bed reactor. Heavy oil were supplied to the packed bed reactor filled with supercritical water. From the experimental results, a flow channeling was observed depending on the experimental conditions.

ARS-5 applied the neutron imaging to boiling two-phase flow at a high temperature conditions. High-speed quenching phenomena was successfully visualized by using our improved imaging system. In addition to such boiling experiments, quantitative method for void fraction was examined.

ARS-6 applied neutron imaging to frosting behavior in cooling heat exchange system. 3-D frost density was clearly visualized by the neutron CT imaging system at the B4 port.

ARS-8 applied neutron imaging to observation of water movement in reciprocal grafts of tomato and eggplant by analyzing movement of D_2O as tracer.

ARS-12 performed quantification of neutron imaging by using two-different neutron source (KUR-E2 and NUANS). Carbon fiber reinforced plastic and its peeling from aluminum alloy was visualized. The spatial resolution of neutron imaging at the two neutron imaging facilities was compared each other.

ARS-13 wanted to develop new measurement technique of the superfluid. However, the experiments could not be performed due to malfunction of laser system.

PR2-1 Measurements of multiphase flow dynamics using neutron radiography

Y. Saito and D. Ito

Institute for Integrated Radiation and Nuclear Science, Kyoto University

INTRODUCTION: Neutron radiography (NRG) is a powerful tool for fluid flow visualization as well as two-phase flow research. Gas-liquid two-phase flows in a metallic pipe have been visualized clearly by using NRG. However, it would be still difficult to obtain dynamic information on such flows by NRG, because of insufficient neutron flux from neutron sources or poor efficiency of imaging devices. In this work, our imaging system was improved for high frame rate NRG. Then, the improved system was applied to investigate the effect of motion blur in the observation of rapidly moving object and to visualize air-water two-phase flow structure.

HIGH-SPEED NEUTRON IMAGING: A high frame rate NRG system was constructed at the B-4 supermirror neutron guide facility [1] of the Institute for Integrated Radiation and Nuclear Science, Kyoto University. In the B-4 port, the neutron flux is 8.5×10^7 n/cm^{2}s at 5MW reactor operation mode, and the beam width and height at the beam exit are 10 mm and 75 mm, respectively. The imaging system for high frame rate NRG consists of a neutron converter, a dark box with a single mirror, an ultrasensitive lens, an optical image intensifier and a high-speed camera. In this system, a high sensitivity high-speed camera (AX-50, Photron) was applied to enhance the temporal resolution. The frame rate of 10,000 fps was achieved using this system at the B-4 port [2]. The spatial resolution and frame rate can be adjusted by selecting the optics.

EVALUATION OF MOTION BLUR: The motion blur cannot be neglected in the imaging of high-speed moving object. A Gd indicator illustrated in Fig.1(left) was rotated using a rotating disc system and the neutron transmission image of the rotating indicator was obtained. A typical image of the static indicator is shown in Fig.1(right). The shape of the Gd indicator could be clearly observed by neutron radiography. The transmission images of the rotating indicator with different velocity are shown in Fig.2. The indicator moved downward and the transmission images were obtained at the frame rate of 10,000 fps. As the rotating velocity increases, the image degradation becomes significant. The effect of this blur should be clarified for accurate measurements by high frame rate NRG.

TWO-PHASE FLOW VISUALIZATION: Air-water two-phase flow was visualized by the present high frame rate NRG system. The test section is a vertical circular pipe which is made from aluminum. The inner diameter is 10 mm and the wall thickness of the test pipe is 1 mm. The water was circulated by a pump and the compressed air was injected from the upstream of the test section. The flow rates of water and air were monitored by flow meters. The typical void fraction distribution estimated from the neutron transmission image is shown in Fig.3. The superficial liquid and gas velocity are 0.72 m/s and 15.3 m/s, respectively, and the flow pattern in the test section was annular flow. The gas phase passes through the center of the cross-section and the liquid film flows along the wall. Fast fluctuation behavior of such liquid film was observed by the high frame rate NRG.

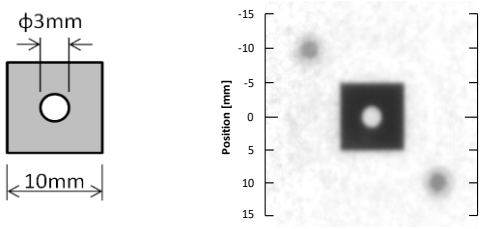

Fig. 1 Detail (left) and neutron transmission image (right) of the Gd indicator.

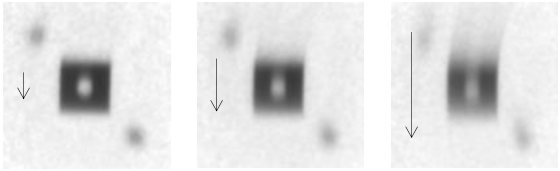

Fig. 2 Neutron transmission images of rotating indicator.

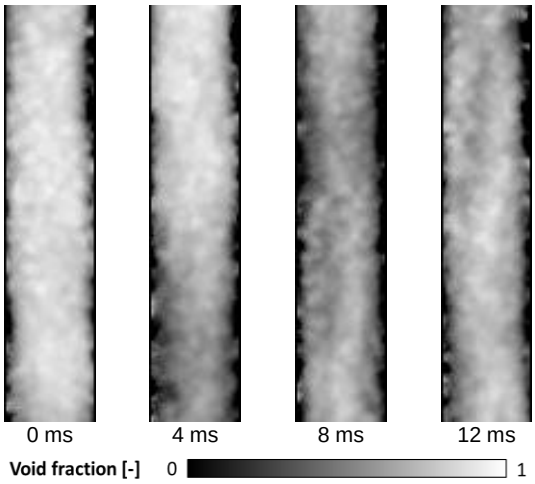

Fig. 3 Void fraction distributions in annular flow (J_L=0.72m/s, J_G=15.3m/s).

REFERENCES:

[1] Y. Saito, *et al*., Nucl. Instr. Meth. Phys. Res., A, **651** (2011) 36-41.

[2] D. Ito, Kei Ito and Y. Saito, WCNR-11, Sydney, Australia (2018).

PR2-2

Simultaneous Measurements of Water Distribution and Electrochemical Characteristics in Polymer Electrolyte Fuel Cell

H. Murakawa, S. Sakihara, K. Sugimoto, H. Asano, D. Ito[1] and Y. Saito[1]

Graduate School of Engineering, Kobe University
[1]Institute for Integrated Radiation and Nuclear Science, Kyoto University

INTRODUCTION: Water management in polymer electrolyte fuel cells (PEFCs) is a key topic for the PEFC operation. If condensed water exists in the gas diffusion layer (GDL) and the gas channel, it may depress the gas diffusion as flooding. In order to clarify the effect of water content in the proton exchange membrane (PEM) and the (GDL) on the electric resistances, simultaneous measurements of water distribution and the electrical impedance were carried out by using the neutron radiography and electrochemical impedance spectroscopy (EIS). Change of water accumulation in the PEM and the GDL were compared with the PEM and the reaction resistances.

EXPERIMENTS: A small size PEFC having nine-parallel gas-channels with cross-sectional area of 1 × 1 mm^2 was used for measuring two-dimensional water distribution and the electrochemical characteristics. Nafion® NR-212 was used as the PEM with a thickness of approximately 90 μm having catalyst layers on both the anode and cathode sides. The GDL was carbon paper (Toray Ind.) with thickness of 190 μm at the cathode side and 280 μm at the anode side. The porosity of the GDL was approximately 78%. Two-dimensional water distributions were obtained every 60 sec during the PEFC operation. The EIS measurements were simultaneously carried out with the neutron radiography for evaluating the PEM resistance R_{PEM} [Ω] and the reaction resistance R_{CT} [Ω]. The EIS was carried out with a frequency range of 0.5 to 30 kHz.

RESULTS: Two-dimensional water distributions at current density i =158 mA/cm^2 are shown in Fig. 1. Liquid water accumulation during the PEFC operation can be confirmed as indicated by the gray-scale. Amounts of water accumulation in the GDL under the lands and channels are different and a large amount of water existed under lands at the earlier results. It indicated that water accumulation is started under the lands. Then, liquid water reaches channel and are particularly concentrated on the land corners.

Fig. 2 shows time series of the cell voltage, R_{PEM} and R_{CT}. The cell voltage rapidly recovered just after the PEFC operation and was almost constant. R_{CT} slightly increased although R_{PEM} slightly decreased with the operation time. Water contents in the PEM, λ, were evaluated from the water distributions. Change of λ and σ based on the initial condition, Δλ and Δσ, are shown in Fig. 3. It can be confirmed that Δσ almost linearly increases with Δλ. This tendency is the same with a proposed correlation by Springer et al. [1]. However, effect of water contents on the protonic conductivity was much less that the literature. This results show that change in the protonic conductivity with respect to the water content becomes small in low range of water content.

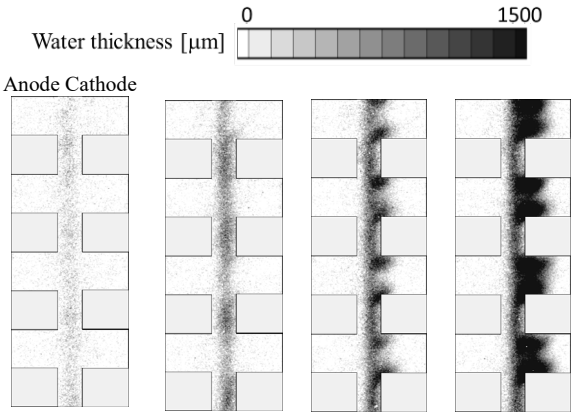

Fig. 1. Two-dimensional water distributions at i =158 mA/cm^2.

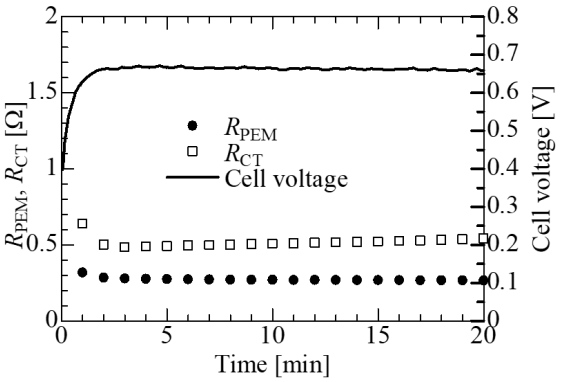

Fig. 2 Relation between the cell voltage and the resistance at i =158 mA/cm^2.

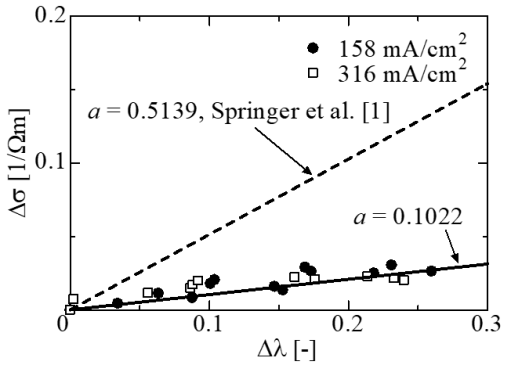

Fig. 3. Relation between water content in MEA and the protonic conductivity.

REFERENCE:

[1] T.E. Springer, T.A. Zawodzinski and S. Gottesfeld, J. Electrochem. Soc., **138** (1991) 2334-2342.

PR2-3

Visualization and Measurement of Distribution of Adsorbed Refrigerant in Adsorbent Particle Layer under Transient Conditions

H. Asano, G. Ren, H. Murakawa, K. Sugimoto,
D. Ito[1] and Y. Saito[1]

Graduate School of Engineering, Kobe University

[1]Institute for Integrated Radiation and Nuclear Science, Kyoto University

INTRODUCTION: Adsorption refrigerator driven by heat at relatively low temperature is one of the efficient tools for waste heat recovery. Refrigerant vapor from an evaporator at low pressure is adsorbed in an adsorbent particle layer in an adsorber. In order to keep the evaporation pressure, the adsorber must be changed to a dry adsorber in a batch operation. Wet adsorber is regenerated by heating. Therefore, the coefficient of performance is low due to its batch operation and the heat capacity of the adsorber. On the other hand, although adsorbed amount increased with decreasing the adsorbent temperature for a refrigerant pressure, the adsorbent is heated by the adsorption heat in the adsorption process. So, quick rejection of the adsorption heat from the adsorbent layer is required in the adsorption process. Metallic fins are often used for higher thermal diffusion. In is required for the optimal design of the fin configuration to clarify adsorption/desorption phenomena in transient changes. Adsorbed refrigerant distribution in an adsorbend particle layer in a cylindrical cell was visualized by neutron radiography.

EXPERIMENTS: Activated carbon and ethanol were used as the adsorbent and refrigerant, respectively. Mean particle diameter of the activated carbon was 86 μm. Activated carbon was installed in a cylindrical cell with thin stainless steel wall and the inner diameter of 21 mm. The depth of the adsorbent layer was 35 mm. The installed amount of dry activated carbon was 3 g. The layer was covered by two aluminum porous plates with the thickness of 10 mm to prevent scatter by vapor flow. The bottom of the cell was brazed on a brass plate whose temperature was maintained by cooling water. The cell was connected to a liquid ethanol reservoir immersed in a temperature controlled water.
The mass attenuation coefficient of liquid ethanol was 3.86 cm^2/g [1]. Radiographs on a scintillation converter were recorded by a cooled CCD camera with the exposure time of 30 seconds and the pixel size of 42.8 μm/pixel. The temperatures of the bottom plate and ethanol reservoir were maintained at 30 °C and 10 °C during the adsorption process, respectively.

RESULTS: Original radiographs under the condition of dry before adsorption and with adsorbed ethanol are shown in Fig. 1 (a) and (b), respectively. It was clearly show that the region of adsorbent layer became darker due to ethanol adsorption. Adsorbed amount was larger closer to the surface. Heat radiation through the side wall to the ambient air might be enough for the heat rejection of the adsorption heat. Attenuation due to ethanol was calculated for each pixel and summed values in the sliced layer with 3 mm height (70 pixels) were evaluated. Temporal change of the summed values are plotted against the elapsed time from the adsorption start in Fig. 2. The value at 31.6 mm was lower because the region included the surface and the adsorbent amount was smaller. It was clearly shown that refrigerant adsorption progressed from the surface to the depth. Figure 3 shows the horizontal distribution at each sliced layer at 2670 seconds from the start. Smooth bold lines show the proportional profile of the chord length of cell along the beam direction. At 28.6 and 25.7 mm, the adsorption ratio might be higher near the wall. On the other hand, at 16.9 mm, the adsorption ratio seemed to be homogeneous because the attenuation distribution agreed well with the cell size.

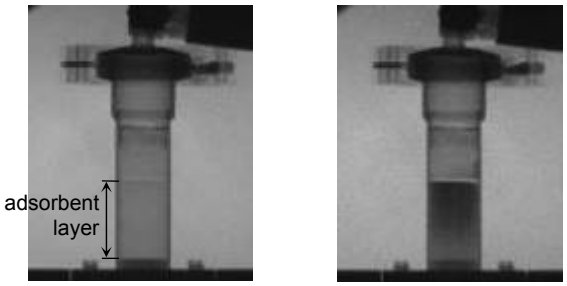

(a) Before adsorption (b) With adsorption

Fig. 1 Obtained neutron radiographs at E2 port of KUR.

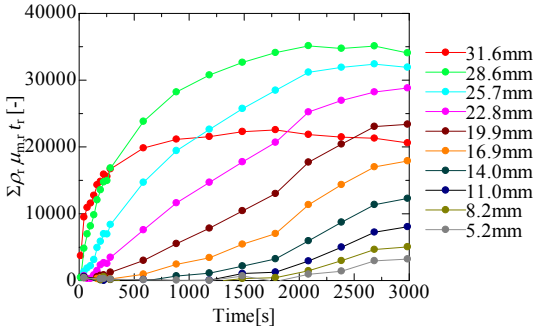

Fig. 2 Change of adsorbed amount at different height.

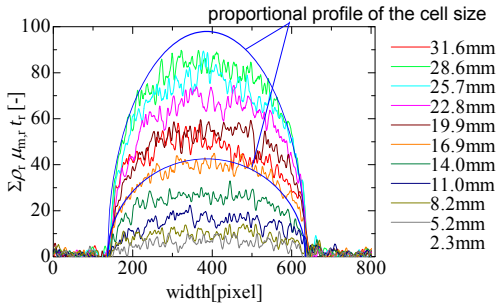

Fig. 3 Horizontal distribution of adsorbed amount.

REFERENCE:

[1] H. Asano, K. Murata, N. Takenaka and Y. Saito, Physics Procedia, **69** (2015) 503-508.

PR2-4 Flow visualization of heavy oil in supercritical water using neutron radiography

T. Tsukada, M. Kubo, E. Shoji, T. Kikuchi, N. Ito, S. Takami[1], K. Sugimoto[2], D. Ito[3] and Y. Saito[3]

Dept. of Chemical Engineering, Tohoku University

[1] Dept. of Materials Science and Engineering, Nagoya University

[2] Dept. of Mechanical Engineering, Kobe University

[3] Institute for Integrated Radiation and Nuclear Science, Kyoto University

INTRODUCTION: With an increase in the demand for petrochemical feedstock and middle distillate, utilization of heavy oil such as atmospheric or vacuum residue is also necessary. Since the heavy oil has high viscosity and its quality is low, desulfurization and upgrading processes are required to use the heavy oil effectively. In such a situation, upgrading process using supercritical water has been proposed and studied recently.

Understanding of flow behavior of heavy oil in reactors filled with supercritical water is important to improve the performance of upgrading process. However, the phenomena are complicated to simulate numerically. Since, in experiment, the reactor is made of metal for operation at high pressure and high temperature, the visualization using visible light is not available. Thus, the numerical simulation and experimental flow visualization of heavy oil flow in supercritical water have not been conducted. In our previous study [1], we have visualized the heavy oil flow in a trickle bed reactor under N_2 atmosphere using neutron radiography, and indicated the potential of neutron radiography to investigate the flow behavior of heavy oil. As a next step, the objective of this study is to visualize the heavy oil flow in supercritical water.

EXPERIMENTS: In neutron radiography for the flow visualization of heavy oil in supercritical water, the Kyoto University Research Reactor (KUR) was utilized as neutron source. A series of neutron radiography experiments was conducted with a thermal neutron flux of 5×10^7 n/cm^2·s.

Fig. 1 shows the schematic diagram of the apparatus used in the experiment. The reactor consists of a 1/2-inch stainless steel tube filled with Al_2O_3 particles having the diameter of 3 mm. The heavy oil was supplied to a reactor from above with the flow rates of 2.5 or 5.0 mL/min. Atmospheric residue (AR) was used as the heavy oil sample. On the other hand, the water was supplied counter-currently with the flow rates ranged from 0.05 to 7.5 mL/min. The reactor was heated to temperatures of 400°C and was operated at 25 MPa.

An image intensifier and a camera at the framerate of 30 fps were used to obtain radiography images of the unsteady flow behavior. An image processing to reduce noises and to calculate neutron attenuation was performed for the obtained radiography images.

RESULTS: The flow behavior of heavy oil in the reactor varied depending on the experimental conditions were visualized using neutron radiography. Fig. 2 shows the time variation of flow behavior of heavy oil in supercritical water at the flow rates of heavy oil and water were 2.5 mL/min and 1.0 mL/min, respectively. The heavy oil spread radially to the wall of the tube. This is because heavy oil diffused in supercritical water. In addition, the heavy oil spread above the nozzle because the lighter components contained in the heavy oil were carried by the supercritical water flow.

CONCLUSION: This study indicated that neutron radiography is a useful technique to visualize the flow behavior of heavy oil in metallic reactor filled with supercritical water at high pressure and high temperature conditions. The results showed that the flow behavior of heavy oil depends on the flow rates of heavy oil and supercritical water.

ACKNOWLEDGEMENT: This research was supported by Kurita Water and Environment Foundation.

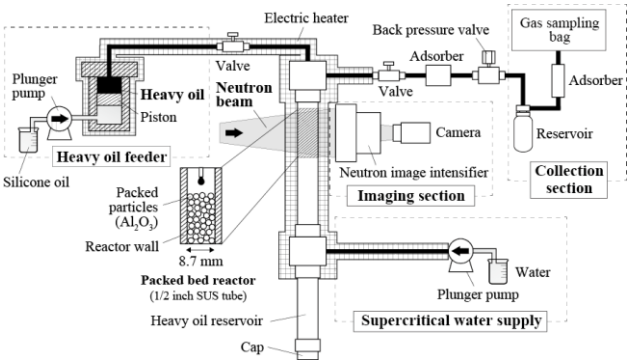

Fig. 1: Schematic diagram of experimental apparatus

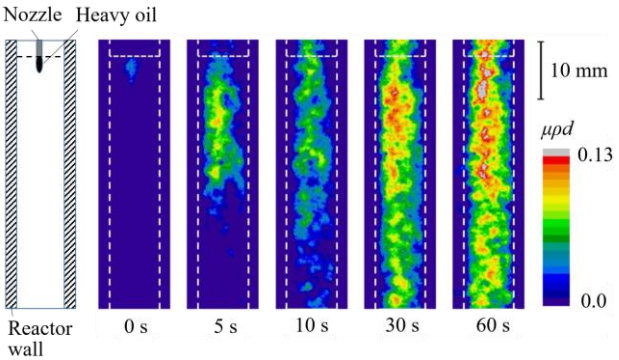

Fig. 2: Flow behavior of heavy oil in supercritical water when the flow rates of heavy oil and water were 2.5 mL/min and 1.0 mL/min, respectively. μ, ρ, and d are mass attenuation coefficient of thermal neutrons [m^2/kg], density of heavy oil [kg/m^3], and thickness along the neutron beam direction

REFERENCES:

[1] E. Shoji *et al.*, Chem. Eng. Sci., **196** (2019) 425-432.

PR2-5 Quantitative Dynamic Measurement of Void Fraction

H. Umekawa, T. Ami, K. Saito, Y. Kawazoe, K. Obata, K. Shibata, H. Sakai, Y. Saito[1] and D. Ito[1]
Dept. Mechanical Engineering, Kansai University.
[1]*Institute for Integrated Radiation and Nuclear Science, Kyoto University.*

INTRODUCTION: In this series of experiments, Void fraction of forced convective boiling is quantitatively visualizing under three kind of conditions, i.e. Micro-channel heat exchanger, Quenching process and Sub-cooled boiling. In each experiment, several technical trials as the neutron radiography technique are included, and one of them is quantitative measurement of dynamic image. In this report, the estimation results of the ability of the dynamic image processing is briefly explained.

EXPERIMENTS: In the quenching experiment, sub-cooled liquid was injected into the superheated test section which was heated until 800 deg.C. After the injection, quenching was propagated, and Inverted annular flow might be constructed in the test section. In this kind of experiment, to estimate the Inverted annular flow, "hot-patch" to prevent the propagation of quenching has been normally equipped so far, but the detail information at the quenching point could not be acquired by this method. In this mean, the dynamic quantitative measurement has been strongly required.

Figure 1 is the visualization result by using the high speed camera (Photron AX-50) with 10,000 frames/sec. Although the movement of liquid slug is clearly observed, it's not enough for the quantitative measurement.

To estimate the required neutron number for quantitative measurement, the neutron flux at the arbitrary location from beam exit has been simply estimated by using the geometric relationship of beam expansion as shown in Fig.2.

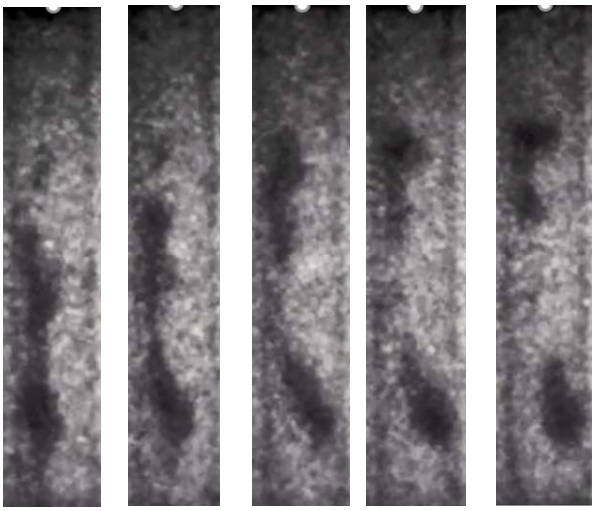

Fig. 1. Example of visualization image at 10,000 frame/s.

On the basis of these neutron flux, the relationship between the frame rate and pixel size is explained at Fig.3. For the purpose of flow observation, approximately 5neutrons/pixel is enough, and this condition corresponds to the condition of Fig.1. The requirement of the quantitative measurement is estimated by using visualization image of 500frames/sec with 0.5ms exposure period, and evaluated by using the standard deviation. As the results, 0.5ms exposure period is not enough and 2.5ms is minimum exposure period for quantitative measurement, and over 10ms is more suitable exposure period. The neutron number under these exposure period corresponds to a.20n/pixel, a.100n/pixel and a.300n/pixel, respectively. This number would be used as the standard value to consider the frame rate of dynamic quantitative measurement.

Author wish to express sincere thanks to Messrs H. Fuiwara and T. Kageyama for their support in the experiment.

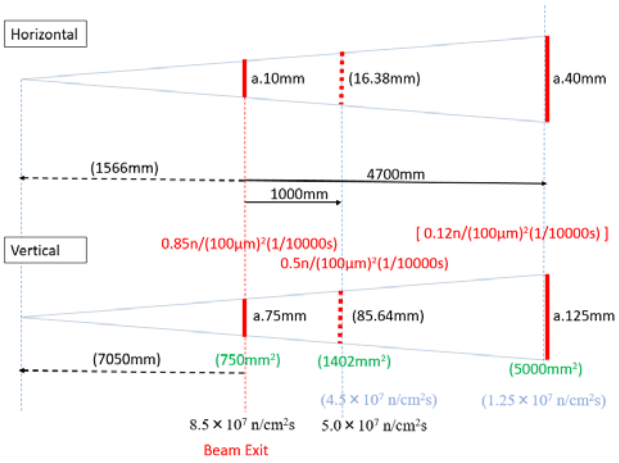

Fig. 2 Rough estimation of visible area and neutron flux.

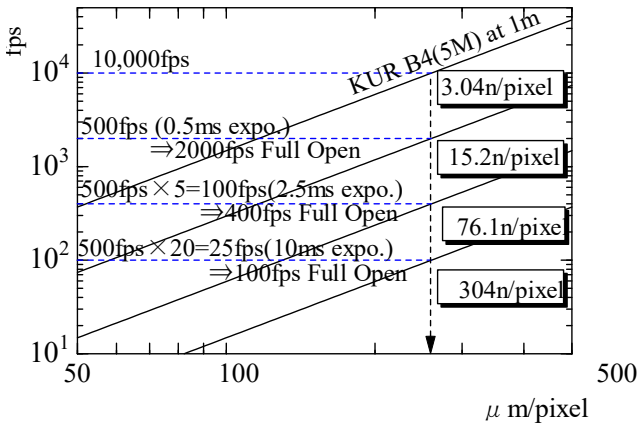

Fig. 3 Requirement of neutron number for qualitative measurement.

30P2-5

PR2-6 Three Dimensional Frost Formation on the Heat Exchanger Measured by Neutron CT

R. Matsumoto, Y. Nagasawa[1], T. Shiokawa[1], Y. Nishiura[1], D. Ito[2] and Y. Saito[2]

Faculty of Engineering Science, Kansai University
[1]Graduate School of Science and Engineering, Kansai University
[2]Institute for Integrated Radiation and Nuclear Science, Kyoto University

INTRODUCTION: Heat exchangers which are operated at 0 deg.C below are subjected to the frost deposition and its growth. The frost layer is a porous structure of ice crystals and air pores. The frost layer has low conductivity, thus, the frost formation on heat exchanger causes serious problem to the heat transfer performance by thermal resistance between the cold surface and the humid ambient air. Matsumoto et al. [1] reported the two dimensional distribution of the frost deposition rate on the plate fin-tube heat exchanger by using neutron radiography. Neutrons are strongly attenuated by the water molecules in the frost layer, but not by the aluminum heat exchanger. The frost formation can be quantitatively estimated based on the neutron beam attenuation. By applying the computed tomography technique, three dimensional frost formation can be visualized. In this study, the three dimensional distribution of the frost deposition and the frost density profiles on the plate fin-tube heat exchanger are quantitatively estimated by using the neutron computed tomography at KUR B-4 radiation port.

EXPERIMENTS: Fig.1 shows the schematic view of the experimental apparatus. Cooled humid air adjusted to the flow rate 70 L/min was supplied to the test section. The test section consisted of Styrofoam block duct with a cross section of 68 mm x 150 mm and the aluminum plate fin-tube heat exchanger. The heat exchanger consisted by 6 fins with 60 mm in height, 28 mm in width, 0.25 mm in thickness, and together with two tubes of an outer 8.5 mm. Fig.2 shows the aluminum heat exchanger used in this experiment. Fin pitch was 5 mm. The heat exchanger was cooled by -22 ºC fluorinert. The frosting duration was 60 min. CCD camera (Princeton Inst., 16-bit, 1024 × 1024 pixels) set in the inside a light-tight camera box. Two mirrors reflect the visible ray image from the converter with the 6LiFZnS scintillator screen mounted onto the front end of the camera box. 600 neutron radiography (NRG) images were taken by the CCD camera with an exposure time of 5 sec by rotating the heat exchanger through 180 degrees.

RESULTS: Fig.3 shows the three dimensional frost formation on the heat exchanger with the horizontal cross section at z=17.5, 30, 42.5 and 60mm. The tomographic image shows the linear attenuation coefficient μ. The frost density ρ can be calculated from $\rho = \mu / \mu_{m,ice,}$ in which $\mu_{m,ice}$ is the mass attenuation coefficient of ice. At the front fin edge, high frost deposition are observed. Inside of the heat exchanger, the frost layer covered whole of the fin surface, however, the frost layer is thin in the wide area of the wake region of the tubes. The three dimensional frost density profile can be estimated by using 3D neutron computed tomography.

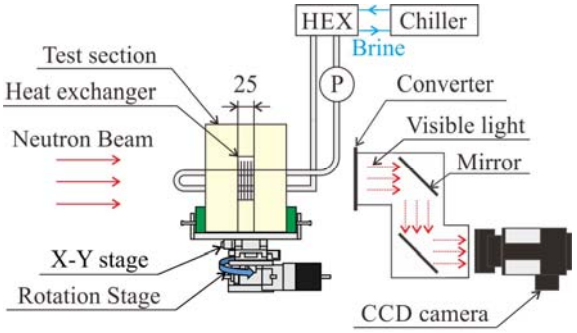

Fig.1 Schematic view of the experimental apparatus.

Fig. 2 Plate-fin tube heat exchanger.

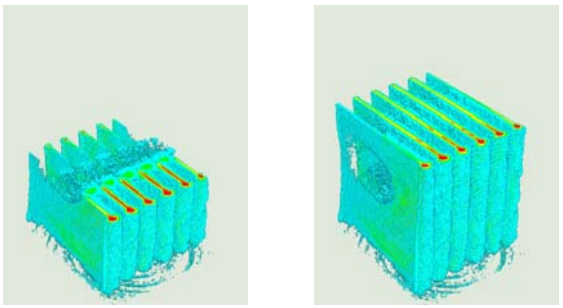

(a) z = 17.5mm (b) z = 30mm

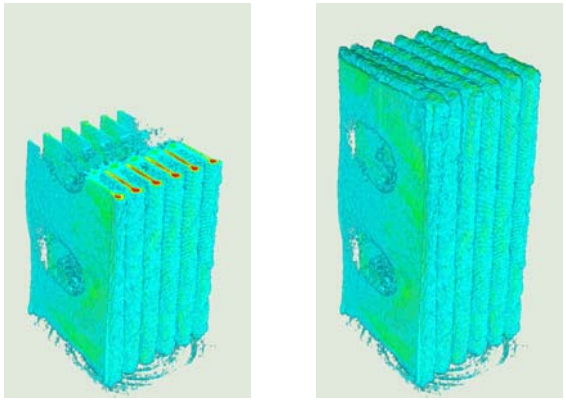

(a) z = 42.5mm (b) z = 60mm

Fig.3 Three dimensional frost density distributions.

REFERENCE:

[1] R. Matsumoto, et al., Proceedings of the International Heat Transfer Conference IHTC-15, IHTC15-9144, Kyoto, pp. 3603-3615.

PR2-7 Analysis of production technology of optics components using neutron radiography

Y. Yamagata[1], Y. Saito[3], T. Hosobata[1], S. Takeda[1], S. Morita[1,2], M. Hino[3] and D. Ito[3]

[1]*RIKEN Center for Advanced Photonics, RIKEN*
[2]*Tokyo Denki University*
[3]*Institute for Integrated Radiation and Nuclear Science, Kyoto University*

INTRODUCTION:

Precision optics are important key components used in imaging devices like digital cameras or smart phones, motor car components like HID head lamps, projection displays, advanced safety systems and medical devices like endoscopes, eye inspection instruments, which are one of the strongest technologies of Japanese industries. Those precision optics recently contains a few aspherical lenses, which cannot be manufactured in conventional grinding and polishing method. Those aspherical optics are mostly manufactured by plastic injection molding or glass press mold using precision dies. Especially glass materials have strong advantage over plastics in terms of optical performance. To make an aspherical glass lens, glass press mold (GM) process is necessary, which use high precision dies made of tungsten carbide to mold glass preforms at temperature of 300 to 1000 degC. Since this molding process is conducted inside the heavy metal die at very high temperature, no attempt has been successful to investigate the process in real-time, whereas optimization of glass press mold condition is done by a number of trial-and-error.

Another issue in aspherical lens production is that there remains some inhomogeneity inside molded lenses, which is not easy to measure. A trial has been made to measure the optical path difference where molded lens is dipped in a high-refractive index liquid, but the stability

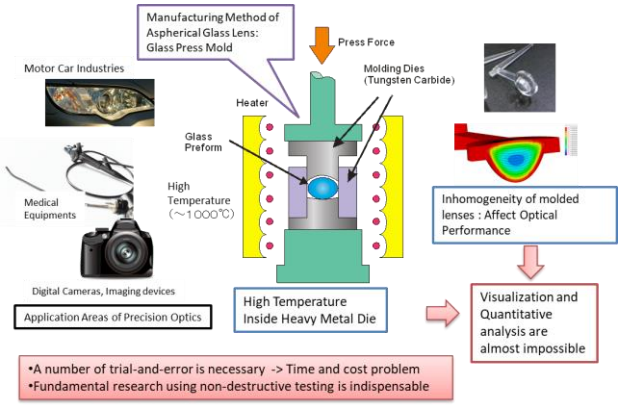

Fig. 1 Background of this Research

is not satisfactory. The final verification of such molded optics is conducted by assembly of all the prototype components, which is quite time-consuming.

Neutron Radiography can be one solution to analyze those issues, since the penetration depth of neutron beams in tungsten is rather good and most of glasses contain boron which is a good neutron absorber.

EXPERIMENTS: For FY2018, we have concentrated on developing a simulation code named V-Glace to understand the situation of glass press molding process. This code is based on V-Struct[1] system, which uses static explicit solver and hexahedral mesh system, which allow very large deformation without volume locking. The V-Glace code introduced a creep constitution to express glass molding process and thermal analysis. In addition, it has structure relaxation model to incorporate with glass relaxation mechanism.

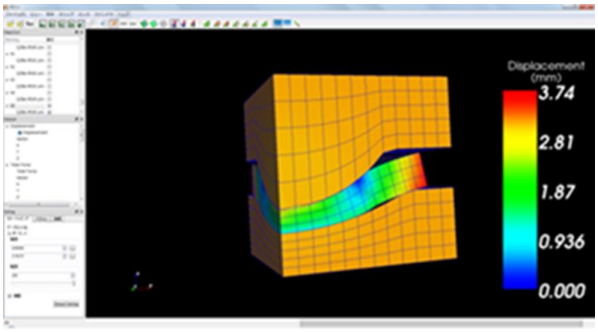

Fig.2 Screen of glass press mold simulation code.

Fig. 2 shows the screen of V-Glace software. It has pre-processor to generate hexahedral mesh from polynomial based aspherical lens profile and post processor to display stress, displacement with stress relaxation.

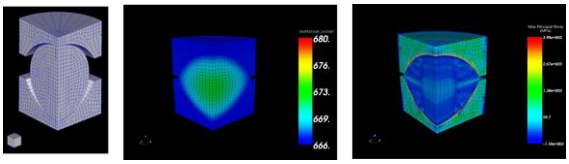

Fig.3 Glass molding simulation of ball-lens.

Fig.3 shows a simulation result of glass ball lens. Press molding process and stress relaxation (right) can be simulated[2].

RESULTS: Unfortunately, we were not able to perform neutron radiography for this year since preparation for molding process was not sufficient. We will try to do neutron radiography of glass molding process in the near future.

REFERENCES:

[1] Sun *et al.*, JSME Transactions A, **77** (773)(2011).
[2] Yamagata *et al.* JSPE Annual autumn meeting (2018).

PR2-8 Observation of Water Movement in Reciprocal Grafts of Tomato and Eggplant

U. Matsushima, R. Kobayashi, D. Ito[1], Y. Saito[1] and H. Shono

Faculty of Agriculture, Iwate University
[1] *Institute for Integrated Radiation and Nuclear Science, Kyoto University*

INTRODUCTION: Fruit sugar content of tomato plants grafted onto scarlet eggplants was higher than that of tomato plants grafted onto rootstocks of tomato [1]. These results suggest a way of obtaining high quality plant products, such as sweet tomato fruits, using this grafting technique. However, larger hydraulic resistance in *Solanum torvum* rootstocks than in tomato rootstock, has been shown to cause delayed graft-incompatibility [2]. We compared water movement at the graft union of tomato plants grafted onto tomato and eggplant, and eggplant plants grafted onto eggplant and tomato, to estimate the effect of graft-incompatibility.

MATERIALS and METHODS: Four types of grafted samples were prepared: tomato grafted onto eggplant rootstock (T/E) and tomato rootstock (T/T), and eggplant grafted onto tomato rootstock (E/T) and eggplant rootstock (E/E). Tomato (TO) and eggplant (EO) without grafts were prepared as control plants. Control samples were selected from seedlings that were sowed at the same time as seedlings for grafted plants. Fourteen days after grafting, we performed neutron imaging at the E2 hole of Kyoto University Research Reactor (KUR). Plant samples were fixed on a piece of thin aluminum board with aluminum tape. Thereafter, 10 mg of deuterium oxide (D_2O) was injected into the plant pot. Immediately after the injection, interval neutron imaging was initiated. Exposure and interval times were 300 s and 360 s, respectively.

RESULTS: The neutron cross section of D_2O is much lower than that of water. However, the chemical characteristics of D_2O are similar to those of water. Therefore, plants can uptake D_2O through the root system. The plant neutron image becomes bright as D_2O replaces water. The gray level of plant shoot images increased according to time after injection of D_2O. Figure 1 shows the changing ratio of the gray level (CRGL) from that of the initial value in the plant shoot images. Exceeding a CRGL value of 1 indicates that the gray level in the neutron image is increased. In Fig. 1, shoot length represents the length from the shoot part nearest to the root system, to the first true leaf. The CRGL of all samples was highest at the part near their root systems. The CRGL then decreased towards the upper part of the shoots. This indicates that water in the shoot vessel has been replaced by D_2O from the lower to upper part. Comparing the types of rootstock, the increase in CRGL was faster in the eggplant group than in the tomato group. In particular, the CRGL of T/E was the not only the highest among all the samples but also the fastest to pass over the value of 1.1. The dry weight of the T/E shoot was 79 mg/plant, which was the smallest of all shoots with an eggplant rootstock (EO had a dry weight of 113 mg/plant and E/E, 107 mg/plant). This fast D_2O uptake by T/E could not be explained according to shoot size. These results suggest that scion with eggplant rootstocks (T/E), require more water than other scion with eggplant rootstocks, EO and E/E.

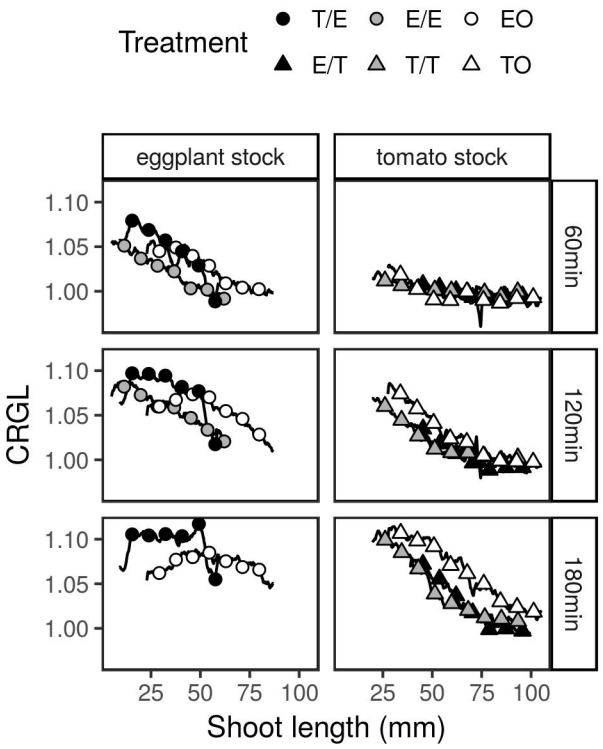

Fig. 1. Profiles of transmittance along plant shoots based on initial gray level. The transmittance is measured as the changing ratio of gray level (CRGL). The left-hand column of the graph shows plants with eggplant rootstock and the right-hand column shows plants with tomato rootstock. The rows of the graph indicate the time elapsed after applying D_2O.

REFERENCES:

[1] M. Oda *et al.*, J. Japan. Soc. Hort. Sci., **65(3)** (1996) 531-536.
[2] M. Oda *et al.*, J. Japan. Soc. Hort. Sci., **74(6)** (2005) 458-463.

PR2-9 Analysis of dehydration in high-strength concrete under high temperature using by neutron radiography

M. Kanematsu[1], Y. Nishio[1], A. Miyabe[1], K. Ueno[1],
T. Koyama[1], D. Ito[2], Y. Saito[2], T. Noguchi [3], M. Tamura[3]

[1]*Department of Architecture, Tokyo University of Science*
[2] *The Institute for Integrated radiation and nuclear science joint-use research, Kyoto University*
[3] *Department of Architecture, The University of Tokyo*

INTRODUCTION: Concrete is commonly known as a material excellent in fire resistance, if ensure a constant cover depth, reinforced concrete (RC) structure is recognized as fire-proof structure in Japan's Building Standard Law. However, chemical and mechanical property of concrete is changed due to influence of high temperature, and damage of concrete suffered from heat is remaining after cooled down. Moreover, when RC structure is subjected to high temperature, surface layer of concrete could be peeled explosively. This phenomena is known as so-called "spalling". JCI reported the evaluation methods for spalling of high-strength concrete [1], such as ring test [2]. On the other hand, some researchers have been attempting to evaluate concrete as composite material composed of aggregate and cement paste matrix, which is representative volume element of meso scale [3].

Therefore, in this study, the authors applied neutron radiography (NR), an imaging technique by using neutron beam, to high-strength concrete under high temperature, and tried to measure water content with high spatial resolution. Furthermore, it was also tried to reveal dehydration of high-strength concrete under high temperature experimentally from the viewpoint of meso scale.

EXPERIMENTS: Mix proportion of concrete was prepared with W / B of 18%. For coarse inclusion, two types were used. One was graywacke from Ome for greywacke concrete, and the other was limestone from Sano for limestone concrete. Specimens were casted in mold of 100 × 100 × 400 mm, demolded after 24 hours and then cured in water until age of 28 days. After that, they were cut into sliced plates with a thickness of 20 mm and holes were produced in the specimens to install thermocouples. Until an experiment initiation, specimens were stored under 20°C RH 60% environment.

Thermocouples were installed in the holes drilled at the position of 10, 20, 40, 60, and 80 mm from the heating surface, respectively. Propane gas burner, controlled by flow meter, was used to raise the surface temperature. The surface temperature became constant in seconds after start of heating and was about 1000 °C.

NR was performed at Thermal Neutron Radiography Facility (TNRF) in the B-4 port by using neutron beams at the time of output 1MW steady-state operation. To minimize influence of scattered neutron

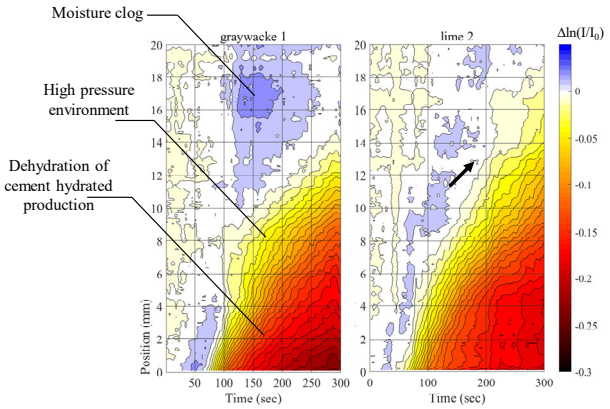

Fig.1 Legend and distribute of amount of substance per matrix unit

beams, distance between specimen and converter was set at 100 mm. Further, the angle of view of CCD camera was 100 × 100 mm, and the spatial resolution in this study was about 0.1 mm / pixel.

RESULTS: **Fig.1** shows contour plots which represent progressing and distribution of amount of substance per unit matrix. Dewater proceeding is indicated at black portion and increasing of water content is indicated at blue portion. With the specimen made of graywacke, **Fig.1** shows that regions of increased water content (moisture clog) are confirmed. Compared with the specimen made of limestone, moisture clog is larger. Therefore, it is considered that specimen made of limestone dissipate moisture easier than specimen made of graywacke from the weight reduction by heated. In addition, using the values obtained from relationship between temperature and decreased amount of substance per unit matrix, color map of contour plots was adjusted to indicate to evaporation of water in high pressure environment at yellow portion and to indicate to cement hydrate dehydrating at red portion. **Fig.1** shows that existence region of the high pressure environment had been moved to deep in specimen with the passage of time. Moreover, the existence region of the high pressure environment has been formed below the moisture clog.

REFERENCES:

[1] JCI, (2017). "Committee Reports:JCI-TC-154A Physical and Mechanical Properties of Concrete at High Temperature, Japan concrete Institut"
[2] M. Ozawa etc., (2014) "Numerical analysis of spalling of HSC restrained with steel rings at high temperatures, Proc. of Annu. Conv. of JCI, vol.36, No.1
[3] Jie Zhao, Klass van Breugel, (2014)." A meso-level investigation into the explosive spalling mechanism of high-performance concrete under fire exposure.", Cement and Concrete Research, vol.65, pp.64-75

PR2-10 Effect of gravity on coolant distribution in flat laminate vapor chamber

K. Mizuta, Y. Saito [1] and D. Ito [1]

Faculty of Engineering, Kagoshima University
[1] KURNS, Kyoto University

INTRODUCTION: Recently, rapid increase in heat dissipation from electric devices leads to various reliability problems and low working efficiency, then effective heat exhausting techniques are desired than ever. The author have developed flat laminate vapor chamber called FGHP (Fine Grid Heat Pipe), which consists of upper and bottom plates, and of some middle plates. All the plates are made of copper, and the coolant used was water. As for thermal performance, FGHP had the lowest thermal resistance among various vapor chambers when the effect of heat receiving area is concerned [1], and the lateral thermal conductivity exceeded 10,000 W m^{-1} K^{-1} when the temperature of heat receiving area exceeded about 360 K [2]. Moreover, the liquid thickness in the wick area scarcely changed with heat input even when the surface of FGHP was set parallel to the gravity direction [3]. In our previous study [3], however, the heat input was below about 15 W, which were smaller than that in the practical use.

In this study, we investigated the gravitational effects on the coolant distribution in the FGHP by using neutron radiography at the Kyoto University Research Reactor (KUR) when the heat input is larger than that in our previous work [3].

EXPERIMENTS: Experiment was conducted at the E-2 port of the KUR, where the thermal neutron flux at the sample position was about 3×10^5 cm^2s at 5 MW operation. The size of the test sample of FGHP heat spreader was 65 mm square and 2 mm thick. The test sample was set vertically, which means that its bottom and top plate was placed parallel to the gravitational direction. A ceramic heater of $25\times25\times1.75$ mm^3 was attached to the central part of the bottom plate as a heat source, and the top plate was cooled by plate fin type heat sink under forced convection conditions. K-type thermocouples were utilized to measure both the surface temperature of the heat spreader and the atmospheric temperature to estimate the thermal resistance of the FGHP. A CCD camera (BU-53LN, BITRAN Co. Ltd.) was utilized, which has 4008×2672 pixels and ^{6}LiFZnS (50 μm thickness) was used as a scintillator screen. The spatial resolution was 9.0 μm/pixel at the present system setup, however, the effective spatial resolution was about 50 μm/pixel due to the scintillator screen characteristics. Neutron imaging of the sample was performed at the 1 MW operation mode of the KUR and the exposure time was 300 s. Neutron images of the sample were utilized to calculate liquid thickness in the FGHP. The effect of gravity on the coolant distribution was evaluated by the calculated liquid thickness in the wick area at different positions as follows:

1. Vertical position 1 (Top),
2. Vertical position 2 (Bottom),
3. Horizontal position 1 (Left),
4. Horizontal position 2 (Right).

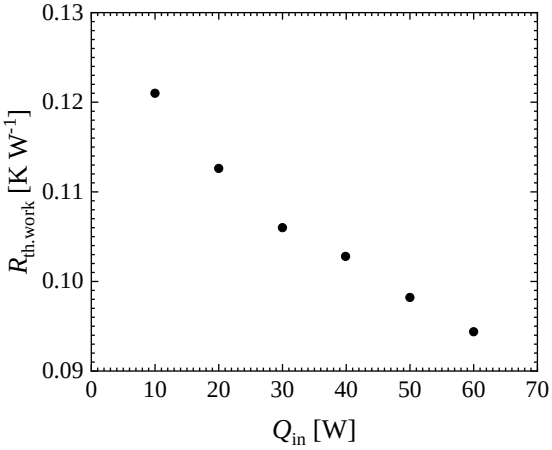

Fig. 1 Variation of the thermal resistance of the test sample with heat input.

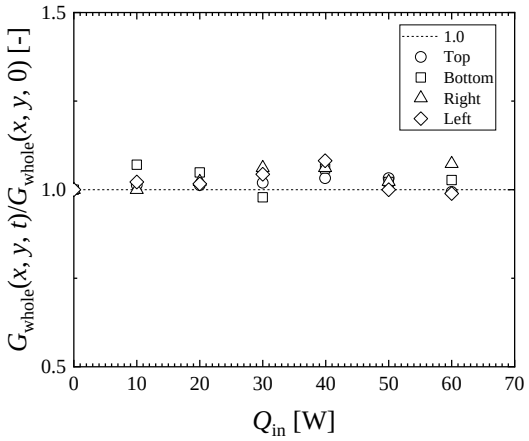

Fig. 2 Variation of the averaged gray level with heat input.

Interrogation window size was 0.4×1.5 mm^2 at each position.

RESULTS: Figure 1 shows the variation of thermal resistance of the test sample with heat input. As shown in Fig. 1, thermal resistance of the test sample decreases with increasing heat input as reported in the previous work [1], which shows that this test sample worked properly under the current experimental conditions. Figure 2 shows the variation of the averaged gray level in the respective interrogation area with the heat input. As shown in Fig. 2, the values of averaged gray level are nearly constant regardless of heat input, which suggests that the thickness of liquid film in the wick area was scarcely affected by the heat input under the current experimental conditions.

REFERENCES:

[1] K. Mizuta *et al.*, App. Therm. Eng., **104** (2016) 461-582.
[2] K. Mizuta *et al.*, App. Therm. Eng., **146** (2019) 843-853.
[3] K. Mizuta *et al.*, Phys. Proc., **69** (2015) 556-563.

30P2-11

PR2-11 Study on the Visualization of Organic Matter between Metals in oder to Contribute to the Advancement of the Industrial Products

K. Hirota, H. M. Shimizu[1], M. Kitaguchi[1], Y. Tsuchikawa[1], S. Imajo[1], S. Awano[1], N. Yamamoto[1], A. Uritani[2], K. Watanabe[2], S. Yoshihashi[2], A. Yamazaki[2] and Y. Saitoh[3]

RCNP, Osaka University
[1]Graduate School of Science, Nagoya University
[2]Graduate School of Engineering, Nagoya University
[3]Institute for Integrated Radiation and Nuclear Science, Kyoto University

INTRODUCTION: Mechanical and industrial products such as automobiles and aircraft are progressing with higher performance and higher accuracy in Japan. One of the demands at the development site of these state-of-the-art products is visualization of the state of organic materials (oil film, grease, electrolyte, etc.) existing between metals, which can not be seen directly by our eyes. In this research, we will explore the possibility of observing the dynamic state of the organic materials (shape, properties, thickness distribution) and its dynamic change mainly between automobile parts as an example.

At present Nagoya University is constructing an accelerator-driven small neutron source (NUANS) and neutron radiography ports [1,2]. We are planning an in-site measurement of fuel cell during the power generation. And we are also proceeding with the quantitative evaluation of the CCD output image. This year, we produced a neutron camera for radiography to be used at NUANS, so we evaluated its performance in KUR E2 port.

EXPERIMENTS: In the fuel cell development, the elimination of water from the electrode during the power generation is very important issue. It was evaluated whether water droplets generated during fuel cell power generation could be identified or not, using fuel cell electrodes by neutron radiography measurement. Since the fuel cell uses a combustible gas, it is impossible at KUR to make measurement while actually generating electricity. So we put water directly into the fuel cell electrodes, and measured the transmission image at E2 port, not using the combustible gas. At the result, we cans see the clear image with 60s neutron irradiation.

In addition, a space of about 1 mm^3 was made on an aluminum plate, water droplets were placed, and measurements were made for a short time, to evaluate how much visual time would be visible in what measurement time. At the result, we can see the water drop is clearly seen with the 1s irradiation time. Next we tried to move the water position quickly, and we also could see the water position.

CFRP(carbon fiber reinforced plastic) is considered to be a effective material for near-future industrial use as a lightweight and durable material. Although it is a strong CFRP, fatigue failure can occur, so when we use it to aircraft we have to evaluate and identify the precursor crack. CFRP is usually covered with aluminum on the surface, X-ray transmission measurement is difficult to see. Neutron transmission imaging is good candidate to check the cracks of CFRP.

Since the CFRP contain a large amount of hydrogen, it is also difficult to measure even in the neutron radiography. And because it has a layered structure, it is desirable to identify the position of the crack in the depth direction by performing CT measurement. In this measurement, we try to get the transmission image and CT measurement of a joined body of CFRP and aluminum alloy, which are 3cm width and 5mm thickness, respectively. In the first trial, we can get the 3D image of CFRP and aluminum joint material, and the crack image is not so clear. We will get the better image to scrutinize the measurement conditions.

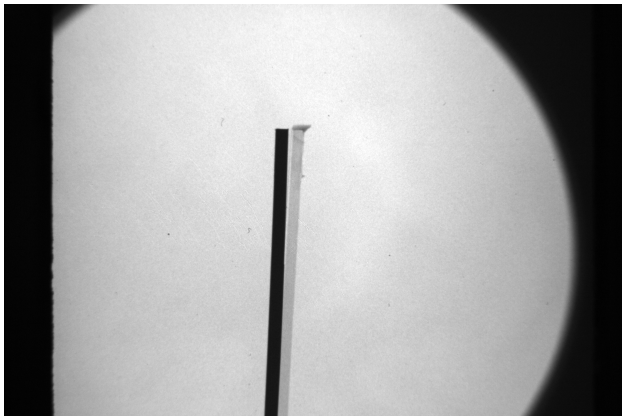

Fig. 1. Measurement of the peeling of CFRP and aluminum alloy.

REFERENCES:

[1] K. Hirota, PoS., (KMI2017) 025.
[2] I. Ito, PoS., (KMI2017) 068.

PR2-12 Development of canalicular-structure-based neutron optical devices

T. Sakai[1], H. Iikura[1], D. Ito[2] and Y. Saito[1, 2]

[1]*Materials Sciences Research Center, Japan Atomic Energy Agency*

[2]*Institute for Integrated Radiation and Nuclear Science, Kyoto University*

INTRODUCTION: In this work, we are developing two neutron devices, namely micro-structured fluorescent plates and Soller slits. The former device consists of capillary plates and fine phosphor grains [1, 2]. The capillary plates are commercially available glass plates on which tiny capillaries are arrayed in two-dimensions periodically [3]. The latter is based on commercial canalicular-structured ceramic devices. Herein, we introduce the development of the Soller slits for neutron optical device.

EXPERIMENTS: The ceramic device is named HONEYCERAM ™ and manufactured by NGK INSULATORS, LTD. [4]. The original ceramic and sliced ones are shown in Fig. 1 (a). The magnified image of the entrance of the ceramic canals is indicated in Fig. 1 (b). The canal size is approximately 0.7 mm x 0.7 mm, and the wall is mere 0.05 mm thick. The outside diameter is 106 mm, and L/D ratios are 11, 30, 163 for 8 mm-length, 21 mm-length, 114 mm-length, respectively. The ceramics are impregnated with gadolinium acetate solution to add neutron absorption capacity. The first test of fabricated Soller slits was performed at KUR E-2. The photograph of the experimental setup and the neutron radiograph were shown in Fig. 2.

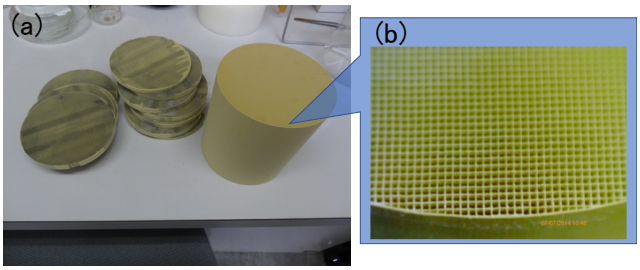

Fig. 1 Photographs of HONEYCERAM ™ and sliced ones (a), and magnified image (b).

RESULTS: The radiograph in Fig. 2 (b) indicated that the ceramic worked well as Soller slits. The neutron absorption in the wall is fairly uniform, though some canals are clogged with shavings. The dependence of neutron transmittance on the slits length is not evaluated yet.

The fabricated Soller slits are expected to be useful to improve the neutron beam parallelism, namely L/D ratio. Impregnation with gadolinium acetate solution is effective to add neutron absorption capacity to the ceramic wall. The fabrication method is simple, and the materials are relatively cheap (~10,000 yen).

The next step of the work is characterization the slits performance and application to the imaging experiments.

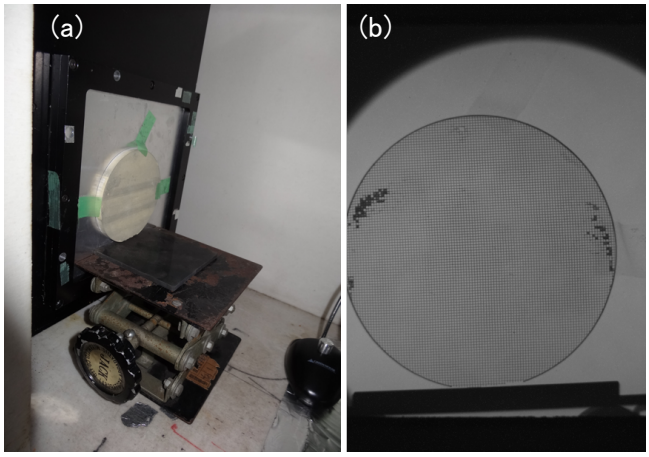

Fig. 2 Photograph of experimental setup at KUR E-2 (a) and the neutron radiograph of the fabricated Soller slits (b), respectively.

REFERENCES:

[1] T. Sakai *et al.*, JPS Conf. Proc. 11, 020005 (2016) .

[2] T. Sakai *et al.,* KURRI PROGRESS REPORT 2017, 29P7-14 (2018) .

[3] HAMAMATSU PHOTONICS K. K. website: <http://www.hamamatsu.com/jp/en/product/category/3200/3032/index.html>

[4] NGK INSULATORS, LTD. website: <https://www.ngk-insulators.com/en/product/automobile/>

I-1. PROJECT RESEARCHES

Project 3

PR3 Project Research on Nuclear Spectroscopy and Condensed Matter Physics Using Short-Lived Nuclei

Y. Ohkubo

Institute for Integrated Radiation and Nuclear Science, Kyoto University

Objective and Participating Research Subjects

The main objectives of this project research are the investigation of the nuclear structure of unstable neutron-rich nuclei and also the local properties of materials using short-lived nuclei.

This period is the second year of the project.

The research subjects reported here are as follows:

30P3-1 Technique of transferring radioactive atomic nuclei implanted in dry ice film
30P3-2 Search for isomer of fission product ^{144}La through the β^-–decay of ^{144}Ba by means of internal conversion electron measurements
30P3-3 Compton scattering asymmetry observed for γ rays from ^{146}La
30P3-5 Direct measurement of the internal pressure in ultrafine bubbles by angular correlation technique
30P3-6 Dynamic behavior of impurity indium ions in magnetite
30P3-7 Observation of local fields at the ^{111}Cd(←^{111m}Cd) sites in $CdTi_{0.95}Co_{0.05}O_3$

Main Points Described in the Reports in the Following Six pages

As a means to measure the charge distribution of an unstable nucleus, it is promising to make a muonic atom composed of the nucleus that are trapped in deuterium film and then to measure the energies of X-ray emitted from the muonic atom. However, it is unavoidable to deal with high radioactivity. One of the technical problems is how efficiently and safely long-lived radioactivity in the apparatus is removed after such an experiment is done. A. Taniguchi *et al*. (30P3-1) attacked this problem using a $^{146}LaO^+$ radioactive ion beam (two ^{146}La states with a half-life of 10 s and 6 s) available at KUR-ISOL and an apparatus designed for the present work. The removal efficiency was at most 30% and how to improve is now under consideration.

At KUR-ISOL, M. Shibata *et al*. (30P3-2) detected γ-rays and internal conversion electrons emitted in the β^- decay of ^{144}Ba (half-life of 11.5 s) using a 31% HPGe detector and a cooled Si(Li) detector, respectively, in order to search for an unknown isomer state in an odd-odd nucleus ^{144}La (a daughter of ^{144}Ba), which is in turn expected to be able to solve the so-called Q_β puzzle. They proceeded with analysis of data previously obtained and newly obtained. At present they could not observe their expected isomer, while they could determine several internal conversion coefficients and detected new γ-rays.

Y. Kojima *et al*. (30P3-3) have been trying to measure the linear polarization of γ-rays from short-lived β decaying nuclei using a clover detector as a Compton polarimeter and additional coaxial Ge detectors in order to obtain the multipolarities of those γ-rays. In AY 2017, they could not obtain clear Compton scattering asymmetry for the 258- and 410-keV γ rays from ^{146}La (half-life of 6.3 s) produced at KUR-ISOL. This was due to large chance coincidences with intense background radiations, in particular, γ rays from the beam collection port. In AY2018, they reduced background radiations by shielding the clover detector and could successfully obtain values of the polarization sensitivity for both the 258- and 410-keV γ rays from ^{146}La, consistent with those measured off-line for other long-lived nuclei, although the obtained values have large uncertainties.

Ultrafine bubbles, attracting a lot of attention in various industrial fields, are of the diameter less than one micro meter. Despite the Young-Laplace equation predicting a high internal pressure for such a small bubble in water so that it should survive only very short time, it is reported to live more than a month. Employing time-integral perturbed angular correlation (TIPAC) technique for ^{125}I(←^{125}Xe), M. Tanigaki *et al*. (30P3-5) successfully obtained the internal pressure of ultrafine bubbles of the average diameter about 200 nm containing Xe gas inside, the value of which is much smaller than that the Young-Laplace equation predicts.

More than three decades ago, magnetic hyperfine field at ^{111}Cd(←^{111}In) chemically doped in Fe_3O_4 was measured with time-differential perturbed angular correlation (TDPAC) technique to study the supertransferred magnetic field from the magnetic (Fe) ions via the oxygen ions to the nonmagnetic (Cd) ions. The location of In was assigned to the tetrahedral (*A*) site. However, recently, a paper was published stating that the location of In was the octahedral (*B*) site. W. Sato *et al.* succeeded in obtaining TDPAC spectra with damping free for the first time, concluded that the location of In is the *A* site, and moreover obtained a signal indicating that at high temperatures some In ions in the *A* sites move to the *B* sites, which is consistent with a density functional theory calculation. In order to observe this In motion at high temperatures, W. Sato *et al.* (30P3-6) synthesized 0.5 at.% In-doped Fe_3O_4 and took a ^{111}Cd(←^{111m}Cd) TDPAC spectrum for this oxide at 900 K (above the Curie temperature of 858 K). As anticipated, they could observe ^{111}Cd nuclear spin relaxation that was considered to be caused by thermally activated In motion.

In some cases, perovskites oxides ABO_3 induce ferroelectricity or assume better ferroelectricity when they are doped with a small amount of metal ions different from the constituent metals. Distortion of the crystal structure by doping can cause these changes. S. Komatsuda *et al.* (30P3-7) synthesized $CdTiO_3$ and $CdTi_{0.95}Co_{0.05}O_3$ and searched any structural difference between the two oxides by applying the room-temperature TDPAC method with ^{111}Cd(←^{111m}Cd) as local probes. They found no noticeable difference in the TDPAC spectra.

PR3-1 Technique of Transferring Radioactive Atomic Nuclei Implanted in Dry Ice Film

A. Taniguchi, P. Strasser[1], M. Tanigaki and Y. Ohkubo

Institute for Integrated Radiation and Nuclear Science, Kyoto University
[1]Muon Science Laboratory, IMSS, KEK

INTRODUCTION: The nuclear charge radius is one of the fundamental parameters that gives information about the effective interactions on nuclear structure, which has been investigated by electron scattering, measurements of muonic atom X-ray energies and optical isotope shifts. Recently the study for unstable nuclei has been advanced by optical isotope shifts, while the study using other methods is little progress mainly because a large amount of radioactivity is needed [1]. The results obtained from these three methods provide complementary information each other. Therefore, R&D for more efficient systems of electron scattering and muonic X-ray measurements is being promoted.

Measurement of the emitted X-ray energy from muonic atoms is a powerful method for the investigation. The muon and the electron have similar properties except for their mass difference, thus a negative muon (μ^-) can be captured in a Bohr orbit of a nucleus just as an electron and then a muonic atom is formed. Because the mass of a muon is 207 times the electron mass, its lower orbits are close to the nucleus and the energies of the states depend sensitively on the nuclear charge distribution. By means of the muonic X-ray spectroscopy, therefore, information on the nuclear charge distribution can be obtained. Recently, a new method using solid hydrogen film has been developed to produce muonic atoms. In this method, negative muons are injected to solid deuterium (D) film in which nuclei of interest (A) are implanted beforehand, thereby muonic atoms being formed through the highly-efficient muon transfer reaction: $\mu^-D + A \rightarrow D + \mu^-A$. The feasibility of this method was demonstrated and promising results were obtained [2]. However, several problems have to be solved before this method is applied to experiments for unstable nuclei. In this study, one such problem, concerned with handling of residual radioactivities in deuterium film after experiments, in particular their highly efficient recovery, was approached experimentally using a radioactive-isotope beam from KUR-ISOL and dry ice film instead of solid hydrogen film.

EXPERIMENTS: An apparatus capable of implanting radioactivities to dry ice film was installed at the beam line of KUR-ISOL [3]. This apparatus has two copper blocks and one CO_2 gas diffuser in the vacuum chamber. Each copper block can be cooled with LN_2 flow internally and movable independently in a horizontal direction between the center of the chamber which is on the axis of the RI beam and the γ-ray measurement port while keeping LN_2 flow. Dry ice film was formed on the surface of one cooled block (catcher) by sprayed CO_2 gas through the diffuser. In the present work, about 10^6 ions of $^{146}LaO^+$ ($T_{1/2}$ = 10 s and 6 s) were implanted into dry ice film on the catcher in every run. After the implantation, the other pre-cooled block (trap) was moved to the frontal vicinity of the catcher, and then the catcher was warmed by stopping LN_2 flow. With this procedure, the atoms of ^{146}Ce ($T_{1/2}$ = 14 m, daughter of ^{146}La) and ^{146}Pr ($T_{1/2}$ = 24 m, daughter of ^{146}Ce) ware released from the catcher and were re-trapped on the trap together with CO_2. The trapped efficiency was measured by detecting the γ-rays emitted from each of the blocks.

RESULTS AND DISCUSSION: In this work, the trapped efficiencies were measured by changing the formation condition of dry ice film on the catcher. Specifically, a single layer film or a multilayer film was formed while changing the spraying speed and total amount of carbon dioxide gas. However, since it takes a long time for one run, the experiments under so many conditions were not performed. Incidentally, a multilayer film was made by alternately repeating formation of dry ice film and ion implantation.

While the detail data analysis also is in progress, the trapped efficiencies remained at most 30% in any run. (For now, the efficiency is defined as the ratio of the radioactivities on the trap to those remaining on the catcher, and the contribution of the radioactivities escaped somewhere other than the trap is not taken into account.) From a practical point of view, these efficiencies are not so high, but the most notable point is that radioactivities remained on the catcher in all runs.

The range in dry ice of $^{146}La^+$ whose acceleration energy is 27 keV is about 27 nm according to SRIM code, on the other hand, a visually recognizable dry ice film was formed on the catcher in any run. That is, the thickness of the dry ice film is considered to be sufficient to stop ^{146}La ions within the film. The cause for the remaining radioactivities on the catcher is not clear. So far, the possible reasons are (1) formation of a non-ideal dry ice film, or (2) chemical interaction between the implanted atoms and the catcher surface material in the process of sublimation of dry ice, etc. If there is a cause in (2), it means that an important issue has been found for applying the solid hydrogen method to experiments on unstable nuclei.

ACKNOWLEDGMENTS: This research was partially supported by the Ministry of Education, Science, Sports and Culture, Grant-in-Aid for Scientific Research (C) (24540303, Akihiro Taniguchi, and 15K05103, Akihiro Taniguchi).

REFERENCES:

[1] I. Angeli and K.P. Marinova, At. Data Nucl. Data Tables **99** (2013) 69-95.
[2] P. Strasser *et al.*, Hyperfine Interact. **193** (2009) 121-127.
[3] A. Taniguchi *et al.*, KURRI Prog. Rep. 2013, p98.

PR3-2 Search for Isomer of Fission Product ^{144}La through the β⁻-decay of ^{144}Ba by means of Internal Conversion Electron Measurements

M. Shibata, S. Ohno[1], H.Sawai[1], Y. Ishikawa[2], M. Kanaji[2], Y. Kojima and A. Taniguchi[3]

Radioisotope Research Center, Nagoya University
[1]Graduate School of Engineering, Nagoya University
[2]School of Engineering, Nagoya University
[3]Institute for Integrated Radiation and Nuclear Science, Kyoto University

INTRODUCTION: Determination of precise decay scheme of fission products of ^{235}U are very important for both nuclear engineering and nuclear physics. Information of nuclear structure are also useful to study nucleosynthesis. Especially, relatively long-lived isomeric states are important to evaluate the r- or s-process of neutron capture in nucleosynthesis. In the last year, we focused on to search for unobserved isomeric states of some elements which are expected from the systematics for doubly-odd nuclei around mass number 150 with an energy-sum γ-ray spectrometry using a clover detector. [1] In this year, to solve the "Q_β-puzzle" in doubly-odd ^{144}La [2], internal conversion electron (ICE) measurements with a cooled Si(Li) detector were carried out to search for isomeric transitions and to determine of their multipolarities, and also data analyses of γ singles, γ–γ and x-γ coincidences were proceeded.

EXPERIMENTS: The experiments were carried out using the on-line mass separator KUR-ISOL at the Kyoto University Reactor. 93%-enriched $^{235}UF_4$ target of 72 mg were inserted in a through-hole facility and the nuclei of interests were produced with the thermal neutron-induced fission of ^{235}U. The fission products were transported by a He-N_2 gas jet system and were ionized by a thermal-ionization type ion source. The mass-separated radioactive beam was implanted in an aluminized Mylar tape set in the computer controlled tape transport system. The tape was moved with a predetermined period to reduce the background from their daughter nuclei. At the measuring position, the γ rays and ICEs were measured, simultaneously, with a 31% HPGe detector (ORTEC GMX, 57 mm⌀ × 68 mm*L*, energy resolution 2.4 keV at 1408 keV) and a cooled Si(Li) detector (Eurisys, 500 mm^2 × 6 mm*L*), respectively. The detectors were set at 180° direction and the source to detector distances were set at 15 mm and 13 mm for the Ge and the Si(Li) detector, respectively. The detailed setup of the detector were described elsewhere [3]. The data were taken with the list mode including the time information using a VME based data acquisition system (A3100 by IWATSU). The collection-measurement cycle was set at 22 s - 22 s for ^{144}Ba ($T_{1/2}$ = 11.5 s), and was repeated for 10 hours. The detectors were shielded with 10 cm-thick lead blocks and borated polyethylene ones outside them in order to reduce the background neutrons and γ radiations. For the efficiency calibration in the geometrical condition as well as the energy calibration, the daughter nucleus of ^{144}La and ^{146}La were measured for 8 hours, respectively, since these nuclei contain well-evaluated pure E2 transitions.

RESULTS: The measured singles ICE spectrum in the decay of ^{144}Ba was shown in Fig. 1. The ICE peaks were observed up to the 260 keV transition. The internal conversion coefficients (ICCs) were determined with the ratio of the measured counts of ICEs to the corresponding γ-rays by normalized by the pure E2 transitions as described above. The ICC of the 260 keV transitions were determined and only the upper limit values of the 418, 422, 431, 516, 571 and 584 keV transitions were determined owing to low statistics. On the other hand, the ICCs of the 43, 69, 82, 104, 115, 153 keV transitions were determined from the x-γ coincidence method. Preliminarily, adding the result of γ-γ coincidence relations, 115 γ-rays including the newly observed 28 ones and the multipolarities of 13 transitions and 28 excited levels were incorporated in the decay scheme. These results were mostly in agreement with the previous results [4]. Nevertheless, isomeric transitions to give the answer of "Q_β-puzzle" were not observed in this experiment.

CONCLUSIONS: The measurements of internal conversion electrons and the analyses of γ-rays of doubly-odd fission product ^{144}La were carried out through the β-decay of ^{144}Ba. The expected long-lived isomer and γ transition having higher multipolarity could not be observed, consequently, the Q_β-puzzle in ^{144}La could not be solved. The construction of detailed decay scheme is in progress.

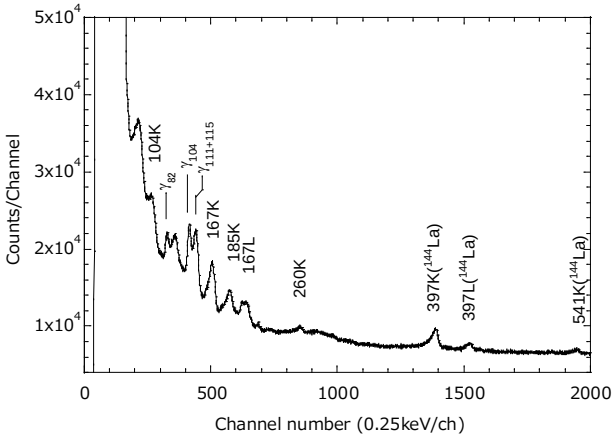

Fig. 1. Singles spectrum of internal conversion electrons in the decay of ^{144}Ba measured with a cooled Si(Li) detector. The electron peaks for daughter nucleus ^{144}La, which were used for the calibration of the detector, are also observed.

REFERENCES:

[1] Y. Shima *et al*., Nucl. Data Sheets, **120** (2014) 30-32.
[2] M. Shibata *et al*., J. Phys. Soc. Jpn., **71** (2002) 1401-1402.
[3] M. Shibata *et al*., Eur. Phys. J., A **31** (2007) 171-176.
[4] C. Chung *et al*., Phys. Rev. C, **26** (1982) 1198-1214.

PR3-3 Compton Scattering Asymmetry Observed for γ Rays from ^{146}La

Y. Kojima, S. Ohno[1], H. Sawai[1], Y. Ishikawa[2], A. Taniguchi[3] and M. Shibata

Radioisotope Research Center, Nagoya University
[1]Graduate School of Engineering, Nagoya University
[2]School of Engineering, Nagoya University
[3] Institute for Integrated Radiation and Nuclear Science, Kyoto University

INTRODUCTION: Gamma-ray multipolarities are one of the most important data for nuclei because they relates to γ-ray emission process. The linear polarization is useful in determining the γ-ray multipolarities, and is usually measured using a Compton polarimeter consisting of two or more γ-ray detectors. Our group is trying to apply a clover Ge detector [1] to the linear polarization measurements for short-lived β-decaying nuclei. In this technique, a Compton scattering asymmetry *A* in orthogonal directions is determined by means of coincidence measurements. After correcting the *A*-value using the polarimeter sensitivity *Q*, the value of *A*/*Q* is compared with the degree of polarization *P* which has been calculated for various multipolarities.

In AY2017, we tried linear polarization measurements for nuclides produced by on-line isotope separator KUR-ISOL [2]. However, we could not clearly observe the Compton scattering asymmetry [3]. As a result of detailed analysis, we found that the main reason was due to chance coincidences with intense background radiations.

In this report, we present the preliminary results of improved experiments in AY2018.

EXPERIMENTS: The detection system consisted of the clover detector as a polarimeter, a coaxial 60% (relative efficiency) HPGe detector as a directional detector, and a coaxial 38% HPGe detector to deduce correction factors of detection efficiencies. The clover detector contains four large Ge crystals packed closely. The size of each crystal is 80 mm in diameter and 90 mm in length. The directional detector was placed perpendicular to the clover detector, and was used to define a *reference plane*. A detector-to-source distance was 10 cm for all detectors. The preamplifier signals from the detectors were processed by a VME-based data acquisition system, and data on the pulse height and the detection time were recorded in event-by-event mode.

Gamma rays from ^{146}La (half-life of 6.3 s) were measured at KUR-ISOL. The ^{146}La nuclei were produced by the thermal-neutron-induced fission of ^{235}U. The fission products were thermalized in the target chamber, and transported to a surface ionization-type ion source using gas jet stream. After ionization, the nuclei were extracted, accelerated to 30 keV, and mass-separated. The mass-separated beams were implanted into an aluminized Mylar tape in a tape transport system. The source was periodically moved to a detector port with time intervals of 13 s. The measuring time was 13 h.

To reduce background radiations, in particular, γ rays from the beam collection port, heavy shield was placed around the clover detector. The shield was extremely effective. Counts due to the background γ rays were reduced to about 1/100 compared with those in experiments in AY2017.

RESULTS: The list data were analyzed using an off-line sorting program. In this analysis, we focused on E2-E2 γ cascade (258-410 keV γ cascade) in the β decay of ^{146}La. Signals recorded within 570 ns were taken as coincident events.

From coincidence spectra gating on the 258-keV γ ray, we found that the Compton scattering perpendicular to the reference plane occurs 6% more often than that parallel to the reference plane for the 410-keV γ ray. After correcting detection efficiencies, the asymmetry value *A* was found to be 0.055(27). Asymmetry was also observed for 258-keV γ ray. The sensitivity $Q = A/P$ was deduced for each γ ray, and compared with values obtained using standard radioactive sources of ^{60}Co, ^{134}Cs and ^{152}Eu. As shown in Fig. 1, the sensitivities obtained in the on-line measurement agree with the values obtained in the off-line measurement, while the statistical uncertainties for ^{146}La are somewhat large.

CONCLUSION: We succeeded in observation of asymmetry of Compton scattering events in the on-line measurements. We plan to measure γ rays from nuclei produced by KUR-ISOL to deduce unknown multipolarities.

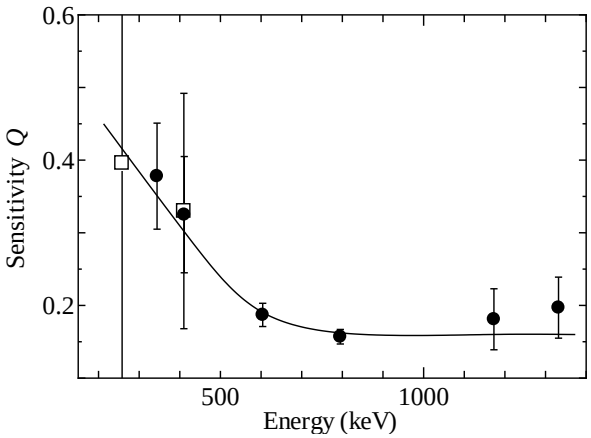

Fig. 1. The polarization sensitivity as a function of incident γ-ray energy. Open and filled marks show data obtained at KUR-ISOL and off-line measurements, respectively. The curve is only a guide to the eye.

REFERENCES:

[1] Y. Shima *et al.*, Appl. Radiat. Isot. **91** (2014) 97-103.
[2] A. Taniguchi *et al.*, Nucl. Instr. and Meth. A, **351** (1994)378-382.
[3] S. Ohno *et al.*, KURRI Prog. Rep. 2017. p.44.

PR3-4 **Direct Measurement of the Internal Pressure in Ultrafine Bubbles by Angular Correlation Technique**

M. Tanigaki, T. Yamakura[1], Y. Ueda[2], A. Taniguchi, Y. Tokuda[3], and Y. Ohkubo

Institute for Integrated Radiation and Nuclear Science, Kyoto University
[1]Graduate School of Science, Kyoto University
Department of Physics, Niigata University
[2]Research Institute for Sustainable Humanosphere, Kyoto University
[3]Faculty of Education, Shiga University

INTRODUCTION: Ultrafine bubbles, the gaseous cavities with diameters less than one micro meter [1], recently attract a lot of attentions because of their multifunctionalities. While applications of ultrafine bubble are extended in wide variety of fields, fundamental studies on ultrafine bubble itself are not well extended because of its small size, smaller than the wave length of radiant ray. Some are even suspicious of the existence of ultrafine bubble itself.
In nuclear physics, the angular correlations measurements of iodine isotopes in Xe gas were reportedly difficult [2][3] because of their large dependences on the pressure of Xe gas [4][5][6]. This means that the gas pressure in a ultrafine bubbles of Xe can be directly measured by a technique of nuclear physics, i.e., the angular correlation measurement of radioactive iodines inside ultrafine bubbles, .
In this paper, the measurement of the internal pres- sure in Xe ultrafine bubble through the angular correla- tion measurement of 55 - 188 keV γ-γ cascade in ^{125}I is described.

EXPERIMENTS: The water containing ultrafine bubbles of natural Xe gas with the average diameter of 200 nm in pure water was generated via the pressurized dissolution method. 4 cm^3 of ultrafine bubble water and saturated solution of natural Xe were separately packed to 4.5 cm^3 polypropylene (PP) cylinders for the irradiation at the reactor and were irradiated by thermal neutrons with the total dose of 6.9×10^{16} n/cm^2 at the slant exposure tube of Kyoto University Research Reactor (KUR) to activate ^{125}Xe ($T_{1/2}$ = 16.9 h) through the thermal neutron capture reaction of ^{124}Xe(n,γ)^{125}Xe. The γ-γ cascades were detected by a conventional fast-slow coincidence method with a 1 cm^3 CdZnTe detector (KROMEK GR1-A) and one of two 1.5-inch ϕ × 1-inch thick BaF_2 detectors. Two BaF_2 detectors are placed at the fixed angle of 90°, and a CdZnTe detector on a turntable moves around the PP cylinder containing the irradiated sample. With this configuration, the angular correlations of both 90° - θ and 180° + θ are measured at a time. The correlation function of γ-γ cascade under the existence of hyperfine interactions is given as,

$$W(\theta) = 1 + A_{22}\overline{G_{22}(\infty)}P_2(\cos\theta),$$

where A_{22}, $\overline{G_{22}(\infty)}$ are asymmetry parameter and the attenuation factor caused by the hyperfine interaction, respectively. $A_{22}\overline{G_{22}(\infty)}$ for 55-188 keV cascade in ^{125}I was determined to be +0.097 ± 0.037 from the obtained angular correlation (Fig. 1), by taking into account the corrections of detector solid angles, size of source and the contribution of ^{125}I existing as the solute in the water.

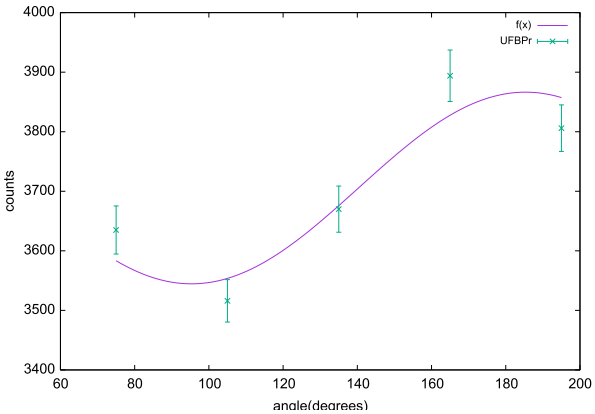

Fig. 1 Angular correlation of 188 - 55 keV γ-ray cascade of 188 keV state in ^{125}I in ultrafine bubble water.

RESULTS: The pressure dependence of $A_{22}\overline{G_{22}(\infty)}$ for the 203 keV state in ^{127}I in Xe gas was well studied by Berek [5], and the result of ^{127}I can be converted to that of ^{125}I by simply applying the ratio of A_{22} for these states [6].
From the obtained pressure dependence of $A_{22}\overline{G_{22}(\infty)}$, the internal pressure of ultrafine bubble is tentatively determined to be $3.4^{+5.4}_{-1.1}\times10^5$ Pa.
The present result is smaller than that expected from Young-Laplace equation, 1.6×10^6 Pa. Some kind of compensation schemes for the present discrepancy are required to maintain an ultrafine bubble. One possible explanation is the repulsive force by the electrostatic charge on the surfaces of ultrafine bubbles. We are planning to measure ζ potential for ultrafine bubble to evaluate the surface charge.

The present work is supported by JSPS KAKENHI Grant Number 18K03948.

REFERENCES:
[1] E. G. Denis, The fine bubble breakthrough. https://www.iso.org/news/2014/05/Ref1844.html
[2] H. J. Leisi, Nucl. Phys. **76** (1966) 308.
[3] T. v Ledebur, Helv. Phys. Acta **49** (1976) 661.
[4] U. Berek, W. Kreisel, H. Schneider, and E. Tierno, Phys. Lett. **A48** (1974) 79.
[5] U. Berek, W. Kreisel, H. Schneider, E. Tierno, and H. Wagner, Phys. Lett. **A55** (1975) 22.
[6] U. Berek, W. Kreisel, H. Schneider, and E. Tierno, Phys. Lett. **A53** (1975) 251.

PR3-5

Dynamic Behavior of Impurity Indium Ions in Magnetite

W. Sato, S. Komatsuda[1], T. Fujisawa[2], S. Takenaka[2], T. Sugimoto[2], M. Takata[2], and Y. Ohkubo[3]

Institute of Science and Engineering, Kanazawa University
[1]National Institute of Technology, Ichinoseki College
[2]Graduate School of Science and Technology, Kanazawa University
[3]Institute for Integrated Radiation and Nuclear Science, Kyoto University

INTRODUCTION: Magnetite (Fe_3O_4) is a promising material applicable to functional devices in such fields as spintronics, drug delivery systems, and chemical catalysts. There are many vacant spaces inherent in the compound comprised of the sublattices called tetrahedral *A* site and octahedral *B* site, and these vacancies could make it possible for impurity ions to move around from site to site. In our previous work, we observed thermal migration of impurity indium ions from the *A* site to the *B* site at temperatures higher than the Curie temperature (T_C = 858 K) by means of time-differential perturbed angular correlation (TDPAC) spectroscopy with the ^{111}In($\rightarrow^{111}$Cd) probe [1]. It is expected that this phenomenon possibly leads to impurity-induced ionic conductivity. However, the observation of the movement of In ions was indirect; we merely measured the field at the probe site after the migration of the parent nucleus (^{111}In), namely, after the disintegration to the daughter nucleus (^{111}Cd). It is thus essential to observe the movement of In ions through "the eyes" of witnessing nuclei. For that purpose, in this work, we performed TDPAC spectroscopy for the observation of dynamic motion of impurity In ions adopting the ^{111m}Cd($\rightarrow^{111}$Cd) probe nuclei as the witnessing eyes. In the report, direct evidence of dynamic motion of In ions is presented.

EXPERIMENTS: A stoichiometric amount of In_2O_3 was mixed well with Fe_3O_4 so as to synthesize 0.5 at.% In-doped Fe_3O_4 (IFO). The mixture was pressed into a disk, and sintered in vacuum at 1073 K for 3 h. It was confirmed that any second phase of the In impurities did not appear in its powder X-ray diffraction pattern.

Neutron irradiation was performed for cadmium oxide (CdO) enriched with ^{110}Cd in Kyoto University Reactor to produce radioactive ^{111m}Cd by a neutron capture reaction. The radioactive Cd(^{111m}Cd)O powder was mixed well in a mortar with IFO prepared in advance, and sintered in vacuum at 1173 K for 45 min. TDPAC measurements were carried out for the ^{111m}Cd($\rightarrow^{111}$Cd) probe on the 151-245 keV cascade γ rays with the intermediate state of I = 5/2 having a half-life of 85.0 ns. In the present work, we obtained the perturbed angular correlation as a function of the time interval of the cascade γ-ray emissions by the following expression:

$$A_{22}G_{22}(t) = \frac{2[N(\pi,t) - N(\pi/2,t)]}{N(\pi,t) + 2N(\pi/2,t)} \quad , \qquad (1)$$

where A_{22} denotes the angular correlation coefficient, $G_{22}(t)$ the time-differential perturbation factor as a function of the time interval t between the cascade γ-ray emissions, and $N(\theta, t)$ the number of the delayed coincidence events observed at an angle θ.

RESULTS: The TDPAC spectra of ^{111m}Cd($\rightarrow^{111}$Cd) embedded in IFO are shown in Fig. 1. The room-temperature spectrum shows an oscillatory structure characteristic of static magnetic interaction with the internal field. Thus, we analyzed the spectrum with the following time-differential perturbation factor $G_{22}(t)$ assuming a relative width δ to the centroid of the Larmor frequency ω_L:

$$G_{22}(t) = \frac{1}{5}\left\{1 + 2\exp\left(-\frac{1}{2}\delta^2\omega_L^2t^2\right)\cos(\omega_L t) + 2\left[\exp\left(-\frac{1}{2}\delta^2\omega_L^2t^2\right)\right]^4\cos(2\omega_L t)\right\} \quad . \qquad (2)$$

The analytical results are as follows: ω_L = 171.9(5) Mrad/s, δ = 3.6(4)%. The ω_L value shows good agreement with that obtained in the previous work [1], verifying that Cd as well as In ions occupy the *A* site. At 900 K ($>T_C$), we observed exponential relaxation in the spectrum, which signifies nuclear spin relaxation caused by dynamic perturbation arising from the fluctuation of the extranuclear field. Thus we analyzed the spectrum with

$$G_{22}(t) = \exp(-\lambda t) \quad , \qquad (3)$$

where λ is the relaxation constant. Taking into account the unperturbed nature of the spectrum for Fe_3O_4 doped only with the ^{111}In($\rightarrow^{111}$Cd) probe measured at 873 K ($>T_C$), this relaxation should be attributed to the doping effect of macroscopic amount of In. Thus it is evident that the observed nuclear spin relaxation was caused by thermally activated dynamic motion of In ions. The present result shows direct observation of In motion through the eyes of ^{111m}Cd.

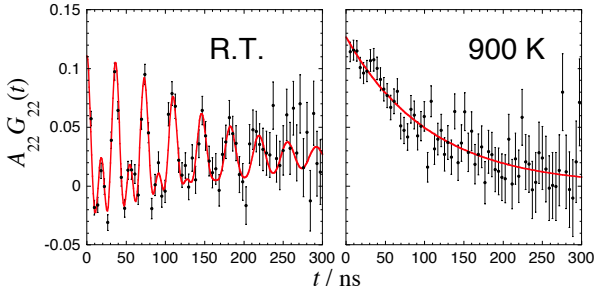

Fig. 1. TDPAC spectra of ^{111m}Cd($\rightarrow^{111}$Cd) in 0.5 at.% In-doped Fe_3O_4 measured at temperatures indicated.

REFERENCE:

[1] W. Sato *et al.*, J. Appl. Phys., **120** (2016) 145104 (1-7).

30P3-6

PR3-6 Observation of Local Fields at the ^{111}Cd(←^{111m}Cd) Sites in $CdTi_{0.95}Co_{0.05}O_3$

S. Komatsuda, W. Sato[1], H. Sakurada[2], K. Oikawa[2], and Y. Ohkubo[3]

Liberal Arts and Sciences, Natural Sciences, National Institute of Technology, Ichinoseki College
[1]*Institute of Science and Engineering, Kanazawa University*
[2]*National Institute of Technology, Ichinoseki College*
[3]*Institute for Integrated Radiation and Nuclear Science, Kyoto University*

INTRODUCTION: The perovskite oxides ABO_3 such as cadmium titanate ($CdTiO_3$) has been attracting much attention as a ferroelectric oxide, and its technological applications are strongly expected. It is reported that substitution of impurity ions at the *A* or *B* sites induces good ferroelectricity because of a distortion of crystal symmetry[1]. Therefore, it is necessary for a practical use of $CdTiO_3$ to obtain microscopic information on this doping effect. In this study, in order to investigate the effect of Co doping on crystal symmetry, we observed the local structures in $CdTiO_3$ and $CdTi_{0.95}Co_{0.05}O_3$ by means of the time-differential perturbed angular correlation (TDPAC) method using the ^{111}Cd(←^{111m}Cd) probe.

EXPERIMENTS: About 3 mg of CdO enriched with ^{110}Cd was irradiated with thermal neutrons in a pneumatic tube at Kyoto University Reactor, and radioactive ^{111m}Cd was generated by ^{110}Cd(n, γ)^{111m}Cd reaction. The neutron-irradiated CdO powder was then added into stoichiometric amount of TiO_2, Co_3O_4 and nonradioactive CdO powder to synthesize the polycrystalline $CdTiO_3$ and $CdTi_{0.95}Co_{0.05}O_3$ powder. The powders were mixed in the mortar. Each powder was pressed into disks and sintered in air at 1373 K for 45 min, respectively. It was confirmed from the powder XRD pattern for the nonradioactive $CdTiO_3$ and $CdTi_{0.95}Co_{0.05}O_3$ samples that calcining at 1373 K for 45 min is sufficient to synthesize a single phase $CdTiO_3$. The TDPAC measurement was carried out for the 151-245 keV cascade γ rays of the ^{111}Cd(←^{111m}Cd) probe with the intermediate state of I = 5/2 having a half-life of 85.0 ns.

RESULTS: Figure 1 shows TDPAC spectra of ^{111}Cd(←^{111m}Cd) probe in $CdTiO_3$ and $CdTi_{0.95}Co_{0.05}O_3$. The measurements were performed at room temperature. The directional anisotropy on the ordinate, $A_{22}G_{22}(t)$, was deduced with the following simple operation for delayed coincidence events of the cascade:

$$A_{22}G_{22}(t)=\frac{2[N(\pi,t)-N(\pi/2,t)]}{N(\pi,t)+2N(\pi/2,t)}. \qquad (1)$$

Here, A_{22} denotes the angular correlation coefficient, $G_{22}(t)$ the time-differential perturbation factor as a function of the time interval, t, between the relevant cascade γ-ray emissions, and $N(\theta,t)$ the number of the coincidence events observed at angle, θ. The oscillatory structure observed in Fig.1 reflects electrostatic interactions between the probe nucleus and the extranuclear field because the sample consists of no magnetic materials. We thus performed least squares fits to the spectra in Fig. 1 with $G_{22}(t)$ expressed as

$$G_{22}(t)=\sigma_{2,0}+\sum_{n=1}^{3}\sigma_{2,n}\cos(\omega_n t) \qquad (2)$$

For all symbols in eq.(2), refer to our previous paper[2]. The electric field gradient (EFG) and asymmetry parameter values obtained for $CdTiO_3$ were estimated to be V_{zz} = 5.5(9)×10^{21} Vm^{-2} (η=0.40). This EFG value shows a good agreement with that obtained for ^{111m}Cd probe in $CdTiO_3$ sample[3]. Since the present spectra can be reproduced by the fit assuming a single component, ^{111m}Cd probes occupy the Cd site in $CdTiO_3$ and $CdTi_{0.95}Co_{0.05}O_3$. For $CdTi_{0.95}Co_{0.05}O_3$ sample, V_{zz} and η values show good agreement with those for $CdTiO_3$ sample: V_{zz} = 5.6(9)×10^{21} Vm^{-2} (η=0.40). These TDPAC parameters show that substitution of Co ions at Ti site has no effect for crystal symmetry at ^{111}Cd probe. The present experimental result suggests that doping into *B* site has negligible effects on crystal symmetry and microstructure for $CdTiO_3$.

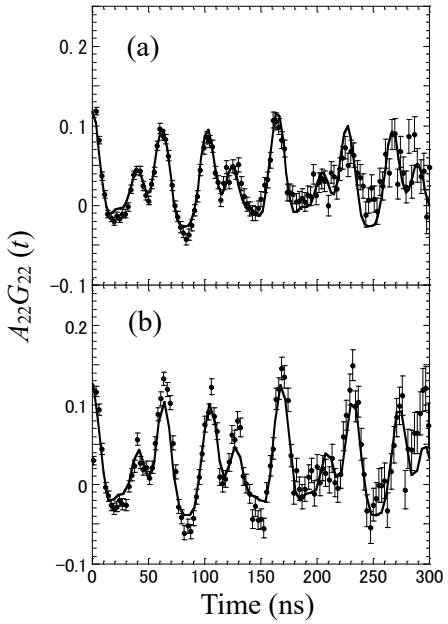

Fig. 1. TDPAC spectra of ^{111}Cd(←^{111m}Cd) probe in (a) $CdTi_{0.95}Co_{0.05}O_3$ and (b) $CdTiO_3$ at room temperature. The line is the result of a least-squares fit with eq.(2).

REFERENCES:

[1] S. Suzuki *et al*., *Phys. Rev. B* **86** (2012) 060102 (1-4).
[2] S. Komatsuda *et al*., *J. Appl. Phys.* **116** (2014) 183502 (1-5).
[3] I. J. R. Baumvol *et al*., *J. Phys. Chem. Solids* **39** (1978) (175-178).

30P3-7

I-1. PROJECT RESEARCHES

Project 4

PR4 Project Research of Accelerator-Driven System with Spallation Neutrons at Kyoto University Critical Assemly

C. H. Pyeon[1], M. Yamanaka[1], K. Hashimoto[2], N. Aizawa[3], A. Ohizumi[4], M. Fukushima[4], G. Chiba[5], K. Watanabe[6] and T. Endo[6]

(Kyoto University)

[1] *Institute for Integrated Radiation and Nuclear Science, Kyoto University*

[2] *Atomic Energy Research Institute, Kindai University*

[3] *Graduate School of Engineering, Tohoku University*

[4] *Nuclear Science and Engineering Center, Japan Atomic Energy Agency*

[5] *Graduate School of Engineering, Hokkaido University*

[6] *Graduate School of Engineering, Nagoya University*

INTRODUCTION: At the Kyoto University Critical Assembly (KUCA), a series of the accelerator-driven system (ADS) experiments [1]-[5] had been carried out with the combined use of A core (solid-moderated and -reflected core) and the fixed-field alternating gradient (FFAG) accelerator. Project research of "Accelerator-Driven System with Spallation Neutrons at Kyoto University Critical Assembly" was composed of six research teams in domestic: Kindai University; Tohoku University; Japan Atomic Energy Agency (JAEA); Hokkaido University, Nagoya University; Institute for Integrated Radiation and Nuclear Science, Kyoto University (KURNS; former the Kyoto University Research Reactor Institute). In the project research organized by KURNS, the ADS core was comprised of EE1 (1/8"p60EUEU) core shown in Fig. 1, and 100 MeV protons generated by the FFAG accelerator was injected onto the lead-bismuth (Pb-Bi) target. For an injection of 100 MeV protons onto the Pb-Bi target, spallation neutrons were observed with a hard spectrum by high-energy neutrons, and were contributed to neutron multiplication of the EE1 core. The objectives of the project research were to examine experimentally neutron characteristics of the EE1 core modeling actual ADS experimental facilities, and to investigate applicability of current measurement technologies to kinetic parameters and numerical methodologies to deterministic and stochastic calculations, in the ADS experiments with spallation neutrons at KUCA.

EXPERIMENTS: In the ADS experiments with spallation neutrons, main characteristic of proton beams by the FFAG accelerator were shown as follows: 100 MeV energy; 30 Hz frequency; 100 ns repetition rate; 30 pA to 1 nA intensity; 40 mm diameter beam spot. The research topics were revealed in each research team as follows:

- Subcriticality measurement by the Noise method (Kindai University)
- Measurement of reaction rate distribution (Tohoku University)
- Minor Actinide irradiation (JAEA and Hokkaido University)
- On-line monitoring of kinetic parameters (Nagoya University)
- Neutronics of EE1 core in ADS

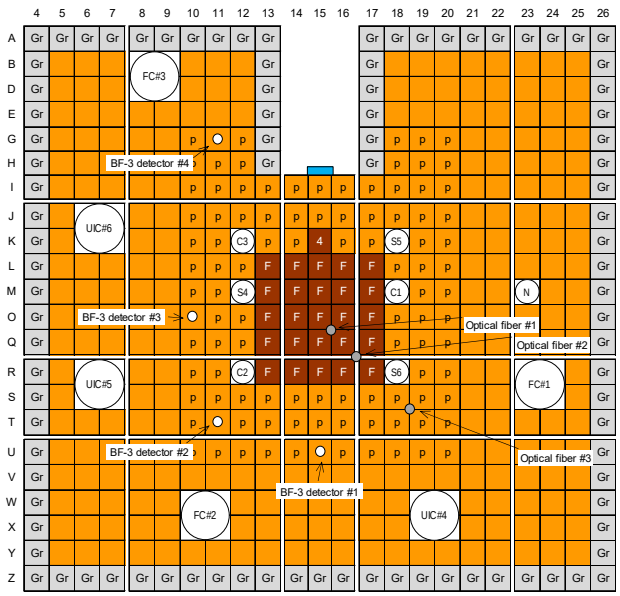

Fig. 1. Top view of EE1 core configuration at KUCA.

RESULTS: From the results of a series of ADS experiments, special attention was made to the following items: applicability of the Noise method to subcriticality measurement in ADS with spallation neutrons (Kindai); subcriticality dependency on reaction rate distributions (Tohoku); feasibility study on MA irradiation by spallation neutrons (JAEA and Hokkaido); applicability of advanced measurement system with optical fibers to on-line monitoring of kinetic parameters (Nagoya); benchmarks on kinetic parameters in EE1 core of ADS with spallation neutrons (Kyoto).

CONCLUSION: The project research of ADS with spallation neutrons at KUCA was successfully conducted with the combined use of EE1 core and FFAG accelerator at KUCA. A series of static and kinetic ADS experiments revealed importantly applicability of current measurement methodologies to upcoming actual ADS facilities in the future, demonstrating remarkable reconstruction of ADS experiments by numerical calculations.

REFERENCES:

[1] C. H. Pyeon, *et al.*, J. Nucl. Sci. Technol., **46**, (2009) 1091-1093.

[2] C. H. Pyeon, *et al.*, Nucl. Eng. Technol., **45**, (2013) 81-88.

[3] C. H. Pyeon, *et al.*, Nucl. Technol., **192**, (2013) 181-190.

[4] C. H. Pyeon, *et al.*, Ann. Nucl. Energy, **105**, (2017) 346-354.

[5] C. H. Pyeon, *et al.*, J. Nucl. Sci. Technol., **55**, (2018) 190-198.

PR4-1 Subcriticality Monitoring for a Reactor System Driven by Spallation Source (II)

K. Hashimoto, A. Sakon, S. Hohara, K. Nakajima[1], K. Takahashi[1],C. H. Pyeon[2], T. Sano[2] M. Yamanaka[2]

Atomic Energy Research Institute, Kindai University
[1]Graduate School of Science and Engineering, Kindai University
[2]Institute for Integrated Radiation and Nuclear Science, Kyoto University

INTRODUCTION: Feynman-α and Rossi- α Methods have been frequently employed to determine subcritical reactivity of nuclear reactor systems driven by Poisson source such as Am-Be neutron source. Recently many advanced formulas for a pulsed non-Poisson source such as spallation source have been derived. The objectives of this study are to confirm experimentally an applicability of these formulas for a subcritical reactor system driven by a spallation source and to investigate the multiplicity information of neutrons emitted by spallation reaction.

EXPERIMENTS: A subcritical system was constructed on the A loading of the Kyoto University Critical Assembly. The system had a lead-bismuth target, to which 100Mev proton beam was drawn to cause spallation reactions. The repetition frequency of the proton pulse beam was 30Hz. Time-sequence counts data from four BF_3 proportional counters were acquired for 30 minutes at several subcritical states. The subcritical reactivity was adjusted by axial positions of control and safety rods.

RESULTS: Figure 1 and 2 show a Feynman-α and Rossi-α analysis result obtained from a counter BF_3#1 placed near the reactor core, where all control and safety rods are completely inserted. The Degweker's formulas [1] with a delayed neutron contribution were fitted to these data to determine the prompt-neutron decay constant α. These fitted curves are in very good agreement with the Y(T) and the P(τ) data, respectively. The decay constants α determined by the Feynman- α and the Rossi-a analyses are consistent with each other.

Figure 3 and 4 show another Feynman-α and Rossi-α result obtained from a counter BF_3#4 placed near the lead-bismuth target and far from the core. These distributions of the Y(T) and the P(τ) are significantly different from those of Figure 1 and 2. The decay constants are significantly larger than those determined from BF_3#1 data. This is because BF_3#4 counter detects spallation source neutrons but no fission neutrons. Therefore, the distributions of Figure 3 and 4 must have only the correlation information of spallation neutrons. However, the decay constant determined by the Feynman-α analysis is significantly different from that by the Rossi-α analysis. The further advancement of data analysis is in progress.

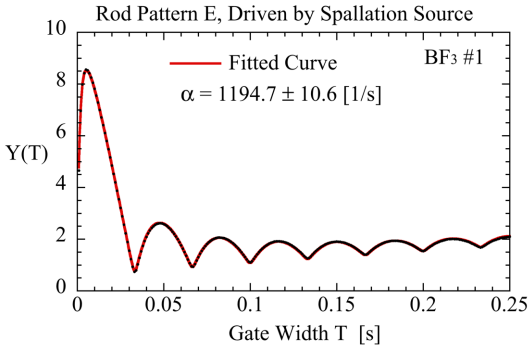

Fig.1. Feynman-α result obtained from BF_3#1.

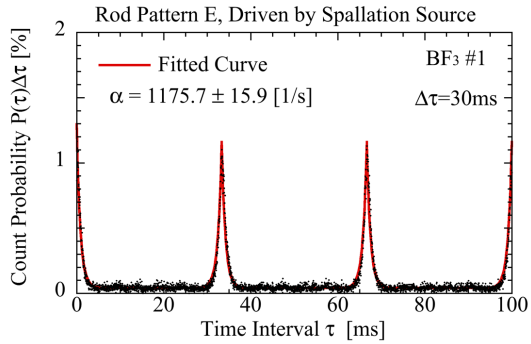

Fig.2. Rossi-α result obtained from BF_3#1.

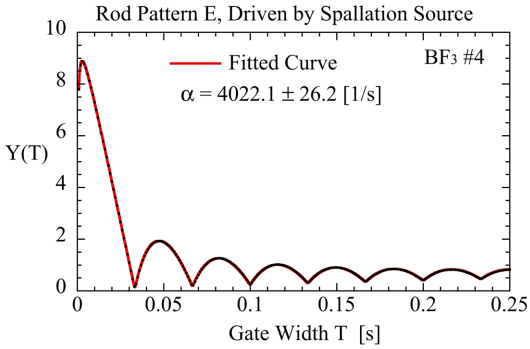

Fig.3. Feynman-α result obtained from BF_3#4.

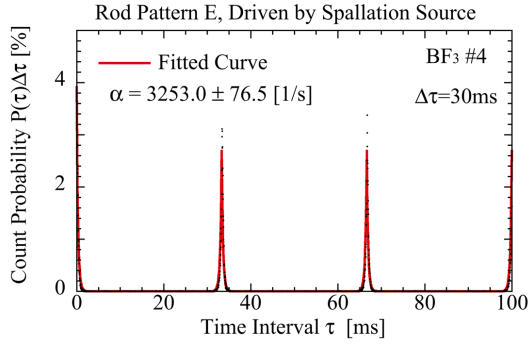

Fig.4. Rossi- α result obtained from BF_3#4.

REFERENCES:

[1]S.B. Degweker Ann. Nucl. Energy, **30** (2003) 223-243. 555-559.

PR4-2 Reaction Rate of Accelerator-Driven System with Spallation Neutrons

N. Aizawa, D. Maeda, K. Nakamura[1], M. Yamanaka[2] and C. H. Pyeon[2]

Graduate School of Engineering, Tohoku University
[1] School of Engineering, Tohoku University
[2]Institute for Integrated Radiation and Nuclear Science, Kyoto University

INTRODUCTION: An accelerator-driven system (ADS) has been investigated for the effective minor actinide transmuter. The neutron reactions in the ADS core are dominated by neutrons with several MeV energy, but the contribution of several tens MeV neutrons to the reactions is not negligible. The experimental studies of the neutron reaction rates in the core region had been carried out in the previous study with the use of the Pb-Bi zoned core with the spallation neutron source generated by 100 MeV protons [1]. In the previous study, the accuracy of the reaction rates in the fixed-source calculation was presented as an important issue. The purpose of the present study is to examine the cause of the calculation accuracy through the measurement of the neutron reaction rates in the different core system with spallation neutron source.

EXPERIMENTS: The ADS experiment was performed in KUCA A-core combined with spallation neutron source generated by 100 MeV protons from FFAG accelerator. Figure 1 shows the core configuration. The core employed in the present study was 1/8"p60EUEU core, which was PE (polyethylene) moderated uranium core. The subcriticality was set from 1449 to 8820 pcm (0.986 to 0.929 in k_{eff}) by changing the number of fuel assembly. In, Al, Fe, Ni, Au foils were employed for the measurement of the neutron reaction rates on the basis of the various reaction threshold energies, and were set at (M-O, 15). In wire was set along (A-P, 13-14) to measure the reaction rate distributions of ^{115}In(n, γ) ^{116m}In and ^{115}In(n, n') ^{115m}In, which were sensitive to thermal and the fast neutrons, respectively.

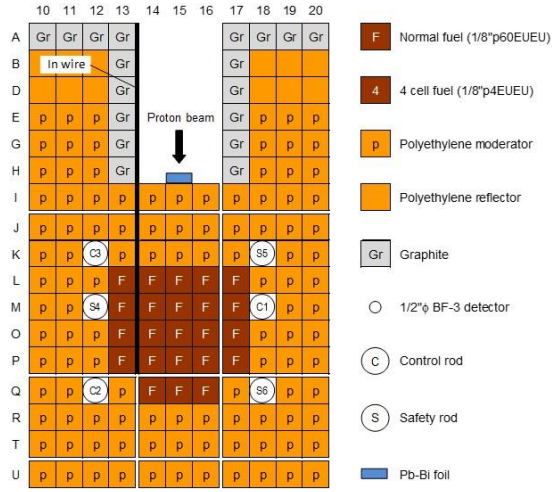

Fig. 1 Core configuration of KUCA A-core.

RESULTS: Figure 2 shows the variation of the reaction rates on each foils normalized by the reaction rates of Au(n,γ). The all reaction rates except for Al foil increased as the subcriticality became deeper, and the gradient of the Fe reaction rate whose reaction threshold was 5.0 MeV was the largest. These trends meant that the contribution of the fast neutrons, especially over 5.0 MeV neutrons, to the neutron reaction increased with increasing the subcriticality level. The discrepancies between experiments and Monte Carlo calculations were seen but the same trends were also obtained in the calculations. The reaction rate distributions of ^{115}In(n, γ) ^{116m}In and ^{115}In(n, n') ^{115m}In were also measured, and the ratios of ^{115}In(n, n') ^{115m}In to ^{115}In(n, γ) ^{116m}In were derived as shown in Fig. 3. The calculated ratios also had the similar distributions, and the spectrum information at the wire positions was considered to be available from the measured reaction rates.
In the future work, the cause of the discrepancies between the experiments and calculations will be analyzed in detail.

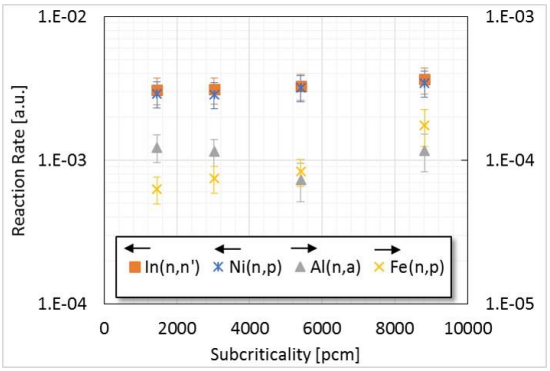

Fig. 2 Reaction rates of activation foils normalized by Au reaction rate.

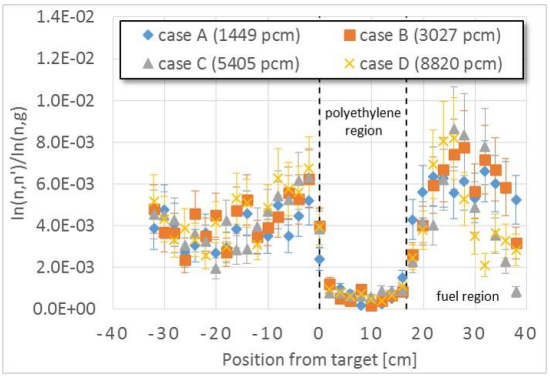

Fig. 3 Distributions of ^{115}In(n,n')/ ^{115}In(n,γ) ratio.

REFERENCES:
[1] C. H. Pyeon *et al.*, J. Nucl. Sci. Technol., **55(2)** (2018) 190-198.

PR4-3

Measurement of MA Reaction Rates Under Sub-Critical Condition with Spallation Neutron Source in A-core of KUCA for ADS

A. Oizumi[1], M. Fukushima[1], K. Tsujimoto[1], G. Chiba[2], M. Yamanaka[3], T. Sano[3], and C. H. Pyeon[3]

[1]*Nuclear Science and Engineering Center, Japan Atomic Energy Agency*
[2]*Graduate School of Engineering, Hokkaido University*
[3]*Institute for integrated Radiation and Nuclear Science, Kyoto University*

INTRODUCTION: In order to transmute minor actinides (MAs) partitioned from the High-level waste, the Japan Atomic Energy Agency (JAEA) has investigated neutronics of an accelerator-driven system (ADS). In the nuclear transmutation system such as ADS, the nuclear data validation of MA is required to reduce the uncertainty caused by the nuclear data of MA. To validate the nuclear data, many independent experimental data need to be mutually compared. An expansion of integral experimental data is the important issue since there is a limited number of experimental data of MA. The Kyoto University Critical Assembly (KUCA) has a potential capability to perform simulated experiments of ADS with injection of spallation neutron sources into a subcritical core. This study aims to measure the reaction rates of neptunium-237 (^{237}Np) and americium-241 (^{241}Am) under the sub-critical condition using the spallation neutron source in KUCA.

EXPERIMENTS: The MA irradiation experiments were conducted at A-core in KUCA with the fixed-field alternating gradient (FFAG) proton accelerator. Fission reaction rates were measured by using a back-to-back (BTB) fission chamber (diameter: 40mm, height: 42mm). The BTB fission chamber having two foils (mass: 10μg/nuclide) such as uranium-235 (^{235}U) and MA (^{237}Np or ^{241}Am) was installed at the center of the core as shown in Figure 1. The pulsed-height distribution from the BTB fission chamber was acquired under the condition of sub-critical core (k_{eff} = 0.998) with proton beam injection, such as 100 MeV energy, 30 Hz period, 100ns beam width, and 0.5 nA current, which corresponds to a reactor power of 1.5W. The measurement times were 112 min for ^{237}Np/^{235}U and 98 min for ^{241}Am/^{235}U.

RESULTS: The distributions of pulse height of ^{237}Np, ^{241}Am, and ^{235}U fission reactions were observed under the sub-critical condition as shown in Figure 2. The fission reaction signals have to be separated from noises due to α and γ rays in small channels. For example, the fission reaction events of ^{237}Np and ^{235}U in Figure 2(a) were determined by integrating the signals from 59 and 51 to 250 and 255 channels, respectively. Similarly, the fission reaction counts of ^{241}Am and ^{235}U in Figure 2(b) were obtained from 45 and 30 to 215 and 240 channels, respectively. Finally, the fission reaction rate ratios of ^{237}Np/^{235}U and ^{241}Am/^{235}U calculated from the each total count using the above method and the number of atoms were 0.014±0.002 and 0.023±0.005, respectively. These measured values will be used for verification of evaluated nuclear data by conducting detailed analyses.

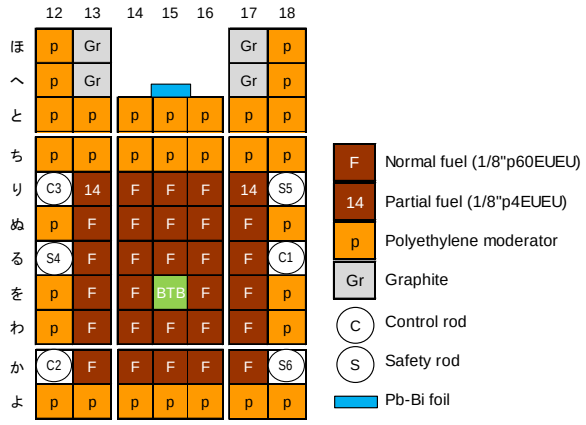

Figure 1. Loaded position of the BTB fission chamber in the A-core of the KUCA.

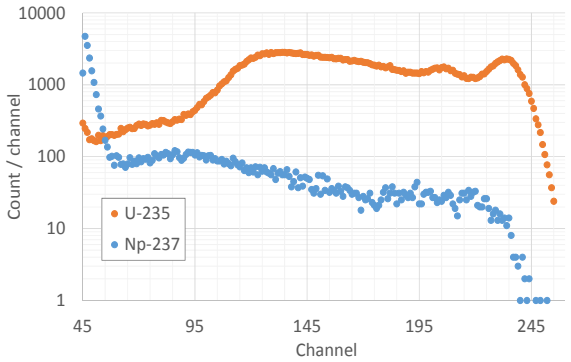

(a)^{237}Np and ^{235}U

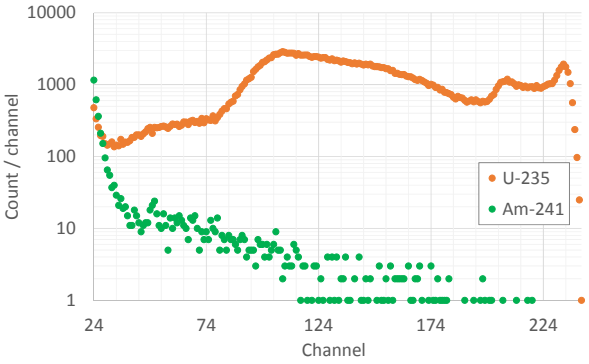

(b) ^{241}Am and ^{235}U

Figure 2. Signals from BTB fission chamber.

Development of Real-time Subcriticality Monitor

K. Watanabe, T. Endo, A. Uritani, A. Yamazaki, M. Yamanaka[1] and C. H. Pyeon[1]

Graduate School of Engineering, Nagoya University
[1] Institute for Integrated Radiation and Nuclear Science, Kyoto University

INTRODUCTION: The accelerator-driven subcritical (ADS) system has been developed for transmuting minor actinides and long-lived fission products [1-2]. The ADS system should be designed to be subcritical condition in any case and the subcriticality should be monitored in real time. Iwamoto et al. already demonstrated real-time subcriticality monitoring for ADS system, in which they used only a pulsed neutron source (PNS) method [3]. So far, we also developed a real-time subcriticality monitoring system. This system uses two methods simultaneously, the PNS and Rossi-α method, to assure validity of the measured subcriticality. In this study, we attempt to improve the detector performance and time resolution of the subcriticality measurements.

EXPERIMENTS: Subcriticality measurement experiments were conducted in A-core of Kyoto University Critical Assembly (KUCA). As a pulsed neutron source, a Pb-Bi target bombarded with 100 MeV protons from a FFAG proton accelerator. The repetition rate of the pulsed proton beam was 20Hz. We fabricated a new optical fiber type detector. Figure 1 shows the fabricated detector. Small LiF/Eu:CaF2 eutectics scintillators were dispersed on side surface of a wavelength shifting fiber. These scintillators were wrapped with Teflon tape reflector and covered with a 2.5 mm dia. aluminum tube to protect the detection element. The PMT signal was digitized and processed with a Field-Programmable Gate Array (FPGA). The information of pulse height, rise time and detection timing were extracted by FPGA and transferred to an analysis computer. The analysis computer processed these data and calculated the subcriticality every seconds. The detector was placed in a core region. The subcriticality was changed by inserting control and safety rods.

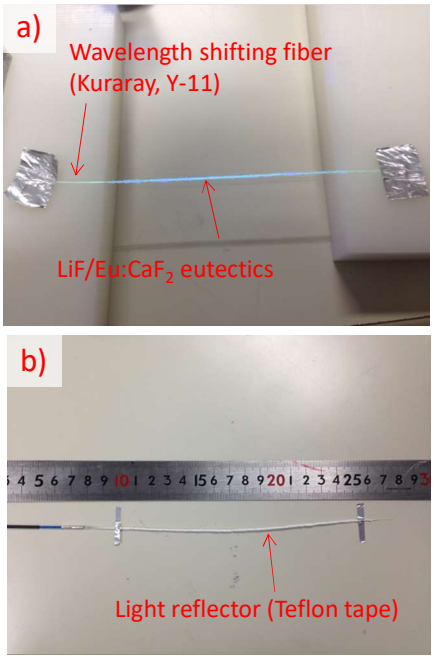

Fig. 1 Photograph of the fabricated new detector. a) Small LiF/Eu:CaF_2 eutectics scintillators were dispersed on side surface of WLSF. b)After wrapped by Teflon tape reflector.

RESULTS: Figure 2 shows the time trends of the measured neutron count rate and measured subcriticality. To determine the prompt neutron decay constant α, Levenberg-Marquardt algorithm, which is non-linear least square fitting method, was used for the both of PNS and Rossi-α method. The estimated α and area ratio were consistent with the reactor operation, such as a control rod insertion. Our system was confirmed to be able to determine the subcriticality every second. This means that the time resolution of this system is one second. This fast response is achieved by highly sensitive optical fiber type neutron detector developed in this study.

REFERENCES:

[1] Pyeon CH, Lim JY, Takemoto Y *et al.*, *Ann. Nucl. Energy,* **38** (2011) 2298–2302
[2] Pyeon CH, Yagi T, Sukawa K *et al., Nucl. Sci. Eng.,* **177** (2014) 156-168
[3] Iwamoto H, Nishihara K, Yagi T, Pyeon CH, *J. Nucl. Sci. Technol.*, **54** (2017) 432-443

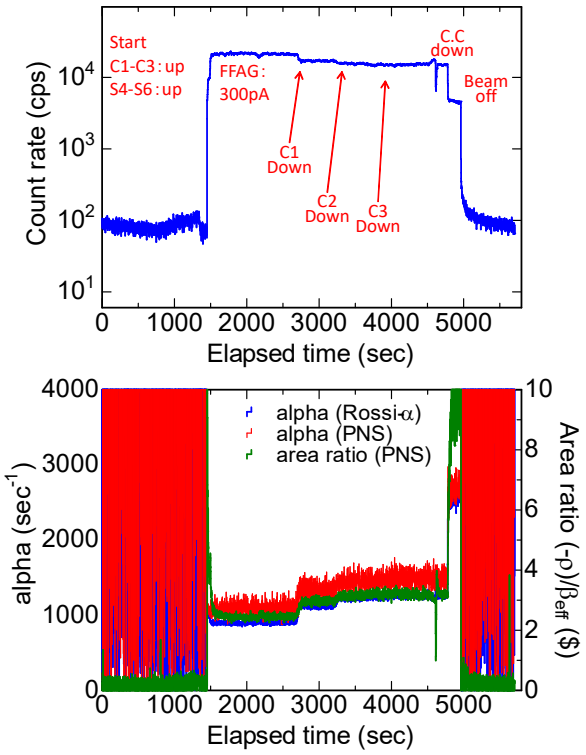

Fig. 2 Time trend of the measured neutron count rate(top) and the measured subcriticality (bottom).

I-1. PROJECT RESEARCHES

Project 5

PR5 Preclinical study for development of new drug for NCT

M. Suzuki

Institute for Integrated Radiation and Nuclear Science, Kyoto University

In this research project, twenty research projects were included. In this summary, three research projects (P5-1, P5-2, P5-3) could not be reported due to unexpected or uncontrolled events.

P5-4: Boronophenylalanine loaded mesoporous silica nanoparticles (BPA-MSN) as a new boron-delivery agent were investigated using chicken egg tumor model. Thermal neutron irradiation following BPA-MSN injection dramatically inhibited tumor growth. Growth inhibition was not observed in the tumors irradiated by thermal neutron with no injection, empty BSA or free BPA injection.

P5-5: As new boron-delivery agents, BPA or BSH bounded to 7-mer IFLLWQR peptide, designated IF7, were tested in this study. Pharmacokinetic studies revealed that IF7-BSH injection accumulate ^{10}B in the tumor more than twice compared with free BSH injection.

P5-6: Cancer-loaded human artificial three-dimentional tissue was investigated as the tool for evaluating accumulation ratio of BPA between cancer cells and normal tissues.

P5-7: Aggregation of boron carbide (B_4C) which is a candidate material for BNCT should be prevented in clinical use. Femosecond laser irradiation reported to enhance colloidal stability of various nanoparticles to aggregated B_4C nanoparticles failed to stable B_4C nanoparticle colloid due to a high hard ness and chemical stability of B_4C.

P5-8: BPA nanosuspensions (median diameter: 144 nm) were made using stabilizers, macrogol 15 hydoroxystearate and soybean lecithin. BNCT with subcutaneous-injected BPA nanosuspensions was equally efficacious in that with intravenous injected BPA-fructose.

P5-9: Therapeutic efficiency of pteroyl *closo*-dodecabrate conjugate (PBC) using F98 glioma-bearing rats *in vivo* boron neutron capture therapy (BNCT) was investigated. BNCT in combination with BPA (i.v) and PBC (convection enhanced delivery, CED) showed significantly longer survival time.

P5-10: Novel *p*-boronophenylalanine based boron carriers (BADB1-3), in which the medium-chain alkyl sulfoniododecaborate is linked to *C*-terminal of L-BPA was evaluated about the cytotoxicity, water solubility, and cellular uptake. The BADB-1 is useful candidate as new boron carrier with viewpoint of low cytotoxicity and high cellular uptake.

P5-11: Novel boron-containing low molecular compound (Compound A) was investigated with tumor-growth delay assay. BNCT with Compound A (250 mg/kg) showed tumor growth inhibitory effect comparable to that with BPA (500 mg/kg).

P5-12: Two different types of phenylboronic acid -installed polymeric nanoparticles with pinacol protection (Pinacol-NP) and without any protection (PBA-NP) were investigated with tumor-growth delay assay. BNCT with Pinacol-NP exhibited comparable antitumor effect with BPA-fructose even at a 100-fold lower effective dose of ^{10}B.

P5-13: As novel boron delivery agents, 2-boryl-1,2-dideoxy-D-glucose derivatives uptaken into the tumor cell via glucose transporters (GLUT) and sodium dependent glucose cotransporters (SGLT) were investigated. The lead compound was found.

P5-14: Poly vinyl alcohol (PVA)-BPA exhibited strong BNCT effect using a hypovascular tumor model (BxPC3). PVA should offer great potential as the additive boosting therapeutic potential of BPA.

P5-15: Newly synthesized boronated polymer exhibited comparable antitumor effect to sorbitol-BPA. The boronated polymer may be useful in the clinical application.

P5-16: This study revealed that disulfide bond-containing maleimide-functionalized *closo*-dodecaborate (SSMID) are bound to form a covalent bond to the albumin through the Lys residues.

P5-17: Doxorubicin DXR-encapsulated boron liposome was tested in this study. All the mice treated with the DXR boron liposome died within 20 days. The boronated liposome significantly suppressed tumor growth.

P5-18: Artificial oligonucleotides bearing hydorophobic boron-containing fluorophore (BODIPY-ODN) was investigated as a new boron compound.

P5-19: BPA-BNCT exhibited suppression of tumor growth using two head and neck tumor models (SAS and HSG.

P5-20: This study reviled that RGD sequence binding GD-DTPA/CaP nanomicelle has the promising possibility as novel active targeting GdNCT agent.

PR5-1 Nanoparticle formulation improves efficacy of BPA for BNCT

K. Matsumoto[1], T. Doan[1], A. Komatsu[1], N. Mai[1], Y. Tamari[2], T. Takata[2], M. Suzuki[2] and F. Tamanoi[1]

[1]Institute for Integrated Cell-Material Sciences, Institute for Advanced Study, Kyoto University
[2]Particle Radiation Oncology Research Center, Institute for Integrated Radiation and Nuclear Science, Kyoto

INTRODUCTION: Advance in Nanotechnology resulted in the generation of nanoparticles that have diameter in the range of 40-400 nm. We have been developing mesoporous silica nanoparticles (MSNs) that contain thousands of pores. An important feature of this type of nanoparticles is that they have a large surface area where a variety of reagents can be attached. MSNs are efficiently taken up into cancer cells. This involves the use of the endocytosis mechanism. MSNs are localized to the perinuclear localization, as lysosomes are located at these sites. MSNs can be designed to accumulate in tumor in animal models.
Our experimental plan is to prepare BPA-loaded MSN (BPA-MSN). We have designed experiments to prepare MSN that has BPA attached. We then examine tumor accumulation of BPA-loaded MSN. Then, the samples will be exposed to neutron beam at the nuclear reactor. BNCT efficacy will be compared to that of free BPA.

EXPERIMENTS: MSN were synthesized by the sol-gel process using TEOS as a building material and CTAB as a templating agent to produce pore structure. Diameter of MSN is 100 nm and the nanoparticle is surface modified by the addition of phosphonate. BPA was attached to MSN and the presence of Boron on MSN was confirmed by ICP-OES.

To carry out BNCT, we employed chicken egg tumor model established by transplanting human ovarian cancer cells. The experiments involved purchasing fertilized eggs and incubating till day 10 of development. A window was made on the egg shell and ovarian cancer cells were transplanted. Tumor was formed on the CAM (chorioallantoic membrane) three days later at which time BPA-loaded MSN were injected intravenously. After a day and half when MSN was accumulated in the tumor, eggs were irradiated with neutron beam at the reactor. The exposure time was set for 1 hour. After the exposure, the eggs were incubated for 3 days and the tumor size and weight were examined.

The setup developed for the exposure to neutron beam is shown in Figure 1. Two different setups have been developed, one accommodating 4 eggs while the other setup accommodating about 20 eggs.

RESULTS: We observed dramatic inhibition of tumor growth when BPA-MSN was injected. The tumor weight at the end of the experiment was 17 mg when BPA-MSN was injected, while control eggs with no injection had a tumor of 50 mg. Tumor weight of eggs with empty MSN injection was 45 mg. Eggs with free BPA injection had tumor weight of 40 mg. These results clearly show the effect of MSN formation of BPA on BNCT efficacy.

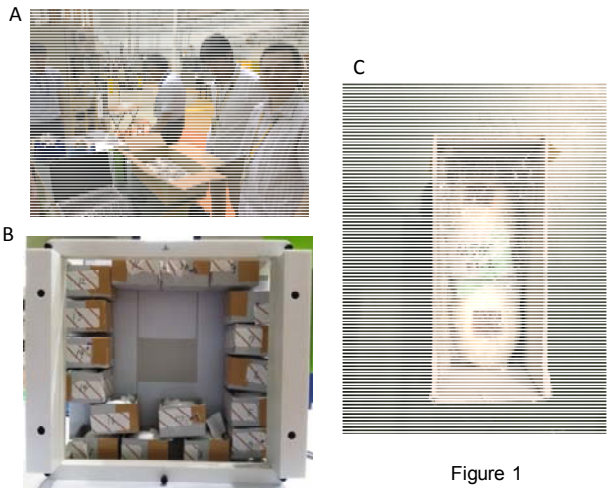

Fig. 1. Two different setups for carrying out BNCT experiments using chicken egg tumor model. A: BNCT experiments. B: Setup for 22 eggs. C: Setup for 4 eggs.

FUTURE PROSPECTS:
We have now demonstrated the power of our nanoparticles to improve BPA efficacy. Systematic experiments will be carried out to further investigate the use of nanoparticles in BNCT.

REFERENCES:
[1] B. Vu *et al.*, Scientific Reports **8** (2018) 8524.
[2] M. Vallet-Regi and F. Tamanoi, Enzymes **43** (2018) 1-10.
[3] T. Doan *et al.*, Enzymes **44** (2018) 61-81.
[4] K. Matsumoto *et al.*, Enzymes **44** (2018) 103-116.

PR5-2

Next Generation A (Aomori) - Research and development of novel boron drugs in BNCT therapy

S. Ishiyama[1], C. Ohyama[2], Y. Hashimoto[2], K. Mori[2], S. Hatakeyama[2], T. Yoneyama[2] , T. Tanaka[2] and M. Suzuki[3]

[1].*Graduate School of Science, Hirosaki University*
[2]*Graduate school of Medicine, Hirosaki University*
[3] *Institute for integrated radiation and nuclear science, Kyoto University*

INTRODUCTION: In Aomori Prefecture, "Prefectural Government Refuge against the shortest life time with high death rate" is taken as the prefectural government, Hirosaki University (Faculty of Medicine / Graduate School of Science and Engineering) received this, "Next generation A (Aomori) - Research and development on BNCT treatment "started. The main core technologies related to next-generation A-BNCT therapy are (1) development of new boron medicines, (2) A-BNCT treatment technology and (3) POST / BNCT regeneration technology, and this joint research aims at technological development for practical application concerning (1). New boron drug development In Hirosaki University, IF7-B series (10B-IF7) in which boron nuclide 10B is bound to 7-mer peptide (IFLLWQR; IF7 peptide) 1) -2) which selectively binds to tumor vascular endothelial cells , 10 BSH-IF 7, 10 BPA-IF 7). In this core research, demonstration experiments on the pharmacokinetics, toxicity test and BNCT treatment effect for practical application of the relevant IF7-B series are conducted by nuclear reactor irradiated animal experiments

EXPERIMENTS: In the fiscal year ending March 31, 2010, we will mainly focus on pharmacokinetic examinations by small animal experiments of IF7-B series drugs (3 species). An animal tumor model in which mouse bladder cancer cells (MBT 2) were seeded at the mouse thigh in Hirosaki University was prepared and injected with a boronic agent (IF 7 - BPA, IF 7 - BSH, BPA, BSH) from the mouse tail vein. Mice were sacrificed after drug administration (after 20 minutes, 40 minutes, 60 minutes, 90 minutes, 120 minutes, 240 minutes), and the tumor area and normal organs (liver, kidney, heart, bladder, lung , Brain, spleen, skin, blood) to Teflon containers (10 in total) and then transported to the Kyoto University Reactor. After transportation, measured boron concentration in prompt gamma ray assay(PGA) in E3 duct compartment.

RESULTS: Fig.1 shows the ^{10}B concentration in the organ of 13 sites taken out from the mouse specimen after 0~40 minutes of BPA, IF7-BPA. From these results, the accumulation amount of BPA and IF7-BPA in tumor cells was up to about 10 ppm of ^{10}B accumulation up to 40 minutes after injection, but no significant difference was observed between the two agents.

Fig.2 shows the ^{10}B concentration in the organ of 13 sites taken out from the mouse specimen after 0~40 minutes of BPA, IF7-BPA. From these results, the accumulation amount of BPA and IF7-BPA in tumor cells was up to about 10 ppm of ^{10}B accumulation up to 40 minutes after injection.

Fig.2 shows BHS and IF7-BSH (Fig.1 (a)) and the new boron drug IF 7-BSH (Fig.1 (b)) by tail injection, respectively. However, in experiments with IF7-BSH, experiments were conducted using multiple specimens.
According to this result, the accumulation degree of 10 B in the tumor site reaches up to about 20 ppm in 10 minutes after the introduction in BSH. On the other hand, it can be seen that IF7-BSH reaches 40 ppm more than twice that at the same elapsed time.

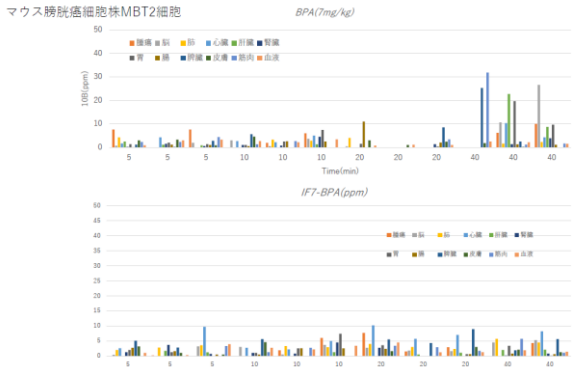

Fig.1 ^{10}B condensation in various internal organs including tumor site. In the case of BPA and IF7-BPA.

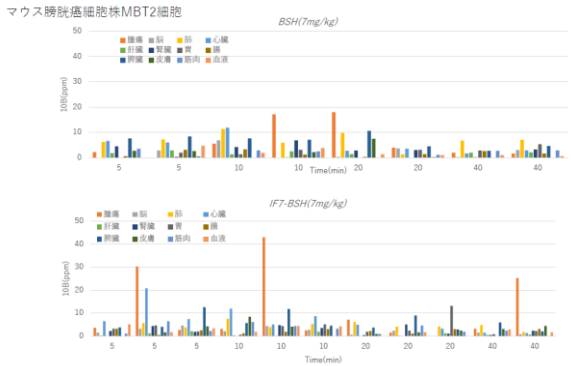

Fig.2 ^{10}B condensation in various internal organs including tumor site. In the case of BSH and IF7-BSH.

From these results, while the accumulation performance of ^{10}B to the tumor site of the newly developed IF7-BPA was not significantly improved as compared with the conventional agent BPA. However, in the case of IF7-BSH, it has been found that it has more than twice the integration performance comparing with the conventional agent BSH.

REFERENCES:

[1] Mirzaei HR, *et al*., J Cancer Res Ther. 2016.
[2] Takahara K, *et al.,* Plos One 2

PR5-3 **Pharmacokinetic status test using 3D artificial tumor cell tissue model prepared by LBLA method**

S.Ishiyama[1],Y.Asano[2], A.Shimoda[2] and M.Suzuki[3]
[1].Graduate School of Science, Hirosaki University
[2]Graduate school of Medicine, Hirosaki University
[3] Institute for integrated radiation and nuclear science, Kyoto University

INTRODUCTION: In Aomori Prefecture, "Prefectural Government Refuge against the shortest life time with high death rate" is taken as the prefectural government, Hirosaki University (Faculty of Medicine / Graduate School of Science and Engineering) received this, "Next generation A (Aomori) - Research and development on BNCT treatment "started [1-5]. The main core technologies related to next-generation A-BNCT therapy are (1) development of new boron medicines, (2) A-BNCT treatment technology and (3) POST / BNCT regeneration technology, and this joint research aims at technological development for practical application concerning (2). Pharmacokinetics experiments of ^{10}BPA drugs using α-radiography were performed using cancer-loaded human artificial three-dimensional tissue NHDF / BxPC3 prepared by the LBLA (Layer By Layer Assembly) method, and the performance of the ^{10}BPA for treatment of BNCT under the $^{10}B(p,n)^{7}Li$ reaction was evaluated.

EXPERIMENTS: Cancer-loaded human artificial three-dimensional tissue were prepared using human neonatal fibroblasts (NHDF (LONZA)) and red fluorescent protein (RFP) labeled (Anti- Cancer Japan) human pancreatic cancer cell line BxPC3 was used[7-13]. Organization of both cells was carried out using bovine serum-derived fibronectin (Wako) and porcine-derived gelatin (Wako) by the LBLA method. DMEM with 10% FBS, antibiotics was used as a medium for culturing after artificial tumor tissue production. Incorporation of ^{10}B into the prepared artificial tumor cell tissue was carried out using boron drug ^{10}BPA (boronophenylalanine $C_9H_{12}BNO_4$ molecular weight 209.01 (treatment concentration of ^{10}B: 20 - 50 ppm) of 3% weight concentration (fructose complex). Irradiation experiments using these samples were conducted at the E-2 port of Kyoto University Reactor KUR, and irradiation was performed for 30 minutes under an irradiation flux of 1.4×10^9 n / cm^2.

RESULTS: Fig.1 shows the respective structures of the NHDF and NHDF/BxCP3 samples and the results of observation of the alpha ray track in each sample after neutron irradiation. The fluorescent tissue (NHDF (a), NHDF / BxCP3 (b) and (c)) is shown on the left side of the figure, and the alpha track images ((a) 'to (c') are shown on the right side. The hole in the middle (black part to white part) is the above position confirmation hole, and the circular broken line (yellow) in both images shows the part with relatively high BxCP3 concentration on the NHDF / BxCP3 sample as a result of fluorescence observation. Comparing the α track concentrations of

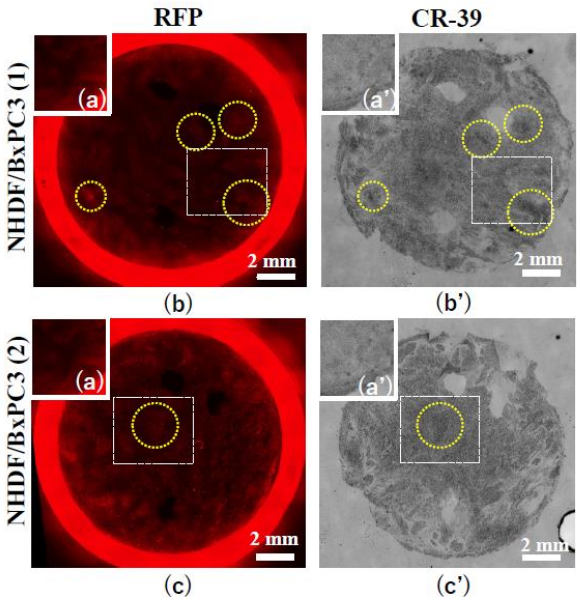

Fig.1 Fluorescence(left) and α radiography imaging(right) of NHDF and NHDF/BxPC3 3D cell structure(×4) :NHDF(a)(a') abd NHDF/BxPC3(b)(b') and (c) (c')

NHDF and NHDF / BxCP3 samples, it can be seen that the concentration in BxCP3 is higher and the track height is higher in the high density BxCP3 site (circular broken line part). This means that it corresponds to the concentration of 10B taken up into each tissue of NHDF and NHDF / BxCP3 samples after BPA immersion and gives a concentration of 10B uptake proportional to each tissue concentration in both samples.

REFERENCES:

[1] Masunaga, H.Kumada and et. al., The dependency of compound biological effectiveness factors on the type and concentration of administered neutron capture agents in boron neutron capture therapy, *Springer Plus*, 3:128(2014).
[2]S.Ishiyama, Y.Baba, R.Fujii, M.Nakamura, Y.Imahori, Synthesis of Lithium Nitride for Neutron Production Target of BNCT by in-situ Lithium Deposition and Ion Implantation, Nuclear Instruments and Methods in Physics Research B293,42-47.
[3]S.Ishiyama, Y.Baba, R.Fujii, M.Nakamura and Y.Imahori, Thermal Stability of BNCT Neutron Production Target Lithium Synthesized by in-situ Lithium Deposition and Ion Implantation, Materials Transactions, Vol.54, No.9,pp.1760-1764.
[4] S. ISHIYAMA and Y. IMAHORI, Deterministic parsing model of CBE factor for Intra-organ ^{10}B Distribution in Boron Neutron Capture Therapy, Journal of Cancer Therapy, 2014, 5, 1388-1398.
[5] S.Ishiyama, Y.Imahori, J.Itami and V.Hanna, Determination of the Compound Biological Effectiveness (CBE) Factors Based on the ISHIYAMA-IMAHORI Deterministic Parsing Model with the Dynamic PET Technique, J. of Cancer Therapy, Vol.6, No.8（2015）759-766.

PR5-4 An Attempt to Prepare Stable Colloid of Boron Carbide Using a Femtosecond Laser

Y. Ishikawa[1], N. Koshizaki[2] and M. Suzuki[3]

[1]*Nanomaterial Research Institute, National Institute of Advanced Industrial Science and Technology (AIST)*

[2]*Graduate School of Engineering, Hokkaido University*
[3]*KURNS, Kyoto University*

INTRODUCTION: Boron carbide (B_4C) is one of candidate materials for boron neutron capture therapy (BNCT) agent because of a chemical stability and high B atom content. Size reduction and aggregation prevention of B_4C particles are necessary for an application study for BNCT to avoid particle sedimentation. Seo, Y. et al. reported that an enhanced colloidal stability of various nanoparticle suspensions by a femtosecond laser irradiation of suspension [1]. In this study, we attempt to disperse aggregates and obtain stable suspension of B_4C nanoparticles by a Ti:sapphire femtosecond laser irradiation.

EXPERIMENTS: B_4C nanoparticles (EMJAPAN CO., LTD. NO-B4C-2-5) were dispersed in ethanol at 200 ppm concentration. The B_4C suspension of 6 ml in a glass vessel was irradiated over surface with a Ti:sapphire femtosecond laser (pulse width: 100 fs (FWHM), wavelength: 800 nm, and energy density: 8.5 mJ $pulse^{-1}$). The suspension was agitated using a magnetic stirrer during the irradiation for 1 h. B_4C nanoparticles were collected with a centrifugation and mounted on a Si wafer to observe a scanning electron microscope (SEM) image. B_4C particle size distribution and zeta potential were analyzed using a dynamic light scattering (DLS).

RESULTS: B_4C particles 100 to 200 nm in diameter were observed before laser irradiation (Fig. 1 (a)). Although primary particles were clearly observed in the particles before irradiation, these particles solidly aggregated and formed agglomerates larger than 1 μm in size as shown in particle size distribution (Fig. 2 black line). No noticeable shape change of particles were observed after laser irradiation (Fig. 1(b)). Particle size distribution after laser irradiation remained almost the same as that before irradiation (Fig. 2 red line). Zeta potentials of B_4C particles before and after irradiation were the same value -12.4 mV. These results are possibly due to a high hardness and chemical stability of B_4C.
A fabrication of stable B_4C nanoparticle colloid is still a future challenge.

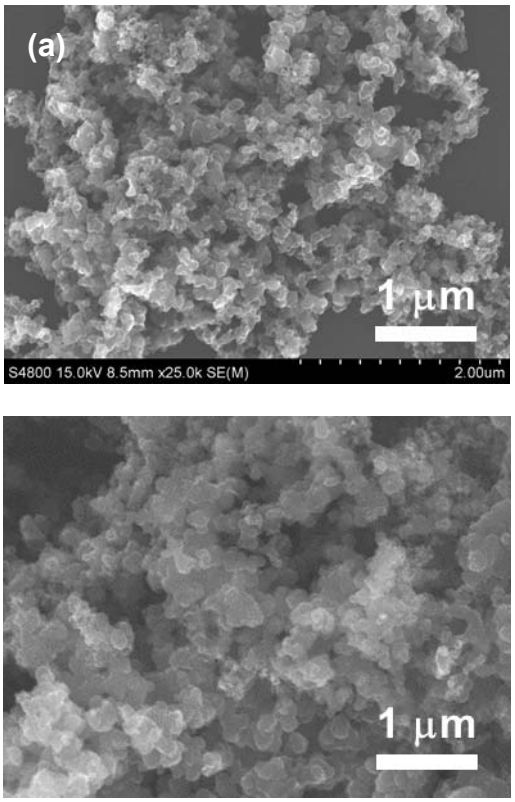

Fig. 1. SEM images of B_4C nanoparticles (a) before and (b) after laser irradiation.

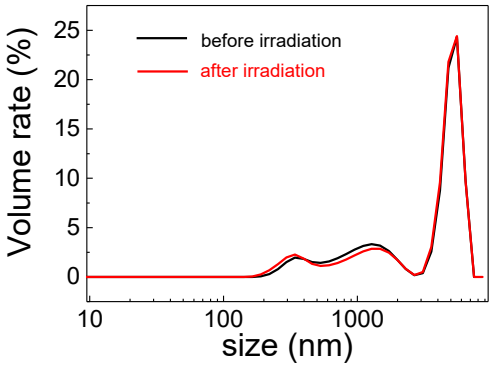

Fig. 2. B_4C particle size distribution analyzed with DLS measurement.

REFERENCE:
[1] Y. Seo *et al.*, J. Appl. Phys., **118** (2015) 114906 1-6.

PR5-5 Nanoparticulate *p*-borono-L-phenylalanine formulations for boron neutron capture therapy: Biodistribution after subcutaneous administration

T. Andoh[1], T. Fujimoto[2], M. Suzuki[3], T. Takata[4], Y. Sakurai[4] and H. Ichikawa[1].

[1]*Faculty of Pharmaceutical Sciences, Kobe Gakuin University, Japan.*
[2]*Department of Orthopaedic Surgery, Hyogo Cancer Center, Japan.*
[3]*Particle Radiation Oncology Research Center, Institute for Integrated Radiation and Nuclear Science, Kyoto University, Japan.*
[4]*Division of Radiation Life Science, Institute for Integrated Radiation and Nuclear Science, Kyoto University, Japan*

INTRODUCTION: The successful treatment of cancer by boron neutral capture therapy (BNCT) requires selective delivery of large amounts of ^{10}B isotope to tumor cells. Although *p*-borono-L-phenylalanine (L-BPA) spontaneously accumulates in tumor cells, pharmaceutical drawbacks include poor water-solubility (1.6 mg/mL) and rapidly decreased tissue concentration after administration. In clinical BNCT, BPA-Fructose complex (BPA-Fr) is a continuously infused intravenously to maintain adequate ^{10}B concentration in blood [1]. A more effective ^{10}B carrier is required to increase the success of BNCT. In the present study, an attempt was made to formulate a BPA nanosuspension (NS) that would be expected to accumulate more efficiently than BPA-Fr after local administration. The biodistribution of the BPA-NS formulation after subcutaneous (s.c.) administration was evaluated. in A tumor bearing animal model was established to investigate the *in vivo* biodistribution of L-BPA and antitumor effects after BNCT.

EXPERIMENTS: Macrogol 15 hydroxystearate (Solutol® HS 15, SO) and soybean lecithin (SL) were used as stabilizers. BPA-NS using SO and SL was prepared by a wet-milling method with the use of a Pulverisette-7 planetary ball mill (Fritsch). The obtained BPA-NS was sonicated using a 2510J-DTH water-bath sonicator (Branson Ultrasonics Co.) for 5 min at room temperature. Biodistribution was assessed using male B16F10 melanoma bearing C57BL/6J mice. BPA-Fr and BPA-NS (500 mg BPA/kg) were administered via s.c. injection to the mice. At a predetermined time after administration, the mice were sacrificed and blood and tissue samples were immediately collected. The concentration of ^{10}B in the blood was measured by inductively coupled plasma atomic emission spectroscopy. In the BNCT trial, tumor-bearing mice were divided into BNCT group and control group. The tumors in the left hind legs were exposed to thermal neutron irradiation at the Institute for Integrated Radiation and Nuclear Science, Kyoto University.

RESULTS: BPA-NS displayed a mass median diameter of 144 nm with 52.1 mg BPA/mL. The BPA concentration of BPA-NS was equivalent to BPA-Fr. After s.c. administration, the maximum ^{10}B concentration in tumors was 43 ppm (1 h) for BPA-Fr and 36 ppm (6 h) for BPA-NS. In addition, concentrations of ^{10}B in tumors were 5 ppm at 12 h after administration of BPA-Fr and 22 ppm 12 h after administration of BPA-NS. The previously described prolonged retention of ^{10}B in blood following s.c. route of administration [2, 3] may account for a longer retention of over 20 ppm in tumors for 12 h. The area under the ^{10}B tumor concentration-time curve (AUC_{tumor}) were calculated to be 313.5 μg･h/mg for BPA-Fr and 599.6 μg･h/mg for BPA-NS. BPA-NS displayed significantly higher AUC_{tumor} values than BPA-Fr ($P<0.0006$), which could reflect the dissimilar transport rate of the BPA formulations into the bloodstream after s.c. administration. In the BNCT trial, growth of tumor masses was observed in the control group, while the BNCT group showed an equivalent suppression of tumor growth. These results suggested that boron accumulates specifically in the tumor after s.c. administration of BPA formulations and that BNCT after s.c. dosing of BPA-NS or BPA-Fr is equally efficacious in the treatment of BNCT after intravenous administration of BPA-Fr.

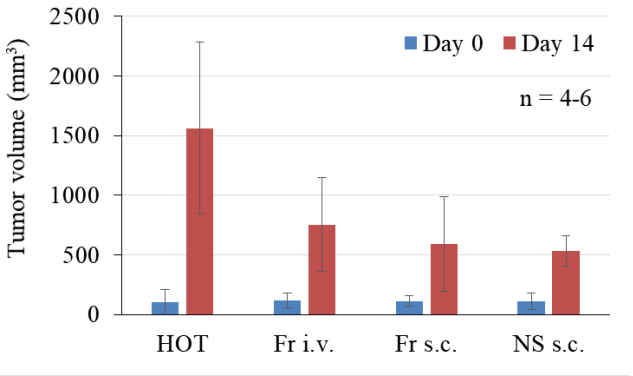

Fig. 1. Tumor volumes after thermal neutron beam irradiation of BNCT and HOT control groups.

REFERENCES:

[1] Y. Ariyoshi *et al.*, Oncol Rep., **18(4)** (2007) 861-866 .
[2] S. Masunaga *et al,* Int. J. Radiation Oncology Biol. Phys., **3** (2004) 920-927 .
[3] S. Masunaga, *et al.*, Springer Plus 2014, 3:128 (2014).

PR5-6

Evaluation of boron neutron capture therapy (BNCT) using brain tumor bearing rats or mice model

Y. Fukuo[1], S. Kawabata[1], T. Kanemitsu[1], R. Hiramatsu[1], T. Kuroiwa[1], M. Suzuki[2], S. Masunaga[2], K. Ono[3], S. Miyatake[4], H. Nakamura[5], Y. Hattori[6], M. Kirihata[6]

[1] *Department of Neurosurgery, Osaka Medical College*

[2] *Institute for Integrated Radiation and Nuclear Science, Kyoto University*

[3] *Kansai BNCT Medical Center, Osaka Medical College*

[4] *Cancer Centre, Osaka Medical College*

[5] *Laboratory for Chemistry and Life Science, Institute of Innovative Research, Tokyo Institute of Technology*

[6] *Osaka Prefecture University, Research Center of Boron Neutron Capture Therapy*

Main study

Introduction

Folic acid (FA) has high affinity for the folate receptor (FR), which is limited-expressed in normal human tissues and over-expressed in many cancer cells, including glioblastoma.

We evaluated a newly developed pteroyl *closo*-dodecaborate conjugate (PBC) as boron carrier in which the pteroyl group is known to interact with FR. The purpose of this study was to evaluate the therapeutic efficiency of PBC using F98 glioma-bearing rats *in vivo* boron neutron capture therapy (BNCT).

Materials and Methods

We used two boron compounds; Boronophenylalanine (BPA) and PBC. For *in vivo* study, F98 glioma bearing rats were divided to five groups: untreated controls, neutron irradiation only, BNCT with BPA (i.v.), BNCT with PBC (convection enhanced delivery; CED), and BNCT in combination with BPA (i.v.) and PBC (CED).

Results

The survival data following BNCT are summarized in Table. 1, and the Kaplan-Meier survival plots are shown in Fig. 1. Median survival time (MST) in all BNCT groups were significantly longer than that in the untreated control group ($p = 0.0013$, $p = 0.0029$, and $p = 0.0013$ by log-rank test, respectively).

Only the combined group showed significantly longer survival compared with the neutron irradiation control ($p = 0.0042$ by log-rank test). In addition, the combined group showed the longest MST and the highest percent increase in life span value among all treated groups (65.2%; Table. 1), as well as a significantly longer survival compared with the other BNCT groups (vs. BPA [i.v.]: $p = 0.0152$, vs. PBC [CED]: $p = 0.0058$ by log-rank test).

Group	n	Survival time
		Median
Untreated controls	6	23.0
Irradiated controls	6	26.0
BPA (i.v.)	6	30.0
PBC (CED)	5	31.0
PBC (CED) + BPA (i.v.)	6	38.0

Table. 1 Survival times of F98 glioma-bearing rats following tumor implantation.

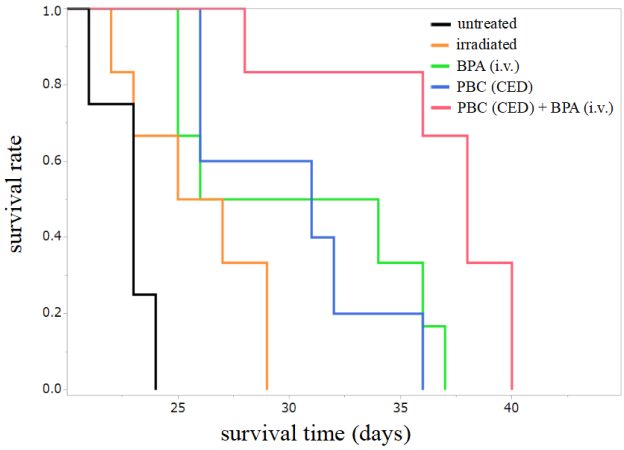

Fig. 1 Kaplan-Meier survival curves for F98 glioma-bearing rats of untreated controls, neutron irradiation only, BNCT with BPA (i.v.), BNCT with PBC (convection enhanced delivery; CED), and BNCT in combination with with BPA (i.v.) and PBC (CED).

Ongoing study

We developed another novel boron drug (AAL) that combines the characteristics of BPA and BSH, which has a boron cluster in its structure and targets an amino acid transporter. As in the main study, BPA was administered i.v. and AAL was administered by CED, neutron irradiation was performed on F98 glioma bearing rats.

As a result, in combination of AAL (CED) and BPA (i.v.), a significant prolongation in survival time was obtained compared with the single agent groups (data not shown).

We will continue this study; the study results will be published in the future.

PR5-7

Development of *S*-Alkylthiododecaborate Containing *p*-Boronophenylalanine for BNCT

Y. Hattori, I. Nakase[1], M. Katayama[1], M. Suzuki[2], and M. Kirihata

Research Center of BNCT, Osaka Prefecture University

[1]Organization for Research Promotion, Osaka Prefecture University

[2]KURNS, Kyoto University

INTRODUCTION: BNCT is based on the nuclear fission reaction of a ^{10}B-atom with thermal and/or epithermal neutrons to yield high linear energy transfer α particles (^{4}He) and recoiling ^{7}Li nuclei in tumor cells, and has attracted attention in term of its potential therapeutic effects on malignant tumors.[1] A boron delivery agent (boron carrier) with high therapeutic efficiency and low adverse effects is crucial for successful BNCT. Although many kinds of boron compounds such as amino acids, nucleic acids and sugars have been reported as boron carriers for BNCT, only two compounds are used clinically for the treatment of cancer with BNCT: *p*-borono-L-phenylalanine (BPA, **1**) and mercapto-*closo*-undeca-hydrododecaborate (BSH, **2**) (Fig. 1).[2,3] Unusual boron amino acids represented by BPA have long being recognized as tumor seeking compounds due to structural analogy to usual L-amino acid, because L-amino acid transport system (LAT1) is enhanced compared with normal tissues to sustain the proliferation of tumor cells.[4]

In the course of our developing studies on new boron carrier for BNCT, we have designed and synthesized thiododecaborate ($[B_{12}H_{11}S]^{2-}$) unit-containing L-amino acids, a new class of tumor seeking and water soluble amino acid. Recently, medium-chain alkyl sulfoniodododecaborate ($[B_{12}H_{11}S^{+}$octyl$]^{-}$) unit containing amino acids (AS-DBA, **3**) showed high cell membrane permeability, low cytotoxicity and high water-solubility, and these compounds could deliver large amount of boron to several kinds of tumor cells.[5]

To develop a new boron carrier for BNCT, we designed and synthesized novel *p*-boronophenylalanine based boron carrier (BADB1-3, **2a-c**), in which the medium-chain alkyl sulfoniododecaborate is linked to *C* terminal of L-BPA. These novel boron compounds have enhanced hydrophobicity and cell membrane permeability owing to a reduced negative charge (-1) and the introduced alkyl chain. Here, we present the biological evaluation of novel boron compounds **2a-c** as boron carriers for BNCT.

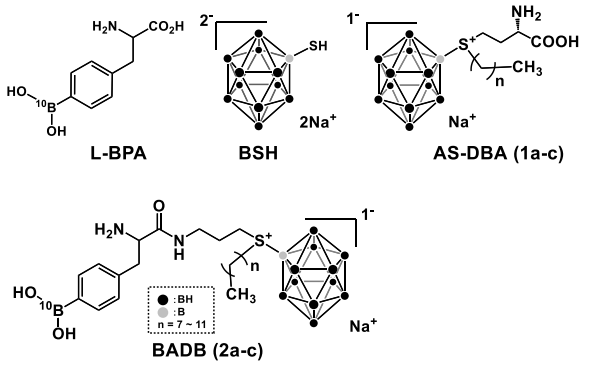

Fig. 1. Boron Carrier.

RESULTS and Discussion: To evaluate the BADBs, we examined the cytotoxicity, water-solubility, and cellular uptake of AS-DBAs, and compared them with that of BPA, BSH, and DBA.

The water solubility of BADB-1 (S-Octyl, **2a**) was higher than that of BPA and **2b**, **2c** (BSH, **1a-c**, **2a**: >40 g/L, BPA: 1.6 g/L, 2b,c: <10g/L). The cytotoxicity of BADB **1a** was marginally low (IC_{50} of **1a** is 0.1 mM in F98 glioma and B16 melanoma cells). However, the cytotoxicity of **2b**,**c** was higher than 0.1mM.

In the next step, we measured the boron concentrations in tumor cells by ICP-OES (Fig. 2). The intracellular boron concentration of BADB-1 in C6 and B16 cells was 2-3 times greater than that of L-BPA, with fewer doses of the compound.

Our results show that BADB-1 is useful candidate as ^{10}B carriers. The *in vivo* evaluation of BADB-1 is ongoing and the results will be reported soon.

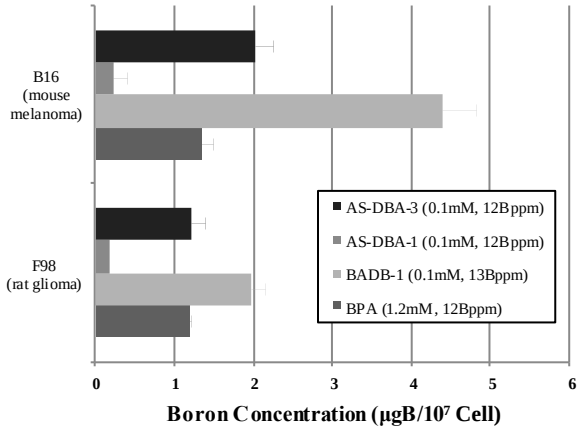

Fig. 2. Boron-uptake test against cancer cells.

REFERENCES:

[1] H. A. Soloway *et al.*, Chem. Rev., **98** (1998) 1515-1562.

[2] M. Ichihashi *et al., Journal of Investigative Dermatology*, **78** (1982) 215-218.

[3] H. A. Soloway *et al., J. Med. Chem.*, **10** (1967) 714-717.

[4] K. kaira *et al*., *Clin. Cancer Res*., **13** (2007) 6369-6378.

[5] Y. Hattori *et al*, *Peptide Science 2016*, 115–116.

30P5-10

PR5-8 *In vivo* Evaluation of Novel Boron-Containing Compound for BNCT

T. Tsurubuchi[1], K. Matsumoto[2], R. Ubagai[2], K. Nakai[1] F. Yoshida[1], A. Zaboronok[1], M. Shirakawa[3] M. Suzuki[4], Y. Sakurai[4], H. Tanaka[4], and A. Matsumura[1]

[1]*Department of Neurosurgery, Faculty of Medicine, University of Tsukuba*

[2]*Institute for Innovation, Ajinomoto Co., Inc.*

[3]*Department of Pharmaceutical Sciences, University of Fukuyama*

[4]*KURNS, Kyoto University*

INTRODUCTION: Boron neutron capture therapy (BNCT) is gaining attention as a state-of-the-art minimally invasive cancer treatment [1]. Up to now, clinical studies using boronophenylalanine (BPA) and sodium borocaptate (BSH) as ^{10}B delivery agents for neutron capture reaction have been conducted [2,3]. However, continuous administration of their high concentrations is needed to keep sufficient ^{10}B tumor concentration. Therefore, we have developed novel boron-containing low molecular compounds efficient in accumulation and retention in tumor.

EXPERIMENTS: 3x10^6 of mouse colon carcinoma (CT26) cells were injected in the right thigh of 5-week-old female Balb/c mice. Two weeks after injection tumor-bearing (avg. 360 mm^3) mice were used in this study. Two dosage of compound A (88.8 mg/kg with 24.1 mg[^{10}B]/kg, n=5 and 250 mg/kg with 68.3 mg[^{10}B]/kg, n=6) were administrated by tail vein injection 24 hours before irradiation. Fructose-BPA (500 mg/kg with 24.1 mg[^{10}B]/kg, n=5) was administrated by tail vein injection 2 hours before irradiation as a positive control. Groups with irradiation only (n=4) and untreated mice (n=6) were used as controls.

The irradiation was performed with thermal neutrons with a flux of 1.8-4.0 x 10^{12} neutrons/cm^2 over 1 hour at Kyoto University Research Reactor (KUR).

The tumor size and body weight were measured in the period starting prior the treatment till 26 days after irradiation. And the tumor volume (mm^3) was calculated using the following formula.

Tumor volume = (long diameter) x (short diameter)^2 / 2

RESULTS: The results of thermal neutron irradiation is shown in Fig. 1. The effect on body weight in all individuals was not found (a). Compound A administrated group and BPA administrated group significantly suppressed the tumor growth as compared with other control groups (b). In particular, Compound A (250 mg/kg) administrated group showed tumor growth inhibitory effect comparable to BPA administrated group until 18th day.

We assume that Compound A is a candidate boron compound for further investigation that showed high accumulation in tumor even 24 hours after injection.

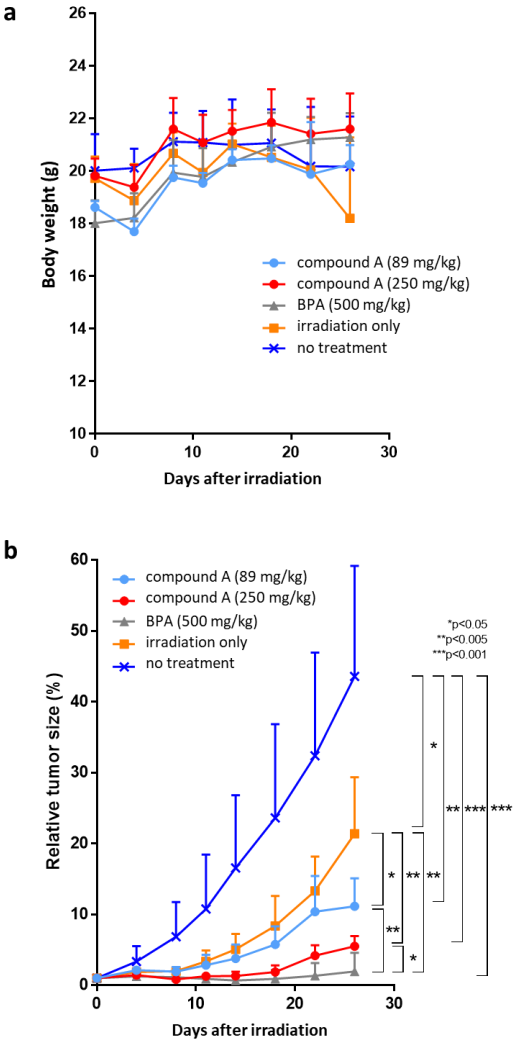

Fig. 1. BNCT of tumor-bearing mice with ^{10}B-enriched compounds. (a) Mice body weight after thermal neutron irradiation. (b) Tumor growth ratio after 1 hour - thermal neutron irradiation (1.8-4.0 x 10^{12} neutrons/cm^2) with the injection of compound A 24 hours, and BPA 2 hours before irradiation, and irradiation only and untreated groups as controls. Comparison using the t-test was performed using mice 26 days after irradiation.

REFERENCES:

1. Sato E, Zaboronok A, Yamamoto T, et al., *J Radiat Res.,* 2018 Mar 1;59(2):101-107.
2. Yamamoto T, Nakai K, Tsurubuchi T, *et al., Appl Radiat Isot.,* 2009 Jul;67(7-8 Suppl):S25-6.
3. Wang LW, Chen YW, Ho CY, *et al., Int J Radiat Oncol Biol Phys.* 2016 May 1;95(1):396-403.

PR5-9 Development of an actively-targeted, phenylboronic acid-installed nanoparticle towards next-generation boron neutron capture therapy

A. Kim[1], Y. Matsumoto[2,3], M. Suzuki[4], N. Fukumitsu[5], and Y. Nagasaki[1,6,7]

[1]Department of Materials Sciences, Graduate School of Pure and Applied Sciences, University of Tsukuba,[2]Faculty of Medicine, University of Tsukuba, [3]Proton Medical Research Center, University of Tsukuba Hospital, Radiation Oncology Research Laboratory, [4]Institute for Integrated Radiation and Nuclear Science, Kyoto University, [5]Department of Radiation Oncology, Kobe Proton Center, [6]Masters Program in Medical Sciences, Graduate School of Comprehensive Human Sciences, University of Tsukuba, [7]Center for Research in Isotopes and Environmental Dynamics (CRiED), University of Tsukuba

INTRODUCTION

The boron neutron capture therapy (BNCT) is based on a binary approach that combines non-invasive thermal neutron irradiation and administration of boron-10 (^{10}B) compounds, which can result in small-range nuclear fission, followed by tumoricidal effects. For the last decade, much efforts have been made on the establishment of safe and stable neutron sources such as linear accelerators, so that in the near future the BNCT could propagate much rapidly and widely, through the local hospitals. Nevertheless, most of the BNCT agents, whether in pre-clinical development or clinical trials, have shown significant obstacles, preventing further clinical translations. For instance, one of only clinically approved BNCT agent, boronophenylalanine (BPA), is a low-molecular weight compound with extremely rapid renal clearance, thus requires continuous intravenous infusion, usually begins few hours before the irradiation and even continues during the irradiation. Thus, the boron concentration in the blood circulation at the moment of neutron irradiation should be considerably high, not only narrowing down therapeutic window of the BNCT agent, but also inducing critical adverse effects to the non-target tissues.

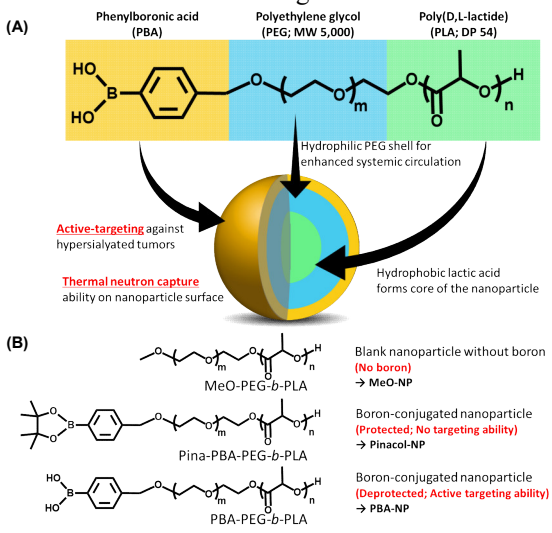

Figure 1. (A) Schematic design of the PBA-installed nanoparticle (PBA-NP). (B) Chemical structure of the MeO-PEG-*b*-PLA, Pina-PBA-PEG-*b*-PLA, and PBA-PEG-*b*-PLA.

Herein, to address aforementioned limitations, we designed and synthesized phenylboronic acid (PBA)-installed polymeric nanoparticles, as illustrated in Fig. 1. The PBA groups on the nanoparticles not only grant thermal neutron capturability but also provide strong affinity to the sialic acid, supposed to facilitate effective accumulation of the nanoparticles to hypersialyated metastatic tumor cells.

EXPERIMENTS

Alkoxylated 4-(hydroxymethyl)phenylboronic acid pinacol ester was used as an initiator for anionic ring-opening, sequential polymerization of ethylene oxide and D, L-lactic acid. Accordingly, ^{1}H NMR analysis confirmed that prepared polymer is comprised of pinacol ester-protected PBA (Pina-PBA), hydrophilic polyethylene glycol (PEG) chain (*c.a.* 110 units), and hydrophobic poly(lactic acid) (PLA) chain (*c.a.* 40 units), hence abbreviated as Pina-PBA-PEG-*b*-PLA (Fig. 1B). Furthermore, deprotection of the pinacol ester was conducted by transesterification with 1,4-phenylenediboronic acid, resulted in PBA-PEG-*b*-PLA. Those polymers were separately dissolved in dimethylformamide and subsequently dialyzed against pure water, to remove organic solvent and to generate the nanoparticles through hydrophilic-hydrophobic interactions. Two different PBA-installed nanoparticles, either with pinacol protection (Pinacol-NP) and without any protection (PBA-NP), were prepared and analyzed by static and dynamic light scattering measurements. In vivo feasibility of those nanoparticles was evaluated on a C57BL6/j mice model, subcutaneously inoculated with B16-F10 mouse melanoma cells on the right thigh. When average tumor volume was reached around 50 mm^3, the mice were subcutaneously injected either with saline, BPA, Pinacol-NP, or PBA-NP (n = 6). It is noteworthy that applied timeframe between drug injection and thermal neutron irradiation was different between low molecular weight compounds groups (2 h for saline and BPA) and nanoparticles groups (48 h for Pinacol-NP and PBA-NP), as their pharmacokinetics were found to be significantly altered. All the irradiation experiments were carried out in the Institute for Integrated Radiation and Nuclear Science, Kyoto University.

RESULTS

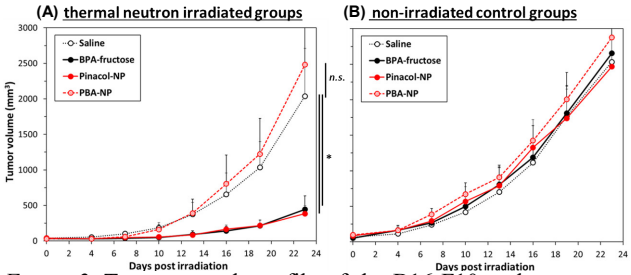

Figure 2. Tumor growth profile of the B16-F10 melanoma tumor bearing mice, subcutaneously injected with saline, BPA-fructose (24 mg ^{10}B/kg), Pinacol-NP and PBA-NP (0.24 mg ^{10}B/kg). (A) thermal neutron irradiated groups and (B) non-irradiated control groups. (n = 6, * $p < 0.05$)

Aforesaid nanoparticles, either with or without pinacol ester protection, were highly stable in physiological condition, as their average hydrodynamic diameters were sustained between 70—80 nm for at least 24 h (data not shown). This suggests that the nanoparticles might demonstrate long-term circulation and attenuated renal clearance profile, once they enter the bloodstream. Notably, in vivo irradiation experiments ensured feasibility of the Pinacol-NP, as it exhibited comparable antitumor effects with the BPA-fructose complex (Fig. 2), even at a 100-folds lower effective dose (0.24 mg ^{10}B kg/kg for Pinacol-NP and PBA-NP, and 24 mg ^{10}B mg/kg for BPA). On the contrary, the PBA-NP exhibited almost no antitumor effect as its tumor growth profile is similar to the saline, presumably because of non-specific association with sialic acids on circulating cells and enzymes, which might accelerate the clearance through reticuloendothelial system. This speculation could be supported by a significantly lower tumor accumulation of the PBA-NP, compared to the Pinacol-NP (data not shown).

PR5-10 Design, Synthesis, and Evaluation of Glucose-type Boron Carriers for BNCT

S. Aoki[1], Y. Hisamatsu[1], K. Tamura[1], H. Ueda[1], B. Shahni[1], M. Suzuki[2], S. Masunaga[2], N. Kondo[2], Y. Sakurai[2], and K. Ono[2]

[1]*Faculty of Pharmaceutical Sciences, Tokyo University of Science*

[2]*KURNS, Kyoto University*

INTRODUCTION: Boron neutron capture therapy (BNCT) is one of powerful therapies for local tumor control in the treatment of brain tumor, melanoma, and so on [1]. To date, only two boron-containing drugs, L-4-boronophenylalanine (BPA) and BSH (sodium mercaptoundecahydrododecaborate, $Na_2B_{12}H_{11}SH$), have been approved as clinically test compounds, and development of better BNCT agents is highly required.

It is well described that tumor cells metabolize D-glucose by anaerobic glycolysis, which provides 2 moles of ATP per mole of D-glucose. Therefore, the rapid growth and proliferation of tumor cells demand a drastic increase in D-glucose uptake and metabolite flux using glucose transporters (GLUT) and sodium dependent glucose cotransporters (SGLT, known as the Warburg effect. An enhanced uptake of D-glucose and glucose transporter expression are common in cancer cells and provide clinically valid targets for cancer diagnosis and treatment using derivatives such as 2-deoxy-2-[^{18}F]fluoro-D-glucose ([^{18}F]FDG) and 2-deoxy-D-glucose (2-DG). In this paper, we report new BNCT agents **4a-d** based on the D-glucose scaffold having borane at the C2 position of D-glucose by the hydroboration of D-glucal derivatives **1** that contain a double bond between the C1 and C2 positions (Fig. 1) [2].

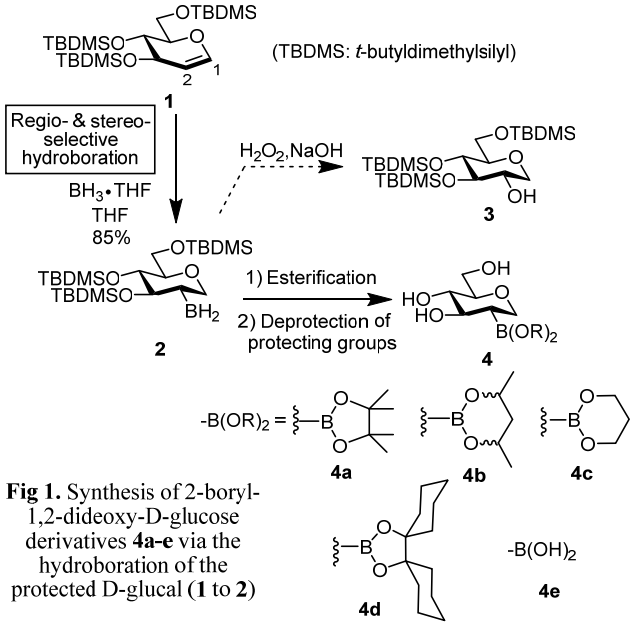

Fig 1. Synthesis of 2-boryl-1,2-dideoxy-D-glucose derivatives **4a-e** via the hydroboration of the protected D-glucal (**1** to **2**)

EXPERIMENTS and RESULTS: Synthesis of 2-boryl-1,2-dideoxy-D-glucose derivatives **4** was carried out via the regio- and stereoselective hydroboration of the protected D-glucal **1**, as shown in Figure 1. Hydroboration is typically used to convert alkenes to alcohols. A boryl intermediate such as **2** is obtained by the treatment of an alkene with a borane reagent, and are then generally converted to alcohol such as **3** by treatment with hydrogen peroxide (H_2O_2) with the retention of stereochemistry. However, we use the boryl intermediate **2** for the synthesis of BNCT agents **4a-e** after esterification of **2** with diols and deprotection of the hydroxyl groups, without the reaction with H_2O_2. Cytotoxicity and cellular uptake activity of **4a-d** in cancer cells was evaluated by MTT assay and ICP-MS (inductivity coupled plasma-mass spectrometer) (Fig. 2). These data and the results of enzymatic phosphorylation indicate that **4e** could be a lead compound of tumor-accumulating BNCT agents.

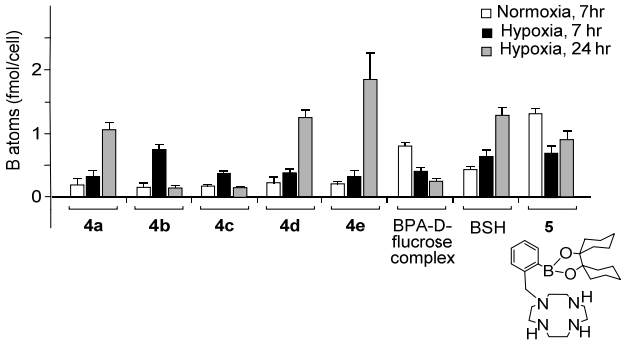

Fig. 2. Cellular uptake assays of **4a-e,** BPA-D-fructose complex, BSH, and the reference compound **5** [3] in HeLa S3 cells, as determined on ICP-MS after incubation with 30 μM of the drugs under normoxic and hypoxic conditions at 37 ºC for 7−24 hr. Data represent the mean ±SD of at least three replicates.

The advantages of **4a-e** are: i) **4a-e** have high solubility in water and low toxicity; ii) **4a-e** are translocated to the cancer cells through GLUT1 and iii) the uptake pathway of 2-borylsugar is different from those of BSH and BPA, which allows us to use the combination of 2-borylsugar, BSH, and/or BPA. These findings suggest that 2-boryl-1,2-dideoxy-D-glucose derivatives, especially **4e** could function as a lead compound of tumor-accumulating BNCT agents. The improvement of the design of these B-carriers are now in progress.

REFERENCES:

[1] a) R. F. Barth *et al.*, *Clin. Cancer Res.*, **11** (2005) 3987-4002. b) R. F. Barth *et al., Rad. Oncol*. **7** (2012) 146-166.

[2] T. Itoh, *et al., Bioorg. Med. Chem.* **26** (2018) 5922-5933.

[3] M. Kitamura *et al., Inorg. Chem.* **50** (2011) 11568-11580.

PR5-11 Investigation of therapeutic potential of poly(vinyl alcohol)-boronophenylalanine complexes in subcutaneous hypovascular tumor models

T. Nomoto, Y. Yao, K. Kanamori, M. Suzuki[1], Y. Sakurai[1], N. Nishiyama

Laboratory for Chemistry and Life Science, Institute of Innovative Research, Tokyo Institute of Technology
[1]KURNS, Kyoto University

INTRODUCTION: Boronophenylalanine (BPA) is the most powerful drug in clinical boron neutron capture therapy (BNCT). BPA can accumulate selectively within target tumors through the large neutral amino acid transporter 1 (LAT1), which is overexpressed on many cancer cells [1]. Although BPA has exhibited strong BNCT effect, its therapeutic effect has been sometimes compromised by quick clearance from tumors. The clearance from the tumor may be due to antiport mechanism of LAT1. Intracellular BPA may be exchanged with extracellular amino acids when extracellular BPA concentration decreases [2].

We recently found that poly(vinyl alcohol) can form the complex with multiple BPA molecules through boronate esters in aqueous solution, and the complex, termed PVA-BPA, can be internalized into cells through LAT1-mediated endocytosis, thereby avoiding the untoward efflux and improving retention in tumors. Importantly, in subcutaneous hypervascular CT26 tumor models, PVA-BPA showed augmented therapeutic effect compared with conventional fructose-BPA complexes. In this study, to examine whether PVA-BPA can exhibit such therapeutic effect even in a hypovascular tumor model, we evaluated the antitumor activity of PVA-BPA in a subcutaneous BxPC3 tumor model.

EXPERIMENTS: BALB/c nude mice bearing subcutaneous BxPC3 tumors were used in this study. PVA-BPA or fructose-BPA complex was intravenously injected to the mouse (10 mg BPA/mouse), and the thermal and epithermal neutrons were irradiated to the tumor using KUR 3 h after the injection. Size of the tumor was measured using a caliper, and tumor volume (V) was calculated using the following equation:

$$V = 1/2 \times a \times b^2$$

where a and b denote major and minor axes of a tumor, respectively.

RESULTS: The pancreatic cancer BxPC3 cells are reported to form a subcutaneous hypovascular tumor having rich stroma inhibiting penetration of drugs, which characteristics can be generally found in intractable cancers. The key to treating such stroma-rich tumors is efficient penetration of drugs in the tumor, and macromolecules sometimes suffer from limited penetration.

As shown in Fig. 1, both fructose-BPA and PVA-BPA exhibited strong BNCT effect, and PVA-BPA more efficiently suppressed the tumor growth. The possible explanation for this enhancement should be prolonged tumor retention of PVA-BPA. The quick clearance of fructose-BPA from the tumor might compromise the therapeutic efficacy. It is noteworthy that the use of PVA did not deteriorate the therapeutic potential, which may be explained by the molecular weight of PVA. We used PVA with the molecular weight of roughly 10,000. This smaller molecular weight compared with the other macromolecules or nanoparticles (including liposomes and polymeric micelles) might facilitate the intratumoral penetration. PVA should offer great potential as the additive boosting therapeutic potential of BPA.

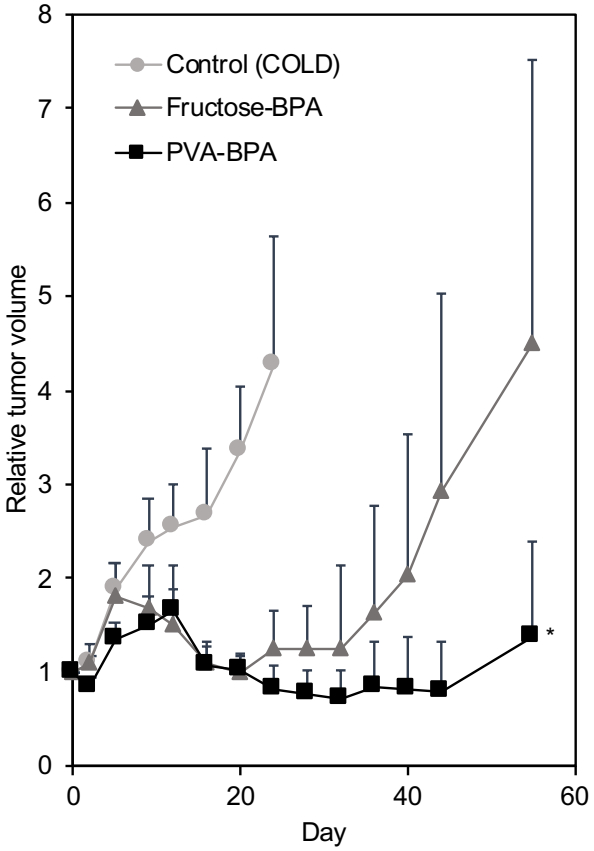

Fig. 1 Antitumor effect of fructose-BPA and PVA-BPA. At day 0, the samples were injected, and neutrons were irradiated to the tumor.

REFERENCES:

[1] M. J. Luderer *et al.*, *Pharm. Res.*, **32** (2015) 2824-2836.
[2] A. Wittig *et al.*, *Radiat. Res.*, **153** (2000) 173-180.

PR5-12 Examination of therapeutic potential of novel boronated polymers

T. Nomoto, M. Suzuki[1], Y. Sakurai[1], W. Kurosawa[2], K. Matsumoto[2], R. Ubagai[2], Y. Kitahara[2], Y. Suga[2], J. Okamatsu[2], Y. Iwai[2], N. Nishiyama[3]

Laboratory for Chemistry and Life Science, Institute of Innovative Research, Tokyo Institute of Technology

[1]*KURNS, Kyoto University*

[2]*Ajinomoto Co., Inc.*

[3]*Innovation center of NanoMedicine, Kawasaki Institute of Industrial Promotion*

INTRODUCTION: In boron neutron capture therapy (BNCT), successful treatment requires boron drugs that can selectively target tumors. Although boronophenylalanine (BPA) has demonstrated its therapeutic potential in many clinical studies, BPA can treat only the tumors overexpressing LAT1. Thus, novel boronated compounds that can accumulate within tumors through the other mechanism should be developed to extend the application of BNCT.

In this regard, polymeric carriers including polymer conjugates and polymeric micelles have attracted recent attention, because these polymeric carriers offer efficient tumor accumulation through enhanced permeability and retention effect [1]. In particular, polymer conjugates have the advantages of efficient penetration in tumors as well as quick clearance from normal tissues owing to their smaller size compared with polymeric micelles [2]. We recently synthesized biocompatible boronated polymers whose molecular weight can be easily controlled. We found that these polymers exhibited molecular weight-dependent tumor accumulation and retention in the blood. In this study, we compared the therapeutic effect of the optimized polymer with that of sorbitol-BPA complexes.

EXPERIMENTS: BALB/c nude mice bearing subcutaneous BxPC3 tumors were used in this study. Boronated polymers or sorbitol-BPA complexes were intravenously injected to the mouse (10 mg BPA/mouse), and the thermal and epithermal neutrons were irradiated to the tumor using KUR 2.5 h after the injection. Size of the tumor was measured using a caliper, and tumor volume (V) was calculated using the following equation:

$$V = 1/2 \times a \times b^2$$

where a and b denote major and minor axes of a tumor, respectively.

RESULTS: As shown in Fig. 1, our synthesized polymer exhibited comparable antitumor effect to sorbitol-BPA. Considering that sorbitol-BPA is the most powerful boron drug in clinical situations, our polymer may also have great potential for clinical BNCT. It is also important that the polymer did not significantly decrease the body weight of the mice, indicating that the polymer should not have acute toxicity. These results suggest that our polymer may be useful in the clinical application.

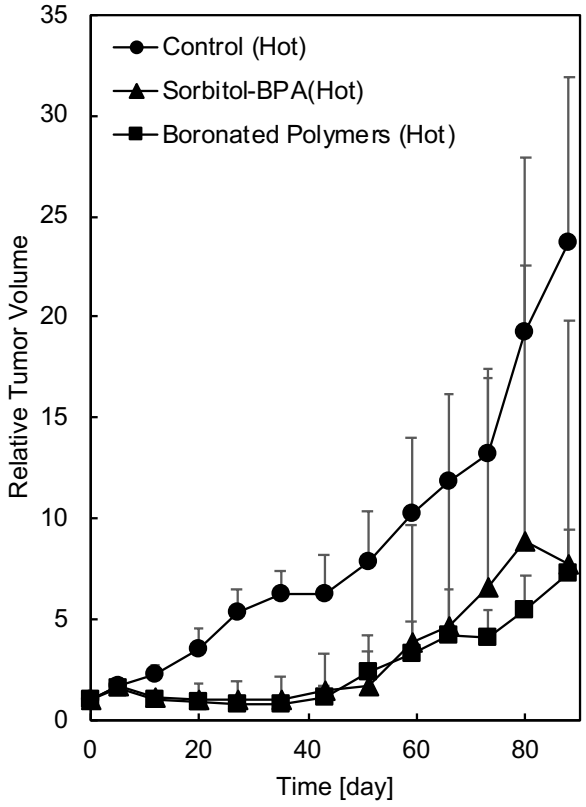

Fig. 1 Antitumor effect of boronated polymers and sorbitol-BPA. At day 0, the samples were injected, and neutrons were irradiated to the tumor.

REFERENCES:

[1] T. Nomoto *et al.*, *Biomaterials,* **178** (2018) 583-596.
[2] P. Mi, *et al.*, *J. Control. Release* **254** (2017) 1-9.

PR5-13 Development of *closo*-Dodecaborate-Conjugated Serum Albumins as Novel Boron Delivery Carriers to Tumor for BNCT

H. Nakamura[1], S. Ishii[1], K. Kawai[1,2], S. Wu[1,2], S. Sato[1], and M. Suzuki[3]

[1] *Laboratory for Chemistry and Life Science, Institute of Innovative Research, Tokyo Institute of Technology*
[2] *School of Life Science and Technology, Tokyo Institute of Technology*
[3] *Institute for Integrated Radiation and Nuclear Science, Kyoto University*

INTRODUCTION: Boron neutron capture therapy (BNCT) has been attracting growing interest as one of the minimally invasive cancer therapies. The phase II clinical study of accelerator-based BNCT for the treatment of brain tumor and head and neck cancer patients has been completed in Japan. We focused on a serum albumin as a nano biocarrier. Albumin is known to accumulate in malignant and inflamed tissues due to enhanced permeability and retention (EPR) effect. We developed maleimide-functionalized *closo*-dodecaborate (MID) for conjugation to bovine serum albumin (BSA).[1] In this paper, we designed disulfide bond containing MID (SSMID) for identification of the biding sites on albumin by MS/MS analysis.

EXPERIMENTS: For the modification with SSMID, a solution of BSA (final concentration 100 μM) in PBS buffer was added SSMID (final concentration 10 mM). The solution was briefly vortexed and incubated at room temperature for 12 h. The mixture was added 5×SDS-PAGE sample buffer, boiled at 95 °C for 5 min and subjected to SDS-polyacrylamide gel (10% acrylamide) electrophoresis (PAGE). The gel was stained by CBB and obtained image with a Molecular Imager ChemiDoc XRS (Bio Rad). The entire acrylamide gel was rinsed with ultrapure water for a few hours, and bands (spots) of interest were excised with a clean scalpel. The gel pieces cut into a cube size was transferred to a tube and they were washed with ultrapure water for 10 minutes three times. The gels pieces were treated with 100 μL of 100 mM ammonium bicarbonate/acetonitrile (1:1, vol/vol) solution and incubate tubes for 10 min at 37 °C. The supernatant was removed and the gels were treated with 100 μL of 100 mM ammonium bicarbonate solution and incubate tubes for 10 min. The supernatant was removed and the gels were treated with 100 μL of 100 mM ammonium bicarbonate/acetonitrile (1:1, vol/vol) solution and incubate tubes for 10 min at 37 °C. The supernatant was removed and the gels were treated with 50 μL of acetonitrile and incubate tubes at 37℃ until gel pieces become white and shrink. The shrunk gels pieces were treated with 50 μL of 100 mM DTT / 100 mM ammonium bicarbonate solution, vortex briefly and incubate tubes for 30 min at 37 °C. The tubes were cooled down to room temperature and the supernatant was removed completely. For capping free SH groups, 50 μL of 100 mM iodoacetamide / 100 mM ammonium bicarbonate solution was added and incubated for 30 min at room temperature in the dark. The gels pieces were washed with 100 μL of 100 mM ammonium bicarbonate solution and 100 μL of 100 mM ammonium bicarbonate/acetonitrile (1:1, vol/vol) solution. The gel pieces were shrunk with acetonitrile. A solution of trypsin in Tris buffer (pH 8.0) were added to the dry gel pieces. The samples were incubated overnight at 37℃. The digestion was quenched with adding TFA (final 0.1 %), and the samples were desalinated through Cleanup C18 Pipette Tips (Agilent). The solution (2 μL) were mixed on MALDI plate mix with 1 μL of CHCA.

RESULTS: Since the *closo*-dodecaborate of SSMID could be cleaved by DTT after conjugation with BSA, SSMID conjugation sites on BSA were identified by MS/MS analysis. After in-gel digestion was performed with trypsin, the resulting peptide fragments were analysed by MALDI TOF-MS. The mascot analysis identified at least three lysine residues, Lys221, Lys413 and Lys431, as conjugated sites in addition to Cys34 (Fig. 1).[2]

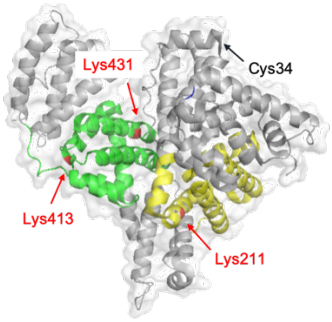

Fig. 1. MID-binding sites of albumin (PDB: 1E7F). Four SSMID modification residues (Cys34, Lys211, Lys413 and Lys 431) were identified by MS/MS analysis.

Because these Lys residues are located in the drug binding sites 1 and 2 in albumin, it is plausible that MID and SSMID are bound to these drug binding sites to form a covalent bond to the protein through these Lys residues. The fact that MID-BSA conjugation was prevented in the presence of warfarin and ibuprofen [3] also supports our hypothesis. We are now in a position to develop protein-based boron carriers with multiple functions, such as for in vivo imaging and active targeting in BNCT.

REFERENCES:

[1] S. Kikuchi, *et al.*, J. Control. Release, **237** (2016) 160-167.
[2] S. Ishii, *et al.*, Org. Biomol. Chem. in press (DOI: 10.1039/C9OB00584F).
[3] H. Nakamura, *et al.*, Pure Appl. Chem. **90** (2018) 745-753.

PR5-14 Experiment on the Therapeutic Effect of Doxorubicin-Encapsulated Boron Liposome by Thermal Neutron Irradiation

M. Shirakawa[1,2], K. Nakai[2], F. Yoshida[2], M. Suzuki[3], T. Takata[3], A. Matsumura[2] and H. Tomida[1]

[1]*Department of Pharmaceutical Sciences, University of Fukuyama*
[2]*Department of Neurosurgery, Faculty of Medicine, University of Tsukuba*
[3]*KURNS, Kyoto University*

INTRODUCTION: There has been a growing interest in Boron Neutron Capture Therapy (BNCT) because they are expected to be next generation in minimally invasive cancer treatment. And the clinical trial was started using boronophenylalanine (BPA) as boron drugs in 2017. However it is difficult that all patients fully remit from cancer by BNCT only. The purpose of this study was to examine whether the combination therapy (BNCT and chemotherapy) using boron liposome get higher anti-tumor effect. Therefore we investigated the therapeutic effect of doxorubicin-encapsulated boron liposome prepared using PBL[1].

EXPERIMENTS:

1. *Preparation of PBL modified liposome*

PBL modified liposome were prepared using bare liposome by post insertion method[2]. The bare liposome were prepared from DSPC and cholesterol (1:1, molar ratio) by conventional lipid-film method[3]. The resulting liposome were extruded with an extruder through a polycarbonate membrane with a 100-nm pour size, yielding each liposomes.

2. *Encapsulation of doxorubicin (DXR) into PBL modified liposome*

The liposome encapsulating doxorubicin were prepared by the pH-loading method[4] and measured inclusion amount by fluorescence spectrometry. DXR concentration of the resulting liposome suspension was 3.3 mM.

3. *Combination therapy using doxorubicin-encapsulated PBL-liposome for tumor-bearing mice*

The tumor-bearing mice were prepared by grafting 5 x 10^6 of mouse colon carcinoma cells (CT26) to the right thigh of female BALB/cA mice (4 weeks old, weighing 16-20 g) to have a tumor diameter of 6-8 mm.

Table.1) Characterization of administration samples.

	PBL-liposome	DXR-encapsulated PBL-liposome	BPA
^{10}B conc. [mgB/kg]	10	10	10
Lipid conc. [mg/mL]	650	500	—
Interval time before irradiation [hour]	12 24	24	2

About 12 days after, each sample (Table.1) was administrated by tail vein injection before irradiation. And the irradiation was performed with thermal neutrons with a flux of 1.8-4.0 x 10^{12} neutrons/cm^2 over 1 hour.

The tumor size was measured over time after the irradiation until Day 26 and calculated using the following formula.

Tumor size [mm^3] =
(Long diameter [mm]) x (Short diameter [mm])^2 / 2

RESULTS: As shown in Fig. 1, significant body weight loss was observed in mice administration of DXR-encapsulated PBL-liposome. And all irradiated mice in this group died within 20 days. This suggests that side effect of DXR in the liposome occur by irradiation.

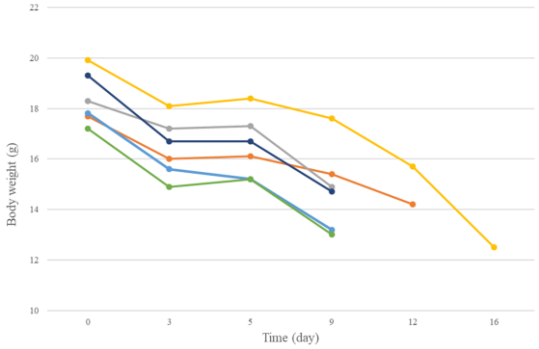

Fig.1) Body weight of mice after irradiation with the injection of DXR-encapsulated PBL-liposome. Data represent each result for six mice.

As shown in Fig. 2, PBL-liposome significantly suppressed the tumor growth as compared to other control groups, indicating its excellent candidate drug potential for BNCT.

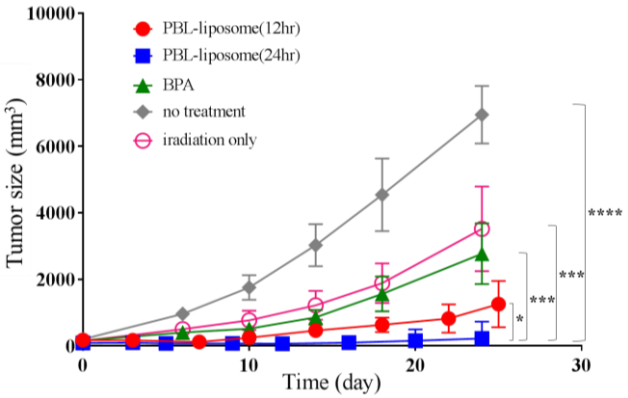

Fig.2) Antitumor effect of BNCT by PBL-liposome.

REFERENCES:

[1] M. Shirakawa, K. Nakai, A. Matsumura., Japanese Patent No. 6206925 and European Patent No.2889302.
[2] Paul S. Uster *et al.*, *FEBS Letters* 1996; 386: 243-246.
[3] A.D. Bangham *et al.*, *J. Mol. Biol*. 1965; 13: 238-252.
[4] L.D. Myer *et al.*,*Biochem. Biophys. Acta*. 1986; 857: 123-126.

PR5-15 DNA aggregates bearing BODIPY units as drugs for BNCT

K. Tanabe,[1] M. Suzuki,[2] R. Kurihara,[1] W. Asahi[1]

[1]*College of Science and Engineering, Aoyama Gakuin University*

[2]*KURNS, Kyoto University*

INTRODUCTION: The functionalized oligonucleotides have been widely used for various scientific fields including gene therapy or diagnosis as well as DNA-based drugs. However, artificial oligonucleotides required toxic gene transfer agent such as cationic lipid for cellular uptake, and therefore there are increasing demands for easy methods to introduce them into cells. Recently, we reported that amphiphilic oligonucleotides with hydrophobic units formed aggregates in aqueous solution, and these aggregates showed unique properties.[1] The aggregate consisted of ODNs smoothly penetrated cell membrane and showed high stability in living cells. Thus, the aggregate act as favorable functional oligonucleotides in living cells. In this study, we attempted to apply artificial oligonucleotides bearing hydrophobic fluorophore BODIPY at strand end (BODIPY-ODN) to drugs for BNCT. We prepared these artificial oligonucleotides and characterized their properties in living cells and tissues.

EXPERIMENTS:

Measurement of critical aggregate concentration (CAC). To form the aggregate, indicated concentrations of BODIPY-ODN in phosphate buffer (5 mM, pH 7.0) were added to 10 μM indocyanine green in acetonitrile. After the removal of solvent in vacuo, the resulting mixture was dissolved in water to form the aggregate and the fluorescence spectra of the resulting samples were measured using excitation at 774 nm.

In vivo experiments using BODIPY-ODN. BODIPY-ODN (100 μM) in 50 μL of saline were intratumorally injected into the A549 tumor-bearing mice. After 1 h, the mice were irradiated (neutron, 1 MW) for 45 min at KUR. Then, the change of the size of the tumors were measured.

RESULTS: Initially, we evaluated an aggregation property of 10 mer BODIPY-ODN. We identified the aggregate formation by measurement of fluorescence of indocyanine green (ICG). ICG showed bright emission in aqueous solution, while encapsulation of ICG into the aggregate consisting of amphiphilic molecules led to a suppression of fluorescence emission due to the concentration quenching even in the aqueous solution. Thus, we evaluated the aggregate formation of BODIPY-ODN by monitoring of ICG emission. As a result, we observed robust fluorescence of ICG in the absence of BODIPY-ODN, while the addition of BODIPY-ODN led to decrease of its emission intensity. Thus, BODIPY-ODN formed aggregate that encapsulated ICG in their hydrophobic core. The CAC values, which indicate the concentration of amphiphiles above which aggregate formation is observed, were estimated to be 430 nM for BODIPY-ODN.

Next, we demonstrated the cellular experiments of BODIPY-ODN using a human cell line of lung carcinoma A549 to characterize their behavior in living cells. We evaluated the cellular uptake of BODIPY-DNA aggregate. A549 cells were incubated with 2 μM BODIPY-ODN for 24 h and imaged the fluorescence emission of BODIPY from the cells by microscopy. We observed high levels of emission from the cells, indicating that BODIPY-ODN penetrated cell membrane smoothly at this concentration. These results strongly indicate that the aggregate formation of BODIPY-ODN was key for its cellular uptake.

Finally, we evaluated the function of BODIPY-ODN aggregate in vivo. For the experiments in vivo, we transplanted A549 tumor cells into the lower thigh of nude mice. To the tumor tissue, the aggregate consisted of BODIPY-ODN were intratumorally injected. After 1 h, the thermal neutrons were irradiated to mice, and then the changes of tumor size were monitored. We expected the shrinking of the tumor size, however, the negligible effects of BODIPY-ODN and irradiation were observed probably due to the low concentration of drugs in the tumor tissue (Fig. 1). The improvements of the method of administration and increase of drug amount were under investigation.

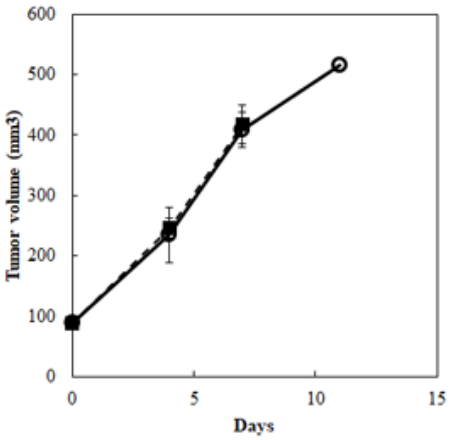

Fig. 1. Monitoring of the tumor volume after administration of BODIPY-ODN and irradiation. Open circle and solid line: administration of BODIPY-ODN. Filled square and dashed line: administration of saline.

REFERENCES:

[1] K. Tanabe *et al.*, ChemBioChem, **19** (2018) 956-962.

30P5-18

PR5-16 *In vivo* evaluation of boron neutron capture therapy for head and neck cancer

K. Igawa, S. Wang[1], A. Sasaki[1], S. Ibaraki[1], Y. Ichikawa, T. Takata[2], M. Suzuki[2]

Neutron Therapy Research Center, Okayama University

[1] Graduate School of medicine, Dentistry and Pharmaceutical Sciences, Okayama University

[2] KURNS, Kyoto University

INTRODUCTION: Head and neck cancer (HNC) is one of main target for Boron neutron capture therapy (BNCT) with consideration for functional and aesthetic outcomes. [1]. However, there are few facilities to evaluate *in vivo* evaluation of BNCT. We optimize HNC model mice to evaluate the novel boron compound in this study.

EXPERIMENTS: In pervious *in vitro* study, we used SAS (JCRB0260, Japan) and HSG-c5 cell line (JCRB1070, Japan) as human head and neck cancer cell line. The intracellular ^{10}B concentration as sodium mercaptoundecahydrododecaborate (BSH, Katchem, Czech) and boronophenylalanine (BPA, Katchem, Czech) in SAS and HSG cell lines were measured by inductively coupled plasma-atomic emission spectroscopy. The result showed that the intracellular uptake and accumulation of BPA was higher than that of BSH in both SAS and HSG cell lines. Also, in boron neutron capture reaction for SAS and HSG cell lines, more suppressive effects on colony formation and cell viability in BPA compared with BSH were observed in each cell lines. Therefore, we used BPA as ^{10}B to optimize in this *in vivo* study.
In this *in vivo* study, SAS or HSG cell lines were subcutaneously injected into the left hind legs of 6-week-old female Balb/c nude mice (Clea Japan Inc., Japan). Using L-boronophenylalanine (BPA, Katchem, Czech), fructose-BPA complex (200 mg/kg) was injected to the HNC tumor bearing mouse 2hrs before irradiation. The average fluence of the thermal neutron (0, 3, 4 $X10^{12}$ n/cm^2) were irradiated. After neutron irradiation, the tumor size was calculated according to the following formula.
Tumor volume [mm^3] = (Long diameter [mm]) x (Short diameter [mm])^2 /2

RESULTS: As shown in Fig. 1, irradiation groups showed significantly decrease in tumor size compared to non-irradiation group at 2 weeks after BNCT for HNC mice. In irradiation of SAS group, gradually tumor regrowth is shown at 3 weeks after irradiation. However, in irradiation of HSG group, the tumor growth is shown as non-irradiation group at 1 weeks after irradiation, at 3 weeks after irradiation, there are no regrowth of tumor. In non-irradiation group, tumor is increased and the growth speed of HSG group is significantly higher than that of SAS group. The optimization of *in vivo* BNCT protocol for head and neck cancer needs more consideration in another factor such as tumor size.

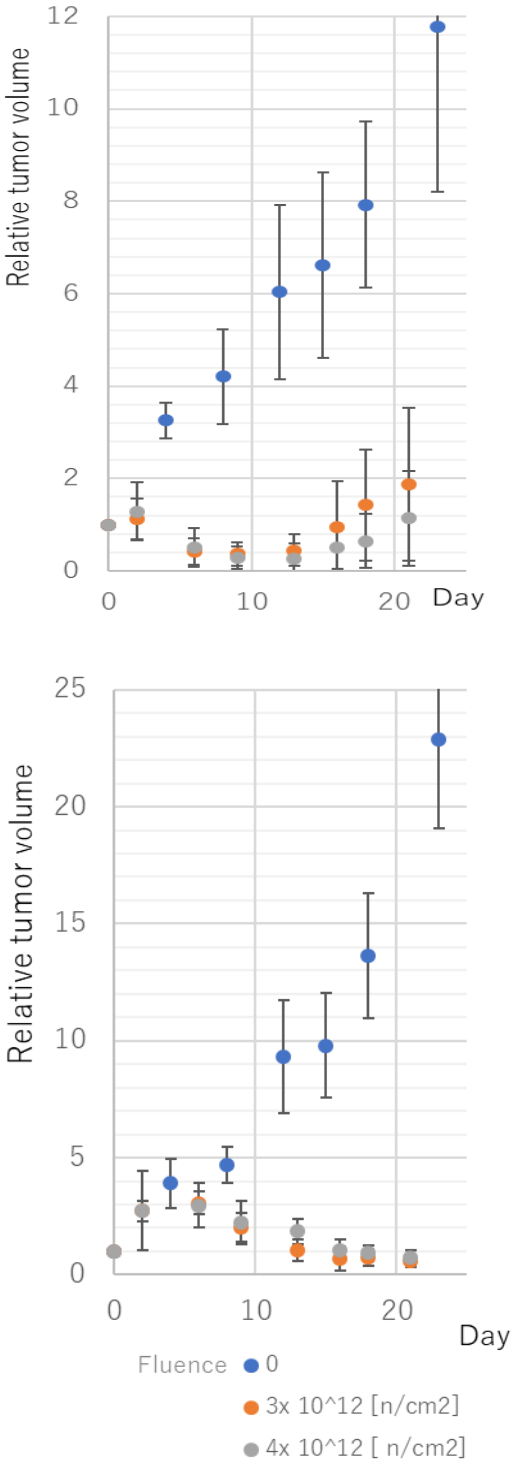

Fig. 1. Tumor growth ratio after thermal neutron irradiation (0, 3, 4 X 10 ^{12} n/cm2, each group n = 5) with BPA 2hrs before irradiation. (a) BNCT of SAS-bearing mice, (b) BNCT of HSG-bearing mice

REFERENCES:

[1] Kato I, Fujita Y, Maruhashi A, et al. Effectiveness of boron neutron capture therapy for recurrent head and neck malignancies. Appl Radiat Isot 2009;67 (Suppl.):S37–S42.

PR5-17

Antitumor effectivity by Gd-neutron capture therapy using Arg-Gly-Asp(RGD) sequence binding Gd-DTPA-incorporated calcium phosphate nanoparticles

H. Xuan [1,2], H. Yanagie[1,3,4], M. Yanagawa[5], Y. Sakurai[3,4], K. Mouri[3,4], N. Dewi[3,4], H. Cabral[2] , S. Dowaki[6], T. Nagasaki[6], Y. Sakurai[7], H. Tanaka[7], M. Suzuki[7], S. Masunaga[7], and H. Takahashi[1,2,3]

[1]Dept of Nuclear Engineering & Management, School of Engineering, Univ of Tokyo, [2]Dept of Bioengineering, School of Engineering, Univ of Tokyo, [3]Cooperative Unit of Medicine & Engineering, Univ of Tokyo Hospital, [4]Niigata Univ of Pharmacy & Applied Life Sciences, , [5]Obihiro Univ of Agriculture and Veterinary Medicine, [6]Osaka City University Graduate School of Engineering, [7]Kyoto Univ Institute for Integrated Radiation & Nuclear Science

INTRODUCTION: We had reported that the gadolinium neutron capture reaction (Gd-NCR) showed the tumour growth suppression, and could be applied to the intensive cancer treatmens in near future [1,2,3].
Gadolinium-157 has been thought one of the attractive candidate atom for neutron capture therapy (NCT) agent because of its high thermal neutron cross section (255 000 barns). The range of induced high LET Auger electrons is few micron, so it is necessary to accumulate the ^{157}Gd atoms in the cancer cells for effective GdNCT [1,2,3].

In the recent targeting fields of pharmaceutical sciences, Arg-Gly-Asp(RGD) sequence is very useful, because RGD sequence can bind to the Integrin receptor of cancer cell surface. So, it can be used for cancer targeting by endocytosis mechanism of RGD sequence [4].

In this work, we prepared the RGD motief binded Gd-DTPA/CaP nanoparticles for selective cancer targeting, and augmentation of 157Gd uptakes to cancer cells.
, then examined the GdNCR by intraveneous injection.

EXPERIMENTS: *In vivo* evaluation was performed on colon-26 tumor-bearing mice irradiated for 60 minutes at nuclear reactor facility of Kyoto Univ Institute for Integrated Radiation & Nuclear Science with average neutron fluence of 2.0×10^{12} n/cm^2. Antitumor effect was evaluated on the basis of the change in tumor growth and survival rate of the mice.

RESULTS:
Tumor growth was suppressed in the groups of RGD sequence binding Gd-DTPA/CaP nanomicelle and bare Gd-DTPA/CaP nanomicelle compared with the non-irradiated groups with the injection of same DDS (data not shown). No acute toxicities were recognized in the treated mice after GdNCT using intraveneous injection of RGD sequence binding Gd-DTPA/CaP nanomicelle and bare Gd-DTPA/CaP nanomicelle.

The tumour volume was decreased after GdNCT. The abnormal change in the liver, the kidney, the heart, and the lung were not found in the histologic examination one month after Gd NCT in the treated groups of RGD sequence binding Gd-DTPA/CaP nanomicelle and bare Gd-DTPA/CaP nanomicelle.

In this experiment, the tumour decresence by bare Gd-DTPA/CaP nanomicelle was superior than the group of RGD sequence binding Gd-DTPA/CaP nanomicelle. We will comfirm the size of nanomicelle and the Gd co centration in the nanomicelle, and the administrated volume of nanomicelle.

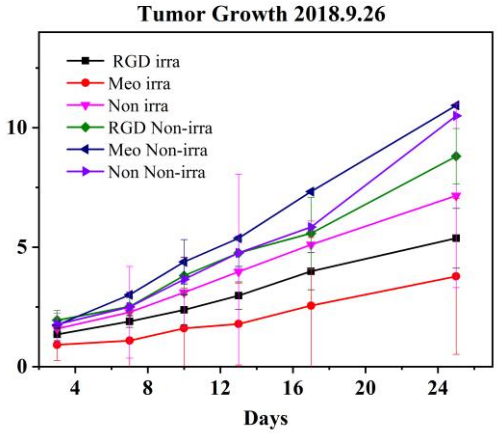

Figure 1. Tumor growth suppression in the group of RGD sequence binding Gd-DTPA/CaP nanomicelle and bare Gd-DTPA/CaP nanomicelle.

In the next experiments, we will check the expression of integrin receptors in many cancer cell lines. We hope to check the uptake of Gd atoms in the cancer cells by endocytosis. We will also evaluate of the mechanism of cytotoxicity on GdNCT, for examples, apoptosis, autophagy, senescence, etc. We hope to refer these results of toxicity examinations to the clinical studies of GdNCT for selection of target cancers in the future.

Thease results indicate that RGD sequence binding Gd-DTPA /CaP nanomicelle has the promising possibility as novel active targeting GdNCT agent.

REFERENCES:

[1] Dewi N *et al.*, Biomed & Pharmacother (2013) **67**:451-7.

[2] Dewi N *et al.*, J Can.Res.Clin.Oncol. (2016) **142**(4):767-75.

[3] Mi P, *et al.*, J Cont. Release (2014) **174**:63-71.

[4] Miyako *et al.,* J Cont. Release (2017) **261**:275-286.

I-1. PROJECT RESEARCHES

Project 6

PR6 Clinical research on explorations into new application of BNCT

M. Suzuki

Institute for Integrated Radiation and Nuclear Science, Kyoto University

Summary

This research projects consists of two clinical research programs on BNCT for malignancies other than malignant brain tumors or head and neck cancers. In P6-1, three patients were treated with BNCT. In P6-2, no patient was recruited in their study.

P6-1

We treated three patients with BNCT in this research program. The malignancies included malignant tissue soft tissue sarcoma, locally recurrent breast cancer and angiosarcoma. Since the patients treated with BNCT in this research problem are under-observation, no preliminary report is available.

P6-2

No patient was enrolled in this clinical research program. Yanagie et al. reported the case report on BNCT for multiple liver metastasis which was carried out previously. Details in this case report is referred to the P6-2 report. The large metastatic liver tumor was diminished, and the local pain derived from the tumor was improved.

Law on Clinical research (*rinsho kenkyu hou*)

New regulation on clinical research, Law on clinical Research (*rinsho kenkyu hou*), has come into effect since April in 2018. Clinical researches conducted by using Drugs and Medical Devices not approved under the Pharmaceutical and Medical Device LAW are categorized into Specified Clinical Research (*tokutei rinsho kenkyu*). Specified Clinical Research Plan should be reviewed by Certified Clinical Research Review Committee. Since BNCT is carried out using unapproved drug (boron compound) and research reactor, BNCT study is categorized into Specific Clinical Research. Six clinical researches on BNCT have been approved as Specific Clinical Research by Certified Clinical Research Review Committee established in medical institutes. Since BNCT studies on locally recurrent breast cancer and angiosarcoma have been approved as Specified Clinical Research, these studies will be carried out in 2019.

PR6-1 Clinical research on explorations into new application of BNCT

M. Suzuki[1], M. Iwamoto[2], J. Sugawara[3], S. Moriwaki[4], H. Tanizaki[4], K. Yoshida[5], S. Kawabata[6], S. Miyatade[7],S. Masunaga[1], Y. Kinashi[1], H. Tanaka[1], Y. Sakurai[1], N. Kondo[1], Y. Tamari[1], T. Fujimoto[8], M. Fukahori[9]

[1.] Institute for Integrated Radiation and Nuclear Science, Kyoto University

[2.]Department of Breast and endocrine surgery, Osaka Medical Collage

[3],Department of Ophthalmology, Osaka Medical Collage

[4.]Departement of dermatology, Osaka Medical College

[5.]Department of Radiology Osaka Medical College

[6.]Department of Neurosurgery, Osaka Medical College,

[7.]Cancer center, Osaka Medical College

[8.]Department of Orthopedic Surgery, Hyogo Cancer Center

[9.]National Institutes for Quantum and Radiological Science and Technology

Introduction

Boron neutron capture therapy (BNCT) has been applied mainly for the treatment of locally recurrent malignant brain tumors or head and neck cancers in the irradiated region using neutron beams from the research reactor. In some BNCT clinical trials, the survival data or tumor response were suggested to be better compared those by other clinical studies. Collaborative project to develop an accelerator-based (AB)-BNCT system between Sumitomo Heavy Industrial and Kyoto University succeeded to construct available cyclotron-based AB-BNCT system.

Clinical trials using the AB-BNCT system are currently in progress. The targets of the ongoing clinical trials are two malignancies as follows: recurrent malignant gliomas and head and neck cancers. In a few years, the system and boron-containing drug is expected to get medical device approval and pharmaceutical approval from national agency. Since the AB-BNCT system installed in the hospital is available to more patients suffering from malignant tumors compared with those by the BNCT using research reactor. However, in a few years before getting medical device approval and pharmaceutical approval, patients with malignant tumors other than malignant gliomas and head and neck cancers will be treated with research reactor-based BNCT. When the AB-BNCT system will be applicable to many clinical trials to search for new application of BNCT in the hospitals, experience of BNCT for new malignancies will be helpful for the new clinical AB-BNCT trials.

We treated three patients with BNCT in this research program. The malignancies included malignant tissue soft tissue sarcoma, locally recurrent breast cancer and angiosarcoma. Since the patients treated with BNCT in this research problem are under-observation, no preliminary report is available. In this report, we present the policy of prescribed neutron fluence adopted in the BNCT studies in this research problem.

Prescribed neutron fluence

Evaluation of irradiated dose is very complicated since irradiation filed in BNCT consists of multiple radiation components including $^{10}B(n,\alpha)^{7}Li$ radiation, high linear energy transfer (LET) proton radiation and γ-ray radiation. The physical dose (Gy) is calculated with an equation as follows,

Physical dose (Gy) = Dose[$^{10}B(n,\alpha)^{7}Li$]* + Dose[γ dose] + Dose[$^{1}H(n,n)^{1}H$] + Dose[$^{14}N(n,p)^{14}C$]

*: Dose[$^{10}B(n,\alpha)^{7}Li$] =7.43 x 10^{-14}xB_{conc} x Φ

Φ: thermal neutron fluence

The equation for converting the physical dose (Gy) to the photon-equivalent dose (Gy-Eq) dose is as follows.

Photon-equivalent dose (Gy-Eq) = CBE x Dose[$^{10}B(n,\alpha)^{7}Li$]* + Dose[γ dose] + RBE x Dose[$^{1}H(n,n)^{1}H$] + RBE x Dose[$^{14}N(n,p)^{14}C$]

*: Dose[$^{10}B(n,\alpha)^{7}Li$] =7.43 x 10^{-14} x B_{conc} x Φ

CBE: compound biological effectiveness

RBE: relative biological effectiveness

In clinical studies of BNCT, the ^{10}B concentration in the blood sampled just before neutron irradiation has been used in deciding irradiation time according to the prescribed dose (Gy-Eq) for normal tissues.

As shown in the equation, the concentration of ^{10}B is necessary to calculate the dose. However, no method to measure ^{10}B concentration during irradiation is developed. Therefore, in evaluating the dose in BNCT, some uncertain is inevitable.

In the clinical pilot studies on BNCT for local recurrent breast cancer and angiosarcoma, we applied the idea of prescribed thermal neutron fluence. In the protocol of the studies, the prescribed thermal neutron fluence was determined as the value of $1.5x10^{12}$ n/cm^2 at the skin of 10-cm diameter circle. Under the condition that ^{10}B concentration in the tumor cells are two times greater than normal cells, the tumor cells received the dose greater than approximately 20 Gy-Eq with keeping the dose for the skin within the tolerant dose.

PR6-2 Literature Consideration of Possibility of Intra-Arterial Immunotherapy after Boron Neutron Capture Therapy to Metastatic Livcer Cancer

H. Yanagie[1,2,3], Y. Nonaka[4], S. Maruyama[5], R. Hatae[5], K. Oyama[5], M. Eriguchi[5], Y. Sakurai[6], H. Tanaka[6], N. Kondo[6], T. Kinashi[6], M. Suzuki[6], S. Masunaga[6], K. Ono[7], S. Higashi[8], K. Seguchi[8], I. Ikushima[9], M. Nashimoto[3], T. Sugihara[3], H. Terada[3], and H. Takahashi[1,2]

[1]Dept of Nuclear Engineering & Management, School of Engineering, Univ of Tokyo, Tokyo, [2]Cooperative Unit of Medicine & Engineering, Univ of Tokyo Hospital, Tokyo, [3]Niigata Univ of Pharmacy & Applied Life Sciences, Niigata, [4]Dept. of Surgery, Keiai-kai Hoyo Hospital, Iwate, [5]Shin-Yamanote Hospital, Japan Anti-Tuberculosis Association, Tokyo, [6]Kyoto Univ Institute for Integrated Radiation & Nuclear Science, Osaka, [7]Kansai BNCT Medical Center, Osaka Medical College, Osaka, [8]Depat. of Surgery, Kojin-kai Medicalcity East Hospital, Miyazaki, [9]Dept. of Radiology, Miyakonojo Metropolitan Hospital, Miyazaki, JAPAN

INTRODUCTION: We had experienced the boron neutron capture therapy(BNCT) to cancers in gastrointestinal regions. Our cases treated by BNCT were 1 case of cervical metastatic gastric cancer(Partial Remission), 2 cases of recurrent rectal cancers(Stable Disease), and 1 case of hepatic metastatic sigmoidal colon cancer(Locally Stable Disease).

In this study, we performed the literature consideration of combination therapies to the case of hepatic metastatic sigmoidal colon cancer.

EXPERIMENTS: The 38y.o. male patient with sigmoidal colon cancer & multiple hepatic metastasis had been performed sigmoidectomy, intra-arterial chemotherapies(CDDP), and molecular targeted therapy (XELOX+ Cmab, XELOX+Pmab, IRIS+Pmab). But the tumour volume of hepatic metastasis was increased, and then the local pain caused tumour swelling was occurred. In order to decrease the chief complaint by the tumour swelling, we performed the BNCT on January 2012. The procedure points were (1) target lesion : S4 hepatic metastatic lesion (Figure 1), (2) ^{10}BPA 400mg/kg drip infusion, (3) Tumour dose:30>Gy-Eq/5cm, Normal Liver dose : <4.9Gy-Eq, (4) Tumour/Blood ration of ^{18}F-^{10}BPA PET:2.6.

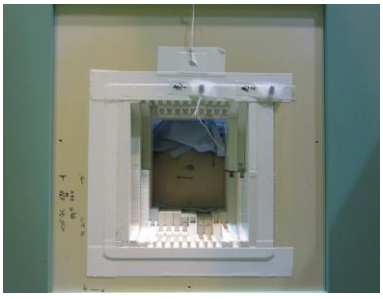

Figure1: Irradiation positioning of BNCT.

RESULTS & DISCUSSION: As shown in Figure 2, Maximum Tumour dose will be 31Gy-Eq, Mean Tumour dose was 20Gy-Eq, Maximum Normal Liver dose was 17Gy-Eq, Mean Liver dose was 3Gy-Eq in 43 minutes BNCT.

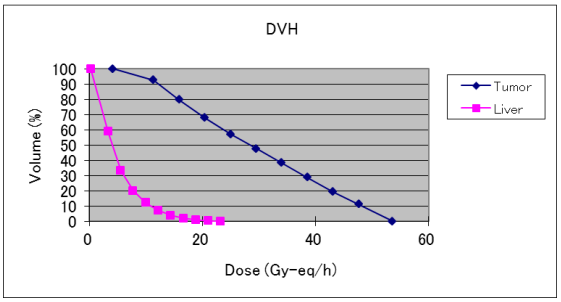

Figure 2: Calculation of Tumour/ Normal Liver Dos.

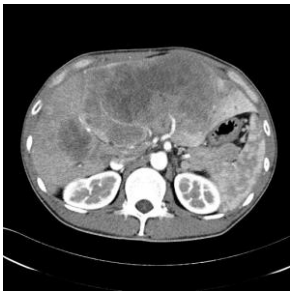

Before BNCT (2011.11.25) **Post 3 months BNCT (2012.04.20)**

Figure 3: Tumour growth was suppressed, and the local pain caused tumour swelling was markidly diminished.

The tumour volume was diminished and the chief complaint of patient was improved. The tumour volume in-hepatic metastasis was regulated in 3 months by single irradiation of BNCT locally.

We had one experienced case of intra-arterial injection of immunostimulating substance, OK432(Picibanil) to the multiple large metastasis of colon cancer patient after operation, and systemic & intra-arterial(IA) chemotherapies. Our case was decrease of tumour volume and recover the QOL of patient. So, we hope to apply the combination therapies with BNCT and Intra-Arterial Immunotherapy in the next step.

Recently, immunotherapies become attractive combination therapies to cancer. Immune checkpoint blockade, Dendritic Cell Therapy, CTL/NK Cell Therapy, OK432-IA will be considered in the consideration of indications to liver cancer in near future.

REFERENCES:

[1] H. Yanagie *et al.*, Jpn J Cancer Clinics,**41** (1995) 306-310.
[2] S. Mikamo *et al.*, Biotherapy, **11** (1997) 634-636.
[3] K.Ando *et al.*, J Radiat Res., **58** (2017) 446-455.

I-1. PROJECT RESEARCHES

Project 7

PR7 Establishment of Integrated System for Dose Estimation in BNCT

Y. Sakurai

Institute for Integrated Radiation and Nuclear Science, Kyoto University

BACKGROUNDS AND PURPOSES:

Several types of accelerator-based irradiation system for boron neutron capture therapy (BNCT) are under development at present. But, there are a number of subjects, which should be improved for the further advance and generalization of BNCT.

In the viewpoints of medical physics and engineering, the advance for dose estimation is one of the important subjects. For the characterization of irradiation field, quality assurance and quality control (QA/QC), clinical irradiation to actual patient, and so on, an ultimate goal is to perform the three-dimensional and real-time dose estimation in discriminating for thermal, epi-thermal and fast neutron doses, gamma-ray dose, and boron dose, with simplicity and low effort. Considering about this ultimate dose estimation, several kinds of dose estimation method are studied. It is so difficult to realize the ultimate dose estimation using only one method, but it is necessary to combine more than two methods.

The purposes of this project research are the advance for the respective dose estimation methods, and the establishment of an integrated system for dose estimation in BNCT.

In the second year of this research project, 2018, the advancement for the respective dose estimation methods were forwarded mainly using Heavy Water Neutron Irradiation Facility and E-3 Neutron Guide Tube at KUR.

RESEARCH SUBJECTS:

The collaboration and allotted research subjects (ARS) were organized as follows;

ARS-1 (30P7-1): Establishment of characterization estimation method in BNCT irradiation field using Bonner sphere and ionization chamber (II). (Y. Sakurai, S. Shiraishi, R. Uchida, T. Takata, H. Tanaka, T. Kawamura, N. Ko, K. Okazaki, M. Sato, A. Sasaki, Y. Kumagai, K. Akita and M. Suzuki)

ARS-2 (30P7-2): Study on new type of neutron spectrometer for BNCT. (A. Ishikawa, A. Uritani, S. Li, K. Watanabe, S. Yoshihashi, A. Yamazaki T. Takada, H. Tanaka and Y. Sakurai)

ARS-3 (29P7-3): Investigation of deterioration characteristics of SOF detector probe. (M. Ishikawa, K. Baba and N. Shimizu)

ARS-4 (30P7-4): Beam profile measurement at E-3 irradiation port by using the self-activation of CsI plate. (A. Nohtomi, R. Kurihara, G. Wakabayashi, Y. Sakurai and T. Takata)

ARS-5 (30P7-5): Characterization of active neutron detector for boron neutron capture therapy. (M. Takada, S. Endo, H. Tanaka, T. Matsumoto, A. Masuda, T. Ueda, M. Ohyauchi, T. Nunomiya, K. Aoyama and T. Nakamura)

ARS-6 (30P7-6): Study for microdosimetry using silicon-on-insulator microdosimeter in the BNCT irradiation field (II). (Y. Sakurai, N. Ko, R. Uchida, T. Takata, H. Tanaka, T. L. Tran, J. Davis, S. Guatelli, A. Rozenfeld, N. Kondo and M. Suzuki)

ARS-7 (30P7-7): Measurement of BNCT beam component fluence with imaging plate. K. Tanaka, Y. Sakurai, T. Kajimoto, Y. Murakami, Y. Ito, H. Tanaka, T. Takata and S. Endo)

ARS-8 (30P7-8): Development of neutron fluence distribution measuring device using thermoluminescence slabs. (K. Shinsho, S. Yanagisawa, R. Oh, G. Wakabayashi Y. Koba and H. Tanaka)

ARS-9 (30P7-9): The study for development and application of tissue equivalent neutron dosimeter. (M. Oita, T. Kamomae, N. Hayashi, T. Takada and Y. Sakurai)

ARS-10 (30P7-10): Development and evaluation of 3D polymer gel dosimeter for the measurement of dose distribution in BNCT. (S. Hayashi, Y. Sakurai, M. Suzuki, T. Takata and R. Uchida)

ARS-11 (30P7-11): Establishment of beam-quality estimation method in BNCT irradiation field using dual phantom technique (II). (Y. Sakurai, T. Takata, H. Tanaka, N. Kondo and M. Suzuki)

ARS-12 (30P7-12): Development of a prompt gamma-ray imaging detector for boron neutron capture therapy. (K. Okazaki, K. Akabori, T. Takata, S. Kawabata, Y. Sakurai and H. Tanaka)

ARS-13 (30P7-13): Radiation damage experiment on novel scintillator material and study on material for development of irradiation monitor in BNCT. (S. Kurosawa, A. Yamaji, T. Horiai, S. Kodama, S. Yamato and H. Tanaka)

ARS-14 (30P7-14): Establishment of the Imaging Technology of 478 keV Prompt Gamma-rays of Boron-neutron Capture Reaction and the Measurement of the Intensity of the Neutron Field. (M. Ishimoto, T. Mizumoto, S. Sonoda, A. Takada, T. Tanimori, T. Takata and Y. Sakurai)

ARS-15 (30P7-15): Feasibility study for establishing quality assurance and quality control for radiation field in boron neutron capture therapy. (S. Nakamura, A. Urushiyama, T. Nishio, M. Tsuneda, T. Masuda, A. Sano, H. Okamoto, S. Nishioka, K. Iijima, M. Takemori, H. Nakayama, Y. Sakurai, H. Tanaka, T. Takata, M. Suzuki and J. Itami)

ARS-16 (30P7-16): Patient-position monitoring by using Kinect sensor for boron neutron capture therapy. (T. Takata, H. Tanaka, Y. Sakurai, Y. Tamari and M. Suzuki)

For ARS-10, no results were obtained because no machine time were used due to the schedule of the collaborators. So, the report of this research subject is not appeared.

PR7-1 Establishment of characterization estimation method in BNCT irradiation field using Bonner sphere and ionization chamber (II)

Y. Sakurai, S. Shirai-shi[1], R. Uchida[1], T. Takata, H. Tanaka, T. Kawamura[1], N. Ko[1], K. Okazaki[1], M. Sato[1], A. Sasaki[1], Y. Kumagai[1], K. Akita[1,2], M. Suzuki

Institute for Integrated Radiation and Nuclear Science, Kyoto University
[1]Graduate School of Engineering, Kyoto University
[2]Osaka Medical School

INTRODUCTION: Research and development into several types of accelerator-based irradiation systems for boron neutron capture therapy (BNCT) is underway [1,2]. In the near future, BNCT using these newly developed irradiation systems may be carried out at multiple facilities across the world. Considering this situation, it is important that the estimations for dose quantity and quality are performed consistently among several irradiation fields, and that the equivalency of BNCT is guaranteed, within and across BNCT systems. Then, we are establishing the quality assurance and quality control (QA/QC) system for BNCT irradiation field.
As part of the QA/QC system, we are developing estimation method for neutron energy spectrum using Bonner sphere [3]. For our spectrometer using Bonner sphere, liquid such as pure water and/or boric acid solution is used as the moderator. A multi-layer concentric-sphere case with several sphere shells is prepared. The moderator and its diameter are changeable without entering the irradiation room, by the remote supply and drainage of liquid moderator in the several layers. For the detector, activation foils are remotely changed, or online measurement is performed using SOF (scintillator with optical fiber) detector containing boron, etc. [4].
In 2018, the detailed optimization was performed mainly by simulation for the development of the Remote-changeable Bonner-sphere Spectrometer (RBS). Concurrently, estimation experiment was performed for the irradiation characteristics at Heavy Water Neutron Irradiation Facility of Kyoto University Reactor (KUR-HWNIF).

METHODS: In the neutron energy spectrometry by Bonner-sphere and activation foils, the combinations of the moderator material and diameter should be previously decided and prepared. Of course, the more information can be obtained as the more moderators and detectors are prepared. However, the information number from those measured data is less than the combination number, because of the overlapped regions among the combinations. The selection is important, in which the more information number is obtained for the combination number.
The combination of moderator and detector is decided, for that the response functions cannot be approximated by the linear functions of the other response functions. The accuracy and precision for the spectrometry can be higher, because the independent information can be obtained from the measurement by the respective combinations. We were developed the selection method, High Independence Selection (HIS) [5].
On the assumption of the application in a typical BNCT irradiation field, the combination of the moderators for boron-10 concentration and diameter was optimized by HIS. Ten types of acrylic container for Bonner sphere is assumed. These container have five hollow shells for supplying moderators and acrylic walls. The thicknesses for the shells and walls in each container are 1 cm and 1 mm, 1 cm and 2 mm, 1 cm and 3 mm, 1 cm and 4 mm, 1 cm and 5 mm, 2 cm and 1 mm, 2 cm and 2 mm, 2 cm and 3 mm, 2 cm and 4 mm and 2 cm and 5 mm. Moderators are pure water and boron acid water (0.14wt%, B-10 solubility at 20 degree centigrade).
Thirty-three combinations for the shells and moderators are simulated. For the ten combinations, only one shell is filled with pure water or boron acid water, and the remaining four shells are empty. For the twenty three combinations, the shells are filled with the moderators in turn from the central shell. Totally, 330 patterns for the spectrometer are simulated.

RESULTS: Some optimized structures of RBS were selected by HIS. Figure 1 shows one of the optimized combinations for RBS.

CONCLUSION: We have a plan to create the RBS, based on the optimization result. Additionally, we have a plan to perform the spectrometry experiments at KUR-HWNIF, etc., in order to confirm the efficacy of RBS.

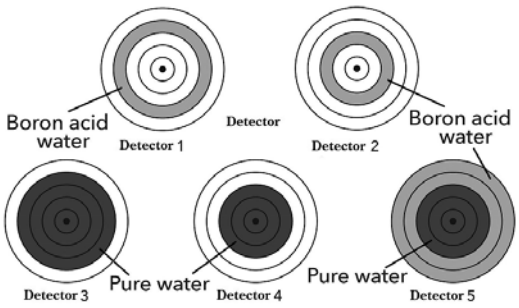

Fig. 1. One of the optimized combinations for the remote-changeable Bonner-sphere spectrometer.

REFERENCES:
[1] H. Tanaka *et al.*, Nucl. Instr. Meth., B **267** (2009) 1970-1977.
[2] H. Kumada *et al.*, Appl. Radiat. Isot., **88** (2014) 211-215.
[3] H. Ueda *et al.*, Appl. Radiat. Isot., **104** (2015) 25-28.
[4] M. Ishikawa *et al.*, Radiat. Oncol., **11** (2016) **105** (1-10).
[5] H. Ueda, Doctoral Thesis (2016).

PR7-2 Study on New Type of Neutron Spectrometer for BNCT

A. Uritani, A. Ishikawa, S. Li, K. Watanabe,
S. Yoshihashi, A. Yamazaki T. Takada[1], H. Tanaka[1] and
Y. Sakurai[1]

Graduate School of Engineering, Nagoya University
[1] Institute for Integrated Radiation and Nuclear Science, Kyoto University

INTRODUCTION: Boron neutron capture therapy (BNCT) is one of the promising treatment methods for cancers such as brain tumors. In recent years, accelerator-driven neutron sources have been developed because of its simplicity of management. In commissioning of these facilities, the irradiation field should be characterized in order to assure designed specifications, such as neutron intensity, the neutron energy spectrum and gamma-ray contamination.

We are developing a new neutron energy spectrometer using an optical fiber type detector. A conventional Bonner sphere neutron spectrometer has only less than ten detectors, typically five or six detectors. Moderation based neutron spectrometers commonly has relatively low response for epi-thermal neutron energy region. One of the solutions to improve the energy response is to increase the number of detectors with different responses. Tamaki et al. proposed a liquid-moderator-based neutron spectrometer, in which liquid moderator volume is changed to make various responses [1]. On the other hand, we propose the spectrometer consisting of a liquid moderator and a thermal neutron flux profile scanner using an optical fiber type detector [2].

In this study, we experimentally conducted response evaluation of the water-moderator-based neutron spectrometer using a thermal neutron profile scanner the optical fiber type detector. Figure 1 shows the response function of the water-moderator-based neutron spectrometer with 200x200x200 mm^3 size calculated by PHITS code.

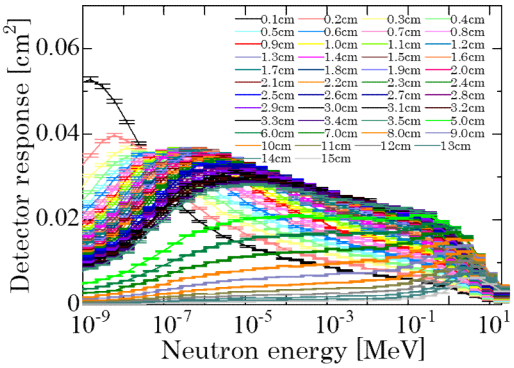

Fig. 1. Response function of the water-moderator-based neutron spectrometer.

EXPERIMENTS: The water phantom with 200 x 200 x 200 mm^3 size was irradiated with epi-thermal neutrons at Heavy Water Irradiation Facility of Kyoto University Reactor. The thermal neutron profile in this phantom was measured by the optical fiber type neutron detector using a small Eu: $LiCaAlF_6$ scintillator. The detector head was moved with a linear stage. The gold foil activation method was also conducted to measure the thermal neutron profile. In order to evaluate pure thermal neutron flux, the Cd subtraction method was used.

RESULTS: Figure 2 shows the depth profile of the thermal neutron flux in a water phantom measured by the gold foil activation method and the optical fiber type detector. Both results well agreed each other. In Fig. 3, we quantitatively compared the both results. The results of the optical fiber detector well reproduce ones of the gold foil activation method within 10% difference.

REFERENCES:

[1] S.Tamaki, *et al.*, Nuclear Instruments and Methods in Physics Research Section A , **870**, 90 (2017)
[2] K. Watanabe *et al.*, Nuclear Instruments and Methods in Physics Research Section A , **802**, 1 (2015)

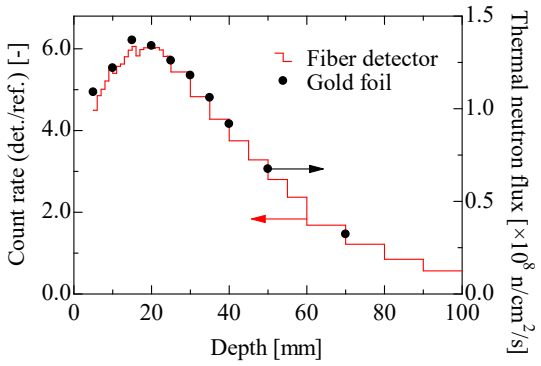

Fig. 2. Depth profile of the thermal neutron flux in a water phantom measured by gold foil activation method and the optical fiber type detector.

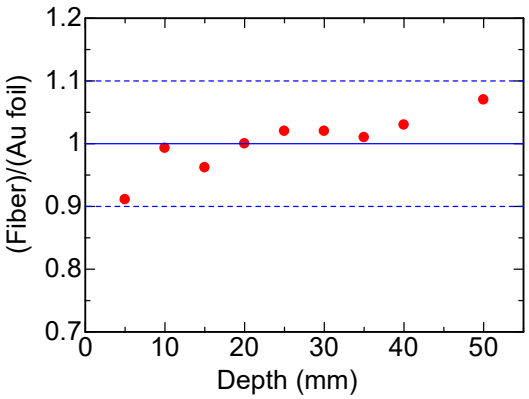

Fig. 3. Comparison between the thermal neutron flux measured by gold foil activation method and the optical fiber type neutron detector.

PR7-3 Investigation of deterioration characteristics of SOF detector probe

M. Ishikawa[1,2], K. Baba[2] and N. Shimizu[2]

[1]*Graduate School of Health Sciences, Hokkaido University*

[2]*Graduate School of Biomedical Science and Engineering, Hokkaido University*

INTRODUCTION: In the conventional BNCT, thermal neutron flux and thermal neutron fluence during treatment could not be measured in real time because gold wire activation was used to evaluate thermal neutron fluence. Therefore, we developed a detector (SOF detector; Scintillator with Optical Fiber Detector) with a plastic scintillator attached to the tip of the optical fiber, tried real-time measurement of thermal neutron flux in neutron capture therapy, and got good results. The long-term stability of the SOF detector and the wide measurement dynamic range (linearity of 10^4 to 10^{10} n/cm^2/s) have been confirmed in previous collaborative experiments. [1,2]
However, signal degradation of SOF detector in long-term exposure was reported [3]. The signal degradation might not be a significant problem in case that calibration can be performed before use. However, signal degradation greatly affects measurement accuracy in case of long-term monitoring because calibration prior to use is difficult. Therefore, in this research, in order to identify the cause of signal degradation, identification of the substance causing the signal degradation was attempted by devising the combination of the materials constituting the probe.

EXPERIMENTS: The experimental geometry is shown in Fig. 1. The Heavy Water Neutron lrradiation Facility (HWNIF) of KUR was used for irradiation. The SOF detector probes were arranged at a surface of a 30 x 30 x 5 cm thick polyethylene block which was placed in the irradiation field, and signal change was monitored online. The combinations of neutron converter and reflectors contained in the irradiated probes are shown in Table 1. All probes used BC490 as a plastic scintillator, and Probes 1 to 3 were mixed with ^{6}LiF as a neutron converter. Moreover, BC642 (PTFE Reflector Tape) and BC620 (Reflector paint) were used as a reflective material for Probe 1 and 2, respectively. Probe 4 used BC620 reflector without any neutron converter. As a reference probe, the probe which consist of BC490 with BC642 was used.

Table 1. Irradiated sample probes with and without neutron converter and reflectors.

Probe #	Neutron converter	Reflector
1	^{6}LiF	BC642
2	^{6}LiF	BC620
3	^{6}LiF	None
4	None	BC620
Reference	None	BC642

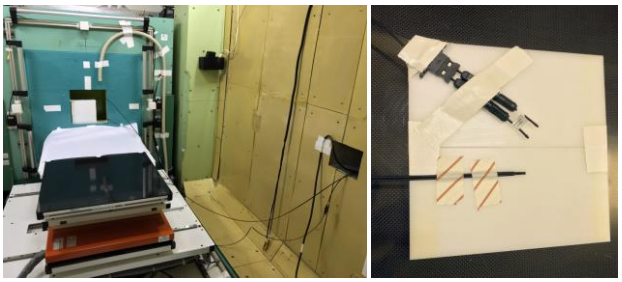

(a) Overview of irradiation (b) detector layout

Fig. 1. Irradiation geometry for on-line assessment of deterioration characteristics.

RESULTS: Figure 2 shows the change in signal strength of the SOF detector by on-line monitoring. Each signal is normalized to the average value of the entire measurement. From Fig. 2, the change of signal intensities of Probes 1 to 3 were relatively decreased, whereas the signal intensity of Probe 4 was relatively increased with neutron irradiation. The 1.64% signal decrease of the Probe 1 which is used in conventional SOF detector was observed from the start of irradiation. This suggests that the deterioration of ^{6}LiF used as a neutron converter may cause a decrease in signal intensity. From the result of Probe 4, it was also found that the reflective material of BC620 reflector paint might be activated by irradiation of thermal neutron.

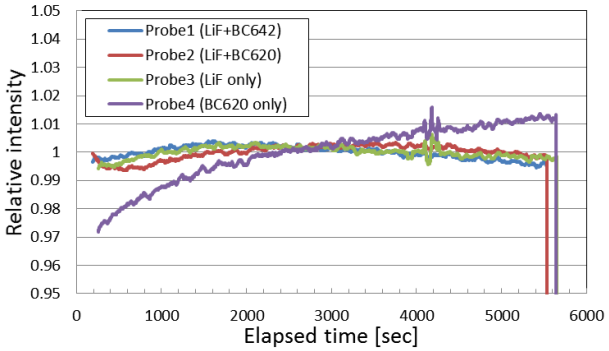

Fig. 2. Irradiation geometry for off-line assessment of deterioration characteristics.

REFERENCES:

[1] M. Ishikawa *et al.*, Appl. Radiat. Isot., **61** (2004) 775-779.
[2] M. Ishikawa *et al.*, Nucl. Instr. Meth., A **551** (2005) 448-457.
[3] M. Komeda *et al.*, Appl. Radiat. Isot., **67** (2009) 254-257.

PR7-4 **Beam profile measurement at E-3 irradiation port by using the self-activation of CsI plate**

A. Nohtomi, R. Kurihara, G.Wakabayashi[1], Y.Sakurai[2] and T.Takata[2]

Graduate School of Medicine, Kyushu University
[1] Atomic Energy Research Institute, Kindai University
[2] Institute for Integrated Radiation and Nuclear Science, Kyoto University

INTRODUCTION: In our previous studies, neutron intensity distribution on a CsI scintillator plate has been observed by a CCD camera and analyzed by using a "decaying self-activation imaging technique" [1, 2]. The decaying self-activation imaging, which has been proposed recently by our group, is based on the analysis of time variation of specific radio-activities generated and remained inside the CsI plate after the termination of neutron irradiation. In the present work, this technique was applied to measure the thermal neutron beam profile at E-3 irradiation port facility of KUR, which is mainly utilized for prompt gamma-ray analysis to evaluate B-10 concentration in a sample.

EXPERIMENTS: A CsI plate (75mm x 75mm x 2mm) which is packed with aluminum container and glass window was irradiated at E-3 irradiation port facility of KUR. After the termination of 75 min. irradiation at the exit collimator of LiF (opening H:14mm x V:18mm). The luminance distributions of a CsI plate are recorded every one minute as a series of images by a cooling type CCD camera (SBIG:STF8300M) with a telescope lens (SIGMA : 30mm F1.4 DC) in a black box. A gold foil was used to evaluate the fluence rate of thermal neutron by the activation analysis.

RESULTS: As the result of activation analysis of gold foil, thermal neutron fluence rate at the irradiation port was determined to be 1.83 x 10^5[n/cm^2/s]. Figure 1 shows a typical I-128 luminance image observed by the CCD camera. The I-128 luminance component was extracted by the decaying self-activation imaging technique. Yellow rectangular indicates 10% level region of the maximum luminance value; the horizontal length is 15 mm and the vertical length is 21 mm.

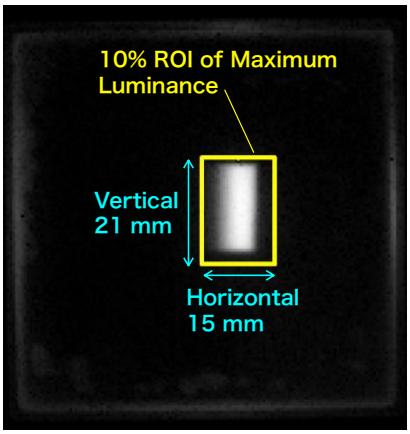

Fig. 1. Typical I-128 self-luminance image observed by a CCD camera.

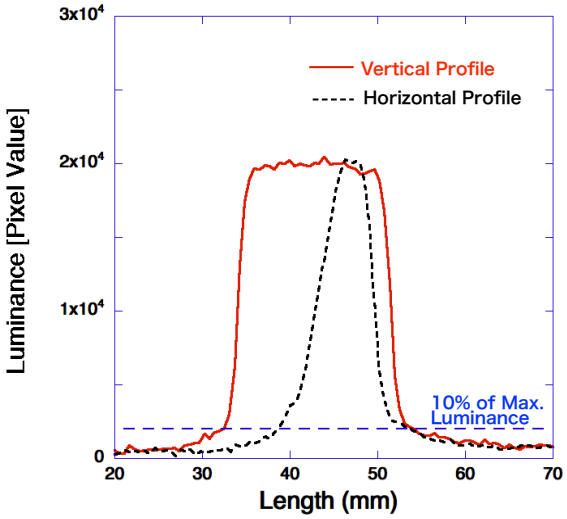

Fig. 2. Horizontal and vertical beam profile of luminance observed by a CCD camera.

So, those are almost consistent with the actual physical dimension of the collimator opening. However, as shown in Fig. 2, horizontal beam profile shows an antisymmetrical peak. Figure 3 displays a 3-D graphical presentation of the beam profile of luminance observed.

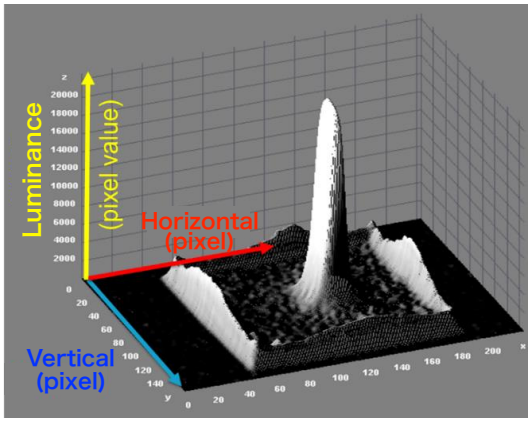

Fig. 3. Three-D graphical presentation of the beam profile observed.

From the results described above, it has been confirmed that the thermal neutron beam profile at E-3 irradiation port facility is almost uniform and symmetrical along the vertical direction. On the other hand, along the horizontal direction, the beam profile indicates a shape like distorted Gaussian distribution and dose not have flat region.

ACKNOWLEDGEMENT: This work was supported by JSPS KAKENHI Grant Number JP16K10320.

REFERENCES:

[1] A.Nohtomi *et al.*, Nucl. Instr. and Meth., **A832** (2016) 21-23.
[2] A.Nohtomi *et al.*, JPS Conf. Proc., **24** (2019) 011041.

PR7-5 Characterization of Active Neutron Detector for Boron Neutron Capture Therapy

M. Takada, S. Endo[1], H. Tanaka[2], T. Matsumoto[3], A. Masuda[3], T. Ueda[1], M. Ohyauchi[1], T. Nunomiya[4], K. Aoyama[4], T. Nakamura[4]

Department of Applied Physics, National Defense Academy of Japan

[1]*Graduate School of Engineering, Hiroshima University*
[2]*Institute for Integrated Radiation and Nuclear Science, Kyoto University*

[3]*National Metrology Institute of Japan, National Institute of Advanced Industrial Science and Technology*

[4]*Fuji Electric Co. Ltd.*

INTRODUCTION: Boron Neutron Capture Therapy, which is called as BNCT, is a binary radiotherapy method developed to treat patients with certain malignant tumors. BNCT has been widely used at nuclear reactors, however, several accelerator-based BNCT facilities have been developed / ready to clinical treatment for more accessible for patients. Measurements of neutron fluences irradiated to the patients are important for BNCT success. The neutron fluence has been measured using passive method of gold neutron activation. In the accelerator-based BNCT, intensity of neutron beam could be varied with time due to instability of the accelerator condition and loss of neu-tron target. We should continuously measure neutron beams in a real time.

For this purpose, we have developed active neutron detector to measure BNCT beam directly, which is named as DAD-BNCT. It can measure both intense neutron beam over $1x10^9$ (n cm^{-2} s^{-1}) and high dose-rate gamma rays around 500 mGy/h [1], simultaneously. The detector consists of thin silicon diode having 40 μm in thickness [2] and thin LiF coated on Teflon plate. Intense neutron beam can be measured by detecting triton produced by the $^6Li(n,t)^4He$ reaction at the LiF neutron converter. In this study, we characterized the active neutron detector for BNCT beam.

EXPERIMENTS: The neutron measurements were performed at the heavy water irradiation facility of research reactor of Institute for Integrated Radiation and Nuclear Science, Kyoto University [3]. The DAD-BNCT was located without any neutron and gamma-ray shields in the irradiation room of this facility. Signals fed from the DAD-BNCT were charge amplified with the commercial preamplifier and main amplifier, and then signals were acquired with a multi-channel analyzer. The thermal neutron beam fluxes and the neutron energy spectrum are changed by the aperture area with Cd plate slits at an upward of the irradiation location. The thermal neutrons from $2x10^7$ to $1x10^9$ (n cm^{-2} s^{-1}) were irradiated to the DAD-BNCT. The response functions are obtained from differences of the measurements under the neutron fields with different areas of Cd slits. Also, the response functions with/without the LiF neutron converter were experimentally obtained to evaluate the responses of detecting secondary particles produced by only the $^6Li(n,t)^4He$ reaction. Bias dependence of the response functions were measured.

RESULTS: The response functions, normalized with the thermal neutron flux, measured under the neutron irradiation with the 600-mm-width Cd slit is shown in **Figure 1**. This setup can irradiate the detectors with highest thermal neutron flux. A clear peak around 650 ch., labeled as (A) in Fig.1, and an edge around 550 ch., labeled as (B), in the spectrum are created by tritons, produced by the $^6Li(n,t)^4He$ reaction, fully stopped in and transmitted through the depletion layer of silicon diode, respectively. Increasing the neutron flux, position of this peak is constant; while, peak widths are slightly broader. Integrating the count rate in this peak region, the detection efficiency of DAD-BNCT to thermal neutron beam was also evaluated. The results are $2.9x10^{-6}$ (# cm^2), temporarily. The continuum from 200 to 550 ch., labeled as (C), is created by alpha particles from the neutron and boron reaction. Below 200 ch., labeled as (D), these events are created by detecting gamma rays. Therefore, the DAD-BNCT can measure BNCT neutron beam directly, well separated from gamma-ray events. Neutron damage have never been observed through the BNCT experiments.

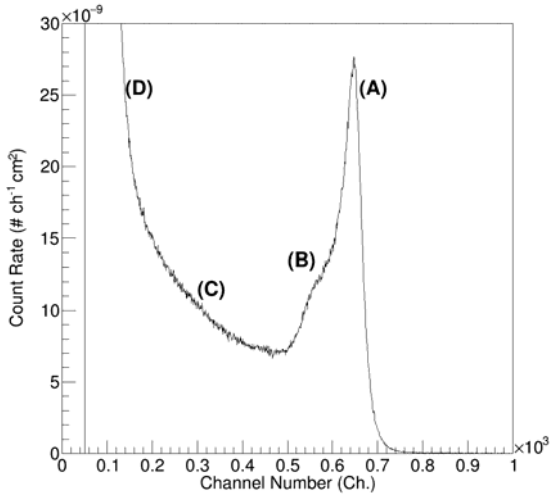

Figure 1. Neutron response functions of DAD-BNCT for BNCT neutron beam under a 600-mm-width Cd slit.

REFERENCES:

[1] M. Takada *et al.*, prepared.
[2] M. Takada *et al.*, Radiat. Meas., 99, 33-54 (2017).
[3] T. Kobayashi *et al.*, Nucl. Technol., 131, 354-378 (2000).

PR7-6 Study for microdosimetry using silicon-on-insulator microdosimeter in the BNCT irradiation field (II)

Y. Sakurai, N. Ko[1], R. Uchida[1], T. Takata, H. Tanaka, T. L. Tran[2], J. Davis2, S. Guatelli[2], A. Rozenfeld[2], N. Kondo, M. Suzuki

Institute for Integrated Radiation and Nuclear Science, Kyoto University
[1]Graduate School of Engineering, Kyoto University
[2]Centre for Medical Radiation Physics, University of Wollongong

INTRODUCTION: Research and development into several types of accelerator-based irradiation systems for boron neutron capture therapy (BNCT) is underway [1,2]. In the near future, BNCT using these newly developed irradiation systems may be carried out at multiple facilities across the world. In contrast to conventional radiotherapy, the types of radiation present in BNCT consists of many distinct radiation components, each having a different biological weighting factor.
Microdosimetry is an effective dosimetry technique in a mixed radiation environment. Using this technique, it is possible to derive the relative contributions of different radiation modalities. The feasibility study of a novel 3D mesa bridge silicon-on-insulator microdosimeter (SIM) in BNCT [3], developed by University of Wollongong (UOW).
In 2018, the more detailed optimization was performed for SIM by Monte Carlo simulation. And also, the experiments for the confirmation of the characteristics of SIM were performed using Heavy Water Neutron Irradiation Facility (HWNIF) and E3 neutron guide tube (E3) of Kyoto University Reactor (KUR).

METHODS: The bridge microdosimeter is comprised of an array of 4248 individual silicon cells fabricated on a 10 μm thick n-type silicon-on-insulator substrate. Figure 1 shows the outline of SIM.
For the optimization simulation, the different boron converter and silicon-on-insulator substrate thickness was modelled and the energy deposition within the detector was simulated using the Particle and Heavy Ions Transport Code System (PHITS). The T-deposit tally in PHITS was used to calculate the energy deposited per event inside the sensitive volume of the bridge microdosimeter. The lineal energy was calculated by dividing the deposited energy per event by the average chord length of the detector. The clinical BNCT field at KUR-HWNIF using both thermal and epithermal irradiation modes were used in this study.
For the experiment at HWNIF, one of the aims was the confirmation for the response characteristics of SIM at the epi-thermal neutron field with larger irradiation area. The other of the aims was the data acquisition for the depth distributions for the SIM response.
For the experiment at E3, the aim was the confirmation for the response characteristics of SIM at the thermal neutron field with smaller irradiation area.

RESULTS: Figure 2 shows one of the microdosimetric spectrum obtained from the optimization simulation. This simulation results showed that the sensitivity of SIM was increased by the boron converter especially in the thermal neutron irradiation field.
For the both experiments at HWNIF and E3, no valid data was obtained foe some reasons. At HWNIF, the effectiveness of neutrons to the electronics of SIM was so large that the data acquisition was stopped immediately after the acquisition start. At E3, the background noise was so large that the response signal of SIM was buried.

CONCLUSION: The simulation results show that this microdosimeter can be utilized as an effective tool for dosimetry in BNCT field. The experiments are planed using KUR again.

Fig. 1. Outline of silicon-on-insulator microdosimeter.

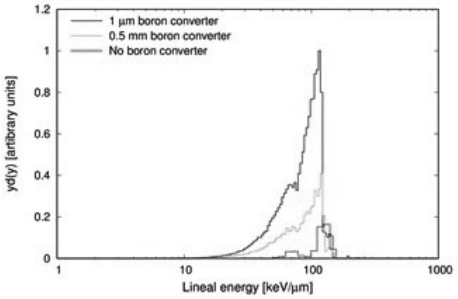

Fig. 2. Microdosimetric spectrum for the boron converter thickness.

REFERENCES:

[1] H. Tanaka *et al*., Nucl. Instr. Meth. B **267** (2009) 1970-1977.
[2] H. Kumada *et al*., Appl. Radiat. Isot., **88** (2014) 211-215.
[3] L. T. Tran *et al*., IEEE Trans. Nucl. Sci., **62** (2015) 3027-3033.

PR7-7 Measurement of BNCT beam component fluence with imaging plate

Kenichi Tanaka, Yoshinori Sakurai[1], Tsuyoshi Kajimoto, Yuto Murakami, Yuto Ito, Hiroki Tanaka[1], Takushi Takata[1], Satoru Endo

Graduate School of Engineering, Hiroshima University
[1]KURNS, Kyoto University

INTRODUCTION: Dose evaluation is required for quality assurance in the irradiation field for boron neutron capture therapy. This study investigated the use of the imaging plate (IP) combined with beam component converter.

EXPERIMENTS: The converter configuration chosen for this study is shown in Fig. 1. The IP is BAS-TR from Fuji Film corporation, Japan. The IP #1 in carbon is for gamma rays, #2 for epithermal neutrons, and #3 for fast neutrons. Here, material #2 is polyethylene. Material #1 is polyethylene infused with LiF, where ^{6}Li is enriched up to 95 at% The concentration of ^{6}Li in Material #1 is 10 wt%. The details of the converter was described previously [1].
The experiment was performed with the standard epithermal neutron irradiation mode of KUR-HWNIF at 1 MW. The beam size was set to about 120 × 120 mm^2 using the collimator. The irradiation was performed for 2 minutes. The nominal value of the flux at the center of the collimator aperture was 7.07 × 10^6 cm^{-2}s^{-1}, 1.33 × 10^8 cm^{-2}s^{-1} and 1.38 × 10^7 cm^{-2}s^{-1} for thermal, epithermal and fast neutrons, respectively. The gamma ray flux was 1.25 × 10^7 cm^{-2}s^{-1}.

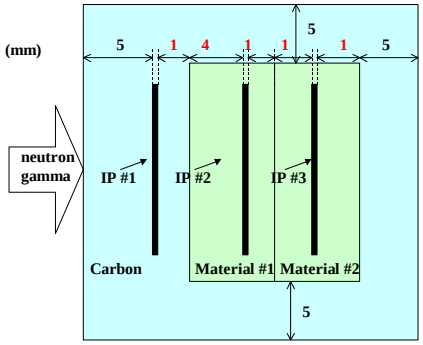

Fig. 1 Converter configuration.
The figure is not in scale.

The fluence ϕ_j of each component was determined using the following model;

$$PSL = \begin{pmatrix} PSL_1 \\ PSL_2 \\ PSL_3 \end{pmatrix} = \begin{pmatrix} a_{11} & a_{12} & a_{13} \\ a_{21} & a_{22} & a_{22} \\ a_{31} & a_{32} & a_{33} \end{pmatrix} \begin{pmatrix} \phi_1 \\ \phi_2 \\ \phi_3 \end{pmatrix} = A \cdot \phi \quad (1),$$

$$\phi = A^{-1} \cdot PSL \quad (2).$$

where a_{ij} denotes the sensitivity of the ith IP for the component j.

RESULTS: The fluence estimated using the results for the three IPs are shown in Fig. 2. All of three beam components yielded positive values successfully. This was intended by setting the each beam component contribution to the total of the energy deposition to the IP at about 10 % or more. The estimated fluence showed reasonable distributions where the values around the beam center was higher than others. The reproducibility of the result is planned to be investigated.

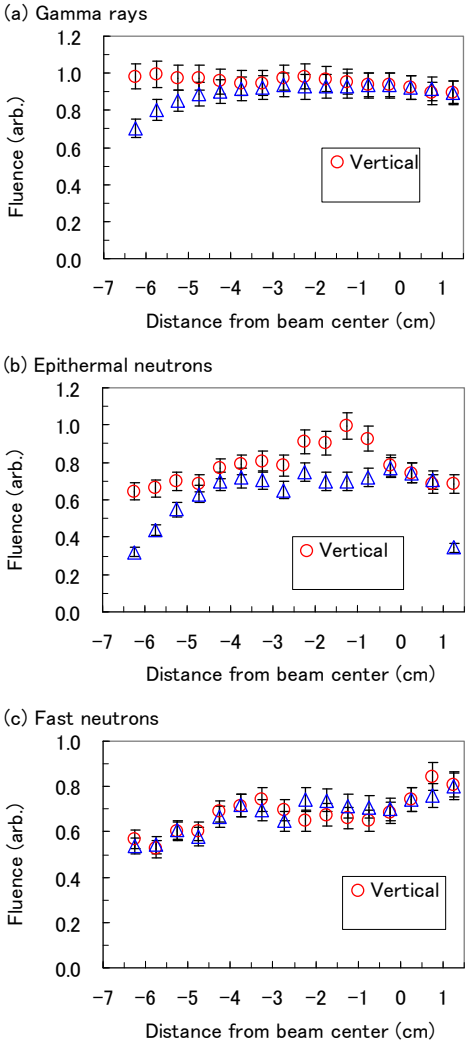

Fig. 2 Estimated fluence distribution

REFERENCES:
[1] K. Tanaka *et al.*, Appl. Rad. Isot., **115** (2016) 212-220.

PR7-8 Development of Neutron Fluence Distribution Measuring Device using Thermoluminescence Slabs

K. Shinsho, S. Yanagisawa, R. Oh, G. Wakabayashi[1], Y. Koba[2], H. Tanaka[3]

Graduate School of Human Health Science, Tokyo Metropolitan University

[1] Graduate school of Science and Engineering Research, Kindai University

[2]Center for Radiation Protection Knowledge, QST-NIRS

[3] KURNS, Kyoto University

INTRODUCTION: Boron Neutron Capture Therapy (BNCT) is one of the radiation therapies using neutrons and ^{10}B drugs which are attracted to tumors. BNCT is expected to be next-generation cancer therapy which will improve the QOL of patient because it is able to irradiate a cancer cell at the molecular level selectively. However, dosimetry techniques in mixed neutron-gamma fields have not been established yet. Therefore we examine the possibility that two dimensional Cr doped Al_2O_3 thermoluminescent slabs can apply to dosimetry in mixed neutron-gamma field. The Cr doped Al_2O_3 thermoluminescent slabs dosimeter have good properties for photons. [1,2] For example, it has a high sensitivity and high special resolution. In this study, we were prepared Cr doped Al_2O_3 thermoluminescent slabs of 10 × 10 × 0.7 mm^3 and 80 × 80 × 0.7 mm^3, then they were investigated TL properties for mixed neutron-gamma field.

EXPERIMENTS: Low melting point Al_2O_3 of Chibaceramic MFG Co. LTD., which was composed of Al_2O_3 > 99.5 wt%, SiO_2 < 0.10 wt%, Fe_2O_3 < 0.05 wt%, Na2O < 0.10 wt%, Cr < 2ppm, Cd < 1ppm, Pb < 1ppm, Hg < 1ppm was used. The bulk density of the plates was 3.7g·cm^{-1}. The dimensions used for the glow curve measurements were 10 × 10 × 0.7 mm^3. The concentration of Cr_2O_3 in the present study was 0.05 wt%. The assumed irradiation fields are the standard thermal neutron irradiation mode, mixed neutron irradiation mode and epithermal neutron irradiation mode in KUR-HWNIF, with a power of 1MW. The glow curves were recorded from room temperature up to 400 °C at a heating rate of 0.1 °C·s^{-1}. The Two-dimensional TL measurement system was made by Seisei Manufactory Co.,Ltd. It consists of a complementary metal oxide semiconductor (CMOS) camera (ORCA®-Flash4.0 V2, C11440 -22CU) , 80 × 80 mm^2 heater (Sakaguchi E.H VOC CORP.), and a dark box. After exposure (irradiation field size of 100 × 100 mm^2), the TL slabs were heated to 400 ℃ for 5 min. The TL images were captured using a CMOS camera equipped with a thermal cut filter.

RESULTS: Figure shows the arrangement of TL slabs, TL phosphor BeOs and ^{197}Au foils (upper) , and the TL imaging (lower). Table shows the thermal neutron fluencies and γ- ray dose for each numbers in Fig.. From these results, we were clear that Cr doped Al_2O_3 thermoluminescent slab has sensitivities for thermal neutron and γ-ray. The TL imaging was high special resolution. Not only thermal neutron and γ- ray imaging but also the β-ray imaging from the $^{197}Au(n,\gamma)^{198}Au \rightarrow {}^{198}Hg$ was able to acquire it clearly.

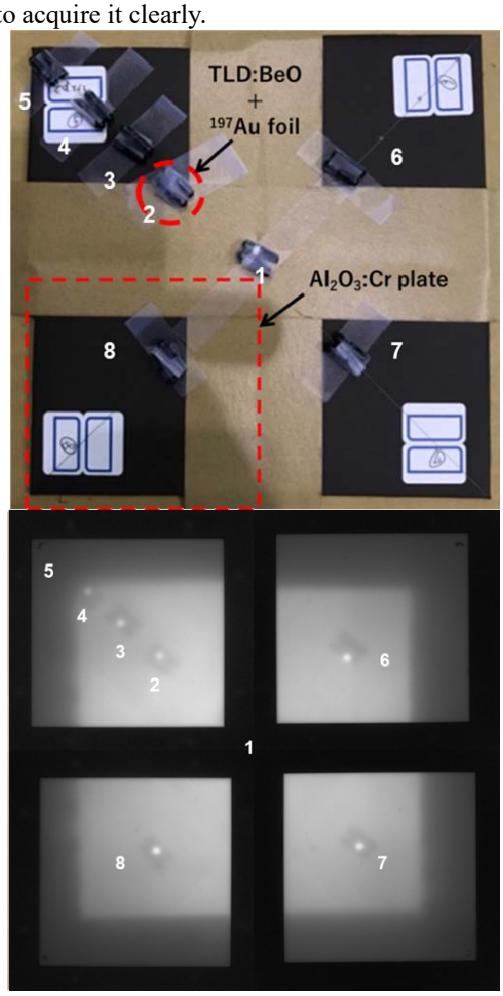

Fig. Arrangement of TL slabs, TL phosphor BeOs and ^{197}Au foils (upper) , and the TL imaging. (lower).

Table Thermal neutron fluencies and γ- ray dose for each numbers in Fig,,

	Thermal neutron fluencies [cm^{-2}]	Epithermal neutron fluencies [cm^{-2}]	γ -ray dose [Gy]
①	2.0 × 10^{12}	3.6 × 10^{11}	0.61
②	1.5 × 10^{12}	2.7 × 10^{11}	0.58
③	1.3 × 10^{12}	2.3 × 10^{11}	0.41
④	8.3 × 10^{11}	1.5 × 10^{11}	0.43
⑤	6.2 × 10^{11}	1.1 × 10^{11}	0.21
⑥	1.6 × 10^{12}	2.8 × 10^{11}	0.47
⑦	1.4 × 10^{12}	2.6 × 10^{11}	0.60
⑧	1.6 × 10^{12}	2.8 × 10^{11}	0.57

REFERENCES:

[1] K. Shinsho *et al.*, Applied radiation and isotopes., **111** (2016)117-123.

[2] K. Shinsho *et al.*, Sensors and Materials., **30** (2018) 1591-159.

PR7-9 The Study for Development and Application of Tissue Equivalent Neutron Dosimeter

M. Oita[1], T. Kamomae[2], N. Hayashi[3], T. Takada[4], K. Sakurai[4]

[1]*Graduate School of Interdisciplinary Science and Engineering in Health Systems, Okayama University*

[2] *Graduate School of Medicine, Department of Radiology, Nagoya University*

[3] *Deviation of Medical Physics, Faculty of Radiological Technology, School of Health Sciences, Fujita Health University*

[4]*KURNS, Kyoto University*

INTRODUCTION: Recent years, the clinical application of Accelerator-Based Boron Neutron Capture Therapy (AB-BNCT) has been introduced to make significant contributions to treatment for intractable cancer such as glioblastoma multiforme, superficial head and neck cancer, and melanoma in Japan.

In BNCT, the boron (n,α)-reaction of the isotope ^{10}B has a high cross section toward thermal neutrons, and the produced alpha and lithium particles have a short range on the micrometer scale. However, the neutron spectrum always spans a broad energy range, which results in different dose distribution and biological effects in tissue. A radiochromic film (RCF) is one of the most useful dosimetry tools in advantages of high spatial resolution, small energy dependence, tissue equivalence, and self-development without processing in a darkroom[1-3]. The hydrogel material is also expected to use for a patient bolus in clinical radiotherapy[4]. In this work, the authors have developed new nanocomposite hydrogel for BNCT, which is highly expected to use for a patient bolus in clinical BNCT. Moreover, the hydrogel can improve dose distribution as well as can be manufactured arbitrary size and thickness using a 3D printer. Therefore, we have investigated to develop a system that enables dose optimization by optimally modulating the neutron beam for each patient using the hydrogel and RCFs.

EXPERIMENTS: We developed a material jetting 3D printing system with a robust nanocomposite hydrogel. To assess the shielding effect of the 3D printed hydrogel for neutron beam, test slabs were fabricated. The thickness and clay nanoparticles concentration of the test slabs were varied from 3 to 35 mm and 2.5 to 5 wt%, respectively. The irradiation experiment was performed using the standard epithermal neutron irradiation mode of the Heavy Water Neutron Irradiation Facility at Kyoto University Research Reactor (KUR-HWNIF). Gold wires were used to estimate the neutron flux at the entrance and exit plane of the test slabs. Thermo-luminescent dosimeters were used for the estimation of gamma-ray doses. The measured data were normalized by the values at the entrance plane of the test slabs.

RESULTS: The relationship between the thickness of the test slab and the relative doses at the exit plane is shown in Fig. 1a. Both results of neutron flux and gamma-ray dose were firstly a slight increase and then continuous reduce. These phenomena would be affected by the buildup of neutron and gamma-ray doses. The relationship between the clay nanoparticles concentration of the test slab and the relative doses at the exit plane is shown in Fig. 1b. As an overall trend, the relative neutron flux at the exit plane of the test slabs decreased and the relative gamma-ray doses increased with increase in the clay nanoparticles concentration.

The relative neutron flux at the exit plane of test slabs of 3, 5, 10, 20, and 35 mm thickness were 67, 74, 71, 47, and 25%, respectively, and the relative gamma-ray doses were 98, 113, 104, 97, and 82%, respectively. The relative neutron flux at the exit plane of the test slabs decreased and the relative gamma-ray doses increased with increase in the clay nanoparticles concentration.

Our results demonstrated the feasibility of utilizing the 3D printed compensator to modulate the neutron beam intensity for BNCT. This result suggested that the dosimetry using RCFs is essential for a better knowledge of fast neutron flux distribution with the KUR neutron source in previous studies. Moreover, it would be feasible for BNCT dosimetry in medical application.

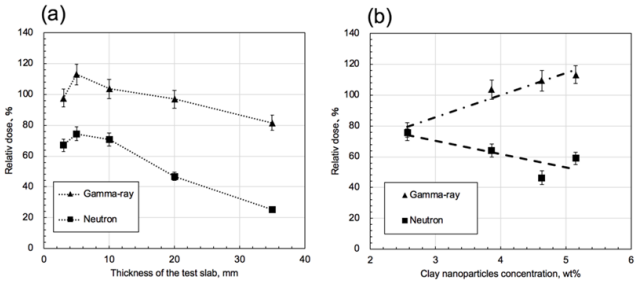

Fig. 1. Relationship between the thickness of the test slab and the relative doses at the exit plane (a), and relationship between the clay nanoparticles concentration of the test slab and the relative doses at the exit plane (b).

REFERENCES:

[1] Niroomand-Rad, Azam, *et al.*, Medical physics **25** (1998) 2093-2115.

[2] Borca, Valeria Casanova, *et al.*, Journal of applied clinical medical physics **14**(2013).

[3] Fiandra, Christian, *et al.* Medical physics **40** (2013).

[4] K. Tanaka, Y. Sakurai, *et al.,* Applied Radiation and Isotopes **127** (2017) 253-259.

PR7-10 Establishment of beam-quality estimation method in BNCT irradiation field using dual phantom technique (II)

Y. Sakurai, T. Takata, H. Tanaka, N. Kondo, M. Suzuki

Institute for Integrated Radiation and Nuclear Science, Kyoto University

INTRODUCTION: Research and development into several types of accelerator-based irradiation systems for boron neutron capture therapy (BNCT) is underway [1,2]. Many of these systems are nearing or have started clinical trials. Before the start of treatment with BNCT, the relative biological effectiveness (RBE) for the fast neutrons (over 10 keV) incident to the irradiation field must be estimated.
Measurements of RBE are typically performed by biological experiments with a phantom. Although the dose deposition due to secondary gamma rays is dominant, the relative contributions of thermal neutrons and fast neutrons are virtually equivalent under typical irradiation conditions in a water and/or acrylic phantom. Uniform contributions to the dose deposited from thermal and fast neutrons is based in part on relatively inaccurate dose information for fast neutrons.
The aim of this study is the establishment of accurate beam-quality estimation method mainly for fast neutrons by using two phantoms made of different materials, in which the dose components can be separated according to differences in the interaction cross-sections. The fundamental study of a "dual phantom technique" for measuring the fast neutron component of dose is reported [3].
In 2018, the optimization simulation was performed for the solid phantom. The solid phantoms were made based on the simulation results. The characteristic experiments were performed for these solid phantoms.

METHODS: One solid phantom was made from polyethylene containing natural LiF, and the other solid phantom was made from polyethylene containing enriched ^{6}LiF. The enrichment was 95% for Li-6. Monte Carlo simulations were used to determine the ideal mixing ratio of natural LiF and/or enriched ^{6}LiF in polyethylene.
Two kids of solid phantom were constructed based on the simulation results. One was made from polyethylene containing 30 weight percent natural LiF, the other was made from polyethylene containing 30 weight percent enriched ^{6}LiF.
Experimental characterization of the depth dose distributions of the neutron and gamma-ray components along the central axis was performed at Heavy Water Neutron Irradiation Facility (HWNIF) of KUR using activation foils and thermo-luminescent dosimeters, respectively.

RESULTS: Simulation results demonstrated that the absorbing effect for thermal neutrons occurred when the LiF concentration was over 1%. Finally, the containing ratio of natural LiF and/or enriched ^{6}LiF in polyethylene was determined to be 30 weight percent.
Experiments confirmed that the thermal neutron flux and secondary gamma-ray dose rate decreased substantially however the fast neutron flux and primary gamma-ray dose rate were hardly affected in the ^{6}LiF-polyethylene phantom. Figure 1 shows one of the results for the neutron-flux distributions in the two phantoms. It was confirmed that the dose contribution of fast neutrons was improved from approximately 10% in the LiF-polyethylene phantom, to approximately 50% in the ^{6}LiF-polyethylene phantom.

CONCLUSION: The dual phantom technique using the combination of LiF-polyethylene phantom and ^{6}LiF-polyethylene phantom provides an effective method for dose estimation of the fast neutron component in BNCT. Improvement in the accuracy achieved with the proposed technique results in improved RBE estimation for biological experiments and clinical practice.
We have a plan to perform the biological experiments at KUR-HWNIF, in order to estimate the RBE distribution in these phantoms.

ACKNOWLEDGMENT: This work was supported by JSPS KAKENHI Grant Number JP 16H05237.

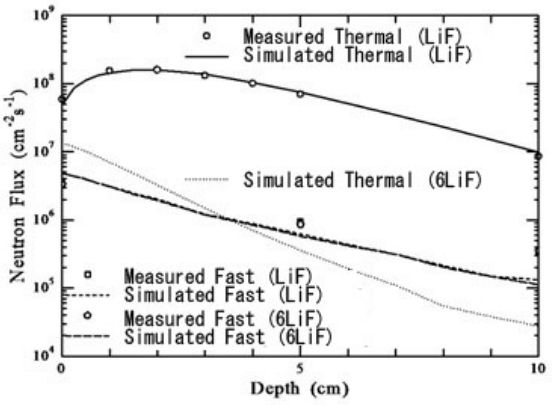

Fig. 1. Comparison between the measured and simulation results for the neutron-flux distributions in the LiF-polyethylene phantom and ^{6}LiF-polyethylene phantom.

REFERENCES:

[1] H. Tanaka *et al*., Nucl. Instr. Meth., B **267** (2009) 1970-1977.
[2] H. Kumada *et al*., Appl. Radiat. Isot., **88** (2014) 211-215.
[3] Y. Sakurai *et al*., Med. Phys., **42** (2015) 6651-6657.

PR7-11 **Development of a Prompt Gamma-ray Imaging Detector for Boron Neutron Capture Therapy**

K. Okazaki, K. Akabori[1], T. Takata[2], S. Kawabata[3], Y. Sakurai[2], H. Tanaka[2]

Graduate School of Engineering, Kyoto University
[1]Sumitomo Heavy Industries
[2]Institute for Radiation and Nuclear Science, Kyoto University
[3]Osaka Medical College

INTRODUCTION: Boron neutron capture therapy (BNCT) is employed to treat cancer cells using a ^{10}B compound and a neutron beam. Basically, the range of the heavy particles, which are produced by the (n, α) reaction between ^{10}B and thermal neutrons, is shorter than the diameter of a cell. A ^{10}B compound accumulates ^{10}B into tumor cells, and into normal cells slightly. To determine the prescript dose during the treatment, it is necessary to measure the ^{10}B concentration in tumor and normal cells in real-time. In addition, it is better to visualize the two-dimensional ^{10}B distribution. At present, it is obtained using a high purity germanium detector with prompt gamma-ray analysis at the Institute for Integrated of Radiation and Nuclear Science, Kyoto University Integrated for Radiation and Nuclear Science (KURNS)[1,2]. However, these procedures are not able to attain the ^{10}B concentration during the irradiation. Thus, a prompt gamma-ray imaging detector system has been developed. It consists of a $LaBr_3(Ce)$ scintillator and an 8 x 8 channel multi-pixel photon counter (MPPC), 64 channels amplifiers, a shaper and analog-to-digital converters (ADCs). This paper reports the concept underlying this system and the results of characterizing this system.

EXPERIMENTS: The size of the $LaBr_3(Ce)$ scintillator was 50 mm x 50 mm x 10 mm[3]. The scintillator was put in front of an 8 x 8 array MPPC. An MPPC is a type of silicon photomultiplier, and the effective active area of one channel of an MPPC is 6 x 6 mm^2. The outputs of 64 channels were fed to an amplifier unit. The 64 analg outputs were digitalized by ADCs. These digital signals were stored in a PC. Firstly, gain in each channel of the MPPC was adjusted. Secondly, gamma ray spectra from an Na-22 source, which emitted 511 keV gamma rays, were attained in order to confirm that the energy resolution at 511 keV was better than 6.5 %. This is required to discriminate between 478 and 511 keV gamma rays. Finally, gamma ray spectra using samples with 50, 100, 250 and 5000 ppm were obtained by irradiating thermal neutrons at the Kyoto University Reactor neutron guide tube. To discriminate between 478 keV and 511 keV gamma rays, the Gaussian distribution for the two gamma rays was defined.

RESULTS: The average energy resolution at 511 keV gamma rays was approximately 5.4 %. Fig.1 shows the spectrum at the center channel of the MPPC obtained with 50 ppm and three ROIs in the Gaussian distribution for 478 keV gamma rays set up. In addition, the count rate of 478 keV gamma rays and the effect from 511 keV gamma rays were calculated in each ROI. The best ROI was ROI2 because the count rate of 478 keV gamma rays on ROI2 was 0.059 that was sufficient to obtain 100 counts for about 28 minutes that was within common treatment time 1 hour, and the average effect was about 2.9 %. In addition, the linearity of the count rate at 478 keV gamma rays and ^{10}B concentration was confirmed. Furthermore, the two-dimensional boron distribution with 50 ppm on ROI2 was measured in Fig.2.

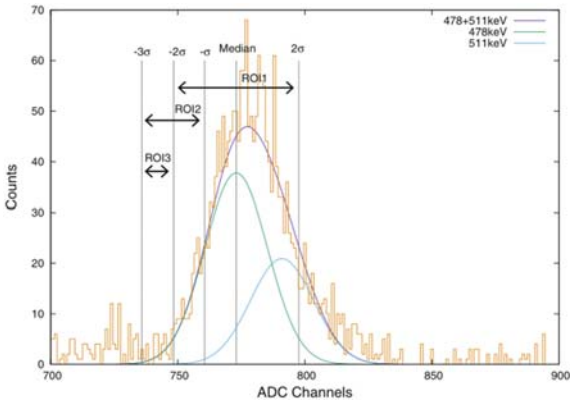

Fig. 1. Gamma rays spectrum at the center channel with 50 ppm.

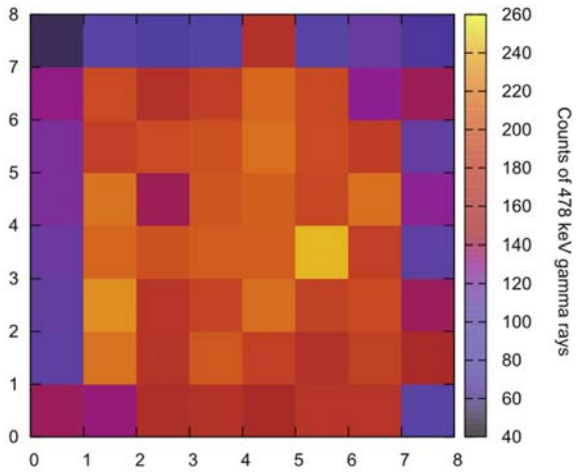

Fig. 2. Two-dimensional boron distribution with 50 ppm.

REFERENCES:

[1] T. Kobayashi and K. Kanda, Nucl. Instruments Methods Phys. Res., vol. 204, pp. 525-531, 1983.
[2] J. Laakso, M. Kulvik, I. Ruokonen, and J. Va, Clin. Chem, vol 47, No. 10, pp. 1796-1803, 2001.
[3] E. V. D. van Loef, P. Dorenbos, C. W. E. van Eijk, K. Krämer, and H. U. Güdel, Appl. Phys. Lett., vol. 1573, pp. 1-4, 2013.

PR7-12 Feasibility Studay on Ultra-High-Dose-Radiation Monitoring System with Bright-Red Scintillator and Fibers

S. Kurosawa[1], S. Kodama[2], H. Tanaka[3], A. Yamaji[2]

[1]*New Industry Creation Hatchery Center, Tohoku University*
[2]*Institute for Materials Research, Tohoku University*
[3]*Institute for Integrated Radiation and Nuclear Science, Kyoto University*

INTRODUCTION: Operation of radiation monitor under ultra-high dose is required in several applications such as the Fukushima Daiichi nuclear plants. Since photon counting mode is hard to measure gamma-ray energy due to pile-up under the ultra-high dose, current mode technique is used. Moreover, photo-detectors cannot be operated under such dose condition, Japan Atomic Energy Agency (JAEA) and other groups proposed to read the scintillation photons outside of high-dose condition using optical fibers [1]. The length of optical fiber is expected to be over 100 m, and noise event would be generated excited by gamma rays in the fiber under such high rate dose.

Red-colored emission (~700 nm) is suitable to low transmission loss region of the optical fiber [2]. Ruby (Cr doped α-Al_2O_3) is a one of the candidates for a scintillation probe, because ruby is known to be red-emitter. However, the scintillation decay of ruby is as slow as a few hundred μs, and scintillation signal intensity (pulse height) is regarded to be insufficient.

Recently, we have developed Cs_2HfI_6 (CHI) with a high light output of ~70,000 photons/MeV and moderately fast scintillation decay of ~2 μs [3]. The emission region was observed around 570 - 750 nm (50% of maximum-intensity). The pulse height of CHI is expected to be around 3-4 orders of magnitude higher than that of the ruby scintillator as shown in Figure 2. Thus, this novel scintillator is expected to be applied to the dose monitor.

EXPERIMENTS: We measured the scintillation light output with optical fiber as a function of dose using current mode. The CHI crysal was grown by the vertical Bridgman method in our laboratory, and the crystalline specimen was covered with optical cement.

Scintillation photons for CHI and ruby irradiated with gamma rays from a ^{60}Co source with an activity of around 100 TBq were detected with Si-photodiode (Si-PD) (ThorLabs, SM1PD1A) under the low dose condition using a optical fiber (Fujikura, Low OH type). The signal of the Si-PD was measured with a source meter (Keithlay, 660).

RESULTS: Figure 3 shows the Si-PD current coressponding to light intensity as a fuinction of the dose. Since CHI has brigter emission than ruby, dose dynamic range of the CHI was found to be wider than ruby. In this setup, the length of the fiber is 20 m, while we need to measure the dose with over 100-m lingth fiber in the Fukushima aplication. We found CHI had an advantage to apply into the monitor in Fukushima with longer fiber compared to ruby. Now we also estimate the noise generated in the fiber exctiecd by some dadiation, and we have developed other system using a CCD or other imaging deveises to select the emission wavelength to reject the noise.

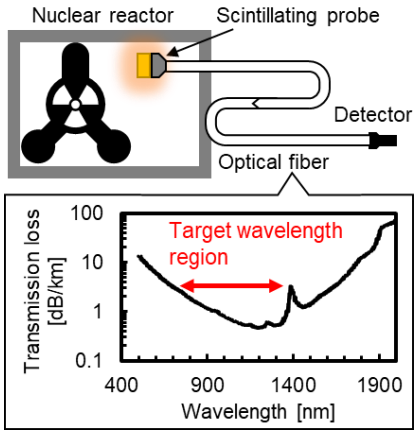

Figure 1. Schematic view of the new radiation detection technique and light transmission loss in an optical fiber.

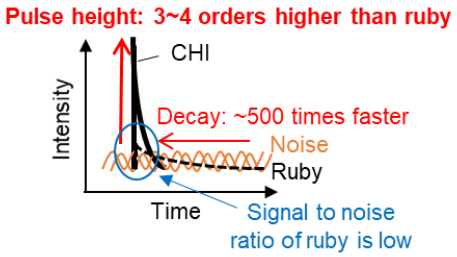

Figure 2. Comparison of time profile of scintillation pulse for CHI and ruby

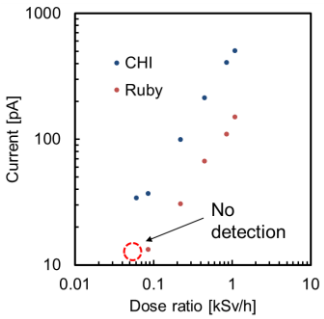

Figure 3. Current from the Si-APD as a function of dose for CHI and ruby

REFERENCES:

[1] TOPICS Fukushima Vol. 70, JAEA (2015).
[2] https://dbnst.nii.ac.jp/view_image/1879/3969?height R =785&width=475
[3] S. Kodama *et al.*, J. Cryst. Growth, 492 (2018) 1.

30P7-13

PR7-13

Establishment of the Imaging Technology of 478 keV Prompt Gamma-rays of Boron-neutron Capture Reaction and the Measurement of the Intensity of the Neutron Field

T. Mizumoto , M. Ishimoto, S. Sonoda, A. Takada[1], T. Tanimori[1], T. Takata[2], Y. Sakurai[2]

Kyoto Space Gamma, Inc.
[1]Graduate School of Science, Kyoto University
[2]KURNS

INTRODUCTION: Although BNCT is one of the promising cancer treatment methods, we have not yet obtained good method to monitor the treatment effect in real time during BNCT. The main reason is that it is difficult to know precisely both the boron concentration and neutron flux intensity in tumor cells and healthy ones. During BNCT, 478 keV prompt gamma rays are generated by the boron-neutron capture reaction. If we get images of 478 keV gamma rays and know their intensity and generation positions in real time, we can check the treatment effect on BNCT. To get gamma-ray images, there have been proposed several detectors such as SPECT gamma cameras and Compton cameras. In the case of SPECT, a very thick collimators are needed to collimate 478 keV gamma rays. It causes the serious decrease of the detection efficiency and also it would be a main reason of the noise source (511keV) of gamma rays. On the other hand, a Compton camera which does not need to use thick collimator, cannot determine the incident direction of the gamma ray only as a circle due to lack of the direction of recoil electron in Compton scattering, and hence never provide a real and quantitative distributions of Boron in body.

As the detector which overcome the shortcomings of two detectors, we have been developing electron tracking Compton cameras (ETCCs). ETCCs are advanced Compton cameras which take the information of the recoil direction of electrons and can uniquely determine the arrival direction of sub-MeV/MeV gamma ray event by event. An ETCC is the complex detector of two sub detectors: a time projection chamber TPC (Compton scatterer and recoil electron detector) and a scintillation camera (scattering gamma-ray absorber). The detail structure of ETCCs are written in [1][2].

EXPERIMENTS: Previously we developed a small ETCC which has a scintillation camera constructed with 576 pixelated GSO scintillators, whose pixel size is 6 mm x 6 mm (26 mm in high), and a TPC whose size is 100 cm^2 (15 cm in high) [2]. To improve the effective area, we developed a prototype middle size ETCC which has the same number of scintillators and a TPC whose size is 400 cm^2 (20 cm in high). We also developed a new middle size ETCC which has a TPC whose size is ~330 cm^2 (20 cm in high). We succeeded in the reduction of the size of ETCC. The total size of the new ETCC is roughly the same as that of the previous small ETCC.

As the first step of the imaging performance test for 478 keV prompt gamma rays, we performed an experiment at KURRI. We irradiated a Boron target (high concentration Boron solution) with thermal neutron beam from Kyoto University Research Reactor (KUR). During the irradiation, we set the ETCC and a germanium (Ge) detector near the target. The exposure time is about an hour. The left part of the Fig.1 shows the photograph and schematic of the experiment.

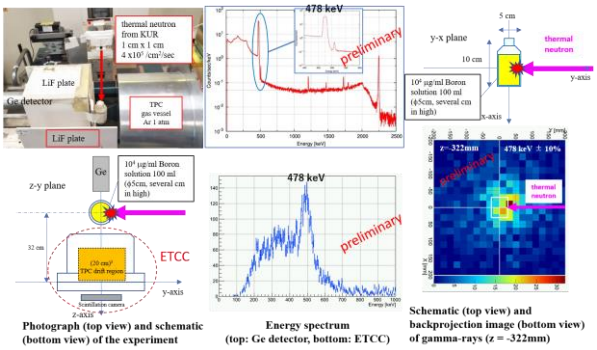

Fig.1: Experimental setup and the results. Left panel: photo and schematic of the experiment. Center panel: Spectra of the gamma-rays taken by Germanium detector and the ETCC. Right panel: schematic and back-projection image of 478 keV gamma-rays.

RESULTS: The center panel of Fig.1 shows energy spectra taken by the Germanium detector and ETCC. As shown in the spectrum of germanium detector, 478 keV gamma-rays have an overwhelmingly larger number of 511 keV gamma-rays. In the ETCC spectrum, we can see a clear peak of 478 keV gamma-rays. The right part of Fig.1 shows the schematic view and the ETCC 478 keV gamma-ray back-projection image on z = -322 mm plane (z axis is defined in Fig.1). In the back-projection image, the light point in the image corresponds to the intersection point of the neutron beam and the surface of the Boron solution container. From the results, we succeeded in imaging 478 keV prompt gamma-rays of Boron neutron capture reaction with ETCC. In the future prospects, it is needed to try the measurement test in the high dose condition and the separation of 478 keV and 511 keV gamma-ray events.

REFERENCES:

[1] Y. Mizumura, JINST, 9 (2014) C05045.
[2] T. Mizumoto, JINST 10 (2015) C0600.

30P7-14

PR7-14 Feasibility study for establihing quality assurance and quality control for radiation field in boron neutron capture therapy

S. Nakamura[1, 2], A. Urushiyama[3], T. Nishio[4], M. Tsuneda[4], T. Masuda[4], A. Sano[4], H. Okamoto[1, 2], S. Nishioka[1, 2], K. Iijima[1], M Takemori[1], H. Nakayama[1], Y. Sakurai[5], H. Tanaka[5], T. Takata[5], M. Suzuki[5], and J. Itami[1, 2, 6]

[1]*Department of Medical Physics, National Cancer Center Hospital.*

[2]*Devision of research and development for boron neutron capture therapy, National Cancer Center Exploratory Oncology Research & Clinical Trial Center.*

[3]*Rikkyo University*

[4]*Department of Medical Physics, Graduate School of Medicine, Tokyo Women's University.*

[5]*KURNS, Kyoto University.*

[6]*Department of Radiation Oncology, National Cancer Center Hospital.*

INTRODUCTION: Boron neutron capture therapy (BNCT) has been performed using the research nuclear reactor as neutron sources [1], [2]. However, recent researches have indicated that accelerator-based neutron sources can be employed in BNCT. Therefore, in order to evaluate the efficacy of BNCT in clinical oncology, the accelerator-based neutron source is installed into the hospital, such as National Cancer Center Hospital, Tokyo, Japan, and Southern TOHOKU General Hospital, Fukushima, Japan [3], [4], [5], [6]. Compared to the research nuclear reactor, the size of facility in the accelerator-based neutron source is small. In the radiation therapy, quality assurance (QA) and quality control (QC) is important to validate the treatment quality. In BNCT, the radiation field has both neutrons and gamma-rays. Hence, methods of the quality assurance (QA) and the quality control (QC) for the radiation field in BNCT have to consider its property. Nevertheless, the detector for neutron and gamma-ray is not enough small to be equipped into the accelerator-based neutron source. The purpose of this study is to establish the QA and QC methods for radiation field in BNCT with considering the property in the accelerator-based neutron source.

EXPERIMENTS: In order to establish the method for QA and QC, three types of films were examined. Two of those consisted of thermo-luminescence phosphor. After radiation exposure, with heating the film, output can be measured. Signal intensity was measured as the amount of the luminescence. The other was EBT3 film (manufactured by Ashland). The experiment of neutron irradiation was performed in Kyoto University Research Reactor (1 MW). Pictures of these experiments were shown in figure 1. TLD detectors for measuring gamma-ray and a gold foil for measuring the neutrons were placed on each of the films, and the neutrons and the gamma-rays were then delivered to those films. The delivered time was set to 30 s, 1 min, and 2 min.

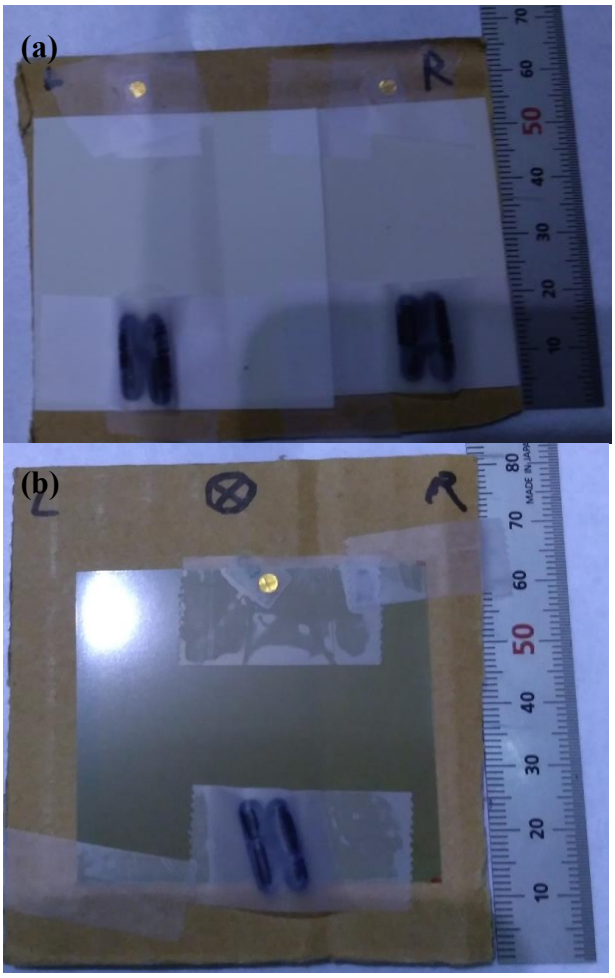

Fig.1. The picture of each experiment. (a): two films consist of thermo-luminescence phosphor. (b): EBT3 film

RESULTS: The output depended on the delivered time in each film. The outputs of three films represented different dose.

REFERENCES:

[1] K. Nakai *et al.*, Appl. Radiat. Isot., **69 (12)**: 1790-1792; (2011).
[2] S. Masunaga *et al.*, Br. J. Radiol., **85 (1011)**: 249-258; (2012).
[3] S. Nakamura *et al.*, Proc. Jpn. Acad. Ser. B Phys. Biol. Sci., **93(10)**: 821-831; (2017).
[4] S. Nakamura *et al.*, Phys. Med., **58**: 121-130; (2019).
[5] S. Nakamura *et al.*, Appl. Radiat. Isot., **125**: 80-85; (2017).
[6] H. Tanaka *et al.*, Appl. Radiat. Isot., **69 (12)**: 1642-1645; (2011).

PR7-15 Patient-Position Monitoring by Using Kinect Sensor for Boron Neutron Capture Therapy

T. Takata, H. Tanaka, Y. Sakurai, Y. Tamari and M. Suzuki

Institute for Integrated Radiation and Nuclear Science, Kyoto University

INTRODUCTION: In boron neutron capture therapy (BNCT) irradiations carried out at Kyoto University Research Reactor, sitting position has been applied in many cases, considering flexibility of patient positioning and structural restriction of an irradiation facility. In some cases, there is difficulty in reproducing a patient position determined by a treatment planning process, which is related to a patient set-up error. Also, the sitting position is sometimes unstable, resulting in displacement from an initial set-up position during an irradiation period, which is related to patient motion. These set-up error and motion cause uncertainty in estimation of delivered dose.

Aiming to improve the dose estimation accuracy, we have been developing a patient-position monitoring system using a Kinect sensor: a real-time range sensing device [1]. This report describes measurement of patient position displacement by using a Kinect sensor.

EXPERIMENTS: Measurement using a human head phantom was performed in a treatment room at KUR heavy water neutron irradiation facility, which is usually used for patient positioning prior to BNCT irradiation. The experimental setup is shown in Fig. 1. The head phantom was placed on a XYZ stage. A Kinect sensor was pointed to the phantom from the downstream of beam axis at a distance of about 2m. The phantom was moved to each of XYZ directions shown in Fig. 1(a) in a range from 3 to 10mm, and 2D range image was acquired with the sensor at each of the positions. An example of the 2D range image is shown in Fig. 1 (b).

Procedure of displacement estimation is described in Fig. 2. The 2D range image at each position was converted to point cloud data format, then the data points in a background region were masked. Displacement was estimated according to the transformation vector to the original position, which was obtained by making registration of point clouds. The VC++, Kinect for Windows SDK v2 and PCL (Point Cloud Library) ver. 1.8.1 [2] were used for handling the 2D range images and point cloud data. The registration of the point clouds was performed by means of Iterative Closest Point (ICP) algorithm [3] implemented in the PCL library.

RESULTS: The estimated displacements are shown in Table 1. Displacements in a range of ~10mm were estimated with good accuracy in directions normal to the y axis. However, there were large discrepancy in the y axis along the sensor-to-object direction. Ambient IR rays can be considered a cause of fail in measurement because a Kinect sensor uses an IR time-of-flight method to measure a range to an object. Especially, the intense IR rays from mercury lamps attached on the ceiling of the reactor room were considered to affected largely on the measurement performance of the Kinect. Shielding the ambient IR can be effectively work to improve the results.

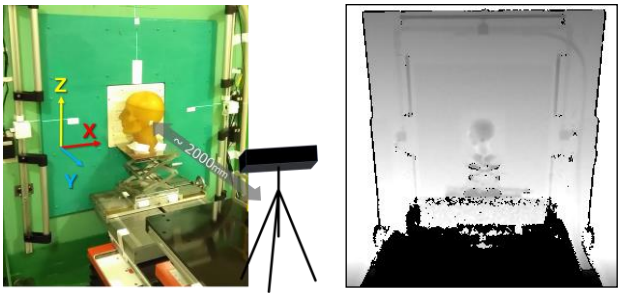

(a) (b)

Fig. 1. Experimental setup for position measurement using a head phantom: (a) arrangement of a phantom and a Kinect sensor, shown with definition of spatial coordinate, (b) an example of range image acquired with the sensor.

Fig. 2. Procedure of displacement estimation. Point cloud presented with white dots is corresponding to original position.

Table 1. Estimation results of phantom displacement measured with the Kinect sensor.

Displacement (mm)	X		Y		Z	
	+3	+10	+3	+10	-3	-10
Estimated (mm)	+2.5	+10	+0.7	+3.5	-7	-9

REFERENCES:

[1] T. Takata *et al.*, KURRI PROGRESS REPORT 2017 (2018) 88.
[2] R. B. Rusu, S. Cousins, 2011 IEEE International Conference on Robotics and Automation (2011).
[3] S. Rusinkiewicz, M. Levoy, Proceedings Third International Conference on 3-D Digital Imaging and Modeling (2001).

I-1. PROJECT RESEARCHES

Project 8

PR8 Analyzing Tumor Microenvironment and Exploiting its Characteristics in Search of Optimizing Cancer Therapy Including Neutron Capture Therapy

Shin-ichiro Masunaga, M.D., Ph.D.

Particle Radiation Biology, Division of Radiation Life Science, Institute for Integrated Radiation and Nuclear Science, Kyoto University

BACKGROUNDS AND PURPOSES: Human solid tumors contain moderately large fractions of quiescent (Q) tumor cells that are out of the cell cycle and stop cell division, but are viable compared with established experimental animal tumor cell lines. The presence of Q cells is probably due, in part, to hypoxia and the depletion of nutrition in the tumor core, which is another consequence of poor vascular supply. As a result, Q cells are viable and clonogenic, but stop cell division. In general, radiation and many DNA-damaging chemotherapeutic agents kill proliferating (P) tumor cells more efficiently than Q tumor cells, resulting in many clonogenic Q cells remaining following radiotherapy or chemotherapy. Therefore, it is harder to control Q tumor cells than to control P tumor cells, and many post-radiotherapy recurrent tumors result partly from the regrowth of Q tumor cells that could not be killed by radiotherapy. Similarly, sufficient doses of drugs cannot be distributed into Q tumor cells mainly due to heterogeneous and poor vascularity within solid tumors. Thus, one of the major causes of post-chemotherapy recurrent tumors is an insufficient dose distribution into the Q cell fractions.

With regard to boron neutron capture therapy (BNCT), with ^{10}B-compounds, boronophenylalanine-^{10}B (BPA) increased the sensitivity of the total cells to a greater extent than mercaptoundecahydrododecaborate- ^{10}B (BSH). However, the sensitivity of Q cells treated with BPA was lower than that in BSH-treated Q cells. The difference in the sensitivity between the total and Q cells was greater with ^{10}B-compounds, especially with BPA. These findings concerning the difference in sensitivity, including other recovery and reoxygenation following neutron irradiation after ^{10}B-compound administration were mainly based on the fact that it is difficult to deliver a therapeutic amount of ^{10}B from ^{10}B-carriers throughout the target tumors, especially into intratumor hypoxic cells with low uptake capacities.

Hypoxia is suggested to enhance metastasis by increasing genetic instability. Acute, but not chronic, hypoxia was reported to increase the number of macroscopic metastases in mouse lungs. We recently reported the significance of the injection of an acute hypoxia-releasing agent, nicotinamide, into tumor- bearing mice as a combined treatment with γ-ray irradiation in terms of repressing lung metastasis. As the delivered total dose increased with irradiation, the number of macroscopic lung metastases decreased reflecting the decrease in the number of clonogenically viable tumor cells in the primary tumor. The metastasis-repressing effect achieved through a reduction in the number of clonogenic tumor cells by irradiation is much greater than that achieved by releasing tumor cells from acute hypoxia. On the other hand, more ^{10}B from BPA than from BSH could be distributed into the acute hypoxia-rich total tumor cell population, resulting in a greater decrease in the number of highly clonogenic P tumor cells with BPA-BNCT than with BSH-BNCT and with neutron beam irradiation only. BPA-BNCT rather than BSH-BNCT has some potential to decrease the number of lung metastases, and an acute hypoxia- releasing treatment such as the administration of nicotinamide, bevacizumab, wortmannin or thalidomide may be promising for reducing numbers of lung metastases. Consequently, BPA-BNCT in combination with the treatment using these agents may show a little more potential to reduce the number of metastases. Now, it has been elucidated that control of the chronic hypoxia-rich Q cell population in the primary solid tumor has the potential to impact the control of local tumors as a whole, and that control of the acute hypoxia-rich total tumor cell population in the primary solid tumor has the potential to impact the control of lung metastases.

The aim of this research project is focused on clarifying and analyzing the characteristics of intratumor microenvironment including hypoxia within malignant solid tumors and optimizing cancer therapeutic modalities, especially radiotherapy including BNCT in the use of newly-developed ^{10}B-carriers based on the revealed findings on intratumor microenvironmental characteristics.

RESEARCH SUBJECTS:

The collaborators and allotted research subjects (ARS) were organized as follows;

ARS-1 (30P8-1): Optimization of Radiation Therapy Including BNCT in terms of the Effect on a Specific Cell Fraction within a Solid Tumor and the Suppressing Effect of Distant Metastasis. (S. Masunaga,*et al.*)

ARS-2 (30P8-2): Development of Hypoxic Microenvironment-Oriented ^{10}B-Carriers. (H. Nagasawa, *et al.*)

ARS-3 (30P8-3)*: Search and Functional Analysis of Novel Genes that Activate HIF-1, and Development into Local Tumor Control. (H. Harada, *et al.*)

ARS-4 (30P8-4)*: Radiochemical Analysis of Cell Lethality Mechanism in Neutron Capture Reaction. (R. Hirayama, *et al.*)

ARS-5 (30P8-5): Development of Neutron Capture Therapy Using Cell-Membrane Fluidity Recognition Type Novel Boron Hybrid Liposome. (S. Kasaoka, *et al.*)

ARS-6 (30P8-6): Drug Delivery System Aimed at Adaptation to Neutron Capture Therapy for Melanoma. (T. Nagasaki, *et al.*)

ARS-7 (30P8-7): Molecular Design, Synthesis and Functional Evaluation of Hypoxic Cytotoxin Including Boron. (Y. Uto, *et al.*)

ARS-8 (30P8-8): Bystander Effect on Malignant Trait of Tumor Cells by Irradiation. (H. Yasui, *et al.*)

ARS-9 (30P8-9): Analysis of the Response of Malignant Tumor to BNCT. (M. Masutani, *et al.*)

ARS-10 (30P8-10): Cell Survival Test by Neutron Capture Reaction Using Boron Compound and Inhibitory Effect on Tumor Growth. (K. Nakai, *et al.*)

ARS-11 (30P8-11): Multilateral Approach Toward Realization of Next Generation Boron Neutron Capture Therapy. (Y. Matsumoto, *et al.*)

ARS-12 (30P8-12): Analysis of Radiosensitization Effect through Targeting Intratumoral Environmental. (Y. Sanada, *et al.*)

ARS-13 (30P8-13)*: Exploratory Research on the Optimal Administration of ^{10}B Compound Aiming at New Enforcement Method of Neutron Capture Therapy (S. Masunaga *et al.*)

ARS-14(30P8-14) *: Examination of Cancer Cell Accumulation Property of New Boron Agent (CbaP14). (J. Hiratsuka, *et al.*)

(*There was no allocated time for experiments using reactor facilities during their operation periods of FY 2018.**)**

PR8-1

Estimation of Therapeutic Efficacy of BCNT Based on the Intra- and Intercellular Heterogeneity in ^{10}B-Distribution

T. Sato[1] and S. Masunaga[2]

[1]*Nuclear Science and Engineering Center, Japan Atomic Energy Agency*
[2]*Institute for Integrated Radiation and Nuclear Science, Kyoto University*

INTRODUCTION: Two types of dose were proposed for use in the treatment planning of boron neutron capture therapy (BNCT) for expressing its high relative biological effectiveness (RBE). On one hand, the RBE -weighted dose is the sum of the absorbed doses weighted by fixed RBE for four dose components of BNCT, which are attributable to ^{10}B(n,α)^{7}Li, ^{14}N(n,p)^{14}C, and ^{1}H(n,n)p reactions as well as photons, respectively. On the other hand, photon-isoeffective dose is the photon dose to give the same biological effect calculated considering the dose dependence of RBE and the synergetic effect between different types of radiation [1]. In this study, the depth distributions of the two types of dose in a phantom placed at an accelerator-based BNCT field were calculated using Particle and Heavy Ion Transport code System, PHITS [2], coupled with an extended stochastic microdosimetric kinetic (SMK) model [3].

MATERIALS AND METHODS: The basic flow of the calculation procedures is shown in Fig. 1. In the PHITS simulation, a cylindrical phantom with the radius of 10 cm and the depth of 20 cm composed of ICRU soft tissue was placed at the beam port of the Linac-based BNCT facility in University of Tsukuba [4]. The absorbed doses were determined from the calculated neutron and photon fluxes multiplied with their corresponding kerma factors for each dose component. The calculated absorbed doses were converted to RBE-weighted dose and photon-isoeffective dose, using the extended SMK model. The parameters used in the model were evaluated by the least-square fitting of the surviving fractions of SCC VII murine squamous cell carcinomas obtained from *in vivo/in vitro* experiments of tumor-bearing mice treated by BNCT [5].

RESULTS AND DISCUSSION: Fig. 2 shows the RBE-weighted dose and photon-isoeffective dose in the phantom administrated with BPA or BSH, or without ^{10}B. The absorbed doses at the entrance of the phantom without ^{10}B were normalized to 2 and 10 Gy in panels (A) and (B), respectively. It is evident from Fig. 2 that the photon-isoeffective doses are larger than the corresponding RBE-weighted doses in panel (A), while the reverse is true in panel (B) except at the locations deeper than 7 g/cm^2. The depth dependence was more apparent in the RBE-weighted doses, which decreased more dramatically with increasing depth. Such tendency is mainly due to the consideration of the dose dependence of RBE in the calculation of the photon-isoeffective dose because RBE decreases with an increase in the absorbed dose. The consideration of the synergetic effect also causes the difference, which raises the photon-isoeffective dose by approximately 10-20%. More detailed discussions can be found in our recently published paper [6].

REFERENCES:

[1] S.J. Gonzalez, *et al.*, Phys Med Biol **62** (2017) 7938-7958.
[2] T. Sato *et al.*, J Nucl Sci Technol **55**, (2018) 684-690.
[3] T. Sato *et al.*, Sci Rep **8** (2018) 988.
[4] A. Masuda *et al.*, Appl Radiat Isot **127** (2017), 47-51.
[5] S. Masunaga *et al.*, Springerplus **3** (2014), 128.
[6] T. Sato *et al.*, Radiat Prot Dosim (2018) DOI: 10.1093/rpd/ncy235

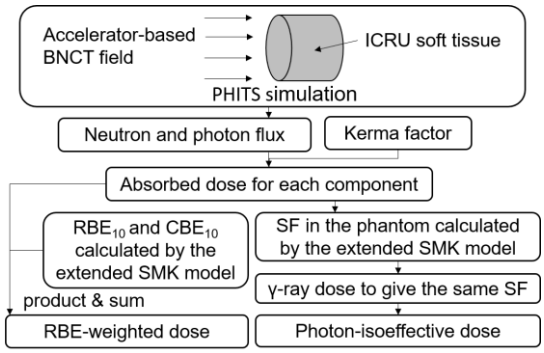

Fig. 1. Basic flow of the calculation carried out in this study.

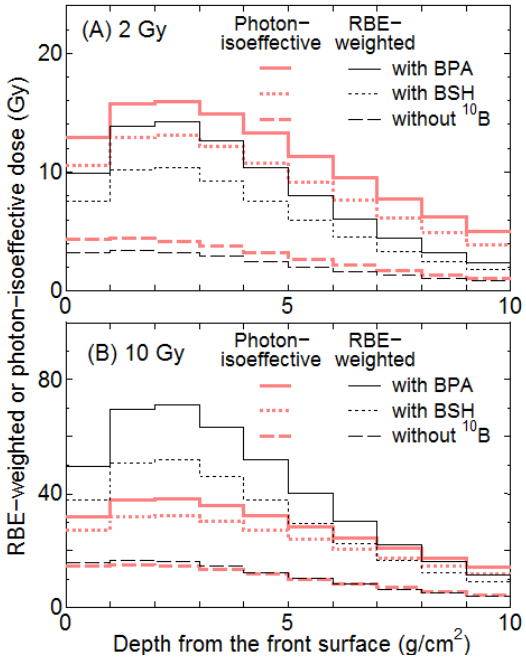

Fig. 2. Calculated RBE-weighted dose and photon -isoeffective dose in the phantom administrated with BPA or BSH, or without ^{10}B.

PR8-2 Design, synthesis and biological evaluation of lipopeptide conjugates of BSH for BNCT

A. Isono[1], M. Tsuji[1], Y. Sanada[2], T. Hirayama[1], S. Masunaga[2] and H. Nagasawa[1]

[1] *Laboratory of Medicinal & Pharmaceutical Chemistry, Gifu Pharmaceutical University*

[2] *KURNS, Kyoto University*

INTRODUCTION: Tumor selective delivery of sufficient quantity of ^{10}B is essential for the success of boron neutron capture therapy (BNCT). The clinically used boron carrier, sodium mercaptoundecahydro-closo-dodecaborate (BSH: Na2B12H11SH) does not penetrate the cell membrane directly, due to its highly hydrophilic and anionic properties. Here, we developed a new membrane-permeable boron cluster using the cell-penetrating lipopeptide pepducin as the vehicle for intracellular delivery of boron clusters. Pepducins are membrane-permeable, lipidated peptides, developed as allosteric modulators of the G-protein-coupled receptor (GPCR). We have previously developed fluorescence resonance energy transfer (FRET)-based pepducin probes to demonstrate the direct membrane penetration of a pepducin by fluorescence imaging in living cells. So, we designed and synthesized pepducin-BSH conjugates and performed structural optimization to improve cellular uptake. (Fig.1)

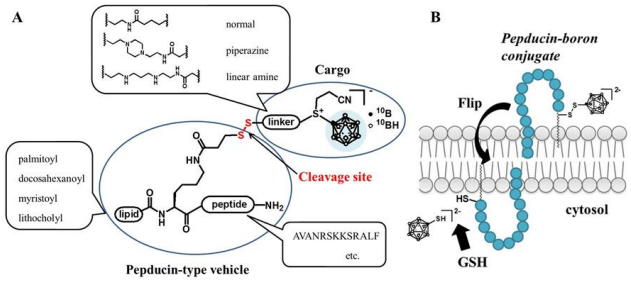

Fig. 1. Molecular design (A) and putative mechanism of intracellular delivery of pepdicin-BSH conjugates.

EXPERIMENTS: All compounds were synthesized based on sol-id-phase synthesis. (Table 1) T98G, cells were treated with the boron carriers (10 or 20 μM) at 37 °C for various times, then, washed with PBS three times, and dissolved in 200 μL HNO3 for 1 h. The boron concentrations of these extracts were measured by ICP-AES. To evaluate neutron sensitizing ability of the compounds, T98G cells were treated with 20 μM boron carriers for 24 h. Then the cells were washed with PBS, suspended in serum containing medium and aliquoted into Teflon tubes for irradiation. Cells were irradiated using the neutron beam at the Heavy Water Facility of the Kyoto University Research Reactor (KUR) operated at 1 MW power output. The survival rates of the irradiated cells were determined using conventional colony assays.

Table 1. Structures of new boron carriers.

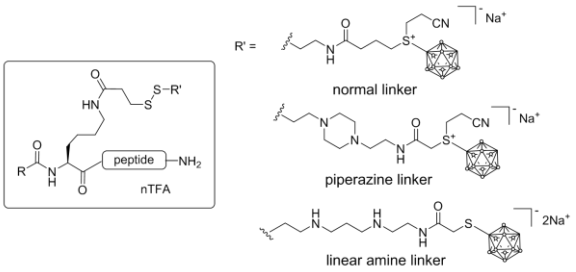

Boron carrier	R	Sequence of peptide	linker
1a[a]	$C_{15}H_{31}$	**AVANRSKKSRALF**	
1b	$C_{15}H_{31}$	**KKSRALF**	
1c	$C_{15}H_{31}$	**NRSKKSRALF**	
1d	$C_{15}H_{31}$	**AVANRSK**	
1e	$C_{15}H_{31}$	**AVANRSKKSR**	
1f	$C_{15}H_{31}$	**ALFAVANRSKKSR**	
1g	$C_{15}H_{31}$	**ARVSAKNKASLRF**	
1h	$C_{15}H_{31}$	**FLARSKKSRNAVA**	
1i	$C_{15}H_{31}$	**AVANRPGKSRALF**	normal
1j	$C_{15}H_{31}$	**AVANRPKKSRALF**	
2a[a, b]	$C_{15}H_{31}$		
3a	CH_3		
3b	$C_{22}H_{19}$		
3c	$C_{13}H_{27}$		
3d	$C_{23}H_{38}OH$	**AVANRSKKSRALF**	
3e	$C_{23}H_{38}OCOCF_3$		
4[a]	$C_{15}H_{31}$		piperazine
5[a,b]	$C_{15}H_{31}$		linear amine

[a] Lipopeptide moiety is derived from P1pal-13. [b] No cyanoethyl group.

RESULTS: Among the pepducin-BSH conjugates, the most effectively incorporated and accumulated in the cells was compound **1a,** which has a peptide of 13 residues derived from the intracellular third loop of PAR1 and a palmitoyl group. Compound **1a** and compound **4** both showed a stronger radio-sensitizing effect than BSH on T98G cells under mixed-neutron beam irradiation. (Table 2)

Table 2. Plating efficiencies without irradiation, D_{10} values and the enhancing effects of boron carriers.

	PE without irradiation (%)	D_{10} value (Gy)	The enhancing effect
Control	19.0±4.4	4.17	-
BSH	32.9±3.6	4.32	0.97
1a	51.2±5.6	0.55	7.69
4	20.0±4.5	0.72	5.79

The results demonstrate that lipopeptide conjugation is apparently effective for enhancing intracellular delivery and accumulation of BSH and improving the cytotoxic effect of BNCT [1].

REFERENCES:

[1] A. Isono *et al.*, ChemMedChem., **14** (2019) 823-832.

PR8-3 Molecular mechanism underlying radioresistance of hypoxic tumor cells

M. Kobayashi[1,2], S. Masunaga[3], A. Morinibu[1,2] and H. Harada[1,2]

[1]Laboratory of Cancer Cell Biology, Graduate School of Biostudies, Kyoto University.
[2]Department of Genome Dynamics, Radiation Biology Center, Graduate School of Biostudies, Kyoto University.
[3] Institute for Integrated Radiation and Nuclear Science, Kyoto University.

INTRODUCTION: Cancer cells are 2-3 times more radioresistant under hypoxic than normoxic conditions, which causes poor prognosis of patients with more hypoxic regions in their tumor tissues [1]. Although the radioresistance is known to be induced by biological mechanisms, at least in part, in a hypoxia-inducible factor 1 (HIF-1)-dependent manner, further studies are needed for better understanding of the nature of hypoxic cell radioresistance [2, 3].

EXPERIMENTS & RESULTS:
Here we found that hypoxia-inducible secretory protein 2, HISP2, which we recently identified as a novel hypoxia-responsive gene through our own DNA microarray analysis, causes radioresistance of hypoxic cancer cells in a HIF-1-independent manner (*in preparation*). qRT-PCR experiments confirmed that HISP2 mRNA levels were significantly upregulated under hypoxic conditions. ELISA experiments for culture media showed that the amount of secreted HISP2 protein levels increases under hypoxic conditions. The hypoxia-dependent increase in the HISP2 mRNA levels was abrogated by a transcription inhibitor, actinomycin D, suggesting that HISP2 were upregulated under hypoxia at transcription initiation levels. A loss-of-function study found that the hypoxia-dependent increase in the HISP-2 mRNA levels was significantly abrogated by silencing of HIF-1β, but not by that of HIF-1α and HIF-2α, suggested that the hypoxia-mediated expression is dependent on HIF-1β. A reporter gene assay with the use of an expression vector for EGFP-53BP1M fusion protein demonstrated that HISP2-overexpression decreased the number of DNA double strand breaks after irradiation. Clonogenic cell survival assay showed that cancer cells acquired radioresistance when transfected with HISP2-overexpression vector. All of these data suggested that HISP2 proteins are secreted under hypoxic conditions in a HIF-1-independent but HIF-1β-dependent manner and decrease the number of double-strand break after irradiation, leading to radioresistance of cancer cells in an autocrine fashion.

REFERENCES:
[1] *Harada H. Hypoxia-inducible factor 1-mediated characteristic features of cancer cellsfor tumor radi-aresistance. J Radiat Res., **57** (2016) 99-105.
[2] Koyasu S, Kobayashi M, Goto Y, Hiraoka M, *Harada H. Regulatory mechanisms of hypoxia-inducible factor 1 activity: Two decadesof knowledge. Cancer Sci. 109:560-571. 2018.
[3] Nagao A, Kobayashi M, Koyasu S, Chow CCT, *Harada H. HIF-1-dependent reprogramming of glucose metabolic pathway of cancer cellsand its therapeutic significance. *Int J Mol Sci*. 20:238. 2019.

PR8-4 Membrane-Targeted Boron Neutron Capture Therapy with Boron Liposomes Composed of Dimyristoylphosphatidylcholine

S. Kasaoka[1], Y. Okishima[1], Y. Tanaka[1], H. Yoshikawa[1], Y. Sanada[2], Y. Sakurai[2], H. Tanaka[2] and S. Masunaga[2]

[1]*Department of Pharmaceutical Science, Hiroshima International University*

[2]*KURNS, Kyoto University*

INTRODUCTION: There are many reports that membranes in cancer cells are relatively more fluid compared to healthy cells. Higher membrane fluidity in cancer cells closely relates to their invasive potential, proliferation, and metastatic ability [1]. Liposomes composed of dimyristoylphosphatidylcholine (DMPC) and polyoxyethylenedodecylether were found to inhibit the growth of human promyelocytic leukemia cells without using any drugs [2]. In this study, we have developed a novel boron delivery system using the membrane-fluidity sensitive boron liposomes (MFSBLs) composed of DMPC and borocaptate (BSH)-conjugated chemical compounds for boron neutron capture therapy.

EXPERIMENTS: Octadecylamine and 1,2-dimyristoyl-sn-glycero-3-phosphorylethanolamine were conjugated with BSH using the optimal hetero-crosslinking agents for boron compounds. MFSBLs composed of DMPC, polyoxyethylenedodecylether and boron compounds at mole ratios of 8:0.9:1.1 were prepared by sonication method in 5% glucose solution at 45°C. The diameter of MFSBLs was measured with a light scattering spectrometer. The boron concentration was measured by inductively coupled plasma atomic emission spectrometry. B16F10 murine melanoma cells, COLO679 human melanoma cells and human fibroblast cells were incubated with 2-6 ppm of ^{10}B at 37℃ for 14 hours before neutron irradiation. The cells were rinsed twice in PBS and suspended in fresh medium. After neutron irradiation the cells were plated into plastic Petri dishes 60 mm in diameter at 200 cells per dish. They were incubated for an additional 7 days to allow colony formation.

RESULTS: MFSBLs had a mean diameter of 59.6 nm. High encapsulation efficiency value from 55% to 89% of ^{10}B in MFSBLs were obtained. MFSBLs had high stability (95-99%) in the retention of ^{10}B during storage at 4℃ for 4 weeks. All borocaptate-loaded formulations had low cytotoxic effects in human fibroblast cells. MFSBLs were efficiently fused to melanoma cells, but were inefficiently fused to human fibroblast cells. Thus, it is essential to elevate the ^{10}B concentration in melanoma cells, while maintain low levels of ^{10}B in normal fibroblast cells. The tumor/normal ratio (T/N ratio) was 2.1-3.0. As shown in Fig. 1, MFSBLs showed higher suppression of growth of murine and human melanoma cells than BSH solution. This result suggested novel MFSBLs is useful for ^{10}B carrier on BNCT for melanoma.

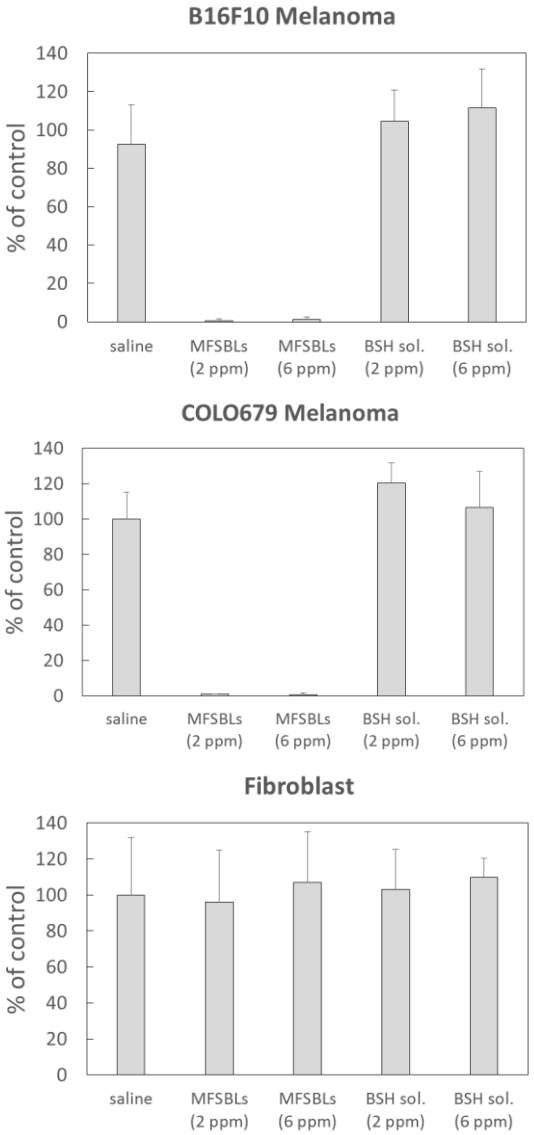

Fig. 1. Suppression of the colony formation of B16F10 cells, COLO679 melanoma cells and fibroblast cells after in vitro BNCT.

REFERENCES:

[1] Sherbet GV. Magalit, Exp Cell Biol., **57** (1989).
[2] Y. Matsumoto *et al.* Int. J. Cancer, **115** (2005).

PR8-5 GLUT1-mediated endocytosis could be a major pathway for internalisation of kojic acid-appended carborane conjugate into melanoma cells

S. Dowaki, K. Matsuura, R. Kawasaki, M. Kirihata[1], Y. Hattori[1], Y. Sakurai [2] and S. Masunaga [2]

Graduate School of Engineering, Osaka City University
[1] BNCT Research Center, Osaka Prefecture University, [2] Institute for Integrated Radiation and Nuclear Science, Kyoto University

INTRODUCTION: Receptor-mediated endocytosis is potent pathways for the internalization of drugs into target cells. It is well known that the expression level of glucose transporter and uptake of glucose are increased in cancer cells [1]. We have previously reported the inclusion complex of kojic acid-appended carborane (CKA) with hydroxypropyl-ß-cyclodextrin (HP-β-CD) as a novel boron agent is potent for melanoma targeting BNCT. CKA/HP-β-CD complex showed melanoma cells selectivity, unique nuclear localization, and high tumor-suppression effect on BNCT toward melanoma-bearing mice. Herein, mechanism of high efficient internalization of CKA/HP-β-CD complex into melanoma cells is evaluated.

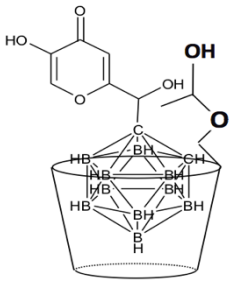

Structure of CKA/HP-β-CD

EXPERIMENTS: B16BL6 cells were maintained in RPMI containing 10% FBS and 1% penicillin/streptomycin. B16BL6 cells seeded on the 6 well plate at the concentration of 2.0×10^5 cells/well. The cells were exposed to CKA/HP-β-CD complex (10 ppm) and the cells were corrected at each time point (12 and 24 hr). The involvement of GLUT1 on the uptake of CKA is confirmed with not only a small-molecule inhibitor of GLUT1 [2] ,but also RNA interference-mediated reduction in GLUT1 [3]. The isolated cells were digested by using aqua regia with heating (95 ºC, 30 min; 115 ºC, 60 min). After centrifugation, the cellular uptake amounts were quantified by ICP-AES.

RESULTS AND DISCUSSION: As shown in Fig. 1 and 2, clear suppression of CKA uptake by melanoma cells were observed in the presence of WZB117 inhibitor and siRNA for GLUT1. Furthermore, CKA uptake obviously reduced when melanoma cells were incubated in the normal medium with glucose. These results suggested that the internalization of CKA/HP-β-CD complex into melanoma cells is enhanced with GLUT1-mediated endocytosis.

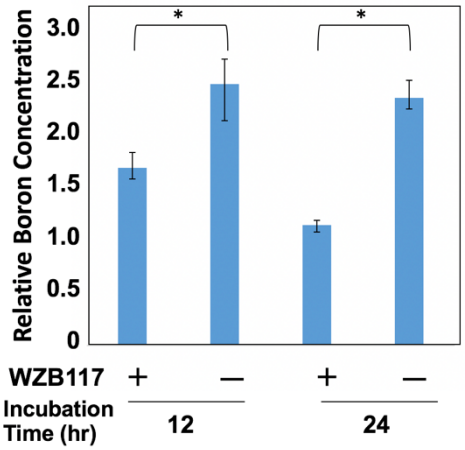

Fig.1 Suppression of CKA uptake by the inhibition of GLUT1 by WZB117. B16BL6 cells were incubated in the presence or absence of WZB117 (30 μM) for 12 and 24 hr. * denotes P < 0.02 between indicated treatments.

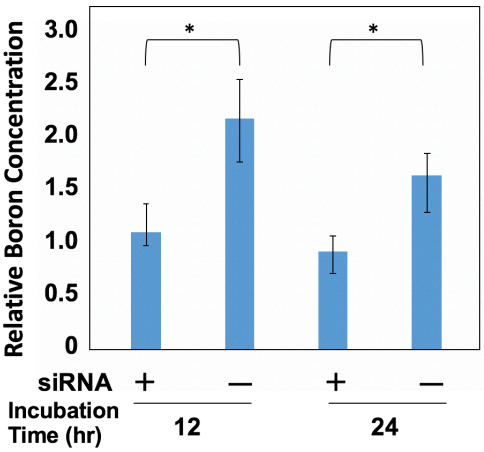

Fig.2 Suppression of CKA uptake by RNA interference-mediated reduction in GLUT1. B16BL6 cells were incubated in the presence or absence of siRNA (100 nM) for 12 and 24 hr. * denotes P < 0.02 between indicated treatments.

REFERENCES:

[1] T. Yamamoto *et al.*, Biochem. Biophys. Res. Commun., **170** (1990) 223-30.
[2] Y. Liu *et al.*, Mol. Cancer Ther., **11** (2012) 1672-82.
[3] L. Al-Khalili *et al.*, Biochem. Biophys. Res. Commun., **307** (2003) 127-32.

30P8-6

PR8-6 Development of novel BPA-Tirapazamine hybrid BNCT agent targeting hypoxic tumor cells

Y. Uto, Y. Tanaka, S. Masunaga[1], Y. Sanada[1]

Graduate School of Technology, Industrial and Social Sciences, Tokushima University
[1]Radiation and Nuclear Science, Kyoto University

INTRODUCTION: Hypoxia is a ubiquitous environment of cancer, it has a resistance to anticancer drugs and X-ray, and accelerated infiltration / metastasis is a problem. Boron neutron capture therapy (BNCT), a kind of radiotherapy, is a treatment method utilizing neutron capture reaction in tumor cells by accumulating ^{10}B in tumor tissue. Hybrid molecules of Tirapazamine (TPZ), as a hypoxic cytotoxin and the neutron scavenger *p*-borono-*L*-phenylalanine (BPA) are useful as selective BNCT agent for hypoxic tumors. Since therapeutic efficiency of BNCT depends on ^{10}B concentration, it is expected to provide an effective therapeutic effect for hypoxic cancer.

In this study, UTX-117 with amide linkage of TPZ and BPA and UTX-118 with ester linkage of TPZ and BPA were designed and synthesized, and antitumor activity and neutron sensitizing activity were evaluated. UTX-117 and UTX-118 exhibit hypoxia selective cytotoxicity and UTX-118 has improved uptake rate compared to BPA fructose complex. Further, UTX-117 and UTX-118 shows neutron sensitizing activity.

EXPERIMENTS: Tirapazamine derivatives and L-BPA were condensed to synthesize UTX-117 and UTX-118 (Fig.1). Using melanoma cells B16-F10 cells, the IC_{50} values of UTX-117 and UTX-118 were evaluated by WST-1 assay. The cell uptake of UTX-117 and UTX-118 was measured by ICP-AES, and the intracellular boron concentration was calculated. Neutron sensitizing activity of UTX-117, UTX-118 and BPA-F to B16-F10 cells were evaluated by WST-1 assay.

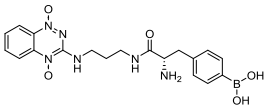

UTX-117

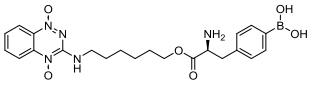

UTX-118

Fig.1

RESULTS: Cytotoxicity tests were performed by WST-1 assay using B16-F10 cells. As shown in Table 1, UTX-117 andUTX-118 exhibited hypoxia-selective cytotoxicity similar to that of tirapazamine.

Table. 1. Cytotoxicity of UTX-117 and UTX-118.

	Normoxia	Hypoxia	N/H ratio
UTX-117	>1000 μM	641.6 μM	>1.56
UTX-118	96.0 μM	33.8 μM	2.84
TPZ	123.2 μM	35.5 μM	3.74

N/H ratio=the IC_{50} value of Normoxia / Hypoxia

The cell uptake test of UTX-117 and UTX-118 was performed using B16-F10 cells (Fig. 2). The maximum uptake of BPA-F, a conventional BNCT agent, was approximately 1.3×10^9 atoms / cell [1]. On the other hand, the maximum uptake of UTX-118 was approximately 7.4×10^9 atoms / cell, it showed higher uptake efficiency than BPA-F. Since the boron concentration required for BNCT is at least 1.0×10^9 atoms / cell, a neutron sensitization effect can be expected for UTX-118.

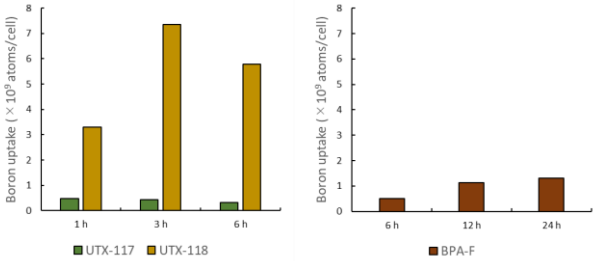

Fig. 2. Intracellular uptake of UTX-117 and UTX-118.

Neutron sensitizing activities of UTX-117, UTX-118 and BPA-F were evaluated using B16-F10 cells (Fig. 3). UTX-117 and UTX-118 showed the neutron sensitizing effect similar to BPA-F.

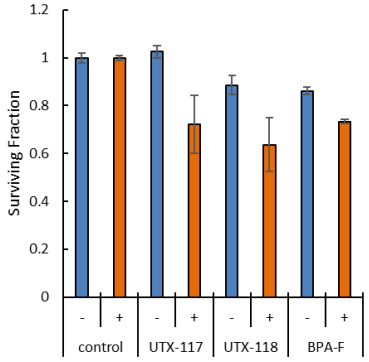

Fig. 3. Neutron sensitizing activity of UTX-117 and UTX-118. +: Irradiation, -: Non-irradiation.

REFERENCES:

[1] F. F. Flores *et al. Radiat. Environ. Biophys.,* **51** (2012) 319-329.

30P8-7

PR8-7 X-irradiation-induced bystander effect enhances invasion in tumor cells

H. Yasui[1], M. Eitaki, S[1]. Masunaga[2], and O. Inanami[1]

[1]*Laboratory of Radiation Biology, Graduate School of Veterinary Medicine, Hokkaido University*

[2]*Particle Radiation Biology, Division of Radiation Life Science, KURNS, Kyoto University*

INTRODUCTION: In cancer studies, it has been suggested that irradiation sometimes enhances invasion of tumor cells. Wild-Bode et al. reported that sublethal dose of γ-ray irradiation enhanced invasiveness of human glioblastoma, and the enhancement was accompanied by the activation and/or up-regulation of integrin and matrix metalloproteinase (MMP) contributed to cellular adhesion and degradation of extracellular matrix (ECM). Fujita et al. also reported that X-ray irradiation enhanced cellular invasive ability via up-regulation of MMP in some human pancreatic tumors. Including these reports, a number of studies suggested that ECM degradation activity was involved in the irradiation-enhanced invasiveness of tumor cells. However, although there are many studies that estimate effects of direct irradiation on tumor cell invasiveness, not so many reports did bystander effects of irradiated tumor cell conditioned medium (CM) on it. Furthermore, the same effect of high LET radiation therapy such as boron neutron capture reaction (BNCT) has not been reported. In this study, we conducted the experiments to examine effects of X-irradiated tumor cell CM on cellular invasiveness in breast cancer and lung cancer-derived cells, prior to BNCT challenge.

EXPERIMENTS: Human breast adenocarcinoma MDA-MB-231 cells and human lung adenocarcinoma A549 cells were seeded on 60 mm dishes (1×10^6 cells/dish), and incubated with RPMI1640/10% FBS overnight. After washing by PBS, serum-free RPMI1640 medium was added to the dishes followed by 0, 2 or 4 Gy X-irradiation immediately. After 24 h incubation, the media were centrifuged for 5 min at 3,000 rpm at 4°C, and supernatants were collected as conditioned media (CM). Hereinafter, CM derived from 0, 2 and 4 Gy X-irradiated cells are described as 0 Gy CM, 2 Gy CM and 4 Gy CM.

Cellular invasive ability was evaluated using a BD BioCoat™ Matrigel™ Invasion Chamber (8 μm pore size, 24-well plate, BD Biosciences, Billerica, MA). Cells (2×10^4 MDA-MB-231 cells or 1×10^5 A549 cells) were suspended in 500 μl of serum-free RPMI1640 medium with or without 500 nM AG1478, and they were loaded into the upper chamber, followed by an addition of 750 μl of CM containing 1% FBS (CM/1 % FBS) into the lower chamber. After incubation for 6 h (MDA-MB-231 cells) or 12 h (A549 cells), non-invading cells were removed from the upper side of the membrane using cotton tips. Invading cells on the lower side of the membrane were fixed with 100% methanol and stained with 1% toluidine blue and 1% sodium borate. All the invading cells were counted using a light microscope. Invasion index was calculated as a relative value which set the number of 0 Gy CM-treated invaded cells to 1.

Cells (1×10^4 cells) were suspended with 100 μl of RPMI1640/10% FBS, and loaded into each well of a 96-well plate. After overnight incubation, the medium was exchanged with CM/1% FBS, and the cells were incubated for 6 h (MDA-MB-231 cells) or 12 h (A549 cells). Ten μl of WST-1 solution (3.24 μg/μl WST-1, 70 ng/μl PMS, 20 mM HEPES-NaOH [pH 7.4]) was added into each well, and 1 h incubation was performed. Absorbance (450 nm) of the each well was measured with Model 680 Microplate Reader (Bio-Rad Laboratories). Cellular proliferation activity was described as relative values which set the absorbance of 0 Gy CM-treated cells to 1.

RESULTS: In order to investigate the influence of CM on the infiltration ability of cells, an invasion assay was first performed. The lower chamber was filled with CM from MDA-MB-231 cells and A549 cells, and the upper chamber was filled with cells to evaluate the infiltration ability of each cell at 6 h and 12 h. As shown in Fig. 1, CM promoted the respective cell infiltration ability in a dose dependent manner of the irradiated X-rays. Next, a colorimetric test using WST-1 was performed to evaluate the effect of CM on cell proliferation activity. When MDA-MB-231 cells are treated with CM from X-irradiated cells for 6 h, 2 Gy CM and 4 Gy CM reduces cell proliferation activity about 2% and 9% as compared to 0 Gy CM. When A549 cells were treated with CM from X-irradiated cells for 12 h, 2 Gy CM and 4 Gy CM reduces cell proliferation activity about 3% and 24% as compared to 0 Gy CM. From these results, it was suggested that the X-ray irradiated cell-derived CM promotes cell infiltration ability even if taken into consideration cell proliferation activity. In next fiscal year, we plan to examine the effect of CM obtained after BNCT-treated cells.

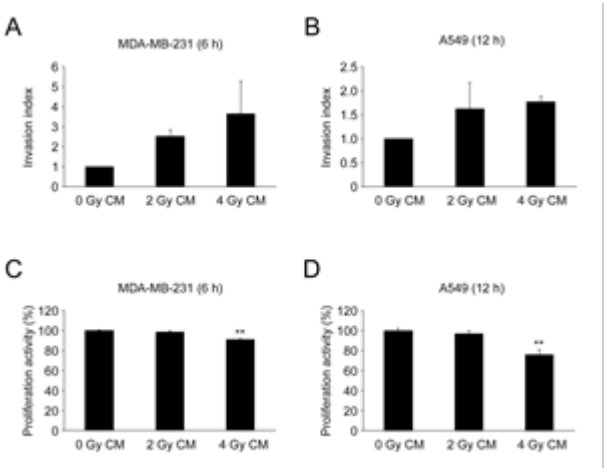

Fig. 1 The effect of X-irradiation CM on cellular invasion and proliferation.

30P8-8

PR8-8 Analysis of the response of tumor and normal tissues to BNCT

S. Imamichi[1,2], L. Chen[2,3], M. Ihara[2,3], Y. Sasaki[2,3], T. Onodera[2,3], Y. Natori[3], N. Toriya[3], A. Takahira[3], J. Itami[1,4,5], S. Masunaga[6] and M. Masutani[1,2,3]

[1]*Division of Boron Neutron Capture Therapy, EPOC, National Cancer Center*
[2]*Lab of Collaborative Research, Division of Cellular Signaling, Research Institute, National Cancer Center*
[3]*Department of Frontier Life Sciences &* [4]*Department of Comprehensive Oncology, Nagasaki University Graduate School of Biomedical Sciences*
[5]*Department of Radiation Oncology, National Cancer Center Hospital*
[6]*Institute for Integrated Radiation and Nuclear Science, Kyoto University*

INTRODUCTION: Boron neutron capture therapy (BNCT) is one of the particle beam radiation therapy based on the boron neutron capture fission reaction, which causes α particle and lithium nuclei of high linear-energy-transfer in a short range that is less than the diameter of typical cells. Boron compounds such as ^{10}B-boronophenylalanine (BPA) are mainly clinically used with neutron sources of nuclear reactors or accelerator-based BNCT systems. The cell death following DNA damage that is induced by BNCT[1)] is affected by various factors including the uptake of boron compounds by tumor cells and the thermal neutron fluence[2)]. Gamma-H2AX, a marker for DNA double strand breaks and poly(ADP-ribose) became high levels 6 or 24 hrs after boron neutron capture reaction (BNCR) in the rat lymphosarcoma model[3)]. The comprehensive analysis of the transcriptome and proteome after BNCR in human squamous carcinoma SAS cells has been carried out[4)]. As one of the factors induced after BNCR conditions, we focused on *CSF2* gene product, granulocyte-macrophage colony stimulating factor (GM-CSF). We studied the dynamic properties of GM-CSF and its mRNA (*CSF2*) after BNCR in cells and also in xenograft models of mice.

EXPERIMENTS: We used human squamous cell carcinoma-derived SAS and malignant melanoma-derived A375 cells. The neutron beam irradiation was operated at 1 MW at the Heavy Water Neutron Irradiation Facility of KUR reactor. Suspended cells were irradiated 2 hrs after incubation in the presence or absence of BPA 25 ppm (boron concentration) on Nov. 28th & Dec. 4th, 2018. For the xenograft models, SAS and A375 cells were transplanted into left hind legs of BALB/c nude male mice of 5 weeks old. Ten days later, neutron beam irradiation was carried out. As a boron compound, ^{10}B-BPA fructose complex was prepared before irradiation. Mice were irradiated approximately 30 min after intraperitoneal administration on Dec. 4th, 2018. Gold foil activation analysis was used for the measurement of thermal neutron fluences and thermoluminescence dosimeter (TLD) was used for the measurement of the γ-ray dose including secondary γ-ray. As previously described, total absorbed dose calculation was carried out using the flux-to-dose conversion factor by the sum of the absorbed doses resulting from ^{1}H(n, γ)^{2}D, ^{14}N(n, p)^{14}C, and ^{10}B(n, α)^{7}Li reactions. The cellular responses including factors present in culture supernatants were analyzed 6 and 24 hrs after irradiation of therapeutic doses of BNCT and γ-ray. Cell survival was analyzed by colony formation assay. The cells were transfected with siRNA of *CSF2* & *CSF2 receptor* using Lipofectamine™ 3000 Reagents (Thermo Fisher Scientific). GM-CSF levels in culture supernatant and mouse blood were measured using ELISA.

RESULTS: The irradiated beam and total radiation doses for cell experiments were exemplified in Table 1. SAS and A375 cells showed an increase in *CSF2* mRNA expression after the therapeutic dose irradiation of neutron beam with BPA, respectively. Growth of tumors derived from SAS cells was decreased 3 and 8 days after neutron beam irradiation in the presence of BPA compared with non-irradiated controls. Three days after irradiation, the DNA double strand break marker was positive in the tumors but not in the surrounding normal tissues. Changes in GM-CSF and other factors in the blood of xenograft models and cell culture are being analyzed. The results suggest that CSF2 and CSF2 receptor pathway is limitedly involved in the cancer cell survival. The dynamic changes of GM-CSF levels in tumors suggest its involvement in the regulation of local tumor microenvironment after BNCR and this point is being studied further.

Table 1. The irradiated thermal neutrons and doses.

Irradiation time (min)	Position	Thermal neutron fluence (/cm^2)	Total dose (Gy-Eq)	Average dose (Gy-Eq)
10	Sample surface	1.3E+12	2.9	2.2
	Back side	6.2E+11	1.5	
60	Sample surface	7.1E+12	9.3	12.1
	Back side	3.6E+12	14.9	
7	Sample surface	7.1E+11	1.6	1.4
	Back side	5.4E+11	1.3	
12	Sample surface	1.2E+12	2.6	2.3
	Back side	8.9E+11	2.0	
36	Sample surface	3.7E+12	8.3	7.4
	Back side	2.8E+12	6.4	

REFERENCES:

[1] S.G. Hussein *et al.*, Proc. Montreal Int. Conf. Eds Harvey, Cusson, Geiger, Pearson (U. Mont Press) (1969) 91.
[2] K. Okano *et al.*, Nucl. Instr. and Meth, **186** (1981) 115-120.
[3] M. Masutani *et al.*, Appl. Rad. Iso., **104** (2014) 104-108.
[4] A. Sato *et al.*, Appl. Rad. Iso., **106** (2015) 213-219.

PR8-9 Radiobiological effect of extratumoral boron distribution and Neutron irradiation

K. Nakai[1], T. Tsurubuchi[3], S. Masunaga[2], Y. Sakurai[2], H. Tanaka[2], F. Yoshida[3], M. Shirakawa[4], A. Matsumura[3] and H. Sakurai

Department of radiation oncology, Faculty of Medicine, University of Tsukuba

[1]Department of Neuro-rehabilitation, Ibaraki Prefectural University Hospital

[2]KURNS, Kyoto University

[3]Department of Neurosurgery, Faculty of Medicine, University of Tsukuba

[5]Department of Pharmaceutical Sciences, University of Fukuyama

INTRODUCTION: Boron Neutron Capture Therapy (BNCT) is a particle radiation therapy for malignant diseases. However, Boron distribution of extra-cellular fluid or interstitial tumor tissue during the neutron irradiation and radiobiological effect of extracellular born neutron reaction is still unclear. In the previous studies, we have focused on intra-cellular boron concentration and tumor tissue boron concentrations. These were special average boron concentration and there have intrinsic heterogeneity. The goal of this study is, to clarify a role of extra-cellular / peri-tumoral boron neutron reaction in BNCT.

EXPERIMENTS:

Materials

Boron compounds were prepared using previously published method [1]. *p*-boronophenylalanine (BPA) were purchased from Interpharma Ltd. (Praha, Czech Republic). Fructose-BSH final concentration was 2400μg/mL ^{10}B.

Cell Lines

CT-26 murine colon cancer cell lines were cultured in D-MEM supplemented with 10% fetal bovine serum and maintained at 37℃ in a humidified atmosphere with 5% CO_2. After trypsinized and counted, cells were suspended in culture medium.

Tumor models

4w female bulb/c mice 1.0x10^{7}cells were implanted to rt. thigh subcutaneously.

Boron Neutron Reaction

BPA was administrated via tail vain or i.p. injection 2hrs before neutron irradiation. Thermal neutron dose was 7.3x10^{12} n/cm^2.

Tumor progression were measured by tumor size in each group.

RESULTS AND DISCUSSIONS:

As shown in Fig. 1, The group which administrated via i.p. has more inhibitory effect than i.v. group. These two groups were administrated the same dose, some boron agent. It is presumed that the area under curve of BPA during neutron irradiation is the difference. It is easily conceivable that the peak boron concentration of i.v. group reached just after administration and blood boron concentration was rapidly reduced by renal excretion. On the other hand, i.p. group reached peak boron concentration of i.p. group reached after a certain period, and supplied from interstitial tissue to blood continuously, then reduced moderately.

Neutron irradiation without boron administration group also showed inhibitory effect. With or without boron, these inhibitory effects were showed as a reducing growth curve rate. It means there are sublethal damaged cells despite high LET radiation, or damaged tumor surrounding normal tissue which supplying a proliferation factor or a nutrient factor to tumor. and such inhibitory effect prolonged after single boron neutron reaction. Ono [2] advocated that the tumor cell density connect with BNCT effectiveness.

To clarify this inference, the detailed boron distribution of intra and extra tumor cells, and interstitial peritumoral tissue should be examined.

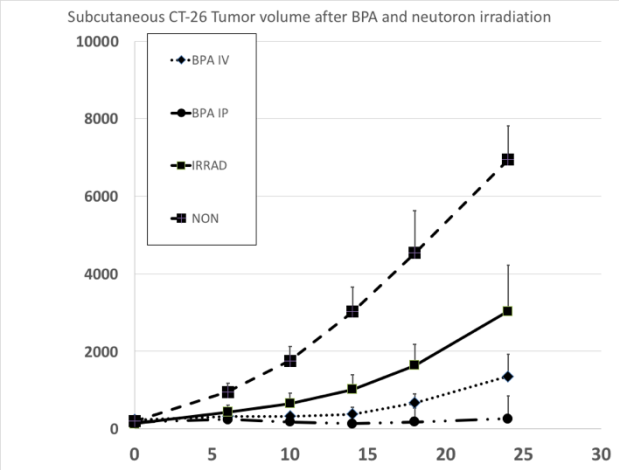

Fig. 1. BNCT treatment of subcutaneous model of colon cancer. Three groups of animals underwent the irradiation treatment at KUR. The first group (irradiated and i.v. treatment group, n=6) received f-BPA at a dose of 250mg^{10}B/kg, i.v. via tail vein 2 hours before neutron exposure. The second mice group (irradiated and i.p. treatment group, n=5) received the same volume of f-BPA i.p. 2hrs before the irradiation. The third group (irradiated only, n=6) received neutron exposure only. Nine mice were followed up as non-treatment group.

REFERENCES:

[1] K.Yoshino *et al.*, Strahlenther Onkol., **165**(2-3) (1989) 127-129.

[2] K. Ono *et al.*, J Rad Res., **60** (2019) 29-36.

30P8-10

PR8-10 Multilateral Approach toward Realization of Next Generation Boron Neutron Capture Therapy

Y. Matsumoto[1,2], K. Hattori[3,4], H. Arima[3,4], K. Motoyama[3,4], T. Higashi[3,4], N. Fukumitsu[1,2], T. Aihara[1,2], H. Kumada[1,2], K. Tsuboi[1,2], Y. Sanada[5], SI, Masunaga[1,2], K. Tsuboi[1,2] and H. Sakurai[1,2]

[1]*Faculty of Medicine, University of Tsukuba*
[2]*Proton Medical Research Center, University of Tsukuba Hospital*
[3]*CyDing Co., Ltd*
[4]*Faculty of Life Sciences, Kumamoto University*
[5]*KURNS, Kyoto University*

INTRODUCTION: Boron neutron capture therapy (BNCT) is a next-generation radiation therapy that irradiates thermal neutrons to boron compounds accumulated in tumor cells and selectively irradiates tumor cells with high LET radiation by the generated α-rays and Li nuclei. The therapeutic effect of BNCT greatly depends on the boron compound which collects boron at the tumor site, and existing boron compounds, L-p-Boronophenylalanine (L-BPA) and disodium mercaptoundecahydrododecaborate (BSH) have limitation with regard to the adaptive cancer type and its sufficient and specific accumulation to tumor. Therefore, new boron compounds and carrier with higher tumor cell accumulation without normal tissue accumulation are being searched. BSH don't have the active accumulation to tumor cells, but it has 12 x 10B in one molecule, BSH induces a strong biological effect even with small accumulation. Folate receptor-α (FR-α) is highly expressed on the many tumor (ovarian, kidney, colorectal, et al.), and it is useful as a target for drug delivery system (DDS) against cancer. It has been reported that the compound which is a cyclic oligosaccharide cyclodextrin modified with folic acid, has improved tumor accumulation and therapeutic effects of paclitaxel (PTX) and doxorubicin (DOX), which are anticancer drugs. In this study, we aimed to construct BSH inclusions with folate-modified cyclodextrin (ND 201) and to realize active accumulation of BSH against folate-targeted tumor and its usefulness.

EXPERIMENTS: Colon-26 cells derived from murine colorectal cancer and A549 cells derived from human lung cancer were purchased from RIKEN BioResource Research Center. Colon-26 cells show the overexpression of FR and A549 cells show low expression level of FR. BALB/c nu/nu mice were used for in vivo kinetics experiments. BSH was purchased from Stella Pharma in powder form and dissolved in a phosphate buffer at the appropriate time before the experiment. ND201 was purchased from NanoDex corporation and dissolved in 0.1 mol/l carbonic acid/bicarbonate buffer (pH9-10). The solution was neutralized with a phosphate buffer (pH 6.8-7.2) and stocked at -30°C freezer. The interaction between BSH and ND201 was evaluated from stability constants and stoichiometric ratio. BSH and BSH containing ND201 (BSH-ND201) were administered from the tail vein to mice at concentrations of 100 and 5 mg/kg, respectively. Boron concentration (ppm) in the tumor and blood was measured with ICPS-8100 (Shimadzu Corporation) and the tumor/blood (T/B) ratio was calculated with each value.

RESULTS: The stability constants Kc was 1.4×104 (/M) in BSH and the value suggests that ND201 and BSH shows stable complex in serum-containing culture medium and human blood. The stoichiometry of a host-guest complex was determined by the continuous variation plot method. The plots made by monitoring the fluorescence intensity change gave a maximum peak at 0.5, indicating that ND201 forms an inclusion complex with BSH at a 1:1 molar ratio. Next, the boron concentration in tumors and blood of BALB/c nu/nu mice was measured by ICP-MS. The concentration in blood showed similar time course kinetics after BSH and BSH-ND201 without depending on the tumor type. On the other hand, the concentration in Colon-26 tumor showed drastic decrease immediately after BSH administration, whereas it increased to 24 hours and showed high value at 72 hours after BSH-ND201 administration. The T/B ratio when the intratumoral boron concentration was peak was calculated and BSH-ND201 showed high T/B ratio (10.6) for Colon-26 tumor, and this value satisfied the T/B ratio > 10 required for clinical safety in BNCT. On the other hand, the ratio was too low (1.6) for A549 tumor.

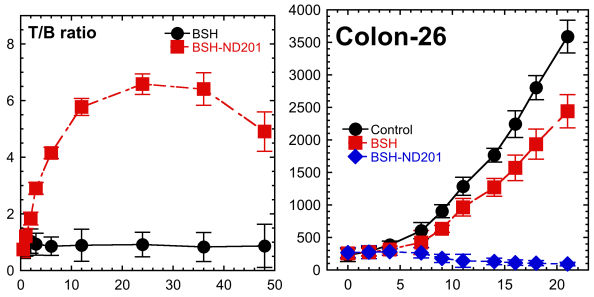

Fig. 1. Comparison of the T/B ratio and anti-tumor effects using BSH and novel boron complex, BSH-ND201.

REFERENCES:

[1] 1.N Parker, *et al.*, Folate receptor expression in carcinomas and normal tissues determined by a quantitative radioligand binding assay. Anal. Biochem., **338** (2005) 284-293.
[2] 2. A Okamatsu, *et al.,* Folate-appended β-cyclodextrin as a promising tumor targeting carrier for antitumor drugs in vitro and in vivo. Bioconjugate Chem., **24** (2013) 724-733.

30P8-11

PR8-11 Attempts to sensitize tumor cells by exploiting the tumor microenvironment

Y. Sanada, T. Takata, Y. Sakurai, H. Tanaka and S. Masunaga

Institute for Integrated Radiation and Nuclear Science, Kyoto University

INTRODUCTION: Hypoxia and glucose deprivation have been suggested to play important roles in resistance to radiation [1]. Attempts to sensitize tumor cells by exploiting the tumor microenvironment have been studied. A major mediator of the cellular hypoxic response, hypoxia inducible factor 1 (HIF-1), is a potential target for cancer therapy, because it transcriptionally regulates a number of genes, including those involved in glucose metabolism, angiogenesis and resistance to chemotherapy and radiation therapy [2]. We previously reported that the disruption of Hif-1α enhanced the sensitivity of murine squamous cell carcinoma (SCC-VII) cells to gamma-ray [3]. In the present study, we investigated whether the disruption of Hif-1α affects the radiosensitivity of SCC-VII cells to the boron neutron capture reaction (BNCR).

EXPERIMENTS: In vitro, SCC-VII and SCC-VII-Hif-1α-deficient (ΔHif-1α) cell suspensions were incubated with 10B-carrier (BPA or BSH) at 20 ppm 2h before neutron irradiation, and cell survival assay was performed.
In order to examine the effect of hypoxia on cell survival, the cells were cultured for 12 h under normoxic or hypoxic (1% O2) condition, and then incubated with 10B-carrier.
In order to examine the influence of the disruption of Hif-1α in vivo, SCC-VII or SCC-VIIΔHif-1α cells were inoculated subcutaneously into the hind legs of C57BL/6 mice. Tumor-bearing mice were irradiated with a reactor neutron beam, and then clonogenic cell survival assay. Irradiation was started from 60 min after the subcutaneous injection of 10B-carrier (BPA 250 mg/kg or BSH 125 mg/kg).

RESULTS: We examined the cell survival fraction of SCC-VII or SCC-VII-ΔHif-1α cells irradiated with the neutron beam. In the presence of BSH (data not shown) or BPA (Fig. 1), the cell survival after neutron irradiation was lowered. Moreover, SCC-VII-ΔHif-1α cells with BPA exhibited lower survival compared to SCC-VII cells with BPA (Fig. 1). We also investigated the influence of oxygen levels on cell survival. In the presence of BPA, SCC-VII cells (hypoxia) showed more resistant to the neutron beam than SCC-VII cells (normoxia), similar to the previous research [1]. However, there was no significant difference in survival of the ΔHif-1α cells between hypoxia and normoxia groups.
In order to examine the influence of the disruption of Hif-1α in vivo, tumor-bearing mice were irradiated with a reactor neutron beam. As shown in Fig. 2, in the absence of BSH or BPA, SCC-VII and SCC-VII-ΔHif-1α cells from tumor-bearing mice showed similar survival fraction. In the BSH-administrated group, ΔHif-1α cells exhibited higher survival than the SCC VII cells. In the BPA-administrated group, ΔHif-1α cells was more sensitive than the SCC VII cells.

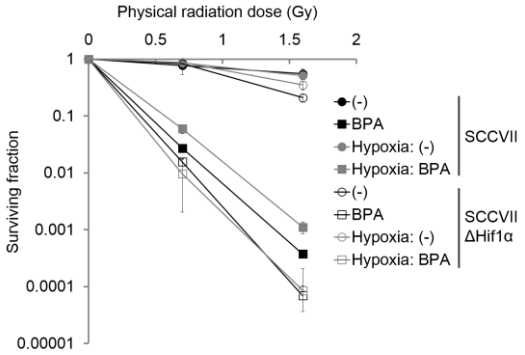

Fig. 1 Cell survival curves for SCC VII or SCC-VII ΔHif-1α cells.

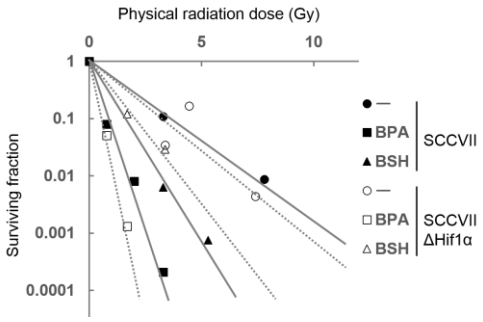

Fig. 2 Cell survival curves for the total cell population from SCC VII or SCC-VII ΔHif-1α tumors irradiated with neutron beam.

REFERENCES:
[1] S. Masunaga *et al.*, Int. J. Rad. Biol., **92** (2016) 187-194.
[2] Z. Luo *et al.*, Neuropharmacology., **89** (2015) 168-174.
[3] Y. Sanada *et al.*, Int. J. Rad. Biol., **94** (2018) 88-96.

30P8-12

I-1. PROJECT RESEARCHES

Project 9

PR9

Production Mechanism of Radioactive Aerosols Released from Fukushima Daiichi Nuclear Power Plant

K. Takamiya

Institute for Integrated Radiation and Nuclear Science, Kyoto University

OBJECTIVE: The high amount of radioactive materials was released in the severe accident of Fukushima Daiichi Nuclear Power Plant. Investigating the chemical and physical properties of the radioactive materials in the air and soil samples are one of the most important problem to understand the exposure dose at the time of the accident and in the future and have been studied by various method. However, the production mechanism of radioactive aerosols generated in the reactor buildings does not be clarified because a part of the inside of the reactor building was under the condition of high temperature, high dose rate, etc. But elucidating the production mechanism of radioactive aerosols inside of the reactor buildings is important to understand the chemical and physical properties of radioactive materials just after the release from the reactor buildings. In addition, understanding the production mechanism will play an important role in decommissioning of the reactors because the environment in the reactor building is under quite unusual condition as used to be. In this project research, the production mechanism and measurement technique of such radioactive aerosols have been investigated experimentally.

RESEARCH SUBJECTS: The project research is composed by three individual subjects in this year period. One is developments of production method of radioactive aerosols for simulation experiments to investigate the production mechanism of radioactive solution aerosols, one is development of measurement technique of radioactive aerosols under high dose condition, and another is investigation of insoluble radioactive micro particles. The respective subjects of the research groups of this project are described as follows;

P9-1: Development of production method of radioactive aerosols by attaching radioisotopes to aerosol particles
P9-2: Development of measurement method of radioactive aerosols under severity conditions
P9-3: Investigation for production process of insoluble radioactive particles released from FDNPP

RESULTS: In the subject P9-1, experimental method using aerosol generating apparatus combined with neutron irradiated UO_2 has been developed to observe the attachment behavior of fission products of thermal velocities to solution aerosol particles. Neutron irradiated UO_2 powder was used as a source of fission products. The fission products were mixed in a cylindrical chamber with solution aerosol generated by an atomizer filled with 0.01 M sodium chloride solution. In the chamber, fission products attached to the aerosol particles to generate radioactive solution aerosol particles. The radioactive aerosol particles were collected on a filter. The gamma-ray spectrometry for the filter was performed to estimate the attachment ratio of fission products to the aerosol particles. It was found that there exist various attachment ratios depending on chemical properties of fission products. The results obtained in the present work is correspond with the previous work summarizing that attachment ratio might depend on electro static interaction between fission products and localized anions at the surface of solution aerosol particles.

Continuing from the previous year, a newly assembled screen-type diffusion battery (SDB) system was applied to measure aerosol particle size in the target room of an electron linear accelerator (LINAC) facility for the purpose of development of measurement method of radioactive aerosols under severity conditions (P9-2). An irradiation chamber was placed at a rear position of a platinum target of LINAC. The size distribution of the radiation-induced aerosols generated in the chamber was also measured by using a scanning mobility particle sizer (SMPS) in advance. The irradiated air containing the aerosol was simultaneously introduced to the SDB cylinder and the compensation line. The irradiated air was sampled continuously from both the upstream and downstream positions of the SDB cylinder, and the penetration ratios were estimated. The number concentrations of the aerosols were mainly measured with a condensation particle counter. The penetration ratios obtained by changing air flow rate were fitted to a theoretical function for lognormal distributions to obtain the geometric mean and geometric standard deviation of particle diameter. In order to confirm the performance of newly developed system, the SMPS was used for comparison with the SDB system. As a result, very good agreement is found in the particle size distribution obtained by both methods, and the performance is confirmed.

In the subject P9-3, morphological observation and elemental analysis for a radioactive insoluble micro particle which was collected from a soil sample around the power plant were performed. The particle was extracted from a soil sample by using an imaging plate at University of Tsukuba. Morphological observation was performed by SEM, and the EDX measurement was performed for particle surface to analyze the elemental composition of the particle. The whole shape is distorted, and the length of the longer direction is about 500 μm. The surface is almost smooth but has small holes partly. Concentrations of main elements are determined by EDX measurement to be 66.4, 18.8, 9.4, 1.8, 1.7 and 1.4% for oxygen, silicon, sodium, calcium, aluminum and magnesium, respectively. The main composition of the particle is thought to be silica dioxide from the elemental analysis, and element ratio is similar to that of basalt concrete containing sodium. In the near future, the generation process was experimentally simulated on the basis of obtained chemical composition to understand the generation process of insoluble radioactive micro particles.

PR9-1 Electrostatic Interaction in Production Process of Radioactive Solution Aerosol Particles

K. Takamiya, Y. Takeuchi, S. Sekimoto, Y. Oki and T. Ohtsuki

Institute for Integrated Radiation and Nuclear Science, Kyoto University

INTRODUCTION: Elucidating generating process of radioactive aerosols is one of the most important problem to understand the behavior of radioactive aerosols released from the Fukushima Daiichi Nuclear Power Plant after the Great East Japan Earthquake in 2011. The generating process has been investigated using an aerosol generating apparatus combined with a spontaneous fission source of ^{252}Cf in our previous work [1-4]. It was found that there are two types of attachment processes of fission products to aerosol particles; one is caused by geometric collision and another is induced by electrostatic interaction between a fission product and surface of an aerosol particle. And dependence of species and concentration of solute on attachment behavior of fission products to solution aerosol particles has been found in the previous study. However, the electrostatic interaction could not be quantitatively clarified because fission products emitted from ^{252}Cf source have recoil velocities which cause the attachment process by geometric collision to increase. Experiments similar to the previous study using fission products with thermal velocity might elucidate the electrostatic interaction qualitatively. In the present work, experimental method using aerosol generating apparatus combined with neutron irradiated UO_2 has been developed to observe the attachment behavior of fission products with thermal velocity to solution aerosol particles.

EXPERIMENTS: The neutron irradiation to uranium dioxide was carried out at Kyoto University Research Reactor (KUR). Powder of UO_2 was encapsulated in a quartz tube under reduced pressure, and the quartz tube covered by a polyethylene tube was inserted into polyethylene capsule to irradiate neutrons using pneumatic transport system (Pn-2) of KUR. The amount of UO_2 was 10 mg, and the neutron irradiation time is 30 min. The experimental setup for production of radioactive aerosol is shown in Figure 1. A part of irradiated UO_2 powder was extracted to another quartz tube placed in an electric furnace. Fission products produced in the irradiated UO_2 powder was released by heating the furnace up to 1100°C. On the other hand, Atomizer filled with 0.01 M sodium chloride solution generate solution aerosol. Both released fission products and solution aerosol particles were aspirated by a suction pomp to be transported and mixed in a cylindrical chamber. And radioactive aerosol particles were produced by attaching fission products to aerosol particles in the chamber. The produced radioactive aerosol particles were collected on a polycarbonate filter at downstream of the chamber. The amount of fission products which attaches to aerosol particles were estimated by gamma-ray spectrometry for the filter using a Ge-detector. On the other hand, the amount of fission products released from the irradiated UO_2 powder by heating was estimated by subtraction of gamma-ray spectra for before and after heating the UO_2 powder.

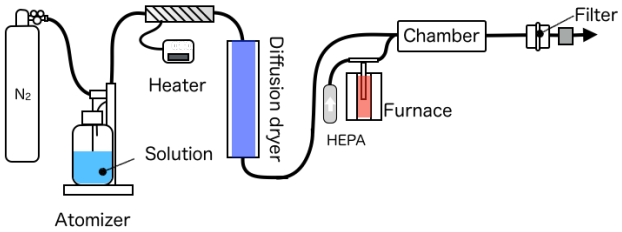

Fig. 1 Experimental setup for generating radioactive solution aerosol using neutron irradiated UO_2.

RESULTS: The attachment ratio of fission products to aerosol particles was estimated as shown in Figure 2. It was found that there exist various attachment ratios among various fission products. Fission products which can forms positively-charged chemical species (Zr, Te and Ce) might show higher attachment ratio compared with those form negatively-charged or neutral species (Ru, I and Xe). These results correspond with our previous work summarizing that attachment ratio might depend on electro static interaction between fission products and localized anions [5] at the surface of solution aerosol particles.

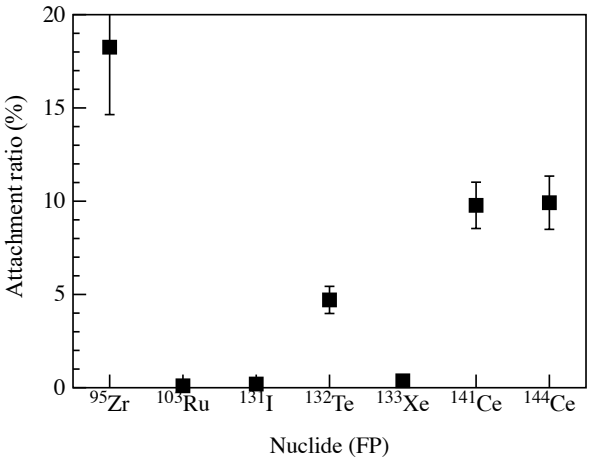

Fig. 2 Attachment ratio of FP released from neutron irradiated UO_2 to 0.01 M NaCl solution aerosol particles.

This work was supported by JSPS KAKENHI Grant Numbers JP24110005 and JP26286076.

REFERENCES:

[1] K. Takamiya *et al.*, J. Radioanal. Nucl. Chem. **307** (2016) 2227-2230.
[2] K. Takamiya *et al.*, J Radiat. Prot. Res. **41** (2016) 350–353.
[3] K. Takamiya *et al.,* KURRI Progress Report 2016 (2017) 45.
[4] K. Takamiya *et al.*, KURRI Progress Report 2017 (2018) 13.
[5] P. Jungwirth *et al.*, Chem. Rev. **106** (2006) 1259-1281.

PR9-2 Particle Size Measurement of Radioactive Aerosol Particles in An Electron LINAC Using A Diffusion Battery System II

Y. Oki and N. Osada[1]

Institute for Radiation and Nuclear Science, Kyoto University
[1]Advanced Science Research Center, Okayama University

INTRODUCTION: Radioactive nuclides are evaporated and released to the environment in target melting accidents in accelerator facilities like the J-PARC accident in 2013. The radionuclides are often incorporated into metallic aerosols emitted from the target metal or ambient aerosols in the target room. Therefore, properties of the ambient aerosols like their particle size and concentration are very important information to clarify the behavior of the radioactive nuclides.

During machine operation the target room is filled with radiation-induced aerosol particles in the size range of several nm to ca. 100 nm. The size for the radioactive particles was often measured using a wire screen technique in accelerator facilities. Convenient size measurement techniques are needed from the viewpoint of radiation protection in accelerator facilities.

In this work, continuing from the previous year [1], a newly assembled screen-type diffusion battery (SDB) system was applied to measure aerosol particle size in the target room of an electron linear accelerator (LINAC) facility.

EXPERIMENTS:

The measurement system: The SDB system used in this work consists of an SDB line (Line A in Fig. 1) and a compensation line (Line B). Each line was connected to a ball valve and a mass flow controller (MFC) to change a flow rate independently. All valves and MFCs were controlled by a PC for automatic measurement of aerosol size distribution. In the SDB line, an air-tight wire screen cylinder containing a stack of stainless steel screens (500 mesh).

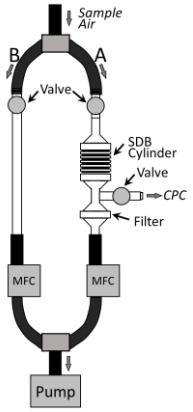

Fig. 1 The SDB system employed in this work

When very fine aerosol particles pass through wire screens, a part of the particles are trapped on the wire surface of the screens by their diffusion according to their particle size. The loss by the screens is expressed as a function of particle size, coarseness and number of screens, and flow rate of particles. The size distribution of the aerosol particles can be calculated by measuring the penetration ratio (N/N_0), where N_0 and N are number concentrations of the aerosol particles before and after penetrating screens, respectively.

Irradiation: The air-irradiation experiment was carried out in the 46-MeV electron LINAC of the Institute for Radiation and Nuclear Science, Kyoto University (KURNS). An irradiation chamber was placed at a rear position of a platinum target. During the irradiation, aerosol-free air was introduced to the chamber from the experiment room next to the target room. The target was bombarded with a 35-MeV electron beam to produce bremsstrahlung. The bremsstrahlung ionizes air and produces the radiation-induced aerosol. The beam current was ca. 40 μA.

Size measurement based on number concentration for the radiation-induced aerosol: The size distribution of the radiation-induced aerosols was confirmed to have a lognormal shape using a scanning mobility particle sizer (SMPS) in advance. The irradiated air containing the aerosol was simultaneously introduced to the SDB cylinder and the compensation line. The air flow rate for the SDB was gradually changed from 0 to 15 L/min, while that for the compensation line was decreased from 15 to 0 L/min so that the total flow rate was maintained constant not to change irradiation rate of air in the irradiation chamber. The irradiated air was sampled continuously from both the upstream and downstream positions of the SDB cylinder, and the penetration ratios were calculated. The number concentrations of the aerosols were mainly measured with a condensation particle counter (CPC).

RESULTS: The penetration ratios (N/N_0) obtained by changing air flow rate were fitted to a theoretical function [2] for lognormal distributions to obtain the geometric mean and geometric standard deviation of particle diameter. An SMPS with nano-differential mobility analyzer was used for comparison with the SDB system.

Figure 2 shows the particle size distribution obtained using the SDB cylinder with a stack of three pieces of 500-mesh screen. It was in very good agreement with that obtained with SMPS.

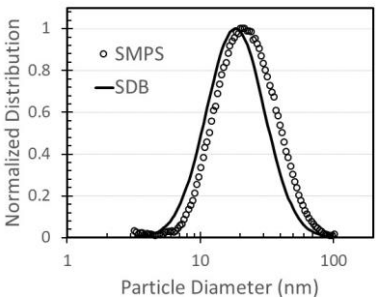

Fig. 2 Comparison of particle size distributions obtained with the SDB system and SMPS

REFERENCES:

[1] Y. Oki, *et al.*, KEK-Proceedings, **2018-7**, 265-269.
[2] Y.S. Cheng and H.C. Yeh, J. Aerosol Sci., **11** (1980) 313-320.

PR9-3 Observation of Insoluble Radioactive Microparticle Released from FDNPP

K. Takamiya, M. Inagaki, S. Sekimoto, Y. Oki T. Ohtsuki and K. Sueki[1].

Institute for Integrated Radiation and Nuclear Science, Kyoto University
[1]Faculty of Pure and Applied Sciences, University of Tsukuba

INTRODUCTION: The characteristics of radioactive micro particles which were released from Fukushima Daiichi Nuclear Power Plant have been analyzed using various method [1-5]. The effect of the micro particles to the environment is important because the particles are mostly insoluble and a part of them has high radioactivity. And these high radioactive microparticles might exist in the reactor building even now and will affect exposed dose in decommissioning process of the reactors. Morphological observation and elemental analysis for the radioactive insoluble micro particle which was collected from a soil sample around the power plant were carried out in the present work.

EXPERIMENTS: The particle observed in the present work was extracted from a soil sample by using an imaging plate at University of Tsukuba. Morphological observation was performed by SEM (Phenom ProX, Thermo Fisher Scientific K.K.). And the EDX measurement was performed for particle surface to analyze the elemental composition.

RESULTS: The SEM image of overview of the micro particle is shown in Figure 1. The whole shape is distorted, and the length of the longer direction is about 500 μm. The surface is almost smooth but has small holes partly. The EDX measurement was performed for a part of smooth surface area to analyze the elemental composition. The obtained EDX spectrum is shown in Figure 2. Concentrations of main elements are determined to be 66.4, 18.8, 9.4, 1.8, 1.7 and 1.4% for oxygen, silicon, sodium, calcium, aluminum and magnesium, respectively. From the elemental analysis for other parts of the particle surface, similar results were obtained. The main composition of the particle is thought to be silica dioxide from the elemental analysis, and element ratio is similar to that of basalt concrete containing sodium. It is impossible to identify a generating process of the particle from the present results, however, following process is conceivable. Basalt concrete was used as pedestals supporting a reactor pressure vessel. The pedestal with sea water which was injected as coolant from outside were heated by contact with melted core, and the microparticles were generated through decomposition, melting, scattering, recooling and other process. In the near future, the generation process was experimentally simulated by heating mixture of concrete and sodium chloride to understand the generation process of radioactive micro particles.

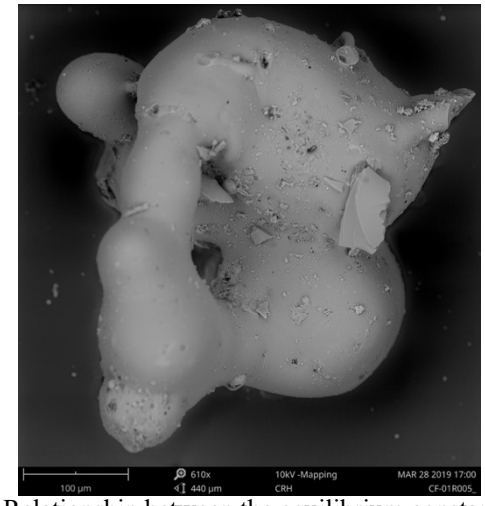

Fig. 1 Relationship between the equilibrium constant and concentration of solute.

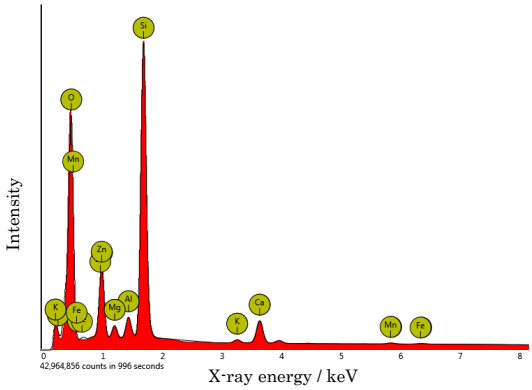

Fig. 2 EDX spectrum of a part of smooth surface of the micro particle.

This work was supported by JSPS KAKENHI Grant Numbers JP18H04150, JP26286076 and Interdisciplibnary Project on Environmental Transfer of Radionuclides F-18-6.

REFERENCES:

[1] K. Adachi, *et al.*, Scientific Reports, 3 (2013) 2554.
[2] Y. Satou, *et al.,* Anthropocene, 14 (2016) 71-76.
[3] T. Kogure, *et al.*, Microscopy, 65-5 (2016) 451-459.
[4] G. Furuki, *et al.*, Scientific Reports, 7 (2017) 42731.
[5] N. Yamaguchi, *et al.*, Scientific Reports, 6 (2016) 20548.

I-1. PROJECT RESEARCHES

Project 10

PR10 Solution Chemical Studies on Actinides and Fission Product Nuclides

A. Uehara

National Institute for Quantum and Radiological Science and Technology

OBJECTIVE:

Chemistry of actinide and fission product nuclides in various kinds of solutions such as aqueous, organic solutions including ionic liquids plays important role on the nuclear fuel cycle and radioactive waste disposal. The ionic species of the actinide and fission products dissolving into the solutions are strongly affected by the various kinds of parameter, concentration of H^+, electrolyte, oxygen, organic/inorganic ligands, and so on. Hot laboratory of KUR is one of core facilities in which various nuclides can be handles. Here, these nuclides can be obtained by the irradiation in the reactor core. Collaboration researches have been progressed with the field of nuclear science as well as material, environmental sciences after the accident in Fukushima Dai-ichi Nuclear Power Plant. The following research subjects have been studied to enhance an activation on science of actinide and fission product nuclides as well as the use of hot laboratory:

P10-1 Kinetic and equilibrium analysis of actinide and FP elements in molten salts (T. Goto, *et al.*)

P10-2 Study on complexation behavior of actinide and FP elements in radioactive waste disposal environment (T. Kobayashi, *et al.*)

P10-3 Study on the redox behavior of uranium and FP elements in molten chloride (Y. Sakamura, *et al.*)

P10-4 Study on dissolution behavior of actinide and FP elements in fuel debris (T. Sasaki, *et al.*)

P10-5 Application of isotope ratio analysis to radio nuclide analysis in environmental samples (Y. Shibahara, *et al.*)

P10-6 Activity measurement of dissolved chemical species in molten salt using halide ion conductor (H. Sekimoto, *et al.*)

P10-7 Effects of neutron irradiation and uranium addi tion on borosilicate glass structure (T. Nagai, *et al.*)

P10-8 Neutron cross section studies of actinides and fission nuclides (S. Nakamura, *et al.*)

P10-9 Interaction of inorganic compounds with trit ium ion in aqueous solution (H. Hashizume, *et al.*)

P10-10 Solvent extraction studies of uranium and fission product elements (T. Fujii, *et al.*)

P10-11 Electrochemical and spectroscopic studies for dry recycling process development (Matsuura, *et al.*)

RESULTS:

Some groups reported the environmental analyses and separation of radio nuclides produced by Fukushima Dai-ichi Nulcear Power Plant. Sasaki, *et al.* studied the preparation of the molten core-concrete interaction (MCCI) debris using a mixture of uranium and zirconium oxides, and a component of cement material such as calcium which is simulated to the bottom of the primary containment vessel. The simulated MCCI debris was irradiated at KUR to produce radionuclides. Shibahara, *et al.* reported the applicability of the thermal ionization mass spectrometry (TIMS) for the analysis of cesium Cs isotopes released on the accident of Fukushima Dai-ichi Nuclear Power Plant. Matsuura, *et al.* proposed selective fluorination using HF to dissolve into molten salt and electrodeposition uranium as a metal or oxides at the electrode in the molten salts. Hashizume, *et al.* studied the change of the ion exchange between tritium in water and proton in a hydroxide to the different concentration of tritium in water, and showed the isotherm for the ion exchange between tritium and proton to the concentration of tritium in water by the hydroxide.

Chemical separation of radioactive elements has been extensively applied in nuclear science fields because there are long-term options for management of spent nuclear fuels: storage for nuclear wastes in a deep geological repository and separation and recycling of the actinide elements. Nagai, *et al.* reported that the structural change of borosilicate glass dissolving simulated high-level radioactive elements was observed by Raman spectroscopy after neutron irradiation at KUR. Fujii, *et al.* focused on the separation of palladium and studied the solvent extraction behavior of palladium from a nitric acid solution using newly prepared organic ligands. Sakamura, *et al.* reported that redox behavior of selenium and tellurium ions in molten lithium-potassium chloride melts were investigated by in-situ uv-vis absorption spectroscopy for developing pyrochemical reprocessing of spent oxide fuels. A new type reference electrode in molten chlorides consisted of silver, pure silver chloride and anion conducting solid electrolyte such as calcium oxide doped lanthanum oxychloride was proposed by Sekimoto, *et al.* The thermal-neutron cross-section of the ^{135}Cs $(n,\gamma)^{136}Cs$ reaction was measured by Nakamura, *et al.* to evaluate the transmutation and reaction rate. For the safety assessment of radioactive waste disposal, it is necessary to predict the solubility limit of radionuclides under relevant repository conditions. Kobayashi, *et al.* investigated the uranium(VI) solubility in the presence of isosaccharinic acid (ISA), which is known as one of the main degradation products, dominant U(VI)-ISA complex was revealed, and the formation constant was determined by the analysis of the solubility data.

ACKNOWLEDGEMENTS:

This project was supported by Profs. Ohtsuki, Takamiya, and Sekimoto in KURNS.

PR10-1 Solubility of U(VI) in the presence of isosaccharinic acid

T. Kobayashi, D. Matoba, T. Fushimi, K. Haruki, T. Sasaki, T. Saito[1]

Graduate School of Engineering, Kyoto University
[1]Institute for Integrated Radiation and Nuclear Science, Kyoto University

INTRODUCTION: For the safety assessment of radioactive waste disposal, it is necessary to predict the solubility limit of radionuclides under relevant repository conditions. Cellulosic material contained in low and intermediate level waste degrades to smaller organic substances and α-isosaccharinic acid (ISA) is known as one of the main degradation products. ISA is a poly-hydroxycarboxylic acid and potentially enhance the solubility of radionuclides. Although several literatures have investigated the interaction of ISA with radionuclides, uranium is one of the elements, on which only very few studies have proposed the dominant ISA complexes and their formation constants [1]. Hexavalent uranium (U(VI)) is relevant under an occasional oxidizing condition in the repository system. Rao et al. has determined the complex formation constants of $UO_2(ISA)^{2+}$, $UO_2(ISA)_2(aq)$ and $UO_2(ISA)_3^-$ based on the potentiometric and calorimetric measurements [2]. In their experiments, the pH range was limited to the acidic pH region and thus U(VI)-ISA species dominant in neutral to alkaline pH range is still unclear. Since the U(VI) solubility in neutral to alkaline pH region is controlled by sparingly soluble $Na_2U_2O_7{\cdot}H_2O$(cr), formation of stable U(VI)-ISA species increases the uranium solubility in the repository system. In the present study, we investigated the U(VI) solubility in the presence of ISA at hydrogen ion concentrations (pH_c) of 7–13 and total concentration of ISA ($[ISA]_{tot}$) of 10^{-4} to $10^{-1.2}$ mol/dm^3 (M). Based on the slope analysis of the solubilities, dominant U(VI)-ISA complex was revealed, and the formation constant was determined by the analysis of the solubility data.

EXPERIMENTS: A stock solution of 0.33 M U(VI) was prepared by dissolving $UO_2(NO_3)_2{\cdot}6H_2O$ in 0.1 M HNO_3. Portions of concentrated NaOH solution was then quickly added into the U(VI) stock solution to obtain $Na_2U_2O_7{\cdot}H_2O$(cr) solid phase at pH_c about 10. Calcium isosaccharinate ($Ca(ISA)_2$) was synthesized from α-lactose and converted to NaISA stock solution. Sample solutions at specific pH_c and $[ISA]_{tot}$ were prepared by an undersaturation method. Before adding the $Na_2U_2O_7{\cdot}H_2O$(cr) to each sample tube, pH_c and $[ISA]_{tot}$ were adjusted in the ranges of pH_c = 7–13 and $[ISA]_{tot}$ = 10^{-4} to $10^{-1.2}$ M by adding appropriate amount of HCl/NaOH and NaISA stock solution. The ionic strength of each sample solution was set to I = 0.5 using 5 M NaCl stock solution. The sample tubes were kept in the Ar glove box up to maximum 123 days. After aging at a given period, the pH_c of the sample solutions was measured and each 0.5 mL of the supernatant was filtrated through ultrafiltration membrane (NMWL) of 10 kDa. The filtrate was acidified with nitric acid and diluted in 0.1 M HNO_3 for the measurement by ICP-MS. The detection limit was about 10^{-8} M.

RESULTS: U(VI) solubility in the absence and presence of $10^{-2.4}$ and $10^{-1.5}$ M ISA was investigated as a function of pH_c. In the absence of ISA, the solubility plots obtained in the present study are in good agreement with the literature values reported as the solubility of $Na_2U_2O_7{\cdot}H_2O$(cr) [3,4]. In the presence of $10^{-2.4}$ and $10^{-1.5}$ M ISA, the solubility was higher than those in the absence of ISA and almost constant against pH_c. Provided that the solid phase is $Na_2U_2O_7{\cdot}H_2O$(cr), the slope of zero suggested that three OH^- ions were involved in the U(VI)-ISA complex. At fixed pH_c 8.4 and 10.5, the U(VI) solubility was investigated as a function of total ISA concentrations ($[ISA]_{tot}$). U(VI) solubility increased with an increase of $[ISA]_{tot}$ with a slope of approximately 2, indicating that two ISA ligands were involved in the U(VI)-ISA complex. In conjunction with the slope of U(VI) solubility against pH_c and $[ISA]_{tot}$, the dominant U(VI)-ISA species was found to be $UO_2(OH)_3(ISA)_2^{3-}$ with the formation reaction of $UO_2^{2+} + 3OH^- + ISA^- \rightleftharpoons UO_2(OH)_3(ISA)_2^{3-}$. Taking the complex formation constant (β_{132}) of $UO_2(OH)_3(ISA)_2^{3-}$, hydrolysis constants of U(VI) (β_{1m}) [1], and solubility product of $Na_2U_2O_7{\cdot}H_2O$(cr) (K_{sp}) [4] into account, U(VI) solubility ([U(VI)]) can be described as

$$[U(VI)] = [UO_2^{2+}] + \sum_{m,n}[(UO_2^{2+})_m(OH)_n^{2m-n}] + [(UO_2^{2+})(OH)_3(ISA)_2^{3-}]$$

The solubility data in the neutral to alkaline pH range were analyzed to determine the complex formation constants β_{132} in the least squares fitting analysis. The formation constant was determined to be $\log \beta_{132} = 27.5 \pm 0.1$. The increase of the U(VI) solubility in the presence of ISA was quantitatively well explained by the formation of $UO_2(OH)_3(ISA)_2^{3-}$.

REFERENCES:

[1] Hummel W *et al.,* Chemical Thermodynamics of Compounds and Complexes of U, Np, Pu, Am, Tc, Se, Ni and Zr with Selected Organic Ligands. Elsevier, North-Holland, Amsterdam (2005).
[2] Rao L *et al.*, Radiochim. Acta, **92** (2004) 575-581.
Baes C. F., Mesmer R. E. The Hydrolysis of Cations. John Wiley & Sons, New York (1976).
[3] Yamamura T *et al.,* Radiochim. Acta, **83** (1998) 139-146.
[4] Altmaier M *et al.,* J. Chem. Thermodynamics **114** (2017) 2–13.

PR10-2 Electronic Absorption Spectra of Sulfer in LiCl-KCl Eutectic Melt

Y. Sakamura[1], T. Murakami[1], K. Uozumi[1] and A. Uehara[2]

[1]*Central Research Institute of Electric Power Industry*
[2]*National Institutes for Quantum and Radiological Science and Technology*

INTRODUCTION: The electrolytic reduction technique in LiCl-Li_2O melts has been developed for pyrochemical reprocessing of spent oxide fuels. At the cathode, actinide oxides are reduced to their metals:

$$MO_2 + 4\ e^- \rightarrow M + 2\ O^{2-} \qquad (1)$$

where M denotes actinides such as U and Pu. Similar to oxygen, chalcogen fission products such as Se and Te are dissolved into the melt in the form of divalent anion.

Recently, the authors have studied electrochemical behaviors of Na_2Se and Na_2Te in LiCl-KCl eutectic melt to extract Se and Te from molten salts [1]. It was indicated that the deposition of Te proceeded in two steps at the anode: the oxidation of Te^{2-} to Te_2^{2-} occurred followed by the oxidation of Te_2^{2-} to Te, which was similar to the electrochemical behaviors of Se and S [2]. Moreover, the absorption spectra of Na_2Se and Na_2Te in LiCl-KCl melt have been already reported [3,4]. In this study, Li_2S was investigated to compare the spectroscopic characteristics among S^{2-}, Se^{2-} and Te^{2-}.

EXPERIMENTS: LiCl-KCl-Li_2S (Li_2S: 0.44 wt%) and LiCl-KCl-Li_2S-S (Li_2S: 0.48 wt%, S: 1.5 wt%) mixtures were prepared by heating quartz tubes containing LiCl-KCl eutectic (59:41 mole ratio), Li_2S (99.9% purity) and S (99.999% purity) at temperatures > 673 K.

LiCl-KCl-Li_2S test

LiCl-KCl eutectic (4.079 g) was loaded in a rectangular quartz cell (10 x 10 mm) used for absorption spectrometry and heated to 673 K in an electric furnace. The experimental apparatus was previously described in detail by Nagai et al. [5] The LiCl-KCl-Li_2S mixture (0.211 g) was then added and the absorption spectrum of the melt was measured by using an UV/Vis/NIR spectropho-tometer (V-570, JASCO).

LiCl-KCl-Li_2S-S test

LiCl-KCl eutectic (4.013 g) was loaded in a rectangular quartz cell and heated to 673 K. The LiCl-KCl-Li_2S-S mixture (0.086 g) was then added and the absorption spectrum of the melt was measured. Subsequently, S (0.012 g) was added.

All of the experiments were conducted in a high-purity argon atmosphere glove box.

RESULTS: Fig. 1 shows absorption spectra of the melts. No peak was present in the wavelength range of 1000-2000 nm. The absorption peak at 333 nm (Fig. 1, (a)) increased as the LiCl-KCl-Li_2S mixture was added, which has not been reported before. The LiCl-KCl-Li_2S-S melt was light blue and there was an absorption peak at 580 nm (Fig. 1, (b)). The cyclic voltammetric studies in LiCl-KCl-Li_2S melts showed that S is deposited on inert anodes such as Au via intermediate products of polysulfide ions (S_n^{2-}) [2]:

$$S^{2-} \rightarrow S_n^{2-} \rightarrow S_n \qquad (2)$$

Therefore, it is suggested that the absorption peak at 580 nm might be due to the S_n^{2-} ions, which is consistent with the results previously measured in a LiCl-KCl melt after the cathodic dissolution of liquid S [6]. The subsequent addition of S into the melt led to a large increase in the peak height (Fig. 1, (c)), and the melt became dark blue. The peak wavelength remained at 580 nm, indicating that the addition of S might not change the polysulfide species. After the measurement, evaporated S was found on the upper part of quartz cell. The mass balance of S in the melt should be examined in detail in future work.

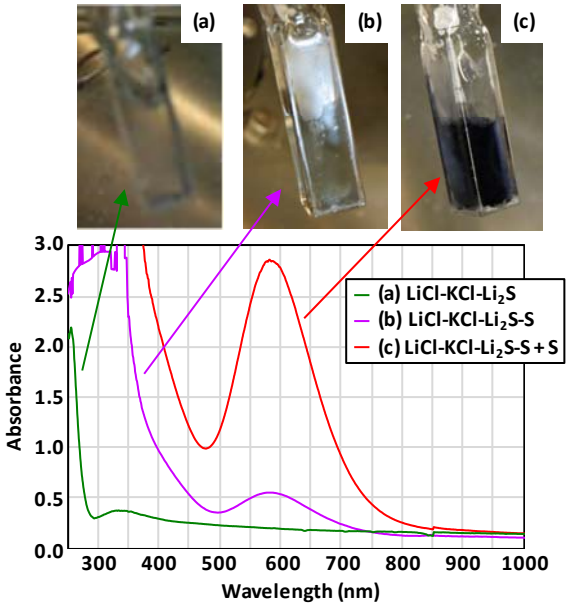

Fig. 1 Absorption spectra of (a) "LiCl-KCl-Li_2S", (b) "LiCl-KCl-Li_2S-S" and (c) "LiCl-KCl-Li_2S-S +S" melts.

ACKNOWLEDGMENTS: The authors are grateful to Drs. K. Takamiya and T. Ohtsuki of Institute for Integrated Radiation and Nuclear Science, Kyoto University, for their support and useful advice.

REFERENCES:

[1] Y. Sakamura, T. Murakami and K. Uozumi, Proc. The 49th Symposium on Molten Salt Chemistry, p. 84, Kansai Univ., Japan, Nov. 30 - Dec. 1, 2017, in Japanese.
[2] D. Warin, Z. Tomczuk and D.R. Vissers, J. Electro-chem. Soc., 130 (1983) 64-70.
[3] Y. Sakamura, T. Murakami, K. Uozumi, A. Uehara and T. Fujii, KURRI Progress Report 2016 (2017) 15.
[4] Y. Sakamura, T. Murakami, K. Uozumi, A. Uehara and T. Fujii, KURRI Progress Report 2017 (2018) 192.
[5] T. Nagai, T. Fujii, O. Shirai and H. Yamana, J. Nucl. Sci. Technol., 41 (2004) 690-695.
[6] F.G. Bodewig and J.A. Plambeck, J. Electrochem. Soc., 117 (1970) 904.

PR10-3 Study on the leaching behavior of fission products in simulated MCCI debris

T. Sasaki, N. Sato[1], A. Kirishima[1], D. Akiyama[1], T. Kobayashi, K. Takamiya[2], S. Sekimoto[2], S. Sakamoto and Y. Kodama

Graduate School of Engineering, Kyoto University

[1] Institute of Multidisciplinary Research for Advanced Materials, Tohoku University

[2] Institute for Integrated Radiation and Nuclear Science, Kyoto University

INTRODUCTION: Information on the radionuclide behavior in fuel debris and surface seawater will be helpful to analyze the forthcoming analysis data about the contents of minor FPs and TRU in the contaminated water, and to manage associated secondary wastes. A molten core-concrete interaction (MCCI) is thought to be a critical event because of the penetration of partially molten core from the reactor pressure vessel to the bottom of the primary containment vessel. The physical and chemical characteristics of the MCCI debris have been studied using the knowledge obtained from similar events in other countries, and by using some calculation codes. Based on these fundamental findings, the initial composition of the debris, high-temperature and atmospheric conditions, and the cooling rate of molten core-concrete have a large impact on the solidification phases. However, the leaching behavior of fission products in MCCI debris has not been fully understood [1]. In the present study, the preparation of the MCCI debris are investigated using a mixture of UO_2, ZrO_2, and a component of cement material.

EXPERIMENTS: The reference cement material 211S was purchased from Japan Cement Association, and used without any preconditioning. Three cement mixing ratios of UO_2–ZrO_2 were adopted to obtain U:Ca mole ratios of 1:0.75 (#OA), 1:1.75 (#OB), and 1:6.75 (#OC). The mole ratio of U:Zr in UO_2–ZrO_2 sample was assumed to be 5:1, as a balance of UO_2 fuel and zircaloy clad. The weighed amounts of UO_2 and ZrO_2 powders and of the cement were mixed using an agate mortar and pestle. The sample was heated in a quartz boat at 1473 K for 2 h in an oxidizing (Ar + 2% O_2) atmosphere. During furnace cooling, pure argon gas was kept flowing. After the cooling, the sample was investigated by XRD. The simulated MCCI debris sealed in a quartz ampoule was inserted into a polyethylene capsule and irradiated using Pn-2 of Kyoto University Reactor (at 1 MW) for 20 min. The gamma-ray activity, which is considered as an initial inventory of each radionuclide in the solid sample, was measured using a Ge detector after cooling in order to allow for the decay of highly radioactive, short-lived nuclides.

RESULTS: The peaks of UO_2 phase in the mixed samples with ZrO_2 and CaO shifted to higher angles, which indicates the formation of a solid solution, $(Ca_yZr_zU_{1-y-z})O_{2+x}$ in #OA. The lattice parameter was 5.339 Å. It is recognized that the lattice parameters of the cubic-fluorite-type solid solution $(Ca_yZr_zU_{1-y-z})O_{2+x}$ changes with the stoichiometric abundances of metals and the O/M ratio. With increasing the Ca (and Si) amount to U, the dominant species changed from $(Ca_yZr_zU_{1-y-z})O_{2+x}$ in #OA (U:Ca = 1:0.75) to the trigonal $CaUO_4$ in #OB (U:Ca = 1:1.75), and Ca_3UO_6 in #OC (U:Ca = 1:6.75) appeared in the presence of further excess calcium. The nuclides were produced by the fission reaction of uranium-235. The peaks for five radionuclides—Zr-95, Ru-103, I-131, Cs-137, and Ba-140—were assigned in γ spectrometry. Zr-95 was produced from the fission reaction of uranium and the (n,γ) reaction of natural Zr-94 in the ZrO_2 matrix, suggesting that Zr-95 from two different origins exists in samples.

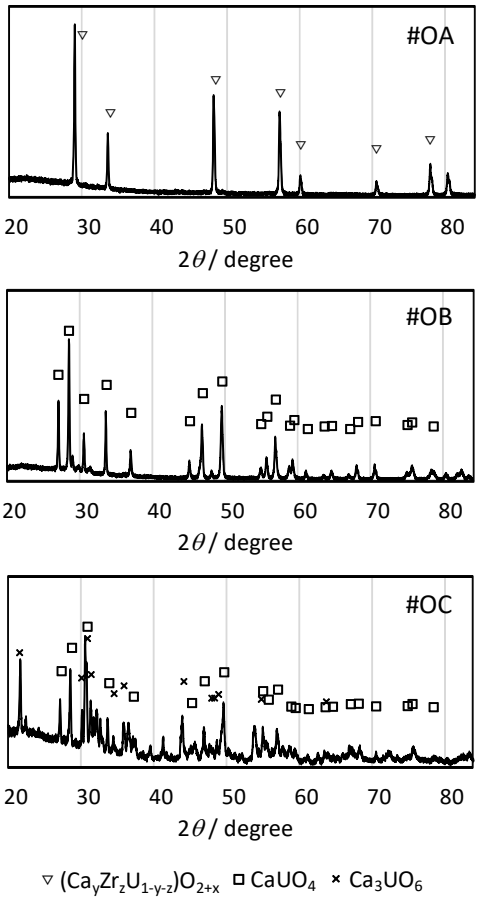

Fig. 1 XRD patterns of samples by heat treatment at 1473 K under O_2 atmospheric condition.

REFERENCES:

[1] Sasaki T., Takeno Y., Kirishima A., Sato N., J. Nucl. Sci. Technol., **53** (2016) 303–311.

PR10-4 Analysis of isotopic composition of Cs recovered from environmental sample obtained in Fukushima prefecture by thermal ionization mass spectrometry

Y. Shibahara, S. Fukutani, T. Kubota,
T. Shibata[1], M. Yoshikawa[1]

KURNS, Kyoto University
[1]Graduate School of Science, Hiroshima University

INTRODUCTION: We have studied the applicability of the mass spectrometry, especially thermal ionization mass spectrometry (TIMS), for the analysis of radionuclide released on the accident of Fukushima Dai-ichi Nuclear Power Plant. In the previous study of the analysis of Cs isotopic composition by TIMS, we compared the analytical result of isotopic composition of Cs in the standard materials and so on with the literature data to discuss the applicability of the isotopic analysis of Cs [1]. In this study, we discussed the analytical results of Cs isotopic composition obtained within the latest 2 financial years from April 2017 to March 2019.

EXPERIMENTS: Cs was recovered from the environmental sample of moss obtained in Fukushima prefecture. The concentration of ^{137}Cs of the environmental sample obtained in Fukushima prefecture was about 2.6×10^{-10} g/g (corrected on 11 Mar 2011). Cs was recovered according to the recovery scheme [2-4]. After the preparation of the samples for the isotopic composition analysis of Cs, the Cs isotopic ratios (= ^{134}Cs/^{137}Cs and ^{135}Cs/^{137}Cs) were analyzed by TIMS.

A thermal ionization mass spectrometer (TRITON-T1, Thermo Fisher Scientific) with a rhenium single filament system was used for the isotopic composition analysis of Cs. The Cs sample prepared for the TIMS analysis was loaded onto a rhenium filament with a TaO activator [2-4] or glucose activator [5]. Because of the loading amount of Cs (max. 1×10^{-12} g), the mass spectrometry was conducted with a secondary electron multiplier detector and the peak jump method [2-4].

RESULTS: The mass spectrum of Cs recovered from the environmental sample of moss was shown in Fig. 1. We can see the peaks corresponding to ^{134}Cs, ^{135}Cs and ^{137}Cs, aside from the peak of ^{133}Cs. Figure 2 shows the time profile of ^{134}Cs/^{137}Cs isotopic ratio. The analytical results obtained within the latest 2 years shows the following correlation as;

^{134}Cs/^{137}Cs =
$(0.070\pm0.001)\times\exp[(-0.000849\pm0.000007)\times T]$ (1),

where T means the time in days (T=0 is March 11, 2011). From Fig. 3 showing the time profile of ^{135}Cs/^{137}Cs isotopic ratio, we also obtained the following equation as;

^{135}Cs/^{137}Cs =
$(0.365\pm0.004)\times\exp[(0.000063\pm0.000005)\times T]$ (2).

From eqs. (1) and (2), the half-lives of ^{134}Cs and ^{137}Cs were evaluated as $T_{1/2(Cs\text{-}134)}$ = 2.08±0.02 y and $T_{1/2(Cs\text{-}137)}$ = 30.2±2.2 y respectively. We found that these values show the good relation with the literature data [6] (2.07 y for ^{134}Cs and 30.2 y for ^{137}Cs).

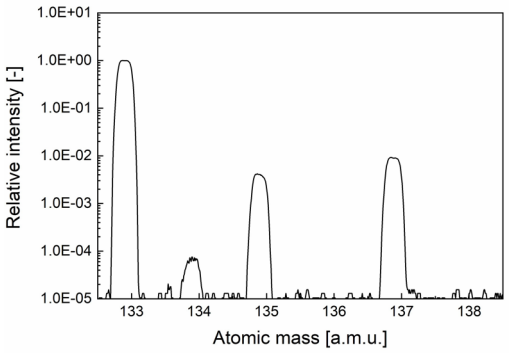

Fig. 1 Mass spectra of Cs recovered from environmental sample obtained at Fukushima prefecture observed at March 2019.

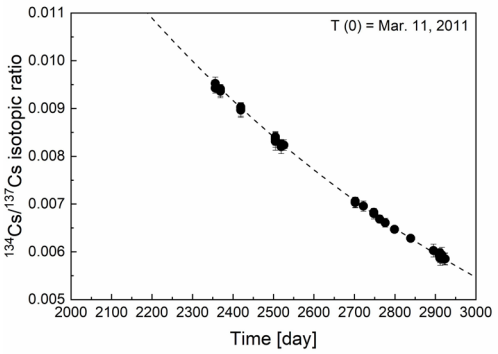

Fig. 2 Time profile of ^{134}Cs/^{137}Cs isotopic ratio. Broken line shows analysis results with equation of $y=a\times\exp[b\times x]$.

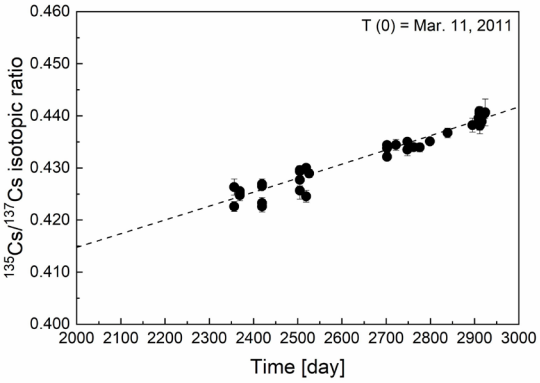

Fig. 3 Time profile of ^{135}Cs/^{137}Cs isotopic ratio. Broken line shows analysis results with equation of $y'=a'\times\exp[b'\times x]$.

REFERENCES:
[1] Y. Shibahara et al. KURRI progress report 2017,157.
[2] Y. Shibahara *et al.*, J. Nucl. Sci. Technol. 2014, 51, 575-579.
[3] Y. Shibahara *et al.,* Radiological issues for Fukushima's revitalized future. Springer. 2016. 33-46.
[4] Y. Shibahara *et al.,* J. Nucl. Sci. Technol. 2017, 54, 158-166.
[5] J. A. Dunne *et al.,* Talanta 2017, 174, 347-356.
[6] R.B. Firestone *et al.,* Table of Isotopes, John Wiley and Sons, New York, 1998.

PR10-5 EMF Mesurements of AgCl Concentration Cell in LiCl-KCl Eutectic Molten Salt Using Chloride Ion Conducting Solid Electrolyte

H. Sekimoto[1], Y. Saito[2] and N. Iwabuchi[1]

[1]*Department of Physical Science and Materials Engineering, Faculty of Science and Engineering, Iwate University*
[2]*Department of Materials Science and Engineering, Division of Science and Engineering, Graduate School of Arts and Science, Iwate University*

INTRODUCTION: Thermodynamic data of chemical species dissolved in molten salts such as activity, and activity coefficient are important to evaluate existing processes for treating nuclear materials. Such thermodynamic data are conventionally determined by measuring electromotive force using silver-silver chloride reference electrode. The electrodes are usually prepared by adding 1-5mol% of silver chloride into the same molten salt as sample and immersing silver wire. At the junction between sample and the electrode, porous ceramics or glass membrane are used. They can be used in limited system. In this study, a new type reference electrode was proposed. The proposed electrode consists of silver, pure silver chloride and anion conducting solid electrolyte. In this study, CaO doped LaOCl reported by Imanaka et al. [1] was employed as chloride ion conducting material.

EXPERIMENTS: CaO doped LaOCl is prepared by solid state reaction. The molar ratio of LaOCl : CaO was 85 : 15. The CaO doped LaOCl was attached on a side of cylindrical mullite tube with ceramic bond. Pure AgCl was inserted in the mullite tube with CaO doped LaOCl and heated at 600 °C to melt AgCl. Afterwards, silver wire was immersed in liquid AgCl. Subsequently, mullite tube with CaO doped LaOCl and silver wire immersed to construct the following AgCl concentration cell.

Ag(*s*) | AgCl(*l*, pure) (a_{AgCl} = 1) | LaOCl-CaO | AgCl (*l*, in LiCl-KCl eu.) (a_{AgCl} < 1) | Ag(*s*) (1)

The electromotive force of the cell (1) is evaluated as follows.

$$emf = -RT/F \ln a_{AgCl\ (l,\ in\ LiCl\text{-}KCl\ eu.)} \quad (2)$$

The addition of AgCl in LiCl-KCl eutectic molten salt and measurement of the *emf* was repeated several times.

RESULTS: As shown in Fig. 1, the relation between the *emf* and the concentration of AgCl in LiCl-KCl molten salt obeyed the Nernst equation. The activity of AgCl in LiCl-KCl eutectic molten salt was evaluated and shown in Fig. 2. The value obtained in this study well agree with the reported values [2-5].

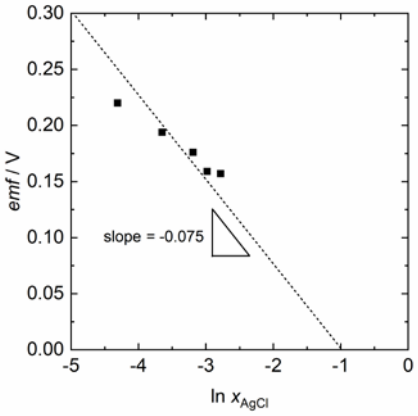

Fig. 1 Relation between the electromotive force of the AgCl concentration cell and the concentration of AgCl in LiCl-KCl eutectic molten salt.

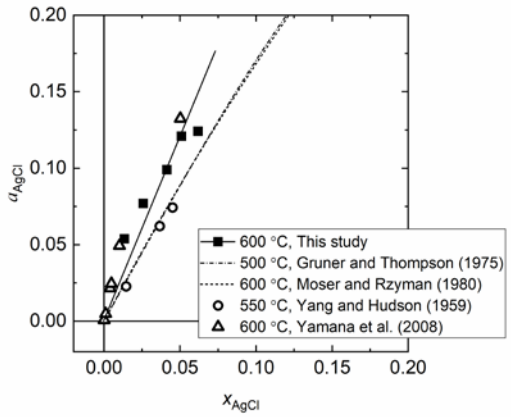

Fig. 2 Relation between the activity and the concentration of AgCl in LiCl-KCl eutectic molten salt.

REFERENCES:

[1] N. Imanaka, K. Okamoto and G. Adachi, Angew. Chem. Int. Ed., **41** (2002) 3890.
[2] O. Shirai, T. Nagai, A. Uehara and H. Yamana, J. Alloy. Compd., **456** (2008) 498.
[3] L. Yang and R. G. Hudson, J. Electrochem. Soc., **106** (1959) 986.
[4] A. C. Gruner and W. T. Thompson, Can. J. Chem., **53** (1975) 1084.
[5] Z. Moser and K. Ryzman, Electrochim. Acta, **25** (1980) 183.

PR10-6 Structural Change of Borosilicate Glass by Neutron Irradiation

T. Nagai, H. Kobayashi, Y. Okamoto, D. Akiyama[1], N. Sato[1], A. Uehara[2], T. Fujii[3], and S. Sekimoto[4]

Japan Atomic Energy Agency (JAEA)
[1]Institute of Multidisciplinary Research for Advanced Materials (IMRAM), Tohoku University
[2]National Institute of Quantum and Radiological Science and Technology (QST)
[3]Graduate school of Engineering, Osaka University
[4]Institute for Integrated Radiation and Nuclear Science, Kyoto University

INTRODUCTION: A high-level radioactive liquid waste from a reprocessing process for spent nuclear fuels is processed into a solidified waste made of a borosilicate glass. In our previous study, the structural change of neutron irradiated borosilicate glass was observed by using Raman spectrometry [1]. In this study, to understand this structural change by a neutron irradiation in detail, the irradiation test was carried out in 2017FY. The glass structure was estimated by using Raman spectrometry in 2018FY. As a mechanism of neutron irradiation on borosilicate glasses, the nuclear reaction $^{10}B(n,\alpha)^{7}Li$ was supposed, which was studied by S. Peuget, et al [2].

EXPERIMENTS: Two kinds of borosilicate glass of $17B_2O_3$-$65SiO_2$-$17Na_2O$-CeO_2-Y_2O_3 and $28B_2O_3$-$54SiO_2$-$17Na_2O$-CeO_2-Y_2O_3 were prepared based on the selection of chemical composition [3]. Raw material reagents of SiO_2, H_3BO_3, Na_2CO_3, CeO_2, and Y_2O_3 were loaded in an alumina crucible and were melted at 1,150°C in an electric furnace. After the molten glass samples were solidified by cooling to room temperature, they were cut into thin plates. In Dec. 2017, these thin plate samples were set in a polyethylene tube and were irradiated under the condition of 1,000 kW for 50 min in the Pn-2 of KUR. After the radioactivity of the samples reduced to the background level, the Raman spectra of the samples were measured by using a Raman spectrometer, NRS-3100 of JASCO.

RESULTS: As a structural change of borosilicate glass by the irradiation, an amount of Li would be increased by the $^{10}B(n,\alpha)^{7}Li$ reaction, and Li was expected to disconnect the Si-O bridging structure. So, the effect of the irradiation would be effectively evaluated by the Raman shifts of Si-O bridging structure. The Raman shifts of Si-O bridging structure of a borosilicate glass lies in the wavenumber of 850-1,250 cm^{-1}, and the peak positions of Raman shifts depend on the number of non-bridging oxygen, NBO. In this measurement, those Raman shifts were observed in 850-1,250 cm^{-1}, and the measured spectra was successfully separated into six Gaussian waves as shown in Fig. 1, where fitting error was negligible compared to the difference by irradiation. The Raman peak of Q^4 structure without NBO appeared in around 1,150 cm^{-1}, and those of Q^3, Q^2, and Q^1 structures with the NBO number = 1, 2, and 3 were in 1,090, 1,000, and 900 cm^{-1} respectively. The peaks of Q^2 and Q^3 structures can be subdivided into plural by the Si-O-X connecting state, and were divided into $Q^{2(1)}$, $Q^{2(2)}$, $Q^{3(1)}$, and $Q^{3(2)}$. Comparing the Raman shifts after irradiation with non-irradiation, it was observed that the peak heights of $Q^{2(1)}$, $Q^{2(2)}$, or $Q^{3(1)}$ decreased and that of Q^1 increased after the irradiation in Fig. 1. This result suggests that $Q^{2(1)}$, $Q^{2(2)}$, and $Q^{3(1)}$ structures change into Q^1 structure by the irradiation. In other words, it was considered that generated Li enters into a part of $Q^{2(1)}$, $Q^{2(2)}$, and $Q^{3(1)}$ structures easily.

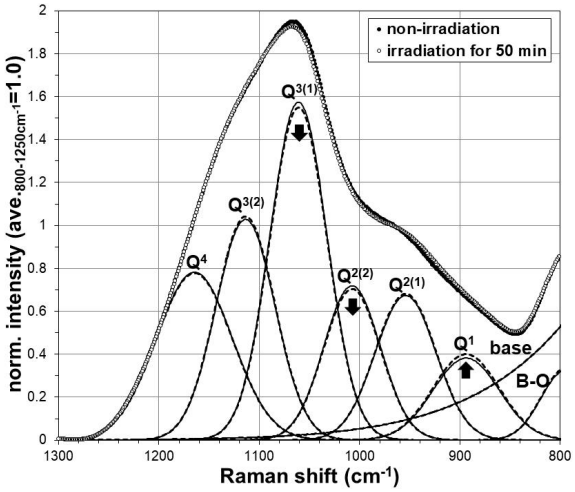

(1) $17B_2O_3$-$65SiO_2$-$17Na_2O$-CeO_2-Y_2O_3 sample.

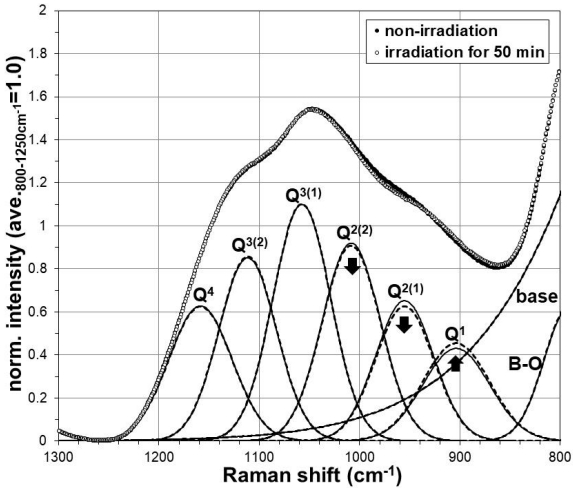

(2) $28B_2O_3$-54 SiO_2-$17Na_2O$-CeO_2-Y_2O_3 sample.

Fig. 1. Raman spectra and separated Gaussian waves. Open circles and dotted lines are after irradiation, and closed circles and fine lines are non-irradiation.

REFERENCES:

[1] T. Nagai, et al, 2014FY KURRI progress report, 26P11-4 (2015).
[2] S. Peuget, et al, Nucl. Inst. Methods in Phys. Res. B, **327** (2014) 22-28.
[3] T. Nagai, et al, 2017FY KURRI progress report, 29056 (2018).

PR10-7 Activation measurement for thermal-neutron capture cross-section of Cesium-135

S. Nakamura[1], A. Kimura[1], O. Iwamoto[1]
Y. Shibahara[2], A. Uehara[3], T. Fujii[4],

[1]*Japan Atomic Energy Agency*
[2]*Institute for Integrated Radiation and Nuclear Science, Kyoto University*
[3]*National Institutes for Quantum and Radiological Science and Technology*
[4]*Graduate School of Engineering, Osaka University*

INTRODUCTION: In recent years, transmutation researches have been reconsidered. The "ImPACT" project [1] is one of such research trends. In this project, following LLFP nuclides are listed to be transmuted: ^{107}Pd, ^{93}Zr, ^{135}Cs, and ^{79}Se. When considering nuclear transmutation of these LLFPs by using neutrons, accurate data of neutron capture cross-sections are required to evaluate the transmutation and/or reaction rate. Two nuclides of ^{107}Pd and ^{93}Zr have been previously measured at J-PARC [2,3]. On the other hand, it is very difficult to obtain ^{135}Cs and ^{79}Se samples for measurements. This is the reason why there are a few ^{135}Cs data and no ^{79}Se data. The authors chose ^{135}Cs for measurements because we got an idea of using ^{135}Cs contained as an impurity in a ^{137}Cs standard solution.
This work is aimed to measure the thermal-neutron cross-section of the ^{135}Cs (n, γ) ^{136}Cs reaction.

EXPERIMENTS: A standard solution of ^{137}Cs was obtained through the Japan Radioisotope Association. The isotope ratio of ^{135}Cs and ^{137}Cs was determined by mass spectrometry. The mass spectrometer TRITON (Thermo Fisher Scientific, Inc.) was used for this analysis. A small amount (about 10 Bq) of the ^{137}Cs solution was pipetted onto a Re filament together with a TaO activator, and then the filament was dried. The loaded filament was attached onto the ion source of the spectrometer. From mass yields of Cs isotopes in the mass spectrum, the ratio of ^{135}Cs and ^{137}Cs was found to be 0.868±0.004 (±2σ).

A small amount of 1 kBq solution was taken from the same ^{137}Cs standard solution, and then dropped onto a 5-mm-square chemical filter. The ^{137}Cs loaded filters were dried by an infrared lamp. The filter was wrapped with high purity aluminum foil together with pieces of Au/Al and Co/Al alloy wires to monitor neutron flux components at an irradiation position. The ^{137}Cs loaded filter with the monitor set was used as an irradiation target (called "a bare target"). The same ^{137}Cs loaded filter and monitor set were sandwiched both sides with a Gadolinium (Gd) foil of 10 mm×15 mm×25 μm^t in size (called "a Gd filtered target") to estimate contributions by epi-thermal neutrons. The irradiations of the targets were performed at the Hydraulic tube of the Kyoto University Reactor (KUR) in 5-MW power operation. The bare target was irradiated for 3 hours, and the Gd filtered one for 6 hours. The γ-ray measurements were performed later from the end of the irradiation. A high-purity Ge detector was used to measure the γ rays emitted from Cs isotopes to obtain their induced activities. **Figure 1** shows an example of γ-ray spectrum of the Gd filtered target. Decay γ rays emitted from ^{137}Cs and ^{136}Cs were clearly observed at the γ-ray energies of 662 keV and 819 keV. Sufficient statistics for the γ-ray peaks were obtained. Since the ratio of ^{135}Cs and ^{137}Cs have been determined in advance, the yield of 662-keV γ ray can give an amount of ^{135}Cs in the target.

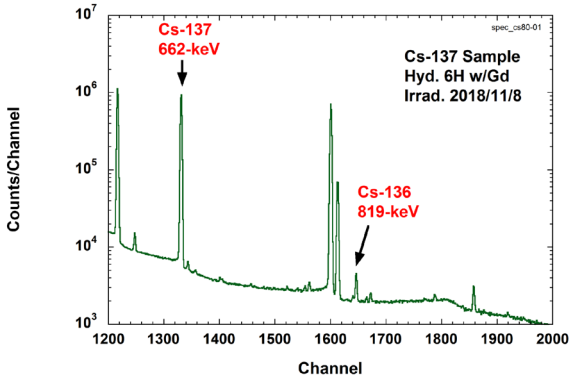

Fig.1 Gamma-ray spectrum of Gd filtered ^{137}Cs target irradiated by reactor neutrons at KUR

Then, the ^{135}Cs(n,γ)^{136}Cs reaction rate can be obtained from the yield of 819-keV γ ray due to ^{136}Cs. The reaction rates in the cases of bare and Gd-filtered targets were determined, and the thermal-neutron capture cross-section can be derived by the analysis based on Westcott's convention [4]. The present result is consistent with the past reported value [5] within the limits of errors. Further analysis is now in progress.

Acknowledgement

The authors would like to appreciate staffs of Kyoto University Research Reactor Institute for their support. This research was funded by ImPACT Program of Council for Science, Technology and Innovation (Cabinet Office, Government of Japan).

REFERENCES:

[1] http://www.jst.go.jp/impact/index.html
[2] S. Nakamura *et al.*, Nuclear Data Sheets, 2014;**119**:143.
[3] J. Hori *et al.*, AESJ fall meeting, 2010.
[4] C.H. Westcott *et al.*, "*Proc.2nd Int.Conf.Peaceful Use of Atomic Energy, Geneva*", 1958;**16**:70.
[5] T. Katoh *et al.*, J.Nucl.Sci.Technol., 1997; **34**: 431.

PR10-8 Exchange Reaction of Proton in Hydroxide with Tritium in Aqueous Solution

H. Hashizume, A. Uehara[1], S. Fukutani[2], K. Fujii, T. Ando

National Institute for Materials Science
[1]National Institute for Quantum and Radiological Science and Technology
[2]Institute for Integrated Radiation and Nuclear Science, Kyoto University

INTRODUCTION: Tritium (T) is one of radioactive elements. Since the characteristics are almost the same as hydrogen (H), it is very difficult to separate tritium from water. We have a large amount of radioactively contaminated water for the Fukushima Daiich Nuclear Power Station Accident. Because HTO is included in the radioactively contaminated water, it can not be discarded and is increasing. For the removal of HTO from water, Koyanaka and Miyatake (2015) reported that about 30% amounts of tritium in water including tritium was caught by manganese oxide for about 20 min [1]. Hashizume et al. (2016) investigated that tritium was discriminated in the formation of a hydroxide from an oxide in water including tritium [2]. They also examined the ion exchange between proton in hydroxide and tritium in water [3]. A few % of tritium was removed in water including T by those treatments.

We investigate the change of the ion exchange between tritium in water and proton in a hydroxide to the different concentration of tritium in water, and show the isotherm for the ion exchange between tritium and proton to the concentration of tritium in water by the hydroxide.

EXPERIMENTS: We used water including tritium which was prepared in Institute for Integrated Radiation and Nuclear Science, Kyoto University. Magnesium hydroxide ($Mg(OH)_2$) and calcium hydroxide ($Ca(OH)_2$) were used as the ion exchange materials. Water including tritium was diluted by deionized water, properly. For the ion exchange, 1g of the ion exchange material and 8 cm^3 of diluted water were put in the glass bottle with stopper. The suspension was shaken for 5 hours by the rotary shaker. Hashizume et al. (2018) showed that 5 hours were enough time to achieve the equilibrium of the ion exchange [4]. After shaking, the suspension was centrifuged and supernatant was filtered by 0.45 or 0.2 μm of a filter. For the measurement by a scintillation detector (Packard, Liquid Scintillation Analyzer), 1 cm^3 of the supernatant or the original water including tritium and 20 $cm^3$of the liquid scintillator were pour into the glass vial.

The extent of the ion exchange was estimated by the following equation.

$$E=(C_0-C)\bullet V/W \quad (1)$$

where E is the extent of ion exchange, C_0 is the concentration of tritium in water, C is the concentration of tritium in supernatant, V is the volume of added water and W is the weight of the ion exchange material.

RESULTS: The isotherms for the ion exchange by $Mg(OH)_2$ and $Ca(OH)_2$ are shown in Fig. 1. The extent of the ion exchange by $Mg(OH)_2$ was higher than that by $Ca(OH)_2$. The isotherms were adopted to Langmuir and Freundlich equation. The Langmuir and Freundlich equation are

Langmuir equation: $E=a\bullet E_s\bullet B/(1+a\bullet B)$ (2)

Freundlich equation: $E= K_f\bullet B^{1/n}$ (3)

where E_s is the saturated ion exchange capacity, B is equilibrium concentration, a, K_f and n are constant.

The parameters of Langmuir and Freunlich equations are shown in Table 1. And the isotherms from Langmuir and Freundlich equations are also shown in Fig. 1. The Freundlich equation might be more fitted than the Langmuir equation.

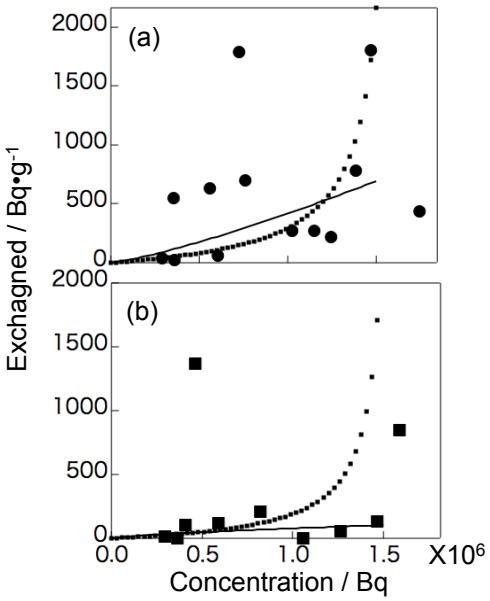

Fig.1 Isotherms for ion exchange of tritium by $Mg(OH)_2$ (a) and $Ca(OH)_2$ (b). The dot and black lines are for Langmuir and Freundlich equation, respectively.

Table 1 Parameters of Langmuir and Freundlich equation.

	Langmuir			Freundlich	
	$Mg(OH)_2$	$Ca(OH)_2$		$Mg(OH)_2$	$Ca(OH)_2$
a	-6.1x10-7	-6.4x10-7	K_f	1.37	0.0033
E_s	-185.2	-106.4	1/n	1.24	0.723

REFERENCES:

[1] H.Koyanaka & H. Miyatake, *Separation Science Technology*, **50** (2015) 2142-2145.
[2] H.Hashizume *et al.,* Tokugann 2016-135839 (2016) (Japanese patent in Japanese).
[3]H.Hashizume *et al.*, Tokugann 2018-43792 (2018) (Japanese patent in Japanese).
[4] H.Hashizume *et al.*, KURRI Progress Report (2017) C05-6.

30P10-9

PR10-9 Solvent Extraction Behavior of Fission Product Elements

Y. Araki[1], M. Morita[1], T. Kawakami[1], C. Kato[1], A. Uehara[2], S. Fukutani[2] and T. Fujii[1]

Graduate School of Engineering, Osaka University
[2]KURNS, Kyoto University

INTRODUCTION: By separating the long lived nuclides from high-level radioactive waste, it is possible to significantly reduce the potential hazard of waste, thereby reducing long-term risk. Palladium (Pd) is a fission product element contained in the spent fuel. The half-life of ^{107}Pd is 6.5×10^6 years, and is subjected to separation. Also, Pd has a large cross section area to the fast neutron, so it is likely to interfere with fission of minor actinides (MA). In this study, we focused on the separation of Pd and studied the solvent extraction behavior of Pd from a nitric acid solution. Furthermore, we compared with nickel (Ni) which is the same group element as Pd for better understanding.

EXPERIMENTS: Palladium and Ni were prepared in nitric acid as the aqueous phase. For the organic phase, tetradodecyl diglycolamide (TDdDGA), N,N,N',N',N",N"-hexaoctylnitriloacetamide (HONTA) and alkyldiamideamine (ADAAM) was prepared in dodecane. HONTA and ADAAM are novel extractants developed by Japan Atomic Energy Agency (JAEA) [1]. After the two phases were stirred for 30 minutes, phase separation was performed by centrifugation. The back extraction was performed using the phase-separated organic phase and diluted nitric acid, which was then separated by centrifugation. The element concentration was measured in the aqueous phase after the fore extraction and back extraction using inductively coupled plasma－atomic emission spectrometry (ICP-AES), and the distribution ratio was determined.

RESULTS and DISCUSSION: The distribution ratio of Pd and Ni and its dependency of nitric acid concentration is shown in figure 1. For Pd, when using the novel extractants, the distribution ratio peaked at a nitric acid concentration around 0.2 M. In addition, it was found that the distribution ratio was up to 103 times higher than using TDdDGA in the high acidity region. For Ni, it was found that the distribution ratio was generally low for all extractants.

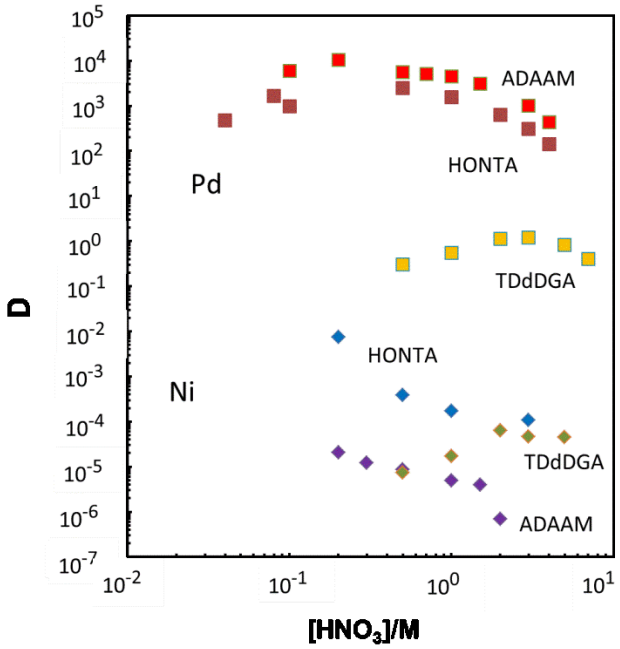

Fig. 1. Distribution ratio of Pd and Ni and its dependency on nitric acid concentration.

REFERENCES:

[1] H. Suzuki *et. al.,* Anal. Sci., **32** (2016) 477-479.

PR10-10 Electrochemical behavior of zirconium in molten lithium – calcium chloride to develop processing nuclear fuel debris

T. Nagasawa, T. Emori[1], H. Matsuura[1,2], A. Uehara[3]

Faculty of Engineering, Tokyo City University, Japan
[1]Graduate School of Engineering, Tokyo City University, Japan
[2]Atomic Energy Research Laboratory, Tokyo City University, Japan
[3]National Institutes for Quantum and Radiological Science and Technology, Japan

INTRODUCTION: In order to develop processing nuclear fuel debris caused by nuclear accident of the Fukushima Daiichi Nuclear Power Plant following from huge earthquake and tsunami on 2011, we have proposed selective fluorination and molten salt electrolysis to separate uranium from nuclear fuel debris. Process concept is as follows; 1) selective fluorination; UO_2 was fluorinated in nuclear fuel debris using HF gas[1], 2) selective dissolution; UF_4 was dissolved in molten salt and 3) molten salt electrolysis; uranium ions were reduced in molten salt, and uranium metal or oxide was deposited on electrode. However coexisting zirconium can be also fluorinated with uranium and zirconium oxide will be remaining at the upstream process. Therefore, electroreduction of uranium cannot be made because standard redox potential of zirconium is more positive than that of uranium. Zirconium electrochemistry due to the presence fluoride and oxide ions should be investigated to reduce zirconium concentration in molten bath. In this year, we choose molten LiCl-$CaCl_2$ for electrolysis bath since no cationic species are disturb at uranium electro-reduction even in co-existence of fluoride anion.

EXPERIMENTS: All the electrochemical measurements using molten LiCl-$CaCl_2$ have been performed in an electric furnace which is built inside a glove box filled with dried argon atmosphere using an electrochemical analyzer. Electrochemical analysis has been performed as both cyclic voltammetry and linear sweep voltammetry by using the electrodes as follows: working electrode: molybdenum, counter electrode: pyrographite and reference electrode: silver wire dipped in molten LiCl-KCl + AgCl inside the borosilicate tube. Aluminium oxide ceramics was used as a crucible, and temperature condition is at 700 ^{o}C. To observe the fluoride addition effect, both zirconium chloride and fluoride were used as a zirconium solute (1 wt%) by addition to the pre-mixed LiCl-$CaCl_2$ electrolysis bath. Duration of pre-reduction before linear sweep voltammetry is 1 minute.

RESULTS AND DISCUSSION: Before going to simulant of fluorinated fuel debris, electrochemical behavior of zirconium in molten LiCl- $CaCl_2$ without fluoride have been performed. In cyclic voltammogram, both 2 steps redox couples (Zr(VI)/Zr(II) and Zr(II)/Zr(0)) were identified. However, as comparison to previously obtained data which was performed by using molten LiCl-KCl eutectic as electrolysis bath, zirconium redox potential related to metal was significantly shifted to positive value. Next, cyclic voltammetry of LiCl-$CaCl_2$-ZrF_4(1wt%) has been also performed. Redox couple of Zr(IV)/Zr(II) was observed at R: -0.77 V and O:-0.18 V and that of Zr(II)/Zr(0) was at R:-0.90 V and O:-0.83 V. Also in this case, zirconium reduction peak was significantly positive shifted from that in molten LiCl-KCl bath and the value of potential was very close to that in LiCl-$CaCl_2$-$ZrCl_4$. With increasing cathodic sweep limit of potential, current density increased rapidly, thus zirconium would be electroreduced with calcium though further characterization of electrodeposit will be necessary. Exactly using the same sample of molten LiCl-$CaCl_2$-ZrF_4(1wt%), linear sweep voltammetry has been applied, which is shown in Fig. 1. In the case of pre-reduction at more negative potential than -0.90V, huge 2 oxidative peaks has been appeared between -0.70 V and -0.60 V. While in the case of pre-reduction at less negative potential than -0.85 V, these huge peak was completely dissapeared. Therefore, by using LiCl-$CaCl_2$ electrolysis bath, co-reduction of zirconium and calcium is unavoidable.

From these results, we can suggest the process design for fuel debris treatment is as follows. 1) As shown in increase of current density using zirconium fluoride as solute, once fluorinated fuel debris will be compatible to molten chloride bath, since $ZrCl_4$ has high vapor pressure. 2) As comparison with the case of molten LiCl-KCl, electroreduction potential of zirconium is positively shifted in molten LiCl-$CaCl_2$. It seems great advantage of electrodeposition but more important factor is how to separate uranium and zirconium. We have also noticed on the local structural variation in each case, so further systematic investigation of related material will be required in order to suggest much concrete process design for treatment of fuel debris. .

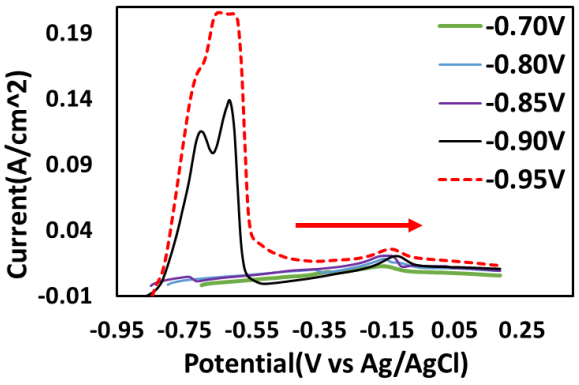

Fig.1 LSV at molten LiCl-$CaCl_2$ containing 1 wt% of ZrF_4.

REFERENCE:

[1]T. Ono, N. Sato, A. Nezu, T. Uchiyama, H. Matuura, *ECS,Tr ans.*,**75** (2016) 87.

I-1. PROJECT RESEARCHES

Project 11

PR11 Project Research on Advances in Isotope-Specific Studies Using Muti-Element Mössbauer Spectroscopy

M. Seto

Institute for Integrated Radiation and Nuclear Science, Kyoto University

OBJECTIVES AND PERFORMED RESEARCH SUBJECTS:

The main objectives of this project research are the investigation of the fundamental properties of new materials and the development of the advanced experimental methods by using multi-element Mössbauer spectroscopy. One of the most irreplaceable features of the Mössbauer spectroscopy is to extract element-specific or isotope-specific information. As the Mössbauer resonance line is extremely narrow, hyperfine interactions are well resolved and give us the information on the surrounding electronic states and magnetism. Therefore, promotion of the variety of Mössbauer isotope provides more useful and valuable methods for modern precise materials science of complex systems, such as biological substances, multi-layer films, and complicated-structured matter.

In this project research, each group performed their research by specifying a certain isotope:

^{57}Fe in P11-1, P11-2, P11-3, and P11-4,

^{197}Au in P11-5, P11-6, and P11-7.

Development for other isotopes in P11-8.

The subjects of research are as follows:

P11-1 EFG tensor of Fe^{2+} in *M2* site of clinopyroxene by single crystal Mössbauer microspectroscopy (K. Shinoda *et al.*)

P11-2 Mössbauer study on the model complexes of heme enzymes (H. Fujii *et al.*)

P11-3 Mössbauer analysis of the nanoclusters prepared by liquid phase pulsed laser ablation on pyrite (Y. Yakiyama *et al.*)

P11-4 Effect of H64L mutation on resonance hybrid of Fe-bound oxygen in myoglobin (Y. Yamamoto *et al.*)

P11-5 Study on the electronic states of gold clusters, $[Au_{25}(SR)_{18}]^n$ (n = +1, 0, -1) by means of ^{197}Au Mössbauer spectroscopy (N. Kojima *et al.*)

P11-6 The state analysis of gold sulfide using ^{197}Au Mössbauer spectroscopy (H. Ohashi *et al.*)

P11-7 ^{197}Au Mössbauer study of supported Au nanoparticles catalysis (Y. Kobayashi *et al.*)

P11-8 Development of Mössbauer spectroscopy for ^{161}Dy and ^{169}Tm (S. Kitao *et al.*)

MAIN RESULTS AND CONTENTS OF THIS REPORT:

K. Shinoda *et al.* (P11-1) have developed Mössbauer microspectrometer using Si-PIN semiconductor detector and applied to studies of crystallographically-oriented single crystals of thin sections of augite. The electric field gradient(EFG) tensor of Fe^{2+} in M2 site of clinopyroxene was evaluated from the intensity ratio of two quadrupole doublets due to Fe^{2+} in M1 and M2 sites by assuming calculated Fe^{2+} in M1 site.

H. Fujii *et al.* (P11-2) studied the effect of the electron-donating ability on the stability of the intermediate spin state for iron(III) porphyrin hexafluoroantimonate complexes. The results indicated that the spin state of iron(III) center changes from intermediate spin state to the high spin state with decreasing the electron-donar ability of the porphyrin ligand.

Y. Yakiyama *et al.* (P11-3) have developed a new method for Fe-S nanoclusters by pulsed-laser ablation in liquid(PLAL) and evaluated the obtained compounds by Mössbauer and Raman spectroscopy. Even the shortage of samples, hematite nanoparticles was suggested to exist. By further investigation, the results clarified the solvent in laser ablation significantly affected the product composition.

Y. Yamamoto *et al.* (P11-4) studied oxy form of the H64L(His64 by Leu) mutant Myoglobin reconstituted with ^{57}Fe-labeled heme cofactor. By comparing the obtained Mossbauer parameters with those of native proteins, the effect of the removal of His64 through mutation on the resonance hybrid of Fe-bound O_2 in the protein was observed.

N. Kojima *et al.* (P11-5) have studied thiolate-protected gold clusters with different oxidation states. The obtained three components were well attributed as outer layer, core surface, and core Au sites. The change of the isomer shifts by oxidation states is consistent.

H. Ohashi *et al.* (P11-6) evaluated gold sulfides synthesized by sulfide deposition precipitation (SDP) method. The ^{197}Au Mössbauer spectra revealed the chemical state of gold in obtained Au_2S_x was estimated to be monovalent(Au(I)).

Y. Kobayashi *et al.* (P11-7) studied the Au nanoparticle catalysis supported on hydroxyapatite(HAp) using ^{197}Au Mössbauer spectroscopy. The results showed the electronic state of the Au nanoparticles does not have much difference from Au bulk.

S. Kitao *et al.* (P11-8) have developed Mössbauer sources for several less-common Mössbauer spectroscopy. As for source materials of ^{161}Dy and ^{169}Tm Mössbauer spectroscopy, $Dy_{0.5}Gd_{0.3}F_3$ and Er-Al alloy were successfully synthesized, respectively. These materials were confirmed as well-performed Mössbauer sources.

PR11-1 EFG tensor of Fe^{2+} in *M*2 site of clinopyroxene by single crystal Mössbauer microspectroscopy

D. Fukuyama[1], K. Shinoda[1], Y. Kobayashi[2]

[1]*Department of Geosciences, Graduate School of Science, Osaka City University*
[2]*Institute for Integrated Radiation and Nuclear Science, Kyoto University*

INTRODUCTION: ^{57}Fe Mössbauer spectroscopy has been widely used for the analysis of Fe in Fe-bearing minerals. Powdered mineral is generally used as a Mössbauer sample, in spite of the usefulness of the conventional method, it is not useful for the Mössbauer analysis of any narrow area in a crystal or mineral grain. To overcome the disadvantage of spatial resolution by powder method, several Mössbauer microspectrometers have been proposed. Mössbauer microspectroscopy will be widely used for measuring spectra of a grain in a thin section in future. Intensities of component peaks in a quadrupole doublet of a thin section as a single crystal are asymmetric and vary depending on the angle between the direction of incident γ-rays and the crystallographic orientation of the thin section. Intensity of quadrupole doublet (I^h / I^{total}) means a ratio between area of the peak of the higher energy (I^h) and total area of the doublet (I^{total}= I^h + I^l) (sum of I^h and area of the lower energy (I^l)). The intensity of component peaks of a ^{57}Fe Mössbauer doublet is related to an electronic field gradient (EFG) tensor of the site containing Fe^{2+} and Fe^{3+} (Zimmermann, 1975 and 1983). Thus, EFG determination is important in Mössbauer measurements of thin section as a single crystal. Zimmermann (1975, 1983) introduced experimental determination of EFG tensor from the Mössbauer spectrum of a single crystal, and proposed a formulation of the EFG tensor from the intensities of the component peaks of asymmetric Mössbauer doublet of a monoclinic crystal as an example. In pyroxene, Fe^{2+} in *M*1, Fe^{2+} in *M*2 and Fe^{3+} in *M*1 sites are possible. As three doublets overlap in Mössbauer spectrum of pyroxene, it is important to reveal EFG of three doublets to analyze Mössbauer spectrum of pyroxene thin section. Tennant *et al*. (2000) revealed the EFG tensor of Fe^{2+} at the octahedral *M*1 site of clinopyroxene. However, EFG tensors due to Fe^{2+} in *M*2 site of clinopyroxene remain unknown. In this study, Zimmermann's method was applied for single crystal ^{57}Fe Mössbauer spectra of an augite crystal on oriented thin sections to determine the EFG tensor of Fe^{2+} at the *M*2 site of *C*2/*c* clinopyroxene.

EXPERIMENTS and RESULTS: A single crystal of augite was used for this study. Three crystallographically oriented thin sections which are perpendicular to ***a**** and ***b****, and parallel to (-2 0 2) plane were prepared by measuring X-ray diffraction using precession camera. Nine Mössabuer spectra of oriented thin sections were measured. In this study, Cartesian coordinate (*X Y Z*) is set as *X*//***c****, *Y*//***a***, *Z*//***b**** in order to set ***b***-axis as *Z* and set ***a***, ***b***, ***c***-axes as right-handed system, where ***a***, ***b***, ***c*** are real and ***a****, ***b****, ***c**** are reciprocal lattice vectors of augite. Mössbauer measurements were carried out in transmission mode on a constant acceleration spectrometer with an Si-PIN semiconductor detector (XR-100CR, AMPTEK Inc.) and multi-channel analyzer of 1024 channels. A 3.7GBq ^{57}Co/Rh of 4mmϕ in diameter was used as γ-ray source. An ^{57}Fe-enriched iron foil was used as velocity calibrant. The two symmetric spectra were folded and velocity range was ±5mm/s. Thickness corrections of raw spectra were not done. Overlapped doublets were observed in nine raw spectra. Two quadruploe doublets due to Fe^{2+} in *M*1 and *M*2 sites are assumed in raw spectra for peak decomposition by MossWinn program. Intensity tensor of Fe^{2+} in *M*1 site was calculated from Tennant *et al*. (2000). Intensity rensor of Fe^{2+} in *M*2 site was obtained by peak fitting under a constraint of intensity tensor of Tennant *et al*. (2000). The residual doublet that is obtained by subtracting doublet due to *M*1 from raw data was assigned as *M*2 doublet. The intensity tensor due to Fe^{2+} in *M*2 site was

$$\begin{pmatrix} 0.65 \pm 0.19 & 0.06 \pm 0.22 & 0 \\ 0.06 \pm 0.22 & 0.38 \pm 0.18 & 0 \\ 0 & 0 & 0.47 \pm 0.66 \end{pmatrix}.$$

Diagonalized traceless intensity tensor was

$$\begin{pmatrix} 0.24 & 0 & 0 \\ 0 & -0.19 & 0 \\ 0 & 0 & 0.05 \end{pmatrix}.$$

REFERENCES

[1] Zimmermann, R. Advances in Mössbauer spectroscopy (Thosar, B.V. Ed.). pp.273-315, Elsevier Scientific Publishing Co. Amsterdam (1983).

[2] Zimmermann, R. Nucl. Instr. and Meth. **128** (1975) 537-543.

[3] Tennant, W.C., McCammon, C.A. and Miletich, R.. Phys. Chem. Min., **27** (2000) 156-163.

PR11-2 Mössbauer Study on the Model Complexes of Heme Enzymes

H. Fujii, Y Kobayashi[1], T. Namba, H. Muto, K. Nishikawa

Graduate School of Science, Nara Women's University
[1]Graduate School of Science, Kyoto University

INTRODUCTION: Iron porphyrin complexes are active sites of many heme proteins in nature. The oxidation state and the spin state of the iron porphyrin complexes are key for controlling the function of the heme proteins. Recently, intermediate spin states have been found in ferrous and ferric porphyrin complexes. These intermediate spin states are unique and have not been clarified well. Previous studies revealed that the intermediate spin state is realized when very weak axial ligand such as hexafluoroantimonate anion is coordinated to ferric iron center. In this project, we studied the effect of the electron-donating ability on the stability of the intermediate spin state by using Mössbauer spectroscopy for iron(III) porphyrin hexafluoroantimonate complexes.

EXPERIMENTS: Mössbauer spectroscopy was conducted in conventional transmission geometry by using ^{57}Co-in-Rh(50 mCi) as γ-ray source. The Doppler velocity scale was calibrated using an Fe metal foil at room temperature. 5,10,15,20-tetraphenyl porphyrin (**F0**) and 5,10,15,20-Tetrakis(pentafluoro phenyl)porphyrin (**F20**) was purchased from Sigma Aldrich. 2,3,7,8,12,13,17,18-Octafluoro-5,10,15,20-tetrakis(pentafluorophenyl)porphyrin (**F28**) was prepared by literature methods. ^{57}Fe was purchased from commercial as a powder and changed to iron(II) acetate. Iron(III) porphyrin chloride complexes were prepared by the published method. Iron(III) porphyrin hexafluoroantimonate complexes were prepared by the reaction of the chloride complexes with silver hexafluoroantimonate in dichloromethane or fluorobenzene in a glove box.

RESULTS: We measured Mössbauer spectra of iron(III) hexafluoroantimonate complexes of **F0**, **F20**, and **F28**. The δ and ΔE_Q values for these complexes are estimated to be 0.4 mm/s and ~4.0 mm/s, respectively. These values indicate the intermediate spin states of these complexes. Importantly, as the electron-withdrawing effect of the porphyrin ligand is stronger, the ΔE_Q value becomes smaller. This indicates that the electron-donor ability of the porphyrin ligand is a key factor to be the intermediate spin state. This result was further confirmed by the aqua complexes. When the hexafluoroantimonate complexes are contacted with air, water in air bind to the iron center to form the aqua complex. Fig 1 shows Mössbauer spectra of the aqua complexes of **F0**, **F20**, and **F28**. As the electron-withdrawing effect of the porphyrin ligand is stronger, the ΔE_Q value becomes smaller (see green lines of Fig 1). All of these results indicated that the spin state of iron(III) center changes from the intermediate spin state to the high spin state with decreasing the electron-donar ability of the porphyrin ligand.

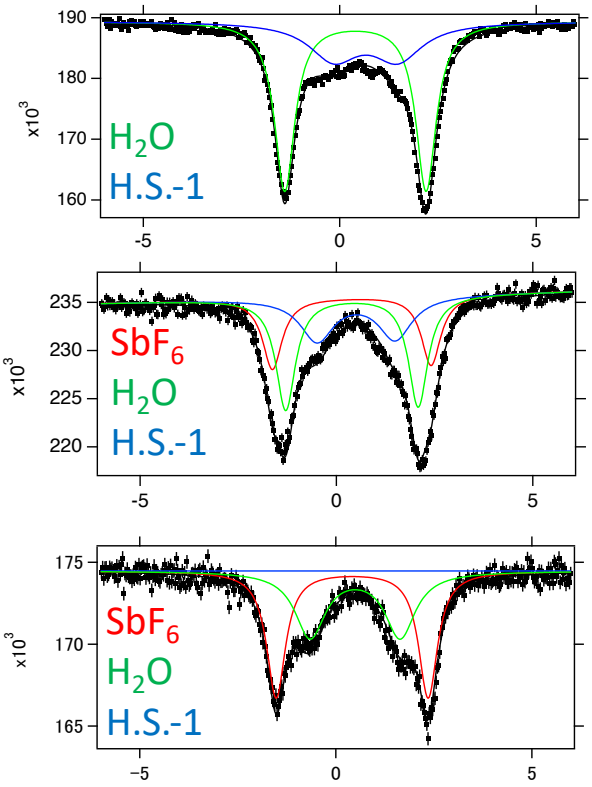

Fig 1. Mössbauer spectra (6 K) of complexes after aeration of iron(III) porphyrin hexafluoroantimonate complexes of **F0** (top), **F20** (middle), and **F28** (bottom). Red line: hexafluoroantimonate complex, green line: aqua complex, blue line: further decomposed complex.

REFERENCES:

[1] Scheidt, W. R.; Reed, C. A. *Chem. Rev.* **1981**, 81, 543-555.

[2] Reed, C. A.; Mashiko, T.; Bentley, S. P.; Kastner, M.E.; Scheidt, W. R.; Spartalian, K.; Lang, G. *J. Am. Chem. Soc.* **1979**, 101, 2948.

[3] Reed, C. A.; Guiset, F. *J. Am. Chem. Soc.* **1996**, 118, 3281-3282.

[4] Woller, E. K.; DiMagno, S. G. *J. Org. Chem.* **1997**, 62, 1588-1593.

[5] Fujii, H. *J. Am. Chem. Soc.* **1993**, 115, 4641-4648.

PR11-3

Mössbauer Analysis of the Nanoclusters Prepared by Liquid Phase Pulsed Laser Ablation on Pyrite

Yuka Motohashi, Yumi Yakiyama, Fumitaka Mafuné,[1] Hajime Okajima,[2,3] Akira Sakamoto,[2] Toshihiko Shimizu,[4] Yuki Minami,[4] Nobuhiko Sarukura,[4] and Hidehiro Sakurai

Graduate School of Engineering, Osaka University
[1]Graduate School of Arts and Sciences, The University of Tokyo
[2]College of Science and Engineering, Aoyama Gakuin University
[3] JST, PRESTO
[4]Institute of Laser Engineering, Osaka University

INTRODUCTION: Pyrite (FeS_2), which composed of Fe-S bonds, is one of the most abundant minerals on the earth and has been recently focused on as a component of photovoltaic semiconductors. In addition, the related compounds, Fe-S clusters represented by Fe_2S_2 and Fe_4S_4, are the most essential structures found in enzymes, which play important roles in metabolism. For example, the Fe-S clusters are the main contributor in hydrogenase or nitrogenase for transferring electrons to the active site. However, studies on their detailed mechanisms are not smoothly progressed, since the conventional synthesis of the model complexes including Fe-S clusters require long steps and special cares. Therefore, the development of new methods for the preparation of Fe-S clusters, especially here, pulsed-laser ablation in liquid (PLAL) using pyrite as a target is meaningful for both materials and biological chemistry. In this project, we tried the PLAL using pyrite and examined the products using Mössbauer and raman spectroscopy, clarifying that the solvent significantly affected the product composition.

EXPERIMENTS: The sample was prepared by the PLAL technique in water with surfactants (polyvinylpyrrolidone (PVP), sodium dodecyl sulfate (SDS) and hexadecyltrimethylammonium bromide (CTAB)) or in organic solvents (EtOH, toluene, and acetone) [1]. ^{57}Fe Mössbauer measurement was performed at KURNS.

RESULTS: As shown in Fig. 1, the presence of hematite was suggested in Mössbauer spectrum for nanoparticles surrounded by PVP (Fig. 1). Other samples prepared by using different surfactants were also afforded hematite as the main product. This was supported by raman measurement for all the samples (Fig. 2). However, because of the shortage of the samples (< 100 μg), further investigation using Mössbauer spectroscopy was impossible. Instead, we continued the sample examination by raman measurement and selected area electron diffraction (SAED) measurement. revealed that the solvent used in laser ablation significantly affected the product composition. Especially the coordinative solvent such as acetone gave the product containing sulfur in addition to hematite.

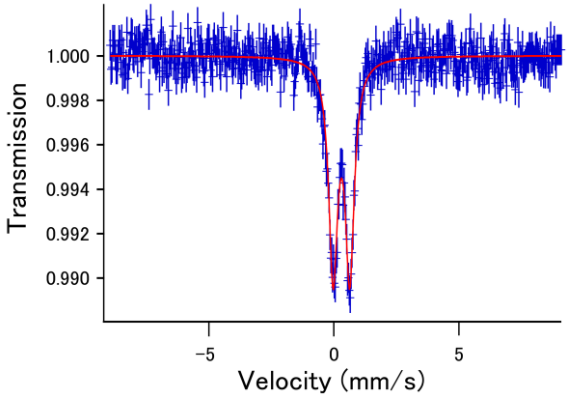

Fig. 1. Mössbauer spectrum for the nanoparticles surrounded by PVP obtained by PLAL method in water.

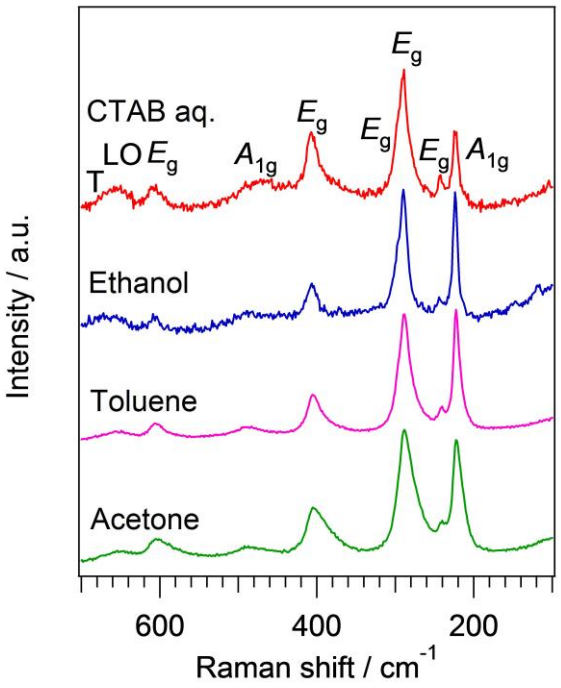

Fig. 2. Raman spectra of the hematite nanoparticles obtained by PLAL of pyrite.

REFERENCES:

[1] Y. Motohashi *et al.*, Chem. Lett., accepted (2019).

PR11-4 Effect of H64L Mutation on Resonance Hybrid of Fe-bound Oxygen in Myoglobin

T. Shibata,[1]M. Saito,[2] M. Seto,[2] Y. Kobayashi,[2] T. Ohta,[3] S. Yanagisawa,[3] T. Ogura,[3] Y. Yamamoto,[1] S. Neya,[4] and A. Suzuki.[5]

[1] *Department of Chemistry, University of Tsukuba*
[2] *KURNS, Kyoto University*
[3] *Graduate School of Life Science, University of Hyogo*
[4] *Graduate School of Pharmaceutical Sciences, Chiba University*
[5] *Department of Materials Engineering, National Institute of Technology, Nagaoka College*

INTRODUCTION: Myoglobin (Mb), an oxygen storage hemoprotein, is one of the most thoroughly studied proteins and has been used as a paradigm for the structure-function relationships of metalloproteins. Dioxygen (O_2) and also carbon monoxide (CO) are reversibly bound to a ferrous heme Fe atom in Mb. As a respiratory protein, Mb must favor the binding of O_2 compared to the toxic ligand CO ubiquitously produced from a variety of sources in biological systems. Distal His (His64) contributes significantly by increasing the O_2 affinity of the protein by stabilizing Fe-bound O_2 through a hydrogen bonding interaction between the His64 $N_\varepsilon H$ proton and the bound O_2 (Scheme 1).[1] We found that both the O_2 affinity and CO/O_2 discrimination of the protein are regulated by the intrinsic heme Fe reactivity through the heme electronic structure.[2] We revealed that the control of the CO/O_2 discrimination is achieved through the effect of a change in the electron density of the heme Fe atom (ρ_{Fe}) on the O_2 affinity, which can be reasonably interpreted in terms of the effect of a change in the ρ_{Fe} value on the resonance process between the Fe^{2+}-O_2 and Fe^{3+}-O_2^--like species[3] (Scheme 1). On the other hand, in contrast to O_2 binding, the CO affinity of the protein was shown to be almost independent of the ρ_{Fe} value.[2] In this study, we characterized the effect of the removal of the distal His64, through the replacement of His64 by Leu (H64L mutation), on the control of the intrinsic heme Fe reactivity through the resonance hybrid of Fe-bound O_2.

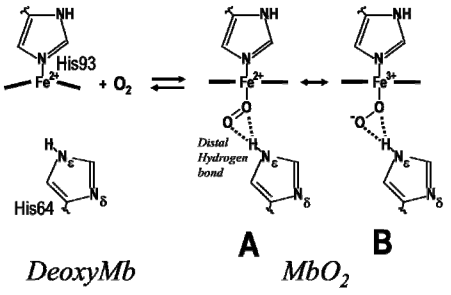

Scheme 1. Oxygenation of deoxy Mb. The binding of O_2 to the heme Fe is stabilized by the hydrogen bonding between the Fe-bound O_2 and His64.[1] Structure (B) of the oxy form is only a proposed one.[3]

EXPERIMENTS: Iron-^{57}Fe (95 atom %, Merck) was used to prepare ^{57}Fe-enriched heme cofactor. The expression and purification of the H64L mutant Mb were carried out according to the methods described by Springer *et al.*[4], and then apoprotein was prepared from the H64L Mb mutant using the procedure of Teale[5]. Apoprotein of the H64L mutant protein was reconstituted with ^{57}Fe-labelled heme cofactor, and oxy form of the reconstituted protein in 50 mM potassium phosphate buffer, pH 7.40, were cooled in liquid nitrogen bath. The Mössbauer measurement was performed at 6 K.

RESULTS: The Mössbauer spectrum of oxy form of the H64L mutant Mb reconstituted with ^{57}Fe-labeled heme cofactor indicated the values of 2.09 ± 0.017 mm/s and 0.322 ± 0.008 mm/s for quadrupole splitting (QS) and isomer shift (IS) of the protein, respectively. These values are compared with the corresponding ones of the native protein, i.e., 2.28 ± 0.008 mm/s and 0.258 ± 0.004 mm/s for the QS and IS, respectively. The differences in the QS and IS between the two proteins possibly reflect the effect of the removal of His64 through the mutation on the resonance hybrid of Fe-bound O_2 in the protein. Unfortunately, the spectrum of CO form of the protein contaminated in the sample appears in Figure 1, and hence another measurement is essential to confirm the QS and IS obtained for the H64L mutant protein.

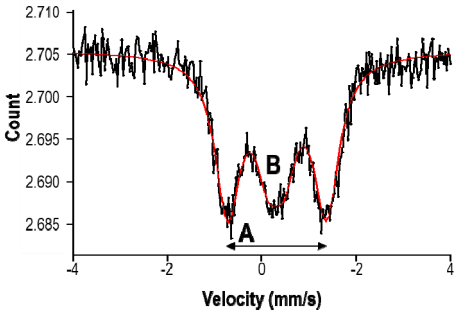

Figure 1. Mössbauer spectrum of oxy form of the H64L mutant Mb reconstituted with ^{57}Fe-labeled heme cofactor at 6 K. The spectrum is composed of two components **A** and **B** due to oxy form and contaminated CO one of the protein.

REFERENCES:

[1] J. S. Olson, A. J. Mathews, R. J. Rohlfs, B. A. Springer, K. D. Egeberg, S. G. Sligar, J. Tame, J.-P. Re-naud, and K. Nagai, *Nature*, **336** (1988) 265-266.

[2] T. Shibata, S. Nagao, M. Fukaya, H. Tai, S. Nagatomo, K. Morihashi, T. Matsuo, S. Hirota, A. Suzuki, K. Imai, and Y. Yamamoto, *J. Am. Chem. Soc.*, **132**, (2010) 6091-6098.

[3] J. C. Maxwell, J. A. Volpe, C. H. Barlow, and W. S. Caughey, *Biochem. Biophys. Res. Commun.*, **58**, (1974) 166-171.

[4] B. A. Springer, K. D. Egeberg, S. G. Sligar, R. J. Rohlfs, A. J. Mathews, and J. S. Olson, *J. Biol. Chem.*, (1989) 3057-3060.

[5] F. W. J. Teale, *Biochim. Biophys. Acta*, **35** (1959) 543.

PR11-5 Study on the Electronic States of Gold Clusters, $[Au_{25}(SR)_{18}]^n$ (n = +1, 0, -1) by Means of ^{197}Au Mössbauer Spectroscopy

N. Kojima, Y. Kobayashi[1] and M. Seto[1]

Toyota Physical and Chemical Research Institute
[1] Institute for Integrated Radiation and Nuclear Science, Kyoto University

INTRODUCTION: Thiolate (SR)-protected gold clusters have attracted much attention as a prototypical system for fundamental studies on quantum size effect and as a building block of nanoscale devices [1]. Among many thiolate-protected Au clusters, the $Au_{25}(SR)_{18}$ cluster has been studied most extensively as a prototype system of stable $Au_n(SR)_m$ clusters. From the single crystal X-ray analysis [2], $Au_{25}(SR)_{18}$ is composed of an icosahedral Au_{13} core whose surface atoms are completely protected by six staples, –S(R)–[Au–S(R)–]$_2$ (Fig. 1). As shown in Fig. 1, the Au atoms in $Au_{25}(SR)_{18}$ are classified into three in terms of chemical environment: twelve Au atoms on the outermost layer, which are bound by two thiolates (**Au1**); twelve Au atoms at the core surface, each of which are bound by a single thiolate (**Au2**); and a single central Au atom at the core (**Au3**). In the present work, we investigated the electronic states of $[Au_{25}(PET)_{18}]^n$ (PET = 2-phenylethanethiol, n = +1, 0, -1) by means of ^{197}Au Mössbauer spectroscopy.

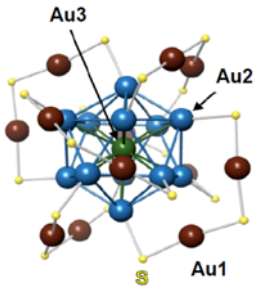

Fig. 1. Molecular structure of $Au_{25}(PET)_{18}$ [2]. Large and small balls represent Au and S atoms, respectively.

EXPERIMENTS: ^{197}Au Mössbauer measurements were carried out at Institute for Integrated Radiation and Nuclear Science, Kyoto University. The γ-ray source (77.3 keV), ^{197}Pt, was generated by neutron irradiation to a 98%-enriched ^{196}Pt metal foil. The γ-ray source and samples were cooled down to 16 K. The isomer shift (*IS*) of Au foil was referenced to 0 mm/s. The spectra were calibrated and referenced by using the six lines of a body-centered cubic iron foil (α-Fe).

RESULTS: The ^{197}Au Mössbauer spectra of $[Au_{25}(PET)_{18}]^n$ (n = +1, 0, −1) were analyzed, which is based on that of $[Au_{25}(SG)_{18}]^{-1}$ (SG = glutathione) [3]. The three sites of Au atoms (Au1, Au2, Au3) in $[Au_{25}(SR)_{18}]^n$ exhibit different isomer shift (*IS*) and quadrupole splitting (*QS*) due to the difference in electronic structures of each site; In Au atoms, the main contribution to *IS* and *QS* are the density of s-electrons at the nucleus and the symmetry of charge distribution around the nucleus, respectively. The ^{197}Au Mössbauer spectra of $[Au_{25}(PET)_{18}]^n$ (n = +1, 0, −1) were fitted by the superposition of two sets of doublet Lorentzians and a singlet Lorentzian, which is listed in Table 1. The doublet with the largest *IS* and *QS* (Au1) is assigned to the twelve Au atoms on the outermost layer coordinated by two thiolates. These parameters, *IS* and *QS*, are typical of Au(I) coordinated by two sulfur atoms [4]. The second doublet (Au2) is assigned to the twelve Au atoms at the surface of icosahedron, which are bound by single thiolate. The singlet (Au3) is assigned to the central Au atom of icosahedron. As shown in Table 1, the *IS* and *QS* values of Au1, Au2 and Au3 for $[Au_{25}(PET)_{18}]^{-1}$ are consistent with those for $[Au_{25}(SG)_{18}]^{-1}$. According to a spherical superatom model [5], the superatomic 6s-electron configuration in the icosahedron (Au_{13}) for $[Au_{25}(SR)_{18}]^{-1}$ is described as $(1S)^2(1P)^6$ corresponding to a noble gas-like configuration, which is responsible for the most stable cluster among $[Au_{25}(SR)_{18}]^n$ (n = +1, 0, -1). When $[Au_{25}(PET)_{18}]^n$ is oxidized from n = -1 to +1, the *IS* values of Au2 and Au3 sites remarkably change from 0.36 mm/s to 1.36 mm/s, and from 1.29 mm/s to 0.40 mm/s, respectively, while the *IS* of Au1 remains almost unchanged, which implies that not only the core surface site (Au2) but also the central core site (Au3) for the icosahedron in $[Au_{25}(SR)_{18}]^n$ is oxidized on going from n = -1 to +1. In connection with this, the following should be noted. The remarkable decrease of *IS* at the central core site (Au3) for n = +1 is attributed to the decrease of 6s-electron density due to the oxidation.

Table 1. ^{197}Au Mössbauer parameters (*IS* (mm/s). *QS* (mm/s), area (%) of $[Au_{25}(SR)_{18}]^n$ (n = +1, 0, -1) at 16 K

$[Au_{25}(SR)_{18}]^n$		*IS* (mm/s)	*QS* (mm/s)	Area (%)
$[Au_{25}(SG)_{18}]^{-1}$	Au 1	2.78	6.36	46.1
	Au 2	0.34	4.14	44.8
	Au 3	0.94	0	9.1
$[Au_{25}(PET)_{18}]^{-1}$	Au 1	2.90	6.55	36.1
	Au 2	0.36	4.48	52.0
	Au 3	1.29	0	11.9
$[Au_{25}(PET)_{18}]^{0}$	Au 1	3.21	5.95	42.0
	Au 2	0.55	3.94	50.4
	Au 3	0.24	0	7.7
$[Au_{25}(PET)_{18}]^{+1}$	Au 1	2.77	6.28	43.4
	Au 2	1.36	4.68	48.7
	Au 3	0.40	0	7.9

[1] T. Tsukuda, H. Häkkinen (Eds.), "Protected Metal Clusters: From Fundamentals to Applications," (Elsevier, 2015).
[2] M. Zhu, E. Lanni, N. Garg, M.E. Bier, R. Jin, J. Am. Chem. Soc., **130** (2008) 1138.
[3] T. Tsukuda, Y. Negishi, Y. Kobayashi, N. Kojima, Chem. Lett., **40** (2011) 1292.
[4] Mössbauer Handbooks: ^{197}Au Mössbauer spectroscopy, Mössbauer Effect Data Center, 1993.
[5] C.M. Aikens, J. Phys. Chem. Lett., **2** (2011) 99.

PR11-6 The State Analysis of Gold Sulfide Using ^{197}Au Mössbauer Spectroscopy

H. Ohashi, T. Sai, R. Takaku, T. Yokoyama[1], H. Murayama[1], K. Yonezu[2], T. Yamada[2], S. Inoue[2], O. Juntarasakul[2], D. Kawamoto[3], Y. Kobayashi[4], S. Kitao[4]

Faculty of Symbiotic Systems Science, Fukushima University
[1]Faculty of Sciences, Kyushu University
[2]Faculty of Engineering, Kyushu University
[3]Faculty of Sciences, Japan Women's University
[4]Institute for Integrated Radiation and Nuclear Science, Kyoto University

INTRODUCTION:

Though sulfide deposition-precipitation (SDP) method was a kind of new DP method, it was a very unique method and different from DP on several points such as preparation pH. However, until now, the structure of gold sulfide as a precursor synthesized by the SDP method was unknown. The purpose of this study aimed to analyze the state of gold valence and Au-S bond on gold sulfide synthesized by a similar method of SDP. using ^{197}Au Mössbauer spectroscopy.

EXPERIMENTS:

The gold sulfide (Au_2S_x) were synthesized by the similar SDP method already reported[1]. In addition, trisodium ditiosulfatoaurate(I) ($Na_3[Au(S_2O_3)_2]$)[2] as a standard material with Au-S bond was measured.

^{197}Au Mössbauer spectra were measured at Kyoto University Research Institute of Nuclear Science. The ^{197}Pt isotope ($T_{1/2}$ = 18.3 h), γ-ray source feeding the 77.3 keV Mössbauer transition of ^{197}Au, was prepared by neutron irradiation of isotopically enriched ^{196}Pt metal at the Kyoto University Reactor. The measurement temperature was 14-20 K, and the measurement was performed by the transmission method.

RESULTS:

The ^{197}Au Mössbauer spectra of the Au_2S_x and the standard sample were showed in Fig.1. It showed that the Mössbauer spectrum of Au_2S_x consisted of doublets in shape. Compared to the spectrum of $Na_3[Au(S_2O_3)_2]$, value of the isomer shift was small, and the FWHM value was large.

Based on the value of IS-QS derived from the synthesized Au_2S_x and $Na_3[Au(S_2O_3)_2]$, the chemical state of gold in Au_2S_x was estimated to be monovalent (Au(I)).

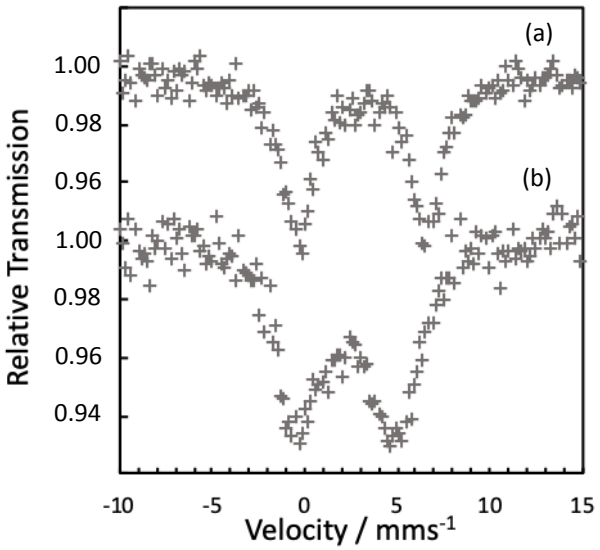

Fig.1.^{197}Au Mössbauer spectra for $Na_3[Au(S_2O_3)_2]$ (a) as a reference and Au_2S_x (b) prepared by similar SDP method.

REFERENCES:

[1] H. Ohashi *et al*., "Method for dispersing and immobilizing gold fine particles and material obtained thereby", Patent No. 5010522.
[2] Marjorie O. Faltens and D. A. Shirley, *J. Chem. Phys., **53*** (1970) 4249.

PR11-7 ^{197}Au Mössbauer study of supported Au nanoparticles catalysis

Yasuhiro Kobayashi, Junhu Wang[1] and Makoto Seto

Institute for Integrated Radiation and Nuclear Science, Kyoto University
[1]*Dalian Institute of Chemical Physics, Chinese Academy of Sciences*

INTRODUCTION: The normal surface of metallic gold does not adsorb small molecules like hydrogen and oxygen, thus, gold is not generally considered as a good catalyst. Small particles have many edges, corners and metastable surfaces, and they are different from bulk for catalytic activities. Dispersing the small particles on supports, the catalytic activity of gold increases. Au small particles supported on some materials shows high catalytic activity to oxidize CO to CO_2 at temperatures as low as 197 K [1,2].

The interaction between particles and supports may give new activity to the catalysts. Hydroxyapatite (HAp) is known as bone mineral, and it is nature-friendly. Furthermore, it is good support of nanoparticles [3]. HAp binds strongly with Au, and it avoid the fusion of the nanoparticles.

We have studied the supported Au nanoparticles catalysis using ^{197}Au Mossbauer spectroscopy to elucidate the origin of the catalytic activity. Using ^{197}Au Mossbauer spectroscopy, we can observe the signals from Au atoms without disturbance from supports. Moreover, it is sensitive to the electronic states of Au atoms. Thus, Mossbauer spectroscopy is powerful for the study of supported catalysts.

EXPERIMENTS: The supported Au nanoparticles catalysis was prepared by the deposition precipitation method and calcination. The mixed solution of $HAuCl_4$ and HAp was kept on pH 9 and 65°C, thus the Au ions were precipitate on HAp as $Au(OH)_3$. After precipitation, the specimens were washed with distilled water, and dried. These specimens were calcined for 4 hours at 600°C in air. At that time, $Au(OH)_3$ was degraded into Au metal, and the Au nanoparticles were firmly fixed on HAp.

^{197}Au Mössbauer measurement was conducted using a constant-acceleration spectrometer with a NaI scintillation counter. The ^{197}Au γ-ray source (77.3 keV) was obtained from ^{197}Pt (half-life; 18.3 hrs) generated by irradiation of neutron to 98%-enriched ^{196}Pt metal foil using KUR. The γ-ray source and samples were cooled to 16 K, and the spectra were recorded in a transmission geometry. The isomer shift value of a gold foil was referenced to 0 mm/s.

RESULTS: Figure 1 shows ^{197}Au Mössbauer spectra of the pure Au bulk and Au nanoparticle catalysis. Observed spectrum shows almost same shape and peak position as pure Au bulk. Thus, the electronic state of the Au nanoparticle catalysis does not have much difference from bulk. However, the different catalytic activity from bulk Au was observed on this catalysis. The activity comes from a very small percentage of the Au atoms, for example in surface, at edge and by lattice defect. And, high activity is owing to the increase of the surface area. We will study the other type catalysis to elucidate the particle-size dependence of the Mössbauer spectra and activity of the catalysis.

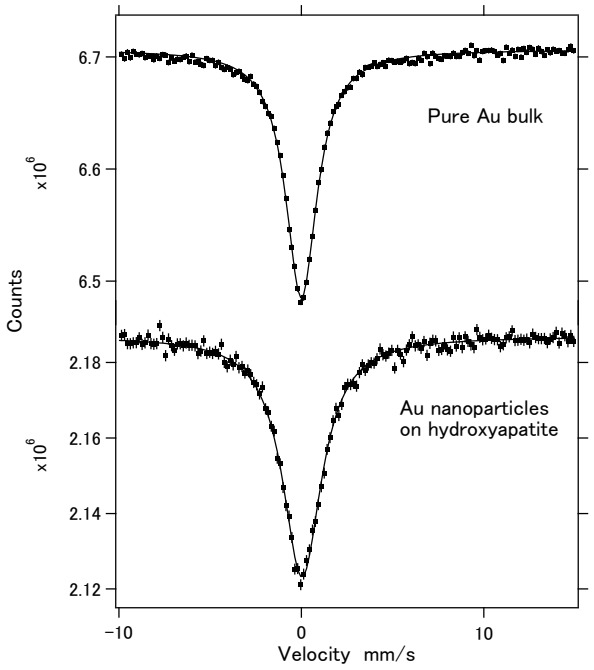

Fig. 1 ^{197}Au Mössbauer spectra of the pure Au bulk and Au nanoparticles catalysis at 16K.

REFERENCES:

[1] M. Haruta, T. Kobayashi, H. Sano and N. Yamada, Chem. Lett., **16** (1987) 405.
[2] M. Haruta, N. Yamada, T. Kobayashi and S. Iijima, J. Catal., **115** (1989) 301.
[3] Yanjie Zhang, Junhu Wang, Jie Yin, Kunfeng Zhao, Changzi Jin, Yuying Huang, Zheng Jiang, and Tao Zhang, J. Phys. Chem. C, **114** (2010) 16443-16450.

PR11-8 Development of Mössbauer Spectroscopy for ^{161}Dy and ^{169}Tm

S. Kitao[1], M. Kobayashi[1], T. Kubota[1], M. Saito[1], R. Masuda[1], M. Kurokuzu[1], S. Hosokawa[2], H. Tajima[2], S. Yazaki[2], and M. Seto[1]

[1]*Institute for Integrated Radiation and Nuclear Science, Kyoto University*
[2]*Graduate School of Science, Kyoto University*

INTRODUCTION:

The Mössbauer spectroscopy is one of the most powerful methods for investigation of electronic states, magnetic properties, chemical properties, and so on. A remarkable feature of this method is to extract the information of the specific isotope. Although about one hundred of Mössbauer energy levels are known, research activities in Mössbauer studies so far are quite limited, except ^{57}Fe and ^{119}Sn. It is partly because commercially available sources at present are only ^{57}Co and ^{119m}Sn for the Mössbauer spectroscopy of ^{57}Fe and ^{119}Sn, respectively.

On the contrary, at the Institute for Integrated Radiation and Nuclear Science, various short-lived isotopes can be obtained by neutron irradiation at Kyoto University Research Reactor(KUR). We have already been performing Mössbauer spectroscopy of some isotopes, such as ^{125}Te, ^{129}I, ^{197}Au, by obtaining ^{125m}Te, ^{129}Te or ^{129m}Te, ^{197}Pt, respectively. Moreover, complementary short-lived isotopes can be produced by high-energy γ-ray irradiation at the electron linear accelerator(KURNS-LINAC).

The main purpose of this research is to develop effective Mössbauer sources for various isotopes to apply many fields of researches for less common isotopes in Mössbauer spectroscopy.

EXPERIMENTS AND RESULTS:

(1) ^{161}Dy Mössbauer spectroscopy

The 25.5keV level of ^{161}Dy is known as the most useful level for Dy-Mössbauer spectroscopy. As for the Mössbauer source, ^{161}Tb with a half-life of 6.88days is effectively usable. Since ^{161}Gd becomes ^{161}Tb in β-decay process with a half-life of 3.7 minutes, ^{161}Tb source is obtainable by neutron irradiation of ^{160}Gd. Since natural Gd contains 21.86% abundance of ^{160}Gd, natural Gd is usable by waiting a few days for decay of a by-product of ^{159}Gd with a half-life of 18.48 hours. In this study, in order to improve the source material, $Dy_{0.5}Gd_{0.5}F_3$ was synthesized[1]. After Dy_2O_3 and Gd_2O_3 was dissolved in HCl, HF was added to obtain precipitation of hydrated $Dy_{0.5}Gd_{0.5}F_3$. Anhydrous $Dy_{0.5}Gd_{0.5}F_3$ was obtained by evacuation of the hydrated compound with careful heating. The neutron irradiation was performed by pneumatic tube(Pn) for 1 hour at 5MW operation of KUR. The expected ^{161}Dy Mössbauer spectra were obtained successfully by using a Xe proportional counter. The ^{161}Dy-Mössbauer spectrum of DyF_3 at room temperature using ^{161}Tb source in $Dy_{0.5}Gd_{0.5}F_3$ is shown in Fig. 1. Since expected single-line spectrum was obtained, this source material can be widely used for many application experiments in Dy-Mössbauer spectroscopy.

(2) ^{169}Tm Mössbauer spectroscopy

The 8.4 keV level of ^{169}Tm is used for Tm-Mössbauer spectroscopy. Its low-energy feature of the γ-ray has an advantage in high recoilless fraction even at high temperature. As for the Mössbauer source, ^{169}Er with a half-life of 9.3 days is obtained by neutron irradiation of ^{168}Er (natural abundance of 26.8 %). Even when natural Er is used as a source material, a by-product of ^{171}Er with a half-life of 7.5 hours from ^{170}Er(natural abundance of 14.9 %) was reduced by waiting a few days. In this study, Er-Al alloy with about 10 wt-% Er was used as a source material[2]. The Er-Al alloy was obtained by the arc-melting method followed by solution treatment. The neutron irradiation was performed by long-term irradiation for 3 weeks at KUR. Since the fluorescent X-rays of Er with energies of 6.9 to 7.8 keV are not separated in an energy spectrum with a Xe proportional counter, the right-half of the γ-ray peak was chosen for Mössbauer measurements. The ^{169}Tm Mössbauer spectra of $TmAl_2$ absorber were obtained successfully as shown in Fig. 2. Therefore, this source material is applicable for various Tm Mössbauer spectroscopy.

REFERENCES:

[1] R. L. Cohen and H. J. Guggenheim, Nucl. Instr. Methods **71**, 27(1969).
[2] G. Kalvius, F. Wagner, and W. Potzel, J. Phys. Colloq. **37**(C6), 657(1976).

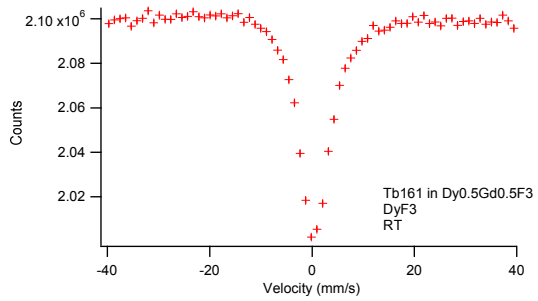

Fig. 1. ^{161}Dy-Mössbauer spectrum of DyF_3 at room temperature using ^{161}Tb source in $Dy_{0.5}Gd_{0.5}F_3$ irradiated at KUR.

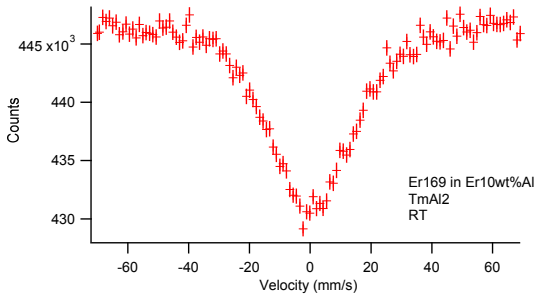

Fig. 2. ^{169}Tm-Mössbauer spectrum of $TmAl_2$ at room temperature using ^{169}Er source in Er-Al alloy irradiated at KUR.

I-1. PROJECT RESEARCHES

Project 12

PR12 Project Research on Boron Dynamics in Plants using Neutron Capture Reaction: Development of Boron Analytical Method and Elucidation of its Physiological Function

T. Kinouchi

Institute for Integrated Radiation and Nuclear Science, Kyoto University

BACKGROUND AND OBJECTIVE

Boron is an essential micronutrient for all plants. In general, boron in the soil dissolves in rainwater to form boric acid, which migrates into the groundwater. Therefore, in Japan or Southeast Asia, where there is a large amount of precipitation, the concentration of boron in the soil tends to decrease. As a result, various crops suffer from a growth disorder, called "boron deficiency," and it significantly reduces the value and productivity as agricultural products. While the use of fertilizers, which contain boron, can restore them from this deficiency, boron overload causes other disorders in plants, such as sterility. Particularly in semi-arid areas such as central Asia, in which the amount of precipitation is small, the agricultural damage caused by boron overload stress is more serious than a simple lack of water. Despite this situation, drastic measures have not been taken, since there is not enough information on the physiological functions of boron to develop the effective measures compared to other essential micronutrients. In order to understand the physiological functions of micronutrients, research has often been carried out to investigate their kinetics in plants by tracer experiments using their radioisotopes. In fact, Tsukamoto *et al*. revealed that iron (Fe) distribution was different depending on the process of plant growth by a tracer experiment using ^{52}Fe (*Plant Cell Physiol.* 2009; 50(1): 48–57). On the other hand, recently it was put to practical use for a novel method by injecting boric-acid water into wood building material. This method is an epoch-making one that incorporates antiseptic properties to the wood by applying the insecticidal activity and cross-linking function in the cell wall of boron. However, if this development goes on without paying due attention to the leaching of boron from this wood, it may cause great adverse impacts on the environment.

If a method to analyze multi-dimensional information of boron in plants is developed, the productivity of agricultural products will be improved by advancing understanding of the physiological functions of boron. Moreover, it is very promising in the contribution to the public interest in many ways, such as reinforcing historical wooden buildings by the injection of a proper dose of boron. Therefore, we decided to establish a method to perform precise detection and quantification of boron in plant tissue using a neutron capturing reaction.

ALLOTTED RESEARCH SUBJECTS

This project research is composed by three individual subjects as follows;

PR-1: Localization of boron in plants using neutron capture radiography (M. Kobayashi and T. Kinouchi)

PR-2: Kinetics of boron artificially injected into wood and its environmental transfer analysis (S. Kitajima and T. Kinouchi)

PR-3: Development of *in situ* visualization of boron distributed in plants (T. Kinouchi)

MAIN RESULTS

PR-1: Kobayashi *et al.* examined various samples with the aim of confirming the usability of neutron capture radiography for the boron analysis, and looking for the suitable plant materials. Through the analyses, radish roots were found to be an excellent material for the boron localization analysis.

PR-2: Since suitable plant material was unobtainable due to unseasonable weather, this allotted research was not carried out.

PR-3: Kinouchi *et al.* tried to develop *in situ* visualization of boron distribution in the root by neutron capture radiography. As a result, it was observed that a large amount of boron was concentrated at the center and outer peripheral tissues of the radish tap root.

PR12-1 Localization of boron in plants using neutron capture radiography

T. Kinouchi and M. Kobayashi[1]

KURNS, Kyoto University
[1]Graduate School of Agriculture, Kyoto University

INTRODUCTION: Boron (B) is one of the essential micronutrients for vascular plants. Boron plays a role as the cross-linker of pectin in cell walls. The structure is considered important for the cell wall architecture, but the exact function of B-pectin cross-linking still remains elusive. Clarifying the localization of B within tissues may give us useful insights on the issue. Therefore, we have been trying to apply neutron capture radiography for the analysis, and reported that the method was applicable to the roots of radish seedlings [1]. Here, we examined the samples from some other plants as well, with the aim of confirming the usability of this method and looking for the suitable plant materials.

EXPERIMENTS: Suspension cultured cells of tobacco (*Nicotiana tabacum* L. cv. Bright Yellow-2) was maintained in the standard culture medium containing 1 mg B L^{-1} as boric acid and subcultured by transferring a 0.2-mL aliquot of 7-d-old culture into a 30-mL new medium. The CR-39 nuclear track detector was overlaid with a mixture of 0.1 mg mL^{-1} poly-L-lysine (PLL; Nacalai Tesque) and 0.1% (w/v) Tween 20 and air-dried at ambient temperature. The PLL-coated CR-39 was then overlaid with an aliquot of 5-d-old culture, incubated for 10 min at room temperature, and washed with new culture medium. The cells adhered onto the detector surface were fixed with 3% (w/v) glutaraldehyde in 0.1 M potassium phosphate buffer (pH 7.0) for 2 h at room temperature. After washing in 0.1 M potassium phosphate buffer (pH 7.0), the cells were dehydrated in a graded ethanol series (20%, 40%, 60%, 80%, and 99.5%). Duckweed (*Lemna minor*) was cultured in a medium containing 0.5 mg B L^{-1} in the laboratory under sunlight through window. Fronds were fixed with glutaraldehyde and embedded in OCT compound (Tissue-Tek), frozen in liquid nitrogen, and subjected to section preparation using freezing microtome. Radish (*Raphanus sativus* L. *sativus*) seeds were grown and used for section preparation as described previously [1].

The bright field-images of the plant specimen on CR-39 nuclear track detectors were taken under microscope. The detectors were then irradiated with neutron for 15 min using Tc-Pn facility at Kyoto University Research Reactor Institute. The irradiated CR-39 plate was etched in NaOH solution, and the resulting pits were observed under microscope.

RESULTS: Figure 1 shows a representative result of analysis using tobacco BY-2 cells as the material, which is the merged image from the bright-field and pit images. The pits shown in pink were found mostly within the cell boundary, suggesting that the observed signals were derived from B in the cells. The result, together with our previous report on the analysis of radish roots, demonstrate the usability of this method to detect B in plants at a cellular level. However, the number of observed B signals was much lower than that expected from the distribution of RG-II as the B acceptor, which distributes in the entire cell wall [2][3]. Thus, the sensitivity of signal detection needs to be increased, to apply this method to subcellular localization of B in plant cells.

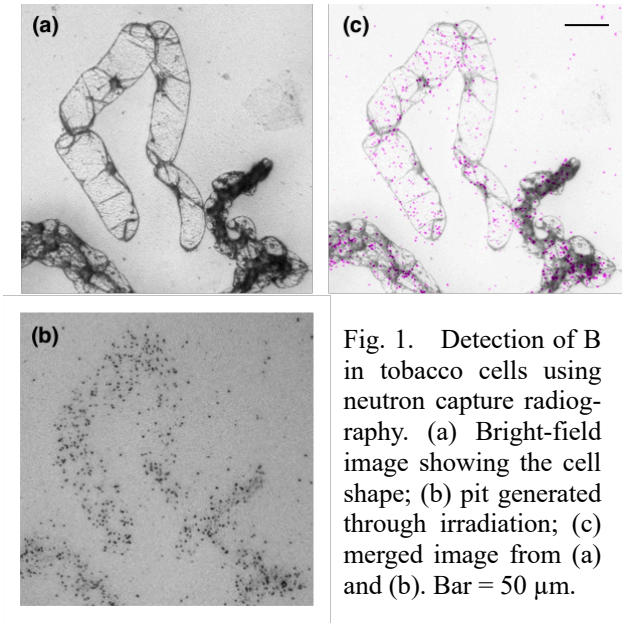

Fig. 1. Detection of B in tobacco cells using neutron capture radiography. (a) Bright-field image showing the cell shape; (b) pit generated through irradiation; (c) merged image from (a) and (b). Bar = 50 μm.

Duckweed is an aquatic monocotyledonous plant that accumulate exceptionally high amount of B. The high tissue concentration of B may lead to a stronger signal, hence we tried using duckweed for the analysis. However, it was difficult to obtain slices of duckweed fronds with high quality, probably because the fronds did not get in contact with OCT compound well. This might be due to water repellency of the fronds of the aquatic plants.

Through the analyses, radish roots were found to be excellent as the material for the B localization analysis. The tip region of tap roots in young seedlings has a diameter suitable for the microscopy used in the analysis. In addition, anthocyanin accumulated in the skin helps finding the specimen in the molded block of OCT during the section preparation. Using the material, we are now planning to analyze the concentration of B in different tissues within a root, based on pit density in each substructures.

REFERENCES:

[1] M. Kobayashi and T. Kinouchi, KURRI Progress Report, **2014** 12929-12929 (2014).
[2] Matoh T *et al*., Plant Cell Physiol. **39** 483-491 (1998).
[3] Zhou Y *et al*. Biosci. Biotech. Bioch. **81** 899-905 (2018).

PR12-2 Development of *In Situ* Visualization of Boron Distributed in Plants

T. Kinouchi

Institute for Integrated Radiation and Nuclear Science, Kyoto University

INTRODUCTION: Boron is known to be the essential element for the growth of plants. In general, boron in the soil dissolves in rainwater to form boric acid, which migrates into the groundwater. Therefore, in Japan or Southeast Asia, where there is a large amount of precipitation, the concentration of boron in the soil tends to decrease. As a result, various crops suffer from a growth disorder, called "boron deficiency", and it significantly reduces the value and productivity as agricultural products.

Figure 1 shows the artificially caused boron deficiency in radish tap roots. As indicated by arrows, brown pigment, which is a kind of phenolics such as anthocyanin, was observed at the center and outer peripheral tissues of the tap root of radish, which was cultured in hydroponics in the absence of boron. In particular, since the phenolics accumulated in the outer periphery was formed a ring-shape, that tissue was considered to be cambium. Although the phenolics accumulation is known as typical symptoms of boron deficiency, it was unknown the reason why plants undergoing boron deficiency produce and accumulate phenolics in those specific tissues. Thus, in order to make clear the relation between boron deficiency and abnormal pigmentation within tissues, we tried to develop *in situ* visualization of boron distribution in the root by neutron capture radiography.

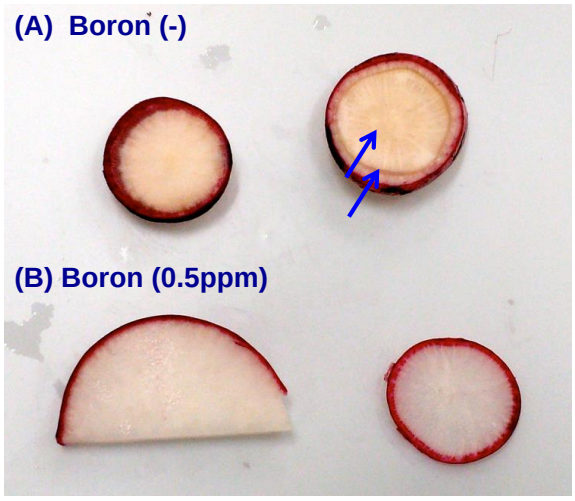

Fig.1 The artificially caused boron deficiency in radish tap roots. (A) Upper two cross sections of the tap root of radish, which were cultured in hydroponics in the absent of boron, exhibits symptoms of boron deficiency: deposition of brown pigment can be observed at the center and the periphery of the tap root as shown by arrows. (B) Lower two cross sections are also obtained from the tap root of radish, which were cultured in hydroponics with boron (0.5ppm).

EXPERIMENTS: Plant materials and growth conditions> Radish (*Raphanus sativus* L. *sativus*) was cultivated at 23°C in hydroponic media containing major nutrients (1 mM $Ca(NO_3)_2$, 0.5 mM KH_2PO_4, 0.5 mM K_2SO_4, 1 mM $MgSO_4$, and 1.5 mM NH_4NO_3) and micronutrients (75 μM EDTA-Fe, 46 μM H_3BO_3, 9 μM $MnSO_4$, 0.8 μM $ZnSO_4$, 0.3 μM $CuSO_4$, and 0.8 μM Na_2MoO_4) under a 16-h light/8-h dark cycle in a 60%-humidified growth chamber.
In situ visualization of boron in plants using neutron capture radiography> Mounted slice (10-μm thickness) of the radish tap root onto a solid-state nuclear track detector, CR-39 (20 mm×30 mm) was irradiated with epithermal neutron for 15 min by applying to the pneumatic tube in the graphite thermal column (Tc-Pn) of Kyoto University Research Reactor (KUR). The irradiated CR-39 plate was etched in 6 M NaOH solution, and the resulting etch-pits were observed under an optical microscope [1].

RESULTS: Pits generated by boron-neutron capture reaction were not distributed equally, but were concentrated at the center and outer peripheral tissues (fig. 2). Therefore, the total pit-image merged well with phenolics accumulating sites. Since cell division is very active at the central part and cambium, a large amount of boron would be distributed in such tissues. On the other hand, the relationship between phenolics accumulation and boron distribution still unknown. We would like to solve this question by analysis using cultured cells.

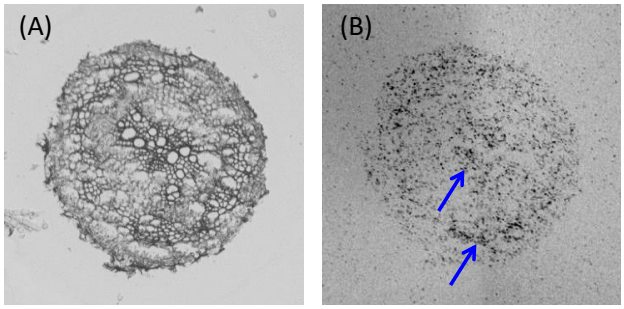

Fig.2 Distribution of boron in the radish tap root. (A) Optical microscopic image of the radish tap root. The root has a diameter of 2 mm. (B) Etch-pit image of the radish tap root after neutron radiation.

REFERENCES:

[1] M. Kobayashi and T. Kinouchi, KURRI Progress Report, **2014** 12929-12929 (2014).

I-2. COLLABORATION RESEARCHES

1. Slow Neutron Physics and Neutron Scattering
2. Nuclear Physics and Nuclear Data
4. Material Science and Radiation Effects
5. Geochemistry and Environmental Science
6. Life Science and Medical Science
7. Neutron Capture Therapy
8. Neutron Radiography and Radiation Application
9. TRU and Nuclear Chemistry
10. Health Physics and Waste Management
12. Others

CO1-1 Quantitative Characerization of Microstructures in Steels using Small-Angle X-ray Scattering

Y. Oba, R. Inoue[1] and M. Sugiyama[1]

Materials Sciences Research Center, Japan Atomic Energy Agency
[1]Institute for Integrated Radiation and Nuclear Science, Kyoto University

INTRODUCTION: Nano- and microstructures are crucial for steels because they are closely related with the mechanical properties. Small-angle scattering (SAS) is a powerful tool to quantitatively characterize the nano- and microstructures because of its large gauge volume. Several research groups have reported the applications of SAS to steel researches [1-3].

However, model alloys having simple nanostructures are often examined by SAS to simplify the discussion. For further progress, it is necessary to apply SAS to more practical materials. Stainless steel is a typical commercial steel and has complex nanostructures. In this case, small-angle X-ray scattering (SAXS) measurements using in-house instruments is suitable as a usual characterization technique closely linked with practical materials processing. Although it takes over several hours for a SAXS measurement using the in-house SAXS instruments, steels are stable for such long measurements.

Therefore, in this study, the nanostructures in the stainless steels were investigated to confirm the ability of the in-house SAXS instrument.

EXPERIMENTS: SAXS measurements were performed using the in-house SAXS instrument with Mo $K\alpha$ radiation. For steels, conventional Cu $K\alpha$ radiation is not useful because of low transmission and high fluorescence X-ray emission. Scattering patterns were obtained using a two-dimensional detector (PILATUS 100k) equipped with a 1000 μm-thick silicon sensor to efficiently detect the high energy Mo $K\alpha$ radiation. The path of X-ray between the entrance slit and up to the detector including the sample area was evacuated to eliminate background scattering from air and vacuum windows. In this study, the original vacuum tubes were changed to thicker vacuum pipes to improve the degree of vacuum and further reduce the background scattering from residual air.

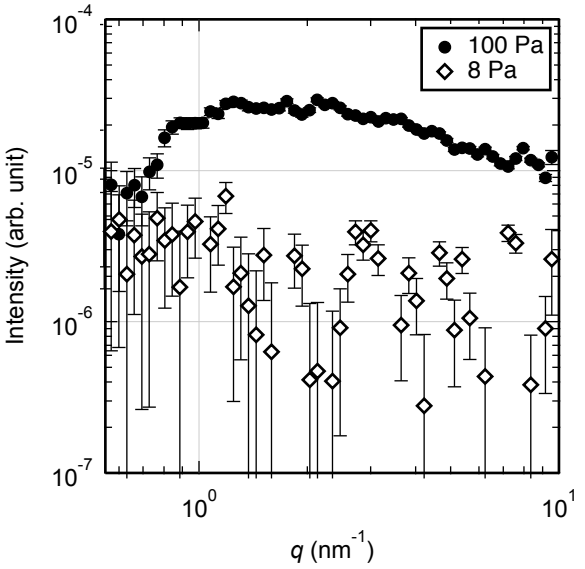

Fig. 1. Background scattering profiles.

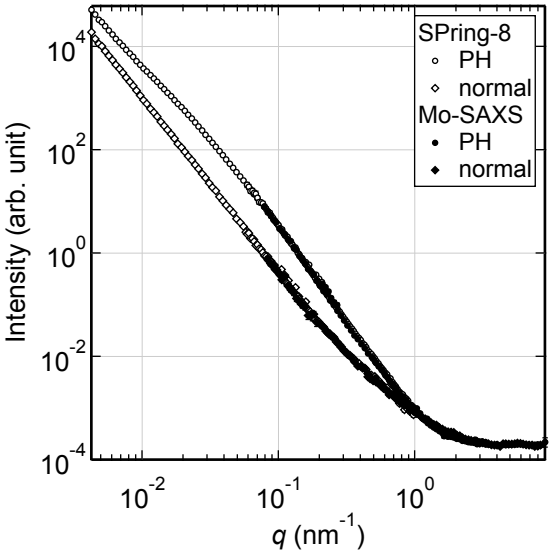

Fig. 2. Scattering profiles of stainless steels. Circles and diamonds denote precipitation hardening (PH) and normal stainless steels, respectively. Open and filled symbols are data obtained using SPring-8 and Mo-SAXS.

RESULTS: Fig. 1 shows the background scattering before and after changing the vacuum pipes. With this changing, the ultimate vacuum was improved from 100 Pa to a few Pa and the background scattering intensity decreases to about 1/10.

Fig. 2 shows the scattering profiles of precipitation hardening (PH) and normal stainless steels. Both the profiles obtained using Mo-SAXS agree well with the corresponding scattering profiles obtained using the SAXS instrument in SPring-8. The profile of the PH stainless steel has a hump at about $q < 1$ nm^{-1} compared to that of the normal stainless steel. This hump is attributed to the scattering from precipitates. Therefore, we successfully observed the precipitates in stainless steels using SAXS.

REFERENCES:

[1] M. Ohnuma *et al.*, Acta Mater., **57** (2009) 5571-5581.
[2] Y. Oba *et al.*, ISIJ Int., **51** (2011) 1852-1858.
[3] A. Deschamps *et al.*, Mater. Lett., **65** (2011) 2265-2268.

CO1-2 Fabrication of *m*=6 spuermirror on ellipsoidal metal substrate

M. Hino[1], T.Hosobata[2], T.Oda[1], H.Yoshinaga[1], S. Takeda[2], Y.Yamagata[2], H.Endo[3], N.L.Yamada[3], F. Funama[4], Y. Kawabata[1]

[1]*Institute for Integrated Radiation and Nuclear Science, Kyoto University (KURNS), Japan*
[2] *RAP, RIKEN, Japan*
[3] *IMSS, KEK, Japan*
[4]*Dept., Nucl. Eng., Kyoto University, Japan*

INTRODUCTION: Progress of neutron optical devices is very significant. Recently we proposed promising fabrication method for aspherical focusing supermirror with metal substrate [1-4]. The metallic substrate is robust and ductile, to which able to fabricate steeply curved surface with high form accuracy. It is also applicable to use under high radiation irradiation and high-temperature filed, even at a place close to the neutron target and moderator. Furthermore, it is possible to fabricate a large focusing mirror by combining multiple segmented mirrors with mechanical fastening entailing the usage of screw holes and fixture tabs. The big problem was required surface roughness for neutron mirror. The roughness should be smaller than 0.3 nm for high-*m* supermirror coating. Here *m* is the maximum critical angle of the mirror in units of critical angle of natural nickel. By using electroless nickel-phosphorus (Ni-P) plating, we overcame the problem and are establishing fabrication process for aspherical focusing supermirror. In this study, we show a latest result for neutron focusing experiment with a couple of ellipsoidal supermirrors with metallic substrates.

EXPERIMENTS: We fabricated ellipsoidal metallic substrates with the Ni-P plating, based on the technology using ultrahigh precision cutting with correction processing, followed by mechanical precision polishing. The first precise manufacturing was conducted at a CNC machine for development of neutron optical devices at workshop of the KURNS. The ultra-precise manufacturing, polishing and cleaning of the metallic substrate were conducted at RIKEN. The supermirror coating was conducted with ion beam sputtering machine at the KURNS (KUR-IBS) [5]. The neutron experiments were conducted at CN-3 beam line at the KURNS and the BL06 (VIN ROSE) beam port at J-PARC MLF [6]. We have succeeded in fabricated a couple of *m*=3 NiC/Ti ellipsoidal supermirrors in which length of 900mm [7]. The semi-major and semi-minor axes of the ellipsoidal supermirror were 1250 mm and 65.4 mm, respectively. The acceptable angle of the minor axis arc of the ellipsoidal supermirror is 20 degree. In this study, we tried to fabricate higher-*m* NiC/Ti ellipsoidal supermirrors in which substrate was same with the *m*=3 NiC/Ti one. Here the required number of layers of high-*m* supermirror increases with the proportional of m^4, in which principle is well known as Porod's law. We have fabricated *m*=5 and *m*=6 NiC/Ti supermirrors in which number of layers were 3000 and 5000, respectively.

RESULTS:
Figure 1 shows photograph of *m*=6 NiC/Ti supermirror fabricated by the KUR-IBS. As shown in Fig. 1(a), the supermirror coating itself was succeeded, however, it was not tough for temperature difference. Here one of three supermirrors peeled off as shown in Fig. 1(b). The performance of supermirrors were not so good and it is still necessary to improve fabrication process for higher-*m* ellipsoid supermirror. By using the ellipsoid supermirror, we succeeded in observation of first neutron resonance spin echo signal of focusing neutron beam at BL06 at the MLF, J-PARC [8].

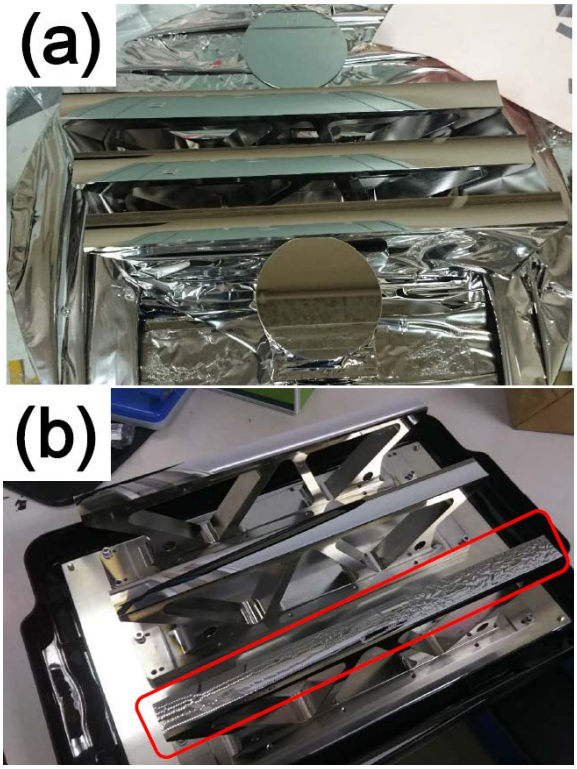

Fig. 1. Photograph of m=6 NiC/Ti supermirror coated by the KUR-IBS. (a) just after the deposition (b) after about 30° temperature change with transportation.

REFERENCES:
[1]J.Guo *et al.*, Optics Express **22** (2014) 063108.
[2]J.Guo *et al.*, Review of Scientific Instruments 86(2015) 86 (2015) 063108.
[3]S.Takeda *et al.*, Optics Express **24** (2016) 12478.
[4]T.Hosobata *et al.*, Optics Express **25** (2017) 20012.
[5]M.Hino *et al.*, Nucl. Instr. and Meth., **797** (2015) 265.
[6]M.Hino *et al.*, J. Nucl. Sci. Technol. **54** (2017) 1223.
[7]M.Hino *et al.*, KURRI Progress report 2017 CO1-8.
[8]H.Endo *et al.*, Physica B, **564** (2019) 91.

CO1-3 Character of DNA damage induced by nuclear palnt neutron beams

H. Terato, Y. Tokuyama[1], K. Mori[1], N. Osada, H. Tanaka[2] and T. Saito[2]

Advanced Science Research Center, Okayama University

[1]Analytical Research Center for Experimental Sciences, Saga University

[2]KURNS, Kyoto University

INTRODUCTION: Radiation biological effects are arrived via DNA damaging by ionizing radiation, because DNA loads genetic information. There have been a lot of studies about radiation DNA damage, and the most of them were for gamma- and X-rays' ones, but less other radiation qualities. We have studied for the DNA damage with heavy ion beams, previously [1, 2]. These studies indicated that the DNA damage with heavy ion beams were unique, indicating that a lot of clustered DNA damage were generated including DNA double strand break (DSB). Clustered DNA damage is a complex damage containing multiple lesions in the local region of DNA. This damage strongly inhibits DNA polymerization, and shows less repairable. Here, we analyze the DNA damage with neutrons from nuclear power plant to unveil the molecular mechanism of neutron biological effect. The neutron beam is also high LET radiation as same as heavy ion beam. Therefore, we will find some interesting character of DNA damage with neutron like heavy ion beam.

EXPERIMENTS: Cultured cells of Chinese hamster ovary (CHO) AA8 strain were irradiated with neutron beams in the Kyoto University Reactor. The cells were cultivated with the conventional method. The logarithmic growing cells were recovered by trypsinization, and set into a polypropylene tube for irradiation. The irradiation time was up to three hours with sampling in every 30 minutes. The estimated dose rate of neutron was 1Gy h^{-1}. After irradiation, the cells were immediately frozen by dry ice, and stored until analysis. The procedures of DNA damage analysis were mass spectrometry and electrophoresis for base damage and strand break, respectively [2 – 4]. For base damage analysis, we focused on the oxidative base damage, that is common damage with ionizing radiation. The chromosomal DNA were extracted from the irradiated cells, and were digested by nuclease to obtain the separated nucleotide units. Then, the nucleotide mixture was analyzed by mass spectrometry. For DSB analysis, the irradiated cells were embedded into low-melting agarose plug just after irradiation. The plugs were digested by protease and then electrophored. The sheared chromosomal DNA are released from the gel plug in electrophoresis gel, but the intact ones stay in the plug. The gel was stained by ethidium bromide, and the DNA bands were visualized. We compared the staying and released DNA bands for DNA shearing by neutron beams.

RESULTS: The result for base damage indicated that 8-oxoguanine as a guanine oxidative damage increased dose-dependently (Fig. 1). DSB were also detected with 1 Gy-irradiation. However, the elevation of this damage was not shown with more than 1 Gy. The reason for the no increment have been still unknown. We consider that DNA repair is involved in no increase of DSB because of the low dose rate of the neutron beam.

We need further study for elucidation of molecular mechanism of neutron biological effect. The future study plan will contain the oxidative pyrimidine analysis such as 5-hydrooxycytosine. Also, the DSB will be analyzed by using of the mutant cell strains without homologous recombination (HR) and hon-homologous end joining (NHEJ). Using of these mutants leads the initial yields of DSB without DNA repair process. Additionally, we will investigate viability of the irradiated cells for concerning of DNA damage participation for neutron biological effect.

REFERENCES:

[1] H. Terato *et al.,* J. Radiat. Res., 49 (2008) 133-146.
[2] Y. Tokuyama *et al.,* J. Radiat. Res., 56 (2015) 446-455.
[3] K. Kudo *et al.,* J. Electrostat., 73 (2015) 131-139.
[4] K. Kudo *et al.,* J. Phys. D. Appl. Phys., 48 (2015) 365401.

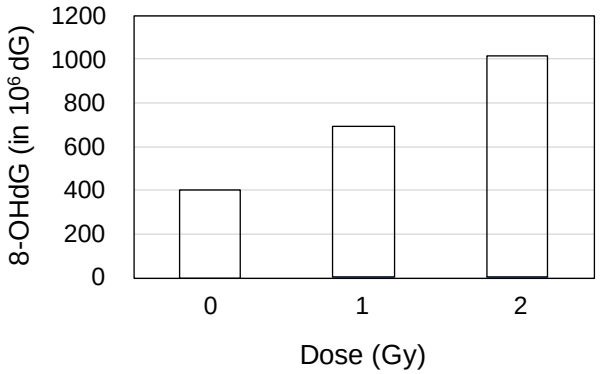

Fig. 1. Yields of 8-oxo-deoxyguanosine (8-OHdG) in the cells irradiated by the neutrons of the reactor.

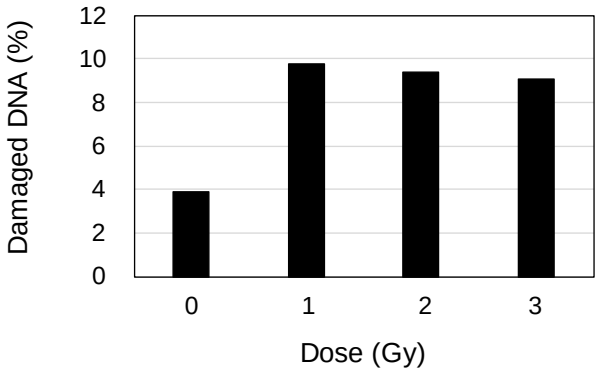

Fig. 2. Yields of DNA double strand breaks in the cells irradiated by the neutrons of the reactor.

CO1-4 Versatile Compact Neutron Diffractometer on the B–3 Beam Port of KUR

K. Mori, R. Okumura, H. Yoshino, M. Kanayama, S. Sato[1], H. Hiraka[2], K. Iwase[3], A. Okumura, and F. Kobayashi[4]

Institute for Integrated Radiation and Nuclear Science, Kyoto University (KURNS)
[1]High Energy Accelerator Research Organization (KEK)
[2]Neutron Science Center, Korea Atomic Energy Research Institute
[3]Department of Materials and Engineering, Ibaraki University
[4]Graduate School of Engineering, Kyoto University

INTRODUCTION: Neutron diffraction is a powerful tool to precisely determine the positions of light elements (e.g., hydrogen and lithium) in solids. This is the main reason why neutron powder diffractometers are critical for structural investigations of energy storage materials, for example, rechargeable lithium-ion batteries and hydrogen absorbing alloys. The B–3 beam port of Kyoto University Research Reactor (KUR) had long been used as a four-circle single-crystal neutron diffractometer (4CND). For the last decade, however, the 4CND was so old that its research activity on neutron science was quite low. Now, the versatile compact neutron diffractometer (VCND) is installed on the B-3 beam port of KUR.

SPECIFICATIONS: Fig. 1 shows the current state of the VCND. The VCND is equipped with a new beam shutter manufactured by the KURNS factory. In addition, the VCND has a wide space around the sample; therefore, we can easily install any other system. The neutron wavelength, λ, which is monochromatized by the (220) plane of a Cu single crystal (i.e., Cu monochromator), is 1 Å. To cover the detector area of $6\,° \leq 2\theta \leq 130\,°$, twenty-five ^{3}He tube detectors (1/2 inch in diameter) are used (see Fig. 2), where 2θ is the scattering angle. A detector bank including twenty-five ^{3}He tube detectors is placed on the arm of the HUBER-440 goniometer. The distance from the Cu monochromator to the sample is approximately 2 m, and the distance from the sample to the detector is 1.2 m.

CRYSTAL STRUCTURE ANALYSIS: The preliminary neutron diffraction measurements have been performed using the VCND. Fig. 3 shows the Rietveld refinement pattern of the standard sample: NIST-Si powder. As a result, an excellent fit was obtained between the observed and calculated intensities. The Bragg reflections at the high Q region (corresponding to the high 2θ region) could be observed using the VCND rather than the Laboratory X-ray diffractometer with a Cu$K\alpha$ radiation, where Q is the magnitude of the scattering vector ($= 4\pi\sin\theta/\lambda$, where θ is half of the scattering angle, 2θ). The complementary use of neutron and X-ray diffraction is very useful for the structural investigations. Further improvements are now in progress.

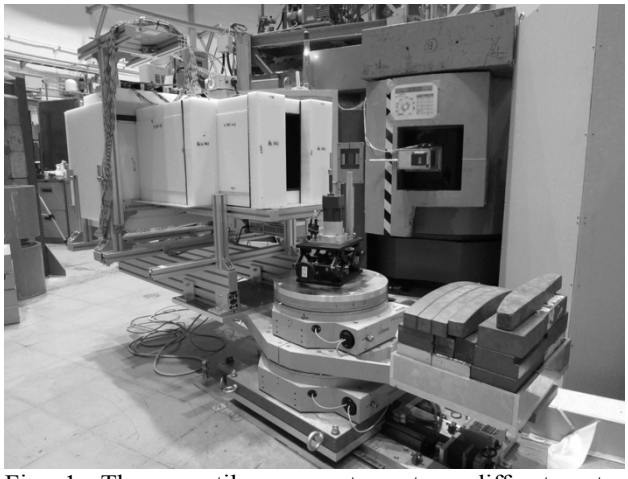

Fig. 1. The versatile compact neutron diffractometer (VCND), installed at the B-3 beam port of KUR.

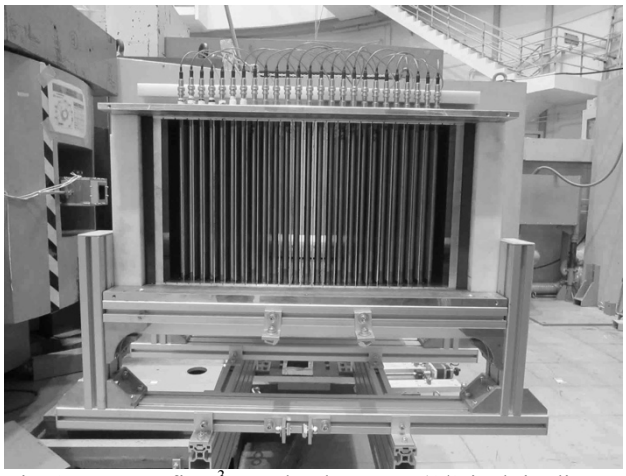

Fig. 2. Twenty-five ^{3}He tube detectors (1/2 inch in diameter) on the detector bank of the VCND.

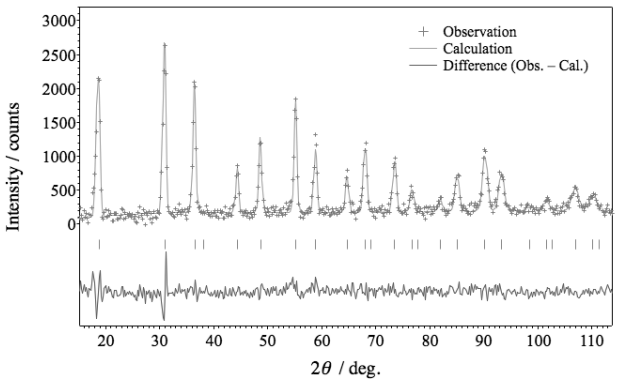

Fig. 3. The crystal structure refinement of NIST-Si using neutron diffraction data collected at the VCND.

CO1-5 Recovery Behaviors of Irradiation-Induced Defects in H_2^+-Implanted SiC and Graphite

N. Kawamura, S. Makimura, S. Matoba, J.-S. Park[1], N. Nakazato[1], H. Kishimoto[1], A. Yabuuchi[2], A. Kinomura[2] and Q. Xu[2]

Institute of Materials Structure Science, High Energy Accelerator Research Organization (KEK)
[1]Graduate School of Engineering, Muroran Institute of Technology
[2]Institute for Integrated Radiation and Nuclear Science, Kyoto University

INTRODUCTION: In J-PARC muon science experimental facility, muons are produced by irradiating a graphite target with a 3 GeV proton beam. A silicon carbide (SiC) attracts our interest for a candidate of new target material to yield more muons. Understanding tritium behavior formed in these target materials by proton irradiation is important for a stable operation in high power beam facilities like J-PARC. Macroscopic studies like TDS show that hydrogen-isotope diffusion in graphite strongly depends on the structure such as the grain size, lattice defects *etc*. Because, in the high-power beam target, the irradiation-induced vacancies are considered to trap tritiums, we investigated the recovery behavior of the vacancies using a slow positron beam.

EXPERIMENTS: 50-keV H_2^+ ions were irradiated to CVD-SiC, NITE-SiC/SiC composite [1], and graphite samples with a dose of 5×10^{16} H_2^+/cm^2. After irradiation, the samples were annealed at 500°C, 700°C, and 900°C for 15 min in N_2 atmosphere. Before and after annealing at each temperature, the samples were probed by the KUR slow positron beam and the Doppler broadening of the annihilation radiation (DBAR) spectra were acquired. The DBAR spectrum is known to be characterized by *S*- and *W*-parameters, which correlate to annihilation with low and high momentum electrons, respectively [2].

RESULTS: Figure 1 shows *S*-parameters obtained for each sample as a function of incident positron energy. They are normalized by that of each unirradiated sample annealed at 900°C. The *S*-parameter of graphite after annealing at 900°C almost recovers to the unirradiated reference-state. This is considered to be due to the recombination of the irradiation-induced vacancies and interstitials [3]. In contrast, the *S*-parameters of CVD-SiC and NITE-SiC samples show no significant change after 900°C annealing. This indicates that the irradiation-induced vacancies survive even after annealing. Figure 2 shows *S*-*W* correlations obtained for the CVD-SiC and NITE-SiC samples. If the defect specie is not changed by annealing, the *S*-*W* data should be marked on the straight line between the unirradiated state and the as-irradiated ones. However, after the annealing, the *S*-*W* points move to lower-left direction. This means that positrons are trapped at different defect species in the annealed samples, as compared to the as-irradiated ones. Although there are no significant changes in the *S*-parameters, the dominant defect species is indicated to be changed by the annealing. This result implies the defect complex of vacancies and hydrogen atoms. For further understanding, theoretical studies and electron-irradiation experiment are necessary.

ACKNOWLDGEMENTS: This study is partially supported by JSPS KAKENHI Grain Number JP16H03994.

REFERENCES:

[1] A. Kohyama *et al.*, Ceramic Transactions **256** (2016) 37.
[2] R. W. Siegel, Ann. Rev. Mater. Sci., **10** (1980) 393–425.
[3] M. Shimotomai *et al.*, J. Phys. Soc. Jpn., **52** (1983) 694–702.

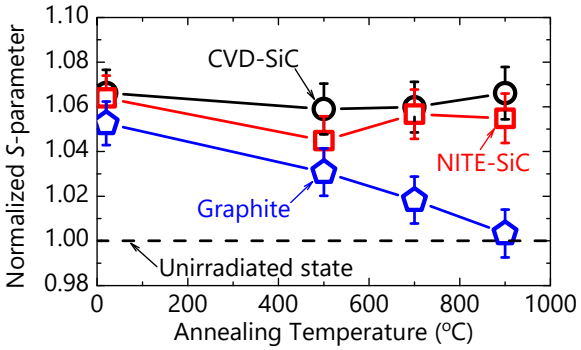

Fig. 1. *S*-parameters for CVD-SiC (open circles), NITE-SiC (open squares), and graphite (open pentagons) samples as a function of annealing temperature. Unirradiated state is also indicated as a dashed line.

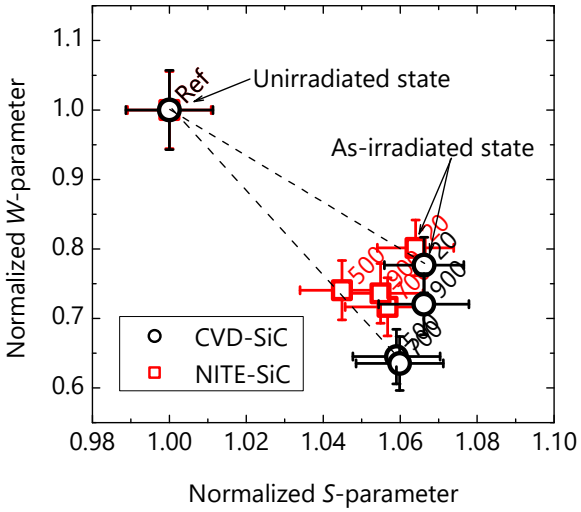

Fig. 1. *S*-*W* correlations for CVD-SiC and NITE-SiC samples. Annealing temperatures are also shown beside each symbol.

CO1-6 Measurements of thermal neutron total cross section of reactor-grade graphite

Jun Nishiyama[1], Jaehong Lee[2], Tadafumi Sano[3] and Jun-ichi Hori[2]

[1]*Laboratory for Advanced Nuclear Energy, Institute of Innovative Research, Tokyo Institute of Technology*
[2]*Institute for Integrated Radiation and Nuclear Science, Kyoto University*
[3]*Atomic Energy Research Institute, Kindai University*

INTRODUCTION: The high temperature gas-cooled reactor is a Generation IV reactor concept that use a graphite moderator. The design takes advantage of the inherent safety characteristics with specific design optimizations. The treatment of thermal scattering caused by crystalline is important for graphite to improve the prediction accuracy of graphite moderated core analysis. There is sufficient thermal scattering law for single crystal graphite, but there is no method has been established to reconstruct thermal scattering cross section for polycrystalline graphite. The differences in the scattering cross section resulting from the size of crystal grains, porosity in the graphite, and the production method of the graphite have been reported [1,2]. In order to provide basic data for thermal neutron scattering law evaluation, the total cross sections of the graphite were measured for reactor-grade graphite samples including a graphite moderator actually used in the critical assembly.

EXPERIMENTS: The total cross sections of reactor-grade graphite were measured in the incident neutron energy region from 0.001 to 10 eV by transmission experiments at the KURNS-LINAC. An experimental arrangement is shown in Fig. 1. Pulsed neutrons were produced from a water-cooled Ta-target by (γ,n) reaction with a pulsed electron beam. The incident neutron spectrum on a sample and the transmitted neutron spectrum were measured by means of a time-of-flight (TOF) method with a ^{6}Li-glass scintillation detector. A 5.0 mm diameter by 5.0 mm thick ^{6}Li-glass was located 12.0 m from the neutron source.

Two reactor-grade graphite samples were used for measurements. The characteristics of the samples are shown in Table 1. The 1/2" thickness sample is used as a moderator in the KUCA facility.

The total cross section of the graphite σ_t is calculated from the transmission spectrum and the thickness of the sample as following.

$$\sigma_t(E) = -\frac{\mathrm{A}}{\rho t N_A}\ln\big(T(E)\big) \qquad (1)$$

where ρ is the sample density, A is the atomic mass, t is the sample thickness and N_A is the Avogadro constant $T(E)$ is the transmission spectrum is derived from

$$T(E) = \frac{S(E) - A(E)}{B(E) - A(E)} \qquad (2)$$

where $B(E)$ is the incident neutron energy spectrum on the sample derived from the TOF spectrum measured with ^{6}Li-glass detector for the Blank run, $S(E)$ is the spectrum transmitted by the sample for the Sample run and $A(E)$ is the background spectrum determined by the Absorber run which performed with the polyethylene block inserted into middle of the neutron flight tube.

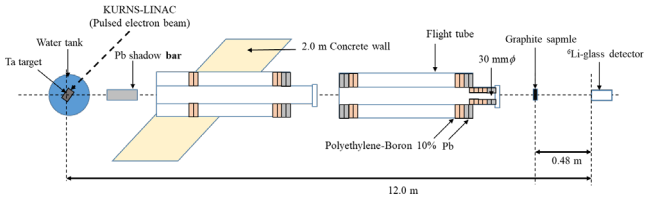

Fig 1. Experimental arrangement

Table 1 characteristics of samples

Sample	Graphite 1.0 cm	Graphite 1/2"
Crystal structure	Polycrystalline	Polycrystalline
Sample shape	Disc	Square plate
Density [g/cm^3]	1.779	1.754
Size [mm]	ϕ50	50.8×50.8
Thickness [mm]	10.0	12.7
[atoms/b]	8.92×10^{-2}	1.12×10^{-1}

RESULTS: The total cross sections of two reactor-grade graphite were derived in the incident neutron energy region from 0.001 to 10 eV. The present results are shown in Fig. 2. A clear first black edge was observed at 0.0018 eV for both samples. In the energy range of 0.1 eV or more, the results are good agreement within the error, but there is discrepancy in the energy region 0.0018 to 0.02 eV.

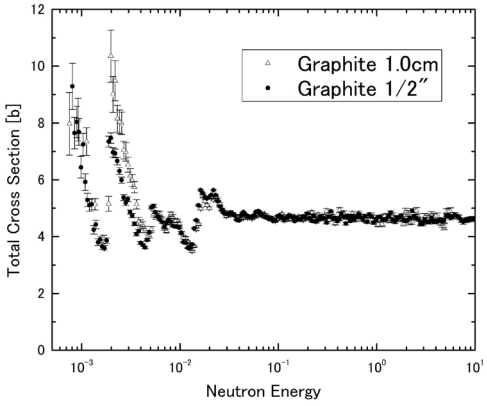

Fig. 2 Total cross section of graphite

REFERENCES:

[1] C. D. Bowman *et al.*, Nucl. Sci. Eng., **159** (2008) 182-198.
[2] S. Petriw *et al.*, J. Nucl. Materials., **396** (2010) 181-188.

CO1-7 Development of neutron spin flipper with large beam acceptance

M. Kitaguchi, H. Okabe[1], T. Oda[2], and M. Hino[2]

Center for Experimental Studies, KMI, Nagoya University
[1]Department of Physics, Nagoya University
[2]Institute for Integrated Radiation and Nuclear Science, Kyoto University

INTRODUCTION: The recent values of neutron lifetime deviate far beyond the systematic errors claimed in the past and require the further improvement for the neutron the lifetime puzzle. We are continuing neutron lifetime measurement at the polarized beam branch of the NOP beamline installed at the port BL05. The system consists of a neutron chopper (SFC) and a gas chamber (TPC) for detecting the electrons from the neutron beta decays. The TPC contains small amount of ^{3}He. The rate of the ^{3}He(n,p)^{3}H reaction is measured by counting the protons. The neutron lifetime is measured as the ratio of the electron events to the proton events [1].
The large background via neutron-induced reactions is suppressed by introducing small neutron bunches into the TPC and selectively detecting decay electrons and reaction protons only when neutron bunches are traveling inside the sensitive volume and they were not transmitting through chamber windows and other materials on the beam path. The SFC is a spin-selective optics to switch the neutron beam using the combination of magnetic supermirrors and spin flippers[2]. Polarized neutrons are injected into the SFC. Controlling the timing of spin-flip makes neutron bunches at the exit of the SFC, which can be reflected by the magnetic mirrors successively. By employing the triple series reflection, the present version of the SFC chops the neutron beam with the intensity contrast of about 400. During the lifetime measurement, the bunch length is adjusted as about 50 cm, which is half of the length of TPC sensitive region for maximizing the signal statistics. The cross section of the output bunches is 2 cm ×2 cm. In order to reduce the statistical uncertainties for the lifetime measurement to the order of 1 s, the incident neutron flux into the TPC must be increased. Although the new mirrors have been already assembled to accept large cross section of the neutron beam, large scale of spin flippers are also required. Now we are also continuing to develop the precision simulation of neutron spin behavior. Numbers of spin flippers, which have various performances, should be investigated and compared with the simulations.

EXPERIMENTS: The experiments were performed at cold neutron beamline CN3 in KUR. Figure 1 shows the experimental setup. Disk chopper provided pulsed neutrons. Magnetic supermirrors were used for neutron polarizer and analyzer. The position and time-of-flight from the chopper to the detector were measured. The behavior of the spin of each neutron was investigated by scanning the position and magnetic field of the flipper coil.

RESULTS: The dependence of spin flipping probability not only for neutron wavelength but also for the position of the flipper coil was observed clearly. It means that the position distribution of the magnetic field of the coil may have non-negligible influences of the spin behavior. This can be reproduced numerically by our simulation (Fig. 2). New flipper coils with large beam acceptance are developed by using the simulation-based design.

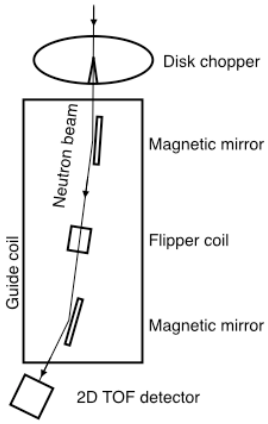

Fig. 1. Experimental setup with polarized neutron beam at CN3 beamline.

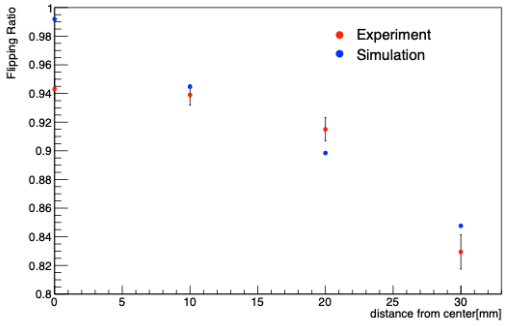

Fig. 2. Position dependence of spin flipping ratio in the flipper coil.

REFERENCES:
[1] K. Mishima *et al.,* Nucl. Instr. and Meth., A600 (2009) 342.
[2] K. Taketani *et al.*, Nucl. Instr. and Meth., A634 (2011) S134–S137.

CO1-8 Development of high spatial resolution cold/ultracold neutron detector using nuclear emulsion

N. Naganawa, M. Hino[1], K. Hirota[2], H. Kawahara[2], M. Kitaguchi[3], K. Mishima[4], N. Muto[2], Y. Seki[5], S. Tada[2], A. Umemoto[2]

Institute of Materials and Systems for Sustainability, Nagoya University

[1]*KURNS, Kyoto University*

[2]*Graduate School of Science, Nagoya University*

[3]*Kobayashi-Maskawa Institute for the Origin of Particles and the Universe*

[4]*High Energy Accelerator Research Organization, KEK*

[5]*Japan Proton Accelerator Research Complex*

INTRODUCTION: We have been developing a high spatial resolution neutron detector using fine-grained nuclear emulsion[1] and a thin converter layer including ^{10}B for measurements of position distributions of cold and ultracold neutrons such as the one of quantized ultracold neutrons under the earth's gravitational field[2]. The detector will also be useful for neutron imaging. In a previous study, we confirmed it having a spatial resolution of less than 100 nm for the one with its converter ($^{10}B_4C$) thickness of 50 nm[3]. In this study, we increased the thickness to 200 nm to increase its detection efficiency with keeping its resolution. It was fabricated by the ion beam sputtering system of KURRI (KUR-IBS). Its detection efficiency of neutrons was measured at CN-3 beamline. Next, also detectors with converter thickness of 2 μm was fabricated and its ability to record microscopic patterns was demonstrated using absorption gratings made of Gd. Exposure experiments was carried out at CN-3 and BL05 of MLF, J-PARC.

EXPERIMENT 1: A converter layer of $^{10}B_4C$ (200 nm)-NiC (60 nm)-C (20 nm) was fabricated by KUR-IBS on a 0.38 mm-thick Si plate. It was coated with 10 μm-thick fine-grained emulsion. Finally, it was covered with two foils of 10 μm-thick aluminum to avoid light. It was exposed to neutrons with typical wavelength of 2.4 Å at CN-3 at the downstream of a 3 mm-diameter pinhole made by Cd. The exposure density of neutrons was 7.36×10^7 n/cm^2. After the exposure, the detector was developed at Nagoya University. Track of α-particles and ^{7}Li nuclei from absorptions were recorded in it was counted manually under an epi-illumination optical microscope.

RESULTS:

A total of 30±5 tracks were found in a view of the microscope whose area is 100 μm×100 μm. Horizontal tracks were not counted for separation from scratch marks on the Si plate. Since a number of neutrons arrived at the area was 7.36×10^4, its detection efficiency turned out to be (0.40±0.07)% for the neutrons of the beam.

EXPERIMENT 2.1: To demonstrate the ability to record microscopic position distributions of neutrons, our detector was exposed to neutrons at CN-3 at the downstream of an absorption grating made of Gd which has apertures of 3 μm wide with a period of 9 μm[4]. In this experiment, a detector with a converter layer of $^{10}B_4C$ (2 μm)-NiC (60 nm)-C (20 nm) was fabricated by IBS-KUR, then coated with the emulsion at Nagoya University. The distance between the grating and the detector was 1.5 mm. They were exposed to neutrons with typical wavelength of 2.4 Å with divergence of ±5 mrad just at the downstream of the guide pipe up to 7×10^{10} n/cm^2. A blur of the neutron image due to the divergence of the beam was assumed to be 7 μm. After development, an image was taken under the microscope with a CMOS camera.

RESULTS: As shown in Fig. 1, a microscopic pattern of the grating was obtained consistently with the dimension of blur due to the beam setting.

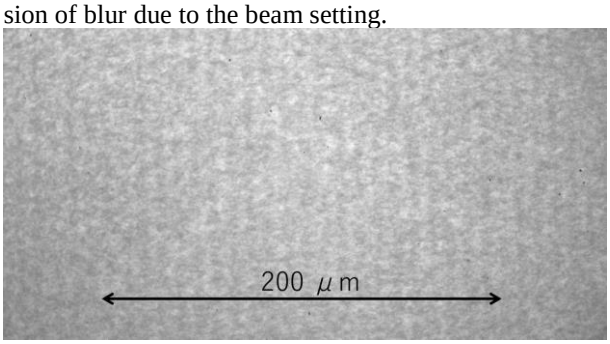

Fig. 1. A neutron image taken by a detector with a 2 μm-thick $^{10}B_4C$ layer at 1.5 mm downstream of the grating with a beam divergence of ±5 mrad. Dark part in the view consists of tracks from absorptions.

EXPERIMENT 2.2: In order to obtain a clearer image, a similar exposure was done at the Low Divergence Beam Line of BL05 in MLF, J-PARC. Another piece of the same detector as EXPERIMENT 2.1 was exposed to 4 Å neutrons with divergence of ±0.056 mrad at 900 μm downstream of the same kind of slit. The amount of neutrons which it was exposed to was 8.2×10^8 n/cm^2. A blur was assumed to be 50 nm.

RESULTS: As shown in Fig. 2, a clear microscopic pattern of the grating was seen.

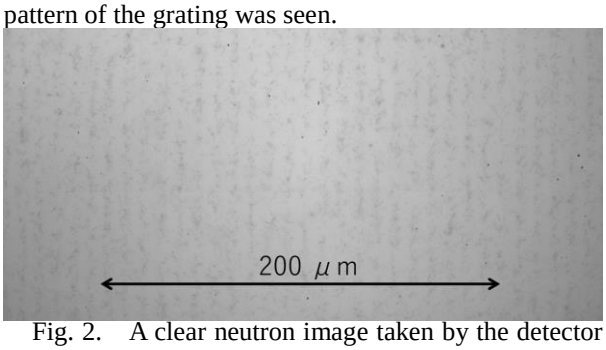

Fig. 2. A clear neutron image taken by the detector at 900 μm downstream of the grating with a beam divergence of ±0.056 mrad.

REFERENCES:

[1] T. Asada *et al,,* Prog. Thor. Exp. Phys., 2017 (2017) 063H01.

[2] V. V. Nesvizhevsky *et al.,* Nature,415 (2002) 297.

[3] N. Naganawa *et al.,* Eur. Phys. J. C, 78(2018)959.

[4] Y. Seki *et al.,* Physics Procedia 88 (2017) 217–223.

CO2-1 Development of Gamma Imager and Its Application to Identification of Nuclear Materials

H. Tomita, K. Kanamori, K. Uema, A. Mukai, K. Watanabe, T. Iguchi, T. Matsumoto[1], J. Kawarabayashi[2], E. Takada[3], and J. Hori[4]

Graduate School of Engineering, Nagoya University
[1] National Institute of Advanced Industrial Science and Technology
[2] Tokyo City University
[3] National Institute of Technology, Toyama College
[4] Institute for Integrated Radiation and Nuclear Science, Kyoto University

INTRODUCTION: Identification of a hidden or shielded gamma radioactive sources and nuclear materials is required in anti-terrorism measures. We are developing passive and active gamma spectroscopy combined with gamma-ray imaging for these applications. Compton gamma imager can measure energy of incident gamma-ray and its direction to the detector. We applied a portable and 4π direction sensitive Compton imager [1-2] to identify ^{10}B sample by prompt gamma-ray with neutron irradiation at the pulsed neutron source at Kyoto University Institute for Integrated Radiation and Nuclear Science Linear Accelerator (KURNS-LINAC).

EXPERIMENTS: A 3D pixel array CdTe detector with 1440 ch. was used as a prototype of the 4π sensitive gamma-ray imager. Three kinds of samples: ^{10}B, natural uranium (NU) and highly enriched uranium (HEU) were irradiated by pulsed neutrons at a distance of around 12 m from the neutron source. In the case of the ^{10}B sample, prompt gamma-ray spectrum was measured by the prototype imager with LiF shielding during neutron irradiation. For spectroscopy of delayed fission gamma-rays, gamma-ray spectra from NU and HEU samples were measured from 0 to 6 hours after neutron irradiation.

RESULTS: In reconstructed image of ^{10}B prompt gamma-rays (478 keV) on a projection sphere around the imager clear peak was found at direction of the sample. LiF shielding had no effect on additional back ground or signal to background ratio. Figure 1 shows a dependence of peak intensity on a distance between the imager and the ^{10}B sample. Even in rather high event rates caused by gamma flash from the neutron source and neutron induced gamma-rays, peak intensity decreased with the distance as expected.

Figure 2 shows typical background subtracted energy spectra of delayed gamma-ray from the HEU sample after 1-2, 2-3, 5-6 hours of neutron irradiation. According to ref. [3], intensity ratios of delayed gamma-rays from 0.8 to 1.5 MeV can be used to identify the fissile materials: ^{235}U and ^{239}Pu. Five peaks of the delayed gamma-rays in the energy region were obviously resolved on the measured spectra as indicated in Fig.2. The ratio of following intensities would be useful for identification:

1031.9 keV (^{89}Rb) / 1000.9 keV (^{142}Ba)
1383.9 keV (^{92}Sr) / 1532.5 keV (^{101}Mo)

In addition, imaging of delayed fission gamma-rays above 1.5 MeV is also useful to localize HEU material because gamma-rays from NU sample had less contributions on the spectra than those from HEU sample in this energy region.

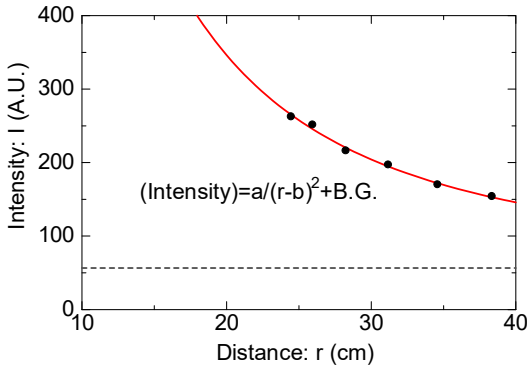

Fig. 1. Dependence of peak intensity of ^{10}B prompt gamma-rays on a distance between the prototype detector and the ^{10}B sample.

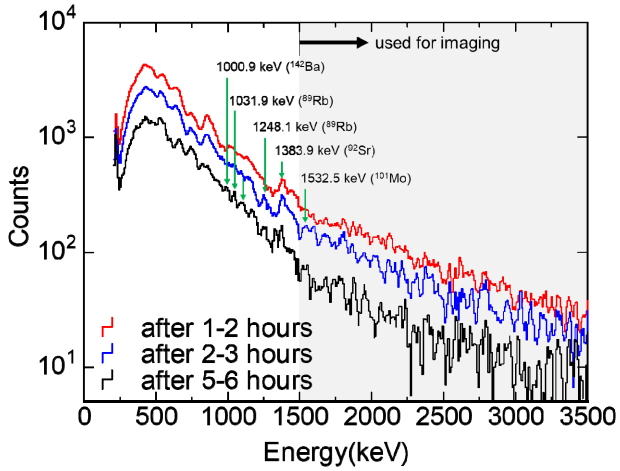

Fig. 2. Typical background subtracted energy spectra of delayed gamma-ray from the HEU sample after 1-2, 2-3, 5-6 hours of neutron irradiation.

REFERENCES:

[1] T. Takahashi, *et al.*, Proceedings ANIMMA, 1332,(2013).
[2] K. Uema *et al.*, JPS Conference Proceedings **24**, 011016 (2019).
[3] D.H. Beddingfield and F.E. Cecil, Nucl. Instrum. Meth. A **417**, 405-412 (1998).

.

CO2-2 Measurement of Doppler Effect by Small Accelerator Neutron Source (III)

T. Sano[1,2], J. Lee[1], J. Hori[1], Y. Takahashi[1], H. Unesaki[1], K. Nakajima[1]

[1]*Institute for Integrated Radiation and Nuclear Science, Kyoto University*

[2]*Atomic Energy Research Institute, Kindai University (Apr. 2019~)*

INTRODUCTION:

We have measured Doppler effect for metal samples which were Nb and Mo by TOF method at KURNS-LINAC since 2016 [1-2]. Doppler effect is depend on the sample and moderator temperature. In numerical calculation of Doppler effect for nuclear systems, the accuracy of neutron spectrum at the moderator is very important. When the moderator in a nuclear reactor is common material such as light-water, researchers and engineers could calculate the accurate neutron spectrum in the moderator by using evaluate nuclear data libraries such as the JENDL-4.0 [3]. On the other hand, if evaluate nuclear data libraries has poor data for moderator materials such as CaH_2, the calculations of accurate neutron spectrum in the moderator will be difficult. CaH_2 is compelling solid moderator for new small nuclear reactor [4]. Therefore, in order to perform a nuclear design for the reactor with CaH_2, it is necessary to experimentally investigate the temperature-dependent neutron spectrum in the moderator.

EXPERIMENTS:

To measure the temperature-dependent thermal neutron spectrum in CaH_2 sample, a preliminary experiment was conducted method in KURNS-LINAC. The CaH_2 sample was set in a heater to be increased the sample temperature from about 300K to 600K. Figure 1 shows the heater. The heater was installed at a positon of 12.6 m from the pulsed neutron source at KURNS-LINAC. In this experiment, a GEM type neutron detector has low sensitivity for gamma-ray from the neutron source was employed. Table 1 shows the experimental conditions and Table 2 is the sample information. The transmitted neutron flux from the sample was observed by the TOF method in the present study.

RESULTS:

Table 3 shows the observed and calculated mean energy of Maxwell peak in each temperature. Here, the numerical calculations were performed with MCNP [5] and JEFF-3.2. The change of the peak energies with increasing the sample temperature were observed, respectively. At the low temperature (21 and 119℃), the experimental data was agreed with the numerical calculations. On the other hand, there were about 13 eV difference of the peak energy between the numerical and the experimental result at 292 ℃. Figure 1 shows the measured and the calcu-lated neutron spectrums.

ACKNOWLEDGEMENTS

This research is a collaborative effort of Toshiba Energy Systems & Solutions, Tokyo Institute of Technology and Kindai University, Kyoto University. This study was supported by Toshiba Energy Systems & Solutions Corporation.

REFERENCES:

[1] T. Sano, *et. al.,* KURRI-Progress report 2016 (2016).
[2] T. Sano, *et. al.*, KURRI-Progress report 2017 (2017).
[3] K. Shibata, *et. al.,* J. Nucl. Sci. Technol., 39(11), (2002).
[4] R. Kimura, *et. al.,* Nucl. Sci. Eng, DOI: 10.1080/00295639.2019.1576454, (2019).
[5] C. J. Werner, Report No. LA-UR-17-29981, (2017).

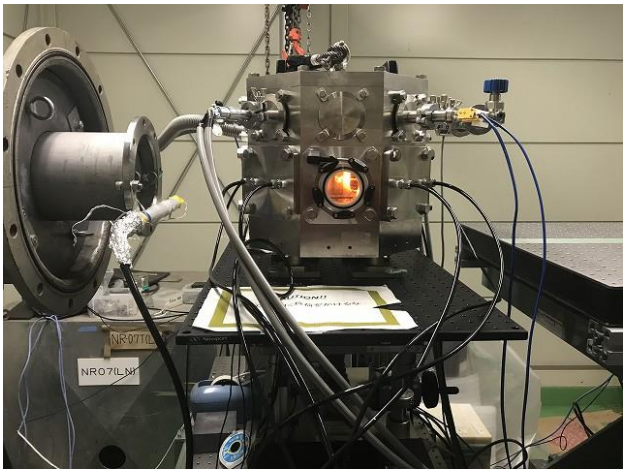

Fig.1 Heater.

Table 1 Experimental condition

Sample	LINAC operational condition (Frequency, pulse width, current)	Sample temperature (degree)	Measuring time (h)
CaH_2	40Hz, 3 μ s, 56 μ A	**21**	**10**
CaH_2	40Hz, 3 μ s, 56 μ A	**119**	**11**
CaH_2	35Hz, 3 μ s, 48 μ A	**292**	**12**
Blank	40Hz, 3 μ s, 56 μ A	**21**	**0.5**

Table 2 Sample information

Chemical formula	CaH_2
Density	1.33 g/cm3
Geometry	70 mm × 70 mm ×60 mm

Table 3 Observed mean energy of Maxwell peak in each temperature

Temperature (degree)	Experiment (eV)	MCNP (eV)
21	0.055±0.005	0.051±0.001
119	0.068±0.005	0.070±0.001
292	0.085±0.005	0.098±0.001

CO2-3 Development of neutron detectors for BNCT fields

T. Matsumoto, A. Masuda, H. Harano, H. Tomita[1], J. Hori[2], T. Sano[2] and Y. Sakurai[2]

National Metrology Institute of Japan, National Institute of Advanced Industrial Science and Technology
[1]Graduate School of Engineering, Nagoya University
[2]Institute for Integrated Radiation and Nuclear Science, Kyoto University

INTRODUCTION: Evaluation of neutron fluence and neutron dose equivalent for the epi-thermal neutron region is very important in work places with neutron sources or nuclear fuels as well as irradiation fields in a boron neutron capture therapy. In the present study, we have developed a precise epi-thermal measurement method that is not affected by nuclear reaction cross sections such as the ^{10}B(n,αγ), ^{3}He(n,p) and ^{6}Li(n,α) reactions. The epi-thermal neutron detection system for absolute measurement is composed of a 50 mm diameter and 5 mm thick LGB scintillation detector and two 50.8 mm diameter and 50.8 mm thick BGO scintillation detectors. In the present study, we tried to demonstrate the epi-thermal neutron measurements using a white neutron source including epi-thermal region. In addition, we have developed a current-mode neutron detector that can be used in intense neutron flux field such as BNCT fields. The neutron detector is composed of a ^{6}Li-glass and ^{7}Li-glass scintillators.

EXPERIMENTS: A collimated neutron beam was obtained by the photo neutron reaction using a water-cooled tantalum target at the KURRI Linac [1]. The LGB scintillation detector was set at the center of beam line. The BGO scintillation detectors were placed on both side of the LGB scintillation detector. For low energy neutrons, monoenergetic gamma rays with energy of 478 keV and alpha particles are produced in the LGB scintillation detector by the ^{10}B(n,αγ) reaction. The alpha particles and a part of gamma rays are observed with the LGB scintillator. The BGO scintillation detectors detects the rest of gamma rays. Characteristics of the neutron detection system were experimentally evaluated by means of the time-of-flight (TOF) method.

The current-mode neutron detector was demonstrated at the E-3 beam port of KUR. The linearity of the neutron detector output to neutron flux was measured.

RESULTS: Fig.1 shows the detection efficiency for 478 keV of the BGO scintillation detectors. Constant detection efficiency of BGO detectors for 478 keV from the LGB scintillator are successfully obtained. Therefore, the neutron fluence is obtained without using nuclear data by the epi-thermal neutron detector.

The response for 4 x 10^5 cm^{-2}s^{-1} neutron flux was obtained for the current-mode neutron detector using the E-3 beam port. The spatial distribution of relative neutron flux in the beam area of the beam port was evaluated using a small-sized ^{6}Li-glass scintillation detector with a plastic fiber. The linearity for the neutron flux region up to 4 x 10^5 cm^{-2}s^{-1} is confirmed as shown in Fig 2.

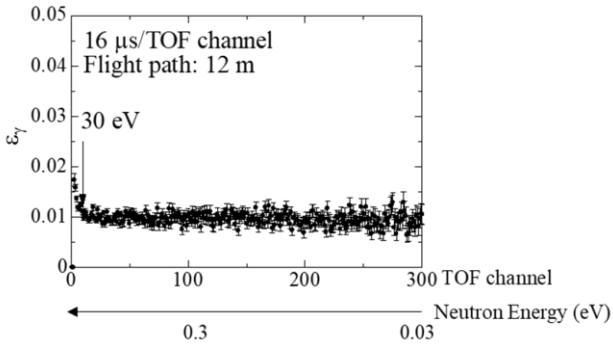

Fig. 1. Detection efficiency for 478 keV of the BGO scintillation detectors in the epi-thermal neutron detector

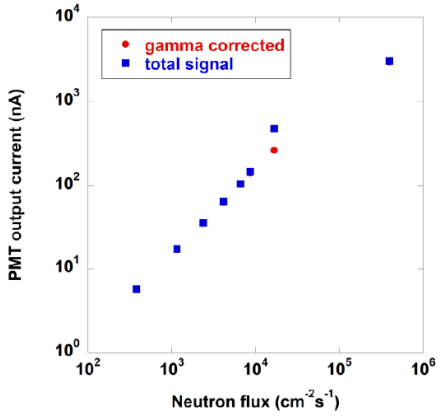

Fig. 2. Relation between the current output of the detector and neutron flux (cm^{-2}s^{-1})

REFERENCES:

[1] K. Kobayashi *et al.,* Annu. Rep. Res. Reactorinst. Kyoto Univ. 22, 142 (1989).

This work was supported by JSPS KAKENHI(JP16K21679, JP16K09030).

CO2-4 Study on the non-destructive nuclide assay for nuclear materials with a self-indication method

J. Hori[1], T. Sano[2], Y. Takahashi[1], J. Lee[1], and K. Nakajima[1]

[1]*Institute for Integrated Radiation and Nuclear Science, Kyoto University*
[2]*Graduate School of Science and Engineering, Kindai University*

INTRODUCTION: For decommissioning of Fukushima Daiichi Nuclear Power Plants, the identification and quantification of the nuclear material in fuel debris are important issues for appropriate nuclear material management. However, it is considered that fuel debris contains unknown amounts of minor actinides, fission products and neutron absorbers except for nuclear materials. Therefore, it is difficult to apply conventional non-destructive assay to fuel debris. Neutron Resonance Densitometry (NRD) is one of the candidate techniques of non-destructive nuclide assay applicable to quantity nuclear materials in fuel debris. Especially, a self-indication method [1] is considered as a suitable technique for the identification and quantification of nuclides in fuel debris.

In the self-indication method, an indicator consisting of the target nuclide is placed at the neutron beam downstream from a sample. The transmitted neutron thorough the sample can be measured indirectly by detecting the reaction products from the indicator with the neutron time-of-flight (TOF) method. The self-indicator is a transmission neuron detector that has high efficiency around the objective neutron resonance energies of the target nuclide, enabling us to quantify effectively the amount of resonance absorption of the target nuclide. Moreover, it is not easily affected by the decayed gamma-rays from the fuel. We carried out the examination of self-indication method for a nuclear material with highly enriched uranium-aluminum alloys.

EXPERIMENTS: The experiment was performed at the 46-MeV electron linear accelerator in Institute for Integral Radiation and Nuclear Science, Kyoto University. The linac was operated with a repetition rate of 50 Hz, a pulse width of 4 μs, a peak current of about 0.5 A, and an electron energy of about 30 MeV. We used a flight path in the direction of 135 degree with respect to the linac electron beam.

An ionization chamber was employed for the measurement of fission fragments from a self-indicator. The chamber is made of aluminum and is 40 mm in diameter and 39 mm in length, and the wall thickness of the chamber is about 2 mm. We used the highly enriched uranium oxide (99.91% of ^{235}U) which was electrodeposited on a stainless steel disk as a self-indicator. The distance between the electrode and the ^{235}U deposited layer in the chamber is 8 mm. The chamber is filled with a mixed gas of 97 % Ar and 3 % N_2 at a pressure of 1 atm.

The signals from the chamber were stored as a two dimensional data of TOF and Pulse-Height (PH). The fission events were selected by PH discrimination between pulses of α ray and fission fragment. The measurements with and without sheets of highly enriched uranium-aluminum alloys (93% of ^{235}U, HU filter) were performed, respectively. Each measurement time was about 40 hours.

RESULTS: The TOF spectra with and without HU filter are shown in Fig. 1. The large resonance peaks of ^{235}U were clearly observed at 1.13, 3.14, 6.99 and 9.70 eV. It can be seen that those resonance peaks were reduced by inserting the HU filter. The counting rates were estimated in thermal energy region from 0.002 to 1 eV and resonance region from 1 to 100 eV. The reduction ratios to the counting rate without the HU filter were obtained as 0.91±0.01 and 0.85±0.05 for thermal and resonance regions, respectively. The reduction in thermal region indicates the neutron absorption by all nuclei in the filter. On the other hands, the reduction in resonance region almost indicates the neutron resonance absorption by ^{235}U in the sample. In the present study, those ratios were good agreement since we used uranium-aluminum alloy with high purity as a filter. When we used a mixture filter, it is expected that the difference between the reduction ratios for thermal and resonance regions is observed. In next stage, we try to measure with a mixture filter and quantify the areal density of ^{235}U in the filter.

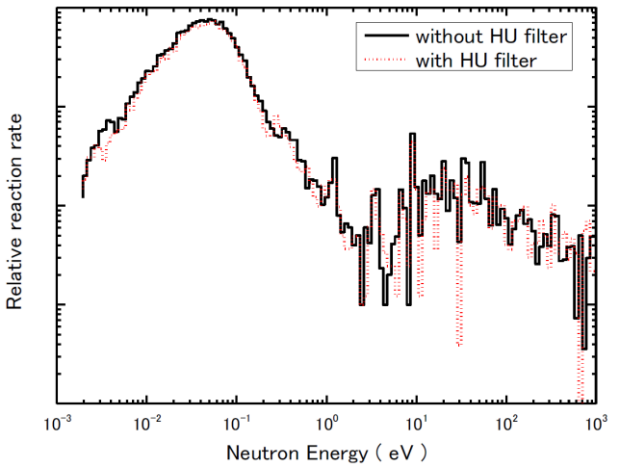

Fig.1 Comparison of TOF spectra for fission events of the ^{235}U indicator with and without HU filter

Present study was supported by JSPS KAKENHI Grand Number JP17K07012.

REFERENCES:

[1] J. Hori *et al.,* EPJ Web of Conferences, 146, 09042 (2017).

CO3-1 Local Two-phase Flow Characteristics for 6x6 Rod Bundle Geometry

Xiuzhong Shen, Shuichiro Miwa[1], and Yigeng Xiao[1]

Institute for Integrated Radiation and Nuclear Science, Kyoto University
[1]Faculty of Engineering, Hokkaido University

INTRODUCTION: The rod bundle two-phase flow is a commonly utilized configuration for nuclear reactor fuel assembly. In the state-of-the-art, the accuracy of the two-fluid model, the most comprehensive and detailed formulation to describe two-phase flow behavior, is heavily dependent on the constitutive equations to close their interfacial transfer terms. In order to develop reliable constitutive equations for rod bundle geometry, understanding of the local flow parameters and their profiles which describe their gas-liquid interaction behaviors is indispensable. In the current joint project between Kyoto University and Hokkaido University, adiabatic air-water two-phase flow experiment using 6×6 rod bundle geometry was carried out. The local void fraction, interfacial area concentration (IAC) and interface velocity were measured using in-house made double-sensor probe, which was manufactures using optical-fiber probe. The bubbly flow regime was selected for the test condition to investigate the phase distribution of the bubbles in spherical and distorted particle regimes. At a cross section of the rod-bundle test section in several axial locations, 16 measurement points were selected in the octant symmetric triangular zone.

EXPERIMENTS: The schematic of the test section utilized in the current project is shown in Fig. 1, which is located in the Institute for Integrated Radiation and Nuclear Science of Kyoto University. In order to visualize the flow behavior, the test section was made of transparent acrylic square duct wit ha cross0section of 100 mm x 100 mm casing. 36 aluminum rods with diameters of 10 mm were inserted inside the test section to form a 6 x 6 rod bundle geometry. These rods were placed 16.7 mm pitch length apart. The hydraulic diameter (D_H) of the test section was 18.7 mm and the overall height of the test section was 3 m. In order to prevent the vibration and unwanted flow disturbances, simplified spacer grids were installed at 4 different axial locations. These spacer grids also represent the actual spacer utilized in the light water reactor. The purified water was supplied from the centrifugal pump attached to the water tank and its volumetric flow rate was monitored by the electromagnetic flow meter. The compressed air was supplied from the air-compressor and its flow rate was monitored using mass-flow meter. They are injected into the mixing chamber located at the inlet section and well-mixed two-phase flow was injected into the test section. Pressure transducers as well as thermocouples were utilized to constantly monitor the axial pressure drop and fluid temperature for the determination of accurate physical parameters.

In the current phase of the project, the local flow parameters were measured using double-sensor optical probe. Measurements at 16 different positions at the axial location (z) of z/D_H=149 were successfully conducted. Both core-peaking and wall-peaking phenomena were observed, depending on the flow conditions. For the data processing, the double-sensor probe algorithm as well as interface-pairing scheme developed by the previous researchers were adopted [1]. In order to convert the local parameters into the area-averaged value, the method proposed by Yang et al. [2] was adopted. According to the methodology, the conversion coefficients of the subchannel center and the rod gap values were determined as 0.662 and 0.243, respectively. for core-peaking profiles and 0.479 and 0.430 respectively for wall-peaking profiles.

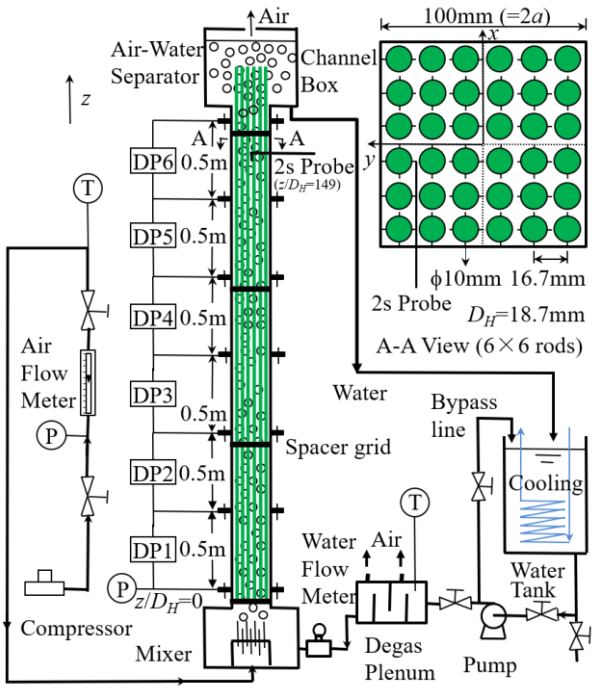

Fig. 1. 6x6 Rod Bundle Test Section [1]

RESULTS: For the local parameters obtained in the experiment, typical core-peaking and wall-peaking profiles in radial direction were confirmed in the present flow conditions. It was also found that the measured parameters in the rod gaps were much smaller than those in the center-region of the sub-channel. Based on the currently established area-averaged void fraction and IAC database, the drift-flux model and an IAC correlation were utilized to examine their accuracy, respectively. It was found that these models are capable of estimating the current experiment within 14.5% and 22.2% error, respectively.

REFERENCES:

[1] X. Shen *et al.*, Exp.Comp.Multiph. Flow, (2019) (In Press).
[2] Yang, X. *et al.,* Int. J. Heat Fluid Fl., Vol. 34, 85-97 (2012).

CO3-2 Basic Research for Sophistication of High-power Reactor Noise Analysis

S. Hohara[1], A. Sakon[1], K. Nakajima[2], K. Takahashi[2], K. Hashimoto[1]

[1]Atomic Energy Research Institute, Kindai University
[2] Interdisciplinary Graduate School of Science and Engineering, Kindai University

INTRODUCTION: Reactor noise for high-power reactors were actively measured in the 1960's and 1970's. The major focuses of those researches were for the abnormality diagnosis or the output stabilization diagnosis, and almost researchers were in the field of system control engineering or instrumentation engineering. High-power reactor noise measurements for dynamics' analysis of reactivity change, reactivity feedback or reactor characteristics itself were few in the time (1960's and 1970's), because of the powerless measurement system. In this research, we plan to measure KUR's output with present-day measurement system and plan to analyze with several analysis methods. The results of this work will supply some knowledges and technics in the aspect of sophistication of reactor noise analysis or simulation methods.

In this year, we tried to measure the reactor nuclide noise of the critical & subcritical state KUR core via the fission chambers which installed into the KUR control console. The experimental work was done in 30 January 2018, 13 – 14 September 2018 and in 2 October 2018. In the analysis of the experimental results, we found that some external electrical noises were inserted into the fission chambers' signals. The noises have bad effect on the analysis results of the reactor noise, and in some case, the noises cannot be separated from the reactor nuclide noise signals. The situation of the external electrical noise on the KUR control console's fission chamber line is reported in this paper.

EXPERIMENTS: In this experiment, the output signal was lined from the control console of KUR. The target signal was of the fission chamber #1 & #2. The signal was binarized in the control console as a 4V/0.5 μ sec-TTL signal. The signal was measured a time-series measurement system (HSMCA4106_LC: ANSeeN Inc.). A schematic view of the measurement is shown in Fig.1.

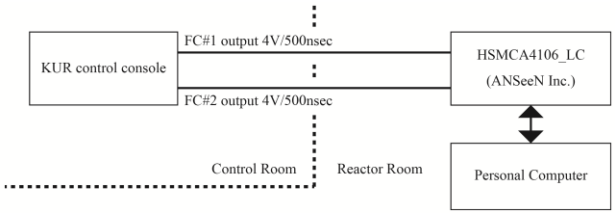

Fig. 1. Schematic view of the measurement.

The experimental condition is shown in Table.1. The criticality was set from -2.9% Δ k/k to critical state. No.1 – 3 were run on 30 January 2018, No. 4 were run on 13 – 14 September 2018 and No.5-10 were run on 2 October 2018. The restrictions of the reactor room IN/OUT were set on No.4-10.

Table 1. Experimental condition

No.	Criticality [% Δ k/k]	Measurement Time [sec]	Restrictions of Reactor Room IN/OUT
1	≈ - 2.9	7,200	×
2	≈ - 2.9	1,800	×
3	≈ - 2.9	1,400	×
4	≈ - 2.9	3,160	○
5	- 2.949	3,600	○
6	- 2.100	3,600	○
7	- 1.153	1,800	○
8	- 0.619	1,800	○
9	- 0.326	1,800	○
10	0 (0.3W)	600	○

RESULTS: The external noise incident was separated from the normal reactor noise by observing the msec order count rate data of each experimental result.

The number of the external noise incident is shown in Table 2. In No.10, the external noise incident cannot be separated from the reactor noise because of the high-count rate of the reactor noise itself.

From the result, it can be founded that the number of external noise incident is strongly related to the restrictions of reactor room IN/OUT. This shows that the external noise on KUR control console occurs with the operation of the reactor room door's interlock circuit or neighbor peripherals.

Generally, the noise link of different circuits is a result of the close connection of power line or ground line. The KUR control console power/ground line should be separated from the other peripherals to keep the control monitors clear from other noise sources. At least, the KUR control console detectors in the present situation are not suitable for the pulse-mode reactor noise measurement.

Table 2. The number of the external noise incident

No.	Number of Ext. Noise Incident	Ext. Noise Incident Rate [/hour]
1	3	1.5
2	4	8
3	3	7.7
4	0	0
5	2	2
6	0	0
7	0	0
8	1	2
9	0	0
10	—	—

CO3-3 Development of In-reactor Observation System Using Cherenkov Light (VIII)

T. Takeuchi, K. Yamamoto*, Y. Namekawa, N. Takemoto, K. Tsuchiya, T. Sano[1,**], H. Unesaki[1], Y. Fujihara[1], Y. Takahashi[1] and K. Nakajima[1]

Waste Management and Decommissioning Technology Development Center, JAEA
[1]Institute for Integrated Radiation and Nuclear Science, Kyoto University
* *Current affiliation: Nuclear Engineering Co., Ltd.,*
** *Current affiliation: Kindai University Atomic Energy Research Institute*

INTRODUCTION: On-line surveillance system which can visualize and quantitatively evaluate reactor statuses will contribute to reactor operation management. Development of an on-line reactor core imaging system using Cherenkov light started in 2009. Previously, reactor power of the KUR was successfully estimated from brightness Cherenkov light using a commercial CCD camera[1]. In this study, in order to assess of a developing Cherenkov light analyzing system, a long- and real-time estimation of the reactor power by the system was performed.

EXPERIMENTS: The CCD camera (AEC-100ZL, Q·I Inc.) was inserted into core-observation pipe of KUR during starting up, keeping the power at 5 MW, and shutting down. The output of the CCD camera had been collected as a movie file and it was used to real-time estimate the reactor power by a developing Cherenkov light analyzing system. Figure 1 shows the setting screen of the system, which was set to obtain the image brightness due to Cherenkov light in the area not overlapping with characters was obtained in real time. The conversion factor from brightness to reactor power was determined assuming that the brightness reached maximum at 5 MW.

RESULTS: Figure 2 shows the comparison of the reactor thermal power from the control system measure value and the estimated value by Cherenkov light. At the reactor start up, the image brightness by Cherenkov light corresponded well to the change of the reactor thermal power. During 5MW, the image brightness showed the behavior of gradually decreasing followed by recovering rapidly several times. After the shutdown, the image brightness decreased more gently than the heat output and showed a hunting-like phenomenon once. The gentle decrease is to be due to the Cherenkov light by radioactive decay of fission products remaining after reactor shutdown. On the other hand, as shown in fig. 2, the drop followed by recovery at 5 MW and the hunting after shutdown were found to be due to the adhesion of air bubbles followed by their detachment and the in-core cable, respectively.

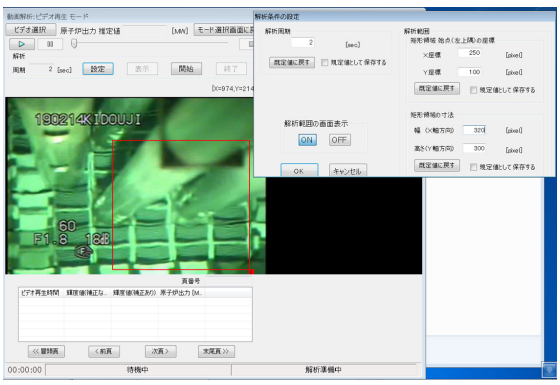

Fig. 1. The setting screen of the Cherenkov light analyzing system. The inside of the red border is analysis area.

CONCLUSION: As part of the development of the visible on-line core surveillance system, a long- and real-time estimation of the thermal power by brightness of Cherenkov light was performed in trial. As a result, It is found that it is necessary to consider the removal of the influence of air bubbles and reactor internals and the influence of FP on the image brightness.

REFERENCES:

[1] N. Ohtsuka, *et al.*, KURRI Progress Report 2013 (2015), P. 215.

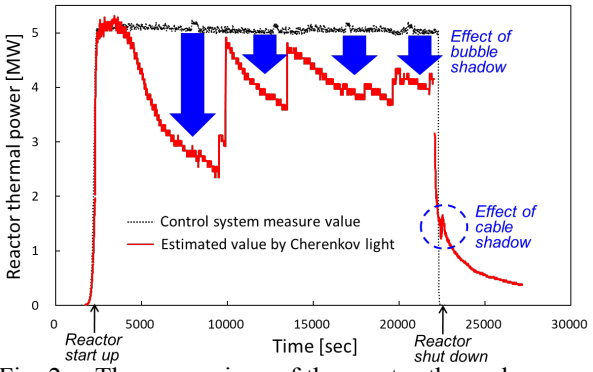

Fig. 2. The comparison of the reactor thermal power from the control system measure value and the estimated value by Cherenkov light.

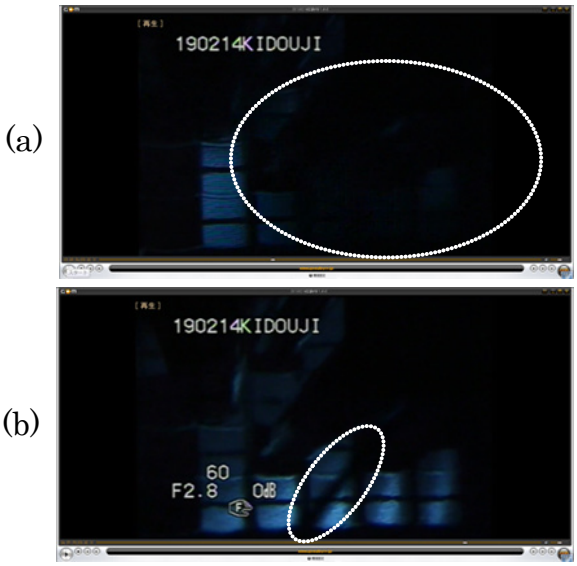

Fig. 3. The shadow of (a) bubble and (b) cable indicated by white dotted circles

30091

CO3-4 Measurements of β_{eff}/Λ in Accelerator-Driven System with 14 MeV Neutrons

C. H. Pyeon[1], M. Yamanaka[1], D. J. Lee[2] and H. J. Shim[3]

[1] *Institute for Integrated Radiation and Nuclear Science, Kyoto University (KURNS)*
[2] *Department of Nuclear Engineering, Ulsan National Institute of Science and Technology (UNIST), Korea*
[3] *Department of Nuclear Engineering, Seoul National University, Korea*

INTRODUCTION: The polyethylene-moderated (solid-moderated) core (A-core) has been designed at Kyoto University Critical Assembly (KUCA) for a subcritical reactivity estimation experiment. The accelerator-driven system (ADS) experiments were carried out at the A-core with 14 MeV neutrons, to estimate β_{eff}/Λ value with the combined use of reactivity in dollar units ($\rho_\$$) and prompt neutron decay constant (α) values obtained by the pulsed-neutron source (PNS) method and the Feynman-α method, respectively. At a near critical state, the value of β_{eff}/Λ was experimentally obtained with an injection of 14 MeV neutrons into the A-core, and examined soundly with the consideration of dependence of measured results on the detector position and kind.

EXPERIMENTS: The core configuration of ADS experiments with 14 MeV neutrons is shown in Fig. 1. "F" is a normal fuel assembly composed of uranium and polyethylene, and "p" is a polyethylene moderator assembly. Subcriticality was attained by full withdrawal of all control (C1, C2 and C3) and safety (S4, S5 and S6) rods from the core, and experimentally deduced by the PNS method (extrapolated-area ratio method): about 80 pcm. The characteristics of pulsed-neutron beams were as follows: 0.1 mA current, 20 Hz pulsed repetition and 97 μs pulsed width.

RESULTS: Experimental results were summarized as shown in Table 1. The values of α [1/s] and $\rho_\$$ [$] were obtained by the Feynman-α (Fig. 2) and the PNS methods, respectively. Moreover, with the combined use of α and $\rho_\$$, β_{eff}/Λ was deduced experimentally by the α-fitting method. As shown in Table 1, objective values of β_{eff}/Λ were observed remarkably to be valid at near critical state (80 pcm), although somewhat depending on the location of detector.

Table 1. Measured results of β_{eff}/Λ [1/s]

Detector	α [1/s]	$\rho_\$$ [$]	β_{eff}/Λ [1/s]
BF-3 #1	319.2 ± 71.6	0.023 ± 0.007	288.2 ± 93.3
BF-3 #2	364.0 ± 75.7	0.016 ± 0.005	223.4 ± 79.5
BF-3 #3	270.4 ± 13.9	0.019 ± 0.003	253.7 ± 37.3
Fiber #1	-	0.021 ± 0.006	243.4 ± 72.1
Fiber #2	268.8 ± 20.7	0.020 ± 0.003	225.4 ± 383.
Fiber #3	310.4 ± 43.0	0.026 ± 0.006	267.0 ± 62.6

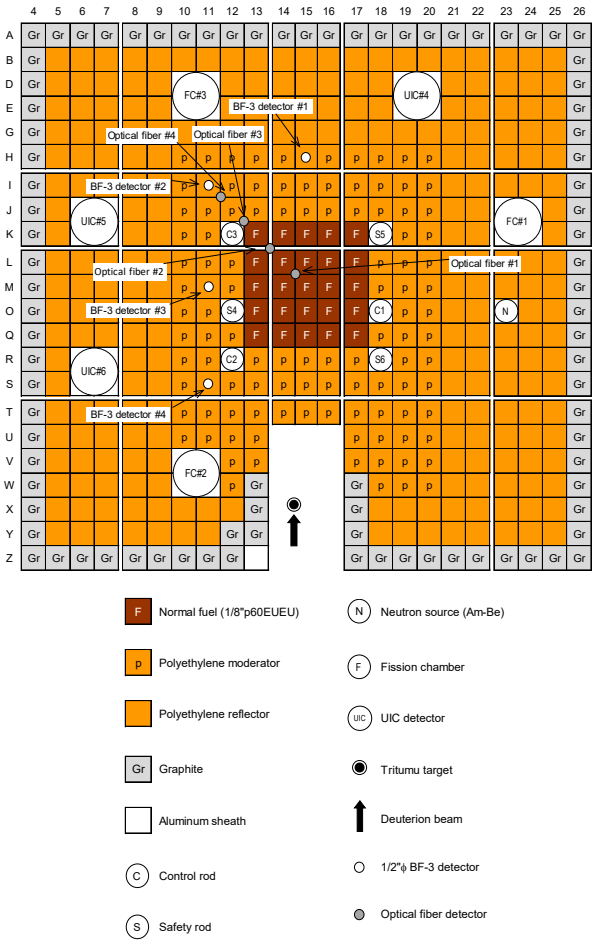

Fig. 1. KUCA core configuration

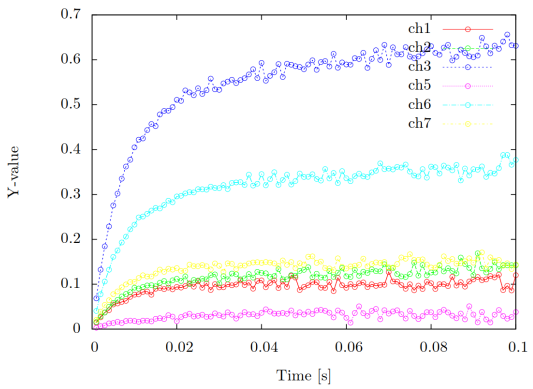

ACKNOWLEDGEMENT: This research was conducted under the International Collaboration Research between UNIST, Korea and Institute for Integrated Radiation and Nuclear Science, Kyoto University.

CO3-5 Transient Analyses of Kinectics on Accelerator-Driven System with 14 MeV Neutrons

C. H. Pyeon and M. Yamanaka

Research Center for Safe Nuclear System,
Institute for Integrated Radiation and Nuclear Science,
Kyoto University

INTRODUCTION: The Kyoto University Critical Assembly (KUCA) has a polyethylene-moderated (solid-moderated) core (A-core), and the accelerator-driven system (ADS) experiments were carried out at the A-core with 14 MeV neutrons, to monitor transients (Fig. 1) of kinetic parameters in time evolution with an injection of 14 MeV neutrons. To estimate prompt neutron decay constant (α), the pulsed-neutron source (PNS) and the Feynman-α method were applied to the ADS experiments.

EXPERIMENTS: The core configuration of ADS experiments with 14 MeV neutrons is shown in Fig. 2. Normal fuel "F" is a normal fuel assembly composed of uranium and polyethylene, and "p" is a polyethylene moderator assembly. Subcriticality was attained by full insertion of C1 control rod into and full withdrawal of control (C2 and C3) and safety (S4, S5 and S6) rods from the core, and experimentally deduced by the PNS method (extrapolated-area ratio method): about 1474 pcm (k_{eff} = 0.985). The characteristics of pulsed-neutron beams were as follows: 0.1 mA current, 20 Hz pulsed repetition and 97 μs pulsed width. Transient behavior of neutron counts was experimentally measured at the subcritical state in the time evolution raging between 1300 and 2800 s, as shown in Fig. 1.

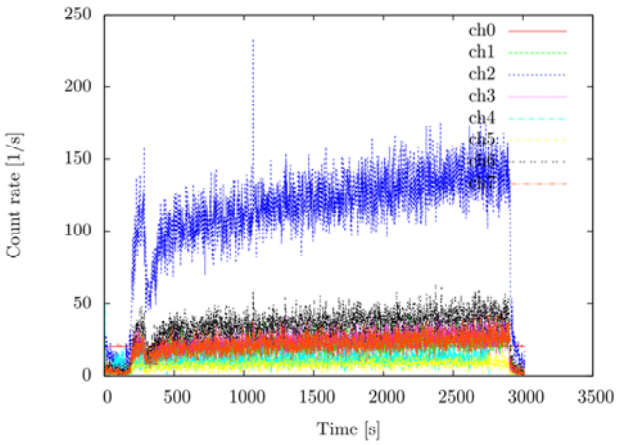

Fig. 1. Neutron counts with beam transients in time evolution ranging between 1300 and 2800 seconds

RESULTS: Experimental results were summarized as shown in Table 1. The values of α [1/s] were obtained by the PNS and the Feynman-α methods. As shown in Table 1, the α values by the two methods were observed to be valid at subcriticality level k_{eff} = 0.985, and resulted approximately in no difference between the measurement methodologies, within an allowance uncertainty. Also, the α values were found remarkably to be independent of detector positions, with in a relative difference of 5%, as shown in Table 1.

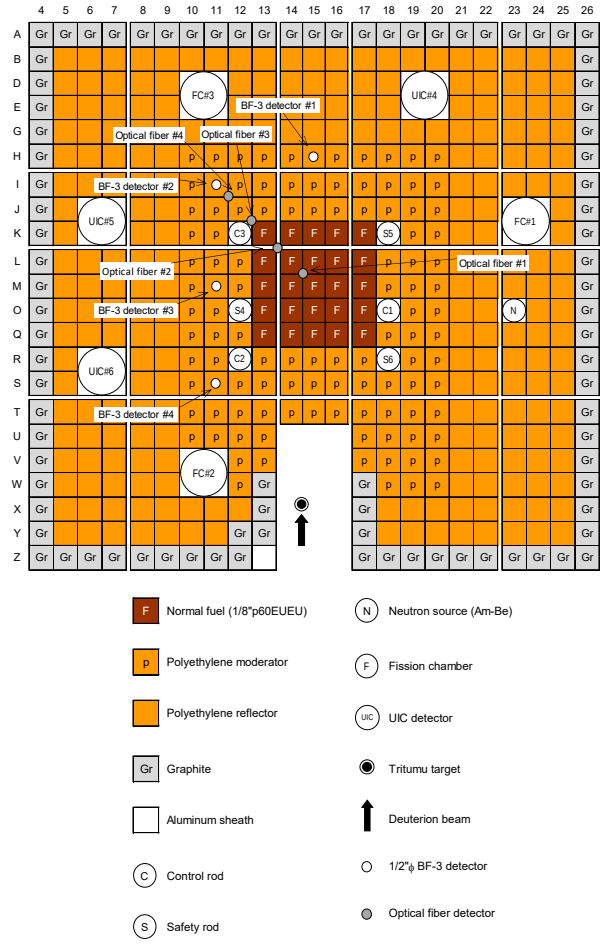

Fig. 2. KUCA core configuration with ADS experiments with 14 MeV neutrons

Table 1. Measured results of α values [1/s]

Detector	PNS method	Feynman-α method
BF-3 #1	528.3 ± 9.0	511.7 ± 7.9
BF-3 #2	528.9 ± 8.2	525.5 ± 6.5
BF-3 #3	532.6 ± 3.4	524.6 ± 2.7
Fiber #1	551.6 ± 16.0	519.0 ± 15.3
Fiber #2	531.1 ± 6.6	535.6 ± 5.6
Fiber #4	538.8 ± 7.9	524.4 ± 7.7

CO3-6 Data assimilation using subcritical measurements: reactor-noise measurement under the shutdown state, and transient experiments for source driven subcritical system

T. Endo[1], K. Watanabe[1], T. Ikeda[1], A. Nonaka[1], T. Sano[2], M. Yamanaka[2], C.H. Pyeon[2]

[1]*Graduate School of Engineering, Nagoya University*
[2] *Institute for Integrated Radiation and Nuclear Science, Kyoto University*

INTRODUCTION: In a general transient in a subcritical system, reactivity, neutron source intensity S, and point kinetic parameters (Λ and β_{eff}) can change simultaneously. The monitoring of the subcriticality by the conventional inverse kinetics is difficult for such a simultaneous transient, because time variations of neutron count rate due to these changes cannot be distinguished in the conventional inverse kinetics method, *e.g.*, the neutron source strength and the point kinetics parameters are assumed to be constant. To address this problem, authors investigate the application of the particle filter (PF) method [1,2] and the time-domain decomposition based integral (TDDI) method [3] to the subcriticality measurement. The purpose of this study is to demonstrate the PF method via subcritical transient experiments conducted at the Kyoto University Criticality Assembly (KUCA). Although the reactor-noise measurements under the shutdown-state and the preliminary experiments of the TDDI method were also conducted, this report focuses mainly on the results of the PF method.

METHODOLOGY: In the case of the PF method, probability distributions of state variables (neutron number density n, delayed neutron precursor density C_i, effective neutron multiplication factor k_{eff}, source strength of external neutron source S, and neutron generation time Λ) are approximated by histograms that consist of N particles having the state-variable vectors. Based on the state-variables at a previous times step, a priori histograms of the state-variables at next time step are calculated using the point kinetic equations. According to the time variation of measurement values (*e.g.*, neutron count rates), the histograms of state variables are successively updated based on the Bayes estimation. In this study, two detector-counts rates were utilized for the likelihood calculations to estimate simultaneously the changes of the reactivity $\rho=(k_{eff}-1)/k_{eff}$, S, and Λ: one is a BF_3 counter to detect mainly fission neutrons; the other is a neutron rem counter for beam monitor. The likelihood function was assumed to be a bivariate normal distribution, where the diagonal components were statistical errors of count rates and the covariance was neglected. To estimate Λ from k_{eff}, the relationship between k_{eff} and Λ was approximated by a linear regression model, which was evaluated using the continuous energy Monte Carlo code, MCNP6.2 [4] with JENDL-4.0u [5] for various control rods patterns and the shutdown state in the EE1 cores. In the PF method, the system noises of ρ and S at each time step were set in proportion to differences of successive count rates of BF_3 and rem counters, respectively. The system noise of Λ was determined by the prediction interval of the linear regression model of Λ with respect to ρ.

EXPERIMENTS: The transient experiments were carried out in subcritical EE1 cores driven by a D-T neutron source. As shown in Fig. 1, two time-variations of neutron count rates [cps] in the 2520 HEU-plates core were measured using a BF_3 counter at the axial center positions in the polyethylene-reflector region and the rem counter above the tritium target. At the time (i) shown in Fig. 1, the pulsed frequency of deuteron beam were changed from 20 to 100 [Hz]. Transients were given by inserting three control rods within the time-range between (i) and (ii). At the time (ii), 3×3 fuel and reflector assemblies were withdrawn for the shutdown. In the estimation of (ρ, S, Λ) using the PF method, the time step Δt and the total number of particles N were set to 1 [s] and 10000, respectively.

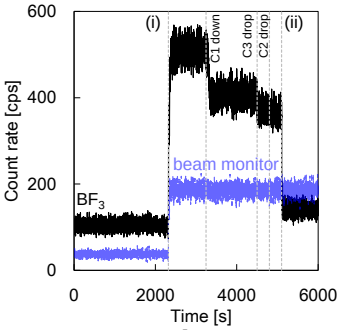

Fig. 1. Measured count rates.

RESULTS: The estimated results of ρ and Λ are presented in Fig. 2, where the reference values of ρ and Λ were numerical results evaluated by MCNP6.2 [4] with JENDL-4.0u [5]. Figure 2 shows that the estimated results of ρ and Λ agreed well with the reference values within 2σ except for after the time (ii), even when S was changed. In this study, Λ was expressed by a simple linear regression model with respect to ρ; thus, other measurements (*e.g.*, epithermal neutron count rate for spectrum index) may be useful to reduce the bias and uncertainty of the estimated results by the PF method.

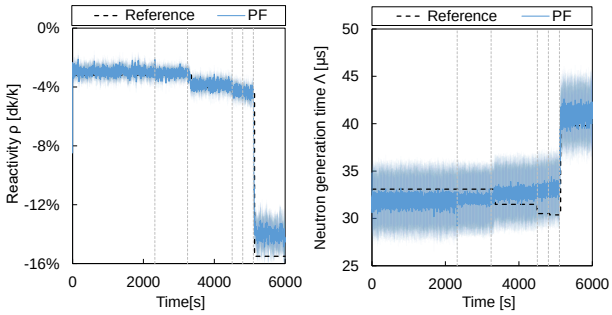

Fig. 2. Estimated results of ρ and Λ by PF method. Error bar represents ±2σ of N particles.

REFERENCES:

[1] G Kitagawa, J. Comput. Graph. Stat., **5** (1996) 1–25.
[2] T. Ikeda, *et al.*, Trans. Am. Nucl. Sci., **118** (2018) 851–854.
[3] A. Nonaka, *et al.*, Trans. Am. Nucl. Sci., **119** (2018) 1112–1115.
[4] C.J. Werner (editor), LA-UR-17-29981 2017.
[5] K. Shibata, *et al.*, J. Nucl. Sci. Technol., **48** (2011) 1–30.

CO3-7 Sample worth measurements with systematically changed mixing ratios of Lead and Bismuth in A-core of KUCA for ADS

M. Fukushima[1], A. Oizumi[1], M. Yamanaka[2] and C. H. Pyeon[2]

[1]*Nuclear Science and Engineering Center, Japan Atomic Energy Agency*
[2]*Institute for integrated Radiation and Nuclear Science, Kyoto University*

INTRODUCTION: The Japan Atomic Energy Agency (JAEA) has investigated neutronics of the accelerator-driven system (ADS) of a lead bismuth eutectic (LBE) cooled-tank-type core to transmute minor actinides discharged from nuclear power plants. For the design study of ADS, integral experimental data of nuclear characteristics of LBE is necessary to validate cross sections of lead (Pb) and bismuth (Bi). In present study, sample worth measurements were carried out with systematically changed mixing ratios of lead and bismuth, which would be complementary to the previous data of Pb and Bi samples individually measured in FY 2013 [1] and FY 2017 [2], respectively.

EXPERIMENTS: The reference configuration had five test rods, which was the same one as the previous experiments. The test fuel rods were composed of 40 test cells with two HEU fuel plates (1/16 inch thick×2) and two Al plates (1/16 inch thick×2) as shown in **Figure 1**.

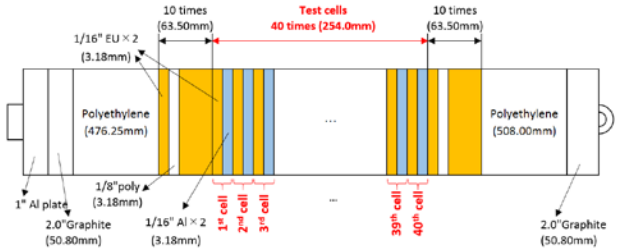

Figure 1. Schematic drawing of test fuel rod.

Table 1 Pattern of mixing ratios

Pattern	Mixing ratio Pb/(Pb+Bi)	# of plates		Cell locations with Pb plates*
		Pb	Bi	
1	100%	40	0	All cells
2	67.5%	27	13	1st, 2nd, 4th, 5th, …, 37th, 38th, 40th
3	50.0%	20	20	1st, 3rd, 5th, …, 37th, 39th
4	32.5%	13	27	3rd, 6th, 9th, …, 36th, 39th

* Bi plates were loaded in the other cells.

In sample worth measurements, 80 plates of Al (1/16 inch thick) were replaced with a total of 40 sample plates of Pb or Bi (1/8 inch thick) per each test rod. The mixing ratio of Pb and Bi plates was systematically changed as shown in **Table 1**. The pattern 1 equivalent to the previous one [1] was carried out to check reproducibility of sample worth measurements. **Table 2** shows the experimental results, together with the previous data for Pb and Bi samples individually. From the results of the pattern 1 (Pb:100%), good reproducibility was confirmed within experimental errors. **Table 2** also shows that the present results smoothly complement between two extremely data of the patterns 1 and 5. The sample worth measurements with systematically changed mixing ratios of Pb and Bi were successfully carried out from the viewpoint of reproducibility with the previous experiment.

Table 2 Experimental results

Pattern	Mixing ratio Pb/(Pb+Bi)	Measured reactivity worth (pcm)	
		Present	Previous
1	100%	156±4	156±8 [1]
2	67.5%	136±4	—
3	50.0%	124±4	—
4	32.5%	109±4	—
5	0.0%	—	84±3 [2]

RESULTS: Numerical analyses were preliminary conducted with MCNP6.1 together with JENDL-4.0 (J40) and ENDF/B-VII.1 (B71). The sample worth was estimated as the difference of the effective multiplication factors between the sample-loaded and reference configurations, without considering the criticality bias. **Figure 2** shows that the calculations by B71 agree with experimental data except for the pattern 1. On the other hand, the calculations by J40 overestimate for all the patterns. To clarify the cause of discrepancies in calculation accuracy between these libraries, nuclide-wise contributions were analyzed changing libraries from J40 to E71 for each nuclide. The discrepancies between them seem to be mainly due to differences in Al cross sections, not in Pb or Bi while the statistical errors should be still reduced.

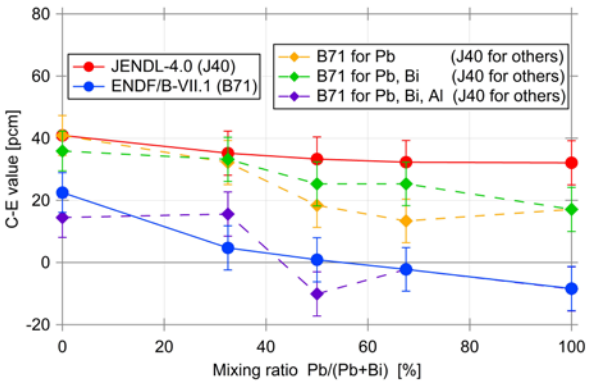

Figure 2. Calculation results (C– E values).

REFERENCES:

[1] C. H. Pyeon, *et al.,* J. Nucl. Sci. Technol., **53**, 602-612, (2016).
[2] C. H. Pyeon, *et al.,* J. Nucl. Sci. Technol., **55**, 1324-1335, (2018).

CO3-8 Measurement of Neutron Reaction Rate on Accelerator-Driven System combined with DT neutron source

N. Aizawa, D. Maeda, A. Sekiguchi, H. Machiya, M. Yamanaka[1] and C. H. Pyeon[1]

Graduate School of Engineering, Tohoku University
[1]Institute for Integrated Radiation and Nuclear Science, Kyoto University

INTRODUCTION: An accelerator-driven system (ADS) has been investigated to reduce the disposal burden of high-level radioactive waste by transmutation. The neutron reactions in the ADS core are dominated by neutrons with several MeV energy, but the contribution of several tens MeV neutrons to the reactions is not negligible. In addition, the multiplication factor k_{eff} ranges from 0.97 to 0.93 in the operation of an industrial scale ADS, and the influence of source neutrons on the total neutron multiplication is considered to vary with the multiplication factor. The experimental studies of the neutron reaction rates in the core region had been carried out in the previous studies with the use of KUCA A-core combined with DT (deuterium-tritium) neutron source [1-2]. DT neutron source is effective to examine the influence of the neutrons below 14 MeV. However, the subcriticalities set in the previous studies were very shallow (0.999 ~ 0.98 in k_{eff}). The purpose of the present study is to examine the influence of the subcriticality on the neutron reactions through the foil activation method by changing the k_{eff} in range of the industrial-scale ADS operation.

EXPERIMENTS: The ADS experiment was performed in PE (polyethylene) moderated uranium core combined with DT neutron source. Figure 1 shows the core configuration. The fuel assembly (1/8"p60EUEU) was composed of 60 unit cells (unit cell: 1/8" PE plate + two 1/16" uranium plates). The subcriticality was set from 1396 to 8752 pcm (0.986 to 0.920 in k_{eff}) by changing the number of fuel assembly. In, Al, Fe, Au foils were employed for the measurement of the neutron reaction rates on the basis of the various reaction threshold energies, and were set at (M-O, 15), and In wire was set along (L-Z', 16-17) to measure the reaction rate distributions of ^{115}In(n, γ) ^{116m}In and ^{115}In(n, n') ^{115m}In, which were sensitive to thermal and the fast neutrons, respectively.

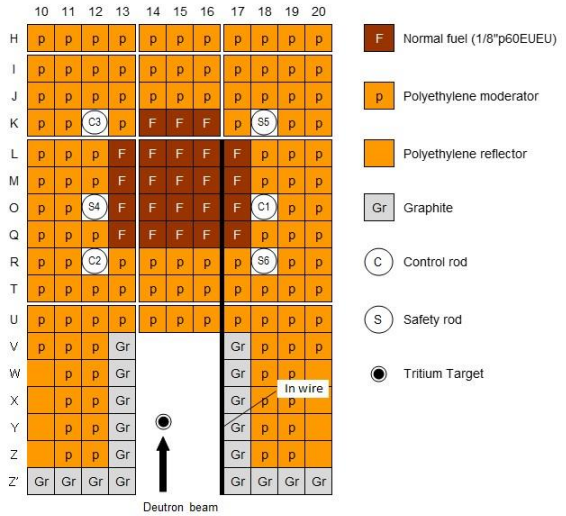

Fig. 1 Core configuration of KUCA A-core

RESULTS: Figure 2 shows the reaction rates of each foil in the various subcrilicalities. The measured reaction rates tended to decrease as the subcriticality became deeper due to the thermal power decrease. (The reaction rates of Al and Fe foils were not obtained due to the small thermal power in deep subcriticalities.) Their calculation/experiment values showed the almost stable values in the same trends as the previous studies. The one example of the measured reaction rate distributions is shown in Fig. 3. The peaks in ^{115}In(n, γ) ^{116m}In and ^{115}In(n, n') were seen in the PE and fuel regions, respectively, and their distributions were considered to reproduce the thermal/fast neutron distributions well in the core.
On the basis of the measured reaction rates, the effect of source neutrons on the reaction rates and the core characteristics is discussed as future works.

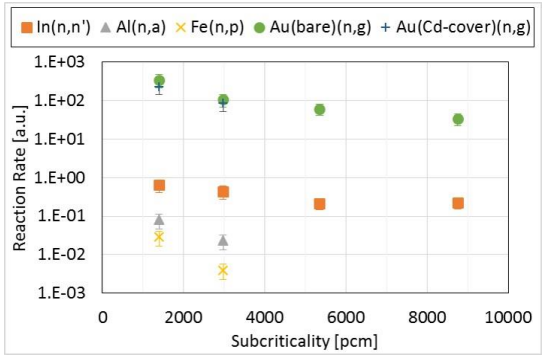

Fig. 2 Reaction rate variations with different subcriticalities

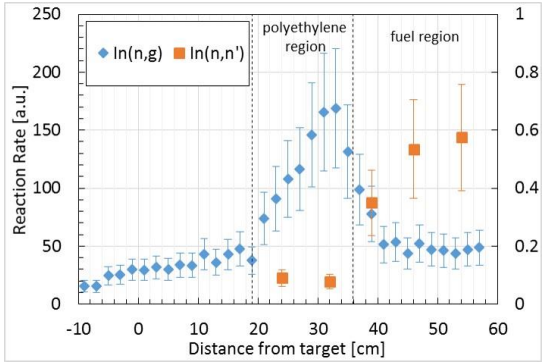

Fig. 3 Measured reaction rate distributions at the subcriticality of 2972 pcm

REFERENCES:

[1] C. H. Pyeon, *et al.*, J. Nucl. Sci. Technol., **46**(10) (2009) 965-972.
[2] C. H. Pyeon, *et al.*, Ann. Nucl. Ene., **40** (2012) 229-236.

CO3-9 Reactor Noise Power-Spectral Analysis for a Graphite-Moderated and -Reflected Core

A. Sakon, K. Hashimoto, S. Hohara, K. Nakajima[1], K. Takahashi[1], Y. Fukaya[2], and T. Sano[3]

Kindai University Atomic Energy Research Institute
[1]Graduate School of Science and Engineering, Kindai University
[2]Sector of Fast Reactor and Advanced Reactor Research and Development, Japan Atomic Energy Agency
[3]Institute for Integrated Radiation and Nuclear Science, Kyoto University

INTRODUCTION: In light-water- or polyethylene-reflected thermal reactors, neutron detector for a reactor noise analysis must be placed closely to core region to observe neutron correlation information. In graphite-reflected thermal reactors, however, the detector may be placed far from the region. This is because mean free path of neutrons in graphite is longer than that in water or polyethylene. The objective of this study is experimentally to confirm a high flexibility of neutron detector placement in graphite reflector for reactor noise analysis.

EXPERIMENTS: The core configuration is shown in Fig. 1. "F" denoted a low-enriched fuel assembly, whose average enrichment is 5.41wt%. "D" is a driver highly-enriched fuel assembly. "G" is graphite reflector. Orange cell is polyethylene reflector. "1", "2" and dots are BF_3 proportional neutron counters (1.0 in. dia., 15.47 in. len.). In a critical state, reactor noise analysis was carried out using BF_3 detector "1" and "2". The distance from core region to detector "1" is about 35cm, and that to detector "2" is about 30cm.

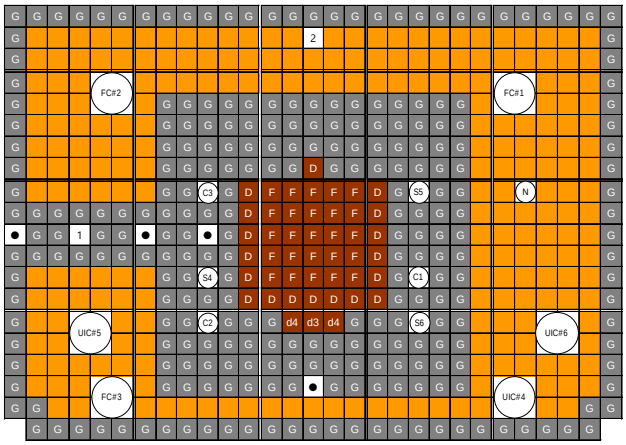

Fig. 1 Core configuration
(B7/4"G2/8"p8EUNU+3/8"p38EU)

RESULTS: Auto-power spectral densities obtained from detector "1" and "2" are shown in Fig. 2 and Fig. 3, respectively. These figures also include least-squares fits of a conventional formula [1] to the spectral densities to determine the prompt-neutron decay constant α_0 (β_{eff}/Λ), where the fitting was confined to a frequency range from 1.25 to 50 Hz. These derived decay constants 67.9±8.2 and 63.3±14.5 [1/s] were consistent with 63.1 [1/s] calculated by the continuous-energy Monte Carlo code MVP version 3 [2] within statistical uncertainty. As can be seen from these figures, however, the correlated component is being buried in the uncorrelated component and the fitting of Fig.3 is severer than that of Fig.2. This is because the detection efficiency of detector "2" is much lower than that of detector "1". The lower efficiency is expected to be responsible for the two-layer polyethylene reflector between detector "2" and graphite reflector. It is confirmed that reactor noise analysis is possible using a detector placed at least 35cm far from core region. The further data analysis is in progress.

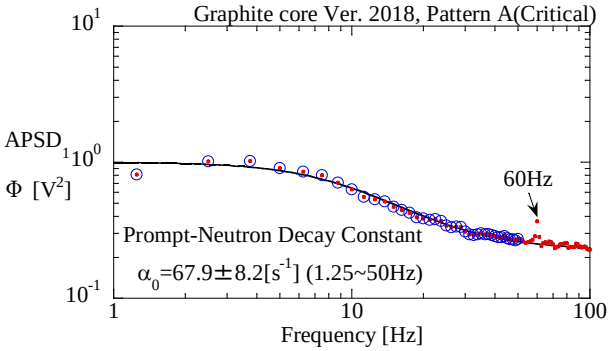

Fig. 2 Auto-Power Spectral Density (Detector "1")

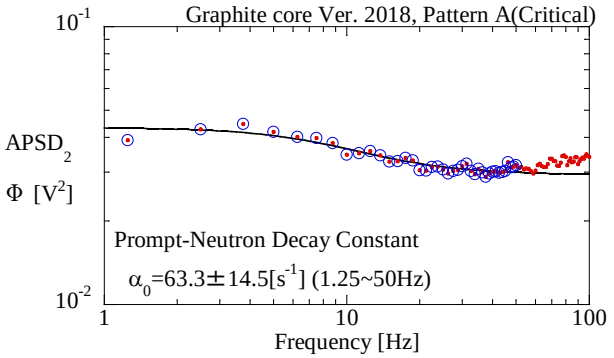

Fig. 3 Auto-Power Spectral Density (Detector "2")

REFERENCES:

[1] M. M. R. Williams, Random Processes in Nuclear Reactors, (Pergamon Press, Oxford,1974), section 3.6.
[2] Y. Nagaya, K. Okumura, T. Sakurai and T. Mori, MVP/GMVP Version 3 : General Purpose Monte Carlo Codes for Neutron and Photon Transport Calculations Based on Continuous Energy and Multigroup Methods, Tokai-mura: Japan Atomic Energy Agency; 2017, (JAEA-Data/Code 2016-018).

CO3-10 Measurement of ^{238}U(n,γ) γ ray from Subcritical System (2)

Y. Nauchi, S. Sato, M. Suzuki, T. Sano[1*] and H. Unesaki[1]

Central Research Institute of Electric Power Industry
[1]Institute for Integrated Radiation and Nuclear Science, Kyoto University.
**Current Affiliation: Atomic Energy Research Institute, Kindai University.*

INTRODUCTION:

Application of the burn-up credit (BUC) is promising for efficient storage and transport of irradiated fuel. To take BUC, measurements are required to certify the residual fissile enrichment of the fuel. For a fresh uranium fuel, the ^{235}U enrichment can be determined by measuring γ rays from decay of ^{235}U and daughters of ^{238}U. However, the method is not available for the irradiated fuel due to intense γ ray radiation from fission products (FP). The highest energy of FP γ ray is around 3.4 MeV. We have measured γ rays of 4.06 MeV from ^{238}U(n,γ) reactions [1] and those of a continuum spectrum (3-8 MeV) from fission reactions [2]. Those γ rays might be measured for the irradiated fuel since the energy is higher than that of FP γ rays. Accordingly, the γ ray pulse height spectra were studied for subcritical cores of different ^{235}U enrichment.

EXPERIMENTS:

In the KUCA-A core, two kinds of subcritical cores of A1/8"p60EUNUNU and A1/8"p70EUNU fuel cells were mocked up with U-Al fuel plates of 93wt% ^{235}U (EU) and the metal uranium of the natural enrichment (NU). The average enrichments of those were 3.1 and 5.4wt%, respectively. In the both cores, 14 fuel cells were loaded as shown in **Fig. 1**. The center of the core was void and the start-up neutron source of Am-Be was inserted. The fuel cells were surrounded by polyethylene and graphite cells. The γ rays from the ^{238}U(n,γ) reactions and the fissions were measured with a HP-Ge detector of 30% relative efficiency. Between the fuel cells and the HP-Ge detector, polyethylene blocks of 35 cm thickness were loaded to shield the detector from the neutron irradiation. From the source, 4.44 MeV γ rays are radiated after de-excitation of ^{12m}C produced by ^{9}Be(α,n)^{12m}C reactions. To reduce the 4.44MeV γ rays from the source, Pb-Bi plates of 15.2 cm thickness is loaded.

RESULTS:

In Fig. 2, the measured γ ray spectrum for A1/8"p60EUNUNU is shown. Different from the previous study where ^{252}Cf was as the neutron source [1], the pulse height spectrum of γ rays from ^{12m}C are significant in spite of the Pb-Bi shield. Another possible source of this component might be the inelastic scattering of ^{12}C induced by the primary neutron from the Am-Be source since the average neutron energy of Am-Be is higher than that of ^{252}Cf [3]. For all these γ rays from ^{12m}C and the fission, the peak spectrum of 4.06 MeV was identified. The counting statistics of the peak are less than 11 % for the both cores. The fission γ ray spectra are overwrapped by those from ^{12m}C below 4.5MeV. Then the relative fission γ ray count rates were assessed by integrating the spectrum over a region from 4.6 to 5.0 MeV. Then the count rate ratio of the 4.06 MeV peak to the fission was evaluated as listed in **Table 1**. The ratio decreases by 46% from A1/8"p60EUNUNU to A1/8"p60EUNU. The relative decrement is consistent with the variation of the number ratio of ^{238}U / ^{235}U loaded in the two cores within the counting statistics of the γ rays. The consistent result indicates the feasibility to determine the enrichment ^{235}U/U of fuel by the way of the neutron induced γ ray spectroscopy.

REFERENCES:

[1] Y. Nauchi *et al.,* KURRI progress report 2017 CO3-6, 2018.
[2] Y. Nauchi *et al.,* Journal of Nuclear Science and Technology, 52(7-8), 1074-1083, 2015.
[3] ISO-8259-1, 2001.

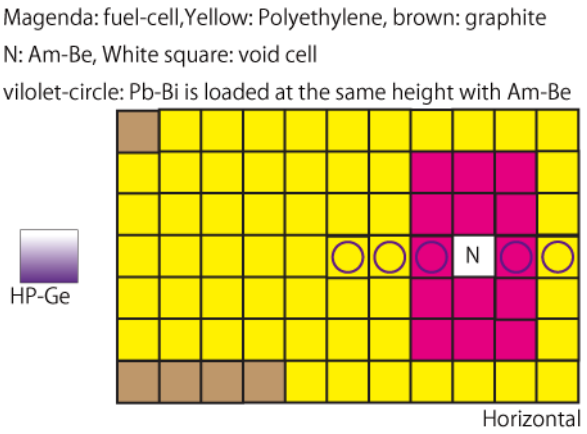

Fig. 1 Mocked up sub-critical core and detector.

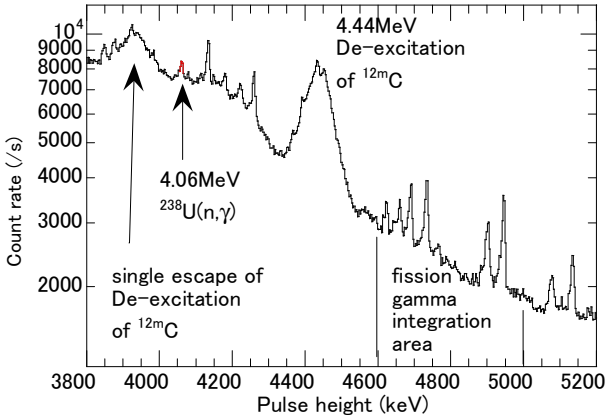

Fig. 2 γ ray spectrum for core of 3.1wt% ^{235}U.

Table 1 Count rate ratio of γ ray and ^{238}U/^{235}U

Fuel cell	Count rate ratio 4.06MeV/fission	Nuclide density ratio 238U/235U
EUNUNU(3.1wt%)	0.00796	30.6
EUNU(5.4wt%)	0.00431	17.3
EUNUNU/EUNU	0.541	0.563

CO3-11 Epithermal Neutron Capture Reactivity of Accident Tolerant Control Rod Materials

H. Ohta[1], Y. Nauchi[1], K. Nakamura[1], S. Sato[1], T. Sano[2*] and H. Unesaki[2]

[1]*Nuclear Research Technology Laboratory, Central Research Institute of Electric Power Industry*
[2]*Institute for Integrated Radiation and Nuclear Science, Kyoto University*
[*]*Present affiliation: Atomic Energy Research Institute, Kindai University*

INTRODUCTION: Since current control rods or blades for light water reactors (LWRs) using Ag-In-Cd alloy or B_4C may be damaged and relocated from the core prior to serious fuel rod failure during severe accident (SA), the Central Research Institute of Electric Power Industry is developing an accident tolerant control rod (ATCR) applying the novel neutron-absorbing materials based on a mixture of RE_2O_3-MO_2 (RE = Sm or Eu, M = Zr or Hf). The ATCR improves the reactor shutdown margin and neutronic lifetime, and reduces the risk of re-criticality accident in any reactor conditions including SAs. A reactivity analysis of ATCR in the representative LWRs indicated that those candidate materials have enough reactivity worth comparable to or higher than the conventional neutron absorbing materials Ag-In-Cd alloy or B_4C [1]. Furthermore, the reactivity worth of RE_2O_3-MO_2 in the thermal neutron field was validated with a criticality experiment [2]. In addition, the applicability of ATCR to the neutron spectrum hardening cores such as a mixed oxide fuel reactor is required in the future. This study aims to validate the epithermal neutron capture reactivity of RE_2O_3-MO_2.

EXPERIMENTS: A critical core with thermal neutron spectrum (E3 core) was assembled in A-core of Kyoto University Critical Assembly (KUCA) as shown in Fig. 1. The unit cell of fuel assemblies is composed of a 93% enriched ^{235}U-Al alloy fuel plate of 2"×2"×1/16" and 3 polyethylene plates of 2"×2"×1/8"/plate. An Al-holder with an inner diameter of 1.2cm and a depth of 1.969cm lined with a 0.5 mm thick Cd foil, containing a mixed powder sample of RE_2O_3-MO_2 was loaded in the center of core. A prior analysis of neutron flux distribution by the continuous-energy Monte Carlo code MVP showed that low energy neutrons less than 0.25 eV are almost completely removed by the 0.5mm thick Cd lining, as shown in Fig. 2. The reactivity worth of each sample was measured with the period method and analyzed using MVP code with 2.58 billion neutron histories. The statistical error of

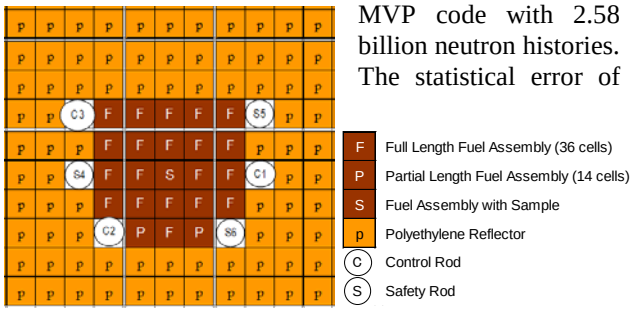

Fig. 1 Configuration of E3 core assembled in KUCA.

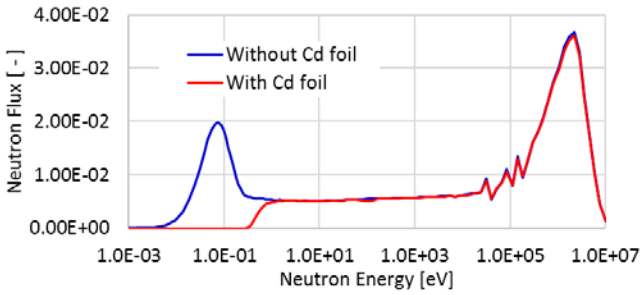

Fig. 2 Thermal neutron removal by 0.5mm thick Cd foil.

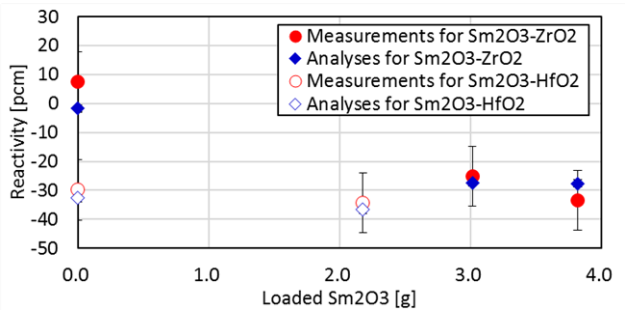

Fig. 3 Measurement and analysis results of reactivity for Sm_2O_3-ZrO_2 or Sm_2O_3-HfO_2.

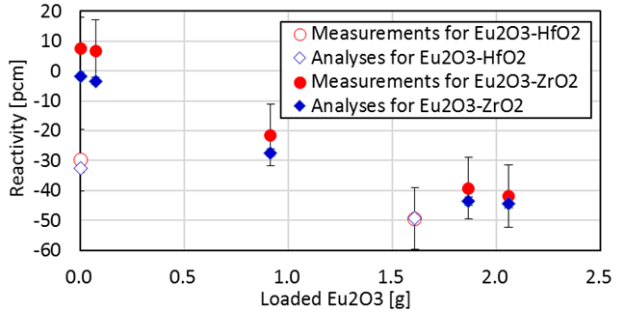

Fig. 4 Measurement and analysis results of reactivity for Eu_2O_3-ZrO_2 or Eu_2O_3-HfO_2.

reactivity analysis was less than 1.5pcm. The neutron cross section libraries were generated using JENDL- 4.0.

RESULTS: The measurement results of the epithermal neutron capture reactivity for mixed powders of Sm_2O_3-MO_2 and Eu_2O_3-MO_2 are shown in Figs. 3 and 4, respectively in comparison with the analysis results. The experimental uncertainty of 10.4pcm was determined from the variation in 6 times measurements of the void sample reactivity. For all samples, the reactivity worth was predicted within the range of the experimental uncertainty. From these results, validity of neutron capture reactivity of Sm, Eu, Zr and Hf in the epithermal energy region was confirmed. As confirmed by the reactivity worth analysis in the mixed oxide fuel loaded LWRs, RE_2O_3-MO_2 is considered to be applicable as the alternative control materials.

[1] H. Ohta, *et al*., *Top Fuel 2016*, 17556 (2016).
[2] H. Ohta, *et al*. *Trans. 2018 ANS winter meeting*, Vol. 119, pp425-428 (2018).

CO3-12 Reactor Physics Experiment in Graphite Moderation System for HTGR (I)

Y. Fukaya, S. Nakagawa, M. Goto, E. Ishitsuka,
S. Kawakami, T. Uesaka, K. Morita, and T. Sano[1]

Sector of Fast Reactor and Advanced Reactor Research and Development, Japan Atomic Energy Agency
[1]Institute for Integrated Radiation and Nuclear Science, Kyoto University

INTRODUCTION: The Japan Atomic Energy Agency (JAEA) started the Research and Development (R&D) to improve nuclear prediction techniques for High Temperature Gas-cooled Reactors (HTGRs). The objectives are to introduce generalized bias factor method [1] to avoid full mock-up experiment for the first commercial HTGR and to introduce reactor noise analysis to High Temperature Engineering Test Reactor (HTTR) experiment. To achieve the objectives, the reactor core of graphite moderation system named B7/4"G2/8"p8EUNU+3/8"p38EU (1) was newly composed in the B-rack of Kyoto University Critical Assembly (KUCA). The core plays a role of the reference core of the bias factor method, and the reactor noise was measured to develop the noise analysis scheme. In addition, training of operator of HTTR [2] was also performed during the experiments.

EXPERIMENTS: The core configuration is shown in Fig.1 "F" is the fuel assembly composed of 8 unit cells, which include a 1/16" thickness enriched uranium plate, a 1 mm thickness natural uranium plate, three 1/2" thickness graphite plates, a 1/4" thickness graphite plate, and two 1/8" thickness polyethylene plates, with axial graphite reflectors. The fuel plates (5.41 wt%) was designed to realize the averaged fuel enrichment of HTTR (5.9 wt%). The polyethylene plate was used to mimic the HTTR spectrum. "D" stands for the driver fuel assemblies composed of 38 unit cells, which include a 1/16" thickness enriched uranium plate, and, three 1/8" thickness of polyethylene, with axial graphite reflector. "d" stands for the partial length driver fuel to adjust criticality.

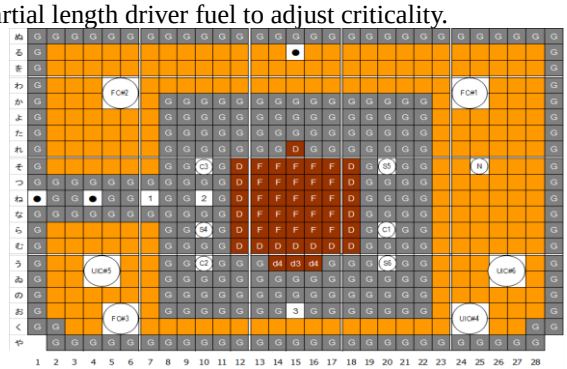

Fig. 1 Core configuration (Experiment)

RESULTS: Figure 2 shows the inverse count rate in an approach to criticality. The detector positions are slightly different with the experimental core shown in Fig.1. Calculated curve is also shown in the figure. The calculation is performed by MVP code which is neutron transport code based on Monte Carlo method with evaluated nuclear data library of JENDL4.0. The calculation curve is obtained only with considering multiplied neutrons. However, in the actual core, directly achieved neutrons from neutron source are also counted in the detectors. Therefore, the curves by the fission chamber from FC#1 to FC#3 are observed upper side of the calculated curve. The trend is significant for that of FC#1 because it is deployed near the neutron source. Finally, the core was reached to criticality with 930 enriched fuel plates and 7 steps of the approach to criticality.

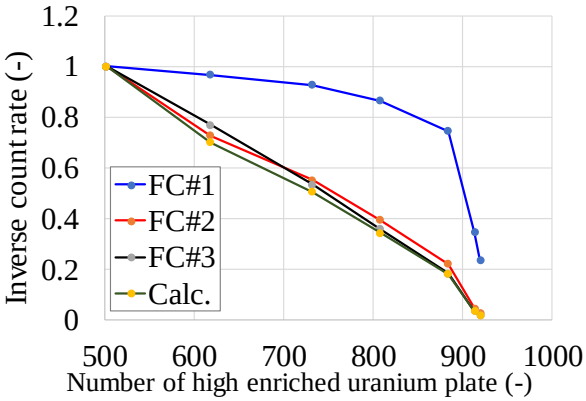

Fig.2 Inverse count rate

After that, reactivity worth of the core was measured. It is summarized in Table 1 with C/E values. The calculations were performed with JENDL4.0, ENDF/B7.0, and JEFF3.2. The experimental values were evaluated by period method for excess reactivity, by rod drop method for control rod, and center rack. Therefore, the C/E value of the center rack is large because the drop velocity of center rack is slow and against the assumption. For other reactivities, the calculations show a good agreement with the experimental values.

Table 1 Measured reactivity and C/E value

	Reactivity	C/E		
	(%Δk/k)	J40	B70	F32
Excess	0.200	1.48	1.19	1.32
Control rod C1	0.871	1.22	1.23	1.20
Control rod C2	0.581	1.15	1.14	1.10
Control rod C3	0.530	1.13	1.12	1.14
Center core	1.813	2.15	2.13	2.13

By the calculation, the well thermalized neutron spectra in fuel assemblies were observed as well. Sensitivity coefficients similar to HTGR were expected to prepare the data base for the generalized bias factor method.

Moreover, reactor noise was also measured. Not only pulse signal for Feynman-α method, but also continuous signal for power spectrum method smoothed by pump circuit were measured.

REFERENCES:

[1] T. Sano, T. Takeda, J. Nucl. Sci. Technol.,43[12] (2006). 1465-1470.
[2] E.Ishizuka, et al., University of Tokyo, UTNL-R 0499 (1969). 9-1.

CO3-13 Measurement of Miner Acinides Reaction Rate Ratio in KUCA (4)

T. Sano[1,2], J. Hori[1] , J. Lee[1], Y. Takahashi[1], M. Yamanaka[1]
C. H. Peyon[1]

[1]*Institute for Integrated Radiation and Nuclear Science, Kyoto University*
[2]*Atomic Energy Research Institute, Kindai University (Apr. 2019~)*

INTRODUCTION:

In order to perform integral evaluation of neutron cross section for minor actinides (MAs), measurements of reaction rate ratios which are MAs/^{235}U fission rate ratio and MAs/^{197}Au at KUCA has been carried out [1]. The measured reaction rate ratio had been ^{241}Am/^{235}U fission rate ratio, ^{237}Np/^{235}U fission rate ratio and ^{237}Np/^{197}Au capture rate ratio at various neutron spectrum fields, respectively. In those experiments, impurities, especially ^{239}Pu in the MAs has not been quantified, exactly. There is some possibility that the fission rate ratios has over estimated, because ^{239}Pu has very large fission cross section in thermal energy region.

Then, the ^{241}Am/^{235}U fission rate ratio in KUCA A core was measured. The ^{241}Am sample which was quantified the amount ^{239}Pu as impurity.

EXPERIMENTS:

An A1/8"p60EUEU core to measure the fission rate ratio was constructed at KUCA A core. A unit cell in the 1/8"p60EUEU fuel element has 2 enriched uranium fuel plates and 1 1/8" thickness polyethylene plate. The core has a void region in the center of core and the Back-to-back (BTB) fission chamber is inserted into the void region as shown in Fig.1. The 241Am foil and 235U foil were set in the BTB fission chamber. The sample information are shown in Table 1. ^{239}Pu in Am sample had been identified and quantified with TOF measurement at KURNS-LINAC [2]. Using BTB fission chamber, a MA foil and a ^{235}U foil are able to irradiate in the neutron spectrums, simultaneously.

In the experiment, the operational condition shows Table 2 and the irradiation time was 240 min.

RESULTS:

Figure 2 shows the PH spectrum from the BTB fission chamber. In the figure, the signals from 500 to 3000 channel are due to 241Am fission events. From those signals, the total fission events were 58680±242.23 counts. In the signal from ^{235}U, the total fission events of ^{235}U were 1390521±1179.204. Then, the fission rate ratio of ^{241}Am/^{235}U were observed as 0.0422±0.0002. On the other hand, the fission rate ratio by numerical calculation with MVP3.0 and JENDL-4.0 was 0.0410. The C/E value was 0.9722±0.42%.

REFERENCES:

[1] H. Unesaki, Doctor Thesis, Nov. 2001 (2001).
[2] T. Sano, 45th Summer Seminar of AESJ Reactor Physics committee, (2016).
[3] Y. Nagaya, et. al., JAERI1348, JAEA, (2005).
[4] K. Shibata, et. al., J. Nucl. Sci. Technol., 39(11), (2002)

Table 1 Sample information [1]

Sample	^{241}Am		^{235}U	
Target Nuclide	^{241}Am	(1.73±0.02) ×10^{16}	^{235}U	(1.49±0.02) ×10^{16}
Impurities	^{239}Pu	1.2ppm [2]	^{234}U	470ppm
			^{236}U	160ppm
			^{238}U	400ppm

Table 2 Operational data for sample irradiation

Control Rod position (mm)	C1	714.93 mm
	C2	715.19 mm
	C3	715.24 mm
	S4, S5, S6	1200 mm
Core temperature (℃)		18.7 ℃
Lin-N		1 μA ×35.2 %
Log-N		2.9×10^{-7} A
Gamma monitor		2.3×10^{3} μSv/h

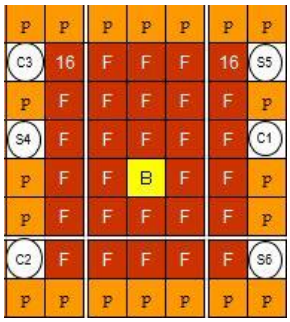

F: 1/8"p60EUEU fuel element,
16: 1/8"p16EUEU Partial Fuel element,
p: 10" polyethylene reflector
C: Control Rod, S: Safety Rod,
B: Void region with BTB fission chamber
Fig. 1 Core configuration

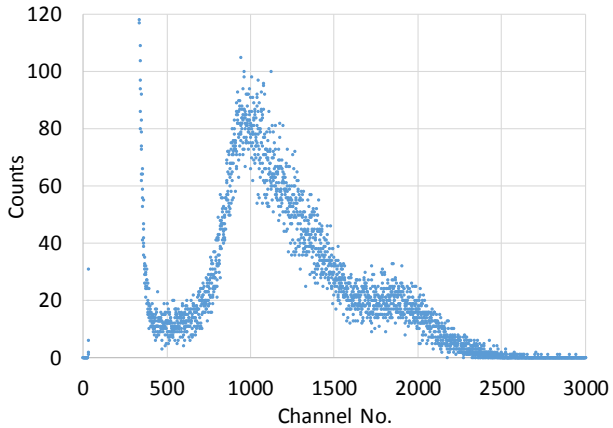

Fig.2 PH spectrum from BTB chamber

CO3-14 Measurement of Neutronics Characteristics for Th loaed core at KUCA

T. Sano[1,2], H. Unesaki[1], J. Hori[1] , J. Lee[1], Y. Takahashi[1], K. Takahashi[3]

[1]*Institute for Integrated Radiation and Nuclear Science, Kyoto University*
[2]*Atomic Energy Research Institute, Kindai University (Apr. 2019~)*
[3]*Graduate School of Science and Engineering, Kindai University*

INTRODUCTION:

In order to perform integral evaluation of the ^{232}Th capture cross section, critical experiments with Th loaded various cores at KUCA has been carried out [1]. The H/^{235}U nuclide ratio in those cores were about 150 – 315 to compensate the negative reactivity worth with Th loaded. The results of numerical analysis for the critical experiments showed magnitude of sensitivity coefficients respected for ^{232}Th capture cross sections in the thermal energy region larger than the resonance energy region. Then, a new critical experiment at KUCA B core which has about 70 of the H/^{235}U ratio was carried out.

EXPERIMENTS:

The new critical core consisted of two type fuel elements. One is Th loaded fuel element, and the other is driver fuel element. A unit cell of Th loaded fuel element has 3 enriched uranium (EU) plates with 1/16" thickness, 1 Th plate with 1/8" thickness and 2 polyethylene plates with 1/8" thickness. The one Th loaded fuel element has 27 unit cells. A unit cell of driver fuel elements consists of the 1 EU plate and the 2 polyethylene plates. The one driver fuel element consists of 49 unit cells.

Figure 1 shows the core configuration of the critical experiment. There were the 37 Th loaded fuel elements (F) and the 17 driver fuel elements (D). In addition, the partial driver fuel element which has 17 or 19 unit cells were loaded in order to adjust an excess reactivity worth of the critical core. Table 1 shows the critical data of the core.

RESULTS:

First of experiments, the neutronics characteristics of the Th loaded core was measured to check on the parameters are fallen within the KUCA regulations. Table 1 shows the measured neutronics characteristics. The all characteristics are satisfied with the KUCA regulations.

In order to observe a effective multiplication factor (k_{eff}) of the core, the excess reactivity worth was measured by the positive reactor period method. As the five-times-measured results, the evaluated excess reactivity worth was 0.086±0.003 (%dk/k) [2] and the k_{eff} was 1.0009 ± 0.0003 [2]. Where, the kinetic parameters shown in Table 3 were calculated by MVP3.0 [3] and JENDL-4.0 [4].

ARKNOWLEGEMENT:

A part of the present study was supported by CHUBU Electric Power Co., Inc.

REFERENCES:

[1] H. Unesaki, Doctor Thesis, Nov. 2001 (2001).
[2] T. Sano, et. al., Abstract of AESJ Spring meeting, 1J11, (2019).
[3] Y. Nagaya, et. al., JAERI1348, JAEA, (2005).
[4] K. Shibata, et. al., J. Nucl. Sci. Technol., 39(11), (2002)

Table 1 Critical data of the Th loaded core

No. of loaded EU plates		3883
No. of loaded Th plates		999
Control Rod position (mm)	C1	1201.15
	C2	1206.11
	C3	735.63
	S4, S5, S6	1200
Core temperature (℃)		20.3

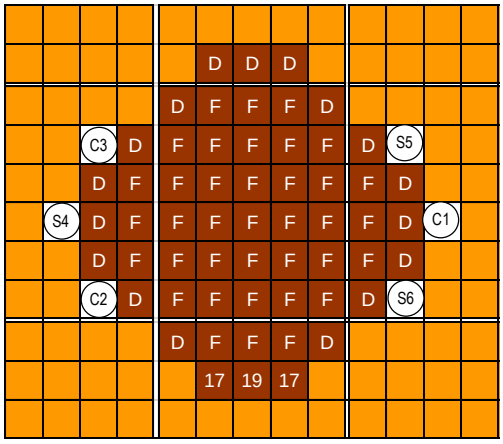

F: Th loaded fuel element, D: Driver Fuel element, 17, 19: Partial Driver Fuel element, C: Control Rod, S: Safety Rod

Fig. 1 Core configuration

Table 2 Measured neutronics characteristics of the Th loaded core

Neutronics Characteristics		Measured (%dk/k)	KUCA Regulation
Excess reactivity (%dk/k)		0.086	< 0.35(%dk/k)
Rod worth (%dk/k)	C1 rod	0.244	Max. worth : < 1/3 of total worth
	C2 rod	0.379	
	C3 rod	0.430	
	Total*	(0.244+0.379+ 0.430)*2 =2.105	>Excess reactivity + 1 (%dk/k)
Center core worth (%k/k)		2.176	>1 (%dk/k)

*S4, S5 and S6 rod worth are assumed same value as C1, C2 and C3 rods by symmetric geometry.

Table 3 Kinetic Parameters

β_{eff}	7.658E-3
Λ	3.257E-5

CO3-15 Neutron measurement experiment using thin type experimental model of the SiC semiconductor detector

M. Nakano[1], T. Saito[1], Y. Harada[1], T. Misawa[2], Y. Kitamura[2]

[1]*MITSUBISHI HEAVY INDUSTRIES, LTD.*

[2]*Institute for Integrated Radiation and Nuclear Science, Kyoto University*

INTRODUCTION: The critical approach monitoring by neutron measurement is considered as one of the critical management methods in the institution which deals with nuclear fuels, such as a domestic nuclear power plant.

In this research, the experimental model of the SiC thin semiconductor neutron detector (called Test-rig in below section) with low gamma ray susceptibility can be used to carry out a neutron measurement examination in which neutron measurement is possible under high gamma ray environment.

When the characteristics of the Test-rig are evaluated, it is expectable to apply from now on as a neutron detector for a nuclear power plant or the fuel debris of a Fukushima Daiichi nuclear power plant.

EXPERIMENTS: As shown in Fig. 1, the reactor core which consists of a fuel bundle and a neutron source was created. The effective multiplication factor of the system at this time was estimated about as 0.93 as a result of the evaluation in an analysis code. The area from cell number “RA14” to “I16" was the space to set the Test-rig, neither fuel nor a polyethylene moderator had set. If this area was filled with polyethylene, the effective multiplication factor was estimated about 0.95.

The Test-rig was installed to the area from cell number “RA14” to “I16", and the neutron from the fuel cell was measured. In addition, a fuel cell and a polyethylene moderator were not set to “SO18” and "SO19" positions of Fig. 1, so that the neutron from the neutron source installed in the "SO20" position reaches a fuel cell directly.

RESULTS: The neutron of about 16,000 counts was measured by the measurement for about 3 hours using Test-rig, namely, sensitivity becomes about 1.34 cps. As a result, it has confirmed that the Test-rig has sensitivity equivalent to the sensitivity estimated in the Test-rig design. It shows that it is possible to measure enough neutrons for the sub-criticality monitoring, without needing gamma ray shielding under high gamma ray environment by manufacturing the SiC thin semiconductor neutron detector with which satisfies the requirement specification.

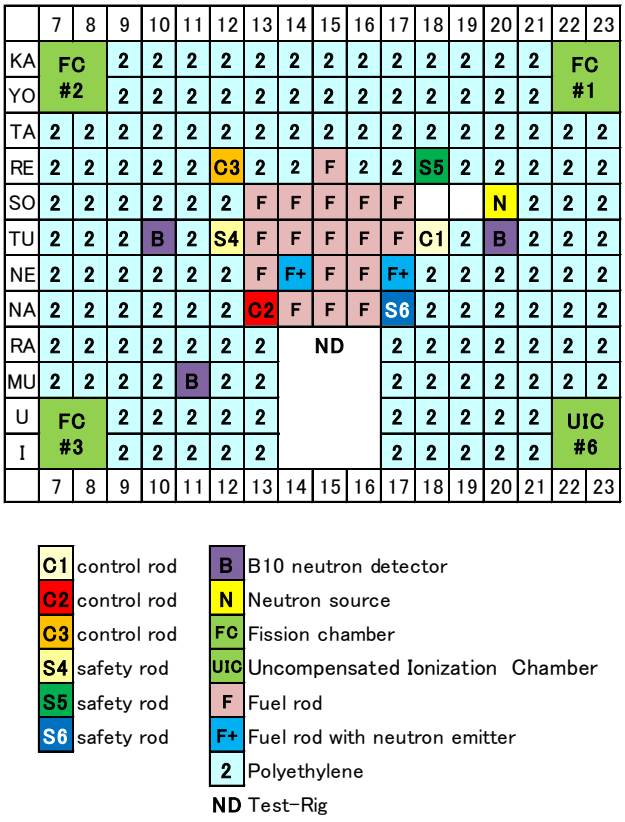

Fig. 1. Core of the neutron measurement examination

From now on, a SiC thin semiconductor neutron detector that satisfies the sub-criticality monitoring requirements can be made. The verification examination is continuously implemented as a neutron detector which can yield high sensitivity with high gamma ray extraction ratio, and application to the sub-criticality monitoring at nuclear power plants or Fukushima fuel debris retrieval work is expected.

CO3-16 Verification of a method to estimate reactivity and fissile composition

Y. Yamane, S. Araki, Y. Kitamura[1], T. Misawa[1]

Japan Atomic Energy Agency
[1]Institute for Integrated Radiation and Nuclear Science, Kyoto University

INTRODUCTION: The estimation of reactivity of an amount of unknown fissile material is one of important issues in the field of criticality safety.
JAEA has been theoretically developing a method to estimate the reactivity and composition of fissile isotope from neutron count rate alone[1-5]. The method is based on a newly developed equation of power in quasi-steady state after prompt jump/drop of power due to reactivity and/or neutron source change.
The purpose of the experiment is to obtain the experimental data for the verification and validation of the developed method. As the first step, the data for the estimation by using new method and other existing methods was obtained for comparison to each other. The reactivity estimation for a subcritical state close to critical one was focused for this time.

EXPERIMENTS: A subcritical core was made by removing fuel elements from the basic critical core configuration known as 3/8" p36EU of A-core. The tritium target irradiated with deutron beam was used as the external neutron source.
BF3 detectors were used. Figure 1 shows the core configuration and the position of the tritium target and BF3 detectors.
The condition of deutron beam was tuned so that the neutron count rate was suitable to Feynman-α method.
For the first 1000s, during 2000s and 3000s, in Fig.2, neutron count data was obtained under steady state. Then the deutron beam was instantaneously cut off. After that, neutron count rate decreased and the measurement terminated in 500s after prompt drop of neutron count rate.

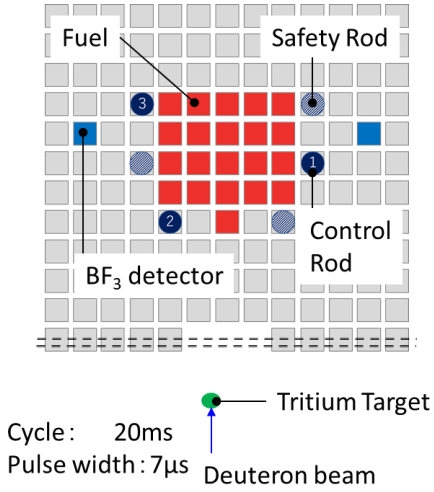

Fig. 1. Configuration of fuels and devices in A-core.

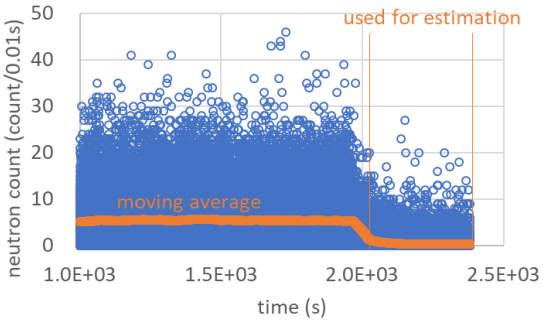

Fig. 2. Neutron count rate data. Blue circle shows neutron counts per 0.01s and orange line shows a profile of averaged neutron counts.

RESULTS: The estimated value obtained by applying the new method to the data was compared to the value calculated by using MVP code with JENDL-4.0 cross section library. The result is shown in Table 1, which shows that the range of C/E was 1.0 and 1.4[5-6]. The worse value was obtained for deeper subcriticality. The reason may be the lowness of the neutron count rate in the quasi-steady state compared to the estimation of TRACY experiment data.
The result indicates that estimated value of reactivity in dollar was reasonable in even not desirable condition in which neutron count rate was very low.
In next step, an experiment will be done in much better condition in deeper subcritical state.

Table 1. The comparison of reactivity values estimated by applying new method and calculated by using MVP code.

CORE	reactivity ($)		C/E	initial count rate (cps)
	MVP	new		
KUCA	-0.49	-0.50	1.0	～50
	-1.0	-0.83	1.2	～30
	-1.3	-0.91	1.4	～20
TRACY	-1.4*	-1.3	1.1	～1000
	* not MVP, solution level diffrence method			

REFERENCES:
[1] Y. Yamane, Proc. 2017 AESJ Spring meeting, 1F04, (2017) [in Japanese].
[2] Y. Yamane, Proc. 2017 AESJ Fall meeting, 3G15, (2017) [in Japanese].
[3] Y. Yamane, Proc. 2018 AESJ Spring meeting, 1F04, (2018) [in Japanese].
[4] Y. Yamane, Proc. 2018 AESJ Fall meeting, 1M08, (2018) [in Japanese].
[5] S. Araki, Y. Yamane, Y. Kitamura, T. Misawa, Proc. 2019 AESJ Spring meeting, 2J01, (2019) [in Japanese].
[6] Y. Yamane, S. Araki, Y. Kitamura, T. Misawa, Proc. 2019 AESJ Spring meeting, 2J02, (2019) [in Japanese].

CO3-17 Measurement of fundamental characteristics of nuclear reactor at KUCA (III)

Y. Kitamura[1], T. Misawa[1], Y. Takahashi[1], Y. Hayashi[2,3], Y. Morimoto[2,4], M. Nakano[2,5]
[1]KURNS, [2]International Research Institute for Nuclear Decommissioning, [3]Toshiba Energy Systems & Solutions Corporation, [4]Hitachi-GE Nuclear Energy, Ltd. [5]Mitsubishi Heavy Industries, Ltd.

ACKNOWLEDGEMENTS: This work is a part of "Development of Technologies for Controlling Fuel Debris Criticality" project supported by the Ministry of Economy, Trade and Industry (METI).

INTRODUCTION: The sub-criticality monitoring system for preventing criticality accident during fuel debris retrieval has been being developed by IRID[1]. This system is based on Feynman-α method[2]. The method is one of well-established sub-criticality measurement methods, but applicability for the sub-criticality measurement of fuel debris in Fukushima Daiichi Nuclear Power Plant is not demonstrated so far. The size of the fuel debris is one of the issues of the sub-criticality measurement. Investigation inside PCV revealed that the size of fuel debris reach approximately 5 meters. The one-point reactor approximation, which is assumed for the formulation of Feynman-α method, could not be valid for such large-scale system. So the sub-criticality may not be measured properly.

EXPERIMENTS: To investigate the applicability of the sub-criticality monitoring system of large-scale fuel debris, the following experiment was performed. It is known that the degree of flux tilt of large-scale system when a perturbation is added is correlated with the first order eigenvalue separation $(E.S.)_1$, which is defined by the difference between the inverse of first order eigenvalue λ_1 and the inverse of zeroth order eigenvalue λ_0[3]. Therefore, the first order eigenvalue separation $(E.S.)_1$ of experimental core was adjusted to simulate the one of large-scale system such as the fuel debris.

The examples of the core configuration are shown in Fig. 1. The core consists of two separated cores, and each core consists of several fuel elements and polyethylene reflectors. The first order eigenvalue separation $(E.S.)_1$ of the core was adjusted to same value (approximately 0.01) of the large-scale fuel debris to simulate it. The B-10 lined neutron proportional counters were set in front of the two separated cores. The neutron multiplication $M(=(1/(1-k_{eff}))$, which is an indicator of sub-criticality, was measured with the prototype of the sub-criticality monitoring system, when the several type of perturbations that are assumed in fuel debris retrieval (e.g. replacement of low reactivity fuel element to high reactivity fuel element, replacement of fuel element to polyethylene reflector, etc.) were added to one of the two separated cores.

RESULTS: The result of the measurement of neutron multiplication M is shown in Fig. 2. The vertical axis of the graph represents measured neutron multiplication M_{meas}, the horizontal axis of the graph represents local neutron multiplication M_{local} of one of the separated core, which is calculated with a Monte Carlo code, MVP[4]. The M_{meas} agreed well with the M_{local}. It is confirmed that the prototype of the sub-criticality monitoring system can be applicable for detecting approach to "local" criticality of large-scale fuel debris.

(a) Core 1 (k_{eff} ~ 0.8)

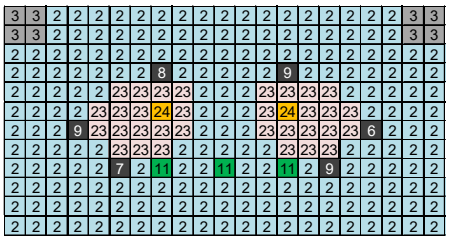

(b) Core 2 (k_{eff} ~ 0.95)

Fig. 1. Examples of core configuration

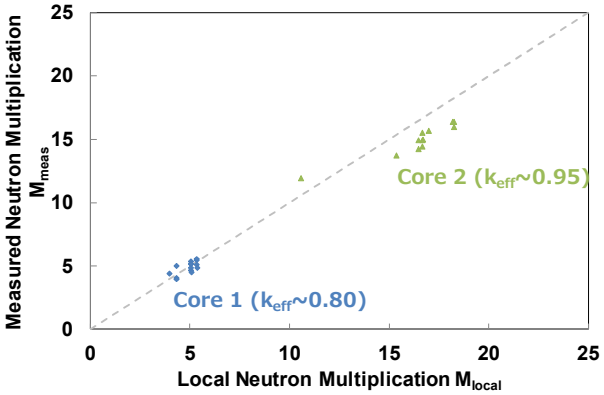

Fig. 2. Measurement results of neutron multiplication M of the cores that simulates large-scale fuel debris

REFERENCES:

[1] 2018. IRID Annual Research Report 2017, International Research Institute for Nuclear Decommissioning. 26-27. http://irid.or.jp/_pdf/pamphleth29_eng.pdf
[2] Feynman, R.P., de Hoffmann, F., Serber, R., "Dispersion of the neutron emission in U-235 Fission", J. Nucl. Energy 3, 64-69 (1956).
[3] K. Hashimoto, Ph.D. Thesis, Nagoya Univ. (1995).
[4] Y. Nagaya *et al.*, MVP/GMVP Version 2 : General Purpose Monte Carlo Codes for Neutron and Photon Transport Calculations based on Continuous Energy and Multigroup Methods, Japan Atomic Energy Research Institute (2004).

CO4-1 Crystal structure analysis of aragonite by neutron diffraction

K. Iwase[1] and K. Mori[2]

[1]*Department of Materials Science and Engineering, Ibaraki University*

[2]*KURNS, Kyoto University*

INTRODUCTION: Creatures form biominerals such as shell, bone, pearl, eggshell, exoskeleton, etc. The process of forming those minerals, which is called biomineralization, takes place usually at ambient temperature and pressure. Biominerals are nanocomposite materials made of inorganic and organic substances [1] and renowned for their mechanical property [2].

The crystal structures of calcium carbonate were reported by Terada [3]. Calcium carbonate have three polymorphs: aragonite, calcite and vaterite phases. Calcite is stable phase among three polymocphs, while aragonite and vaterite are unstable phases in the temperature range 273 K to 1243 K. The aragonite phase is orthorhombic with the space group of *Pnma*, while the calcite phase is trigonal with the spae group of *R*-3*c*. The vaterite phase has the $P6_3/mmc$ spece group. Among shells, Tapes philippinarum, Meretrix lusoria, corbicula, etc, are composed of the aragonite phases, while oyster and scallop shell are of the calcite one. The vaterite phase is seldom obtained in the usual biological systems.

Taylor and Layman reported the mechanical propertys and structures of bivalve shell [2]. The mechanical properties were investigated by bending, impact and microhardness tests. Seven to ten specimens, Pinctada martensi, Mercenaria mercenaria, Glycymeris glycymeris, Pecten maximus, etc, were used for the tests. Pinctada martensi with nacre structure indicated highest stress at fracture by bending and impact tests. The microhrardness of various shell structures, aragonite prisms, composite prisms, sheet nacre and crossed-lamellar, etc, were measured. The microhardness of composite prisms was harder than other structures. The shell of Strombus gigas is formed with 95 % (by volume) inorganic phase and 5 % organic phase. The nacre of Strombus gigas is 3000 times as tough as its pure constituent mineral [4]. The texture of nacre of Strombus gigas is called crossed lamellar microarchitecture, which affords uncracked structural feature of surface [6]. Strombus gigas contains structure at five distinct length scales and the texture size is controlled from 5 μm to 2 mm.

In this study, aragonite was synthesized for NPD measurement. Structural parameters of synthesized aragonite were refined by Rietveld method.

EXPERIMENTS: NPD data were collected by using the step-scan mode of a diffractometer (B-3) with 1.0294 Å wavelength. The powdered sample was sieved to a particle size of < 20 μm for the NPD measurements.

Synthesized aragonite was prepared by the following procedure. An 1.0-L Erlenmeyer flask was used as the reactor, and 1.6 g $NaHCO_3$ was added slowly to an aqueous solution (600 mL) containing 0.8 g $CaCl_2$ at 353 K. During the reaction, the sample was stirred at 1030 rpm. The aragonite phase could be synthesized in the laboratory under stirring at high temperature, when there is no Mg^{2+} in the solution.

RESULTS: Rietveld refinement pattern of synthesized aragonite is shown in Fig. 1. The structural model based on space group $P6_3/mmc$ was developed. The goodness of fit *S* was 1.8. The refined lattice parameters *a*, *b* and *c* were 0.5739(3), 0.4962(2) and 0.7968(4) nm, respectively, which agreed with the values reported by Terada [3]. The refined lattice parameters and atomic position of synthesized are obtained using B-3. In the next stage, biogenic aragonite will be measured by B-3.

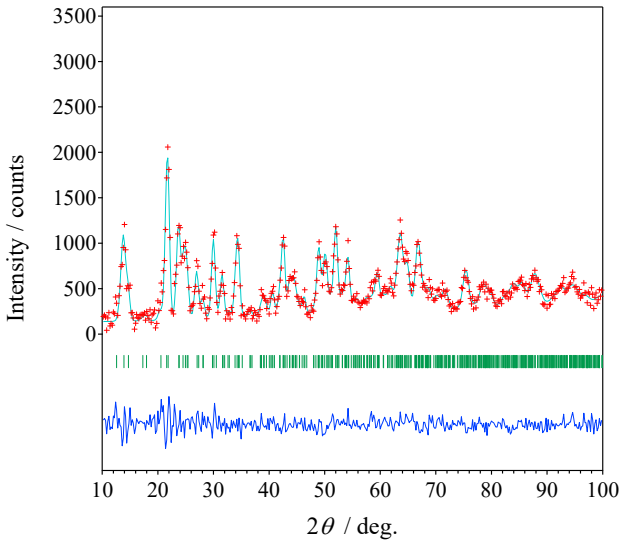

Fig. 1 NPD profile of synthesized aragonite

REFERENCES:

[1] Y. Dauphin, Structures, organo-mineral compositions and diagenetic changes in biominerals, Curr. Opin. Colloid. Interface. Sci. 7 (2002) 133-138.

[2] Y. Dauphin, J.P. Cuif, J. Doucet, M. Salome, J. Susini, C.T.Willams, In situ chemical speciation of sulfur in calcitic biominerals and the simple prism concept, J. Struct. Biol. 142 (2003) 272-280.

[3] J. Terada, Crystal structure of the Ba, Sr, and Ca triple carbonate, J. Phys. Soc. Jpn. 8(2) (1953) 158-164.

[4] A.P. Jackson, J.F.V. Vincent, R.M. TURNER, The mechanical design of nacre, Proc. R. Soc. Lond. B 234 (1988) 415–440.

[5] S. Kamat, X. Su, R. Ballarini, A. H. Heuer, Structural basis for the fracture toughness of the shell of the conch Strombus gigas, Nature 405 (2000) 1036-1040.

CO4-2

Radiochemical Research for the Advancement of $^{99}Mo/^{99m}Tc$ Generator by (n, γ) Method

Y. Fujita, M. Seki, Y. Namekawa, K. Nishikata, A. Kimura, A. Shibata, N. Sayato, K. Tsuchiya, T. Sano[1], Y. Fujihara[1], J. Zhang[1], T. Suzuki[2] and H. Suematsu[2]

Department of JMTR, Japan Atomic Energy Agency
[1]Institute for Integrated Radiation and Nuclear Science, Kyoto University
[2]Graduate School of Engineering, Nagaoka University of Technology

INTRODUCTION: The research and development (R&D) has been carried out for the production of Molybdenum-99 (^{99}Mo) by the neutron activation method ((n, γ) method) from viewpoints of limited availability of high-enriched uranium, no-proliferation and nuclear security, and disposal of nuclear fissile materials. It is essential to improve the properties of Alumina (Al_2O_3) used widely as Mo adsorbent for the $^{99}Mo/^{99m}Tc$ generator. In this study, four kinds of Al_2O_3 specimens[1] were prepared, and molybdenum adsorption and technetium-99m (^{99m}Tc) elution properties of these Al_2O_3 specimens were evaluated. Three kinds of MoO_3 pellets with different ^{98}Mo enrichment rations were also irradiated and evaluated the ^{99}Mo production amounts.

EXPERIMENTS: The MoO_3 pellets were fabricated by the cold pressing and sintering Method. Density of MoO_3 pellets was about 60%T.D. The MoO_3 pellet pieces (about 1.5 g) were irradiated in the Pn-2 of the KUR for 20 min. After the irradiation tests, the irradiated MoO_3 pellet pieces were dissolved with 6M-NaOH solution. Then, the Mo adsorption tests of the Al_2O_3 specimens were carried out with the sodium molybdate solution (10mg-Mo/mL, pH4) at RT. After the tests, each Al_2O_3 specimen adsorbing Mo was packed in the polypropylene column. The saline was flowed through in this column about every 24 h and the ^{99m}Tc was eluted from each Al_2O_3 specimen.

Three kinds of MoO_3 pellets with different ^{98}Mo enrichment ratios (>98.5%, 58.82% and natural isotope ratio (24.13%)) were prepared and irradiated in the Pn-2 of the KUR for 20 min. The activities of ^{99}Mo and ^{99m}Tc in the solution were measured by the γ-ray spectrometer.

RESULTS: Table 1 shows the result of ^{99}Mo adsorption amounts of Al_2O_3 specimens and ^{99m}Tc elution rates from Al_2O_3 specimens. The Mo adsorption amounts of the 3 types of developed Al_2O_3 (D-201-300, V-V-300, V-B-300) exceeded the medical alumina used in current commercial generators. The ^{99m}Tc elution rate was higher in the order of V-V-300, Medical, V-B-300, D-201-300. The ^{99m}Tc elution rate of V-B-300, that the Mo adsorption amount is the largest, was about 80% in 3 mL and the obtained ^{99m}Tc specific radioactivity was also highest as compared with other Al_2O_3 specimens. The Mo desorption rate was dependent on the ^{99m}Tc elution rate.

Table 2 shows the result of ^{99}Mo production amounts of MoO_3 pellets with different ^{98}Mo enrichment ratios. The ^{98}Mo enrichment ratios were re-evaluated from the results of the ^{99}Mo production ratio. The enrichment ratio of MoO_3 pellet with 58.82% was almost the same value as the measurement results. On the other hand, the experimental value was small in the enrichment ratio of MoO_3 pellet with >98.5%. After dissolution of the enrichment ratio of MoO_3 pellet with >98.5%, a white precipitate was observed in the solution and it is considered that the result was affected. In future, the experimental methods should be considered for the high accuracy results.

Table 1 Results of ^{99}Mo adsorption amounts of Al_2O_3 specimens and ^{99m}Tc elution rates from Al_2O_3 specimens

Items	^{99}Mo adsorption amounts		^{99m}Tc elution rates at 3 mL in Milking (%)		
	(MBq/g-Al_2O_3)	(mg-Mo/g-Al_2O_3)	1st run	2nd run	3rd run
Specimen-1 (D-201-300)	0.91	57.4	65.3	69.1	72.7
Specimen-2 (V-V-300)	0.88	55.4	92.4	91.2	91.1
Specimen-3 (V-B-300)	1.44	88.8	79.1	78.1	79.6
Specimen-4 (Medical)	0.63	39.0	89.4	83.3	83.6

Table 2 ^{99}Mo production amounts of MoO_3 pellets with different ^{98}Mo enrichment ratios

Enrichment ratio of ^{98}Mo	^{99}Mo production amounts (MBq/g-MoO_3)		Evaluation of ^{98}Mo enrichment ratio * (%)	
	Run 1	Run 2	Run 1	Run 2
> 98.5%	91.1	-	91.29	-
58.82%	56.3	57.4	51.17	60.87
Natural (24.13%)	26.5	22.7	(24.13)	(24.13)

* Based on specific radioactivity of natural abundance (24.13%)

CONCLUSION: The MoO_3 pellets were irradiated in the Pn-2 at KUR, and ^{99}Mo adsorption/^{99m}Tc elution properties of the Al_2O_3 specimens were evaluated with the solution of the irradiated MoO_3 pellets. As a result, it was suggested that V-B-300 could be used as Mo adsorbent for $^{99}Mo/^{99m}Tc$ generators using the (n, γ) method. However, in order to apply it to the generators, further improvement such as suppressing Mo desorption amount is required. It confirmed that ^{99}Mo production amounts increased with ^{98}Mo enrichment ratio and it is necessary to establish an evaluation method to improve the accuracy.

REFERENCES:

[1] Y. Suzuki *et al.*, Transactions of the Materials Research Society of Japan, **43** (2018) 75-80.

CO4-3 Precise Solution Stucture of Artificial Molecular Self-Assemblies in Water

N. Sato, K. Morishima, M. Sugiyama, Y.-Y. Zhan[1] and S. Hiraoka[1]

Institute for Integrated Radiation and Nuclear Science, Kyoto University
[1]Department of Basic Science, The University of Tokyo

INTRODUCTION: Binding of negatively charged species i.e. anions is one of the modern issues in molecular sciences, because binding of anions as well as cations has often seen in regulation and signal transduction in biological systems. Although artificial molecular hosts that bind cations have widely been developed so far, the progress in design and synthesis of those for anions is slower than that for cations. Now a day, several artificial anion-hosts have been reported, most of which have several hydrogen bonding donors to make strong multi-point hydrogen bonding between these donor atoms in the host and anions. Considering that desolvation is needed to bind anions in the molecular host, anion recognition in water, which strongly solvates the anions, is a challenging issue in anion recognition, but the understanding of the binding of anions in water is most closely related to biological events.

Recently, we found that a discrete, cube-shaped molecular self-assembly i.e. nanocube, which is composed of six gear-shaped amphiphiles (GSAs), is assembled in water.[1] The driving forces of this molecular self-assembly are the hydrophobic effect, van der Waals interactions, and cation-π interactions.[2] The thermodynamic[1] and kinetic[3] stabilities of the nanocube can rationally be tuned by the introduction of the substituents in the GSA. Furthermore, the nanocube can encapsulate relatively hydrophobic anion(s) in the 1-nm-sized hydrophobic cavity in water.[4] As the GSA has two positive charges on the pyridinium rings, the nanocube is a polycationic well-defined particle with 2 nm in diameter, so one of the driving forces of the binding of the anions in the nanocube would be electrostatic attraction between the anions and the cationic nanocube. The binding of anions in the nanocube in water is simply expressed by the following equation.

$$\text{X@nanocube} + \text{A}\cdot\text{S} \rightleftarrows \text{A@nanocube} + \text{X} + \text{S} \quad (1)$$

where A, X, and S indicate anion, the molecule(s) that stay in the cavity of the nanocube before the encapsulation of the anion (A), and solvent molecules (H_2O), respectively. Although we determined the thermodynamic parameters for the binding of anions in the nanocube by ITC measurement,[4] in order to precisely interpret the binding phenomenon, what is/are filled in the cavity of the nanocube before the encapsulation of the anions. As the counter anion of the nanocube is Cl^-, it is highly probable that Cl^- and/or several water molecules is/are tapped in the cavity. Thus in this study, to clarify whether Cl^- or water molecules is/are filled in the nanocube, we planned to measure SAXS of an aqueous solution of the nanocube because the SAXS profile should be affected by what occupies the cavity of the nanocube.

EXPERIMENTS: SAXS profiles were measured with a laboratory SAXS instrument (Rigaku NANOPIX) installed at Institute for Integrated Radiation and Nuclear Science, Kyoto University. X-ray wavelength was 1.54 Å and the typical sample-to-detector distance was 350 and 95 mm. A sample of the nanocube was prepared by dissolving solid sample of GSA in Milli-Q water. The concentration of the nanocube was determined by UV spectroscopy to be 0.758 mg/mL before the SAXS measurements.

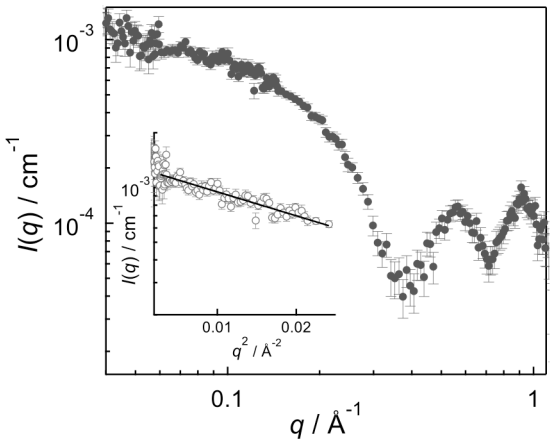

Fig. 1. A SAXS profile of a solution of **BM** nanocube in water. The inset shows the Guinier plot of the same data.

RESULTS: The SAXS profile and the Guinier plot for the nanocube are shown in Figure 1. It was found that the SAXS profile of the nanocube showed mainly two peaks, suggesting a discrete structure in water, which is consistent with the results obtained by other spectroscopic measurements, and that the discussion on the precise structure of the nanocube is possible based on the position and the intensity of the peaks. The radius of gyration (R_g) of the nanocube determined by the Guinier plot is 9.5 ± 0.4 Å, which is also consistent with the size of the nanocube determined by single-crystal X-ray analysis and ^{1}H DOSY spectroscopy. As it was confirmed that SAXS is powerful to discuss the precise solution structure of the nanocube, we are planning to investigate the change in the SAXS profiles by the encapsulation of several anions to conclude what are trapped in the cavity of the nanocube in water.

REFERENCES:

[1] Y.-Y. Zhan *et al.*, *Commun. Chem.*, **1** (2018) 14.
[2] Y.-Y.Zhan *et al.*, *Chem. Eur. J.*, **24** (2019) 9130–9135.
[3] Y.-Y. Zhan *et al.*, *Nature Commun.*, **10** (2019) 1414.
[4] Y.-Y. Zhan *et al.*, *Nature Commun.*, **9** (2018) 4530.

CO4-4

Correlation between Damage Accumulation by Neutron Irradiation and Hydrogen isotope Retention for Plasma Facing Materials

Y. Oya, M. Nakata, A. Koike, S. Yamazaki, T. Wada, M. Zhao[1], F. Sun[2], Y. Iinuma[3] and R. Okumura[3]

Graduate School of Integrated Science and Technology, Shizuoka University
[1]Graduate School of Science and Technology, Shizuoka University
[2]Faculty of Science, Shizuoka University
[3]Institute for Integrated Radiation and Nuclear Science, Kyoto University

INTRODUCTION: Due to the higher melting point and lower sputtering yield, tungsten (W) is considered as a candidate for plasma facing materials (PFMs) in the future fusion reactors. During the operation, W will be exposed to 14 MeV neutrons produced by D-T fusion reaction, as well as energetic particles such as hydrogen isotope, helium ion and charge-exchanged particles. The damages introduced by charge-exchanged particles are concentrated near the surface region, while that induced by 14 MeV neutrons are extended throughout the bulk. For the development of the effective fuel recycling and the safety operation, it is necessary to clarify the hydrogen isotope retention behavior in W with the consideration of damage distribution. In this study, irradiation damages were introduced by both of neutron and 6 MeV Fe ion irradiation with various damage distributions, and the D retention behaviors were evaluated by thermal desorption spectroscopy (TDS).

EXPERIMENTS: A disk-type polycrystalline W (6 $mm^{\varphi} \times 0.5\ mm^{t}$) purchased from A.L.M.T. Co. Ltd. was used. To remove impurities and damages introduced during the polishing processes, the samples were heat-treated at 1173 K under ultrahigh vacuum (< 10^{-6} Pa). Thereafter, the samples were damaged by 6 MeV Fe^{2+} irradiations at room temperature with the damage concentrations of 0.01–0.1 dpa (displacement per atom) by a 3 MV tandem accelerator in Takasaki Ion Accelerators for Advanced Radiation Application (TIARA) at National Institutes for Quantum and Radiological Science and Technology (QST), and the fission neutron irradiations under 323 K by Kyoto University Research Reactor Institute (KUR) with the damage concentration up to 0.015 dpa. After the damage irradiation, the 1.0 keV deuterium ion (D_2^+) implantation was performed on the W sample at Shizuoka University. The D ion fluence was set to be 1.0×10^{22} D^+ m^{-2} with the ion flux of 1.0×10^{18} D^+ m^{-2} s^{-1}. The D desorption behavior was evaluated by TDS at the temperature up to 1173 K with the heating rate of 0.5 K s^{-1}.

RESULTS: Fig. 1 shows D_2 TDS spectra for neutron - Fe^{2+} damaged W samples with various damage distributions. For the comparison, D_2 TDS spectra for only Fe^{2+} damaged samples are shown in Fig. 2. The D_2 TDS spectra were assumed to consist of four major D desorption

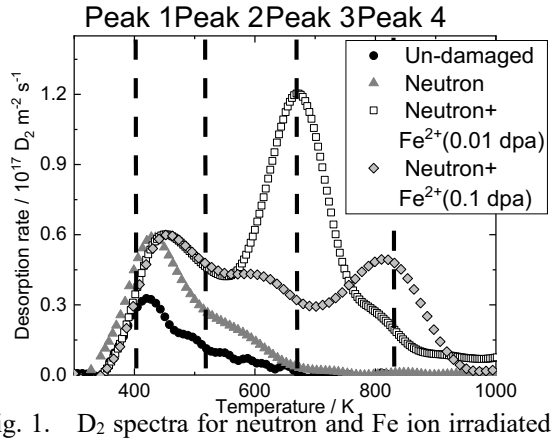

Fig. 1. D_2 spectra for neutron and Fe ion irradiated samples with various damage concentrations

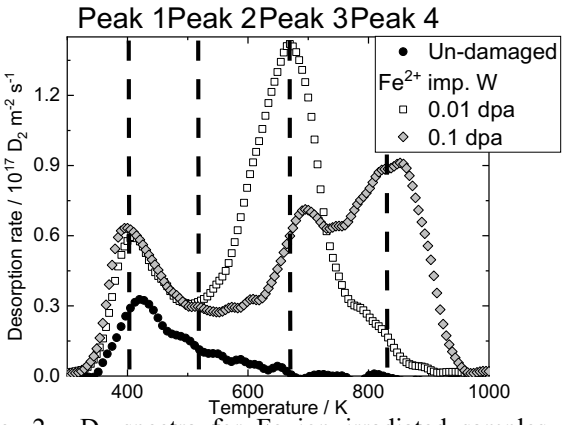

Fig. 2. D_2 spectra for Fe ion irradiated samples with various damage concentrations

stages located at 400 K, 550 K, 650 K and 850 K, respectively. Based on our previous studies, the D desorption stages at Peaks 1 to 4 were corresponded to the desorption of D adsorbed on the sample surface or trapped by dislocation loops, vacancies, vacancy clusters and voids, respectively [1]. In the neutron irradiated sample, D was adsorbed on the surface and/or trapped by dislocation loops and vacancies. The D retentions at Peaks 3 and 4 for multiple neutron - Fe^{2+} damaged W were decreased by neutron irradiation, as shown in Figs. 1, 2. In our previous report [1, 2], the hydrogen isotope recycling was enhanced by the dense damage introduction in the shallow region, and the damages would suppress D diffusion according to the result of HIDT simulation. It was considered that the D diffusion was limited by the increase of point defects by neutron irradiation. It was concluded that total D retention was decreased in the multiple neutron - Fe^{2+} irradiated samples.

REFERENCES:

[1] H. Fujita, K. Yuyama, X. Li, *et al.,* Phys. Scr. **T167** (2016) 014068.
[2] M. Nakata, K. Azuma, A. Togari, *et al.,* Fusion Engineering and Design, In press.

CO4-5 Electron Emission Properties of Field Emitter Array for Image Sensor under Gamma-ray Irradiation

Y. Gotoh, T. Morito, M. Nagao[1], T. Okamoto[2], N. Sato[3], M. Akiyoshi[4] and I. Takagi

Graduate School of Engineering, Kyoto University

[1]*National Institute of Advanced Industrial Science and Technology*

[2]*Naational Institute of Technology, Kisarazu College*

[3]*Institute for Integrated Radiation and Nuclear Science Kyoto University*

[4]*Radiation Reactor Center, Osaka Prefecture University*

INTRODUCTION: We have been developing a radiation tolerant vacuum-type image sensor [1]. The image sensor consists of a matrix-driven field emitter array (FEA) and a photoconductor. It has already been proven that the FEAs have sufficient radiation tolerance against cobalt 60 gamma-rays, up to 1.2 MGy [2]. Following this result, operation of the FEAs under gamma-ray irradiation was conducted last year, with a small vessel that can maintain the pressure at 10^{-6} Pa with an aid of non-evaporation getter (NEG) pump [3]. The FEA and the anode made of stainless steel was set into a glass tube, but it was difficult to realize an image sensor configuration due to a small space. In this study, the vessel was re-made to realize a vacuum image sensor.

EXPERIMENTS: The image sensor could be realized by setting the FEA, mesh electrode, and the photoconductor on a base flange with the size of ICF152. The holder of the FEA was made of machinable ceramics. Unlike the previous vessel, the light or the image could be introduced through a view-port. The vacuum gauge could be mounted on the vessel to monitor the pressure of the vessel. The NEG pump adopted in the present study was the same one with the previous report [3]. Prior to the exposure to gamma-ray, the pressure of the vessel with an NEG pomp activated was recorded, and the vessel maintained the pressure less than 10^{-6} Pa for about 10 days. At the practical test, the pressure was about 1.2 x 10^{-6} Pa. The FEA tested in this study was a matrix-type single-gated Spindt-type with 1024 emission tips. The emitter material was nickel. Before the measurements under irradiation, sufficient aging was performed prior to the exposure to gamma-ray. The measurements of the electron emission property of the FEA was performed at Co-60 Gamma-ray Irradiation Facility, Institute for Integrated Radiation and Nuclear Science, Kyoto University. The dose rate of irradiation was roughly estimated to be 1.3 kGy h^{-1}.

RESULTS: Among the 168 FEAs fabricated on the present sample, one of them that located at the center of the sample was chosen. The electron emission property was measured with the following parameters: gate voltage of 30 V for the selected gate but 0 V for the other, anode voltage of 200 V, gate series resistor of 1 MΩ, emitter series resistor of 1 MΩ. For the selected emitter, a ramp voltage or a constant voltage was applied to observe the variation of the properties under the gamma-ray irradiation. Figure 1 shows the variation of the anode current with and without gamma-ray irradiation. No significant change was observed between with and without gamma-ray irradiation.

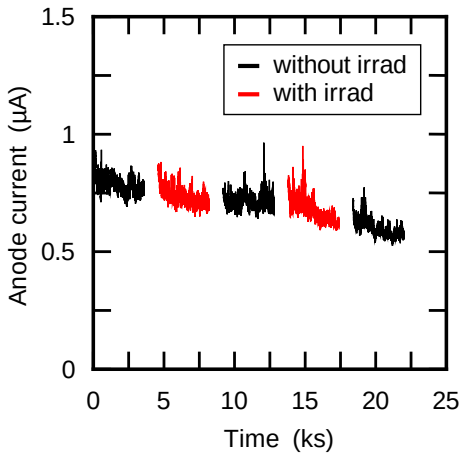

Fig. 1. Variation of the anode current with and without the gamma-ray irradiation.

Detailed analysis of the electron emission was performed with the Seppen-Katamuki analysis which was developed by the authors to evaluate the field emitters [4]. This method enables us to evaluate the surface state (mostly work function) even though the deviation in electron emission. The results suggested that the surface state did not vary even under the gamma-ray irradiation. However, a separate experiment showed a possible changes of surface microstructure of the emitter, which results in the step noise of the anode current.

ACKNOWLEDGMENTS: The present study was partially supported by Japan Society for the Promotion of Science, through a Grant-in-Aid for Scientific Research, KAKENHI 16H04631 and also by Futaba Electronics Memorial Foundation.

REFERENCES:

[1] Y. Gotoh *et al.,* IEEE 28th International Vacuum Nanoelectronics Conference (2015) p. 240.
[2] Y. Gotoh *et al.*. IEEE 29th International Vacuum Nanoelectronics Conference (2016) p. 20.
[3] Y. Gotoh *et al.,* KURRI Progress Report 2017 (2017).
[4] Y. Gotoh *et al.,* J. Appl. Phys. **121** (2017) 234503.

CO4-6 Neutron Irradiation to Liquid Breeders for Fusion Reactors and Tritium Recovery

S. Fukada, K. Tsukahara, Y. Iinuma[1], K. Katayama, M. Oya

Interdisciplinary Graduate School of Engineering Sciences, Kyushu University
[1]KURNS, Kyoto University

INTRODUCTION: Liquid blanket materials such as Li liquid metal, $Li_{17}Pb_{83}$ eutectic alloy or $LiNaBeF_4$ (Flinabe) molten salt are expected to work for a tritium breeding material through the $^6Li(n,\alpha)^3T$ reaction in D-T fusion reactors. These liquid breeding materials have appropriate properties of high Li density necessary for the high tritium breeding ratio, good thermal conductivity for high heat transfer and high γ -ray shielding in fusion reactor blankets. However, there were few experimental studies of tritium recovery from liquid blanket materials using neutron irradiation facility [1-5]. In the present study, tritium recovery from liquid Li or molten Flinabe after neutron irradiation is demonstrated experimentally. In case of the Li breeder, tritium equilibrium pressure is extremely low because of high tritium affinity to Li, which is estimated as $2.2x10^{-9}$ Pa at T/Li=$1x10^{-6}$ in atomic ratio and 500°C. Yttrium metal is selected to work for a tritium recovery material from the Li blanket. On the other hand, tritium (TF) in Flinabe is recovered by the isotopic exchange reaction of $TF + H_2 \rightarrow HT + HF$.

EXPERIMENTS: Li and Flinabe were selected as the tritium breeder for neutron irradiation through the pneumatic facility (pn-2) in KUR having thermal power of 5 MW. One gram of Li or Flinabe is irradiated under the conditions of the neutron flux $2.75x10^{13}$ n/cm^{2}s and irradiation time of one minute. Samples were remained in glovebox for one month to decrease radioactivity of radio nuclides, which have short decay time of ^8Li ($\tau_{1/2}$=0.84 s) or ^{24}Na ($\tau_{1/2}$=15 hr). Irradiated Li samples were contacted with Y metal tips at 300°C in a reaction chamber for specified time. Li is contacted with metallic Y tips shown by Photo 1 and tritium is distributed between Li and Y. Tritium activities in Li and Y are measured by using the two chemical dissolution reactions of $2LiT_X + H_2O \rightarrow Li_2O + 2xHT + (1-x)H_2$ and $YT_X + HNO_3 \rightarrow Y(NO_3)_3 + xHT + ((3-x)/2)H_2$. HT released in purge Ar gas is converted to HTO by a CuO particles bed, and a liquid scintillation counter is used for tritium detection.

RESULTS: Fig. 2 shows the recovery ratio of tritium from Li to Y. When Y surfaces are treated by HF solution before contact with Li and Y, the recovery rate is enhanced. This is because surfaces of Y metal tip without HF treatment are oxidized and it affairs tritium diffusion into metal bulk. So, the Y oxides are removed by HF solution. Its surfaces are converted to YF_3. Tritium in Li is correlated by the first-order reaction rate equation regardless of HF treatment of not.

Photo 1 Overview of Y Tips for T recovery from Li.

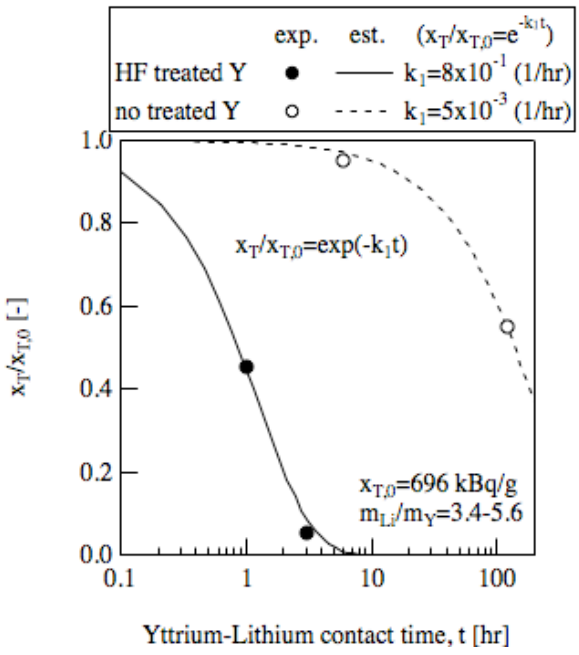

Fig. 2 Tritium recovery ratio from neutron irradiated Li by Y metal tips at 300°C.

REFERENCES:

[1] Y. Yamasaki, S. Fukada, K. Hiyane and K. Katayama, Fusion Science and Technology, 71(4) (2017) 501-506.
[2] S. Fukada, T. Nishikawa, M. Kinjo and K. Katayama, Fusion Engineering and Design, 135 (2018) 74-80.
[3] K. Hiyane, S. Fukada, Y. Yamasaki, K. Katayama and E. Wakai, Fusion Engineering and Design, 109-111 (2016) 1340-1344.
[4] K. Kumagai, T. Tanaka, T. Nagasaka, J. Yagi, T. Watanabe, G. Yamazaki, F. Sato, S. Tamaki, I. Murata, S. Fukada, K. Katayama and A. Sagara, Plasma and Fusion Research, 14 (2019) 1405044.
[5] J. Yamashita, R. Nishiumi, S. Fukada, K. Katayama, A. Sagara and J. Yagi, Fusion Engineering and Design, 136 (2018) 173-177.

CO4-7 Damage Evolution in Neutron-irradiated Metals during Neutron Irradiation at Elevated Temperatures

I. Mukouda and Q. Xu[1]

Hiroshima International University
[1]Institute for Integrated Radiation and Nuclear Science, Kyoto University

INTRODUCTION: It is accumulated an attention that a damage structure in neutron irradiated metals differs if the temperature is varied during irradiation [1]. Especially effect of lower temperature irradiation on the development of damage structure in metals which are irradiated subsequently at higher temperature was reported to be remarkable because the point defects nucleate at lower temperature more frequently during an irradiation. Recently the temperature controlled irradiation devices were developed at KUR [2]. It becomes possible to irradiate continuously at two stage of temperature. In the present work, effects on damage formation in neutron-irradiated copper for the temperature variation were examined for an irradiation at low fluence regime.

EXPERIMENTS: Copper disks of 3mm in diameter were prepared with 99.999% nominal purity specimen. Before an irradiation, they were annealed for 5 hours at 1273 K in vacuum of 10^{-5} Pa. Specimens were irradiated by fission neutrons in a temperature controlled irradiation device in KUR-SSS. In the previous temperature varying irradiation, specimens were irradiated at first at 473 K for 10 hours and subsequently at 573K for 10 and 20 hours at 5MW. After a radiation cooling, they were observed by electron microscopy. A TEM observation was carried out using g = (002) reflection with (g, 5g) condition for the specimens of (110) configuration. Voids were observed in a bright field image by taking a slightly under forcussed image. A triangular image was taken as stacking fault tetrahedra (SFT) and diffused dot image was tentatively taken to be an interstitial cluster.
Present temperature varying irradiation, specimens were irradiated at 473K-6hrs/573K-40hrs and 473K-23 hrs/573K-23 hrs at 1MW. TEM observation are carried out recently.

RESULTS: In 473K-10hrs/573K-10hrs irradiation at 5MW, the number density of voids and SFT was smaller than those of constant temperature irradiation at 573K. Especially the decrease of number density of voids was significant as shown in Figure 1. Fig. 1(a) shows dislocations in the specimen. Dislocations were not decorated by interstitial clusters. Fig. 1(b) shows point defects clusters. The number density of SFT was smaller than the value in copper which were irradiated at constant temperature of 573 K. Only one void was observed in specimens as in this picture, which means the formation of voids was suppressed significantly by the present temperature elevation irradiation.
Neutron-irradiated copper at 573K for 10 hours at 5MW, the dislocation structure show no decorated interstitial clusters around dislocation. Interstitial clusters, which were accumulated along dislocation lines, were unified to grow to dislocations. This makes development of complicated structure of dislocations as reported by Mukouda and Shimomura [3].
The suppression of void formation in temperature-varied irradiation suggests that the nucleation of voids during a constant temperature irradiation at 573K in copper occurs during the period of dislocation decoration by interstitial clusters. Detail consideration are progress by lower irradiation dose at 1MW.

REFERENCES:
[1] N. Yoshida, Q. Xu, H. Watanabe, Y. Miyamoto and T. Muroga, J. Nucl. Mater., 212-215 (1994) 471.
[2] T. Yoshiie, Annual Reports of KUR (1998).
[3] I. Mukouda and Y. Shimomura, Material Science & Engineering A309-310 (2001) 190-197.

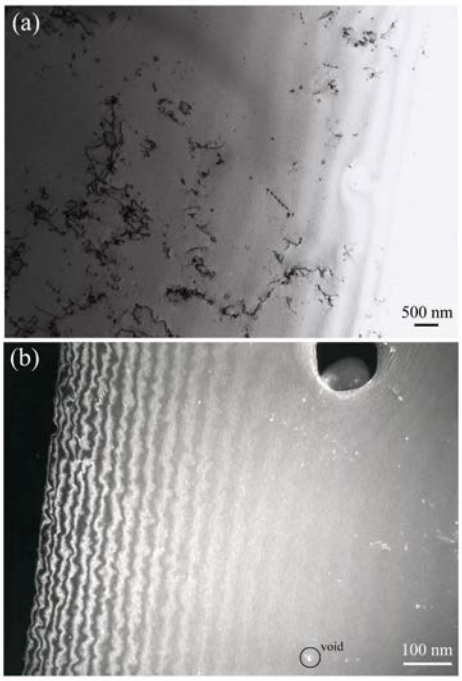

Fig. 1. Damages observed in neutron-irradiated copper with temperature varying schedule. The irradiation was carried out at first at 473K for 10 hours and subsequently at 573 K for 10 hours.

CO4-8 The correlation between microstructural evolution and mechanical property changes in neutron-irradiated vanadium alloys

K. Fukumoto[1] and Xu Qiu[2]

[1] *RINE, Univ. of Fukui*
[2] *KURNS, Kyoto Univ.*

INTRODUCTION: In order to understand the thermal stability of defect clusters, and investigate a recovery method for irradiation hardening and embrittlement, post-irradiation annealing experiments are performed to evaluate the recovery of microstructure and mechanical properties of vanadium alloys irradiated below 300°C.
In this study, experiments to determine the influence of post-irradiation annealing on mechanical properties and microstructures in neutron-irradiated V-Cr-Ti alloys are described. Two groups of specimens (as-irradiated specimens and specimens which underwent the post-irradiation annealing treatment) were subjected to tensile tests at room temperature and 500°C. Post-irradiation annealing experiments with long intervals of up to 50 hr were used to recover the original strength and ductility.

EXPERIMENTS: The majority of test specimens for this study were prepared from V-4Cr-4Ti alloys. The tensile specimens had nominal gauge dimensions of 0.25mm(t) x 1.2mm(w) x 5mm(l). Before irradiation, all specimens were annealed in vacuum at 1000°C for 2hrs. The specimens were irradiated at 228°C to 280°C with 3 to 5 displacements per atom (dpa) in the ATR-A1 or at 306°C with 6 dpa in the HFIR-11J. Post-irradiation annealing was carried out for 2 to 50 hr at 500°C and 600°C in a vacuum. Tensile tests were conducted at room temperature and 500°C. TEM samples were punched from non-deformed areas of tested specimens. The microstructural TEM observations were performed in KUR/Kyoto Univ.

RESULTS: As-irradiated V-4Cr-4Ti alloys in ATR-A1 and HFIR-11J showed the reduction of ductility below 1% and remarkable irradiation hardening above 700MPa in RT tensile tests. A recovery of ductility to 3% and hardening to 500MPa could be observed in an annealed V-4Cr-4Ti alloy at 600°C for 2hrs. On the other hand, no typical changes in uniform elongation and yield stress increase could be seen in an annealed one at 500°C for 2hrs in tensile test. The V-4Cr-4Ti alloys annealed at 500°C for 20hrs showed no change of yield stress increase compared to as-irradiated one in the tensile test at RT, but the total elongation was recovered to 5% with the stress-strain curve like complete elasto-plastic behavior. Even at 500°C tensile test, recovery of ductility could be seen in annealed sample at 500°C for 20hrs. In the case of annealed sample for 50hrs, the ultimate tensile strength decreased significantly with 5% of uniform elongation.
Figure 1 shows the changes in the damage microstructure of V-4Cr-4Ti for different post-irradiation annealing times. In the as-irradiated specimens, the density of defect clusters was very high and the size of each cluster was very small (i.e., about a few nm). With increasing annealing time at 773K, the density of defect clusters decreased gradually. After annealing for 50 h at 773K, the clusters grew into large dislocation loops. Those large loops were identified as dislocations with a/2<111> Burgers vector. No Ti(OCN) precipitates could be seen on {100} habit plane in the as-irradiated and annealed V-4Cr-4Ti alloys. Figure 5 shows the effects of annealing time on the density and average size of the defect clusters and dislocation loops in the post-irradiation annealed V-4Cr-4Ti alloys. With increasing annealing time, the density of defect clusters decreased and the defect clusters grew into dislocation loops. It was found that the recovery of mechanical behavior can be appeared after 10 hour anneal at 500C in order to improve the low-temperature irradiation embrittlement behavior of V-4Cr-4Ti alloys.

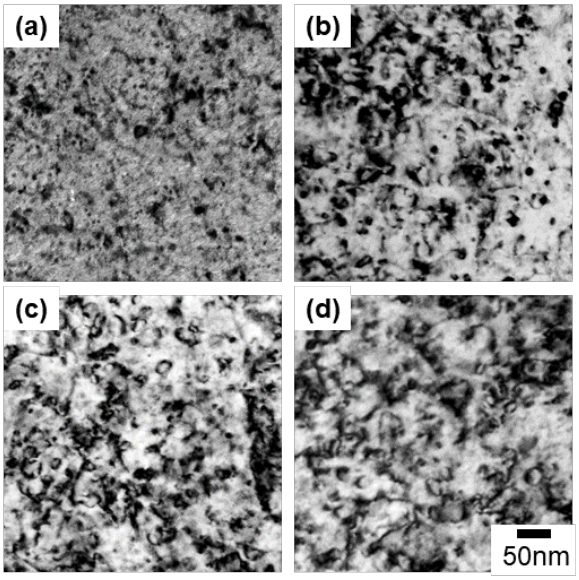

Fig.1. A set of transmission electron micrographs of as-irradiated and post-irradiation annealed V-4Cr-4Ti alloys: (a) as-irradiated, (b) 10 h annealed, (c) 20 h annealed, (d) 50 h annealed.

CO4-9 Search of materials forming nano-porous structures by high-energy ion irradiation and study on its formation mechanisms

J. Yanagisawa, Q. Xu[1], A. Yabuuchi[1], K. Takamiya[1], and A. Kinomura[1]

School of Engineering, The University of Shiga Prefecture
[1]*Institute for Integrated Radiation and Nuclear Science, Kyoto University*

INTRODUCTION: We have been reported that the formation of porous structures with nanometer size (nano-porous structures) can be formed on Ge surfaces by high-energy (100-200 keV) Ga, Au or Si ion irradiations, but no such structures were formed by low-energy (15-30 keV) Au or Si ion irradiations [1]. Last year, large-area ion irradiations on Ge surfaces with 60 keV Ar ions were performed at Research Reactor Institute, Kyoto University, and the formation of nano-structures were confirmed using such ion irradiation conditions [2]. In the present study, lower-energy Ar ion irradiation was performed and the S (line shape) parameters of the positron annihilation was measured as a function of the positron energy to confirm the formation mechanisms of such nano-structures in an early stage by ion irradiation.

EXPERIMENTS: After cleaning of Ge(110) chip samples with an area of about 1.5 x 1.5 cm^2, a corner part of each sample was covered with aluminum foil to prevent the ion irradiation. Three kind of samples were prepared by the Ar ion irradiations using the different ion energy and total fluence, that is, 50 keV and 5 x 10^{16} cm^{-2}, 25 keV and 1 x 10^{16} cm^{-2}, and 50 keV and 1 x 10^{16} cm^{-2}, respectively. S parameters was obtained from the Doppler broadening of annihilation gamma-rays as a function of incident positron energy by the KUR slow positron beam system.

RESULTS and DISCUSSION: Figure 1 shows the optical microscope images of the sample surfaces. It is found that the ion irradiated region was changed to dark, indicating that the formation of nano-structures on the Ge surfaces was confirmed even after such lower ion energy irradiations.

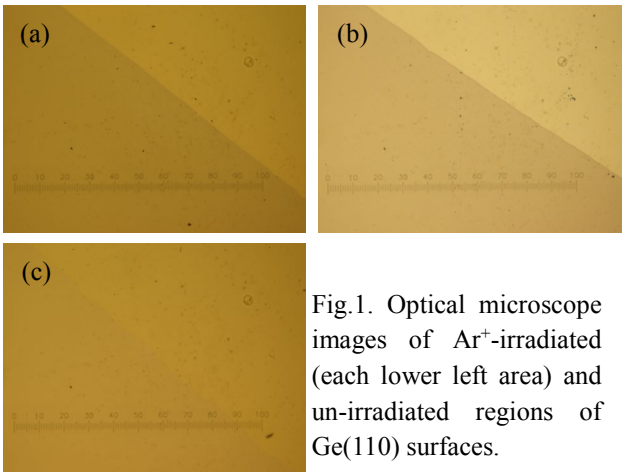

Fig.1. Optical microscope images of Ar^+-irradiated (each lower left area) and un-irradiated regions of Ge(110) surfaces.
(a) 50 keV, 5x10^{16} cm^{-2}, (b) 25 keV, 1x10^{16} cm^{-2}, and (c) 50 keV, 1x10^{16} cm^{-2}.

Figure 2 shows the S parameters for the ion-irradiated and un-irradiated Ge samples plotted as a function of incident positron energy. VEPFIT code was used for the fitting in the figure. After Ar ion irradiation, S parameters were increased compared to the un-irradiated sample. For the samples with the same ion fluence of 1x10^{16} cm^{-2}, the increase in S parameter for the sample with the ion irradiation energy of 50 keV (solid diamonds in Fig. 2) was larger than that of 25 keV (solid squares), indicating that the total amount of the atomic vacancies and/or voids induced by the ion irradiation becomes larger for higher ion energy irradiation. On the other hand, dependence of the ion fluence on the S parameter was not observed for the 50 keV-Ar-ion irradiation (solid triangles and diamonds in Fig. 2).

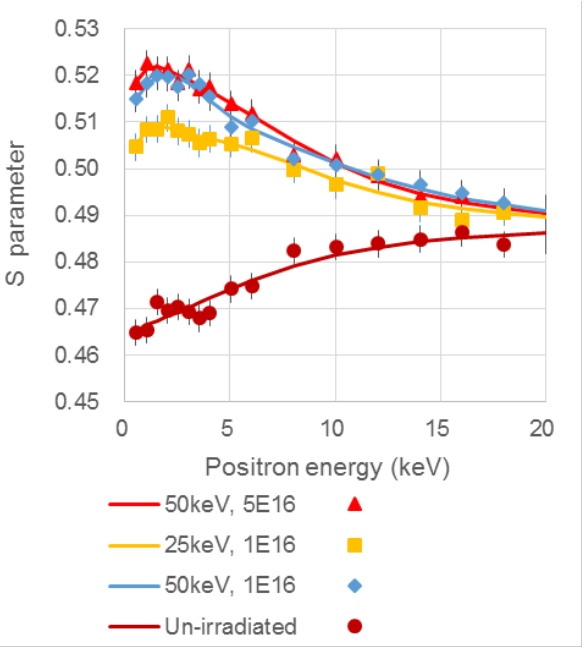

Fig.2. S parameters for Ar^+-irradiated and un-irradiated Ge(110) samples as a function of positron energy.

CONCLUSION: Effect of the low-energy Ar ion irradiation on Ge (110) surfaces was studied using S parameters of the slow positron beam measurements. It is confirmed that the atomic vacancies and/or voids formed inside the surface region increase with increasing the ion energy. Further discussion, such as the influence of the ion fluence and the size and distribution of voids, is an issue in the future.

REFERENCES:

[1] J. Yanagisawa, K. Takarabe, K. Ogushi, K. Gamo and Y. Akasaka, J. Phys.: Condens. Matter **19** (2007) 445002 (10pp).
[2] J. Yanagisawa, Q. Xu, A. Yabuuchi, K. Takamiya, and A. Kinomura, KURRI Progress Report 2017 (Kyoto University), 129 (CO4-15, 29061).

CO4-10 Irradiation Experiment of Accident Tolerant Control Rod Materials

H. Ohta[1], Y. Nauchi[1], K. Nakamura[1] and T. Sano[2*],
H. Unesaki[2]

[1]*Nuclear Research Technology Laboratory, Central Research Institute of Electric Power Industry*
[2]*Institute for Integrated Radiation and Nuclear Science, Kyoto University*
[*]*Present affiliation: Atomic Energy Research Institute, Kindai University*

INTRODUCTION: To improve the safety of light water reactors (LWRs) against severe accidents (SAs), various concepts of "enhanced-accident tolerant fuels and core components" are developed in many countries. The Central Research Institute of Electric Power Industry (CRIEPI) has been developing an accident tolerant control rod (ATCR) to which the novel neutron absorbing materials including rare-earth sesquioxides (RE_2O_3) are applied[1], since current control rods using Ag-In-Cd alloy or B_4C may be damaged and removed from the core in early stage of SAs before serious fuel rod failure occurs. The ATCR improves the reactor shutdown margin and neutronic lifetime, as well as reduces the risk of re-criticality accident in any reactor conditions. For the ATCR candidate materials RE_2O_3-MO_2 (RE = Sm or Eu, M = Zr or Hf), a high temperature compatibility with steel, which is a control rod cladding material, and physicochemical stability under high temperature steam atmosphere were experimentally confirmed so far[2]. Furthermore, a reactivity analysis in representative LWRs indicated that these candidate materials have enough reactivity worth comparable to or higher than the conventional neutron absorbing materials Ag-In-Cd alloy or B_4C[3]. In addition, thermal neutron irradiation characteristics of these candidate materials are needed to be confirmed to evaluate the applicability as a control rod for LWRs. In this study, dimensional stability of a candidate material by neutron irradiation will be confirmed.

SAMPLE PREPARATION: The powders of Sm_2O_3 and ZrO_2 were mixed at a molar ratio of 1 : 1 and sintered to form a pellet with a diameter of 8.1 mm and a height of 8.1 mm as shown in Fig. 1. The pellet density was measured to be 6.55 g/cm^3 corresponding to 93.7 % of the theoretical density. Sintered Sm_2O_3-ZrO_2 mixture with a molar ratio of 1 : 1 is known to form a fluorite crystal structure and its long-term stability in water or steam has been confirmed by previous study[1]. Since Sm_2O_3-HfO_2, Eu_2O_3-ZrO_2 and Eu_2O_3-HfO_2 also have the same fluorite crystal structure as Sm_2O_3-ZrO_2, the results of this irradiation experiment are expected to be applicable to the other candidate materials. For the purpose of minimizing the radioactivation induced by the neutron irradiation, the sintered pellet was cut into small pieces.

Fig. 1 Sm_2O_3-ZrO_2 pellet.

The appearance of the cut sample pieces was observed with an optical microscope and measured the external dimensions, as shown in Fig. 2. Major specifications of the samples prepared for the irradiation experiment are summarized in Table I.

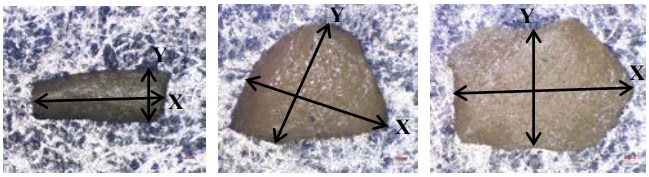

(1) (2) (3)

Fig. 2 Appearance of irradiation samples of Sm_2O_3-ZrO_2.

Table I. Irradiation Sample Specifications

	(1)	(2)	(3)
Composition	Sm_2O_3-ZrO_2	←	←
Density	93.7%TD	←	←
Weight	1.95mg	6.21 mg	5.15 mg
External dimension			
X direction*	1.397mm	1.569mm	1.851mm
Y direction*	0.562mm	1.371mm	1.236mm

*: See Fig. 2.

EXPERIMENTS: Irradiation experiment has been carried out from 11/27/2018 to 02/14/2019 using long-term irradiation plug in Kyoto University Research Reactor (KUR). The above three samples were enclosed in an Al capsule dedicated for long-term irradiation experiment and irradiated for 259 hours at a rated power of 1 MW and 45 hours at a high power of 5 MW. It is estimated that the thermal and epithermal neutron fluences at the end of irradiation experiment are 1.69×10^{19} n/cm^2 and 5.96×10^{17} n/cm^2, respectively. Currently, the irradiated Sm_2O_3-ZrO_2 samples are cooled to reduce the radioactivity (3.23×10^{10} Bq) induced by the irradiation.

POSTIRRADIATION OBSERVATION PLAN: After appropriate cooling period, the appearances of the irradiated samples are observed and their external dimensions are precisely measured. Then, the weights of the samples are also measured to assess density changes during irradiation. Furthermore, the morphology of the sample surface is observed in detail with an electron microscope to confirm the irradiation damage. On the basis of these irradiation experiment and postirradiation observation results, applicability of RE_2O_3-MO_2 to control rod for LWRs will be discussed.

REFERENCES:

[1] H. Ohta, *et al.*, TopFuel 2016, 17556 (2016).
[2] K. Nakamura, *et al., AESJ 2017 spring meeting*, 1I06 in Japanese.
[3] H. Ohta, *et al., Trans. 2018 ANS winter meeting*, Vol. 119, pp425-428 (2018).

CO4-11 Valence change behavior of Cu ions in oxide glasses by γ-ray irradiation

R. Hashikawa, A. Kinomura[1], T. Saito[1], A. Okada[2], T. Wakasugi[2], K. Kadono[2]

Graduate School of Science and Technology, Kyoto Institute of Technology
[1]Institute for Integrated Radiation and Nuclear Science, Kyoto University
[2]Faculty of Materials Science and Engineering, Kyoto Institute of Technology.

INTRODUCTION: Exposure to high energy radiation generates electron-hole pair in glass. A part of the electrons and holes are captured by metal ions present in the glass, resulting in the change in valence of the metal ions. Using this phenomenon, new luminescent centers are generated in the glass. This is known as "Radiophotoluminescence (RPL)", which is applied to luminescent glass used for personal dosimeter [1]. The absorbed dose can measured from the luminescence intensity because it is proportional to the absorbed dose. We have reported that a Cu-doped glass exhibits RPL phenomenon and a well proportionality between the luminescence intensity and absorbed dose [2]. Here we carried out quantitative analyses for the relationship between the variation in the valence of copper ions, absorbed dose, and the RPL intensity.

EXPERIMENTS: Glass was prepared through a conventional melting-cooling method using reagent grade raw materials, $NaNO_3$, Al_2O_3, SiO_2, B_2O_3, and CuO. The glass composition is $25Na_2O \cdot 25Al_2O_3 \cdot 10B_2O_3 \cdot 40SiO_2$ (mol%) doped with CuO of 0.005 mol% for the 100 mol% glass. The prepared glass was cut to the size of 15 x 15 mm^2 and 1 mm in thickness. Gamma-ray irradiation experiments were performed with ^{60}Co γ-ray at the Co-60 Gamma-ray Irradiation Facility at Institute for Integrated Radiation and Nuclear Science, Kyoto University. The irradiation dose was represented as absorbed dose for water.

RESULTS: The mechanism proposed for the RPL phenomenon in the Cu-doped aluminoborosilicate glasses is considered to be as follows [2]. Copper in the glass mainly exists as divalent Cu^{2+} or monovalent Cu^+ ions. Although Cu^{2+} ions has no luminescence, Cu^+ ions has a bright one around 2.5 eV (500 nm) by excitation at 240 nm. A part of the electrons and holes generated in the glass by the high energy radiation are captured by the Cu^{2+} and Cu^+ ions, respectively.

$$\text{Glass} \rightarrow h^+ + e^-$$
$$Cu^{2+} + e^- \rightarrow Cu^+$$
$$Cu^+ + h^+ \rightarrow Cu^{2+}$$

Since the molar fraction of Cu^{2+} is larger than that of Cu^+ in the aluminoborosilicate glass, the electron-captured reaction is predominant. Therefore, the intensity of Cu^+ luminescence increases after the high energy irradiation.

Figure 1 shows the variation of absorption spectra of the Cu-doped aluminoborosilicate glass before and after the γ-ray irradiation. The inset shows the variation of the absorption band assigned to the d-d transition of Cu^{2+} ions. The intensity of the absorption band is decreased because the Cu^{2+} ions became Cu^+ by the capture of the electrons which are generated by the irradiation.

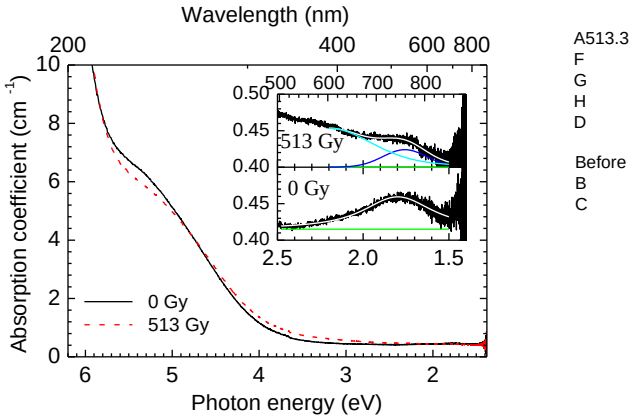

Fig. 1. Absorptions spectra of Cu-doped aluminoborosilicate glass before and after the γ-ray irradiation with the absorbed dose of 513 Gy

The dependences of the absorption and RPL intensities on the absorbed dose are presented in Fig. 2. Absorption and RPL intensities decreased and increased lineally with the absorbed does until about 800 Gy. This is well consistent with the RPL mechanism for the Cu-doped glass. The slop of the proportional line between the absorption intensity and the dose was -1.89×10^{-5} $cm^{-1} \cdot Gy^{-1}$. From this value and the molar absorption coefficient of Cu^{2+} in aluminoborosilicate glass, 26.9 $L \cdot mol \cdot cm^{-1}$ [3], 95 % of Cu in the glass existed as the divalent state, Cu^{2+}, before irradiation and the 0.041 % of Cu^{2+} was varied to Cu^+ ions per 1 Gy irradiation.

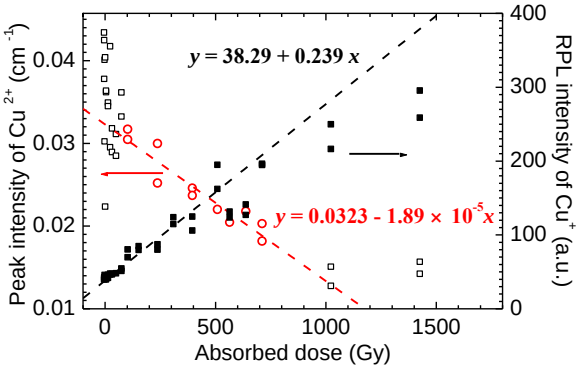

Fig. 2. Dependences of the intensities of the absorption band due to Cu^{2+} ions and RPL of Cu^+ on the absorbed dose.

REFERENCES:

[1] R. Yokota, *et al.*, J. Phys. Soc. Jpn., **23** (1966) 1038-1048.
[2] H. Hashikawa, *et al.*, J. Am. Cer. Soc., **102** (2019) 1642-1651.
[3] W. Thiemsorn, *et al.*, J. Solid Mech. Mater. Eng., **1** (2007) 508 - 518.

CO4-12 Elucidation of the Mechanism of the Solvent-dependent Helix Inversion of Polymer Main Chain Based on the Small Angle X-ray Scattering

Y. Nagata[1], M. Suginome[1], M. Sugiyama[2], R. Inoue[2], N. Sato[2], and K. Morishima[2]

[1] *Graduate School of Engendering, Kyoto University*
[2] *Institute for Integrated Radiation and Nuclear Science, Kyoto University*

INTRODUCTION: Much attention has been paid to the structural control of artificial helical polymers because of their potential applications for asymmetric catalysts, chiral stationary phase, and chiroptical materials. Recently, we found that single-handed helical poly(quinoxaline-2,3-diyl)s (PQXs) bearing chiral side chains exhibit a solvent-dependent helix inversion,[1-3] which can serve as effective scaffold for chirality-switchable materials. [4-7]

In order to elucidate the mechanism of the solvent-dependent helix inversion of PQXs, we have revealed detailed structures of a PWX with right- or left-handed structures in tetrahydrofran-d_8 (THF-d_8) or a mixed solvent of 1,1,2-trichloroethane-d_3 (1,1,2-TCE-d_3) and THF-d_8 (8/2, v/v) by using small-angle neutron scattering (SANS) experiments, in conjunction with theoretical calculations.[8] The obtained structures of the PQX suggested that the right-handed structure in THF-d_8 is well solvated, while the left-handed structure in 1,1,2-TCE-d_3/ THF-d_8 (8/2, v/v) is less solvated. Although SANS measurements was quite useful for the elucidation of the detailed structure of the PQXs, it was also found that the exhaustive screening of the conditions (temperature, solvents, additives, and so on) were difficult because of the limited neutron beamtime. In this study, we have tried to use small-angle X-ray scattering (SAXS) on a laboratory system.

EXPERIMENTS: A PQX bearing (*R*)-2-octyloxymethyl side chains (100mer) was prepared. The PQX was dissolved in tetrahydrofurane (THF, 4.0 mg / mL) to measure the SAXS patterns by using the Rigaku NANOPIX SAXS/WAXS measurement system (CuKα) or the Rigaku Nano-Viewer X-ray Scattering System (MoKα).

RESULTS: Firstly, we tried to use the Rigaku NANOPIX SAXS/WAXS measurement system (CuKα, λ = 1.54 Å) with an aluminum cell with thin quartz windows (the thickness of the quartz films was 20 μm). However, the adhesive agent (epoxy resin) between the aluminum cell and the quartz films was dissolved in THF, which caused the leak of the liquid sample. Although we have also used the indium seal or other adhesive agents, the leak of the sample was not fully sealed. Subsequently, we tried to use the Rigaku Nano-Viewer X-ray Scattering System (MoKα, λ = 0.71 Å) with a quartz cell with a Teflon cap (the thickness of the quartz windows was 1.0 mm, and the optical path was 2.0 mm), which was used in the SANS measurements. Here, we expected that the wavelength of the X-ray was short enough to measure SAXS patterns using this cell, however, the transmission was found to be not enough. Therefore, we have newly developed a quartz cell with a Teflon cap with thin windows and a short cell path (Fig. 1). The thickness of the quartz windows was shortened to 0.5 mm, and the optical path was also shortened to 1.0 mm. The leak of organic solvents including THF, chloroform, and 1,1,2-tetrachloroethane was not observed at least 24 hours at room temperature. Now we are trying to measure the SAXS pattern of the PQX in various organic solvents using the newly developed quartz cell.

Fig. 1 A quartz cell with a Teflon cap. The thickness of the quartz windows was 0.5 mm, and the optical path was 1.0 mm

REFERENCES:

(1) Yamada, T.; Nagata, Y.; Suginome, M. *Chem. Commun.* **2010**, *46*, 4914-4916.
(2) Nagata, Y.; Yamada, T.; Adachi, T.; Akai, Y.; Yamamoto, T.; Suginome, M. *J. Am. Chem. Soc.* **2013**, *135*, 10104-10113.
(3) Nagata, Y.; Nishikawa, T.; Suginome, M. *J. Am. Chem. Soc.* **2015**, *137*, 4070-4073.
(4) Nagata, Y.; Nishikawa, T.; Suginome, M. *Chem. Commun.* **2012**, *48*, 11193-11195.
(5) Nagata, Y.; Takagi, K.; Suginome, M. *J. Am. Chem. Soc.* **2014**, *136*, 9858-9861.
(6)Nagata, Y.; Uno, M.; Suginome, M. *Angew. Chem. Int. Ed.* **2016**, *55*, , 7126-7130.
(7) Nishikawa, T.; Nagata, Y.; Suginome, M. *ACS Macro Lett.* **2017**, *6*, 431-435.
(8) Nagata, Y.; Nishikawa, T.; Suginome, M.; Sato, S.; Sugiyama, M.; Porcar, L.; Martel, A.; Inoue, R.; Sato, N. *J. Am. Chem. Soc.* **2018**, *140*, 2722-2726.

CO4-13 Vacancy-Type Defects in Tb-Doped GaN Films Probed by a Slow Positron Beam

S. Hasegawa, A. Yabuuchi[1], and A. Kinomura[1]

The Institute of Scientific and Industrial Research, Osaka University
[1]Institute for Integrated Radiation and Nuclear Science, Kyoto University

INTRODUCTION: Rare-earth-doped gallium nitride (GaN) is attracting attention as a candidate material for room temperature ferromagnetic semiconductors. Although the amount of vacancies introduced into the film is considered to be different depending on the crystal growth conditions, they will affect the magnetic properties. In this study, terbium-doped GaN (GaTbN) films were prepared by MBE (molecular beam epitaxy) or ion-implantation techniques, and vacancy-type defects in them were investigated using a slow positron beam.

EXPERIMENTS: Two kinds of MBE-grown GaTbN films with a thickness of around 200 nm were fabricated with different growth conditions. Additionally, a Tb^+-implanted GaN film with a dose of 2×10^{14} Tb^+/cm^2 was also prepared. These films were probed by the KUR slow positron beam and the Doppler broadening of the annihilation radiation (DBAR) spectra were acquired. The DBAR spectra were characterized in terms of an *S*-parameter, which is defined as the peak intensity. When positrons are trapped at vacancy-type defects, the value of *S* increases [1].

RESULTS: Figure 1 shows *S*-parameters obtained for the MBE-grown GaTbN films as a function of incident positron energy. No increase in S-parameters was observed for both GaTbN films compared to the GaN template layer (E > 15 keV). This indicates that Ga vacancies are not introduced by Tb-doping at least under the growth conditions of these samples. Figure 2 shows the annealing temperature dependence of the *S*-parameter obtained for the Tb^+-implanted GaN sample. The increase of the *S*-parameter with increasing the annealing temperature suggests the clustering of the irradiation-induced vacancies. In addition to *S*-parameters corresponding to positron annihilation with low-momentum electrons, *W*-parameters corresponding to annihilation with high-momentum electrons were also determined from the DBAR spectra. The *S*-*W* correlation is shown in Fig. 3. With increasing the annealing temperature, the position of the *S*-*W* plot deviates to the right-hand side from the straight line connecting between the unimplanted-state and the as-implanted-state. This indicates that the irradiation-induced vacancies are clustered by annealing. To observe the interaction between Tb atoms and vacancies, annealing with higher temperatures and comparison with self-ion-irradiated (N^+-implanted) samples are desired.

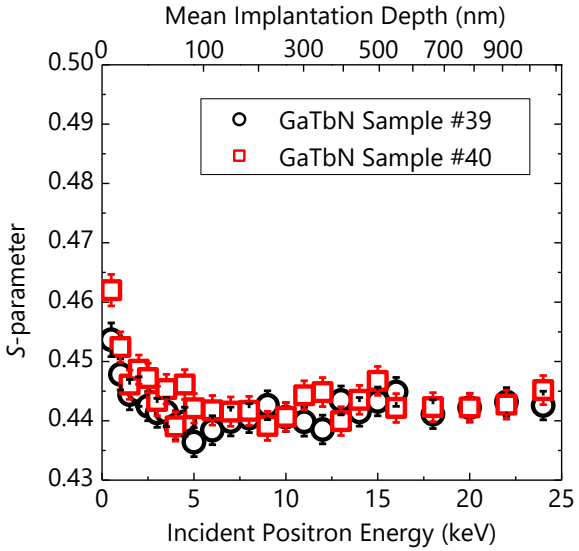

Fig. 1. S-parameters for MBE-grown GaTbN films as a function of incident positron energy. Mean implantation depth is also shown on the upper axis.

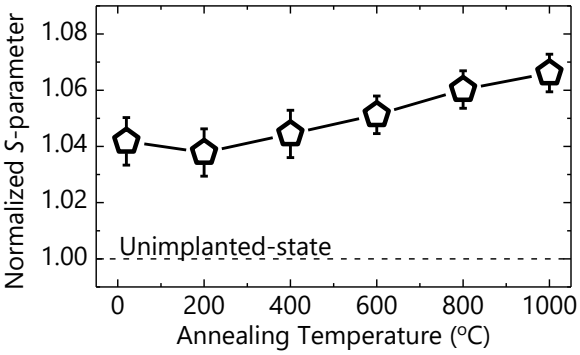

Fig. 2. *S*-parameters for Tb^+-implanted GaN films. The sample was annealed at each temperature for 10 s in N_2 atmosphere by infrared-lamp heating.

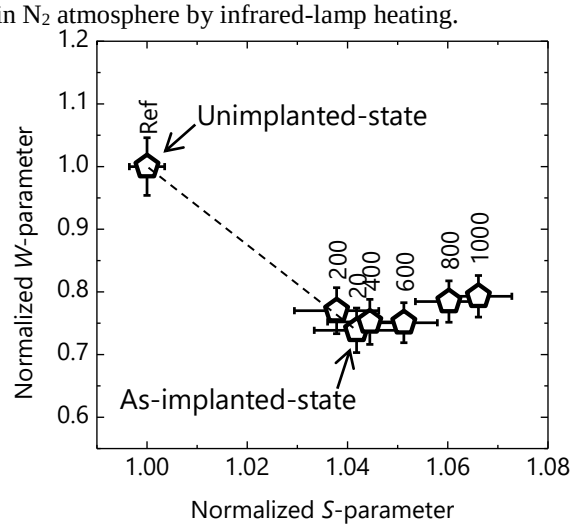

Fig. 3. *S*-*W* correlations for unimplanted (Ref) and Tb^+-implanted GaN films. Annealing temperatures are also shown beside each symbol.

REFERENCES:

[1] R. W. Siegel, Ann. Rev. Mater. Sci., **10** (1980) 393–425.

CO4-14 Fundamental Study on Radiation-Induced Surface Activation under Subcritical Conditions

T. Hazuku[1], T. Ihara[1], R. Taguchi[1], W. Susanto[1], S. Morooka[2], S. Kano[3], H. Abe[3], D. Ito[4] and Y. Saito[4]

[1]*Tokyo University of Marine Science and Technology*
[2]*Waseda University*
[3]*The University of Tokyo*
[4]*KURNS, Kyoto University*

INTRODUCTION: A supercritical water-cooled reactor (SCWR) is one of the 4th generation nuclear reactors, which is based on the light water reactor technology [1], and considered to have high safety and economic performance. On the other hand, radiation-induced surface activation (RISA) phenomenon enhances metal surface wettability, boiling heat transfer and anticorrosive effects by the electrochemical interaction between the base metal and the oxide film on the metal surface [2]. It implies that RISA phenomenon can contribute to the much higher performance of SCWR and improve the safety features.

This study is aimed at evaluations of the RISA effect on the electrochemical characteristics and surface wettability of metals at high-temperatures and pressures.

RESULTS AND DISCUSSIONS:

Effect of RISA on electrochemical characteristics

In order to evaluate the effect of the RISA on the electrochemical characteristics of stainless steels at the subcritical water conditions, corrosion potentials and polarization curves of stainless-304 specimens (SUS-304) before and after radio-activation were measured at the temperatures up to 350 °C. Three types of specimens: the normal SUS-304 with a surface finished by #2000 emery paper, the SUS-304 with SCW oxide film formed in supercritical water with a temperature of 510 °C and pressure around 35 MPa for 90 hours, and the SUS-304 with ZrO_2 spraying film, were used for the electrochemical measurements. The radio-activated specimens were produced by neutron irradiation for 20 minutes at 1 MW in the operation of Kyoto University Research Reactor (KUR). A decrease in corrosion potentials due to radio-activation or the RISA were confirmed for all specimens at temperatures equal to or less than 300 °C (Fig. 1) while the effect of radio-activation on the potentials at a temperature of 350 °C was insignificant for the normal specimen and the specimen with ZrO_2 sprayed film. The decrease in the corrosion potential due to the RISA was, however, more enhanced for the specimen with SCW oxide film even at the temperature of 350 °C. This study first revealed that the electrochemical characteristics of SUS-304 was improved by RISA under the subcritical condition.

Effect of RISA on surface wettability

Next, the capillary action in mini pipes before and after γ-ray irradiation was observed to evaluate the effect of RISA on the metal surface wettability under a subcritical condition. Neutron imaging was used to visualize the water-gas interface in stainless steel capillary pipes. The capillary pipes with various inside diameters such as 0.5, 0.8, 1.2, 1.4, and 1.8 mm were used as a test section which was heated up to a temperature of 320 °C at a pressure of 21 MPa. The pipes irradiated by 60-Co γ-ray with an integrated irradiation dose of approximately 500 kGy and non-irradiated pipes with various diameters are installed in parallel and water levels in each pipe were compared to evaluate capillary action differences (Fig. 2). The measured water level data showed a good agreement with the calculation. The data in the irradiated pipes showed the wettability was decreased compared to non-irradiated pipes at the temperature of 320 °C. Microscopic observation will be required to clarify the relationship between surface wettability and the formation of the hydroxyl groups on the irradiated surface material under high temperatures.

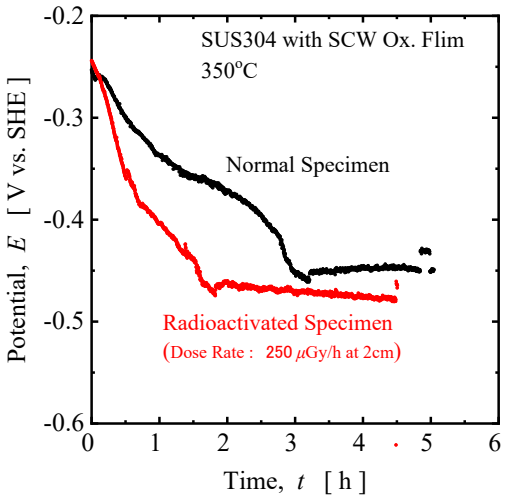

Fig. 1. Corrosion potential of SUS-304 with SCW oxide film before and after radio-activation at 350 °C

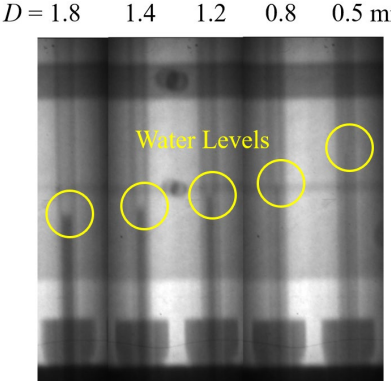

Fig. 2. Typical images in non-irradiated capillary pipes at 320 °C taken by neutron imaging

REFERENCES:

[1] Y. Oka and H. Mori, Supercritical pressure light water cooled reactor, Springer (2014).
[2] T. Takamasa, *et al*., J. AESJ, 49-1 (2007) 45-50.

CO4-15 Salt effects on nanostructure of gliadin hydrates as revealed by SAXS

N. Sato, R. Urade, R. Inoue, K. Morishima, M. Sugiyama

Institute for Integrated Radiation and Nuclear Science, Kyoto University

INTRODUCTION: Wheat flour has been one of the most essential staple foods since ancient times. The quality of wheat flour foods is largely dependent upon the physical property of what dough, which is formed by kneading wheat flour with water and salt. It is well-known that the physical property of wheat dough is mainly attributable to gluten, a composite of major wheat storage proteins: gliadin and glutenin. The former is a monomeric protein responsible for viscosity; the latter is a polymeric protein responsible for elasticity. Therefore deeper understanding on these proteins must be necessary to improve the processability of wheat dough and the quality of wheat food products.

For a long time, gliadins have been believed to be insoluble in water, and accordingly they were extracted with 60–70% ethanol or weak acids. However it has recently been found that gliadins can be extracted into pure water from wheat dough containing NaCl [1]. Seeing that the actual wheat dough is composed of water not alcohols or acids, gliadins in water are more suitable for investigation on the behavior of gliadins in real situation. Based on this view, we have been investigating nanostructure of gliadins in pure water by small-angle X-ray scattering (SAXS). SAXS is a powerful technique for examining structure of disordered condensed materials such as gels, colloids and rubber, and this merit is also effectively applicable to food materials. Our previous study [2] revealed that gliadin monomers dispersed isolatedly at a low concentration of aqueous solution gradually associate together to form multimolecular domains with interdomain interference. The SAXS profiles for gliadin hydrates at higher concentrations also disclosed that density fluctuation exists in the gliadin aggregates and the correlation length of this fluctuation becomes smaller with increasing gliadin concentrations. It was also found that nanostructure of gliadin hydrates is strongly affected by the presence of salts. As the concentration of NaCl increases, the correlation length of density fluctuation reduces significantly, suggesting that gliadin hydrates are strongly contracted. The rheological property of gliadin hydrates also highly depend on the presence of salts. Compression modulus of gliadin hydrates increases with increasing NaCl concentrations. This means that gliadin hydrates become hard when NaCl is added. However it is still unknown what interaction induces the change of structure and property of gliadin hydrates in the presence of salts. In this study, we conducted SAXS measurements on gliadin hydrates containing various classes of salts to elucidate the mechanism of salts affecting on the hydration and association of gliadin molecules.

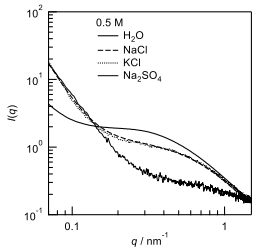

Fig 1. SAXS profiles of 40% gliadin hydrates containing various salts at a concentration of 0.5 M.

EXPERIMENTS: Gliadins prepared by the same method as reported before [1] were dispersed into water containing various kinds of salts at a concentration of 0.5 M. Total gliadin concentration was adjusted by adding the salt-containing solvents whose volume was the same as that of the 40 wt% salt-free solution. Samples were put into 1-nm-thick aluminum cells with optical windows of 7-μm-thick PEI films. SAXS measurements were performed with a laboratory SAXS instrument (NANO-PIX, Rigaku) installed at Institute for Integrated Radiation and Nuclear Science, Kyoto University. The wavelength of X-ray was 1.54 Å and the camera length was 1300 mm. Typical exposure time was 300 sec. All measurements were carried out at 25 °C.

RESULTS: Fig. 1 shows the results of SAXS measurements with 40 wt% gliadin solutions with 0.5M NaCl, KCl and Na_2SO_4. A broad peak due to density fluctuation was found at q = 0.4 nm^{-1} in pure water, and it became small and shifted higher to q = 0.4 nm^{-1} by adding 0.5M NaCl. This profile was almost unchanged by altering salt with KCl, implying that cation variation has little effect on the nanostructure of gliadin hydrates. In contrast, the profile for Na_2SO_4 was drastically different. The broad peak due to density fluctuation was hardly recognizable. This fact indicates that anion change has more significant influence on aggregation structure of gliadin hydrates. Also it should be noted that valence number of the anion is larger than chloride ion, which affects the electrostatic interaction between the gliadin molecules.

REFERENCES:

[1] T. Ukai, Y. Matsumura, R. Urade, *J. Agric. Food Chem.*, **56**, (2008) 1122-1130.

[2] N. Sato, *et al., J. Agric. Food Chem.*, **63**, (2015) 8715-8721.

CO4-16 Ar$^+$-Irradiation-Induced Defects in $GdB_2Cu_3O_y$ Superconducting Films Probed by Positrons

T. Ozaki, T. Sueyoshi[1], H. Sakane[2], A. Yabuuchi[3] and A. Kinomura[3]

School of Science and Technology, Kwansei Gakuin University
[1]Faculty of Advanced Science and Technology, Kumamoto University
[2]SHI-ATEX Co., Ltd.
[3]Institute for Integrated Radiation and Nuclear Science, Kyoto University

INTRODUCTION: $GdBa_2Cu_3O_y$ (GdBCO) is attracting attention as a candidate material for superconducting wires that can be used in liquid nitrogen temperatures. Recently, it has been found that ion-irradiation-induced defects allow the magnetic flux to be pinned and remain superconducting-state even under high magnetic fields. However, it has not been clarified what defects formed by ion irradiation are effective as pinning points. In this study, to investigate what kind of defect that improves high magnetic field resistance in superconducting materials, Ar$^+$ ions irradiated GdBCO samples were probed by a slow positron beam.

EXPERIMENTS: 350 keV Ar$^+$ ions were irradiated to GdBCO(500 nm)/CeO_2(150 nm)/Y_2O_3(150 nm)/Ni/Cu/SUS samples with doses of 5.6×10^{12} Ar$^+$/cm^2 or 3.5×10^{13} Ar$^+$/cm^2. In this Ar$^+$ beam energy, irradiation-induced defects are formed only in the GdBCO layer with a thickness of 500 nm. The unirradiated and Ar$^+$ irradiated GdBCO samples were probed by the KUR slow positron beam and the Doppler broadening of the annihilation radiation (DBAR) spectra were acquired. The DBAR spectra were characterized by *S*-parameter (*W*-parameter), which corresponding to annihilation with low (high) momentum electrons [1]. When positrons are trapped at vacancy-type defects, the value of *S* increases [1].

RESULTS: Figure 1 shows the *S*-parameters obtained for each sample. Contrary to our initial expectations, decreases in S-parameters are observed after Ar$^+$ irradiation. Since the value of S does not increase even when the irradiation dose becomes 6 times or more, almost all incident positrons are considered to be trapped at irradiation-induced defects. Figure 2 shows *S*-*W* correlations obtained for each sample acquired at incident positron energies of 6–11 keV. In the two irradiated samples, the *S*-*W* correlations are plotted in approximately the same region. Almost all positrons are trapped at defects in the irradiated samples, thus, this result indicates that positrons are trapped at the same defect species in both samples. On the other hand, the *S*-*W* correlations of the unirradiated sample are plotted in the region where *S* is higher than that of the irradiated samples. This means that the unirradiated sample contains larger vacancy-type defects (vacancy clusters or voids) than in the irradiated samples. The observed decreases in S parameters due to Ar irradiation will be caused by the mechanism as shown in Fig. 3. Briefly, the unirradiated sample contains larger as-grown defects than Ar$^+$-irradiation-induced defects.

REFERENCE:

[1] R. W. Siegel, Ann. Rev. Mater. Sci., **10** (1980) 393–425.

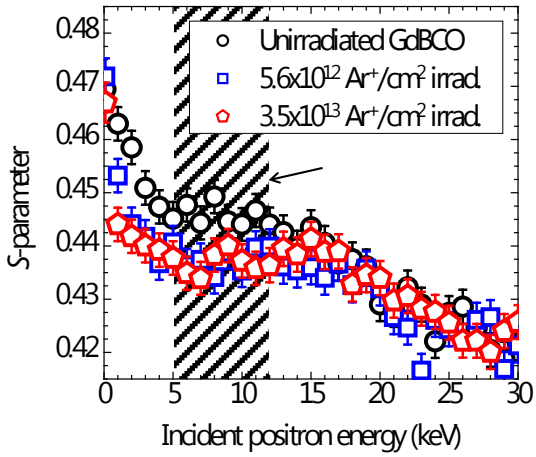

Fig. 1. *S*-parameters for unirradiated and Ar$^+$ irradiated GdBCO samples.

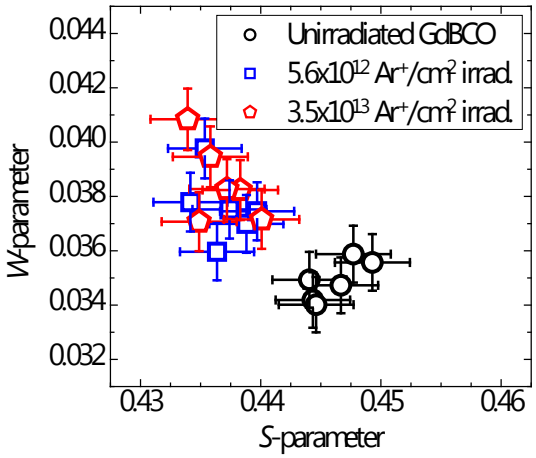

Fig. 2. *S*-*W* correlations for unirradiated and Ar+ irradiated GdBCO samples acquired at incident positron energies of 6–11 keV.

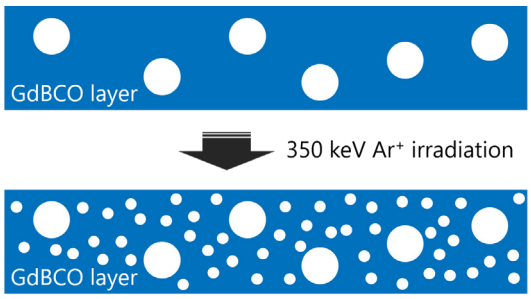

Fig. 3. Picture explaining the change of positron annihilation characteristics in the GdBCO layers before and after Ar$^+$ irradiation.

CO4-17 Vacancy migration behavior in Co-Cr-Fe-Mn-Ni medium/high entropy alloys

K. Sugita, M. Mizuno, H. Araki, A. Yabuuchi[1] and A. Kinomura[1]
Graduate School of Engineering, Osaka University
[1]*Institute for Integrated Radiation and Nuclear Science, Kyoto University*

INTRODUCTION: The alloy design has been conventionally performed by choosing a base metal and adding suitable elements to achieve desired properties. Over the last decade, a new type of multicomponent alloys called as "high entropy alloys", which include equiatomic / near-equiatomic proportion of constituent elements, have been proposed by Yeh et al. [1-3]. They often show simple solid solution structures at high temperature due to high configurational entropy of mixing for a random solid solution. High entropy alloys have been reported to have the following promising properties of practical interest, such as high strength combined with ductility, high fracture toughness, excellent oxidation and corrosion resistance. "Sluggish diffusion" kinetics is believed to be a main contributor to these properties. Therefore, it has also created fundamental interest for atomic diffusion in a multiprincipal element matrix, and the diffusion kinetics in high entropy alloys has been actively investigated by diffusion couple method and tracer-diffusion method.
In this work, we contribute to a debate about hypothetical sluggish diffusion phenomena in high entropy alloys by investigating the vacancy migration behavior in Co-Cr-Fe-Mn-Ni medium/high entropy alloys during the isochronal annealing after electron-irradiation.

EXPERIMENTS: Metal pieces of Co, Cr, Fe, Mn and Ni with 99.9% up purity were added together in equiatomic proportions to produce $Co_{20}Cr_{20}Fe_{20}Mn_{20}Ni_{20}$, $Co_{25}Fe_{25}Mn_{25}Ni_{25}$, $Co_{25}Cr_{25}Fe_{25}Ni_{25}$, $Cr_{33.4}Fe_{33.3}Ni_{33.3}$, $Cr_{15}Fe_{45}Ni_{40}$ alloy ingots by arc melting or vacuum induction melting followed by homogenization at 1373 K for 24 h. The alloy ingots were cut into square plate specimens with dimensions of 10 × 10 × 0.5 mm^3. The specimens were subjected to strain relief annealing at 1373K for 10 h and then rapidly cooled to prevent secondary phase precipitation and to stabilize single-phase FCC structures. The specimens in water flow were exposed to 8 MeV electron beam irradiation for 3 h in KURNS-LINAC. The irradiation damage was evaluated at (1.3 - 1.8) $\times 10^{-4}$ dpa. In order to investigate the thermal stability of vacancies, the electron irradiated specimens were subjected to the subsequent isochronal annealing for 1 h at 373-673 K.
Positron lifetime measurements were carried out by using a digital oscilloscope system with photomultiplier tubes mounted with BaF_2 scintillators, having a time resolution (FWHM) of 180 ps. The positron lifetime measurements require data acquisition for approximately 15 hours with a Na-22 positron source of 0.5 MBq activity in order to acquire 3 million counts in the positron lifetime spectrum. The measured spectra were analyzed using the programs RESOLUTION and POSITRONFIT Extended.

RESULTS: Mean positron lifetime in the electron-irradiated specimens after isochronal annealing is shown in Fig.1. The positron lifetime spectra of as-irradiated specimens show a clear splitting into two exponential components with the longer lifetime values of 185-195 ps. This indicates that a part of positrons is trapped by monovacancies and relatively small vacancy clusters produced during the electron beam irradiation. After the subsequent isochronal annealing, the mean positron lifetime is observed to decrease sharply around 473K. This can be attributed to the decrease in vacancy concentrations triggered by the free vacancy-migration. It demonstrates the vacancy migration enthalpy in the CoCrFeMnNi high entropy alloy is very similar to that in the CrFeNi alloy. These results indicate that the "'sluggish diffusion" hypothesis is not supported in Co-Cr-Fe-Mn-Ni medium/high entropy alloys at least in view of vacancy migration behavior.

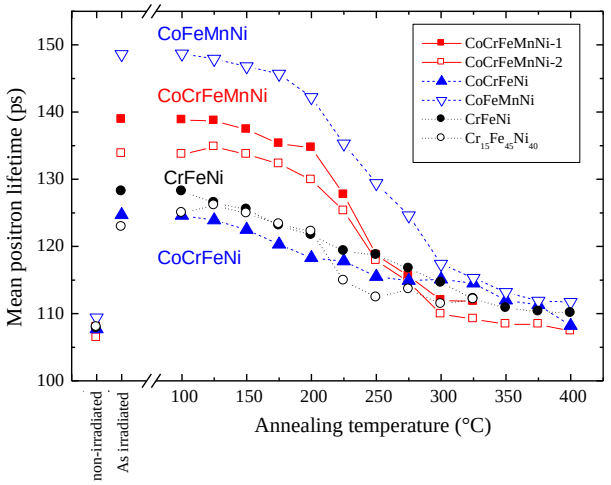

Fig. 1 Mean positron lifetime in the electron-irradiated CoCrFeMnNi, CoFeMnNi, CoCrFeNi, CrFeNi alloys after isochronal annealing.

REFERENCES:
[1] C. Y. Hsu, J. W. Yeh, S. K. Chen, T. T. Shun: Metall. Mater. Trans. 35A, (2004), 1465.
[2] J. W. Yeh, S. K. Chen, S. J. Lin, J. Y. Gan, T. S. Chin, T. T. Shun, C. H. Tsau, S. Y. Chang: Adv. Eng. Mater. 6 (2004). 299.
[3] J. W. Yeh: Ann. Chim. Sci. Mat. 31, (2006), 633.

CO4-18 **Recovery Behaviors of Irradiation-Induced Vacancies in Tungsten Probed by Positrons**

A. Yabuuchi, M. Tanaka and A. Kinomura

Institute for Integrated Radiation and Nuclear Science, Kyoto University

INTRODUCTION: Generally, excess-introduced vacancies agglomerate in the annealing process and develop into vacancy clusters. However, in recent years, vacancies in tungsten (W) have been predicted to repulse each other in theoretical studies based on the first principle calculations [1,2]. In this study, recovery behaviors of electron-irradiation-induced vacancies in W were investigated using positron annihilation lifetime spectroscopy.

EXPERIMENTS: W plates ($5\times10\times0.8$ mm^3) with a purity of 99.999% (5N) were annealed at over 2273 K in vacuum to eliminate lattice defects. After the annealing, 8 MeV electrons were irradiated to the samples at around 373 K using the KURNS-LINAC with total doses of 5×10^{19} e$^-$/cm^2 or 1×10^{18} e$^-$/cm^2. The irradiated samples were isochronally annealed in steps of 15 min/50 K in a vacuum. Positron annihilation lifetime measurements were performed at room temperature for each annealing temperature.

RESULTS: Figure 1 shows the change in positron lifetimes obtained for the 5×10^{19} e$^-$/cm^2 irradiated sample during the isochronal annealing. A positron lifetime component corresponding to a monovacancy [3] is observed in the as-irradiated state with a relative intensity of about 90%. The longer positron lifetime component τ_2 clearly increases at about 600 K. This indicates that monovacancies in W aggregate to form vacancy clusters. Such vacancy clusters are substantially eliminated after the 1423 K annealing. On the other hand, it is noticed that the observed τ_1 is longer than τ_1^{TM} estimated from τ_2 and I_2 with assuming only one defect species exists in the sample. This means that positrons are also trapped at other defect species having a shorter positron lifetime than monovacancies. Figure 2 also shows the change in positron lifetimes obtained for the 1×10^{18} e$^-$/cm^2 irradiated sample during the isochronal annealing. In this measurement, the observed τ_1 agrees with the calculated τ_1^{TM}, which indicates that positrons not trapped at the defect corresponding to the longer positron lifetime τ_2 are annihilated in the delocalized state. However, the longer lifetime component is shorter than that of the high dose sample mentioned above and is less than 150 ps. These results suggest that interstitial impurities are bound with vacancies. Our recent theoretical calculation also supports the interpretation.

REFERENCE:

[1] L. Ventelon *et al.*, J. Nucl. Mater., **425** (2012) 16-21.
[2] Y. Oda *et al.*, Plasma Fusion Res., **9** (2014). 3401117-1-3401117-4.
[3] K. Sato *et al.*, Nucl. Mater. Energy, **9** (2016) 554-559.

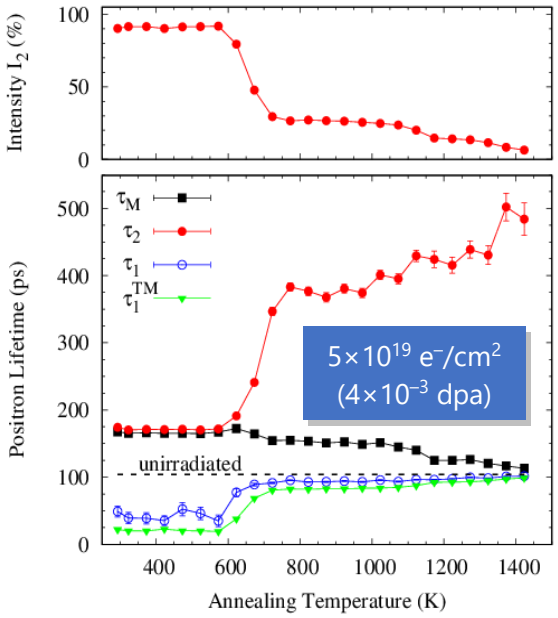

Fig. 1. Change in mean positron lifetime (τ_M), resolved lifetimes (τ_1, τ_2), and the relative intensity of the longer lifetime component (I_2) on isochronal annealing (15 min/50 K) of 5N-W irradiated around 373 K with 8 MeV electrons to a total dose of 5×10^{19} e$^-$/cm^2. The τ_1 calculated from τ_2 and I_2 assuming the presence of only one defect species is shown as τ_1^{TM}. Unirradiated-state is indicated by a horizontal dashed line.

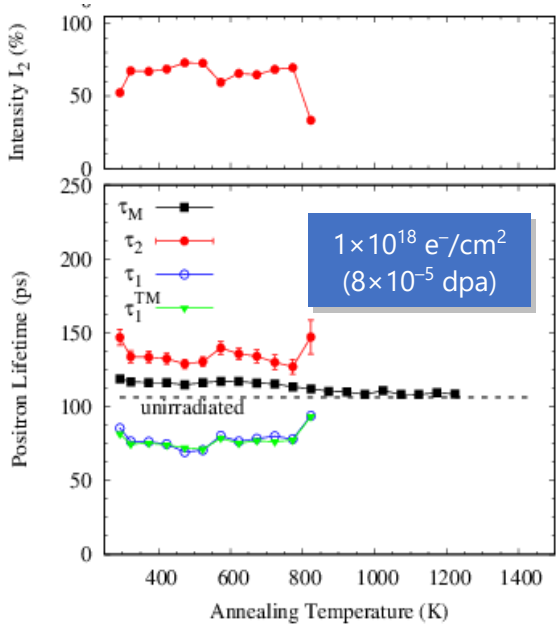

Fig. 2. Change in mean positron lifetime (τ_M), resolved lifetimes (τ_1, τ_2), and the relative intensity of the longer lifetime component (I_2) on isochronal annealing (15 min/50 K) of 5N-W irradiated around 373 K with 8 MeV electrons to a total dose of 1×10^{18} e$^-$/cm^2. The τ_1 calculated from τ_2 and I_2 assuming the presence of only one defect species is shown as τ_1^{TM}. Unirradiated-state is indicated by a horizontal dashed line.

CO4-19 Spectrum of Amino Acid in the Sub-THz region using Coherent TR (II)

T. Takahashi

Institute for Integrated Radiation and Nuclear Science, Kyoto University

INTRODUCTION: In recent years various types of coherent radiation emitted from a short bunch of relativistic electrons have attracted a considerable attention as a bright light source in the THz-wave and millimeter wave regions for the spectroscopic purpose. Coherent transition radiation (CTR), which is emitted from a boundary between two media, is one of such a coherent light source. CTR is usually utilized as a non-polarized light source, because the electric vector of transition radiation (TR) emitted from a metallic screen is axially symmetric with respect to the trajectory of an electron beam. In my previous reports [1] the circularly polarized CTR using a pair of wire-grid radiators with the different polarization has been developed with a new idea. Circularly polarized light has been useful in the circular dichroism spectroscopy. In my previous reports [2] spectra of some kinds of chiral amino acid have been measured using linearly polarized CTR. In this report spectra of Adenine and Thymine, which construct DNA, have been measured.

EXPERIMENTAL PROCEDURES: The experiment was performed at the coherent radiation beamline [3] at the L-band linac of the Institute for Integrated Radiation and Nuclear Science, Kyoto University. The energy, the width of the macro pulse, and the repetition rate of the electron beam were 42 MeV, 47 ns, and 60 Hz, respectively. The average current of the electron beam was 2.0 μA. The spectrum of CTR was measured by a Martin-Puplett type inter- ferometer and a liquid-helium-cooled Si bolometer. The schematic diagram of the experiment was shown in Fig.1.

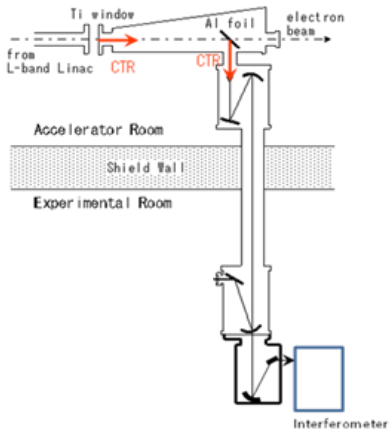

Fig.1 The schematic diagram of the experiment.

Figure 2 is the photograph of the spectrometer and the detector.

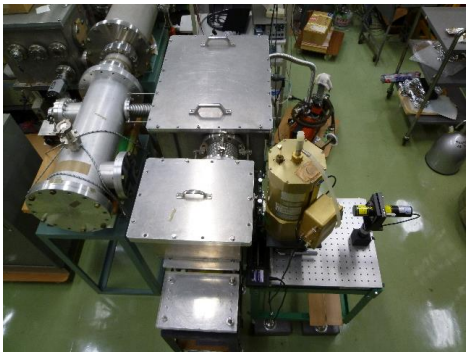

Fig.2 The photograph around the spectrometer.

RESULTS: Measured spectra of Adenine and Thymine are shown in Figs. 3. In the spectrum of Thymine some absorptions are observed at 15, 14, and 19 cm^{-1}. The identification of observed absorption is now in progress

REFERENCES:

[1] T. Takahashi, *et al.*, KURRI-PR 2015 CO4-7.
[2] T. Takahashi, *et al.*, KURRI-PR 2016 CO4-8.
[3] T. Takahashi *et al.*, Rev. Sci. Instrum. **69** (1998) 3770.

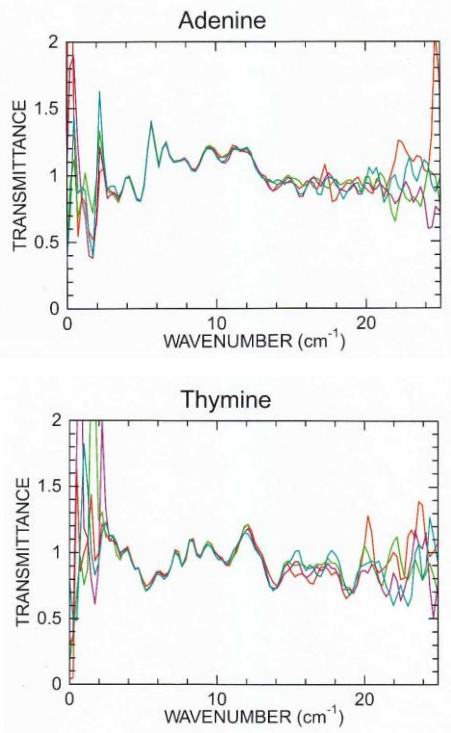

Fig.3 Spectra of Adenine and Thymine.

30080

CO4-20

Hydrogen retention on plasma facing material irradiated by high energy particle beam

K. Tokunaga, M. Matsuyama[1], M. Hasegawa, K. Nakamura and Q. Xu[2]

Research Institute for Applied Mechanics, Khushu University
[1]Hydrogen Isotope Research Center, University of Toyama
[2]Institute for Integrated Radiation and Nuclear Science, Kyoto University

INTRODUCTION: It is of importance to clarify phenomena of implantation, retention, diffusion and permeation of tritium on surface of the armor materials of the first wall/blanket and the divertor on fusion device from a viewpoint of precise control of fuel particles, reduction of tritium inventory and safe waste management of materials contaminated with tritium (T). Refractory metals such as tungsten (W) is potential candidate for an armor of the first wall and the divertor plate of the fusion reactor because of its low erosion yield and good thermal properties. The armor material will be subjected to heavy thermal loads in the steady state or transient mode combined with high energy neutron irradiation that will cause serious material degradation. In addition, high energy runaway electrons would bombard the armor materials along the equatorial plane in fusion device. It is considered that these cause radiation damage and enhance tritium retention. In the present works, T exposure experiments have been carried out on W samples which were irradiated by high energy electrons using LINAC in KURRI of Research Reactor Institute, Kyoto University to investigate effects of high energy electrons irradiation and microstructure on tritium retention of W. In this fiscal year, pure W and recrystallized W were irradiated by high energy electron beam. After that, positron annihilation experiment was carried out to identify the radiation defect. In addition, tritium exposure experiments have been carried out using a tritium (T) exposure device.

EXPERIMENTS: W samples used were ITER grade W (IG-W) and recrystallized W. In the case of IG-W, one was W sample (ITER grade W(1)) which the surface were manufactured to be oriented parallel to the rolling surface and rolling direction. The other W sample (ITER grade W(3)) which the surface were manufactured to be oriented perpendicular to the rolling surface and rolling direction. On the other hand, heat treatment was performed at 1800 ºC for 1h at high vacuum to recrystallize IG-W. The sizes of W samples were 10mm x 10mm x 1mm. The surface of the both samples were polished to be mirrored. High energy electrons irradiation has been carried out using LINAC in KURRI of Research Reactor Institute, Kyoto University. An energy of electron irradiated was 10 MeV and DPA was 2.8 x 10^{-3}. Temperature during the irradiation was measured by thermocouples which was contacted with a backside of the W samples. After the electron beam irradiation, positron annihilation experiment was carried out. In addition, T exposure experiments have been carried out using a T exposure device in University of Toyama. Pressure of the T gas was 1.3 kPa and T exposure was kept for 4 h. T concentration in the gas was about 5 %. Temperatures of pre-heating and T exposures were 400 ºC and 350 ºC. After the exposure to T gas, T amount retained in surface layers of the sample was evaluated by β-ray-induced X-ray spectrometry (BIXS) and imaging plate (IP) measurements.

RESULTS: In the condition of 10 MeV electrons irradiation, electrons go through in 1 mm thickness W sample. As a result, uniform defects were formed in the W samples. Figure 1 shows amount of T measured by the IP measurement. Large amount of T traps comparing with that of samples exposured at 100 ºC, which was reported in the last fiscal year. In the case of non-irradiated samples, T retention of non-recrystallized samples is larger than that of recrystallized samples. These results indicated that some kinds of defects which can trap T decreased by the recrystallization. After the electron beam irradiation, amount of T of non-recrystallized samples is almost the same of that of the un-irradiated ones. However, in the case of the recrystallized samples, the amounts of T of electron beam irradiated samples are a few times of that of non-irradiated samples. As at 400 ºC, vacancies which were produced by electron irradiation at RT, can move enough, vacancy clusters were also formed. It is considered that these vacancy clusters also trap T.

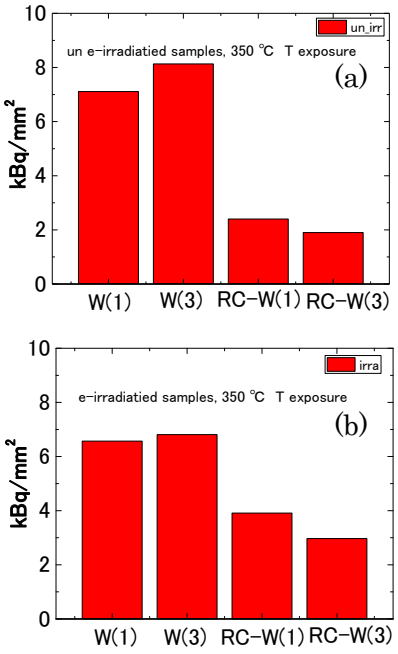

Fig. 1. Amount of tritium on before(a) and after(b) electron beam irradiation measured by IP measurement. RC-W(1) and RC-W(3) are recrystallized W(1) and W(3), respectively.

CO4-21 Defects structure and characterization of electron irradiated B2 ordered alloys

F. Hori, K. Sugita, Y. Sumikura, A. Takano, K. Ohsawa[1], Q. Xu[2] and N. Abe[2]

Dept. of Quantum & Radiation Eng., Osaka Pref. Univ.
[1]*Res. Inst. of Appl. Mech., Kyushu University*
[2]*KURNS, Kyoto University*

INTRODUCTION: Fe-Al alloys, which is B2 ordered intermetallic compound, have good properties such as specific strength to weight ratio, oxidation resistance and strength in elevated temperature. However, the nature of basic defects in this alloy is not necessarily cleared yet. Namely, intermetallic compound alloys possibly include more than two types of vacancies, basically A-vacancy and B-vacancy in A-B type compound. It is difficult to distinguish these vacancies and their characteristic features are distinguishable. For instance, different interaction of hydrogen atoms and different type of vacancies in B2 ordered Fe-Al alloy is suggested by the first principle calculation. So far, we have successfully produced Rh-vacancy and Fe-vacancy by different energy of electron irradiation in Fe-Rh alloys and also detected these defects by positron annihilation techniques. On the other hand, hydrogen is nowadays receiving a lot of attention for various kinds of materials research. It is important to clear the interaction between hydrogen and metallic materials for example hydrogen embrittlement, hydride formation and hydrogen induced transformation in hydrogen storage material. In this study, we have studied the interaction between hydrogen atom and non-equilibrium vacancies in B2 ordered intermetallic alloys.

EXPERIMENTS: Fe-50%Rh alloy specimens with B2 ordered structure were prepared by arc melting method. Sliced samples with the thickness of 0.5 mm were annealed at 1073 K for 3 h followed by quenched into water. These specimens were irradiated with 2 MeV electron to the fluence of 1×10^{17} and 1×10^{18} /cm^2 at JAEA-Takasaki and with 8 MeV electron to the fluence of 5×10^{17} and 1×10^{18} /cm^2 at KURRI, Kyoto University. In both cases, irradiations were carried out at about 330 K controlled by water flow system. Cathodic charged hydrogen implantation have performed for before and after irradiated samples. All samples were measured by X-ray diffraction, positron annihilation lifetime and coincidence Doppler broadening measurements. Also thermal desorption spectroscopy (TDS) measurement have done for hydrogen implanted alloy samples with annealing up to 800K.

RESULTS: Figure 1 shows the CDB ratio profiles of Fe-Rh alloys before and after electron irradiation and hydrogen charged alloy with irradiation. Positron lifetime and CDB results reveals that this irradiation mainly introduces V_{Fe} in this alloy. Changing profile of CDB after hydrogen charging showing trapping of hydrogen atoms by the vacancies. Figure 2 shows the hydrogen desorption from cathodic charged Fe-Rh alloy with or without irradiation. In this figure, desorption peak at 770K appears for hydrogen charged with irradiation sample. Then it can be concluded that hydrogen atoms are trapped by vacancies and released them at this temperature.

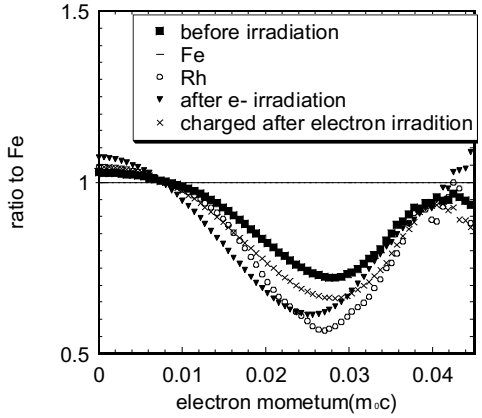

Fig. 1 CDB ratio spectra of electron irradiated and cathodic charged samples.

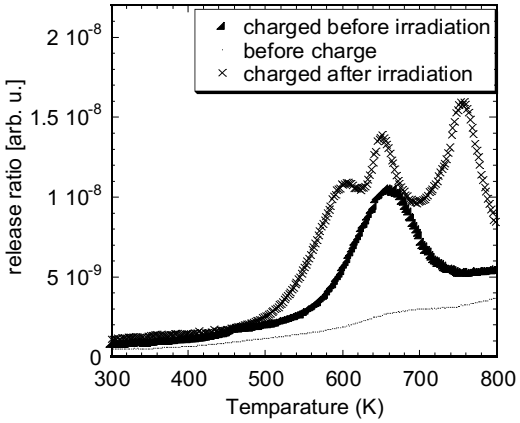

Fig. 2 TDS spectrum for all samples. Hydrogen desorption behavior with annealing temperature.

CO4-22 **Synthesis of Pd nanoparticles on various support materials by γ-ray irradiation reduction method**

F. Hori, S. Toda, Y. Uchimura, T. Matsui[1], Y. Mizukoshi[2] and Q.Xu[3]

Dept. of Engineering, Osaka Prefecture University
[1] Center for Advanced Education of Entrepreneurship and Innovation, Osaka Prefecture University
[2]Institute of Materials Research, Tohoku University
[3]KURNS, Kyoto University

INTRODUCTION: It is well known that metal nanoparticles (NPs) have some specific properties, which are not appeared in bulk materials such as catalytic activities, magnetic properties, electric conductivity and light absorption. These properties depend on its size, shape, structure, chemical composition and so on. They have many possibilities to applied for various industrial fields. Generally, many kinds of metal NPs commercially are synthesized by using chemical reaction method, which is not necessarily in water solution. We have been trying to synthesize various kinds of metal nanoparticles with size and shape controlled by gamma-ray irradiation reduction method. Generally, NPs are not only used itself but supported on large particles with the order of micrometer in almost case. So far, nanocomposites composed of graphene support material and noble metal NPs were successfully synthesized in one-pot process by gamma-ray irradiation. In this study, we have tried to control the size distribution of noble metal NPs on support materials by adsorbing the metal ions on the surface of support material before gamma-ray irradiation.

EXPERIMENTS:
Aqueous solutions with a given concentration of Pd(II) ($PdCl_2 \cdot 2NaCl \cdot 3H_2O$) and 2-propanol. Al_2O_3 and PMMA (Polymethyl methacrylate) powders were added into each water solution respectively. The solution was argon gas purged and sealed into polystyrene vessels. After dispersion by an ultrasonic cleaning bath, they were irradiated with γ-rays from ^{60}Co radio active source at gamma irradiation facility in KURRI, Kyoto University. In order to compare the adsorbing effect of Pd ions on the support materials, one sample was irradiated just after ultrasonic irradiation and another one was gamma irradiated after leave standing for 96 hours. The total dose of gamma irradiation was fixed to 10 kGy with dose rate of 13.6 kGy/h. After irradiation, the products were separated by centrifugation, washed with water and dried by freeze-drying. UV–vis absorption spectra were measured and all products were observed by conventional TEM (JEM-2000FX). X-ray Photoelectron Spectroscopy (XPS) measurement at KEK-PF BL-27 has performed.

RESULTS:
Fig. 1 shows the TEM images for Pd NPs formed on Al_2O_3 particles in aqueous solutions by gamma-ray irradiation reduction. Fig. 2 shows the TEM images for Pd NPs formed on PMMA in aqueous solutions by gamma-ray irradiation reduction. X ray diffraction and XPS measurements show that all of these particles are pure Pd with fcc structure. In both figures, it found that the size of NPs on the support materials irradiated after leave standing for 96 hours becomes smaller than 10 nm and their size distribution is mono-dispersive compared with no leave standing treated samples. In our previous work and preliminaly experiments, no size change was observed for same experiments of Pd NPs synthesis with graphene support material [1, 2]. Al_2O_3 and PMMA have a fuctional group on their surface but graphene has not. Then, it is considred that the metal ions are adsorped on the surface of support materials and it becomes the nucleation site of NPs growth during reduction by gamma irradiation.

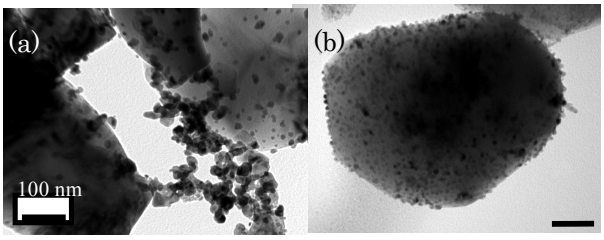

Fig.1 TEM images of Pd NPs reduced with Al_2O_3 by gamma-irradiation method, (a) irradiated just after stirring and (b) irradiated after leave standing for 96 hours.

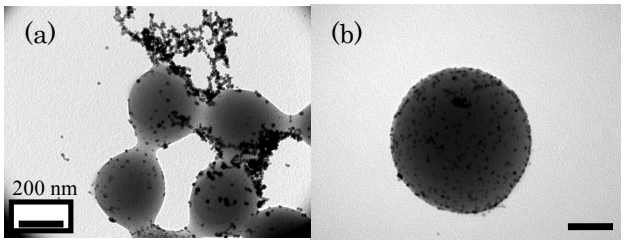

Fig. 2 TEM images of Pd NPs reduced with PMMA by gamma-irradiation method, (a) irradiated just after stirring and (b) irradiated after leave standing for 96 hours.

Reference
[1] A.Tokai and F.Hori et al, Rad. Phys. Chem. 123 (2016) 68.
[2] F.Hori, *et.al,* KURRI Progress Report 2016 (2017) 71 .

CO4-23

Free volume in γ-rays-irradiated Fused Quartz by Positron Age-MOmentum Correlation (AMOC) measurements

H. Tsuchida[1,2], S. Konishi[1], Q. Xu[3]

[1]*Department of Nuclear Engineering, Kyoto University*
[2]*Quantum Science and Engineering Center, Kyoto University*
[3]*Institute for Integrated Radiation and Nuclear Science, Kyoto University*

INTRODUCTION: We study the effect of radiation dose on properties of a free volume in fused quartz under γ-rays irradiation. Fused quartz is a candidate material for use under a radiation environment. A systematic investigation concerning the change in its optical properties has been reported for various types of ionizing radiation such as photons (UV lights and γ-rays), neutrons [1], and fast ions [2]. In this work, Positron Age-MOmentum Correlation (AMOC) technique was applied for investigating radiation damage in the vicinity of free volume by high dose γ-rays irradiation. The AMOC measurement combines positron lifetime and annihilation γ-ray Doppler-broadening spectroscopy by correlated measurements of the positron age and the Doppler shift of one of the annihilation quanta.

EXPERIMENTS: The irradiation experiments were performed at Co-60 γ-rays irradiation facility at KURNS. Fused quartz, with purity of 99.9%, mass density of 2.2 g/cm^3 and thickness of 2 mm (Goodfellow Co.), was used as a target sample. The sample was irradiated with γ-rays at two different radiation doses of 30 kGy and 300 kGy at room temperature. The dose rate was 10 kGy/h. Position annihilation analysis was performed by our developed AMOC system combined with $\beta^+-\gamma$ coincidence positron lifetime spectroscopy. The positron source used was Ge-68.

RESULTS: Fig. 1 shows comparison of positron lifetime spectra obtained before and after irradiation. The spectra in upper left and right indicate results observed at radiation doses of 30 kGy and 300 kGy, respectively. There is a difference in long-lived lifetime component in the time range above approximately 1 ns. This component is attributed to the pick-off annihilation of ortho-positronium (o-Ps) in a free volume of fused quartz. Its intensity is significantly decreased in the spectrum observed after irradiation.

To obtain information about positron lifetimes and corresponding intensities of the spectra, we performed spectrum analysis using the PALSfit program [3]. The results are listed in Table 1. The lifetime and intensity remain unchanged up to 30 kGy, while those values were significantly decreased at high radiation dose of 300 kGy. This suggests that the o-Ps formation in a free volume is suppressed owing to the radiation-induced damage.

The *S* parameter was significantly decreased at 30 kGy, and then it becomes constant. This implies that γ-rays irradiation does not affect a change in a density of free volume in fused quartz. We will perform further investigation on processes of o-Ps annihilation depending on radiation dose by AMOC measurements.

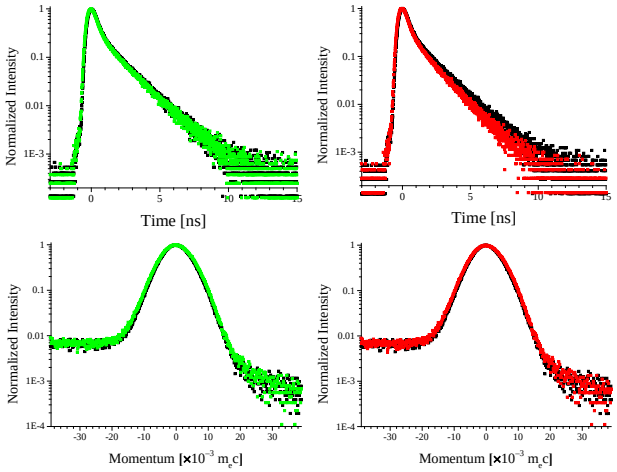

Fig. 1. Spectra of positron lifetime (upper) and annihilation γ-ray Doppler-broadening (bottom) obtained from AMOC measurements for fused quartz sample obtained before and after irradiation of Co-60 γ-rays. The data in left and right shows results for radiation doses of 30 kGy and 300 kGy, respectively. Black symbol indicates data observed before irradiation.

Table 1. Radiation does dependence of the o-Ps lifetime (τ) and intensity (*I*), and the line-shape parameter *S*. The results were obtained from analysis of data shown in Fig. 1.

Dose (kGy)	τ (ns)	*I* (%)	*S*
0	1.580 ± 0.005	53.0 ± 0.2	0.535 ± 0.001
30	1.591 ± 0.005	50.0 ± 0.2	0.509 ± 0.001
300	1.455 ± 0.005	47.8 ± 0.2	0.512 ± 0.001

REFERENCES:

[1] C.D. Marshall *et al.,* J. Non-Crystal. Solids, **212** (1997) 59.
[2] H. Tsuchida *et al.*, Mater. Res. Express, **3** (2016) 055201.
[3] *PALS-Fit Computer Program* (http://palsfit.dk/).

CO4-24 Complex Structure of Ions Coordinated with Hydrophilic Polymer 19. Application for Metaric Plating on Resin Surface. (3)

A. Kawaguchi and Y. Morimoto

KURNS, Kyoto University

INTRODUCTION:

We have reported interacted structures between iodine (polyiodide ions, I_n^{m-}, *m*, *n*: integer, $n > 1$) and polymers.[1] While polyiodide ions (and their counter-ions, ex. K^+ ion presented within I_2-KI(aq)) are prepared as solutes in aqueous solution, they can be diffused into various polymeric matrix without softening nor melting. Such structures and procedures are expected to introduce novel functionality and wide applications to modify polymeric materials with easy operation.[2]

Or, ionic diffusion of polyiodide ions and their counter ions from aqueous solution of polyiodides ("(1st) iodine doping") can advance not only into hydrophilic polymers, such as polyamide-6 (PA6) or polyvinyl-alcohol (PVA), but also into hydrophobic polymers, such as polyethylene (PE) or polyethylene-terephthalate (PET); polyiodide ions in the aqueous solutions can easily diffuse even into *hydrophobic* matrices at room temperature. without melting.

Furthermore, posterior ionic diffusion on the previous presence of polyiodides ("secondary doping") can also advances for both hydrophilic polymers and hydrophobic ones. As phenomena, (previously) iodine-doped polymers can be regarded as "pseudo solvents" for ionic diffusion.[3,4]

These results suggest that coordination between iodine and polymers is dynamic and pliable and activated process, and that previous existence of polyiodide ion drastically enhances posterior ionic diffusion or exchange in polymers. Such posterior diffusion means can be applied for functionalization for matrices with arbitrary shape or size, occasionally, beyond hydrophobicity. As an application for plating, "iodine doping" (and following "secondary doping") is available for metallic plating on hydrophobic matrices.

EXPERIMENTS: Samples are industrial products of micron-sized particles, which designed for ACF (anisotropic conduction film) or spacer with 2 or 5 mm diameters; they are synthesized as spherical particles of acryl resin showing fine-controlled dispersion of diameter. Some particles are products grafted with polystyrene (PS) on their spherical surface. [5]

These matrixes were "iodine-doped" by immersing in I_2-KI(aq) or I_2-NH_4I(aq) (0.1-3.0N) for more than one week. For "secondary doping" of Ag^+, each samples were immersed in $AgNO_3$(aq) (0.1-2.0M) for a few days.

On electroless Cu-plating in aqueous solution, THRU-CUP PSY (UYEMURA) was used. All operation were done at room temperature (c.a. 25℃).

RESULTS: As previously reported, since the resin beads samples have chemically hydrophobic surface as grafted PS, the non-treated sample powder can be little dispersed in water, and ionic treatment (ionic diffusion or electroless plating) for them can be also achieved hardly with ordinal aqueous solutions.[6] Nevertheless, process with the polyiodides aqueous solutions can easily introduce iodine on "(1st) iodine doping" and following Ag^+ ion on "secondary doping" into such hydrophobic surface; coloring with inner-diffused polyiodide (brown) or inner-precipitated AgI (light yellow) had been achieved in a few days or less.

Furthermore, electroless plating with aqueous "THRU-CUP PSY" can advance easily and actively; "iodine-doped" and following "Ag secondary-doped" micro beads, which was originated as hydrophobic surface, could be easily dispersed to aqueous solution of electroless plating reagent, bubbles of H_2 gas were created and light blue color of Cu ion vanished gradually. (Fig.1)

These results means that "iodine doping" (and following "secondary doping", occasionally) is available for posterior introduction of functionality into surface of polymeric materials. Such process has potential availability independent from shape or size of targeted objects, or from if polymeric region is ordered (crystallite) or non-ordered (amorphous), or from if the objects are hydrophilic or hydrophobic.

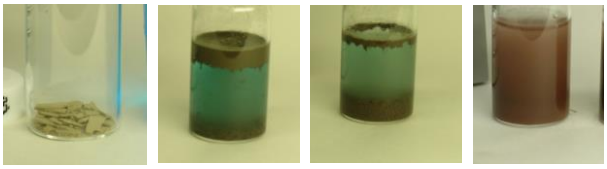

Fig.1: (a) micro particle after "iodine doping" and following "Ag-secondary doping" with $AgNO_3$(aq); (b)-(d) development after injection of electroless Cu-plating aqueous solution, "THRU-CUP PSY".

ACKNOWLEDGMENTS: These results are researched with Dr. Gotoh (Shinshu Univ.) and his staff and are partially funded by NEDO.[5]

REFERENCES:

[1] A. Kawaguchi, Polymer, **35**, 3797-3798. (1994)

[2] patent. JPN-5444559 (2014).

[3] KAWAGUCHI Akio, *et.al.,* SPring-8 User Exp. Rep. **5** (2000A), 354-354. (2000)

[4] A. Kawaguchi, Polym.Prep.Jpn., **62**,5116-5117. (2013).

[5] "Projects for Practical Use from Innovation" sponsored by NEDO (2007-2009).

[6] A. Kawaguchi, *et.al.,* KURRI Prog.Rep.2016, 78-78. (2017).

CO4-25 Compositional Dependence of Mössbauer Spectra for Fe_2O_3-Al_2O_3 Solid Solution

S. Takai[1], H. Nakaishi[1], H. Chen[1], T. Yabutsuka[1], T. Yao[2], S. Kitao[3], M. Seto[3]

[1]*Graduate School of Energy Science, Kyoto University*
[2]*Kyoto University*
[3]*Institute for Integrated Radiation and Nuclear Science, Kyoto University*

INTRODUCTION: While α-Fe_2O_3 and α-Al_2O_3 possess corundum-type structure, the reported solid solution ranges are restricted as approximately 10 % from the both end members due to the 5.6% smaller *c*-axis for Al_2O_3 compared with Fe_2O_3. In recent years, we have found that solid solution of $(Fe_2O_3)_{1-x}(Al_2O_3)_x$ is available for all the compositional range through the mechanochemical synthesis route. Although only the electrochemical property has been investigated on this solid solution system, further magnetic or physicochemical properties have not been clarified yet. Assuming that spin interaction of Fe is diluted by Al substitution, present Fe_2O_3-Al_2O_3 solid solution system is the model case to discuss the magnetization of the corundum-type structure, which has not achieved without the solid solution formation.

In the present investigation, as a relatively early study for the magnetism of Fe_2O_3-Al_2O_3 solid solution, we measured the Mössbauer spectra at room temperature for various compositions of $(Fe_2O_3)_{1-x}(Al_2O_3)_x$. Assuming that α-$Fe_2O_3$ shows weak ferromagnetism with canted magnetic structure at room temperature, contribution of the partial substation of aluminum is important. We focused on the variation of magnetism of the solid solution from the profile of Mössbauer spectra.

EXPERIMENTS: Stoichiometric mixture of γ-Fe_2O_3 and γ-Al_2O_3 reagents were put into a silicon nitride milling pod with 10 milling balls with the diameter of ϕ10. The compositions were selected as x = 0, 0.01, 0.25, 0.33, 050 and 0.67 for $(Fe_2O_3)_{1-x}(Al_2O_3)_x$ system. Mechanical alloying was carried out using a planetary ball milling machine operated at 800 rpm for 240 min. The crystalline phase of the obtained sample was confirmed by X-ray diffraction.

For the measurement of Mössbauer spectroscopy, ^{57}Co in Rh was employed as the γ-ray source. Doppler velocity scale has been calibrated by using Fe foil. The Mössbauer spectra were collected at room temperature. Lorentzian line shapes were assumed for the spectral profile analyses.

RESULTS: Fig. 1 shows the measured Mössbauer spectra for $(Fe_2O_3)_{1-x}(Al_2O_3)_x$. For the spectrum of the sample of x = 0 synthesized by milling γ-Fe_2O_3, sextet peaks were observed, which corresponds to the typical spectrum of α-Fe_2O_3. With increasing the amount of Al_2O_3, additional doublet peaks appear decreasing the sextet peaks. The profiles become almost doublet at x = 0.50 and only the sharp doublet can be seen for x = 0.67. This indicates that weak ferromagnetism diminishes with the substitution of aluminum ions to show the paramagnetic feature. From the sexted component, internal magnetic field is estimated from the peak position and plotted versus Al_2O_3 amount in Fig. 2. The deduced internal magnetic field decreases with x for $(Fe_2O_3)_{1-x}(Al_2O_3)_x$. Therefore, dilution with non-magnetic aluminum ions would reduce the long-range spin ordering to change the magnetic properties, and hence attribute to the internal magnetic field.

Additional experiments as magnetization, XAFS, or heat capacity measurements are now in progress. Precise magnetic behavior in this system would be investigated with these aspect as well as the present results.

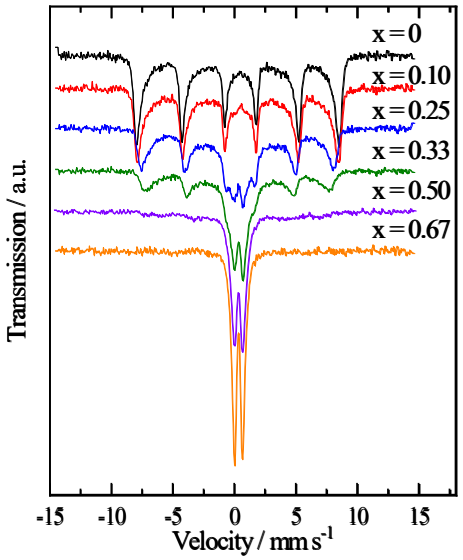

Fig. 1. Mössbauer spectra for $(Fe_2O_3)_{1-x}(Al_2O_3)_x$ measured at room temperature.

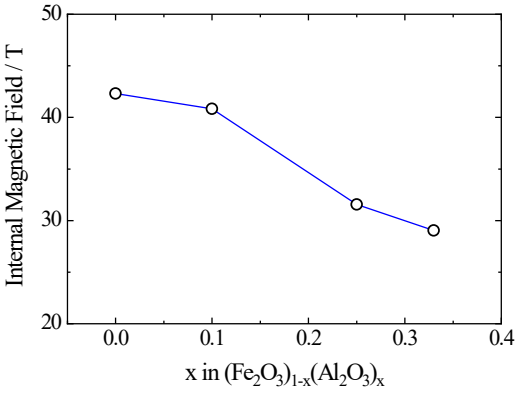

Fig. 2. Internal magnetic field of $(Fe_2O_3)_{1-x}(Al_2O_3)_x$.

REFERENCES:

[1] A. Muan *et al., J. Am. Ceram. Soc.*, 39 (1956) 207-214.
[2] S. Takai *et al., Solid State Ionics*, 313 (2017) 1-6.

CO4-26 Study of resonant frequency change with irradiation dose of piezoelectric PZT element

M. Kobayashi, T. Miyachi, S. Takechi[1], N. Konishi[1], Y. Morita

Planetary Exploration Research Center, Chiba Institute of Technology
[1]Graduate School of Engineering, Osaka City University

INTRODUCTION: In the previous studies, we have performed experiments that a piezoelectric element was irradiated with high intensity 400 MeV/n Xe beam at HIMAC of the National Institute of Radiological Sciences [1][2]. As a result, we found that when irradiating high intensity heavy ions to a piezoelectric element, its resonance frequency and anti-resonance frequency are shifted and also the impedance at the resonance frequency and anti-resonance frequency are changed by beam irradiation. Electromechanical coupling coefficient of the piezoelectric element is decreased.

Since the piezoelectric element is a crystalline material, it is considered that the crystal is damaged by the beam irradiation, and thus the characteristic parameter such as the resonance frequency has changed. Although it is considered to be some radiation damage, detailed mechanism such as its mechanism is not known.

Therefore, in this study, we investigated the response of the piezoelectric parameter to energetic electron beam which has dominantly ionizing effect (less non-ionizing effect).

EXPERIMENTS: From on from irradiation tests in the last year, we performed several runs in which piezoelectric elements were irradiated with electron beam in KURRI-LINAC as an electron beam source. For this year, we varied the condition of electron beam irradiating the test piece, current, energy and so on. There were three conditions in terms of input energy rate into the test PZT element, which were (A) 0.62kJ/sec, (B) 0.55kJ/sec and (C) 0.51kJ/sec. The test piece of PZT element have been warmed by the input electron beam energy, and in the same time, the pieces were air-cooled by a fan to prevent from warming up too much to maintain piezoelectricity. Hence, the temperatures of test pieces were at (A) 118ºC, (B) 100ºC and (C) 80ºC, respectively. Table 1 summarized the other experimental parameters as experimental conditions.

Table 1. Summary of experimental conditions

	Run (A)	Run (B)	Run (C)
Duration (min)	123	129	263
Beam energy (MeV)	18.8	15	20
Beam current (μA)	0.52	0.52	0.4
Input power (j/sec)	6.42	5.5	5.12
Achieved Temp (ºC)	118	103	80
Input energy rate (kJ/sec)	0.62	0.55	0.51

RESULTS: Qualitatively, the same results as last year's experiment were obtained. When irradiation is started, as the temperature of the PZT element rises, the resonance frequency of the PZT element also increases. The resonance frequency also increases with the irradiation amount after the temperature reaches equilibrium. The resonance frequency shift behavior during irradiation is different between Xe beam and electron beam, namely, during beam irradiation and warmed-up of the PZT test piece, the resonance frequency is shifted lower for Xe beam while the frequency is shifted higher for electron beam (in this study), in compared with one at room temperature.

Even after the irradiation is stopped, the resonance frequency is higher than that before the irradiation, while the electromechanical conversion coefficient was decreased, which is the same behavior as one in Xe beam experiment [1][2]. However, among the three tests summarized in Table 1, Run (C) does not have significant change in the electromechanical conversion coefficient. In fact, we performed three runs under the condition of (C) shown in Table1 and found no change in the electromechanical conversion coefficient.

Table 2 summarized the results of those runs and shows also the results of Xe beam experiment for comparison. Two things can be said from this result. First, although Run A and B have a change in the electromechanical conversion coefficient, Run C has no change. It is difficult to interpret this result. One assumption is that changes in the electromechanical conversion factor may require other conditions in addition to beam illumination. For example, the temperature must be above 100 ° C. We will verify this in future experiment.

The other is that the rate of change of the electromechanical conversion coefficient is about twice larger than that of the Xe beam irradiation experiment. Since it is thought that there is some uncertain factor in the estimation of the energy injection amount of the experimental result shown here, this will be further studied in the future.

Table 2. Summary of experimental conditions

	Electron beam (this study)			Xe beam
	Run (A)	Run (B)	Run (C)	
Decrease rate of electromechanical conversion factor[%/kJ]	0.126	0.124	0.0	0.22

REFERENCES:

[1] M. Kobayashi *et al.,* Japanese Journal of Applied Physics 53, 066602 (2014).
[2] M. Kobayashi *et al.,* Japanese Journal of Applied Physics 52, 126604 (2013).

CO4-27 Evaluation of Structural Vacancies in Icosahedral Cluster Solids using Positron Annihilation

J. Takahashi[2], R. Nakajima[3], K. Kitahara[1], A. Yabuuchi[3], N. Oshima[4], I. Kanazawa[2], A. Kinomura[3], K. Kimura[1]

[1]*Department of Advanced Materials Science, The University of Tokyo*
[2]*Department of Physics, Tokyo Gakugei University*
[3]*Institute for Integrated Radiation and Nuclear Science, Kyoto University*
[4]*National Institute of Advanced Industrial Science and Technology (AIST)*

INTRODUCTION: Since the discovery of icosahedral Quasicrystals(i-QCs), extensive studies of i-QCs have been devoted to clarify their structures and electronic transport properties. Unlike crystalline and amorphous metals, stable icosahedral Al-based quasicrystals exhibit anomalous "non-metallic" properties. The term "non-metallic" means a high electrical resistivity and its large negative temperature coefficient. Kimura et al [1] have indicated that the vacant centers of the icosahedral clusters play an important role for stabilities and chemical bonding nature of cluster. Kirihara et al. [2] have reported that 12-Al icosahedral cluster, of which the center of the first shell of cluster is vacant, have covalent bonding nature, while 13-atoms icosahedral cluster with a central atom have metallic bond nature. Positron annihilation method is powerful one for detecting structural vacancies of quasicrystals [3]. Recently Kimura and coworkers [4] have estimated structural vacancies for 1/1-AlReSi approximant crystals by positron annihilation spectroscopy. Positron annihilation measurement of the positron lifetime, coincidence Doppler broadening (CDB), and depth profiling by slow positon beams have shown that structural vacancies in the order of 10^{-3} , which are identified to be centers of the first shell of icosahedral clusters. They found that the structural vacancy density of metallic 1/1 AlReSi with less Re is lower than that of no-metallic AlReSi with more Re. In this study, we have measured the Doppler broadening of quasicrystal AlPdRu, 2/1 approximant crystal AlPdRu, and 1/0 approximant crystal AlPdRu.

EXPERIMENTS and RESULTS:
By using the slow positron beam, we have estimated the change in S-parameter with positron-incident energies in quasicrystal AlPdRu, 2/1 AC AlPdRu, and 1/0 AC AlPdRu. Figure 1 shows the change in S-parameter with positon-incident energies in quasicrystal AlPdRu. The closed circles show the S-parameter, and the open squares show the total counts within the positron annihilation spectra. As shown in Figure 1, S-parameter seems to increase as the positron-incident energy increases from ~0 to 2 keV. But the fluctuation of the values of S-parameter is relatively large. The important point is that the total counts of the positon annihilation spectra decrease remarkably below the positron-incident energy ~ 2keV. So, in order to obtain better data, we must measure the annihilation spectra for longer accumulation time below the positron-incident energy ~ 2 keV.

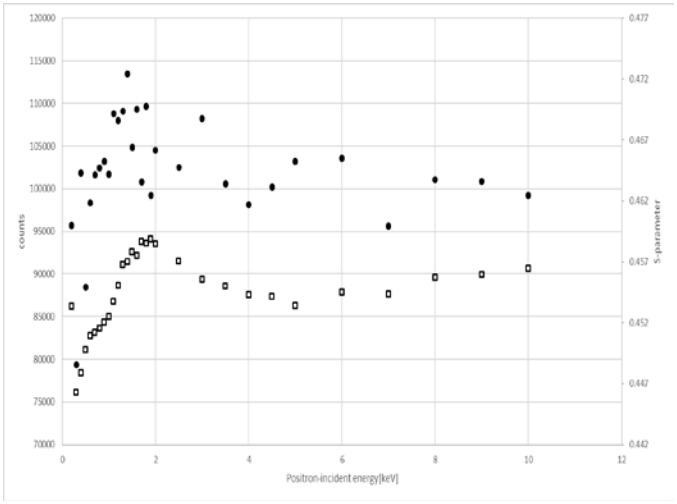

Fig. 1. The closed circles show the S-parameter of quasicrystal AlPdRu. Open squares show the total counts of the positron annihilation spectrum.

REFERENCES:
[1] K. Kimura *et al.*, J. Solid State Chem. **133** (1997) 302.
[2] K. Kirihara *et al.,* Phys. Rev. Lett. **85** (2000) 3468.
[3] I. Kanazawa *et al.,* Phys. Rev. Lett. **79** (1997) 2269.
[4] K. Yamada *et al.,* Philog. Mag. **98** (2018) 107.

CO4-28 Porosity Measurements of Sintered-Silver Bonding Plates

K. Wakamoto[1], T. Otsuka[1], K. Nakahara[1], A. Yabuuchi[2] and A. Kinomura[2]
[1]*Power Device R&D Department, ROHM Co., Ltd.*
[2]*Institute for Integrated Radiation and Nuclear Science, Kyoto University*

INTRODUCTION: Sintered silver has attracted much attention as a die-attach material for the power electronics, owing to its high heat dissipation capability [1]. On the other hand, the coefficient of thermal expansion (CTE) inevitably does not match each other of the materials used in a power system. Thus the heat-cycle oriented mechanical stresses deteriorate die-attach materials, and therefore the mechanical properties of sintered silver impinge on the reliability of electricity systems.

However, nobody can predict how long sintered silver sustains, because the material is porous and its mechanical properties heavily depends how porous it is. Accordingly, the research is highly demanded to measure the porosity.

The porosity rate (p) of sintered silver is reported by some papers [2-3], where p is measured by using cross sectional scanning electron microscopy (SEM). These studies focus on only the μm-order pores of sintered silver materials, not nm-order pores such as crystalline defects. Positron lifetime measurement method has advantages for this purpose. To this end, therefore, the authors used a conventional positron annihilation lifetime spectrometer in Kyoto University to estimate the nm-order pore sizes embedded in sintered silver with various p's by measuring the positron lifetime of the material.

EXPERIMENTS: Four samples were prepared for this research. The fabrication process is described as follows.

Paste including silver nm-particles was stencil printed on a metal plate, and the containing organic solvent was dried at 140ºC for 1 h. These dried films were sintered at 300 ºC for 10 min with uniaxial press via a carbon buffer sheet with 5-, 10-, and 60-MPa pressure. The film shape were 5 mm square and 40-μm thick. As reference, a 500-μm bulk silver sheet annealed at 550 ºC for 2 h was prepared. The process pressure used and the p of each sample are shown in Table I.

Table I Material, pressure, and p of the specimens.

Sample		Material	Pressure (MPa)	p (%)
A		Bulk silver	–	–
B		Sintered silver	60	5
C		Sintered silver	10	14
D		Sintered silver	5	25

p is determined by using cross-sectional SEM images. p is 5%, 14%, and 25% for sample B, C, and D, respectively.

Positron annihilation lifetime spectroscopy was performed to evaluate bulk lifetimes of the samples by using a ^{22}Na source sealed with 7.5 μm Kapton foils. The thickness of the samples B, C, and D was approximately 40 μm. Five sample plates were stacked and measured together to stop all the positrons from the source inside the samples. The spectrometer consists of two scintillation gamma-ray detectors with BF_2 crystals and a digital oscilloscope.

RESULTS: Fig. 1 shows the positron lifetime spectra for the samples B and D together with the reference Ag. The lifetime spectra were decomposed into one or two components apart from the source component. A lifetime of 0.138 ns was obtained for the reference Ag and it was in good agreement with the Ag lifetime previously reported. Average lifetime of the samples B, C and D decreased from 0.24 to 0.22 with increasing pressure during sample formation. Two component analysis of the lifetime spectra showed that the first lifetime changed in the range of 0.17 – 0.20 ns, while the second lifetime changed in the range of 0.29 – 0.33 ns. Changes of lifetimes as a function the formation pressure were not simple, differently from those of the average lifetimes. Balance between the first and second lifetimes changed with increasing the pressure. Further analyses are required to clarify the origin of each lifetime component.

In summary, porosity of sintered Ag plates was characterized by conventional positron annihilation lifetime spectroscopy. The preliminary data were successfully obtained suggesting the correlation between the positron lifetime and the formation pressure.

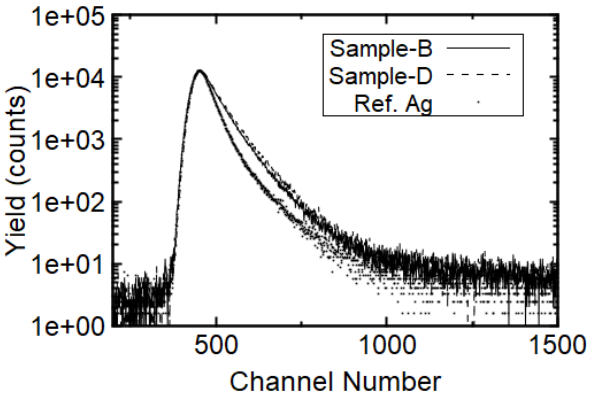

Fig. 1 Typical lifetime spectra of the samples.

REFERENCES:

[1] KIM S. SIOW, Journal of ELECTRONIC MATERIALS., **43** (2014) 947-961.
[2] T. Yousseff *et al*., Microelectronics Reliability., **55** (2015) 1997-2002.
[3] M. Takesue *et al*., Proc. PCIM., (2018) 14

CO4-29 Radiation Resistivity of Ferrite Permanent Magnets Against Neutrons

Y. Iwashita[1], M. Abe[1], T. Yako[1], T. Kurihara[2], M. Fukuda[2], M. Sato[2], T. Sugimura[2], Y. Iinuma[3], Y. Fuwa[3] and K. Takamiya[3]
[1]*Institute for Chemical Research, Kyoto University*
[2]*Accelerator Laboratory, KEK*
[3]*Institute for Integrated Radiation and Nuclear Science, Kyoto University*

INTRODUCTION: Permanent magnets are used as material of beam optical elements. While rare earth magnets, such as neodymium and samarium cobalt, are known to have radiation demagnetization [1], there is not enough information for ferrite magnets, which are economical but have less remanent field strength. In order to verify the resistivity of ferrite magnets, we carried out a trial experiment on radiation demagnetization of ferrite magnets irradiated by neutrons at Kyoto University Research Reactor (KUR).

EXPERIMENTS: We purchased cylindrical anisotropic ferrite magnets with 10 mm diameter and 10 mm length that have easy-axis parallel to the cylinder axis. Since they seemed to have common non-uniformity on the easy-axis and they were randomly magnetized, they were re-magnetized to have better magnetic uniformity. We measured their magnetic field at both end surfaces with a Tesla meter (SENIS 3MH3) using a magnet fixture jig prepared for this experiment. The jig has a 0.5 mm thick plastic plate between the Hall probe and the magnet end surface to avoid a direct contact between them. The irradiation times were starting from 10 seconds and up to maximum 4 hours at 1 MW operation, and 12 minutes and 36 minutes at 5 MW operation. A permanent magnet sample packed in a polyethylene bag was placed into a capsule together with absorbent cotton and sent to the reactor by pneumatic transporter. After the residual radioactivity of the magnet and capsule decayed sufficiently, we took out the magnet sample from the capsule and measured the magnetic field. We compared the magnetic field strength before and after irradiation.

RESULTS: Fig. 1 shows the ratios of the magnetic field strength before and after the irradiation. The error bars show the standard deviations of measured data for each magnet. The resulted data points scatter wider than the error bars, which may come from the magnet fixture configuration of the jig and the measurement procedure. Since the magnets were measured with the polyethylene bag, the distance between the Hall probe and the magnet may not have been defined well, which can be improved for next experiment. In spite of the scattered data points of this preliminary experiment, we conclude that radiation demagnetization of ferrite magnets was not significant up to the range of irradiated dose. The blue line in Fig. 1 denotes neutron dose at which radiation demagnetization becomes significant for neodymium magnets[1]. Ferrite magnets were found to be more resistant to the radiation than neodymium magnets. According to the data taken so far, neutron dose of about 2×10^{18} seems necessary even for 10% reduction of magnetization. Fig. 2 shows comparisons of ratios of magnetic field on 1MW and 5MW operation, showing more decrease at 5MW. Since the temperature in the reactor at 5MW operation is higher than at 1MW, the magnet temperature may have affected the demagnetization process. More data points are desired for better understanding, and the threshold level may become clear.

PERSPECTIVES: More irradiation dose with improved magnetic field measurement procedure will clarify the demagnetization as a function of the dose level.

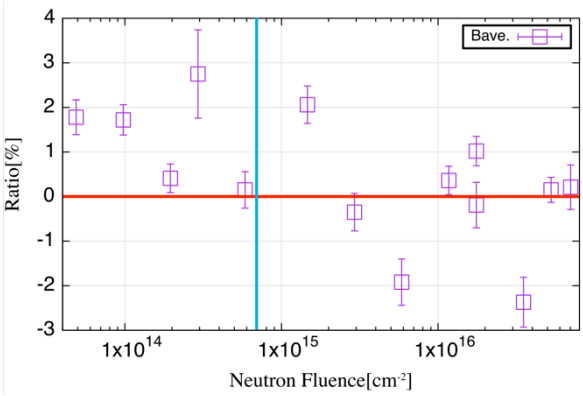

Fig. 1: Ratio of radiation demagnetization of ferrite permanent magnet.

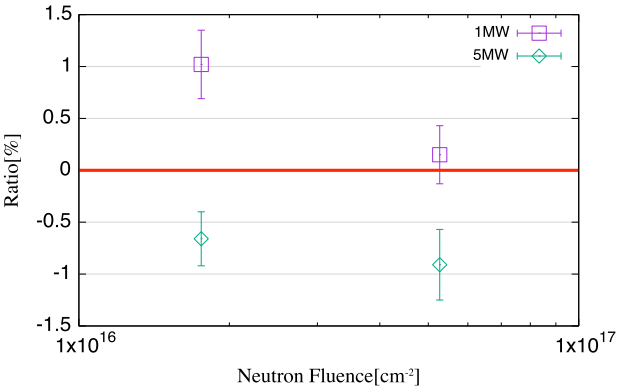

Fig. 2: Ratio of radiation demagnetization on 1MW and 5MW operation.

REFERENCES:

[1] X. -M. Marechal, T. Bizen, Y. Asano, H. Kitamura, Proceedings of EPAC, Edinburgh, Scotland, 2006.

CO4-30 Neutron Irradiation to Optiacal Devices for ITER Diagnostics System

E. Yatsuka and M. Ishikawa,

Fusion Energy Research and Development Directorate, National Institutes for Quantum and Radiological Science and Technology (QST)

INTRODUCTION: QST is developing Diagnostic systems for ITER, which is a fusion experimental reactor. In the development, it is important to verify the radiation resistance of each component of the Diagnostic systems, in particular, the neutron resistance. The purpose of this study is that the high neutron flux generated from Kyoto University Research Reactor (KUR), which is equivalent to the fluence experienced by the diagnostic components during 20 years operation of ITER, irradiates to the component. Then, it is clarified whether the performance of the optical element can be maintained even after high neutron irradiation.

EXPERIMENTS: Neutron irradiation to the optical element (main material is SiO_2) for ITER Edge Thomson Scattering System [1], which is one of the diagnostic system procured by Japan Domestic Agency is performed at the Slant Exposure Tube in KUR in order to investigate the degree of deterioration of the element.

RESULTS: After 20 hours of neutron irradiation at the Slant Exposure Tube, the surface dose rate of the irradiated optical device was measured. It was found that it was relatively high (>300μSv/h: immediately after irradiation, $\gamma \sim 50$ μSv/h, $> \beta\ \gamma 300\mu$ Sv/h). Therefore, it was decided that optical measurements of the irradiated optical element would be performed the next fiscal year (FY2019)

REFERENCES:

[1] E. Yatsuka, T. Hatae, M. Bassan, *et. al.,* Fusion Eng. Design, **100** (2015), 461-467.

CO4-31 A study on destruction of cesium aluminosilicate compounds by gamma ray irradiation

H. Ohashi, R. Takaku, T. Saito[1]

Faculty of Symbiotic Systems Science, Fukushima University
[1]Institute for Integrated Radiation and Nuclear Science, Kyoto University

INTRODUCTION: In recent years, aluminosilicate compounds have attracted attention as a final disposal method of ^{137}Cs contained in radioactive contaminated waste. One of the most considered to be a promising material is pollucite. Pollucite has various properties that favor the immobilization of Cs ions, and in situ synthesis from soil is also possible [1]. However, the damage to the aluminosilicate framework by radiation decay is concerned because it contains ^{137}Cs. Several reports have been made on the effect by β-decay of ^{137}Cs on aluminosilicate framework [2, 3], and no significant damage to the framework has been confirmed in any of the reports. On the other hand, the effects of gamma rays have not been reported. The purpose of this study was to investigate the influence of gamma rays on the synthesized pollucite with aluminosilicate framework.

EXPERIMENTS: The solution with Na_2SiO_3, $NaAlO_2$, CsCl, NaOH, and water was prepared and placed in a Teflon inner cylinder pressure container. Pollucite was synthesized by hydrothermal method, holding the container at 180 ℃ for 5 hours. The resulting precipitate was washed and collected by filtration, and dried at 110℃ for 16 hours at least.

The powder samples were irradiated with ^{60}Co gamma rays at 228 kGy. Characterization was performed by XRD. The 7 days leaching test by PCT-A method was carried out to evaluate the change of Cs retention performance by framework damage. The normalized leaching rate, NR_i [g/m^2·d], was calculated by equation (1).

$$\mathrm{N}R_i = \frac{c_i}{f_i \frac{SA}{V} t} \qquad (1)$$

Where c_i [g/L] was the concentration of element "i" in the solution, f_i was the weight ratio of the element "i" in the sample before leaching, SA [m^2] was the sample surface area, V [L] was the volume of the leaching liquid, and t [day] was the test duration.

RESULTS: Fig.1 shows the XRD patterns of pollucite sample and gamma irradiated pollucite. All the patterns showed that they contained only single-phase pollucite, and gamma irradiated pollucite did not significantly change compared to pollucite without irradiation, indicating that there was no change with irradiation in the crystal structure in bulk phase.

Table 1 shows the various parameters obtained by the leaching test according to the PCT-A method, and the normalized leaching rate. In previous report [4], the normalized leaching rate of pollucite was around 10^{-5} to 10^{-6} g/(m^2·d), and was close value to the sample with gamma ray irradiation at this study.

From the above results, it was considered that the effect of gamma ray irradiation on the aluminosilicate framework of pollucite was not observed in this study.

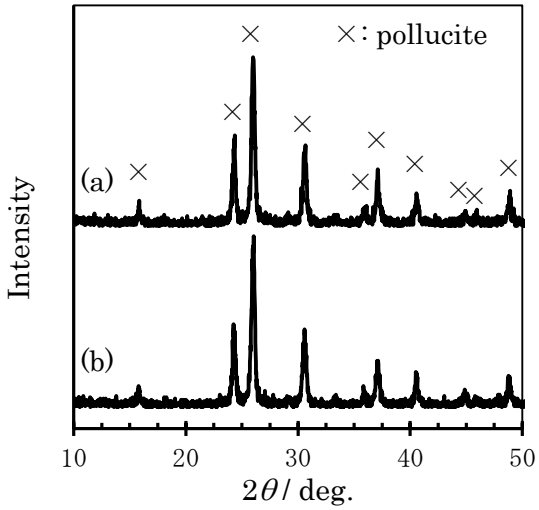

Fig. 1. XRD patterns of (a) pollucite and (b) γ-irradiated-pollucite

Table 1. Leaching test parameters in this study

	f_{Cs}	SA/V [m^2/L]	NR_{Cs} [g/m^2·d]
pollucite	0.40	3.1×10^{3}	1.1×10^{-6}
γ-irr.-pollucite	0.40	3.1×10^{3}	1.0×10^{-6}

REFERENCES:

[1] Y. Yokomori *et al.*, *Sci. Rep.*, **4** (2014), 4195
[2] J. Fortner *et al.*, Radiogenic transmutation effects in a crystalline aluminosilicate ceramic: a TEM study, Scientific Basis for Nuclear Waste Management XXV Materials Research Society 2001 Fall Meeting, November 26–30 2001, Boston, Massachusetts.
[3] N. J. Hess *et al.*, *J. Nucl. Mater.*, **281** (2000), 22-33.
[4] Z. Jing *et al.*, *J. Hazard. Mater.*, **306** (2016), 220–229.

CO5-1 Ar-Ar Dating of Sub-milligram Extraterrestrial Materials and Evaluation of the Irradiation Conditions

R. Okazaki[1] and S. Sekimoto[2]

[1]*Department of Earth and Planetary Sciences, Kyushu University*

[2]*KURNS, Kyoto University*

INTRODUCTION:
Radiometric dating using a combination of K and Ar is useful for rock minerals. In the Ar-Ar dating method concentrations of the parent and daughter nuclides are determined simultaneously as ^{39}Ar / ^{40}Ar ratio, which is an advantage comparing to the K-Ar method. The parent ^{39}K is converted to ^{39}Ar via the $^{39}K(n, p)^{39}Ar$ reaction. In order to obtain precise data of the $^{39}Ar/^{40}Ar$ ratio, it is important to adjust the irradiation condition, such as irradiation duration, neutron flux and its energy. Especially for fine-grained crystalline or small particle samples, temperature attained during the irradiation should also be consideration.
In this study, we have investigated two irradiation conditions by using the hydraulic conveyor and the long-term irradiation plug, for the Ar-Ar dating of small extraterrestrial samples with sub-milligram.

EXPERIMENTS: Several tens to several hundred micron-sized rock fragments were recovered from meteorites (Agoult and HAH262 eucrties) and standard minerals (JG-1, orthoclase, sanidine, and wollastonite). Each of the sample particles was placed in a conical dimple (φ1, depth ~ 0.5 mm) of a sapphire disk (φ5.5, 1.5 mm thick), and covered with a sapphire disk (φ5.5, 0.3 mm thick). Each of the sapphire container was wrapped with pure aluminum foil. These Al-wrapped containers were stacked and sealed in the capsules for Hydro and Long-term irradiations. Condition of the Hydro irradia-tion was 36 hours under 1MW-operation + 7h under 5MW-operation, and that of the Long-term irradiation as 36 hours under 1MW-operation + 7h under 5MW-operation. After irradiation, the samples were moved to non-irradiated glass container with similar di-mension from the sapphire one in order to reduce the radioactivity from the sapphire containers and Al foil. The irradiated samples were moved to Kyushu Univ. to measure noble gas isotopes. Isotopic ratios of Ar extract-ed from each sample by using stepped heating extraction method were determined with a modified MM-5400. Isotopes with mass of 35-39, and 41 were measured with an ion-counting detector, while ^{40}Ar was measured with the ion-counting detector or a Daly detector.
RESULTS: We have measured noble gases in JG-1, and orthoclase samples irradiated by the Hydro and Long-term irradiations. The eucrite samples irradiated by Hydro irradiation were also measured.

Based on the $^{39}Ar/^{40}Ar$ ratio determined for the Hydro and Long-term orthoclase samples, we calculated the neutron flux and obtained J-values to be 0.013 and 0.0069 by using the K of 126400 ppm determined by EPMA and the K-Ar age of 461 Ma [1-2]. The J-value for the Long-term sample is about half of that for the Hydro orthoclase, which means that the bulk conversion rate from K to Ar is better for the Hydro than the Long-term. However, in the case of the Hydro irradiation there is a machine time limitation, so the Long-term irradiation is easier to use for Ar-Ar dating. In order to evaluate the difference in the neutron energy spectrum between the two irradiation conditions, we will conduct NAA for the standard minerals and a meteorite sample (Holbrook) that was already measured for NAA previously.

The two meteorite samples were plagioclase-rich fragments separated from eucrites, Agoult and HaH202. Plateau ages were observed between 900 and 1400 °C and between 1000 and 1400 °C for Agoult and HaH202, respectively. The average Ar-Ar ages are 4348 ± 64 and 4355 ± 60 Ma, respectively, by using the J-value calculated from the Hydro-orthoclase. These Ar-Ar ages matched well with Pu-Xe ages for the bulk samples of these meteorites.

No influence was observed in Ar isotopic ratios of the 600 °C fractions for the meteorites and orthoclase samples. However, by comparison between the orthoclase and JG-1 samples, there is a clear difference in the J-values. In both cases of the Hydro and Long-term irradiations, the J-values for JG-1 are lower than those for the orthoclase, which suggests loss of ^{39}Ar due to recoil during the irradiations. JG-1 is a biotite separate, which is a sheet silicate and is expected to cause recoil loss [3]. Therefore, the orthoclase standard mineral is better for our experiment for small rock samples.

REFERENCES:
[1] Wartho J. A. *et al.,* (1999) Earth Planet. Sci. Lett. 170:141-153. [2] Nägler T. F. and Villa I. M. (2000) Chemical Geology 169:5-16. [3] Foland K. A. *et al.* (1992) Chemical Geology 102:269-276.

CO5-2 Volcanic and Tectonic History of Philippine Sea Plate (South of Japan) Revealed by $^{40}Ar/^{39}Ar$ Dating Technique

O. Ishizuka, S. Sekimoto[1], R. Okumura[1], H. Yoshinaga[1], Y. Iinuma[1], T. Fujii[2]
Geological Survey of Japan, AIST
[1]Institute for Integrated Radiation and Nuclear Science, Kyoto University
[2]Graduate School of Engineering, Osaka University

INTRODUCTION: Submarine volcanic rocks are known to give ages different from their true eruption ages in some cases. This is due to the existence of excess ^{40}Ar in the rapidly quenched glass or Ar loss and K remobilization caused by reaction with seawater or hydrothermal fluids. Stepwise-heating analysis in $^{40}Ar/^{39}Ar$ dating is particularly useful for dating submarine volcanics.

The origin and characteristics of juxtaposing plates is critical for understanding the tectonic setting and requirements leading to subduction initiation. In case of Izu-Bonin-Mariana (IBM) arc in the Western Pacific, arc basement could be preserved in rear arc area of its ancient rear arc (i.e., Kyushu-Palau Ridge). International Ocean Discovery Program Expedition 351 recovered basement of the IBM arc in its rear arc area (Amami Sankaku Basin), and revealed that ocean crust of this basin was generated by seafloor spreading at the time of subduction initiation (Arculus et al., 2015: Ishizuka et al., 2018). However, origin and formation age of the rest of the Philippine Sea basins in the ancient rear arc is still unknown, and this hampers the understanding of the tectonic setting leading to the subduction initiation along the IBM arc.

Recent cruises in the Philippine Sea basins recovered basalts from ocean crust along the major tectonic lines such as the Oki-Daito Escarpment and Mindanao Fracture Zone of the West Philippine Basin. These samples were dated by $^{40}Ar/^{39}Ar$ dating method to obtain age of formation of the basins.

EXPERIMENTS: Samples were wrapped in an aluminum foil packet and the packets were piled up in a pure aluminum (99.5% Al) irradiation capsule (9 mm diameter and 30 mm long). The irradiation capsule was partitioned into 3 compartments to minimize the
For the experiments described here, 5 mg of sample was analysed. Due to alteration of poorly-crystallized part of groundmass, the sample was treated at 100°C on hot plate with stirrer in 6N HCl for 30 minutes and then 6N HNO_3 for 30 minutes to remove possible alteration products (clays and carbonates) prior to irradiation. This procedure effectively separated and concentrated fresh plagioclase in groundmass and of microphenocryst. After this acid treatment, the separates were examined under binocular microscope before packed for irradiation.

RESULTS: $^{40}Ar/^{39}Ar$ dating of fresh basalt lavas returned some good results, show ages between 49 and 58 Ma (Fig. 1, 2). These ages are oldest ages from the WPB reported so far. Even though stratigraphic context of the samples are not clear, the data strongly implies that a part of the West Philippine Basin formed prior to subduction initiation along the Izu-Bonin-Mariana margin, and this further implies that West Philippine Basin spreading did not start as backarc spreading against Izu-Bonin-Mariana arc.

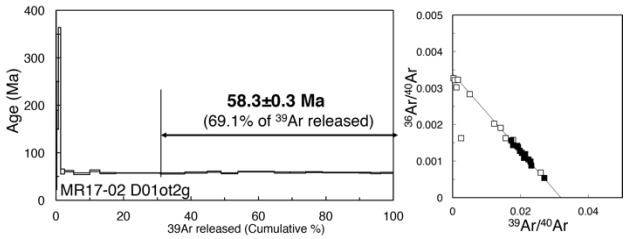

Fig. 1 Age spectrum for the basalts from the West Philippine Basin.

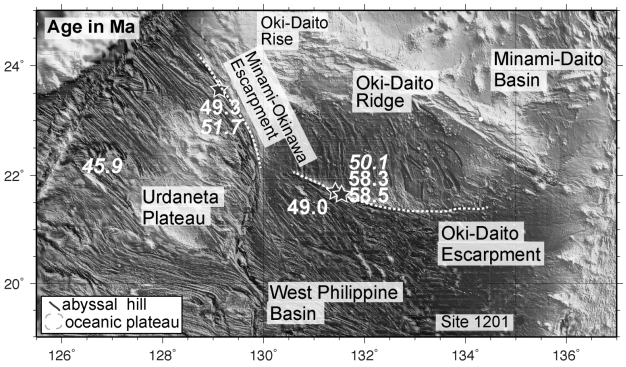

Fig. 2 Preliminary ages from the northern part of the West Philippine Basin.

REFERENCES:
[1] O. Ishizuka *et al.* , Earth Planet. Sci. Lett., 481 (2018) 80-90.

CO5-3 Concentration change of soil origin elements(Al,Ca,Th) in the aerosols observed at Sakai, Osaka

N.Ito A. Mizohata, R. Okumura 1and Y. Iinuma1
Radiation Research Center, Osaka Prefecture University,
[1] Institute for Integrated Radiation and Nuclear Science, Kyoto University

Soil aerosols which are observed mostly in coarse aerosols have various emission sources such as local or regional land surface, road dust and long distant land and desert(China continental land and dessert). Because of the different source profiles appearing the different element composition in the aerosols from these emission sources, the change in the effect from these sources would made the concentration change in the element in the aerosols that are mainly effected soil particles.

We have observed concentration of some elements, Al,Ca,Th,which might be mainly contributed from soil aerosols observed in 12 periods (P1-P12 shown in Fig.1)in 2017. Concentrations of these elements were measured by neutron activation analysis using Kyoto University Nuclear Reactor.

Samples were collected by the impactor sampler (Andersen sampler) which can obtain the aerosols by 9 particles size rages(μm),>11,7-11, 4.7-7.0,3.3-4.7,2.1-3.3,1.1-2.1,0.65-1.1,0.43-0.65,<0.43 with one week sampling period.

In this report, we have examined three elements Al, Ca, Th those might be mainly contributed from soil aerosols in coarse particle (>2.1μm) and have different chemical behavior in the soil. Concentration change in Al,Ca and Th(Fig.1) show the period in high concentration ,P5 and P9 for Al and Ca, P5,P6 and P9 for Th, suggesting the change in effect of soil aerosol effect , P5(rich Al,Ca), P6(rich Th), P9(very rich Th).

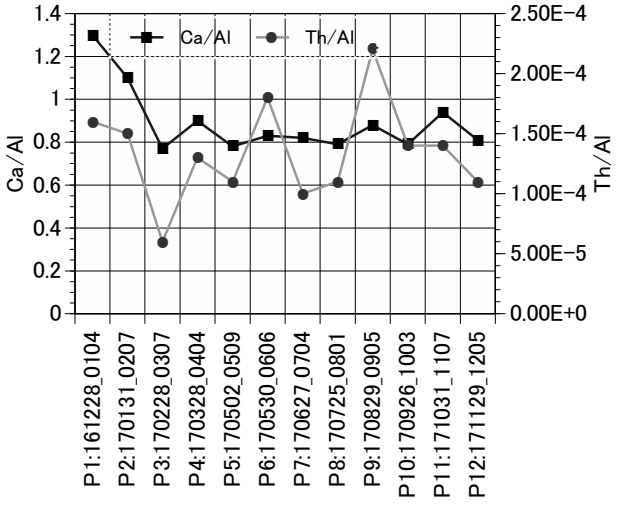

Fig.2 Change in elemental ratio based on Al concentration, Ca/Al, Th/Al.

Another indicator of emission source profile for the soil aerosols is the elemental ratio based on A l such as Ca/Al,Th/Al for which result are drawn in Fig.2. Element ratio based on Al (Ca/Al,Th/Al) in Fig.2 suggest some results as follows

1)Variation in ratio Ca/Al is smaller than that of Th/Al, showing very small variation for P3 to P12 on Ca/Al and large changing in Th/Al ($5E10^{-5}$ to $2E10^{-4}$.)

2) Ratio Th/Al has apparent change in P5,P6 and P9,suggesting ratio Th/Al is a good indicator for the emission source of soil particle.

3) Smallest ratio for Th/Al was observed in P3,in this period Kosa event is frequently observed for ordinary year , expecting Th/Al to be a good indicator for Kosa.

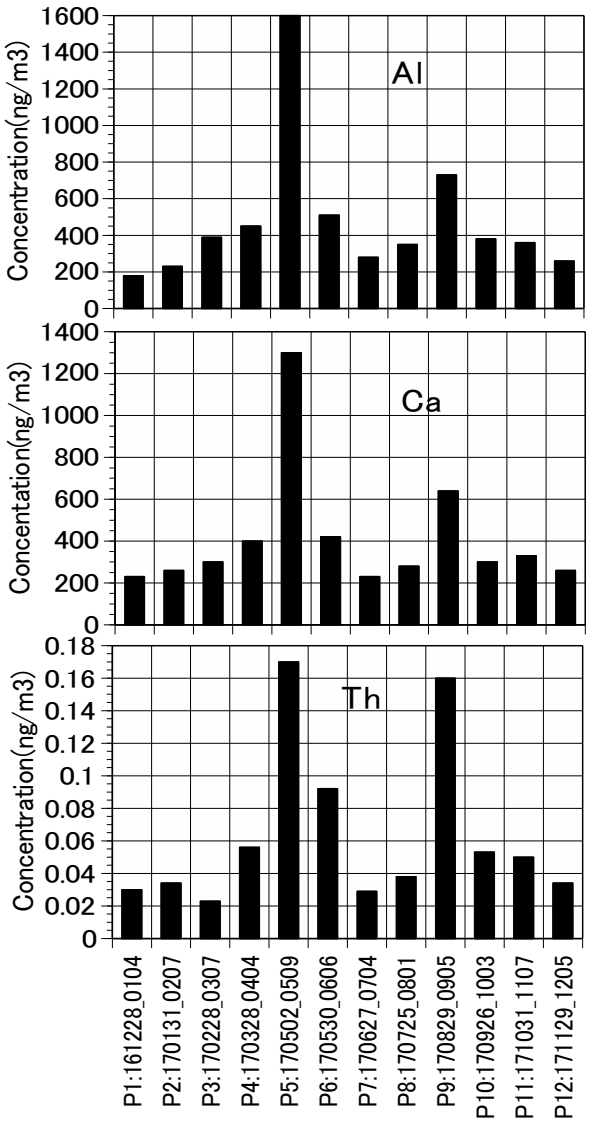

Fig.1 Concentrations of Al,Ca and Th in coarse(>2.1μm) aerosols observed in 12 periods, 2017 at Sakai.

CO5-4 Instrumental Neutron Activation Analysis of the Steelmaking Slag, Compost and Their Mixtures in Artificial Seawater with Various Redox Conditions

M. Matsuo[1], K. Shozugawa[1], M. Yamamoto[2], D. Liu[3], H. Iwai[4], R. Okumura[5], Y. Iinuma[5] and K. Takamiya[5]

[1]*Grad. School of Arts and Sciences, The Univ. of Tokyo*
[2]*Ocean Alliance, The Univ. of Tokyo*
[3]*National Institute of Technology, Ariake College*
[4]*Osaka Prefecture University*
[5]*Institute for Integrated Radiation and Nuclear Science, Kyoto University*

INTRODUCTION: We have been conducting environmental evaluation focusing on redox sensitive elements in coastal areas. For example, Fe, Mn, Ce and Th are used because their concentration possibly increase in oxidative conditions [1]. And U is used for the evaluation of weak reductive conditions because the redox potential of U(VI)/U(IV) is between Mn(IV)/Mn(II) and S(VI)/S(-II) [2]. Recently we paid attention to serious seaweed depletions in coastal areas of barren grounds in Japan. The lack of dissolved iron is one of the possible reasons. So, we have developed a methods for restoration of seaweed beds using the mixture of steel making slag and composts [3]. The influences of redox conditions on the iron elution from the mixture were investigated by laboratorial iron elution test using artificial seawaters. In this study, as a part of above investigation, the steelmaking slag, compost and their mixtures were kept in artificial seawaters with various redox conditions and concentrations of Fe, Mn, U, Th and Ce in samples were analyzed by instrumental neutron activation analysis.

EXPERIMENTS: As test samples, steelmaking slag, compost and their mixtures were prepared. In order to get various redox conditions artificial seawaters were bubbled with oxygen, air and nitrogen. By this operation dissolved oxygen (DO) was achieved 15, 8 and 2 mg/L, respectively. Na_2S were used to achieve 0 mg/L DO. Artificial seawater was replaced every 3 days and aeration was performed. After 30 days samples were taken out and desalted by pure water washing three times and dried.

About 30 mg of samples were packed in double polyethylene film bags to perform INAA. All samples were irradiated at Kyoto University Research Reactor. Three types of gamma-ray measurement were carried out corresponding to half-lives of elements. For analysis of Mn, samples were irradiated for 10 seconds at 1 MW, and gamma-ray was measured for 600 seconds after 600 seconds. As for U, samples were irradiated for 10 minutes at 1 MW, and gamma-ray was measured for 1800 seconds after 3-6 days. As for Fe, Th and Ce, same samples as U were measured for 12000 seconds after 2-4 weeks.

RESULTS: Analysis of redox sensitive elements in samples was done by INAA method. As a result, the higher concentration of Mn was found in the samples kept in more oxidative conditions, whereas there was no significant difference in Fe. It is probably because Fe is a main element in all samples, so the small effect of change was not detected.

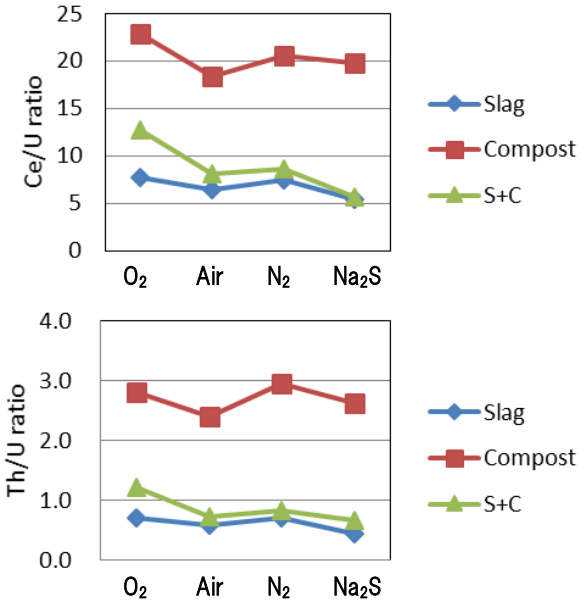

Fig. 1. Ce/U and Th/U ratios of the steelmaking slag, compost and their mixtures in various redox conditions.

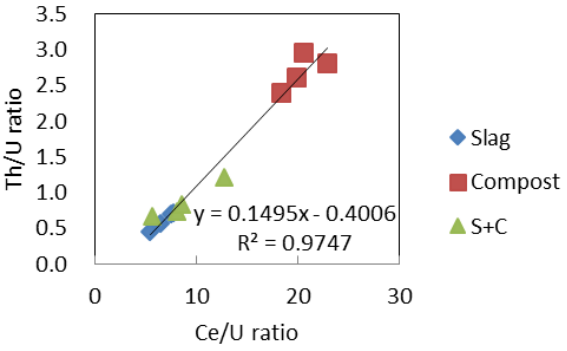

Fig. 2. Th/U-Ce/U plots of the steelmaking slag, compost and their mixtures in various redox conditions.

Ce/U and Th/U ratios for all three types of test samples were found to decrease under reductive conditions (Fig.1). In addition, we plotted the relations between Th/U and Ce/U ratios (Fig.2). The values of Th/U and Ce/U ratios at different types of samples existed on a same line. It is thought that the fact is caused by redox conditions. The chemical states of iron in same samples are also measured by ^{57}Fe Mössbauer spectroscopy.

REFERENCES:

[1] D.G. Brookins, in *Eh-pH diagrams for geochemistry* (Springer-Verlag, 1988).
[2] D.R. Turner, M. Whitfield and A.G. Dickson, Geochim. Cosmochim. Acta, **45** (1981), 855-881.
[3] M. Yamamoto, M. Fukushima, E. Kiso, T. Kato, *et al.*, J. Chem. Eng. Jpn., **43** (2010), 627-634.

CO5-5 Analysis of Cd and As in the rice seed detected from the remains in the Yayoi period by NAA

T. Inamura, S. Fukutani[1] and K. Takamiya[1]

Graduate School of Agriculture, Kyoto University
[1] Institute for Integrated Radiation and Nuclear Science, Kyoto University

INTRODUCTION: The concentration of Cd and As of brown rice is influenced by submerged condition of a paddy field. The submerged condition of the paddy field at the Yayoi period can be estimated from the concentration of Cd and As of the rice seed detected from the remains in the Yayoi period. However, the detected rice seed which is cultural assets must be analyzed by a non-destructive method. We have tried to analyze the concentration of Cd and As of the detected rice seed by NAA (neutron activation analysis) using pneumatic irradiation system and normal Ge-detectors, and succeeded to determine the amount of As. On the other hand, there has been found a difficulty in determination of Cd in the detected rice seeds because the seeds buried in the ground contain more mineral elements compared to fresh seeds. High concentration of mineral components such as iron and sodium would disturb the determination of other elements caused by large Compton-background observed in gamma-ray measurements. In order to decrease the Compton continuum in gamma-ray measurement to determine the amount of Cd in the rice seeds, determination of Cd has been tried by using a Ge-detector combined with Compton suppression systemin in the present work.

EXPERIMENTS: Buried rice seeds which weight was 1 g were double-sealed with polyethylene bags and encapsulated in a polyethylene capsule for neutron irradiation. Neutron irradiation for samples was performed using Pn-2 neutron irradiation system for 10 min and 1 hour under 5 MW operation of KUR. After the irradiation, sample stands for a few hours to decrease activities of short-lived nuclides such as ^{38}Cl, ^{56}Mn and ^{24}Na produced by neutron irradiation. The gamma-ray spectra of irradiated samples were measured twenty times for one hour continuously by the Ge-detector combined with Compton suppression system. The detector system is composed by the Ge-detector surrounded by a well-type high-volume sodium iodine scintillation detector. The coincidental timing signals from two different detectors are processed by an anti-coincidence circuit to generate a gate signal inhibiting signals of which all energy of photon does not absorbed in the Ge-detector from registering on data acquisition system. Finally, the gamma-ray spectra of the neutron irradiated rice seeds were obtained with reduced Compton continuum and analyzed.

RESULTS: The background count rate was reduced by 30 to 70 percent at the photo peaks which energies are 93, 245 and 527 keV arisen from nuclear decay of ^{107}Cd ($t_{1/2}$ = 6.5 h), ^{111m}Cd ($t_{1/2}$ = 48.5 m) and ^{115}Cd ($t_{1/2}$ = 53.5 h) produced by neutron activation of cadmium. However, there did not found definitive photo peaks around the energies.

The amount of Cd contents in the rice seeds was assumed to be around 100 ppm producing a few tens Bq isotopes by neutron irradiation as a basis for initiation of the present experiment. But the concentration of Cd is estimated to be less than a few to a few tens ppm by detection limits of these measurement.

In order to determine cadmium of these low concentration, more irradiation time or more amount of sample is necessary. However, both the irradiation time of the Pn system is limited and the amount of sample is also limited because the sample is the detected buried rice. One possible method to determine those low concentration cadmiums is NAA using hydraulic irradiation system of KUR. The produced activities of long-lived Cd isotopes such as ^{109}Cd ($t_{1/2}$ = 462 d) and ^{115}Cd after one week of irradiation by the hydraulic system for maximum irradiation time are estimated as 34 and 300 Bq for 1ppm Cd in 1 g of rice seeds sample. In the near future, the higher activation by the hydraulic irradiation system will be performed to determine low concentration of cadmium in buried rice seeds sample.

CO5-6 Trace amounts of halogens (Cl, Br and I) in U.S. Geological Survey reference materials

S. Sekimoto, N. Shirai[1], M. Ebihara[1]

Institute for Integrated Radiation and Nuclear Science, Kyoto University

[1]Graduate School of Science, Tokyo Metropolitan University

INTRODUCTION: Accurate and reliable data of halogen abundance have been rarely reported for terrestrial samples, as can be witnessed in the data library for geological rock samples prepared by United States Geological Survey (USGS) (at http://crustal.usgs.gov/geochemical_reference_standards/powdered_RM.html). Since halogens differ in volatility from element to element, their content and relative abundance are highly informative when discussing the petrogenesis of such samples. Recently, we have improved the radiochemical neutron activation analysis (RNAA) procedure for trace amounts of halogens (Cl, Br and I) [1]. In this study, our RNAA was applied to five reference materials that are available in USGS.

EXPERIMENTS: All the materials were in powder and were not subjected to any additional treatment such as drying. About 20-300 mg of each powder sample was weighed, inserted into a clean, small plastic vial that was sealed and then re-sealed inside a clean polyethylene bag. Chemical standard solutions of the three halogens of interest were prepared for use in the quantification by RNAA. An appropriate amount of each halogen solution (containing 90 μg of chlorine, 50 μg of bromine, and 10 μg of iodine) was dropped onto a paper disk (17 mm diameter), weighed, dried under a heat lamp and doubly sealed into polyethylene bags. Extreme care was taken when preparing the iodine reference sample.

Two USGS materials, together with a set of three reference halogen samples, were irradiated for 10 min with a thermal neutron flux of 3.3 x 10^{12} cm^{-2} s^{-1} at Kyoto University Research Reactor Institute (KURRI) When a high flux reactor is used, samples need to be cooled to prevent iodine loss, however no such cooling was required with the neutron flux used in this study. After irradiation, the USGS materials were held for a few minutes to enable the decay of ^{28}Al, and were then subjected to radiochemical separation of neutron-activated halogen radionuclides (^{38}Cl, ^{82}Br, and ^{128}I).

The procedure of radiochemical purification for halogens, gamma-ray measurement and yield determination was essentially the same as that described in our previous work [1-2].

For the determination of iodine and chlorine, the radioactivity of ^{128}I and ^{38}Cl was measured by using a Ge detector for 300–1,000 s and 500–1,000 s, respectively. For bromine, ^{82}Br was measured for 50,000–100,000 s on the following few days after the radiochemical procedure. The three halogen reference samples were measured individually after the completion of the measurements, for for 200-500 s for Cl and I, and 1,000–2,000 s for Br.

Chemical yields of the three halogens were determined by the reactivation method. After the completion of all gamma-ray measurements, a set of 4-6 samples (either of PdI_2 or AgBr+AgCl mixture), along with reference samples for the corresponding halogens, were irradiated for 10 sec at the same irradiation facility as used earlier. The radioactivity of ^{38}Cl, ^{82}Br, and ^{128}I was measured for 100 s for each nuclide.

RESULTS: Each material was analyzed two to four times. For COQ-1 (carbonatite) and DGPM-1 (disseminated gold ore) which were analyzed twice, the two analytical values for the three halogens are in agreement within uncertainties, and mean values between those two analytical values are summarized in Table 1. An uncertainty quoted for each mean value between two analytical values is just the value calculated from two individual uncertainty values accompanied by the two analytical values. Since DTS-2b (dunite), CLB-1 (coal), and SBC-1 (marine shale) have three or four analytical values for the three halogens, mean values with one sigma of standard deviation for those ten materials are also summarized in Table 1. These five USGS materials have no literature values for halogens.

Since we have demonstrated that the RNAA procedure applied in this study is effective in determining halogens in geological rock samples [1], we envisage that our RNAA data will be reflected in any future compilation in the establishment of a database of USGS geochemical reference materials.

Table 1: Cl, Br and I contents in USGS materials analyzed by RNAA in this study
([a] Not reported. [b] Number of analysis was two.)

sample	N	Cl (mg kg^{-1})	Br (mg kg^{-1})	I (mg kg^{-1})
DTS-2b	3	10.7 ± 0.3	0.093 ± 0.002	0.789 ± 0.148
COQ-1	2	27.5 ± 1.1	0.071 ± 0.006	0.331 ± 0.094
CLB-1	4	1190 ± 150	52.1 ± 6.8	599 ± 52
SBC-1	3	24.9 ± 2.4 [b]	0.355 ± 0.005 [b]	5.07 ± 0.19 [b]
DGPM-1	2	315 ± 12	0.843 ± 0.033	3.55 ± 0.13

REFERENCES:

[1] S. Sekimoto and M. Ebihara, Anal. Chem., **85** (2013) 6336-6341.

[2] S. Sekimoto and M. Ebihara, Geostand, Geoanal. Res., **41** (2017) 213-219.

CO5-7 Application of Neutron Activation Analysis to Micro Gram Scale of Solid Samples

S. Sekimoto, N. Shirai[1], M. Ebihara[1]

Institute for Integrated Radiation and Nuclear Science, Kyoto University
[1] Graduate School of Science, Tokyo Metropolitan University

INTRODUCTION: Neutron activation analysis (NAA) has been used in various research fields, such as geo- and cosmochemistry, environmental science, biology, archeology, etc. Since instrumental NAA (INAA) is a non-destructive and multi-elemental analysis method, it is suitable for precious samples and, especially, for such specimens as those highly desired to be neither physically decomposed nor chemically dissolved. Meteorites are the best example for such samples. Chondritic meteorites (chondrites) and iron meteorites contain relatively high contents of Co and Ir compared with those in the earth crust. As Co and Ir have high sensitivity in NAA, they can be good markers for the identification of such extraterrestrial materials. In NAA of chondrites, generally, a few tens mg of specimen is used. For such a case, a few hundred μg kg-1 of Ir and a few hundred mg kg-1 of Co can be reliably determined. When an extremely small size (e.g., micro gram) of samples such as micrometeorites recovered on the Earth surface and tiny particles returned from extraterrestrial asteroids are to be analyzed by INAA, the conventional INAA procedure used for a few tens mg is not suitable. For such tiny samples, neutron irradiation with high neutron flux and long irradiation time (namely, high neutron dose) is required. For the irradiation with high neutron dose, polyethylene bags for holding samples are not usable because they are prone to radiation damage. Polyethylene bags are also not suitable for holding tiny grain samples. It is, therefore, very important to design an appropriate sample holder for irradiating small grain samples. In our previous study [1], we have developed the INAA procedure for analyzing a single grain of down to micro and sub-micro grams in mass, and present that the INAA procedure is applicable to such samples. In this report, detection limits in the procedure is described in detail

RESULTS: Detection limits of the 11 elements measured in this study are estimated under the present experimental condition (45 h-irradiation under 1 MW operation [1]) and listed in Table 1. A detection limit is defined as a value corresponding to three sigma of background counts at the peak area of the gamma-ray emitted by a nuclide of interest. Calculated values are listed in the table, in which data for the previous experimental runs (28 or 19 h-irradiation under 5 MW operation) also are shown for comparison. Detection limit values were obtained based on data on either or both of the samples analyzed in individual runs [1-3]. The detection limit values for this study are higher than those for the previous one by factors of 2 to 20. Detection limits are dependent on experimental conditions such as the sample size, irradiation time, neutron flux, gamma-ray counting time and counting efficiency. In INAA, the detection limit is also largely controlled by the co-existing elements in the matrix. Therefore, detection limit values are to be regarded as information values but the values in Table 1 must be informative in the analysis of similar samples to those analyzed in this study, for example, micro meteorites, meteorite pieces and cosmic spherules. To evaluate the applicability of the INAA procedure described in this study, the deduced detection limits are compared with the estimated elemental contents in 0.05 μg of chondritic meteorites in Table 1. It is obvious that Na, Cr, Fe, Co and Ni can be easily determined for 0.05 μg of chondrite by INAA with 45 h irradiation under 1MW operation (this work), while INAA with more than 28 h irradiation under 5MW operation is required to determine Sc, Zn, Ir and Au. Even with the highest neutron doze (53 h irradiation under 5 MW operation) available at KUR, La and Sm may not be determined for such a small sample.

Table 1 Detection limits for individual elements

	Detection limit (pg)		Concentration range in Chondrite	Content range in Chondrite of 0.05 micro-g (pg)
	This work 45 h irradiation (1MW)	Previous work 28 h irradiation (5MW)		
Na	20	1	1800 - 6900 mg kg^{-1}	90 - 345
Sc	0.4	0.03	6 - 11 mg kg^{-1}	0.30 - 0.55
Cr	40	4	2650 - 4160 mg kg^{-1}	133 - 208
Fe	2800	270	18 - 38 %	9100 - 19000
Co	3	0.4	480 - 1100 mg kg^{-1}	24 - 55
Ni	340	110	1.1 - 2.6 %	550 - 1285
Zn	150	12	18 - 315 mg kg^{-1}	0.9 - 15.8
La	0.5	0.1	235 - 585 μg kg^{-1}	0.012 - 0.029
Sm	0.1	0.02	140 - 294 μg kg^{-1}	0.007 - 0.015
Ir	0.3	0.02	380 - 1070 μg kg^{-1}	0.019 - 0.054
Au	0.02	0.01	120 - 330 μg kg^{-1}	0.006 - 0.017

REFERENCES:
[1] S. Sekimoto *et al.*, J Radioanal Nucl Chem, **307** (2016) 1757-1764.
[2] M. Ebihara *et al.*, Science, **333** (2011) 1119-1121.
[3] M. Ebihara *et al.*, Meteoritics & Planetary Science, **50** (2015) 243-254

CO5-8 Determination of Abundance of Rare Metal Elements in Seafloor Hydrothermal Ore Deposits by INAA Techniques-5: Evaluation of analytical accuracy

J. Ishibashi, Y. Tada[1], Y. Sekiya[1], S. Kawaguchi[1], K. Yonezu[1], R. Okumura[2], Y. Iinuma[2] and K. Takamiya[2]

Department of Earth and Planetary Sciences, Faculty of Science, Kyushu University
[1]Department of Earth Resources Engineering, Faculty of Engineering, Kyushu University
[2]Institute for Integrated Radiation and Nuclear Science, Kyoto University

INTRODUCTION: To meet recent increased demand for rare metal elements as mineral resources, high sensitive multi-element analysis becomes more important as geochemical tools for mineral exploration. Instrumental neutron activation analysis (INAA) has the advantage of non-destructive analysis, which eliminates possible failings to exclude concentrate of elements included in specific mineral poorly soluble during acid digestion. We have conducted preliminary studies using mineralized samples collected from active seafloor hydrothermal fields, with a view to confirm and extend the range of application of this technique. Here, we report evaluation for analytical accuracy of INAA techniques, using reference ore materials.

EXPERIMENTS: We conducted a series of analysis of "Certified Reference Materials" which are provided by Natural Resource Canada. Samples were irradiated at Pn-2 (thermal neutron flux = 5.5×10^{12} n/cm^2/sec at 1 MW) for 4housr (Run-1) and for 25 minutes (Run-2). For each run, the gamma ray activity was measured for 15-30 minutes after adequate cooling time (~5days for Run-1 and ~1day for Run-2). Content of each nuclide was calculated by comparison of gamma ray intensities between samples and artificial standard materials which contain known amount of Mn and Na.

RESULTS: Analytical results of the Certified Reference Materials, CCU-1d, WMA-1a, CH-4, and DS-4 are listed in Table 1. Nuclides used for the determination of elemental content are listed with their energies and half-life in minutes. Content of elements is shown together with one sigma deviations for counting the peak intensity of the gamma ray spectra. The determined contents are basically agreed with the literature values (which are reported as informational values, provisional values, or certified values in the document provided by Natural Resource Canada).

Table 1 Analytical results of "Certified Reference Materials" provided by Natural Resources Canada. Content of elements is shown with one sigma deviation for counting the peak intensity. The digits expressed in blankets are certified values reported for the Reference Materials.

Element (unit)	Na (ppm)	As (ppm)	La (ppm)	Au (ppm)	Sb (ppm)
Nuclide	Na-24	As-76	La-140	Au-198	Sb-122
energy (kev)	2733	559/657	1596	412	564/692
half-life (day)	0.610	1.095	1.677	2.693	2.7
CCU-1d	[200]	[545]	[3]	[14.01]	[61.9]
Run-1	45.6±6.6	230±22	1.3±0.1	52.0±0.2	102±12
Run-2	93.8±4.6	534±53	N.D.	9.8±0.8	88±13
WMS-1a	[329]	[30.9]	[4.3]	[0.300]	[6.92]
Run-1	92±10	20.9±2.0	1.0±0.1	0.55±0.04	5.3±0.6
Run-2	216±3	37.6±5.9	N.D.	0.39±0.12	13.2±1.7
DS-1	[400]	[6960]	[20]	[32.59]	[107]
Run-1	75.5±8.5	5435±48	6.8±0.3	44.3±0.2	124±12
Run-2	139±2	4298±23	0.5±0.1	30.8±0.2	274±5
CH-4	[32600]	[8.8]	[16]	[0.88]	[0.77]
Run-1	1035±98	N.D.	5.6±0.4	0.46±0.04	N.D.
Run-2	not cooled down enough because of high Na content in the sample				

N.D. means too small peak intensity of the gamma ray spectrum.

CO5-9 Siderophile element fractionation in impact glass from the Wabar impact crater

N. Shirai[1], S. Sekimoto[2], M. Ebihara[3]

[1]*Department of Chemistry, Tokyo Metropolitan University*
[2]*Institute for Integrated Radiation and Nuclear Science, Kyoto University*
[3]*Department of Earth Sciences, Waseda University*

INTRODUCTION: Siderophile elements such as Co, Ni and PGE are depleted in crustal materials because these elements are strongly partitioned into core. In contrast, these element abundances of extraterrestrial materials such as chondrites and iron meteorites are several orders of magnitude higher than those for crustal materials. Therefore, the elevated siderophile element abundances in implact-related rock samples are due to the incorporation of meteoritic components into crustal materials. Individual chondrites and iron meteorites have characteristic absolute and relative abundances of siderophile elements. Thus, siderophile elements have been used for the detection and identification of projectile materials [e.g., 1]. Recent studies indicated that there is a possibility of elemental fractionation during impact events [e.g., 2-4]. However, processes of elemental fractionation and interaction between projectile and target materials during impact events are poorly understood. Thus, elemental fractionation leads to a difficulty in identifying projectile materials. Both projectiles and impact-related materials were collected from small and young craters such as Kamil Crater of Egypt [5] and Wabar crater of Saudi Arabia [6]. In this study, elemental abundances of impact glass from Wabar cater were determined by using instrumental neutron activation analysis (INAA) and instrumental photon activation analysis (IPAA) in order to constrain the processes of elemental fractionation during impact event.

EXPERIMENTS: Impact glass from Wabar crater was received from National Institute of Polar Research and roughly ground into small pieces. Black and white melts were separated by using tweezers and analyzed by using INAA and IPAA. INAA and IPAA were performed at Institute for Integrated Radiation and Nuclear Science, Kyoto University for the determination of elemental abundances of impact glass. For INAA, sample was irradiated for 10 sec and 4 hrs at the pn-3 and pn-2, respectively. For IPAA, the irradiation was carried out using the linear accelerator operated at 20 MeV electron beam energy and 102 μA current for 36 hrs.

RESULTS: Our analytical results of black and white melts are consistent with the previous studies [2,6,7]. As observed by [7], black melt has higher abundances of Co, Ni, Ir and Au than those of white melt. Black melt contains 300 ppm for Co, 3710 ppm for Ni, 336 ppb for Ir and 5.72 ppb for Au. Mass fractions of Wabar iron in the black melt analyzed in this study were estimated to be 4 to 6% based on Co, Ni and Ir abundances for Wabar iron [2] and black melt [this study]. Assuming that target material has similar siderophile element abundances to those of upper continental crust, impact-related material having 4 to 6% mass fraction of projectile has similar chemical characteristics of siderophile elements. Figure compares siderophile elements abundances of black melt with those of bulk Wabar iron. Siderophile element abundances were normalized to Ni and those for bulk Wabar iron. Black melt has higher Co/Ni ratio and lower Ir/Ni and Au/Ni ratios compared with those of bulk Wabar iron. For comparison, siderophile element abundances of kamacite and taenite from Wabar iron are shown in Fig. Ir/Ni ratio of black melt falls in the range between those of kamacite and taenite. However, Au in black melt are highly depleted compared with kamacite and taenite. Based on our analytical results of INAA and IPAA, projectile could not be simply incorporated into target material.

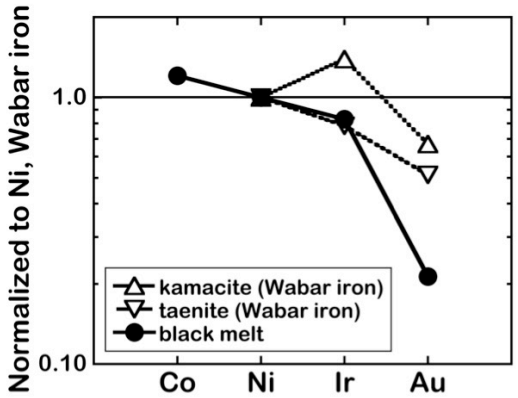

Fig. Siderophile elements of black melt (this work) and kamacite and taenite from Wabar iron (Mullane et al. [8]).

REFERENCES:

[1] R. Tagle and J. Berlin Meteorit. Planet Sci., **43** (2008) 541-559.
[2] D. W. Mittlefehldt *et al.*, Meteoritics, **27** (1992) 361-370.
[3] S. Jonásová *et al.*, Geochim. Cosmochim. Acta, **190** (2016) 239-264.
[4] S. Goderis *et al.*, Geochim. Cosmochim. Acta, **217** (2017) 28-50.
[5] A. Fazio *et al.*, Meteorit. Planet Sci., **49** (2014) 2175-2200.
[6] E. Gnos *et al.*, Meteorit. Planet Sci., **48** (2013) 2000-2014.
[7] F. Hörz *et al.*, Proc. Lunar Planet. Sci Conf., **19th** (1989) 697-709.
[8] E. Mullane *et al.*, Chem. Geol., **208** (2004) 5-28.

CO5-10 Change of uptake of radioactive cesium from contaminated soil to rice plants

M. Yanaga, Y. Dezawa[1], H. Yoshinaga[2], R. Okumura[2] and Y. Iinuma[2]

Center for Radioscience Education and Reseach, Faculty of Science, Shizuoka University
[1]*Department of Science, Graduate School of Integrated Science and Technology, Shizuoka University*
[2]*KURNS, Kyoto University*

INTRODUCTION: A large quantity of radioisotopes, such as ^{131}I, ^{134}Cs, ^{137}Cs, ^{140}Ba and ^{140}La, were released in to the atmosphere by the Fukushima Daiichi Nuclear Power Plant accident and contaminated the air and ground [1-3]. Radioactive cesium is especially a problem because of its long half-life (30 years for ^{137}Cs) among the released radioisotopes. Paddy field soil was also contaminated with radioactive cesium. Separating radioactive cesium from the soil is necessary to prevent damage by rumors although there have been no reports that activity of rice produced in Fukushima prefecture exceeding the reference value was detected in recently.

However, simple removal of contaminated soil would create a vast quantity of radioactive waste. Recently, we found that the absorption of radioactive cesium from artificially contaminated soil into rice plants increased by adding a stable isotope to irrigation water. In this study, cultivation experiments in laboratory were conducted by using paddy field soil collected in Fukushima city to examine whether rice grow normally or not even if stable isotope of cesium is added, based on a change of the trace element concentration, and also to confirm whether the absorption of radioactive cesium from really contaminated soil increase or not.

EXPERIMENTS: *Materials and Method* Soils contaminated with radioactive cesium were collected from paddy fields located in two areas (O area and Y area) of Fukushima city. Rice seedlings were transplanted to 9 Wagner pots (1/5000 a) filled with 2.7 kg air-dried soil of O area and to another 10 pots filled with soil of Y area. The transplanted pots for each area were divided into three groups, respectively, such as O-I, O-II and O-III; Y-I, Y-II and Y-III. Ground water in Shizuoka city was used as irrigation water through a period of cultivation. The number of pots for each group was three except for group Y-III(4 pots). After midseason drainage followed by irrigation, 2.0×10^{-3} mol and 6.0×10^{-3} mol of CsCl were added as aqueous solution into the pots of group I (O—I and Y-I) and group II (O-II and Y-II), respectively. The rice plants were separated into brown rice, straw and leaf after harvest. They were dried and transferred to U8 containers. After measurements of radioactivities of ^{137}Cs and ^{134}Cs in them, 50 - 60 mg of each sample were doubly wrapped in a polyethylene film and subjected to INAA.

INAA The samples in polyethylene capsules were irradiated in Pn-3 for 90 seconds and in Pn-2 for 4 hours, for short and long irradiation, respectively. As comparative standards, the certified NIST Standard Reference Material 1577b Bovine Liver as well as elemental standard for Cs was used. The γ-ray spectroscopic measurements with an HPGe detector were performed repeatedly for the short-irradiated samples: the first measurements for 120 – 900 seconds after decay time of 5 - 15 minutes and the second one for 250 - 1200 seconds after 60 - 150 minutes. The long-irradiated samples were measured for 1 - 24 hours after an adequate cooling time (15 - 60 days).

RESULTS: The absorption amount in groups which were added with cesium stable isotope increased compared with the groups which were not added. This indicates that addition of stable cesium isotope is effective for the removal of radioactive cesium from soil. However, as shown in Fig. 1, addition of large amount of stable cesium caused an obstacle to growth of rice plant. INAA results showed that the concentrations of Mn in leaf and straw of group O-II and Y-II were distinctly lower than the others.

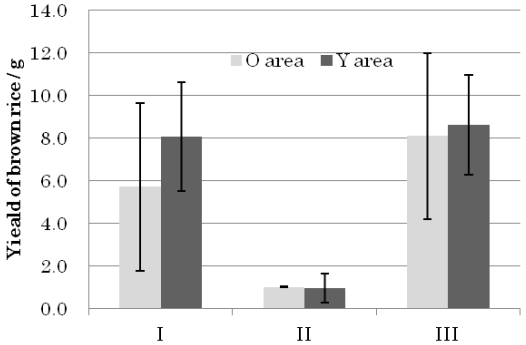

Fig. 1 Yield of brown rice harvested

REFERENCES:

[1] S. Endo *et al.*, J. Environ. Radioact., **111** (2012)18-27.
[2] M. Yanaga and Y. Oya, Radiation Safety Management, **12** (2013)16-21.
[3] M. Yanaga *et al.*, Radiation Safety Management, **12** (2013)37-42.

CO5-11 Thermal History of Early Archean Metamorphic Rocks

H. Hyodo[1], K. Sato[1,2,3], H. Kumagai[3]and K. Takamiya[4]
[1] *Institute of Frontier Science and Technology, Okayama University of Science*
[2]*Department of Applied Chemistry and Biochemistry, National Institute of Technology, Fukushima College*
[3] *Submarine Resources Research Center, Japan Agency for Marine-Earth Science and Technology*
[4] *Institute for Integrated Radiation and Nuclear Science, Kyoto University*

INTRODUCTION: Gneisses in the east coast of Labrador area consist a part of potential oldest crust, as they have recorded several early Archean events. The oldest zircon age reported is 3.9 Ga [1] in the area. It is of much interest to compare the thermal history with that of the Acasta area where the oldest rocks are found [2]. We have carried out $^{40}Ar/^{39}Ar$ dating on zircon grains from the Labrador area. Zircon normally does not have potassium as its component, but it often has inclusions in forms of fluid and/or minerals which may contain potassium. If zircon could behave as a solid container for its inclusions against later disturbances, the inclusions may keep the primary record when they are formed, and may provide some insights on the Precambrian environments. Variety of inclusions might behave separately, but average behavior could be determined from the experiment.

EXPERIMENTS: Experimental procedure is the same as described previously [3]. Rock samples were crushed, and sieved in #25-100 mesh. After ultrasonic cleaning in distilled water, single mineral grains were handpicked. The zircon grains were irradiated in the KUR for 22 hours at 1 MW and subsequently 6 hours at 5MW. The total neutron flux was monitored by 3gr hornblende age standard [4], which was irradiated in the same sample holder. In the same batch, $CaSi_2$ and $KAlSi_3O_8$ salts were used for interfering isotope correction. A typical J-value was $(1.183 \pm 0.009) \times 10^{-2}$. In stepwise heating experiment, temperature of a mineral grain was measured using infrared thermometer whose spatial resolution is 0.3 mm in diameter with a precision of 5 degrees. The amount of argon isotopes in inclusions seems to be small. In some cases when grain sizes are too small for the analyses, mutiple (3-5) grains were heated under defocused beam in order to increase the sample size. Extracted argon isotopes were measured using a custom-made mass spectrometer [3].

RESULTS: Figure 1 illustrates one of $^{40}Ar/^{39}Ar$ age spectra of a single zircon grain. Because of the difficulty in temperature control and small amount of argon release, number of heating steps was only a few. Most zircon grains did not release much argon below 1000 degrees starting from 600 degrees. However, 3.8 Ga age was found in the first step in this case. This probably reflects the characteristics of the inclusions. Average behavior of the zircons was heat resistant.

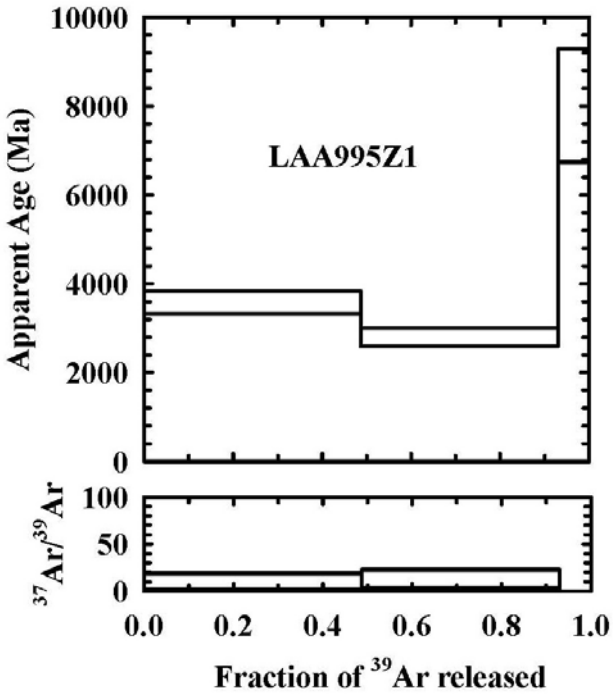

Fig. 1. $^{40}Ar/^{39}Ar$ age spectra of zircon from east coast of the Labrador area, Canada. Although the error seems to be large due to the small amount of ^{39}Ar, some apparent ages are comparable to the U-Pb zircon age.

It is difficult to define a plateau in this diagram. However, the apparent ages seem to be surprisingly old compared to the results from the Acasta gneisses [5]. The similar trend of Archean ages was also found in the results of other Labrador zircon. Presence of variety of inclusions is probably disturbing to obtain a plateau age in the zircons. In this case, the results suggest a possibility of recovering the Archean ages by $^{40}Ar/^{39}Ar$ method comparable to the U-Pb results.

REFERENCES:

[1] T. Komiya, *et al., Geoscience Frontiers* **8** (2017) 355-385.
[2] S.A.Bowring and I.S. Williams, *Contributions to Mineralogy and Petrology*, **134** (1999) 3–16.
[3] H. Hyodo, *Gondwana Research* **14** (2008) 609-616.
[4] J.C. Roddick, *Geochim. Cosmochim. Acta* **47** (1983) 887-898.
[5] H. Hyodo, K. Sato and H. Kumagai, KURRI Progress Report 2017 CO5-15.

CO5-12 Fission track age and cooling history of granitoids in Oku-Izumo area, Shimane Prefecture

H. Ohira, T. Kondo and Y. Sampei

Department of Earth Science, Shimane University

INTRODUCTION: Cretaceous to Paleogene granite in Oku-Izumo area is strongly weathered into granite sand. From the 16th Century to the 1900s, the "Tatara" steel manufacture, using iron sands (magnetite grains) extracted from the granite sand was operated in this area. In the process of extraction of magnetite, the landform of this area was considerably transformed by Kanna-Nagashi, in which outcrops of weathered granite was cut out and large amount of quantity of granite sand was washed in running water along gutter. The granitic basement of this area is classified into several bodies and the age of typical granite body (the Yokota granite) is measured to be 59.6±5.5Ma by Rb-Sr whole rock isochron method [1]. The age of another body (the Abire granite) which produced large amount of iron sand was also measured to be 60.5±6.3Ma [2]. These ages show the period of emplacement of granite, considering with the higher closure temperature of Rb-Sr system. However ages with lower closure temperature which enables estimation of cooling history of rocks has not been reported. Cooling and uplift history might have some kind of relationship with weathering of this area and the formation of granite sands. In this report, apatite and zircon fission track ages with relatively lower closure temperature and schematic cooling history are discussed.

EXPERIMENTS: Rock was crashed, sieved and washed to separate fractions less than 0.3mm. Heavy minerals were concentrated using conventional method of heavy liquid and magnetic separator. Apatite grains were mounted in epoxy resin, polished to reveal a complete internal surface, and etched in 7%HNO_3 solution in 20-25seconds at 25℃. Zircons were mounted in PFA Teflon, polished and etched in a NaOH-KOH eutectic melt at 225˚C [3]. Samples were irradiated at pneumatic tube of graphite facility (Tc-pn) of Kyoto University Reactor (KUR). After irradiation, external detectors (mica) were etched in 46% HF at 25˚C for 6-7 minutes (for mineral mounts) and for 20-50min (for NIST-SRM612 glass). FT density was measured at 1000× magnification with a dry objective.

RESULTS: Apatite and zircon ages from typical outcrops of granite sand near the Hanaidani (the ruin of "Kanna-Nagashi") were measured to be 43.4±3.4Ma and 53.9±2.8Ma, respectively. This sampling site belongs to the Abire granite measured to be 60.5Ma by Rb-Sr method [2]. The discrepancy of above radiometric ages is probably due to the difference of closure temperature of each dating method. Closure temperature of apatite and zircon FT and whole rock Rb-Sr method are thought to be around 100℃ [4], 240℃ [5] and 700℃ [6]. Considering with above closure temperatures and obtained ages, the age-temperature plot (cooling history) is illustrated as shown in Fig.1. The evidence of remarkable hydrothermal alteration such as sericite veins are rarely observed in thin section of granite sand, suggesting that thermal influence for fission track system is probably negligible. The cooling curve shows relatively fast cooling rate (69.7℃/Ma) at a higher temperature range probably due to conductive cooling after emplacement of granite at a deeper depth. In contrast, the lower cooling rate (1.96℃/Ma) at a temperature range less than 100℃ is presumably due to uplift and exhumation of granite of this area. Assuming a constant and normal geothermal gradient of 3℃/100m, surface temperature of 15℃ and simple constant uplift, a schematic denudation rate of 6528m/Ma (0.065mm/year) is obtained. Fission track length measurement is required to discuss more detail cooling history. Fission track age of fine-grained granodiorite which sporadically distributed among the granite was additionally measured to be 26.5±1.1Ma. Thermal influence of such younger intrusion affects the cooling history of the older granite should be examined.

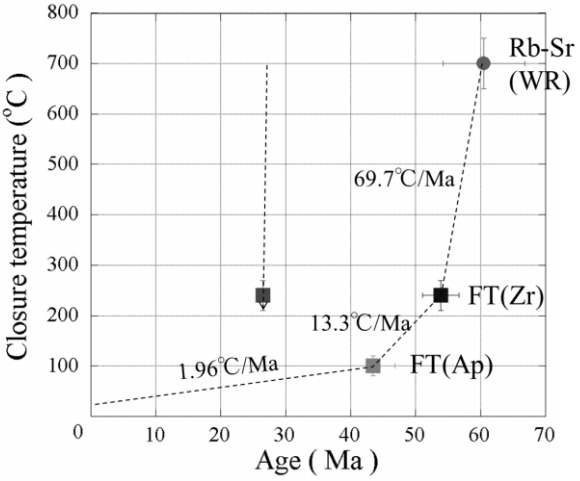

Fig. 1. Schematic cooling history of typical weathered granite collected near the Hanaidani ruin and the younger plutonism newly identified in Oku-Izumo area.

[1] Nishida K. *et al.,* 2005, J. Geol. Soc. Japan, 111, 123-140. (in Japanese with English abstract)
[2] Iwata C. *et al.,* 2013, J. Geol. Soc, Japan, 119, 190-204. (in Japanese with English abstract)
[3] Gleadow A.J.W. et al., 1976, Earth and Planetary Science Letter, 33, 273-276.
[4] Sueoka S. *et al.,* 2016, Geoscience Frontiers, 7, 197-210.
[5] Hurford. A.J., 1986, Contrib. Mineral Petrol., 92, 413-427.
[6] Yuhara *et al.,* 2013, Earth Science (Chikyu Kagaku), 67,161-168. (in Japanese with English abstract)

CO5-13 Halogen Systematics in Mantle Xenoliths from the Western Pacific Subduction Zones

H. Sumino, A. Takenouchi, M. Koike, R. Okumura[1], Y. IInuma[1] and S. Sekimoto[1]

University of Tokyo
[1] Institute for Integrated Radiation and Nuclear Science, Kyoto University

INTRODUCTION: Volatiles, such as water, carbon dioxide, halogens, and noble gases, concentrate on the surface of the Earth, because of their high volatilities. They are continuously expelled from the interior of the Earth by volcanisms at mid-ocean ridges, hot spots, volcanic arcs. On the other hand, oceanic plates transport volatiles into the interior of the Earth via subduction processes. Through decomposition of volatile-bearing minerals such as hydrous minerals, those volatiles are released into the mantle wedge, which may result in major changes to the chemical and physical properties of mantle rocks. However, despite their importance, the detail of volatile cycling in subduction zones remains poorly constrained.

Halogens are among the most powerful tracers of volatile cycling in subduction zones. Based on elemental compositions of heavy halogens (Cl, Br, and I) in subduction zones, the importance of sedimentary pore fluid-like iodine-rich halogens transported by serpentine has been pronounced (e.g., [1,2]). Halogen compositions in mantle beneath volcanic fronts have been overwhelmed by the sedimentary pore fluid-like halogens [2]. Whereas subducted seawater- or sedimentary pore fluid-like heavy noble gases (Ar, Kr, and Xe), which are also powerful tracers of volatile cycling, significantly extend into the convecting mantle [3], mantle xenoliths from intraplate settings suggest that subducted sedimentary pore fluid-like halogens have been negligible in the convecting mantle [4]. However, there is a large missing link between volcanic fronts and the convecting mantle. In this study, we measured compositions of halogens and noble gases in mantle xenoliths from rear-arc region in the Western Pacific subduction zones.

EXPERIMENTS: The mantle xenoliths used in this study are from rear-arc regions in the Western Pacific subduction zones: the Ichinomegata volcano (the Oga peninsula, Northeast Japan), the Jeju Island (south of the Korean peninsula), the Oki-Dogo Island (Southwest Japan), the Ilchan and Sveyagin volcanic bodies in Sikhote-Alin (Far Eastern Russia), and the Takashima Island (Southwest Japan).

Halogens in the samples were analyzed using neutron irradiation noble gas mass spectrometric technique (e.g., [5]). In this method, halogens (F, Cl, Br, and I) and some elements (K, Ca, Ba, and U) are converted to corresponding isotopes of noble gases (Ar, Kr, and Xe) by neutron irradiation in a nuclear reactor. Because of relatively high cross-sections for neutron capture and high sensitivity of noble gas mass spectrometer, trace amounts of heavy halogens (Cl, Br, and I) in mantle xenoliths, which are difficult to analyze using conventional methods in geochemistry, can be quantified.

The mantle xenolith samples were coarsely crushed into 0.5–2 mm. Neutron irradiation for the mantle xenoliths were irradiated neutron in the Kyoto University Research Reactor (KUR) for 5 hours. Thermal and fast neutron fluxes were determined by analyses of Hb3gr hornblende that was irradiated with the mantle xenoliths samples. Noble gases in the neutron-irradiated samples were analyzed using a noble gas analysis system at the University of Tokyo [5]. The samples were crushed using a hydraulic press and the remaining powder was melted in a W-coil furnace to extract noble gases.

RESULTS: The mantle xenoliths from rear-arc regions showed a wide range of I/Cl and Br/Cl ratios. All of data can be explained by mixing among sedimentary pore fluid-like high I/Cl component, high Br/Cl component, and MORB source mantle-like component. Correlation between the Cl and CaO concentrations suggests that clinopyroxenes controls halogen signatures in bulk lherzolites at least in the mantle beneath the Ichinomegata volcano. The high I/Cl and Br/Cl samples showed arc type signatures in trace element compositions, suggesting that these halogens are slab-derived halogens. These evidences indicate that multiple halogen components are present in the mantle beneath rear-arc regions and that they are not a consequence of elemental fractionation from a common source. The presence of halogens inherent in the mantle indicates that subducted halogens are not overwhelming in rear-arc regions, whereas subducted halogens are overwhelming in the mantle beneath volcanic fronts [2]. This difference in the extent of subduction influence is also observed in halogen/^{40}Ar* ratios, where ^{40}Ar* is non-atmospheric ^{40}Ar. The ratios decrease toward the depleted mantle values in the order of volcanic front > rear-arc region > intraplate setting, indicating that the extent of subduction influence decreases in this order. Halogen/^{40}Ar* ratios have an advantage that the ratios are less affected by contamination, especially that from air. This advantage and the variation of the halogen/^{40}Ar* ratios of mantle xenoliths from various geological settings suggest that halogen/^{40}Ar* ratios can be used as a reliable proxy of the extent of subduction influence.

REFERENCES:

[1] H. Sumino *et al.*, Earth Planet. Sci. Lett., **294** (2010) 163-172.
[2] M. Kobayashi *et al.*, Earth Planet. Sci. Lett., **457** (2017) 106-116.
[3] G. Holland & C. J. Ballentine, Nature **441** (2006) 186-191.
[4] M. Kobayashi *et al.*, Geochemistry, Geophysics, Geosystems **20** (2019) 952-973.
[5] M. Kobayashi, Ph.D. Thesis, Univ. Tokyo (2017).

CO5-14 Neutron activation analysis for environmental materials (sediments of Lake)

Y. Okada, N. Hagura[1], H. Matsuura[1], T. Uchiyama and Y Iinuma[2]

Atomic Energy Research Laboratory, Tokyo City University

[1]Department of Nuclear Safety Engineering, Tokyo City University

[2]KURNS, Kyoto University

INTRODUCTION: Contamination of radioactive Cs of Lake Akagi Onuma Lake in Gunma Prefecture was observed due to the accident at Fukushima Daiichi Nuclear Power Station. Recently, the levels of radioactive Cs in wakasagi that live there have been slowly decreasing with the decrease of that of the lake water. In order to clarify the cause of the gradual collapse, we have been investigating the inhabiting organisms and their surrounding areas for 7 years ^{1, 2)}.
This study will be conducted as part of investigating the contribution of sediments to lake water.

EXPERIMENTS: Environmental materials were sediments of Lake Onuma on Mt. Akagi. Sediment samples were collected from the center of Lake Onuma (N36 ˚ 33'46",E39 ˚ 10'46") using a Satake-type core sampler. The core sediment samples were then cut every 2cm from the surface up to the 50cm length depth. The cut samples were dried at 105°C, pulverized in a mortar. The analysis samples were 3 samples respectively from sediments of 10 mm, 160 mm and 390 mm in depth. Those samples were prepared by doubly packing in clean poly-ethylene bags. Six samples(ca.50mg) and comparative standards (JLK1-1,NIES8) were irradiated for a short time (30s) at thermal neutron flux of 4.68×10 ¹² n cm ⁻²s ⁻¹ and for a long time (3600s) at a thermal neutron flux of 5.5×10 ¹² n cm ⁻² s ⁻¹ in KUR. For monitoring the neutron flux, about 9mg of aluminum wires containing 1.5% Sb and about 11mg Fe wires were doubly packed in clean polyethylene bags and irradiated together with the samples and comparative standards. The irradiated samples were measured by conventional [γ]-ray spectrometry using a coaxial Ge detector. Analysis of [γ]-ray spectrometry were at Gamma Station (SEIKO EG&G Co.,LTD).

RESULTS: As a result of measuring the neutron flux in the irradiation capsule, the flux ratio of the upper stage and the lower stage in the capsule was approximately 1.0. Table 1 lists the concentration of 19 elements in sediments from sediments of 10 mm, 160 mm and 390 mm in depth of Lake Onuma on Mt. Akagi. This time, only the results obtained from long-time irradiation were reported. The determined values of many elements in three samples at the same depth showed good agreement. Fig. 1 York,1996), Vol. 1.

shows the concentrations of trace elements in sediments by depth.
The elements that tend to increase in concentration with increasing depth were Lu, Eu, Yb, Ce, Sc and Co. On the contrary, the elements which tend to decrease in concen tration with increasing depth were Br, Sb and Cs.

Table 1 Element concentrations in the core sediments of Lake Onuma on Mt. Akagi. Unit: μg/g

elements	10mm				160mm				390mm			
	1	2	3	Av.	1	2	3	Av.	1	2	3	Av.
U	0.655	0.674	0.676	0.668	1.196	0.994	1.525	1.24	ND	ND	1.046	1.05
Lu	0.162	0.134	0.146	0.147	0.222	0.217	0.236	0.225	0.281	0.275	0.273	0.28
Eu	0.597	0.610	0.580	0.596	0.673	0.656	0.691	0.673	1.00	1.027	0.988	1.01
Ba	182	220	158	187	272	244	264	260	203	182	195	193
Hf	1.64	1.67	1.56	1.62	2.15	2.22	2.20	2.19	1.84	1.94	1.93	1.91
Yb	1.21	1.27	1.30	1.26	1.31	1.34	1.60	1.42	1.90	1.87	1.95	1.91
Ce	22.3	20.1	18.5	20.3	26.1	22.8	25.8	24.9	32.6	38.1	49.1	39.9
Pt(ng/g)	1.23	1.24	1.33	1.27	1.26	1.25	1.51	1.34	2.86	3.12	3.22	3.07
Fe(%)	3.01	3.03	2.71	2.92	3.34	3.25	3.13	3.24	3.13	3.15	3.17	3.15
Th	2.39	2.35	2.22	2.32	3.31	3.40	3.54	3.42	1.75	1.71	1.81	1.76
Cr	15.9	18.1	15.5	16.5	27.6	23.4	21.9	24.3	7.08	8.03	8.37	7.83
La	8.71	8.52	8.40	8.54	10.8	11.0	11.1	11.0	9.99	10.8	10.8	10.5
Br	35.4	35.4	34.3	35.0	32.6	28.5	30.4	30.5	19.6	14.9	15.6	16.7
Sb	0.84	0.85	0.87	0.856	1.03	0.98	1.06	1.02	0.40	0.33	0.31	0.345
Cs	4.16	4.13	4.16	4.15	4.38	4.20	4.52	4.37	2.20	2.12	1.89	2.07
Sc	9.19	9.21	8.92	9.11	10.1	10.2	10.4	10.2	12.7	12.9	15.4	13.67
Rb	19.1	19.6	17.8	18.8	26.6	22.6	25.7	25.0	ND	ND	ND	ND
Co	6.57	6.61	6.32	6.50	6.92	6.74	7.03	6.90	9.47	9.58	9.78	9.61
Ta	0.295	0.208	0.271	0.258	0.348	0.272	0.242	0.287	ND	ND	ND	ND

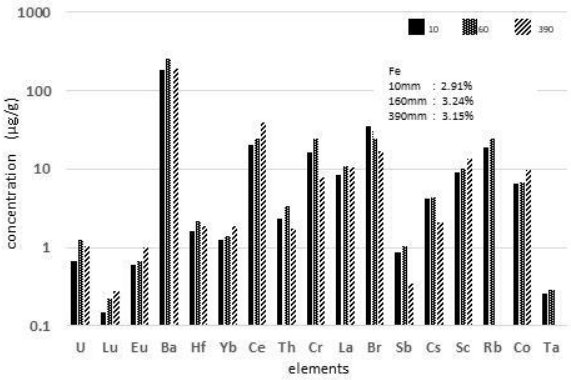

Fig. 1. Determination of trace elements in sediments of Lake Onuma on Mt. Akagi

Fe contained about 3%. Ba was at a concentration of 100 μg / g to 200 μg / g. Also, Ce, Cr, Br and Ba are at concentration range levels of 10 μg / g to 100 μg / g, and Hf, Yb, Th, Cs, Sc and Co are concentration range levels of 1 μg / g to 10 μg / g.

REFERENCES:

[1]K.Suzuki *et al.*, Science of the Total Environment, **622-623**(2018)1153-1164.
[2] M.Mori *et al.*, Science of the Total Environment, **575**(2017)1247-1254.

CO5-15 Research on Earth Surface Processes by Use of Mineral Luminescence

N. Hasebe, K. Miura[1], M. Ogata, U. Uyangaa[1], K. Kinugawa[1], R. Januar[1], K. Oohashi[2], Y. Minomo[2], and Y. Iinuma[3]

Institute of Nature and Environmental Technology, Kanazawa University
[1]Graduate School of Natural Science and Technology, Kanazawa University
[2]Graduate School of Science and Technology for Innovation, Yamaguchi University
[3] Institute for Integrated Radiation and Nuclear Science, Kyoto University

INTRODUCTION: Luminescence dating observes the natural accumulated radiation damage caused by radioisotopes such as U and Th as the form of glow after stimulation by heating or lightening. Because of age range applicable, luminescence dating has been applied to Quaternary active fault (e.g., Ganzawa et al., 2013). However, little comprehensive studies on the effect of rock deformation or destruction through the faulting on luminescence signal have been reported so far. In this study, quartz with known radiation dose is prepared and artificially ground to understand the behavior of luminescence sites during the faulting.

EXPERIMENTS: First, quartz were extracted from granitic specimen by conventional mineral separation processes. To cancel naturally accumulated doses in the environment, quartz were left under the LED light at 80°C for 12 hours. Samples were then wrapped with aluminum foil and irradiated at gamma-ray irradiation facility at KUR to give a known dose of 60 Gy. To check the initial status, some part of samples were brought to Kanazawa University and optically stimulated luminescence (OSL) was measured. Afterwards, samples were brought to Yamaguchi University and friction experiment to mimic fault activity was performed.

RESULTS: The OSL shows typical quartz signal with rapidly decreasing intensity (Fig. 1). When intensity of stimulated light is linearly increased, LM-OSL signal profile is obtained and it can be deconvoluted depending on the sensitivity in releasing light (Fig. 2). The main is the fast component. After the measurement, additional artificial dose of 5 Gy was given by built-in x-ray facility and OSL was measured again. When main 60 Gy signal is compared to the 5 Gy x-ray signal, the signal intensities were smaller than expected (Fig. 3) and showed a wide variation. The reason they show smaller values may be attributable to the unstable luminescence sites in the granitic quartz. Because luminescence signal is too small to perform friction experiment, additional irradiation experiment will be necessary to move to the next step.

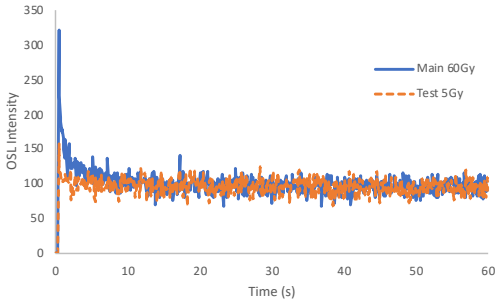

Fig. 1. Example of OSL signal after gamma irradiation (main 60 Gy) and x-ray irradiation (Test 5 Gy).

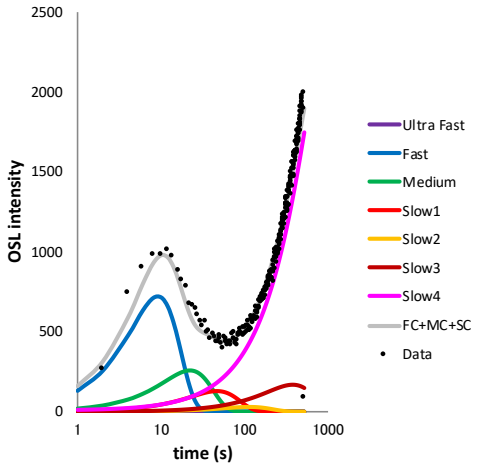

Fig. 2. Example of LM-OSL signal and the results of deconvolution.

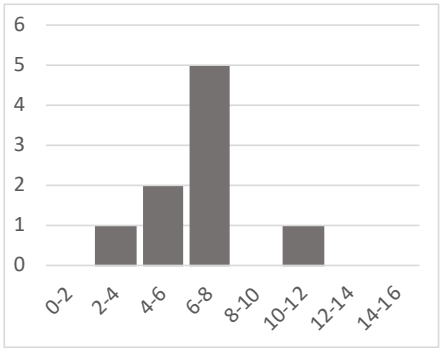

Fig. 3. Histogram for main/x-ray intensity ratio.

CO5-16 Elemental Composition of Atmospheric Fine Particulate Matter (PM2.5)

Y. Oura, J. Kaneko, R. Taniguchi, Md. S. Reza

Department of Chemistry, Tokyo Metropolitan University

INTRODUCTION: Although various sizes of particulate matters suspend in the atmosphere, an influence of very fine particles of less than 2.5 μm of aerodynamic radius (PM2.5) on human health has been attracting attention. Organic compounds, which are considered to be harmful, in PM2.5, are actively determined, but inorganic analysis such as elemental composition is also indispensable for particle characterization. We collected PM2.5 in Hachioji and Koto for 4 years from 2006, and their elemental compositions were determined by instrumental neutron activation analysis (INAA). Recently the environmental standards of PM2.5 are almost achieved every year in Tokyo. But PM2.5 is still a matter of concern at present. Therefore, elemental composition of the present PM2.5 was determined by INAA and compared with ones of PM2.5 collected about 10 years ago.

EXPERIMENTS: Using a NILU filter holder with successive PM10 and PM2.5 inlets, PM2.5 was collected on a Nuclepore polycarbonate filter of 0.2 μm of pore size for two weekdays every week from June to December at a rooftop of a building in Minami-Osawa campus of Tokyo Metropolitan University. Mass concentration in μg m^{-3} was determined by weighing the filter before and after collection of PM2.5.

Polycarbonate filters on which PM2.5 had been collected were cut in half, then one half was folded in square (10 mm × 10 mm). Quadrangular sample in clean polyethylene bag was irradiated together with reference materials (NIST 1648, NIST 1632c, NIES No.8, and GSJ JB-1a) and sulfamic acid by neutrons for 5 minutes in Pn-3 at KUR (1 MW operation) and 1 hour in Pn-2 at KUR (5 MW operation). After irradiation only filters were transferred to a new polyethylene bag and gamma-rays were measured by Ge detector.

RESULTS: Distribution of mass concentrations in 2008, 2009, and 2018 are shown as a boxplot in Fig.1. In 2008 and 2009 PM2.5 was collected by the same way as in 2018 but collection periods in 2008 and 2009 were different from 2018. Average of mass concentration in 2018 was about 1/2 of one in 2008 and slightly smaller than one in 2009.

Annual averages of elemental concentrations determined using radionuclides produced by the irradiation for 5 minutes are shown in Fig.2. Determined elements are arranged in order of decreasing their average in 2018. Although ^{27}Mg was also detected, its average is not shown in Fig.1 because a contribution of the interference reaction, $^{27}Al(n, p)^{27}Mg$, had not been corrected. Sulfur was most abundant among elements determined for 3 years and In was least abundant. The similar tendency of elemental abundances was observed for 2008, 2009, and 2018. Although mass concentrations in 2008 were generally higher than ones in 2009 and 2018, elemental concentrations in 2008, 2009, and 2018 were not largely different from each other. It is guessed that concentration of carbon, which is one of the major compornents, varies from year to year. For Al, the difference between averages in 2008 - 2009 and one of 2018 is slightly larger than other elements. In March 2008 and 2009, some Al concentrations of larger than 450 ng m^{-3} were observed due to probably yellow sand. On the contrary collection of PM2.5 had been started in July in 2018 and such high Al concentration was not observed. It is the main reason of the difference for Al.

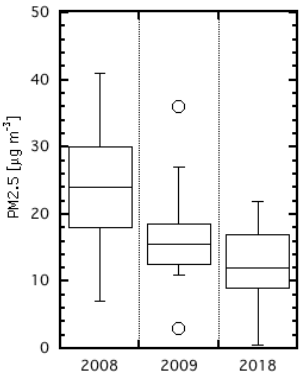

Fig. 1. Mass concentrations of PM2.5 in 2008, 2009, and 2018.

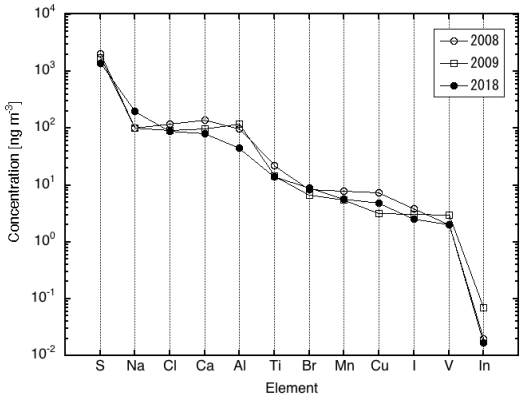

Fig. 2. Elemental concentration of PM2.5 in 2008, 2009, and 2018. Elements are arranged in order of decreasing their average in 2018.

CO6-1 Study of DNA DSB end structure induced by ionizing radiation

K. Akamatsu[1], N. Shikazono[1] and T. Saito[2]

[1]*Radiation DNA Damage Research Group, Kansai Photon Science Institute, National Institutes for Quantum and Radiological Science and Technology (QST)*

[2]*KURNS, Kyoto University*

INTRODUCTION:

Clustered damage site, that is a DNA region with multiple lesions within a few helical turns, is believed to hardly be repaired. However, chemical and spatial details of them are not known. We are developing a methodology for studying structural feature of DNA DSB end and affinity between the DSB end and a repair protein. We have tried to irradiate gamma-rays and iron ion beam with LET of ~0.2 and ~200 keV/μm, respectively, to pUC19 in a cell-mimetic buffered solution. As a result, we found that these ions tend to produce *direct* DSB (except for a DSB by sequentially-produced opposed close SSBs) compared with ^{60}Co γ-rays. We will isolate linear pUC19 with DSB ends and study how a repair protein recognize and process a DSB end.

EXPERIMENTS:

●*Sample preparation and irradiation*

The plasmid DNA (pUC19, 2686bp) was used. The DNA was dissolved to be 0.1 g/L in 0.2 M Tris-HCl buffer (pH 7.5) which is a cell-mimetic condition in relation to radical scavenging capacity. Twenty microliters of the DNA solution was transferred to a micro chamber (20-μL size), and was irradiated with Fe ion beam (LET: ~200 keV/μm; HIMAC QST) and ^{60}Co γ-rays (LET: ~0.2 keV/μm; KURNS Kyoto University) as a standard radiation source. The irradiated DNA sample was purified by ethanol precipitation and was dried in vacuum, followed by being kept at -20ºC until use.

●*Agarose gel electrophoresis of irradiated DNA*

The dry irradiated DNA samples were dissolved to TE buffer (~2g/L). The electrophoresis was performed for 4h, 70V at 4ºC. The gel was stained by ethidium bromide (EtBr). The different DNA forms separated (supercoiled (sc), open circular (oc), and linear (L) form) were quantified by a gel imager (Pharos FX, BioRad).

●*Large-amount Isolation of lin fraction using agarose electrophoresis*

We have constructed a protocol for collecting large amount of lin fraction using general agarose electrophoresis (1% agarose in 0.5xTBE, 25V, 18h) pUC19/SmaI was used as a marker. EtBr staining was performed only to the marker lane. L fraction was collected from L-containing gel fragments by electroelution (D-Tube Dialyzer, Maxi, Novagen), followed by buffer exchange to TE (Amicon Ultra-4, Millipore). The collected L fraction will be used for several biochemical and physicochemical analysis.

RESULTS:

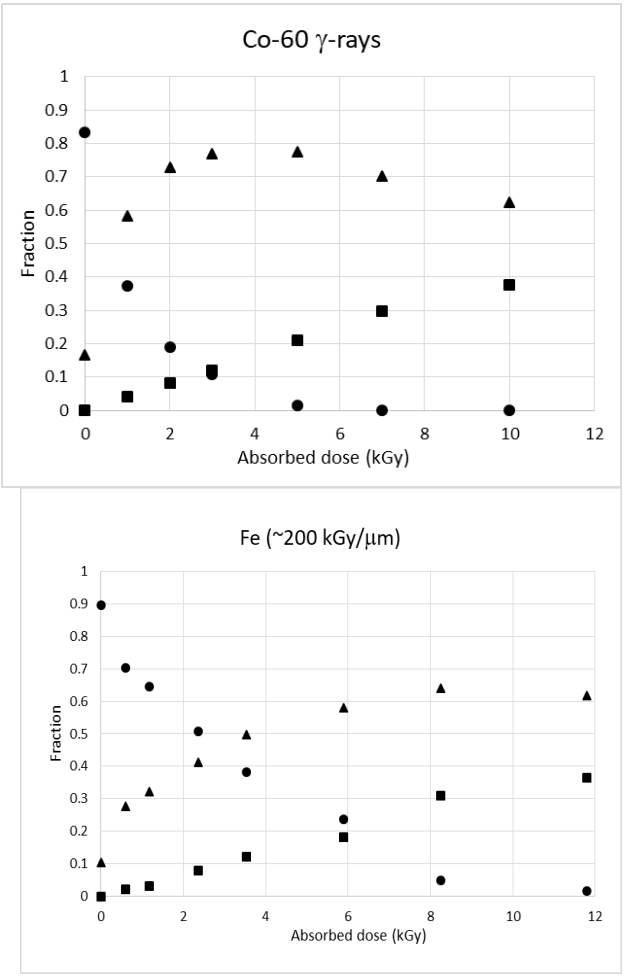

Fig. 1. Relationship between absorbed dose and DNA fractions (●: sc, ▲: oc, ■: L) for ^{60}Co γ-rays (upper panel) and Fe ion beam (lower panel).

The fraction maximum of L for ^{60}Co γ-rays is ~0.8, whereas that for Fe beam dose is ~0.6, suggesting that Fe beam is likely to induce *direct* dsb formation from sc form compared with the γ-rays. The yield ratios of dsb to total strand breaks for γ and Fe are calculated to be 0.067 and 0.17, respectively, according to Cowan's theory [1].

What is a *direct* dsb? How difference are shown between a *direct* dsb and successive dsb (by ssb + ssb)? How is a *direct* dsb repaired? These are our issues to be solved.

REFERENCES:

[1] R.Cowan, *et al.,* J.Theor.Biol. **81** (1987) 229-245.

30001

CO6-2 Oligomeric structures of HspB1 from CHO cell

M. Yohda, K. Ankai, R. Inoue[1], K. Morishima[1], N. Sato[1], M. Sugiyama[1]

Department of Biotechnology and Life Science, Tokyo University of Agriculture and Technology
[1]Institute for Integrated Radiation and Nuclear Science, Kyoto University

INTRODUCTION: Small heat shock proteins (sHsps) endow cells with stress tolerance [1]. They bind to partially folded or denatured proteins, thereby preventing irreversible aggregation or promoting correct substrate folding. Various species of sHsps are present in mammals [2]. HspB1, also known as Hsp27, is a ubiquitous sHsp [3]. The sHsps of mammals, which reflect their status as homeotherms, are regulated by phosphorylation. To examine the structure and function of HspB1, we expressed, purified and characterized HspB1 from Chinese hamster (*Cricetulus griseus*) ovary cells (CgHspB1) (Manuscript in preparation). CgHspB1 forms a large oligomeric structure. In dilute conditions, CgHspB1 dissociates into small oligomers at the elevated temperatures. In contrast, dissociation of the oligomer was not observed at the relatively high protein concentrations. The phosphorylation mimic mutant of CgHspB1 with the replacement of Ser15 to Asp (CgHspB1_S15D) exhibited relatively lower oligomer stability and higher ability for protecting thermal aggregation than the wild-type protein. The result clearly showed the correlation between oligomer dissociation with chaperone activity. In this study, we compared the oligomeric structures of CgHspB1 wild type and CgHspB1_S15D by various methods.

EXPERIMENTS: CgHSPB1 variants (CgHspB1_WT, CgHspB1_S15D) were expressed in *E. coli* and purified by anion exchange chromatography with DEAE-TOYOPEARL, anion exchange chromatography with RESOURCE Q and size-exclusion chromatography with Superdex 200. The molecular weights of the oligomers of CgHspB1 variants were analyzed by Size-exclusion chromatography - multiangle light scattering (SEC–MALS) using a multiangle light-scattering detector (MINI DAWN, Wyatt Technology). The oligomeric conformation of CgHspB1 variants were analyzed by small angle X-ray scattering (SAXS) using NANOPIX (Rigaku) and analytical ultracentrifugation (AUC) using XL-1 (Beckman Coulter Diagnostics).

RESULTS: CgHspB1 variants were analyzed by SEC–MALS. The molecular mass of CgHspB1_WT and CgHspB1_S15D were estimated to be about 470 kDa and about 780 kDa, respectively.

Then, they were applied for the analysis by AUC (Fig. 1). The sedimentation velocities were calculated to be 15.1 S (403 kDa) for CgHspB1_WT and 18.2 S (829 kDa) for CgHspB1_S15D. The values well coincide with the molecular mass determined by SEC-MALS.

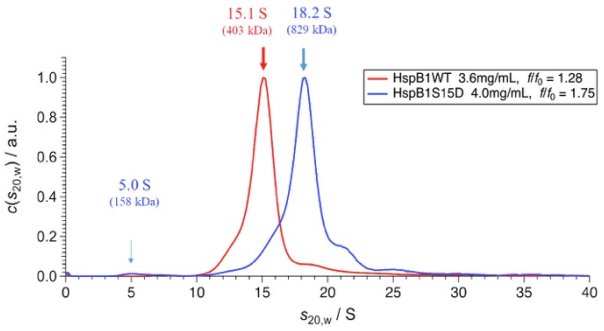

Fig. 1 Analytical centrifugation of CgHspB1 variants

Finally, we have analyzed CgHspB1 variants by SAXS (Fig. 2). *R*g values were calculated to be 58.4 (± 0.6) Å for CgHspB1_WT and 66.9 (± 1.2) Å for CgHspB1_S15D, respectively. SAXS also showed that CgHspB1 changes to the larger oligomeric conformation in the phosphorylated state.

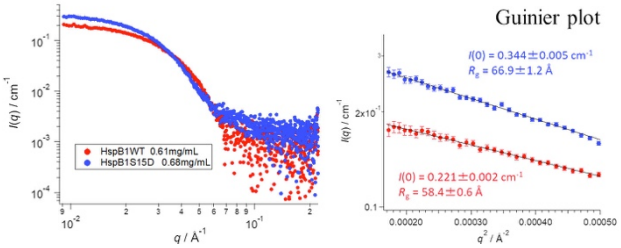

Fig. 2 SAXS profiles of CgHspB1 variants (Left) and the Guinier plots (Right)

Previously, we have shown that the oligomer of CgHspB1_S15S, the phosphorylated mimic mutant, is relatively unstable and dissociates to small oligomers even at the room temperature. In this study, we have shown that the oligomeric structure of CgHspB1_S15S is larger than that of the wild type. Since similar change was observed for CgHspB1_WT at the elevated temperature (Manuscript in preparation), the structure might be the activated conformation of CgHspB1 before dissociation.

REFERENCES:

[1] U. Jakob *et al.,* J. Biol. Chem., 268 (1993) 1517-1520.
[2] C. Garrido *et al.,* Int. J. Biochem. Cell. Biol., 44 (2012) 1588-1592.
[3] A.P. Arrigo., Cell Stress Chaperones., 22 (2017) 517-529.

CO6-3 Effect of ligand Binding on Solution Structure of Multi-domain protein, MurD

H. Nakagawa, T. Saio[1,2], M. Sugiyama[3], R. Inoue[3]

Materials Science Research Center, Japan Atomic Energy Agency

[1]*Graduate School of Chemical Sciences and Engineering, Hokkaido University*

[2]*Department of Chemistry, Faculty of Science, Hokkaido University*

[3]*KURNS, Kyoto University*

INTRODUCTION: In structural biology, precise determination of three-dimensional structures of proteins has been focused, and the structures with an atomic-resolution have given solid platforms to understand their biological functions. Recently, the idea of structural biology has extended beyond the static structural information with atomic resolution, in order to cover more complex and dynamical structures at different levels of space and time resolution. SAXS measurement can observe the solution structure of flexible protein under the physiological conditions [1].

MurD (UDP-N-acetylmuramoylalanine--D-glutamate ligase) is a typical multi-domain protein (Fig.1), which is one of the ATP-driven Mur ligases that are responsible for peptidoglycan biosynthesis. The crysital structure of MurD has been determined, but the ATP-bound form is not detemied.

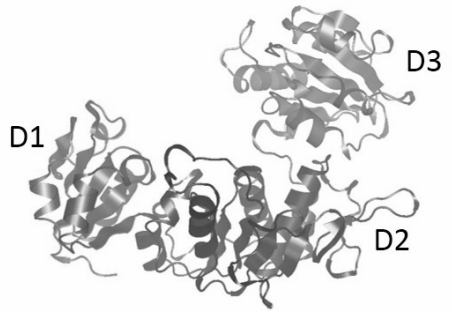

Fig. 1. Multi-domain protein, MurD, which are composed of three domains, D1, D2 and D3.

EXPERIMENTS: MurD were expressed in E. coli strain BL21 (DE3). Small angle X-ray scattering (SAXS) were measured for MurD in ATP-unbound and bound states at the concentration of 5, 10, 20 and 50 mg/ml. The buffer conditions were 20 mM Tris-HCl at pH=7.2. For the sample of ATP-bound state, AMP-PNP and $MgCl_2$ were added at the concentration of 2 mM and 5 mM, respectively. For the sample of Compound1-bound state, Compound1 was added at 3 eq.

RESULTS: SAXS profiles of MurD were successfully obtained for Apo, ATP-bound and Compound1-bound states at 5 mg/mL, where the inter-particle interaction effects were not observed in the profiles. As shown in Fig. 2, SAXS profiles are different among the three samples, indicating the structural change by ATP or Compound1 binding. The previous NMR measurement predicted that the domain orientation of MurD is changed into semi-closed conformation by ATP binding, and closed conformation by Compound1 binding [2]. And our preliminary MD simulation shows that the conformation and fluctuation of MurD domains are changed by ATP- or Compond1-binding, and that these are consistent with the NMR results. The comparison of the SAXS profiles with the results of the NMR and MD simulation are in progress.

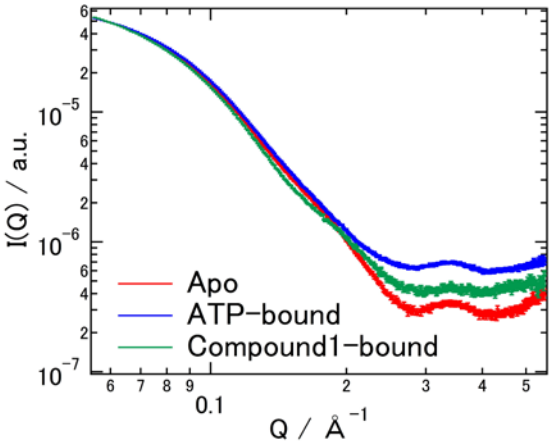

Fig. 2. SAXS profiles in Apo, ATP-bound and Compound1-bound states of MurD at the concentration of 5 mg/ml.

REFERENCES:

[1] J. Trewhella *et al.*, Acta Cryst. **D73** (2017) 710-728.
[2] T. Saio *et al.*, Sci. Rep., **5** (2015) 16685.

CO6-4 Structural characterization of circadian clock potein complexes

H. Yagi, Y. Yunoki, K. Morishima[1], N. Sato[1], R. Inoue[1], and M. Sugiyama[1]

Graduate School of Pharmaceutical Sciences, Nagoya City University,
[1]Institute for Integrated Radiation and Nuclear Science, Kyoto University

INTRODUCTION: The central oscillator that generates the circadian rhythm in the cyanobacterium comprises only three proteins—KaiA, KaiB, and KaiC. Through interactions among these proteins in the presence of ATP, KaiC undergoes phosphorylation and dephosphorylation cycles with the period of 24 h, which proceeds *in vitro* without daylight oscillation, indicating that the internal clock mechanism can be autonomous irrespective of transcriptional and translational feedback systems. Although the formation of several complexes, such as KaiA-KaiC, KaiB-KaiC, and KaiA-KaiB-KaiC oscillated in a circadian manner, their stoichiometry or the detailed structures remains to be elucidated. Herein, in order to understand the oscillation mechanism mediated by the clock protein complex, we characterized the complexes by using analytical ultracentrifugation (AUC) and small angle X-ray scattering (SAXS) analyses. Especially, in this study, we focused on the characterization of KaiA-KaiB-KaiC complex.

EXPERIMENTS: The expression and purification of clock proteins, KaiA, KaiB and KaiC were performed according to methods previously described [1]. SAXS pattern was collected with NANOPIX (Rigaku Corporation, Japan) equipped with HyPix-6000. A Cu Kα line (MicroMAX-007HF) was used as a beam source, which was further focused and collimated with a confocal multilayer mirror (OptiSAXS). The camera length was set to 1.326 m and the range of the scattering vector q was from 0.007 to 0.24 A^{-1}. The AUC experiments were performed using an ProteomeLab XL-I analytical ultracentrifuge (Beckman-Coulter) at 25 °C and an angular velocity of 60,000 rpm. Data were recorded with Rayleigh interference optical system, followed by the analysis with a $c(s)$ distribution of the Lamm equation solutions calculated by the SEDFIT v15.01. The sedimentation coefficient s were converted to the value in water at 20 ºC.

RESULTS: To date, we have reported that KaiB and KaiC formed a complex exclusively in a 6:6 stoichiometry, indicating that KaiB bound to the KaiC hexamer with strong positive cooperativity [1]. Herein we conducted the titration analysis of KaiB-KaiC complex and KaiA for characterization of stoichiometry by SAXS and AUC analyses.

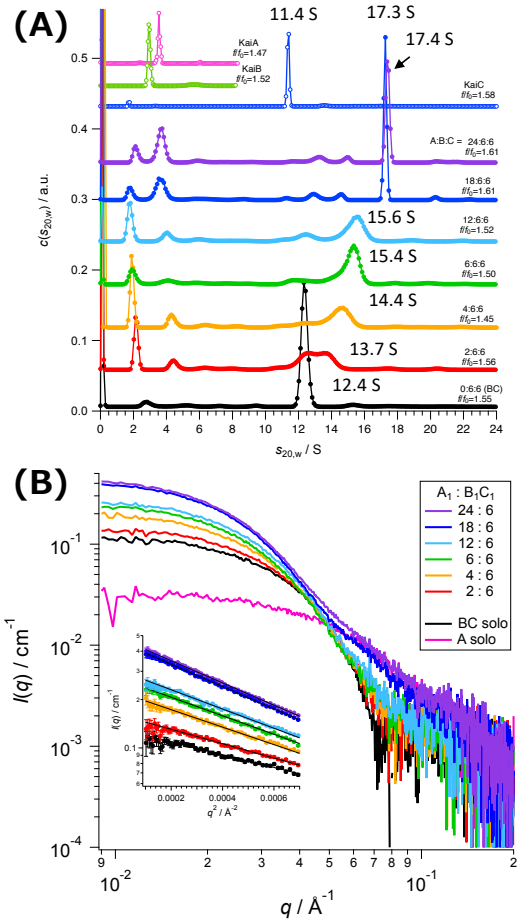

Fig. 1. (A) AUC and (B) SAXS data from titration series with KaiA and KaiBC complex.

The AUC data confirmed that KaiA, KaiB, and KaiC form complexes containing different number of KaiA molecules and form a 12:6:6 complex with a sedimentation coefficient of 17.4 S under the excess amount of KaiA (Fig.1A). The forward scattering $I(0)$ as well as the radius of gyration (Rg) were calculated with the Guinier approximation (Fig.1B). These data also indicated the complex shows the 12:6:6 stoichiometry under the excess amount of KaiA. These data consistent with the model resulting from X-ray crystal structures of KaiB-KaiC 6:6 complex and ternary complex containing KaiA, KaiB, and CI domain of KaiC.

On the basis of our data, we conclude that KaiB-KaiC complex was capable of binding a maximum of 12 KaiA molecules. These findings provide mechanistic insights into the circadian periodicity in cyanobacteria.

REFERENCES:

[1] M. Sugiyama *et al.*, Si. Rep., **6:35567** | (2016).

CO6-5 Sustainable Photoproduction of Medical ^{18}F and ^{99m}Tc Isotopes

T. Takeda, M. Fujiwara[1,2], M. Kurosawa[1], N. Takahashi[1,] M. Tamura[1], T. Kawabata, Y. Fujikawa, K.N. Suzuki, N. Abe[3], T. Kubota[3] and T. Takahashi[3]

Department of Physics, Kyoto University
[1]Research Center for Nuclear Physics, Osaka University
[2]National Institutes for Quantum and Radiological Science and Technology
[3]Institute for Integrated Radiation and Nuclear Science, Kyoto University

INTRODUCTION:

We examined two sustainable methods for producing the medical ^{18}F and ^{99m}Tc isotopes. A new method is proposed for producing medical ^{18}F isotopes as an alternative to the ^{18}F cyclotron production. ^{18}F isotopes are produced via the photoreaction on ^{20}Ne. Natural neon gas is used as a target in the gas recycling flow system. The ^{18}F-FDG radio-pharmaceuticals are obtained by blowing small bubbles of irradiated neon gas in the FDG liquid. Another method is the production of ^{99m}Tc isotopes via the photoreaction on natural MoO_3. In these two methods, both ^{99m}Tc isotopes for the SPECT inspections and ^{18}F isotopes for the PET inspections are sustainably produced using the photoreaction on natural MoO_3 and Ne targets. We have demonstrated the feasibilities of practical usages of these two new methods.

^{18}F EXPERIMENTS:

We used an electron beam from the linear accelerator facility at Institute for Integrated Radiation and Nuclear Science of Kyoto University (KURNS-LINAC) for producing RI from photoreactions. A 40 MeV electron beams with an intensity of 3-9 μA is used to bombard a platinum target with a thickness of 4 mm to generate bremsstrahlung photons for producing ^{18}F via the photoreaction on natural Ne gas.

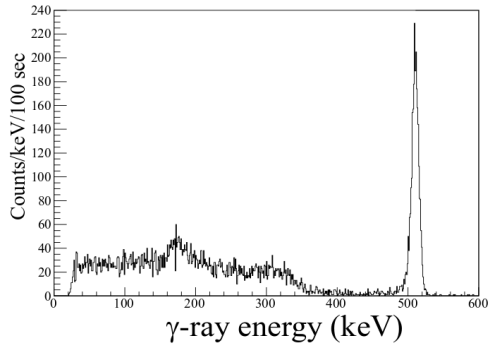

The Ne-gas circulation system has been newly constructed for the present experiment. The irradiation time of bremsstrahlung photons was one hour. The produced ^{18}F isotopes are expected to circulate with Ne gas. When the Ne gas is blow with ^{18}F isotopes in the FDG liquid, ^{18}F isotopes are trapped by FDG, resulting 18F-FDG. The first purpose of the experiment was to examine this principle. Instead of FDG, we used a sodium hydroxide (NaOH) aqueous solution to trap ^{18}F in the first trial.

Figure shows the γ-ray spectrum measured with a CdZnTe detector as a function of the elapsed time in step of 100 second. The decay curve of the 511 keV γ-ray peak is found to be well fitted with a half-life of 110 minutes, demonstrating that the radio-activities trapped in the NaOH water solution are only due to the ^{18}F isotopes. On base of this initial experiment, we have obtained a patent [1].

There are the remaining problems to be solved: One is the trapping efficiency of produced ^{18}F radio-activities in the used gas flow system. We now improve the system to avoid the surface absorption of ^{18}F activities at the inner pipes of the gas flow system. In order to drastically increase the trapping efficiency, we have introduced the SiC ceramic chamber with Teflon coating at inner surface. Another problem is the small yield of ^{11}C with a short half-life of 20.3 minutes, which should be reduced to be as small as possible by replacing the Teflon chamber to SiC chamber. This reduction is also possible by properly collimating the bremsstrahlung photons at the Ne gas target. At present, we are preparing a new paper concerning the ^{18}F production on Ne gas [3].

^{99m}Tc EXPERIMENTS:

Our new paper [2] on the ^{99m}Tc production published in August 2018 has attracted experts of attention. The download amounts to 320 in a half year. In order to refine the project furthermore, a technology to easily extract the ^{99m}Tc isotopes from the radioactivities produced via the (γ,n) reaction on natural Mo are being developed in connection with the noble technologies in materials science.

REFERENCES:

[1] N. Takahashi, Patent Number 6274689 (Japan).
[2] T. Takeda *et al.*, ^{99m}Tc production via the (γ,n) reaction on natural Mo, Journal of Radioanalytical and Nuclear Chemistry (2018) **318**: 811-821.
[3] M. Kurosawa, M. Fujiwara, M. Tamura, N. Takahashi *et al.*, to be submitted to JRNC.

CO6-6 Conformational Characterization of Archaeral Homolog of Proteasome-assembly Chaperone PbaA

M. Yagi-Utsumi, R. Inoue[1], N. Sato[1], M. Sugiyama[1] and K. Kato

Institute for Molecular Science, National Institutes of Natural Sciences
[1]Institute for Integrated Radiation and Nuclear Science, Kyoto University

INTRODUCTION: Recent bioinformatic analyses identified proteasome assembly chaperone-like proteins, PbaA and PbaB, in archaea. PbaB forms a homotetramer and functions as a proteasome activator, whereas PbaA does not interact with the proteasome despite the presence of an apparent C-terminal proteasome activation motif [1, 2]. The C-terminal α6 helices of the PbaB tetramer show tentacle-like structures that project from the core domain, whereas the corresponding C-terminal helical segments of a PbaA pentamer are packed against the core. These structural features may explain the distinct proteasome-binding capabilities of PbaA and PbaB, although the conformational difference may be due to different modes of crystal packing [3]. Interestingly, previous proteome and SAXS-based structural proteomics analyses revealed that PbaA forms a stable complex with an unknown function protein PF0014 [4]. Existence of the putative binding partner protein raised possibilities that it might have some specific role in the PbaA structural design. However, there are no detailed structural information about the protein complex. Thus, we attempted to characterize the structural features of PbaA together with the PF0014 protein by an integrative structural analysis including small-angle X-ray scattering (SAXS).

EXPERIMENTS: The expression and purification of *P. furiosus* PbaA, PbaB and the 20 S proteasome were performed according to methods previously described [1, 2]. SAXS experiments were performed with NANOPIX (Rigaku) at 20°C. X-rays from a high-brilliance point-focused X-ray source (MicroMAX-007HF) were focused and collimated with a confocal multilayer mirror (OptiSAXS) and low parasitic scattering pinhole slits (ClearPinhole). The scattered X-rays were detected using a two-dimensional semiconductor detector (HyPix-6000). The SAXS pattern was converted to a one-dimensional scattering profile, and then standard corrections were applied for initial beam intensity, background scattering and buffer scattering. HS-AFM and EM analyses were also performed.

RESULTS: To obtain information on the overall structure of PbaA/PF0014 complex, we performed HS-AFM and SAXS experiments of PbaA/PF0014 in solution. The HS-AFM data revealed that PbaA/PF0014 complex makes dumbbell-shaped structure in solution and the central pore of PbaA was closed upon complex formation of PF0014. The Ab initio shape modelling from SAXS data (Fig. 1) also demonstrated the dumbbell-shaped structure, in which the estimated radius of gyration (Rg) and the maximum dimension (Dmax) were 55.3±0.1 Å and 178 Å, respectively. Furthermore, using EM and small-angle neutron scattering, we determined the spatial arrangement of PbaA and PF0014 in their dumbbell-shaped complex.

Our study underscores the idea that the functional binding partner of PbaA in archaeal cells is not the proteasome but the PF0014 protein. Although the function of this protein tholos remains unexplored, the structural architecture suggests its capability for molecular encapsulation in archaeal cells.

The unique assembly state of PbaA with PF0014 can provide a new direction to think why this complexity does exist or whether it has some sophisticated novel functional roles in the living system. For example, because of its conformational versatility, PbaA may form different oligomeric structures in response to environmental changes surrounding the organism.

In summary, this study revealed unique structural architectures involving the archaeal homologs of proteasome assembly chaperones, giving new insights into the structural design underlying the dynamic ordering of biomolecules that have internal complexities for the creation of integrated functions.

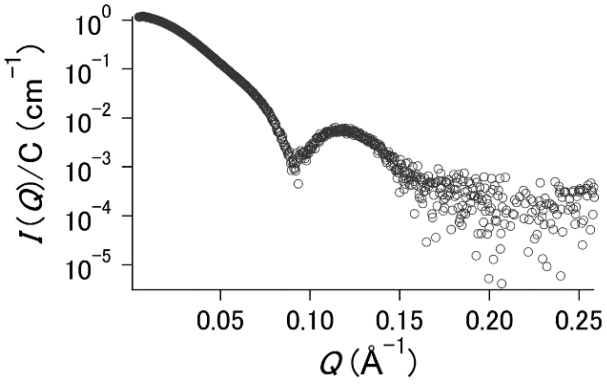

Fig. 1. The SAXS profile of PbaA/PF0014 complex.

REFERENCES:

[1] K. Kumoi *et al.*, PLoS ONE, **8** (2013) e60294.
[2] A. Sikdar *et al.*, Biochem. Biophys. Res. Commun., **453** (2014) 493-497.
[3] M. Yagi-Utsumi *et al.*, Protein Eng. Des. Sel., **31** (2018) 29-36.
[4] Hura, G. L. *et al*. Nat Methods **6** (2009) 606-612.

CO6-7 Time-Resolved Small Angle X-ray Scattering (SAXS) Measurements on the Formation of Insulin B Chain Prefibrillar Intermediates

N. Yamamoto, E. Chatani, R. Inoue[1], K. Morishima[1], and M. Sugiyama[1]

Graduate School of Science, Kobe University
[1]KURNS,Kyoto University

INTRODUCTION: Amyloid fibrils are a kind of protein aggregates associated with a numerous number of diseases. Amyloid fibrils typically exhibit fibrous morphology and β-sheet-rich structure, and the formation of amyloid fibrils typically follows a nucleation-dependent polymerization mechanism. Although a one-step nucleation has widely been accepted as the simplest scheme, a variety of oligomers have been identified in early stages of fibrillation. The oligomers have recently been focused on as an intermediate species involved in the nucleation process as well as molecular species responsible for cytotoxicity [1].

We recently found that prefibrillar intermediates were formed in the early phases of amyloid fibril formation of an insulin-derived peptide (insulin B chain) [2]. In this study, to elucidate the formation mechanisms of the prefibrillar intermediates, we performed time-resolved SAXS measurements of the fibrillation reaction of insulin B chain. Among the wide variety of established analytical techniques stated above, SAXS is one of the most useful approaches to monitor the early events that direct the formation of fibril nuclei [3,4].

EXPERIMENTS: Human insulin was dissolved in 50 mM Tris-HCl, pH8.7. Dithiothreitol was then added to start the reduction of insulin. The solution was kept under 25 °C overnight and a precipitate formed was separated by ultracentrifugation. After rinsed with cold water, the precipitate was dissolved in 10 mM NaOH to 2.5–3.5 mg/ml. The purity of the B chain was confirmed to be > 95 % by the ^{1}H signals of ε protons in tyrosine residues obtained using the NMR spectrometer. The purified insulin B chain was stored at -80 °C before use.

The stock insulin B chain in 10 mM NaOH was diluted with 50 mM Tris-HCl buffer at a concentration of 1.4 mg/ml, which was then put in a 1-mm path-length quartz cell. The small angle X-ray scattering (SAXS) pattern was collected at 25 °C with NANOPIX equipped with HyPix-6000 (Rigaku Corporation, Japan). A Cu K-α line (MicroMAX-007HF) was used as a beam source, which was further focused and collimated with a confocal multilayer mirror (OptiSAXS). The camera length was set to 1.33 m and the range of the scattering vector q was from 0.006 to 2.35 Å^{-1}. Scattering data were collected with an exposure time of 30 min at an interval of 30 min.

RESULTS: Fig. 1 shows representative SAXS profiles of insulin B chain monitored in the formation process of the prefibrillar intermediates. Significant changes in these scattering profiles indicated that the SAXS profiles successfully tracked the formation process of the prefibrillar intermediates. Interestingly, the slope of the log-log plot of the scattering profile was close to −1 from the beginning, suggesting that insulin B chain aggregates in a rod-like shape.

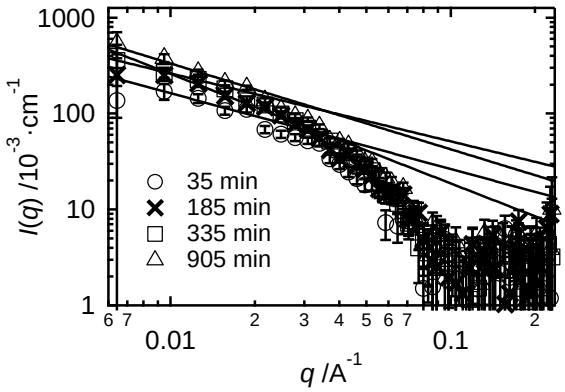

Fig. 1. Representative one-dimensional SAXS profiles of insulin B chain monitored at 35, 185, 335, and 905 minutes. The lines indicate slopes obtained by curve fit.

Data analysis is now ongoing to investigate details about time evolution of conformational development from monomers towards the prefibrillar intermediates. A preliminary analysis of the cross-section plot suggested that the base radius (R_c) of the rod-like aggregates gradually increased from 20 to 25 Å during the measurement. Furthermore, dynamic light scattering measurement allowed us to obtain the hydrodynamic radius, R_h. With the R_c and R_h values, we are now attempting to estimate the length of the prefibrillar intermediate based on Broersma's relationship. The accomplishment of the analysis will reveal detailed mechanisms of the formation of the prefibrillar intermediates of insulin B chain.

REFERENCES:

[1] E. Chatani and N. Yamamoto, Biophys. Rev., **10** (2018) 527-534.
[2] N. Yamamoto *et al*., Sci. Rep., **8** (2018) 62.
[3] E. Chatani and R. Inoue *et al.,* Sci. Rep., **5** (2015) 15485.
[4] A.E. Langkilde and B. Vestergaard, FEBS Lett. **583** (2009) 2600-2609.

CO6-8 Analysis of the initial step of fibrillation by amyloid-β peptide

T. Nakagawa, D. Tsuri, I. Nishii[1], K. Morishima[2], R. Inoue[2], M. Sugiyama[2] and M. Hoshino

Graduate School of Pharmaceutical Sciences, Kyoto University
[1]Faculty of Science, Nara Women's University
[2]KURNS, Kyoto University

INTRODUCTION: Alzheimer's disease is a progressive neurodegenerative disorder. One of its pathological hallmarks is the extracellular deposition of senile plaques in the brain. The major component of these plaques is fibrillar aggregates (amyloid fibrils) of amyloid β-peptide (Aβ). Although the conversion of soluble Aβ monomers to insoluble amyloid fibrils is considered to be a key step to understand the development of Alzheimer's disease, little is known about the molecular mechanism of this process.

The difficulty to analyze the initial step of fibril formation is mainly originated from the extraordinarily high cooperativity of the reaction. While the solution of monomer peptides seems quiescent before the formation of the "nucleus" of amyloid fibrils, a numerous number of molecules rapidly and almost irreversibly bind to the "nucleus" once it formed. As a result, the most important intermediate, "nucleus" or "soluble oligomer", exists only rarely and temporarily.

Here, we examine the conformation of a covalently linked Aβ dimer peptide as a model compound for the initial intermediate of the amyloid fibril formation. We found that the aggregation reaction was enhanced remarkably by the covalent link of two molecules. However, the conformation of tethered molecule was, by itself, very similar to that of random coil structure. We also found that morphology of the aggregates depended significantly on the peptide concentrations. From these observations, we propose that formation of amyloid fibrils are governed by a delicate balance between association and dissociation rate constants.

EXPERIMENTS: The wild type and mutant Aβ(1–40) peptides were constructed as fusion proteins with ubiquitin. The proteins were expressed and purified as described previously [1].

Transmission electron microscopy observations were performed on a JEOL JEM JEM-2100F electron microscope with an acceleration voltage of 100 kV. Samples were applied to Formvar-coated grids and negatively stained with 2% (w/v) uranyl acetate.

NMR experiments were performed on a Bruker Avance 600 spectrometer with triple-resonance probe. A typical ^{1}H-^{15}N HSQC experiments were performed at protein concentration of 50 μM. The solvent conditions used were 20 mM sodium acetate (pH 5.0), and 10% D_2O. The chemical shift value was referenced to DSS.

The kinetics of the aggregation of Aβ peptides was monitored as the increase in fluorescence of thioflavin T (ThT) measured at 490 nm with an excitation wavelength of 446 nm on a Shimadzu RF-5300 spectrofluorometer.

RESULTS: In order to prepare a covalently linked-dimer Aβ peptide, we introduced a cysteine residue by substituting alanine residue at the second N-terminal position. By oxidizing two ceysteine residues, Aβ molecules were covalently linked in the parallel orientation, which was called as A2C-dimer. In contrast to the wild type Aβ peptide, in which fibril formation is preceded by a long lag-period (typically 12~24 hrs), incubation of A2C-dimer resulted in a rapid increase in ThT fluorescence. Dynamic light scattering experiments also suggested rapid formation of aggregates with hydrodynamic radius of several hundred nm. A detailed analysis by TEM observation revealed, however, the morphology of rapidly formed aggregates by A2C-dimers was different from those by wild type Aβ.

Next, we attempted to examine the conformation of A2C-dimer peptide by high resolution NMR spectroscopy in detail. Because rapid formation of aggregate by A2C-dimer hampered analysis by solution NMR, we encapsulated a molecule of A2C-dimer into a reverse micelle formed by mixture of Aerosol-OT(AOT) and hexane to prevent spontaneous aggregation. Surprisingly, the NMR spectrum of A2C-dimer isolated in AOT micelle was almost identical to that of wild type Aβ molecule, suggesting that both Aβ species assume a random coil like structure (Fig. 1).

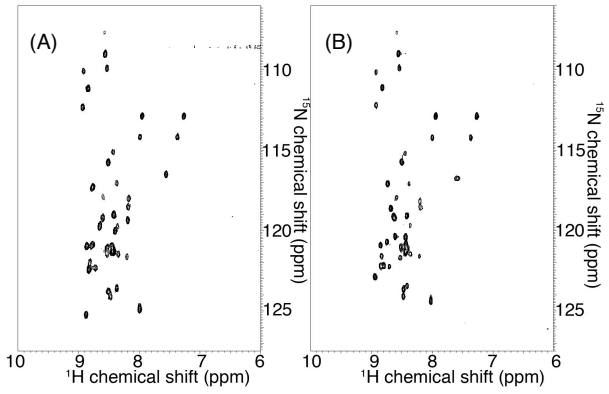

Fig. 1. ^{1}H-^{15}N HSQC spectra of wild type Aβ peptide in aqueous solution (A) and A2C-dimer in AOT/hexane reverse micelle (B).

The results of NMR analysis suggested that the molecular structure of Aβ peptides was, by itself, not significantly changed. Instead, the difference in the kinetics of aggregate formation as well as the morphology of them might attribute too strong tendency of aggregate formation in A2C-dimer peptide. The results emphasizes the importance of delicate balance of the association and dissociation rate constants for the formation of "one-dimensional crystal", amyloid fibrils.

REFERENCES:

[1] T. Yamaguchi *et al*., Biochemistry (2010) 49, 7100-7107.

CO6-9 Generation of radioresistant *Escherichia coli* by adaptive evolution using gamma rays as selection pressure

T. Saito

Institute for Integrated Radiation and Nuclear Science, Kyoto University

INTRODUCTION: In nature, organisms have evolved diversely by adapting themselves to various environmental conditions. Some organisms have been found to survive in environments that can be easily perceived as extremely severe. Elucidating the adaptive mechanisms of organisms to severe environmental conditions can provide meaningful information regarding evolution and diversity overall. Some bacteria, known as radioresistant bacteria, demonstrate extreme resistance to ionizing radiations. The extreme resistance mechanism of these bacteria to ionizing radiation is an interesting area of research from the standpoint of adaptive mechanisms employed by organisms in nature. In order to elucidate the mechanisms of radioresistance in these organisms, it is important to investigate their biological defense mechanisms against external stresses at the molecular level. However, studies conducted on radioresistant organisms existing in nature are likely to encounter many challenges due to limited knowledge of their genetic and biochemical properties. Therefore, in this study, the generation of radioresistant cells of *Escherichia coli* was attempted by experimenting on their ability to undergo adaptive evolution when exposed to gamma rays The following operations were repeated in this experiment: gamma-ray irradiation of *E. coli* cells whose genetic and biochemical properties are sufficiently known, growth of the surviving cells, and irradiation of the grown cells.

EXPERIMENTS: Evaluation of the sensitivity of *E. coli* cells to gamma irradiation: *E. coli K*-12 cells were grown to the early log phase in LB medium at 37°C at 200 rpm. One milliliter of the culture was centrifuged at 4000 × *g* at 20°C for 10 min. The supernatant was discarded and the pellet was suspended in 1 mL of PBS (–). The cell suspension was irradiated with gamma rays at a dose rate of 22 Gy/min at 20 ± 3°C. Gamma irradiation was carried out at the Co-60 Gamma-ray Irradiation Facility of the Institute for Integrated Radiation and Nuclear Science, Kyoto University. The gamma-irradiated cell suspension was diluted appropriately with PBS (–), plated on LB agar, and incubated at 37°C for 12 hr. After incubation, the colonies were counted, colony forming units were determined, and survival rates were calculated.

Selection with gamma rays: *E. coli K*-12 clone cells obtained by single colony pick-up were cultured to the early log phase in LB medium at 37°C at 200 rpm. The cell suspension was prepared as described above and irradiated with the 1% survival dose of gamma rays at a dose rate of 22 Gy/min at 20 ± 3°C. One milliliter of the gamma-irradiated cell suspension was inoculated in 100 mL of LB medium and cultured at 37°C at 200 rpm till the cells reached their early stationary phase. The glycerol stock was prepared and stored at –80°C. This procedure was repeated after culturing the glycerol stock cells to the early log phase.

RESULTS: In order to generate radioresistant *E. coli* cells by adaptive evolution to gamma rays as the selection pressure, *E. coli* cells were irradiated with a 1% survival dose of gamma rays, and the surviving cells were grown. The 1% survival dose of the surviving cell population to gamma rays was evaluated, and the cell population was once again irradiated with the 1% survival dose. The 1% survival dose to gamma rays of the wild type *E. coli* clone without selection was 242 Gy, whereas that of the *E. coli* population obtained after 20 selection cycles was 1872 Gy; the resistance of *E. coli* to gamma rays was increased 7.7 fold in this adaptive evolution experiment (Fig. 1). Furthermore, the resistance gradually increased in the process of the adaptive evolution. These results indicate that mutations and changes in the expression levels of many genes are likely to be involved in this increase of resistance. In the future, further studies, namely that the gene expression levels of radioresistant *E. coli* cells obtained by the adaptive evolution experiment are analyzed and compared with those of wild type *E. coli* cells, will be required.

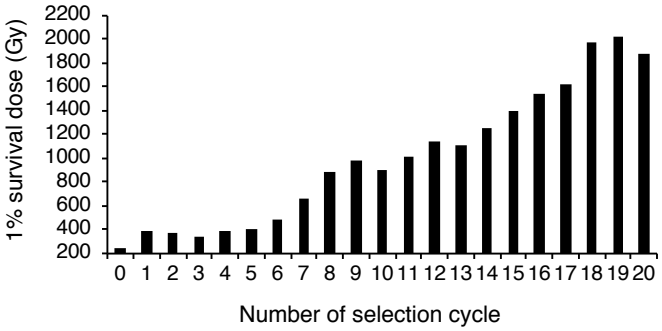

Fig. 1. Increase in resistance of *E coli* cell populations to gamma rays during adaptive evolution.

REFERENCES:

[1] T. Saito, Viva Origino, **30** (2007) 85–92.

CO6-10 Physicochemical study on ILEI suppressing amyloid-β generation

E. Hibino[1], K. Morishima[2], R Inoue[2], M Sugiyama[2], M Nakano[1], N Watanabe[1], T Sugi[1] and M Nishimura[1]

[1]*Molecular Neuroscience Research Center, Shiga University of Medical Science*

[2]*KURNS, Kyoto University*

INTRODUCTION:

The number of patients with Alzheimer's disease (AD) is increasing in Japan. However, any effective AD modifying drug is still undeveloped. The pathogenic processes of AD are thought to be triggered by accumulation of amyloid-β protein (Aβ) in brain. Previously, we have identified a secretory protein named interleukin-like epithelial-mesenchymal transition inducer (ILEI, also known as FAM3 superfamily member C) as a negative regulator of Aβ production by the unique activity[1]. ILEI is secreted from cell to bind to the extracellular region of Presenilin-1, a component of the γ-secretase complex.

The interaction of ILEI with Presenilin-1 enhances nonspecific degradation of Aβ precursor protein. However, the molecular mechanism based on the structural findings is still to be clarified. Although the monomeric and dimeric forms of ILEI have been reported recently[2], the structure-function relationships are also still unclear.

The objective of this study is to elucidate whether the dimerization of ILEI is indispensable for the function on Aβ generation.

EXPERIMENTS:

Human ILEI (residues 55-227) tagged with His was over-expressed in Rosetta-gamiB (DE3) pLysS stain and purified using Ni-NTA resin and size exclusion chromatography (SEC). CBB-stained SDS-PAGE gels and SEC profile on non-redox condition showed a single band and peak, respectively. Subsequently, around 1.5 mg/mL ILEI protein solution was diluted with buffer at each pH condition (6.0, 7.3 and 8.0).

To confirm the monomer-dimer transition of ILEI at 25˚C, ILEI solution was analyzed by analytical ultracentrifugation at 60,000 r.p.m. or 20,000 r.p.m.

RESULTS:

The profiles measured at 60,000 r.p.m. of the rotating speed by Rayleigh interferometer are shown in Fig. 1. The peak derived from around 40 kDa was identified although the main peak corresponding to 20 kDa accounted for the greater part. Most ILEI molecules existed as monomeric state since the molecular weight of ILEI monomer was predicted to be 20.0 kDa. In addition, the abundance ratios of multimer, which were 4.5%, 3.7% and 15.2% at pH 6.0, pH 7.3 and pH 8.0, respectively, were increased in correlation with an increase in pH value.

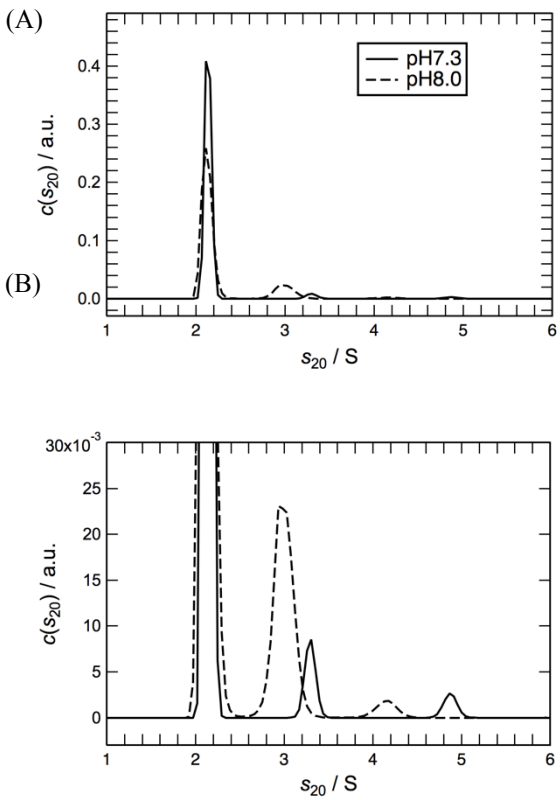

Fig. 1. (A) The solid line, dashed line and dotted line show distributions of sedimentation coefficient derived from ILEI at pH 6.0, pH 7.3 and pH 8.0, respectively. (B) The expanded of the lower range of A.

Furthermore, to identify whether ILEI proteins were dissociated or not, we also measured the profiles at 20,000 r.p.m, so that, the peaks were put into one peak (data not shown). This suggested that ILEI was in monomer-multimer equilibrium state. Moreover, the dissociation constants calculated from the populations were 4.3×10^{-4} M (25℃, pH 7.3) and 1.0×10^{-4} M (25℃, pH 8.0).

In conclusion, although ILEI can form homodimers, most ILEI molecules are thought not to dimerize, taking it consideration that population of dimer is low at pH 7.3 and that ILEI is a secretory protein. We speculate that ILEI functions in monomeric state, although a possibility that ILEI dimers have functions dissimilar from the monomer cannot be ruled out.

REFERENCES:

[1] H. Hasegawa *et al*., *Nat. Commun.*, 5:3917 (2014).
[2] A.M. Jansson *et al*., *J. Biol. Chem.*, **297** (2017) 15501-15511.

CO6-11 **Structural characterization of the *S. pombe* nucleosome containing histone variant H2A.Z**

M. Koyama[1], R. Inoue[2], K. Morishima[2], W. Nagakura[3], M. Sugiyama[2], H. Kurumizaka[1,3]

[1] *Institute for Quantitative Biosciences, The University of Tokyo*

[2] *KURNS, Kyoto University*

[3] *Division of Advanced Science and Engineering, Waseda University*

INTRODUCTION:

In the eukaryotic cells, genomic DNA binds histone proteins to form the chromatin structure, and stored in the nucleus. The structural unit of the chromatin is the nucleosome, in which about 145-base-pairs of DNA are wrapped around the histone octamer, containing two molecules of each of four core histones (H2A, H2B, H3, and H4) [1, 2].

The fission yeast *S. pombe* is a single cell eukaryote that shares many characteristics of the chromatin structure and function with higher eukaryotes. *S. pombe* has only one H2A variant, H2A.Z, which is preferentially associated with actively transcribed chromatin. In this study, to analyze the structural property of the *S. pombe* H2A.Z nucleosome, we reconstituted the nucleosome *in vitro*, and measured its small angle X-ray scattering profile.

EXPERIMENTS:

The *S. pombe* canonical (H2A) or H2A.Z nucleosomes were reconstituted *in vitro*, by mixing a 146-base-pair DNA fragment with *S. pombe* four core histones (SpH2A or SpH2A.Z, SpH2B, SpH3, and SpH4). The reconstituted nucleosomes were further purified by polyacrylamide gel electrophoresis using the Prep Cell apparatus (BioRad). The purified samples were concentrated using a Millipore concentrator (Mw cutoff of 30,000). After filtration, the samples were used for the SAXS measurement.

RESULTS:

SAXS profiles of the *S. pombe* canonical nucleosome, and the *S. pombe* H2A.Z nucleosome are shown in Fig. 1. Guinier plots of the data are shown in Fig. 2. The straight line represents the least-square fitting for the data. This result revealed that the gyration radius (R_g) of the *S. pombe* H2A.Z nucleosome is 46.2 ± 0.3 Å, which is larger than that of the *S. pombe* canonical nucleosome (R_g = 45.0 ± 0.2 Å). The distance distribution functions of the nucleosomes are shown in Fig. 3. The longest distances, D_{max} values, are 150 Å for the canonical H2A nucleosome, and 157 Å for the H2A.Z nucleosome. These findings suggest that the H2A.Z nucleosome has more stretched structure, as compared to the canonical nucleosome in *S. pombe*.

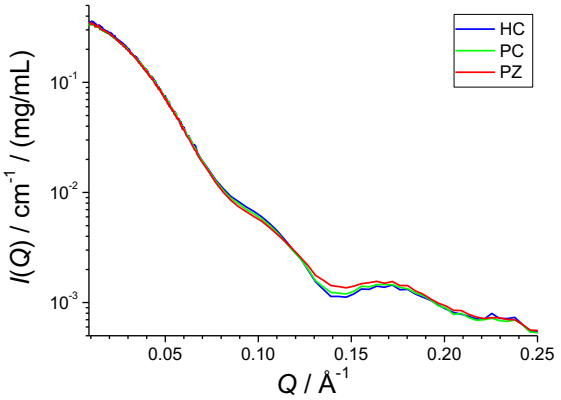

Fig. 1. SAXS profiles of the *S. pombe* canonical nucleosome (green), the *S. pombe* H2A.Z nucleosome (red), and the human canonical nucleosome (blue).

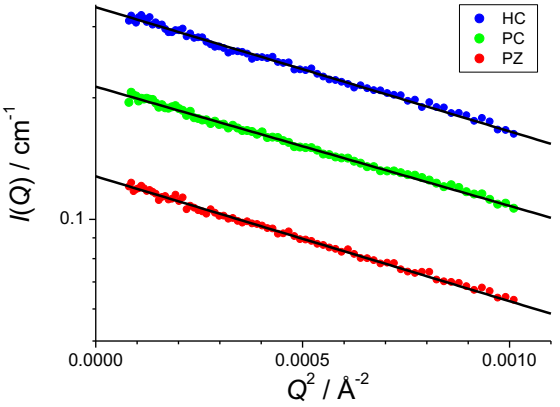

Fig. 2. Guinier plots of the nucleosomes. The color coding is the same as in Fig. 1.

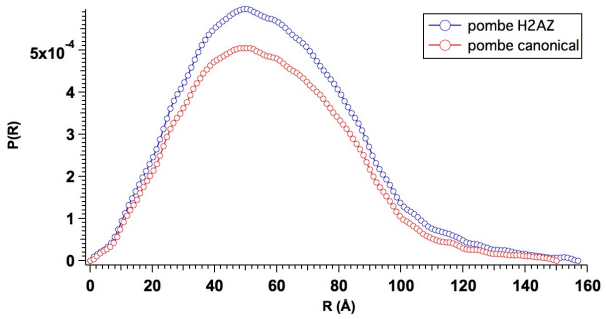

Fig. 3 Distance distribution functions of the *S. pombe* H2A.Z nucleosome (blue) and *S. pombe* canonical nucleosome (red).

REFERENCES:

[1] K. Luger *et al.*, Nature, 389, 251-260 (1997).
[2] M. Koyama and H. Kurumizaka, J. Biochem., 163, 85-95 (2018).

CO6-12 Production of medical radioisotopes using electron linear accelerator

S. Sekimoto, T. Ohtsuki

Institute for Integrated Radiation and Nuclear Science, Kyoto University

INTRODUCTION: A shortage in the supply of ^{99}Mo resulting from the shutdown of reactors used for its production is a global problem. Because ^{99}Mo is an indispensable source of ^{99m}Tc, which is used in nuclear medicine to make diagnoses using techniques such as scintigraphy and single photon emission computed tomography (SPECT), a stable supply of ^{99}Mo is vital. Therefore, production of ^{99}Mo by using neutrons or protons generated in accelerators has been investigated [1–3]. To separate ^{99m}Tc from ^{99}Mo produced by an accelerator, methods based on sublimation, solvent extraction, and ion-exchange column chromatography have been examined and developed [2,4–6]. In addition, Gopalakrishna et al. have reported the preparation of ^{99}Mo by the ^{100}Mo(γ,n) reaction using bremsstrahlung photons [6], followed by conventional solvent extraction using methyl ethyl ketone (MEK) and zirconium (Zr) molybdate gel to separate ^{99m}Tc. According to the regulations of the Japanese pharmacopeia, the extraction using organic materials and the gel method using heavy metal elements such as Zr are not approved for the ^{99m}Tc-separation methods. Additionally, it is also difficult and impractical to use the sublimation method, which requires complicated and/or large scale devices for the mass-production of pure ^{99m}Tc.

In the previous work, we carried out the production of ^{99}Mo by the ^{100}Mo(γ,n) reaction using bremsstrahlung photons generated in an electron linear accelerator (LINAC), a technique that has not been investigated significantly in Japan. The amounts of ^{99}Mo produced at several electron energies (E_e) were examined. In this report, the amounts are compared with those predicted by calculation. The experimental condition and results are described in ref. [7].

RESULTS: The ^{99}Mo activities in the pellets were calculated by using the particles and heavy ion transport code system (PHITS) [8], and the calculated values are shown in Fig. 1 for comparison with the experimental values. Although the experimental value at an E_e of 32 MeV agrees with the calculated value, the experimental values are lower than those calculated at E_e's of 21 and 25.5 MeV and higher than those calculated at E_e's of 35 and 41 MeV. These differences between experimental and calculated values can be explained by the dispersion of the photon beams. At higher E_e, in general, the intensity of electrons in the longitudal direction is greater than that of electrons in the transverse direction; *i.e.*, the dispersion of higher energy electron beams (higher E_e) tends to be smaller than those at lower E_e due to the space charge density of electrons. Therefore, the dispersion of photon beams generated by electrons at higher E_e becomes smaller. This tendency can be confirmed by simulation using the Geometry and Tracking (GEANT) code. Because the dispersion of the photon beams in the PHITS calculation performed in this work is assumed to be identical at E_e's between 21 and 41 MeV, a disagreement was found between the experimental and calculated values. However, the validity of the experimental ^{99}Mo is supported by those found for ^{196}Au produced via the ^{197}Au(γ,n) reaction, *e.g.*, the E_e dependence of the rate of ^{99}Mo-production is similar to that of ^{196}Au-production. This trend depends on the fact that the shape of the excitation functions for the photon energies in the ^{100}Mo(γ,n) and the ^{197}Au(γ,n) reactions are similar, although the absolute values are different by about one order of magnitude [9].

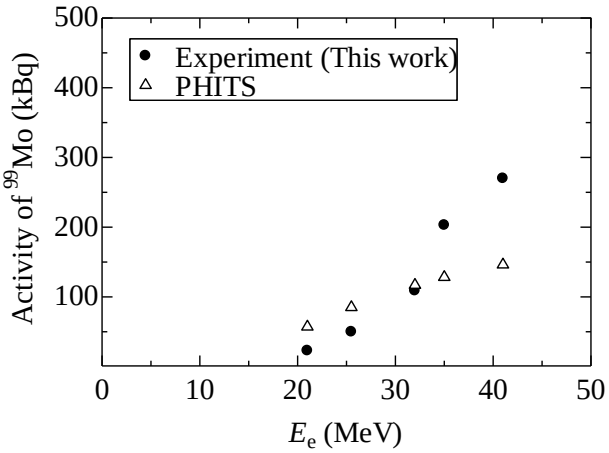

Fig. 1. Activity of ^{99}Mo produced using electron linear accelerator (The irradiation time, beam current of electrons, and amount of target material ($^{100}MoO_3$) were normalized to 5 min, 100 micro-A, and 10 mg, respectively.)

REFERENCES:

[1] Y. Nagai *et al.,* J. Phys. Soc. Jpn. , **82** (2013) 064201.
[2] Y. Nagai *et al.,* J. Phys. Soc. Jpn. , **83** (2014) 083201.
[3] K. Nakai *et al.,* Proc. Jpn. Acad. Ser. **B 90** (2014) 413–421.
[4] M. Kawabata *et al.,* J. Phys. Soc. Jpn. , **84** (2015) 023201.
[5] K. Mang'era *et al.,* J. Radioanal. Nucl. Chem., **305** (2015) 79-85.
[6] A. Gopalakrishna *et al.,* J. Radioanal. Nucl. Chem., **308** (2016) 431-438.
[7] S. Sekimoto and T. Ohtsuki, KUR-progress report (2017) CO6-14.
[8] Niita K *et al.,* (2010) PHITS: Version 2.23, JAEA-Data/Code 2010-022, JAEA.
[9] Dietrich SS, Berman BL (1988) Atlas of photoneutron cross sections obtained with monoenergetic photons. Atomic Data Nucl Data Tables. 38:199–338.

CO6-13 Determination of degree of deutteartion level of deuterated protein through small-angle neutron scattering

R. Inoue, K. Morishima, N. Sato, M. Sugiyama

Institute for Integrated Radiation and Nuclear Science, Kyoto University

INTRODUCTION: Small-angle Neutron (SANS) technique gives the overwhelming opportunities for structural analyzes on target samples in solution. Especially, contrast-variation SANS (CV-SANS) method [1], which utilizes the modulation of scattering length density (scattering contrast) between solute and solvent, offers the fascinating opportunity for studying the partial structure of complex biological samples. It is known that the scattering length density of normal (or hydrogenated) protein is nearly equal to that of 40% D_2O. Namely, hydrogenated protein is invisible in 40% D_2O in terms of CV-SANS. With this characteristic feature, the CV-SANS method has been applied for various hydrogenated proteins. On the other hand, on of the big disadvantages associated with above CV-SANS method is high incoherent signal from 60% H_2O, hindering the detailed structural analyzes on target biological samples. In order to overcome such a situation, the inverse contract matching SANS (ICM-SANS) method [1] has been paid attention. The essence of this technique is that the scattering length density of protein is tuned to be matched with that of 100% D_2O by modulating the deuteration level of protein. The most stressing point in ICM-SANS is the realization of high S/N SANS data attained by the suppression of incoherent scattering from solvent. However, the procedure for preparation of partially deuterated protein that is perfectly contrast-matched with 100% D_2O has not been well established up to now. For this purpose, we have to grasp the proper deuteration condition and the protocol for the determination of degree of deuteration of prepared partially deuterated protein. It is considered that SANS and mass spectrometry are usable for the determination of degree of deuteration of prepared partially deuterated protein. Prior to usage of SANS meausremnets, we try to determine the degree of deuteartion of partially deuterated protein with mass spectrometry.

EXPERIMENTS: In addition to the preparation of hydrogenated αB-crystallin, we prepared partially deuterated αB-crystallin by mixing ratio of hydrogenated and deutearted glucose 3:1 in 75% D_2O. Mass spectrometry measurements were performed with microflex, BRUKER.

RESULTS: Fig. 1 shows mass spectrum from hydrogenated αB-crystallin and partially deuterated αB-crystallin, respectively. It can be clearly seen that main peak shifted to high *m*/*z* value by deuteration, implying the exact increase of mass during cultivation.

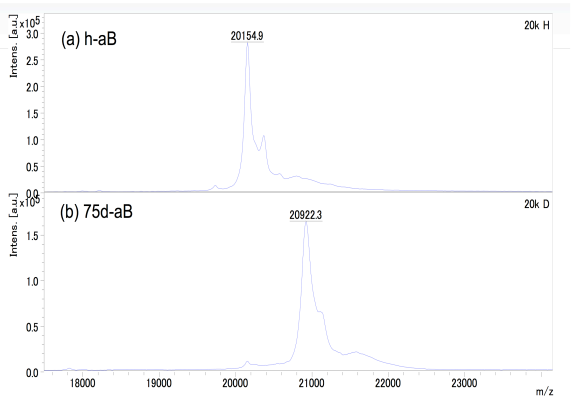

Fig. 1 (a) Mass spectrum from hydrogenated αB-crystallin. (b) Mass spectrum from partially deuterated αB-crystallin.

Considering the amino acid sequence of αB-crystallin, we have calculated the degree of deuteration of partially deuterated αB-crystallin. The degree of deuteartion of partially deuterated αB-crystallin was found to be 70.0%. As written at the experimental section, we have cultivated partially deuterated αB-crystallin in 75% deuterated glucose and 75% D_2O. Hence, the resulting degree of deuteartion of prepared αB-crystallin is much lower than 75%. It is expected that further control of cultivation condition such as mixing ratio of deuterated glucose must be taken into account.

As a next step for this project, we are now trying to evaluate the degree of deuteartion of αB-crystallin by changing the mixing ratio of deuterated glucose and D_2O. It will contribute to realizing the perfectly contrast-matched partially deuterared protein in 100% D_2O. It will further reinforce the powerfulness of ICM-SANS.

REFERENCES:

[1] M. Sugiyama *et al.*, BBA, **1862** (2018) 253-274.

CO6-14 Measurement of Trancemitance Spectra of a Humann Calcificated Aorta Tissue in the Sub-Terahertz Region, which Related with a SEM-EDX Elements Imaging (II)

N. Miyoshi and T. Takahashi[1]

Department of Molecular Chemistry, Kyoto Institute of Technology
[1]Institute for Integrated Radiation and Nuclear Science, Kyoto University

INTRODUCTION: The LINAC (Electron linear accelerator) technology in the millimeter- and terahertz-waves had been unique and had been used as a coherent synchrotron light source in the Institute for Integrated Radiation and Nuclear Science of Kyoto university (KURNS) to observe the transmittance spectra of a human calcified aorta tissue as a collaborate study. The absorption spectra in the sub-terahertz region had been not so clear for the raw tumor tissue although Ashworth-PC. *et al.* [1] had reported for the excised human breast cancer by a terahertz pulsed spectroscopy observed at 320 GHz, which was estimated a longer relaxation time component of the induced electricity for water molecules [2-3] in the raw tumor tissue for three years at the linear analysis.

We had started to measure of new biological sample of a calcified human aorta dried tissue sampling from the pathological autopsy in the last year. Furthermore, the getting spectral information was estimated with the SEM-EDX elements images of the calcified aorta tissue with a biological meaning in this year. It was reported the relation of the biological information between both of the element images and sub-THz spectral components in this report.

EXPERIMENTS: (1) Instrument of Near-field in Terahertz Region: The photograph of the instrument was shown in Fig. 1. Mark-A: Pre-probe Wiston cone; 50-10mm diameter, Length=60mm; the irradiate diameter=0.775mm; Mark-B: The concentrate light probe (diameter=3mm). The instrument was developed by Dr. T. Takahashi [4] for the transmittance measurements.

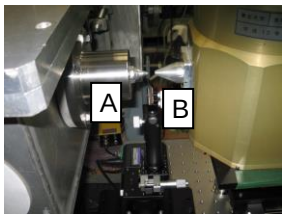

Fig. 1. The near field area of sample holder position.

(2) Sample Preparation for SEM-EDX Elements (P, and Ca) Images of Calcified Aorta: A calcified aorta tissue was cryo-sectioned in vertical of the blood wall at -20 ℃ at 8 μm depth. The sample tissues was measured by a Scanning Electron Microscope (JEOL) combined with Energy Dispersion X-ray (EDX) analyzer.

RESULTS and DISCUTION: (1) The morphological images were observed in side of the calcified aorta tissue by the SEM-EDX analysis as shown inf Fig. 2.

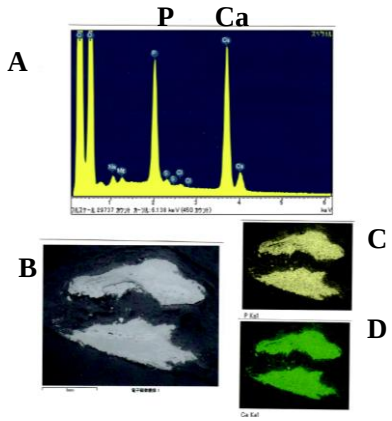

Fig. 2. The SEM-EDX spectrum (A), the SEM, the elements (P and Ca) vertical images (B, C and D) of a human calcified aorta blood vessel wall, respectively.

(2) The transmittance spectra of the sample tissue for each points A, B and C were measured (Fig. 3).

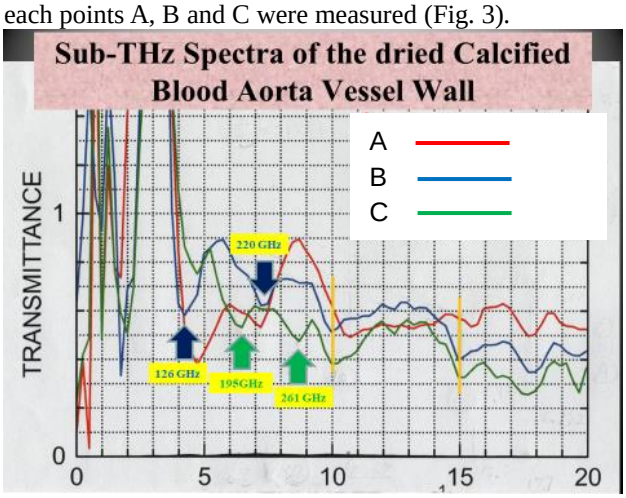

Fig. 3. Sub-THz spectra of the dried calcified blood aorta vessel wall. (A: calcified; B: cholesterol; C: normal)

In the results, the absorbance of the dried tissue at 195 and 261 GHz were observed in the calcified area (included of $CaPO_4$ components from the data of SEM-EDX analysis of calcified aorta tissue), and the absorption peaks of 125, 220 GHz were observed in the cholesterol adhesion area. In the both areas, it was observed the absorption peaks at 300 and 450 GHz also.

In future, it will be needed more measurements and analysis combined with the depth information data of the dried tissue by an ultrasound measurement technology.

REFERENCES:

[1] Phillip C. Ashuworth *et al.*, Optics Express, **17** (2009) 12444-12454.
[2] Toshiko Fukasawa, *et al.*, Phys. Rev. Lett., **95** (2005) 197802.
[3] Hiroyuki Yada, *et al.*, Chem. Phys. Lett., **464** (2007) 166-170.
[4] T. Takahashi, *et al.*, J. Phys.: Conf. Ser. **359** (2012) 012016-1-4.

CO6-15 Preparation of bovine intact FoF1ATP synthase for a cryo-EM structural analysis

C. Jiko[1], C. Gerle[2] and Y. Morimoto[1]

[1]*Institute for Integrated Radiation and Nuclear Science, Kyoto University*
[2]*Institute for Protein Research, Osaka University*

INTRODUCTION: Atomic resolution structure analysis of biomolecules using cryo-electron microscopy (cryo-EM) has been developed (Henderson et al., Nobel Prize, 2017) and the analysis is currently overwhelming for study of membrane proteins that are extremely difficult to crystallize. Although it is powerful, the key to success in structural analysis by a cryo-EM is the ability to purify large quantities of stable and intact samples as well as crystallization.

In this study, we aim to analyze the full length of mammalian mitochondrial FoF1 ATP synthase with atomic resolution. An FoF1 ATP synthesis is an important energy conversion mechanism for maintaining mammalian life activities, and is driven by proton transport in the mitochondrial inner membrane. The FoF1 ATP synthase responsible for this is a membrane protein complex with a molecular weight of 600,000 consisting of 29 subunits. The enzyme not only produces 90% of ATP but also plays an important role in the formation of the inner mitochondrial membrane. It is also suggested that dysfunction of this enzyme leads to apoptosis (cell death). Threfore elucidation of the precise three-dimensional structure of this enzyme is considered to be an important basis for drug molecule design in the future, and is widely studied.

Because of this biological and medical importance, efforts to elucidate the structure of the FoF1 ATP synthase have been made for over 50 years, but the understanding of the function of the FoF1 ATP synthesis enzyme is delayed by the fact that the entire structure has not been elucidated at the atomic level.

The enzyme is a membrane-bound protein of the macromolecule complex and is highly flexible and unstable because of its rotation, which makes it difficult to obtain a purified preparation having a uniform three-dimensional structure throughout the enzyme.

EXPERIMENTS: Bovine heart was obtained immediately after slaughter, and mitochondrial inner membrane was separated followed by solubilization of FoF1 ATP synthase. At this time, purification was required in order to solubilize other proteins. As a purification method of this enzyme, one using an affinity column such as ion exchange chromatography is generally used, and we have also purified by the same method.

However, it was found that this method led to low uniformity of the purified sample. This is because the enzyme has extremely high flexibility as it rotates, and the subunit of this enzyme, which is composed of as many as 29 subunits per monomer, starts dissociation from the intermembrane domain during the purification process

Although this ion exchange chromatography is effective for improving the purification purity, it is considered that the interaction with the ion exchange resin places a burden on the original structure of the enzyme and the degradation of this enzyme is caused. Therefore, it is necessary to establish a purification method that can replace ion exchange chromatography. Dealing with this issue, we developed a purification method by density gradient centrifugation without loading the protein (column-free purification) and succeeded in purifying the enzyme in a very stable and intact state.

RESULTS and DISCUSSION: Using this stable enzyme with full subunits, prepared by the column-free purification developed by the applicant, it was possible to produce a cryogrid suitable for high-resolution single particle analysis by cryo-EM (Fig. 1).

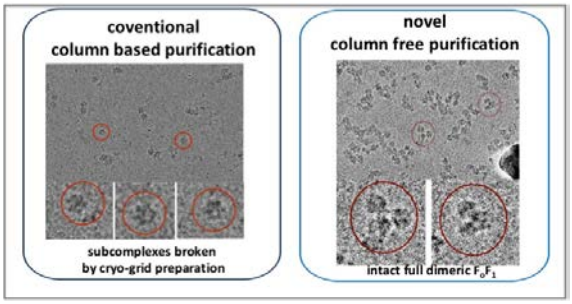

Fig.1 Recent images of mammalian FoF1 dimers by cryo-electron microscopy.

Although the greatest obstacle to collecting high quality data of membrane proteins is the detergent (Rubinstein, Methods, 2007), usually, when the detergent is removed from solution, membrane proteins aggregate and denatures instantaneously. On the other hand, the method developed by Gerle et al. (GraDeR; Hauer et al., Structure, 2015) makes it possible to remove the detergent in the solution before the instant freezing of grid preparation. Currently, grid adjustment is carried out using this method, and observation by cryo-EM is being conducted.

ACKNOWLEDGEMENT: This work is partly supported by the grant of Naito foundation 2018, the grant-in-aid for the young researchers of the JSPS 2019 (C.J.) and the TERUMO foundation 2018, the grant for an advanced research of the KURRI 2018 (Y.M.) .

CO6-16 Preclinical study of boron neutron capture therapy for bone metastasis using human lung cancer cell lines

T. Andoh[1], T. Fujimoto[2], Y. Nagasaki[1], M. Suzuki[3], H. Tanaka[4], T. Takata[4], Y. Sakurai[4], and H. Ichikawa[1].

[1]*Faculty of Pharmaceutical Sciences, Kobe Gakuin University, Japan.*
[2]*Department of Orthopaedic Surgery, Hyogo Cancer Center, Japan.*
[3]*Particle Radiation Oncology Research Center, Institute for Integrated Radiation and Nuclear Science, Kyoto University, Japan.*
[4]*Division of Radiation Life Science, Institute for Integrated Radiation and Nuclear Science, Kyoto University, Japan*

INTRODUCTION: Lung cancer is the leading cause of cancer-related death globally [1]. Rapid metastasis to the bone can occur in 25-40% of lung cancer patients, which has a poorer prognosis [2]. When systematic pharmacotherapy is not effective, the disease is difficult to control. Boron neutron capture therapy (BNCT) may be the sole option in such cases. We have previously demonstrated the effectiveness of BNCT with the use of *p*-borono-L-phenyl-alanine (L-BPA) on tumors in the limbs of human clear cell sarcoma-bearing nude mouse models [3]. In the present study, we established a bone metastasis model for lung cancer and investigated *in vivo* biodistribution of L-BPA and antitumor effects after BNCT in the bone metastasis model.

EXPERIMENTS: Cells of A549-luc, a lung cancer cell line of human origin, were suspended in Matrigel® and injected into the tibia of the left hind leg of nude mice [4]. After 3-4 weeks, a tumor mass was observed in tibia of the mice using a computed tomography scan and luminescence imaging. The biodistribution of ^{10}B was explored by the intravenous administration of BPA-fructose complex (BPA-Fr, 24 mg ^{10}B/kg) to a bone metastasis mouse model of lung cancer. At a predetermined time after administration, the mice were sacrificed and blood and tissue samples were immediately collected. The concentration of ^{10}B in the samples was then measured by inductively coupled plasma atomic emission spectroscopy. In the BNCT trial, the model mice were allocated into a BNCT and control groups. The tumors in the left hind legs were exposed to thermal neutron irradiation at the Institute for Integrated Radiation and Nuclear Science, Kyoto University.

RESULTS: Bone metastasis was successfully produced in the human lung cancer-bearing mouse model. The formation of a solid tumor mass in the left tibia of mice was confirmed by macroscopic observation, micro-computed tomography scans, and luminescence imaging. At 1.5 h after the administration of BPA-Fr, the concentration of ^{10}B in the bone metastasis model tumor tissue reached 50 μg ^{10}B/g wet tumor tissue. Tumor-to-blood and tumor-to-normal tissue (normal bone) ratios were 6.3 and 5.7, respectively, at 1.5 h after injection. In the BNCT trial, tumor growth was observed in the control group, while the BNCT group displayed suppressed tumor growth (Fig. 1). These results suggested that ^{10}B accumulates specifically in the bone tumor and that BNCT destroys tumor cells only at the site of lung metastasis.

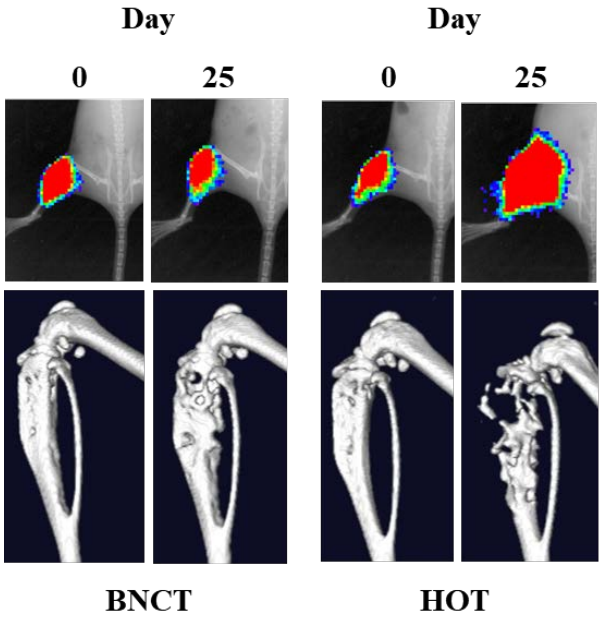

Fig. 1. IVIS images and X-ray CT images after thermal neutron beam irradiation of BNCT and HOT control groups.

REFERENCES:

[1] H.K. Weir *et al.*, J Natl Cancer Inst, 95, 1276–1299 (2003).
[2] H. Fujita, *et al*., PLOS ONE. 11(10) e0164830. DOI:10.1371/journal.pone.0164830 (2016).
[3] T. Fujimoto *et al*. Appl. Radiat. Isot. 73, 96-100 (2013).
[4] J.P. Campbell *et al.*, J. Vis. Exp., 4(67), e4260 (2012).

CO6-17 Coherent Transition Radiation mm-Wave Light Source with an Electron Linac for Absorption Spectroscopy and Irradiation

S. Okuda[1], Y. Tanaka[1] and T. Takahashi[2]

[1]*Organization for Research Promotion, Osaka Prefecture University, Sakai, Osaka, Japan*

[2]*Institute for Integrated Radiation and Nuclear Science, Kyoto University, Kumatori, Osaka, Japan*

***Abstract*—The coherent transition radiation from bunched electron beams of a linear accelerator has continuous spectra in a sub-mm to mm range and has extremely high peak intensity. In Kyoto University the coherent transition light source was developed by using a 45 MeV electron linear accelerator. In this work the characteristics of the light source have been measured and the system has been modified for the applications to absorption spectroscopy and irradiation.**

I. INTRODUCTION

THE coherent transition radiation (CTR) from high-energy bunched electron beams of a linear accelerator (linac) has continuous spectra in a sub-mm to mm wavelength range. The CTR light source has been established [1, 2] by using the electron beams of the 45 MeV L-band electron linac in Kyoto University. It has extremely high peak-intensities in a picosecond light pulse compared with the other THz light sources. The light source has been applied to absorption spectroscopy for various kind of matters. In the present work the detailed properties of the light source have been measured. The light source system has been changed for the applications to absorption spectroscopy and irradiation to investigate the nonlinear effects or biological effects.

II. EXPERIMENTAL

The configurations of the light source system changed for the absorption spectroscopy and the irradiation with CTR are schematically shown in Fig. 1. The electron linac in Kyoto University was used in the experiments. In most experiments the beam energy, macropulse length and the repetition rate are 42 MeV, 47 ns and 60 Hz, respectively. The output CTR light from a light source chamber was transported out from the accelerator room. The spectrum of the CTR light was measured with a Martin-Puplett type interferometer and a liquid-He-cooled silicon bolometer. In the absorption spectroscopy the sample was located on the light path between the interferometer and the detector. The wavenumber resolution was 0.1 cm^{-1} in most experiments, which can be changed. In the interferometer the incident light is divided into two parts by a polarizer: one for spectroscopy and another for irradiation experiments.

III. RESULTS

The light source spectrum has a peak at a wavenumber of about 7 cm^{-1}. The wavenumber range used for spectroscopy was evaluated to be 2-35 cm^{-1}, in which the highest number is limited by the sensitivity of the detector. The intensity of light was estimated to be about 10^{-7} W/0.1%b.w. about the spectral peak and was found to be sufficiently high even if it reduces by 6 orders from the initial one after transmission through the sample with relatively strong absorption. The pulse structure of the CTR corresponds to that of the electron beam from the linac. The micropulse length of the CTR was evaluated by the interferogram obtained by the interferometer to be about 3 ps. Such a relatively short pulse length is due to the special bunching process in the optimized operational conditions of the linac. These results indicated that the peak light intensity in the micropulse is about $3x10^6$ W. In order to increase the peak intensity the electron-gun pulser has been developed to generate the single-bunch electron beam. By using this system it is expected to be a few tens of MW. While the averaged CTR power is sufficiently low not to induce thermal effects in the samples, the comparatively high peak power might cause any nonlinear effects.

Some results for the absorption spectroscopy for liquid samples and the irradiation to investigate the biological effects especially on the gene of fruit fly, *Drosophila melanogaster*, are ongoing to be analyzed.

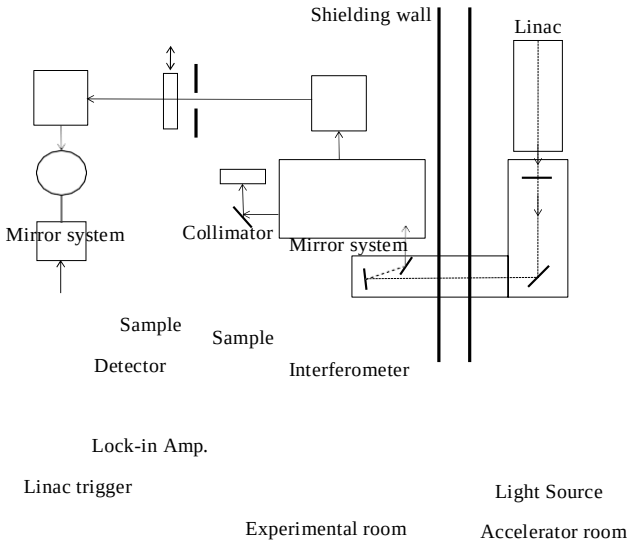

Fig. 1. Schematic diagram showing the configurations for absorption spectroscopy and irradiation using CTR.

In conclusion, the characteristics of the CTR light source in Kyoto University have been measured and the system has been changed for absorption spectroscopy and irradiation experiments. The light source will be applied to investigating some nonlinear effects and biological effects.

This work has been carried out in part under the Visiting Researcher's Program of the Research Reactor Institute, Kyoto University, and supported by JSPS KAKENHI Grant Number JP15K04733.

REFERENCES

[1]. T. Takahashi, T. Matsuyama, K. Kobayashi, Y. Fujita, Y. Shibata, K. Ishi and M. Ikezawa, "Utilization of coherent transition radiation from a linear accelerator as a source of millimeter-wave spectroscopy", *Review of Scientific Instruments*, vol. 69, pp. 3770-3775, 1998.

[2]. S. Okuda and T. Takahashi, "Absorption spectroscopy using a coherent transition radiation mm wave light source", *Infrared Physics and Technology*, vol. 51, pp. 410-412, 2008.

CO7-1 Establishment of protocol for neutron capture therapy for head and neck cancer

I. Ota[1], H. Uemura[1], A. Nishimura[1], T. Kimura[2], S. Mikami[1], T. Yamanaka[1], M. Suzuki[3] N Kondo[3], T. Tamamoto[2], M. Hasegawa[2] and T. Kitahara[1]

[1]Department of Otolaryngology-Head & Neck Surgery,
[2]Department of Radiation Oncology, Nara Medical University
[3]Institute for Integrated Radiation and Nuclear Science, Kyoto University

INTRODUCTION: Neutron capture therapy (BNCT) for head and neck tumors has been clinically studied since 2001, with the BNCT research group at Kyoto University Reactor Laboratory, which is a co-investigator, highly effective, with high safety. It is being established. Since November 2012, we implemented the therapy as a joint research with Kyoto University Reactor Laboratory, with the consent of the patients in 4 cases of refractory recurrent head and neck cancer. As a result, the response rate was a very high 100%. The tumor reduction effect in recurrent cases after radical irradiation, which could not be achieved by conventional treatment methods, strongly suggests the possibility of expanding the indications for BNCT for refractory carcinomas as well as for head and neck cancer cases. Here, we will perform BNCT for refractory and recurrent head and neck tumors and examine their efficacy and optimal protocol.

EXPERIMENTS: We will treat BNCT for refractory and recurrent head and neck tumors that meet the following criteria and examine their efficacy and optimal protocol.
Inclusion Criteria
(1) The patient with local recurrence of head and neck cancer who can not perform the standard therapy any more after radiotherapy.
(2) The patient with local recurrence of head and neck cancer by the imaging diagnosis, such as CT, MRI and PET.
(3) The patient with previous radiotherapy (total 40-75 Gy, 2Gy/fq) for the recurrent region.
(4) The patient with the period of more than one month since the previous treatment.
(5) The patient with recurrence lesion in the less than 6cm of depth from skin as GTV for BNCT.
(6) The Patients who have PS less than 2 and are expected to survive more than 6 months after BNCT.
(7) The patient with good condition of renal function: creatinine <1.2 mg/dl for male and
<1.0 mg/dl for female.
(8) The patient with the age between 20 and 80.
(9) Written informed consent with one own will.

Exclusion Criteria
(1) The patient with active multiple primary cancers; synchronous or metachronous (within 5 years) double cancers .
(2) The patient with metastatic lesion.
(3) The patients with severe complications.
(4)The patients with infection requiring systemic treatment.
(5) The patient with severe adverse event
(>Grade3, CTCAE v4.0) in the BNCT region.
(6) The patient with cardiac pacemaker.
(7) The patient judged to have difficulty in maintain posture during the protocol treatment.
(8) The patient with WBC; < 3000/mm3, PLT; < 100000/mm3
(9) The patient with recurrence lesion invasive to carotid artery and toskin.
(10) Patients with phenylketonuria.

RESULTS: We enrolled 2 patients and undertook BNCT during this period as follows:

Patient #1: 66 y.o. male
Recurrence of oropharyngeal carcinoma
Histology: squamous cell carcinoma
Effect: SD
SAE: none; oral mucositis, Grade 2

Patient #2: 61 y.o. male
Recurrence of unknown head and neck carcinoma
Histology: squamous cell carcinoma
effect: PR
As an Severe Adverse Event (SAE) on Patient #2, on the second day after BNCT treatment, a cardiopulmonary arrest was detected at midnight, and cardiopulmonary resuscitation was started immediately. Fortunately, cardiopulmonary function recovered, but post-resuscitation encephalopathy was noted, and treatment is currently underway. The direct involvement of BNCT is unknown.

CONCLUSION:
We will continue to accumulate the cases carefully to establish a safe and stable treatment of BNCT.

CO7-2 Adjuvant therapy with BNCT for advanced or recurrent Head and Neck Cancer

N. Kamitani[1], Y. Fukuda[2], M. Suzuki[3], Y. Sakurai[3], J. Hiratsuka[1]
[1]*Department of Radiology, Kawasaki Medical School*
[2]*Department of Otolaryngology Kawasaki Medical School*
[3]*KURNS, Kyoto University*

INTRODUCTION

BNCT has been undergone to advanced head and neck (AHNC) cancer and recurrent head and neck cancer (RHNC). Most patients developed, lymph or distant metastasis within 6 months after BNCT [1]. BNCT has achieved a good local control, however patient's survival rate has never been good. That's why these cancer cells have already spread to another organ at the first of BNCT [2]. We report the therapeutic effect and safety of BNCT combined with systemic therapy.

METHODS AND MATERIALS

11patients were treated by BNCT with BPA [3] at KURNS (Institute for Integrated Radiation and Nuclear Science, Kyoto University) between Sep. 2017 and Feb. 2019. All patients were taken F-BPA-PET to estimate the tumor/blood boron ratio (T/B ratio), and these values ranged from 2.5 to 6 (median 3.2). In eight out of 11 patients, systemic therapy was initiated as neoadjuvant therapy prior BNCT. Systemic therapy was administered for 0.7-17.2(median 10.2) months. Most patients, six out of 11, were administered nivolmab as adjuvant therapy. Cetuximab, TS-1 and Immunotherapy were used to three, one and one patient respectively.

RESULT

Follow-up time was 1.8-16 (median 5.2) months. Local recurrence appeared in three patients out of 11 patients in 2.8-12.5 months (median 4.5) after BNCT. Local relapse developed in BNCT field without findings of any lymph node or distant metastasis. Eight out of 11 patients have achieved good local control and good QOL. Two of 4 relapse patients were taking cetuximab and other two patients were taking nivolmab. The relapse patients using nivolmab had had already resistance to nivolmab, though, they were kept taking nivolmab because had no other medical therapy to be chosen. Five patients, the rest of patients who took nivolmab, were controlled.

Adverse effect was not enhanced by systemic therapy. Severe adverse effect which is more than grade 3 on CTCAE v4.0 had never seen after BNCT. No patients died while the follow-up period.

CONCLUSION

BNCT combined with adjuvant anti-cancer therapy, such as chemotherapy, molecular-targeted drug or immunotherapy, was safe and has possibility of improving the therapeutic effect and survival rate. Especially, BNCT combined with nivolmab seems to be good combination for the control of cancer, when tumor has good response to nivolmab.

Patients characteristic	
Number of patients	11
Age (median)	48.5 y.o. (34-75 y.o.)
Gender	
Male	5
Female	6
Pathlogical type	
SCC	10
Mucoepidermoid carcinoma	1
Prior treatment	
Operation	6
Chemotherapy	10
Radiation therapy	11
Disease Presentation	
Local recurrence	8
Cervical lymph node metastasis	3
Systemic therapy	
Nivolmab	6
Other	5
Result	
Controlled	8
Relapse	3
Metastasis	0

REFERENCES

[1] Suzuki M, *et al.,* Boron neutron capture therapy outcomes for advanced or recurrent head and neck cancer, J Radiat Res (2014).
[2] Aihara T, BNCT for advanced or recurrent head and neck cancer, Appl Radiat Isot. (2014).
[3] Aihara T, *et al.,* New Challenges in Neutron capture therapy (2010).

CO7-3 Synthesis and Biological Evaluation of *closo*-Dodecaborate Ibuprofen Conjugate (DIC) as a New Boron Agent for Neutron Capture Therapy

H. Nakamura[1], S. Ishii[1,2], T. Takata[3], and M. Suzuki[3]

[1] *Laboratory for Chemistry and Life Science, Institute of Innovative Research, Tokyo Institute of Technology*
[2] *School of Life Science and Technology, Tokyo Institute of Technology*
[3] *Institute for Integrated Radiation and Nuclear Science, Kyoto University*

INTRODUCTION: The icosahedral symmetrical cluster, *closo*-dodecaborate, contains twelve boron and twelve hydrogen atoms. The sodium form of *closo*-dodecaborate is water-soluble and has low toxicity. Indeed, mercaptoundecahydrododecaborate (BSH; $[B_{12}H_{11}SH]^{2-}$) was developed as a boron agent and used to treat brain tumors via boron neutron capture therapy (BNCT) for many years. We previously developed maleimide-containing *closo*-dodecaborate (MID) that was conjugated not only with cysteine residue–SH but also with lysine residue–NH_2 in proteins.[1,2] We focused on serum albumins, which are essential transporter proteins for many drugs and endogenous compounds, using these as boron carriers for BNCT. As expected, the MID albumin conjugate (MID-AC) accumulated selectively in mouse tumors. It is known that human serum albumin has two primary drug binding sites (i.e., sites 1 and 2) located in subdomains IIA and IIIA. Ibuprofen exhibits high affinity to human serum albumin (HSA) via binding to site 2, and we believe that the ibuprofen *closo*-dodecaborate conjugate will be a novel boron agent, binding to human serum albumin at site 2 for delivery to tumors. In this study, we report the design and synthesis of *closo*-dodecaborate ibuprofen conjugate (DIC) **1** (Figure 1).

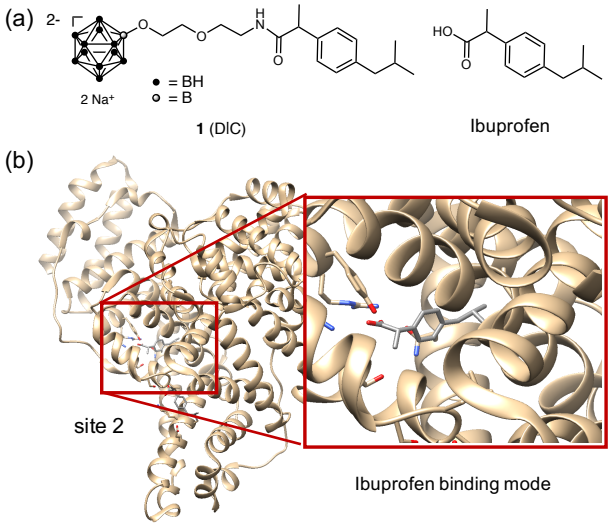

Fig. 1. (a) Chemical structures of ibuprofen and *closo*-dodecaborate ibuprofen conjugate (DIC) **1**. (b) Ibuprofen-human serum albumin (HSA) cocrystal structure (PDB: 2BXG). Ibuprofen binds to site 2 of HSA.

EXPERIMENTS:
Human cervical cancer HeLa cells were seeded at a density of 8×10^5 cells/ml with media 1 mL in the 6 well plate dishes, and incubated for 12 h. Each sample solution was added to a final 300 ppm boron concentration, and the cells were incubated for 1, 3, and 6 hours. Then the medium was removed and cells were washed three times in the dish with 1 mL of PBS buffer. A mixed solution of $HClO_4$ and H_2O_2 ($HClO_4$: H_2O_2 = 1: 2, 2 mL) were added to dishes and the cells were collected. The resulting solution was heated at 70 °C for 1 h. and filtered through 500 nm hydrophobic filter. The boron concentration of the obtained solution was measured by ICP-AES.

RESULTS: The cell uptake of DIC by HeLa cells was examined. The cells were incubated with boron agents for 1-6 h at a 300 ppm boron concentration with and without fetal bovine serum (FBS) to investigate the effect of BSA in medium on the cell uptake. The results are shown in Figure 2. The boron uptake reached a maximum 3 h after administration and became a plateau in the case of BSH. In contrast, the time-dependent boron uptake in the cells was observed in the case of DIC. The boron concentration of DIC in HeLa cells reached at 0.68 μg/10^6 cells 6 h after administration. The uptake of DIC by HeLa cells was similar in the presence or absence of FBS, suggesting that FBS does not affect the uptake of DIC by the cells.

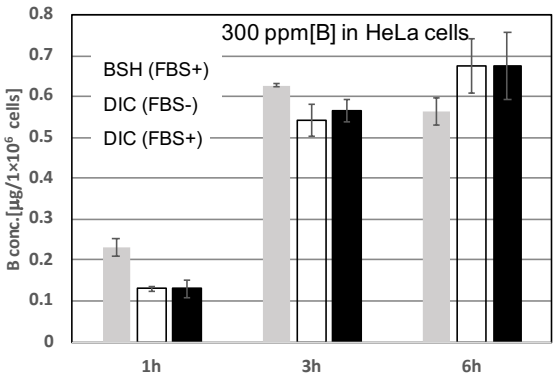

Fig. 2. Cell uptake of DIC by HeLa cells.

In conclusion, DIC was accumulated into HeLa cells in a time-dependent manner. The boron concentration of DIC in the cells 6 h after administration was higher than that of BSH whereas the boron concentration of BSH in the cells was higher than that of DIC 1 h after administration, suggesting that, once accumulated, DIC retains in HeLa cells longer than BSH.

REFERENCES:
[1] S. Kikuchi, *et al.*, J. Control. Release, **237** (2016) 160-167.
[2] S. Ishii, *et al.*, Org. Biomol. Chem. in press (DOI: 10.1039/C9OB00584F).
[3] H. Nakamura, *et al.*, Pure Appl. Chem. **90** (2018) 745-7.

CO7-4 The Effect of Boron Neutron Capture Therapy to Normal Bones in Mice

R. Iwasaki, R. Yoshikawa[1], T. Mori, Y. Tamari[2], Y. Sakurai[2], M. Suzuki[2] and K. Ono[3]

Faculty of Applied Biological Sciences, Gifu University
[1]United Graduate School of Veterinary Sciences, Gifu University
[2]Institute for Integrated Radiation and Nuclear Science, Kyoto University
[3]Kansai BNCT Medical Center, Osaka Medical College

INTRODUCTION: Primary malignant bone tumors have been mainly treated with preoperative chemotherapy followed by surgery. Wide or radical margins including limb amputation are required for local control. Although surgical techniques named limb-salvage therapy become a mainstay of treatment to avoid the limb amputation, complications such as postoperative infection, fracture, or local recurrence often occurred.

Although primary bone tumors have been generally considered as radio-resistant tumors, radiation therapy has been used for the purpose of the functional and cosmetic status of patients. When a large single dose of photon radiation therapy is delivered to achieve the effective tumor control, clinically relevant late effects in the surrounding normal tissues include skin ulceration, neuropathy, and fracture.

Boron neutron capture therapy (BNCT), a tumor cell -selective particle radiation therapy, is considered to be effective for the tumors without any late effects to the normal bone. However, an appropriate BNCT dose irradiated safely to the normal bone, that is evaluated using experiment animals, is not determined.

In this study, we performed BNCT to normal bone in mice, and evaluated the influence on their bone strengths.

EXPERIMENTS: Eight to ten-week-old C3H/He mice were used for the study. As boron compound, p-boronophenylalanine (BPA) was prepared at a dose of 25 mg/ml. Irradiation was carried out using X-ray and thermal neutron at Gifu University and Kyoto University Reactor, respectively.

Boron concentration measurement After subcutaneously injected into mice at doses of 125, 250, 500 mg/kg of BPA, the boron concentrations at each time point (30, 60, 90, 120 min after administration) in the blood and bone were measured by prompt gamma ray spectroscopy. Five mice were used for each group.

X-ray irradiation Mice were irradiated to their right hind limb at single doses of 12, 24, 36, 48 Gy. Five mice were used for each X-ray dose.

Neutron irradiation On the next day after X-ray irradiation of 24 Gy, which was the dose that did not affect bone strength evaluated by X-ray irradiation experiments, mice were irradiated with a reactor neutron beam at a power of 1 MW. Following types of irradiation were carried out; neutron beam only, neutron beams with 125, 250, and 500 mg/kg of BPA administration. Based on a preliminary study of the biodistribution of BPA, irradiation was performed between 30 and 120 min after the injection. Five mice were used for each group.

Bone strength analyses Tibias were collected at 12 weeks post-irradiation. Subsequently, they were mechanically tested in three-point bending to determine the bone strength. Tests were performed at HAMRI CO., LTD.

RESULTS: As shown in Fig. 1, both boron concentrations in blood and bone increased dose dependently. While blood concentrations decreased over time, bone concentrations maintained until 120 min after BPA administration.

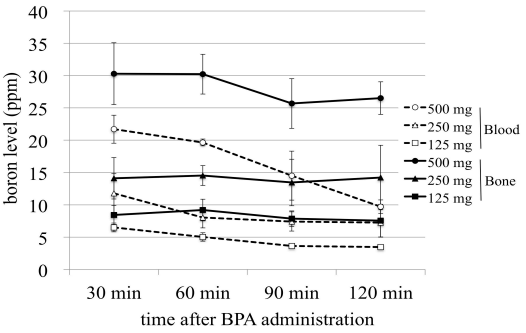

Fig. 1. Boron concentration levels in blood and bone

Tibial bending strengths at 12 weeks after X-ray irradiation decreased at doses of 36 Gy and 48 Gy compared to that at doses less than 24 Gy (Fig. 2).

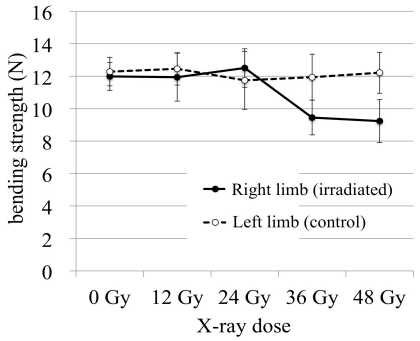

Fig. 2. Bone strengths at 12 weeks after X-ray irradiation.

Tibial bending strengths at 12 weeks after X-ray irradiation (24 Gy) followed by neutron irradiation did not have significant differences between any groups (Fig. 3).

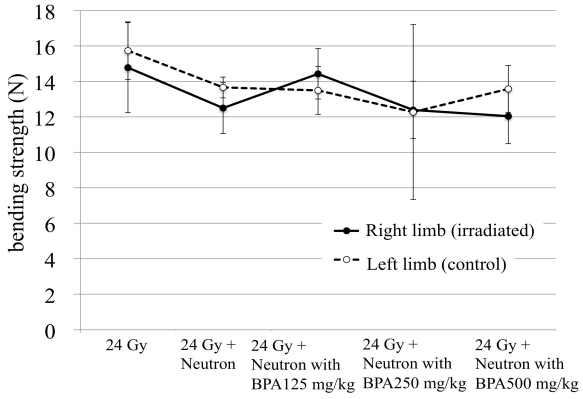

Fig. 3. Bone strengths at 12 weeks after X-ray irradiation followed by neutron irradiation.

CO7-5

Establichment of a novel mutation breeding using Boron Neutron Capture Reaction (BNCR)

M.Kirihata, S. Segami[1], Y. Hattori, Y. Kinashi[2]

Research Center of BNCT, Osaka Prefecture University
[1]Research Institute of Environment, Agriculture and Fisheries, Osaka Prefecture
[2]KURNS, Kyoto University

INTRODUCTION: Mutation breeding has provided significant benefits to breed improvement. The type of mutagenic treatment for plant breeding have been used chemical mutagens, such as EMS and MNU, or physical mutagens, such as gamma rays, X-rays and ion beams[1, 2, 3, 4]. In this present study, we focused on Boron Neutron Capture Reaction (BNCR) which based on the nuclear reaction of ^{10}B atom with thermal/epithermal neutron already applied to cancer treatment (BNCT)[5, 6].

The purpose of this study is to establish a novel mutation breeding using BNCR (Fig. 1). This method uses the principle of inducing mutation by an alpha particle and ^{7}Li recoil nuclei high linear energy transfer and short range when irradiated with neutrons (low energy thermal neutrons (< 0.5 eV) can be absorbed the ^{10}B atoms, leading to generating high linier energy transfer alpha particles (~ 150 keV/μm) and ^{7}Li nuclei (~ 175 keV/μm)) that are produced by BNCR of ^{10}B selectively taken into the meristematic cell with thermal neutron.

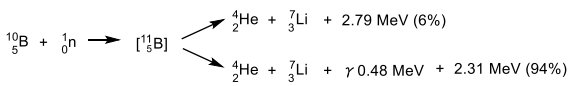

Fig 1. BNCR Reaction.

In other words, the mutagenic effect depends on chemical and physical factors, such as ^{10}B concentration, thermal neutron intensity, and irradiation time. This method is expected as a new approach of mutagenesis.

EXPERIMENTS: The experimental material used *Oryza sativa* L. cv. Nipponbare. The dry seeds were immersed into different concentrations (0, 10, 100, 200ppm) of ^{10}B-enriched *p*-boronophenylalanine (BPA)[7, 8] (Fig. 2) for 16hours. The samples were washed with water and re-dried at room temperature. The seeds in 2-mL tubes were irradiated with thermal neutron for 90 minutes in the Kyoto University Research Reactor (KUR). To provide four different levels of neutron fluence, the tubes were set to four columns microtube rack at the time of irradiation. Irradiation experiments were carried out three times.

As preliminary experiment, the immersed seeds into BPA were germinated on petri-dishes with continual moistening of filter paper at 25℃, it was investigate the germination rate.

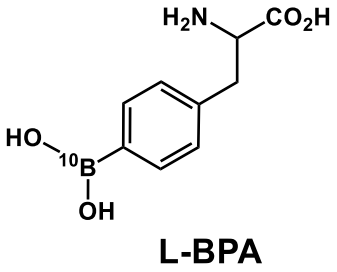

Fig. 2. Boron Carrier.

RESULTS: The immersed seeds were germinated normally at four BPA concentrations at the range of from 70% to 100%. Thermal neutron fluence were 1.1~1.2x10^{13} cm^2, 7.7~8.3x10^{12} cm^2, 5.3~6.3x10^{12} cm^2, 3.7~4.2x10^{12} cm^2, at the time of irradiation. We are set to confirm effects of irradiation. To verify the mutagenic effects of different mutagens. Because of that, the efficiency, mutation rate spectrum, and optimum processing conditions need to be examined. Also, as basic research, ^{10}B selectively accumulate to meristematic cells. If not accumulate, we try the search of suitable ^{10}B compound for plant.

REFERENCES:

[1] Fujii T. *et al., Radiat. Bot.* **6** (1966) 297-306.
[2] T. C. Yang *et al., Gamma Field Symp.* **18** (1979), 141-154.
[3] Tanaka A. *et al., Gamma Field Symp*. **38** (1999), 19-27.
[4] H. Doll *et al., International Atomic Energy Agency* (1969), 195-206.
[5] H. A. Soloway *et al.,* Chem. Rev., **98** (1998), 1515-1562.
[6] B. Farhood, *et al., Rep. Pract. Oncol. Radiother.* **23** (2018), 462-473.
[7] H. R. Snyder, *et al., J. Am. Chem. Soc.* **80** (1958), 835-838.
[8] Mishima Y. *et al., Journal of Investigative Dermatology,* **78** (1982**),** 215.

30055

CO7-6 A Fundamental Investigation on Using Known Samples as a Standard to Evaluate Various Constrction Materials

K. Kimura, T. Takata[1], Y. Sakurai[1], H. Tanaka[1], and K. Takamiya[1]

Fujita Corporation
[1]Institute for Integrated Radiation and Nuclear Science, Kyoto University

INTRODUCTION: Concrete is widely used as radiation shield in nuclear reactors and irradiation facilities, because of its flexibility and sufficient supply. However, there are few discussions on the content of the shielding concrete composition, and very old data (which have uncertain information regarding material properties beside of elemental data) are still used in the shielding calculation. For the above situation, Radiation Shielding Material Standardization Working Group under Atomic Energy Society of Japan (AESJ) was established in order to proceed the standardization of shielding concrete[1]. On the other hand, once those facilities start to operation, the concrete for the shield are affected by the radiation ray from the operating radiation source in the facilities and activated. For the above situation, low activation concrete[2]-[4] is the one of the ways to solve the problem. Especially, boron neutron capture therapy (BNCT) should be effective facilities to apply the low activation concrete.

For the above two points (standardization of concrete composition and low activation), elemental analyses for the materials in concrete for radiation shielding are necessary and important by neutron activation analysis in KUR. As a fundamental study, investigation of variation of three kinds of known sample were conducted in order to discuss proper standard material for the above purpose.

METHODS: More than 3000 of raw material for low activation concrete and ordinary concrete were gathered from all over the Japan and oversea, including hundreds of raw materials newly corrected during the period of KUR shut down. Several tenth of the materials were chosen among the material stock library. These materials were crushed to certain size (typically under 0.7mm or less), and were packed for 0.1 to 0.3 g with special treatment for the irradiation in KUR. After the irradiation with 10 to 60 minutes and with the certain cooling period, these samples were measured by Ge detector one by one. The quantity of the target elements, which were selected by former investigations as Co, Cs, Sc, Fe and Eu[2]-[4], in each sample were estimated by the comparison of the known standard material in the same package for the irradiation. Three kinds of known materials were prepared, such as JSAC0411[5], JSAC0522[6] and fused alumina with Eu and Co (FAwEC). Table 1 shows the content of target elements for the samples, and Table 2 shows the relative standard variation of estimating elements for focused gamma ray peaks. These tables were introduced that the samples for FAwEC had less variation compared to those for JSAC0411 and JSAC0522.

CONCLUSION: Investigation on estimation of the variation for standard samples was conducted in order to estimate the quantity of target elements in concrete raw materials. Fused alumina samples with Europium and Cobolt have less variation compared to those for JSAC0411 and JSAC0522.

REFERENCES:

[1] https://www.hzdr.de/workshops/satif13/wednesday_afternoon/Kimura_SATIF13.pdf
[2] K. Kimura, *et al.,* Proceedings of 8th International Conference on Radiation Shielding, vol. 1, pp.35-42, ANS inc, Arlington, USA, 1994.
[3] M. Kinno, *et al.,* ANS Radiation Protection and Shielding Conference, pp.673-678, Spokane, USA, 2002.
[4] K. Kimura, *et al.*, Proc. of Int. Conf. on Nuclear Engineering (ICONE16), Florida, USA, May 11-15, (2008) 48484.
[5] https://www.jsac.or.jp/srm/srm-n3-11.pdf
[6] https://www.jsac.or.jp/srm/srm-n23.pdf

Table 1 Content of target elements in samples

	K	Fe	Co	Cs	Eu
	g/kg		mg/kg		
JSAC0411	2.4	33	6.5	3.97	1.4
JSAC0522	9.3	29.2	47.4	–	–
FAwEC	–	–	15.1	–	75.9

Table 2 Relative standard variation (%) of estimating elements for focused gamma ray peaks

Sample name	Eu-152		Co-60		Cs-134		Irradiation		Number
	344keV	1408keV	1173keV	1332keV	605keV	796keV	Month	time(min)	of sample
JSAC0411	5.55	2.99	5.21	3.74	4.71	3.52	2018/8	30	4
JSAC0411	4.44	4.60	1.69	2.02	ND	7.28	2018/8	10	6
JSAC0411	6.75	2.64	4.90	6.85	8.25	9.73	2018/11	30	4
JSAC0411	16.28	10.84	10.34	10.45	ND	18.35	2018/11	10	6
JSAC0522	12.92	2.61	2.32	1.43	24.24	6.92	2018/11	10	3
FAwEC	1.64	1.88	1.65	1.16	ND	ND	2018/11	10	6

CO7-7

Pathological findings after GdNCT using Gd-DTPA-incorporated calcium phosphate nanoparticles

H. Xuan [1,2], H. Yanagie[1,3,4], M. Yanagawa[5], Y. Sakurai[3,4], K. Mouri[3,4], N. Dewi[3,4], H. Cabral[2] , S. Dowaki[6], T. Nagasaki[6], Y. Sakurai[7], H. Tanaka[7], M. Suzuki[7], S. Masunaga[7], and H. Takahashi[1,2,3]

[1]*Dept of Nuclear Engineering & Management, School of Engineering, Univ of Tokyo,* [2]*Dept of Bioengineering, School of Engineering, Univ of Tokyo,* [3]*Cooperative Unit of Medicine & Engineering, Univ of Tokyo Hospital,* [4]*Niigata Univ of Pharmacy & Applied Life Sciences, ,* [5]*Obihiro Univ of Agriculture and Veterinary Medicine,* [6]Osaka City University Graduate School of Engineering, [7]Kyoto Univ Institute for Integrated Radiation & Nuclear Science

INTRODUCTION: Gadolinium-157 has been paid the most attention as a novel atom for neutron capture therapy (NCT) agent because of its high thermal neutron cross section (255 000 barns). The ^{157}Gd atoms can induce Auger electrons and gamma rays on gadolinium neutron capture reaction (Gd-NCR). The range of high LET Auger electorn is few micron, so it is necessary to accumulate the ^{157}Gd atoms in the cancer cells, especially in the nucleus for effective GdNCT [1,2,3].

In this work, we performed checking the pathological findings in the evaluation of tumor growth suppression on Colon26 tumour bearing mice by GdNCT with the intraveneous injection of Gd-DTPA/CaP nanoparticles as continued work from previous evaluation on single/multiple-injected group [2, 3].

EXPERIMENTS: *In vivo* evaluation was performed on colon-26 tumor-bearing mice irradiated for 60 minutes at nuclear reactor facility of Kyoto Univ Institute for Integrated Radiation & Nuclear Science with average neutron fluence of 2.0×10^{12} n/cm^2. Antitumor effect was evaluated on the basis of the change in tumor growth and survival rate of the mice. The pathologicl findings of each organ were checked with H.E. stainings.

RESULTS: No acute toxicities were recognized in the treated mice after GdNCT using intraveneous injection of Gd-DTPA/CaP nanomicelle. Tumor growth was suppressed until four times of the non-treated group in the same manner of previous experiments (data not shown). The tumour volume was decreased after GdNCT, and the infiltration of mononuclear cells were seen in the tumour. Non-treated group shows normal histology with clear cytoplasm and nucleus(Fig.1). The abnormal change in the liver, the kidney, the heart, and the lung were not found in the histologic examination one month after Gd NCT (Figure1). Thease results indicate that Gd-DTPA /CaP nanomicelle has the promising possibility as novel GdNCT agent.

In the next experiments, evaluation of the mechanism of cytotoxicity on GdNCT is necessary. We must check the mechanisms, for examples, apoptosis, autophagy, senescence, etc. We hope to increase a dose in quantity of Gd-DTPA /CaP nanomicelle. We hope to refer these results of toxicity examinations to the clinical studies of GdNCT for selection of target cancers.

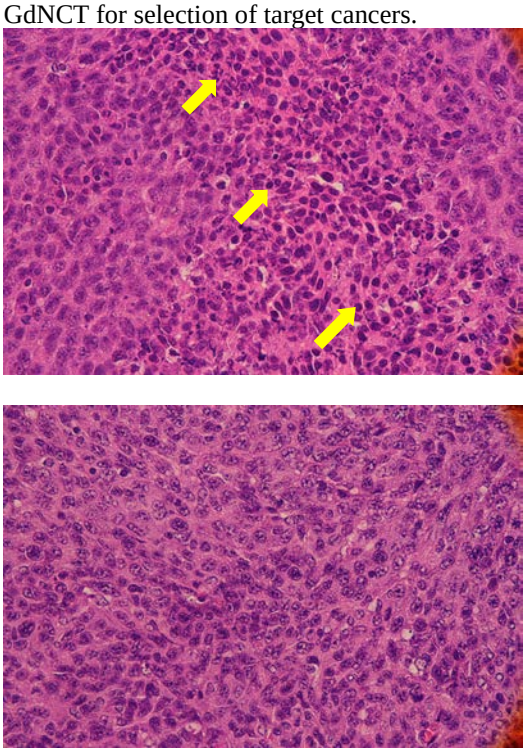

Tumour: The tumour volume was decreased after GdNCT, and the infiltration of mononuclear cells were seen in the tumour(Upper:GdNCT, Lower: Non treated, x400).

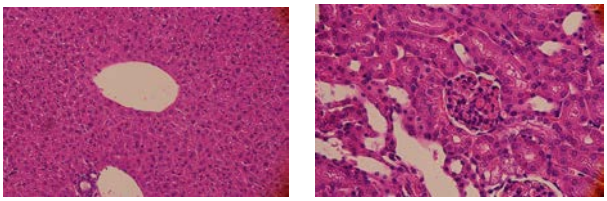

Liver: Hepatocellular denaturation and the destruction are absent(Lt:x400). Kidney: There is no glomerulus or tubular denaturation(t:x400).

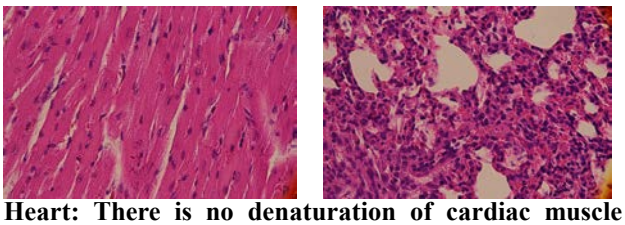

Heart: There is no denaturation of cardiac muscle cells (Lt:x400). Lung: There is no denaturation of alveolar cells (Rt:x400).

REFERENCES:

[1] Dewi N *et al.,* Biomed & Pharmacother (2013) **67**:451-7.

[2] Dewi N *et al.,* J Can.Res.Clin.Oncol. (2016) **142**(4):767-75.

[3] Mi P, *et al.:* J Cont. Release (2014) **174**:63-7.

CO7-8 The feasiblity study of Eu:LiCAF neutron detector for an accelerator-based BNCT

D. Nio, K. Sakasai, T. Nakamura, H. Nakashima
R. Okumura[1], K. Takamiya[1], S. Tanaka[2], H. Kumada[2],

Japan Atomic Energy Agency
[1] Institute for Integrated Radiation and Nuclear Science, Kyoto University
[2] University of Tsukuba

INTRODUCTION: The stability of neutron flux at an accelerator-based BNCT facility is relatively worse than that at a reactor-based one. Therefore, it is necessary to measure the neutron flux precisely in real-time to optimize the patient's exposure dose for the accelerator-based BNCT. However, the neutron flux is so intense (about 10^9(n/cm^2/s)) that the real-time measurement has not been realized yet. Hence we tried to measure the neutron flux with a small detector using a Eu:LiCAF scintillator [1] on the tip of optical fibers, as shown Fig.1. For this detector, the linearity to the neutron flux higher than 10^8(n/cm^2/s) has not been measured and we have measured the linearity of the detector to the neutron flux of 10^8 to 10^9(n/cm^2/s) with the correlation coefficient of 0.99 last experiment done at KUR [2]. In this experiment, we have tried to check the linearity of the detector to the neutron flux higher than 10^9(n/cm^2/s).

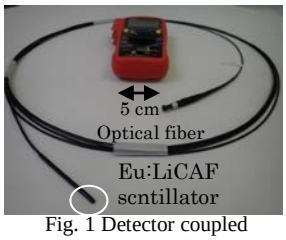

Fig. 1 Detector coupled with the optical fiber.

****

EXPERIMENTS: The experiments were performed at the KUR-SLY where the maximum neutron flux of about 10^{12}(n/cm^2/s) is available at the bottom when the reactor power is 1MW [3]. Figure 2 shows the experimental set-up for the measurement, where the photon counting unit C8855 and 871 is able to count up to 1 Mcps. The optical output from the Eu:LiCAF scintillator through the optical fibers was properly converted to an electric signal and counted with the counting units. Prior to the measurement, the detector was put into the plastic bottle, where Figure 3 shows the situation, and loaded to 20 cm from the bottom of the KUR-SLY. At this position, the maximum neutron flux is about 10^{11}(n/cm^2/s). Figure 4 shows the loading of the detector into the KUR-SLY, which is same method done in 2017. The measurement was carried out from the starting-up to 1 MW-arrival of the reactor.

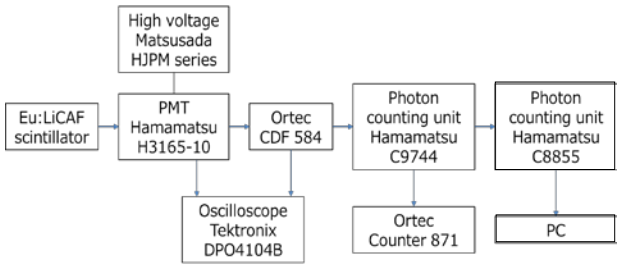

Fig. 2 Experimental setup.

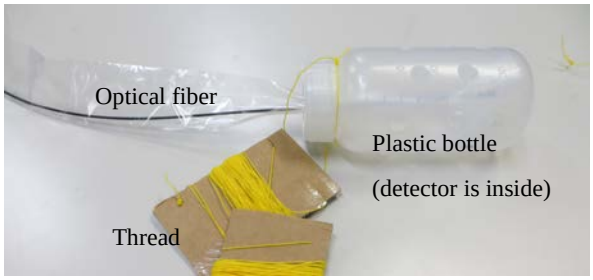

Fig. 3 Situation about the putting into the plastic bottle. (Same method done in 2017)

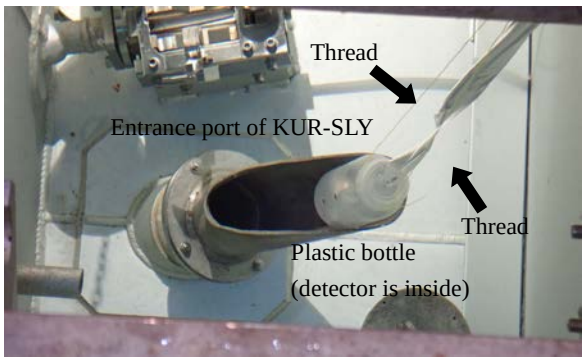

Fig. 4 Loading of the detector into the KUR-SLY. (Same method done in 2017)

****

RESULTS: In this experiment, the count-rate measured by C8855 and Ortec counter 871 has saturated before the reactor reached 1 MW and the linearity to the neutron flux could not be identified. I think that the effect to the count-rate from Cherenkov radiation in optic fiber was high and the setting of the high voltage was high.

****

CONCLUSIONS: A small detector using a Eu:LiCAF scintillator has been tested at the KUR-SLY experimental port. Unfortunately, the linearity to the neutron flux could not be identified.

To overcome the results, we will review two points. First, we will investigate the influence of Cherenkov radiation of which wavelength spreads from 400 nm to 750 nm. Since the scintillation peak of the Eu:LiCAF is about 370 nm, using the optical filters, the influence of the Cherenkov radiation should be estimated.

For the setting of high voltage, we will experiment at the iBNCT in Tsukuba University and we will decide the suitable setting of high voltage.

****

REFERENCES:

[1] N. Kawaguchi., Doctor Thesis, Tohoku University, http://hdl.handle.net/10097/56580
[2] KURRI PROGRESS REPORT 2017 CO7-2
[3] KUR-SLY http://www.rri.kyoto-u.ac.jp/JRS/

CO7-9 Evaluation of Relative Biological Effectiveness of the splenic cells in SCID mice following Thermal Neutron Irradiation

Y. Kinashi[1]and T. Takata[1]

[1]*Institute for Integrated Radiation and Nuclear Science Kyoto University*

INTRODUCTION: It is reported that immune response is activated by partial radiation [1]. The influence on immune organization of the mouse at the time of the head irradiation is not well known. The purpose of this study is to evaluate the relative biological effectiveness in the severe combined immunodeficiency (SCID), so-called SCID mice, those are having well-known high radiation sensitivity following thermal neutron irradiation for mice cranial.

EXPERIMENTS: CB17/Icr-*Prkdc*^{scid}/CrICrIj (SCID mice) were obtained from Charles River Inc. As a comparison experiment for the SCID mice, C3H/He mice were obtained from Japan Animal Inc.
Neutron irradiation and Gamma-ray irradiation was performed as follows. The Heavy Water Facility of the Kyoto University Research Reactor (KUR) was used. Mice were restrained in a plastic box on a radiation board. Neutron fluence was measured by radio-activation of gold foil and gamma-ray doses by TLD. Gamma rays were delivered with a ^{60}Co gamma ray machine. Mice were restrained in a plastic box on a radiation shelf. After irradiation, the splenic cell suspension were adjusted and incubated for 1weeks. At 1 hour, 24 hours and 7 days after irradiation, apoptotic induction of the cells was examined by Cell Death Detection ELISA (Roche).

RESULTS: As shown in Fig. 1, the apoptotic changes of the SCID mice splenic cells increased with a radiation dose.

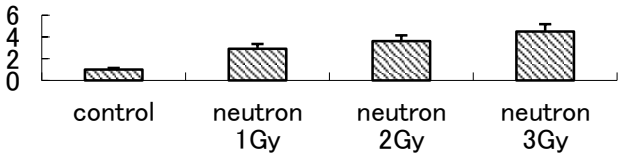

Fig.1. Apoptotic induction of the splenocytes of SCID Mice at 24 hour after neutron irradiation. The vertical axis shows an enrichment factor level.

The apoptotic induction of the splenocytes of SCID mice was larger than that of C3H mice at 1 hour, 24 hours and 7 days after irradiation. The difference of the apoptosis of the splenic cells between SCID mice and C3H mice was the biggest at the 24 hours after the neutron radiation.

The values of relative biological effectiveness were biological effectiveness were shown in below (Table 1).

Table1. RBE (Relative Biological Effectiveness) calculated from apoptosis of splenic cells following neutron radiation

	SCID	C3H
RBE*	1.47	2.08

*RBE was calculated the Enrichment factor at 2Gy neutron radiation dose / the Enrichment factor at 2Gy gamma-ray radiation dose.

DISSCUSSION
Previously we reported the RBE values for SCID mice of the LD50 by radiation oral death assay and gamma H2AX foci number of the lymphocytes. The RBE values calculated from radiation oral death assay and gamma H2AX foci number of the lymphocytes were 1.6 for SCID mice and 2.0 for C3H mice and 1.5 for SCID mice and 1.9 for C3H mice, respectively. In the radiation sensitive mice study, the RBE values of SCID mice was 1.5-1.6, comparing the neutron and the gamma studies. The RBE values of C3H/He mice was 1.8-2.0. SCID mice show extreme sensitivity to ionizing radiation, because cells lack functional DNA-dependent protein kinase. Our results suggest that the difference of RBEs for radiation sensitive mice were smaller than the wild type mice, that is to say, the hyper radiation sensitivity does not have a disadvantage in BNCT.

REFERENCES:
[1] K Reynders *et al.*, Cancer Treatment Reviews, **41**(2015)503-510.
[2] Y Kinashi *et al.*, 15th International Congress of Radiation Research, Abstracts (2015)83.

CO7-10 Effect of BNCT on dissemination and invasion of brain tumor cells

N. Kondo[1], T. Kinouchi[2], M. Natsumeda[3], Y. Sakurai[1], T. Takata[1], M. Suzuki[1]

[1]*Particle Radiation Oncology Center, Institute for Integrated Radiation and Nuclear Science, Kyoto University (KURNS)*
[2]*Div. of Radiation Life Science, KURNS*
[3]*Department of Neurosurgery, Niigata University*

INTRODUCTION: The prognosis of patients with high grade gliomas remains poor despite surgical resection followed by radiation therapy and concomitant adjuvant chemotherapy with temozolomide (TMZ). Tumor recurrence is almost inevitable and the median survival time (MST) of patients with newly diagnosed glioblastomas (GBMs) is only 14.6 months [1]. We have utilized boron neutron capture therapy (BNCT) for the treatment of patients with either recurrent or newly diagnosed high grade gliomas. A significant survival benefit was seen in those patients with newly diagnosed GBMs who received BNCT, followed by photon boost, with a MST of 23.5 months [2,3]. Furthermore, for those patients with recurrent gliomas, especially those with poor prognosis who were classified as 3+7 by recursive partitioning analysis (RPA) [4], had a MST of 9.1 months compared to 4.4 months for those in the same RPA class [3] who had been treated by current standard therapy. In our experience with all clinical trials of BNCT, the most frequent cause of death following treatment has been leptomeningeal dissemination (LMD) [2,3]. Assuming that more than 85% of tumor recurrence following conventional treatment is local, that is within 2 cm of the original margin of the contrast-enhancing lesion [5,6], local control by BNCT is significantly better than that obtained by current conventional radiotherapy [5,6]. The aim of this research is to investigate whether BNCT influences invasion or dissemination of brain tumor stem like cells. Emerging evidence suggests that exosomes (extracellular vesicles) serve an important role in intercellular communications. Therefore, we focus on exosome from brain tumor stem cells after BNCT in this study.

EXPERIMENTS: Cells: U87MG and U87 delta *EGFR* cells were cultured in DMEM with 10 % fetal bovine serum at 37° C in a humidified atmosphere of 95% air and 5% CO_2. Two days before irradiation, we changed the medium without serum. In case of neutron irradiation, we added boronophenylalanine (BPA) at 25 ppm in medium for 24 hrs.
Irradiation: we irradiated the cells in T25 flasks using X-ray or neutron.
Preparation of exosomal fraction: 48hrs after irradiation, the culture medium was collected and centrifuged at 2000 *g* for 20 min at 4° C and supernatant was filtered with 0.22 μm PVDF filter (Millipore). Then the supernatant was centrifuged at 100000 *g* for 70 min. The pellet was rinsed with PBS and centrifuged at 100000 *g* for 70 min.
Sample preparation for western blot: Irradiated cells were collected 48 hrs after irradiation and lysed in RIPA lysis buffer containing protease inhibitors.

RESULTS: We obtained enough amount of exosomes to analyze for non-irradiated control. However, we did not obtain enough exosomes for irradiated groups.
We are performing western blot analysis for irradiated cells.

CONCLUSION: We will change the method for exosome isolation using qEV kit etc next year.

REFERENCES:
[1] R. Stupp *et al*., Lancet Oncol;**10** (2009) 459-466.
[2] S. Kawabata *et al.*, J Radiat Res. **50** (2009)51-60.
[3] S. Miyatake *et al.*, J Neurooncol. **91** (2009) 199-206.
[4] KA Carson, *et al.*, J Clin Oncol **25**(2007) 2601–2606.
[5] SW Lee *et al.*, Int J Radiat Oncol Biol Phys **43**(1999) 79–88.
[6] KE Wallner *et al.*, Int J Radiat Oncol Biol Phys **16**(1989) 1405–1409.

CO7-11 Response Assessment of Meningioma Treated by BNCT

S-I. Miyatake[1], A. Kanbara[2], S.Kawabata[2], T. Kuroiwa[2], N. Kondo[3], Y. Sakurai[3], M. Suzuki[3], and K. Ono[4]

[1]*Cancer Center, Osaka Medical College*
[2]*Departmentof Neurosurgery, Osaka Medical College*
[3]*KURNS, Kyoto University*
[4]*Kansai BNCT Medical Center, Osaka Medical College*

INTRODUCTION: High-grade meningioma (HGM) is a good candidate for boron neutron capture therapy (BNCT). BNCT shows good local response to this entity. However the response assessment is still under developing. Generally speaking, one dimensional RECIST is widely accepted for response assessment for solid cancers. However meningioma has dural attachment and this may make difficult for the one dimensional assessment. Therefore we evaluate the response assessment with two dimensional Macdonald assessment and three dimensional volumetric method.

MATERIALS and METHODS: From August 2017 to February 2019, we treated 14 cases of HGM in KUR. Among them, we applied above 3 methods for the response assessments, RECIST, Macdonald and volumetric assessments for best response, for 7 selected cases.

RESULTS: Here we demonstrated 3 typical cases of HGM treated by BNCT. Patient 6582368 was grade 2 HGM (Fig. 1). She was operated 6 times and applied IMRT and SRT, prior to BNCT. Five months after BNCT, MRI showed transient enlargement of enhanced volume. One dimensional RECIST assessment was 16.8% increase, two dimensional Macdonald assessment was 28.4% increase. The lesion became shrunk after this study. Therefore this transient increase in size seemed to be pseudoprogression. Patient 7081295 showed 1.3% decrease, 2.1% increase and 62.1% decrease in RECIST, Macdonald and volumetric assay, respectively 5 months after BNCT (Fig. 2). Patient 7103553 showed 1.2% increase, 26.5% decrease, 40.8% decrease in RECIST, Macdonald and volumetric assay, respectively 5 months after BNCT (Fig. 3). Table 1 showed the response assessment of BNCT in cumulative 7 cases of HGM.

DISCUSSION: Response assessment for meningioma has not yet been established [1]. RECIST is most popular for response assessment for solid cancer, however, meningioma usually has dural attachment which **is** not affected by any treatments. Therefore, MacDonald may be better than RECIST for this purpose. However, even by Macdonald it may be difficult to exclude treatment-related necrosis for the assessment. Thus volumetric analysis may be adequate for response assessment of HGM treated by BNCT. Case 7081295 and 7212464 demonstrated this theory in Table 1.

Fig. 1
Before BNCT **5M after BNCT**

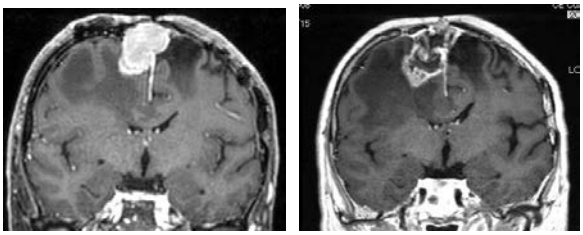

Fig. 2
Before BNCT **5 M after BNCT**

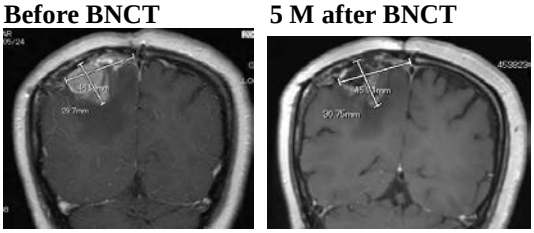

Fig. 3
Before BNCT **2M after BNCT**

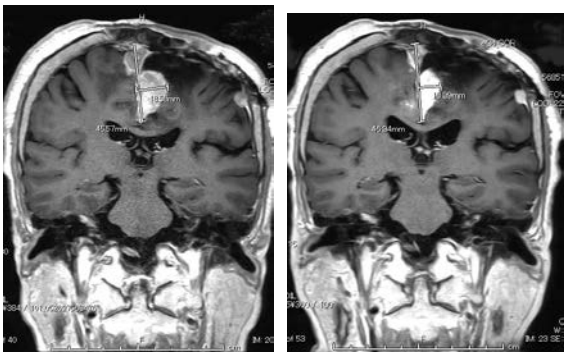

Table 1

ID	6562368#	7081295	7212464	7103553	7277315*	5919134	6795335
RECIST	+16.8%	-1.3%	+4.0%	+1.2%	-11.8%	-10.4%	-14.8%
Macdonald	+28.4%	+2.1%	+6.4%	-26.5%	-67.0%	-14.0%	-10.6%
Volumetry Excluding necrosis	+1.0%	-62.1%	-52%	-40.8%	-41.9%	-35.2%	-46.1%

REFERENCES:

[1] R. Y. Huang, et al., Proposed response assessment and endpoints for meningioma clinical trials: report from the Response Assessment in Neuro-Oncology Working Group. Neuro-Oncology 21(1):26-36, 2019.

CO7-12 Development of a Silica Nano Particle Installed with Gd(III)-Thiacalixarene Complex as a Gadolinium Carrieres to Tumor for Gd-NCT

T. Yamatoya[1], T. Nagasaki[2], N. Iki[1], and M. Suzuki[3]

[1]*Graduate School of Environmental Studies, Tohoku University*

[2] *Graduate School of Engeneering, Osaka City University*

[3]*KURNS, Kyoto University*

INTRODUCTION: Owing to a large thermal neutron capture cross section and total kinetic energy of $^{157}Gd(n,\gamma)^{158}Gd$ larger than that of $^{10}B(n,\alpha)^{7}Li$, gadolinium attracts growing attention as an alternative to boron in neutron capture therapy [1]. Because free gadolinium ($Gd(OH_2)_9$) has toxicity, a safe carrier of Gd to tumor not to release free Gd is required. We recently found that thiacalix[4]arene-*p*-tetrasulfonate (TCAS) self-assembled three lanthanide (Ln) cores including Gd to form a sandwich-type complex, Ln_3TCAS_2 (Fig. 1) [2], the characteristic features of which are high kinetic stability, luminescence signal [3], and ^1H relaxation arising from the Ln center [4]. Nano-sized particles are frequently used as a drug carrier toward tumor by enhanced permeability and retention (EPR) effect. Here we attempted to prepare a silica nano-particle (SiNP) containing Gd_3TCAS_2 and evaluate its ability as the NCT agent by cell viability.

EXPERIMENTS: *Preparation of SiNP installed with Ln.* The trinuclear complexes Ln_3TCAS_2 (Ln = Gd, Tb) were prepared as reported elsewhere [2]. The Ln_3TCAS_2-installed SiNP was prepared by a Stöber's method [5], which was modified with using 3-aminopropyltrimethoxysilane (APTES) as an anchor of negatively charged Ln_3TCAS_2. Furthermore, the surface was modified with poly(ethylene glycol) (PEG) by PEG-NHS (MW 2000) to retain water-dispersibility and biocompatibility.

Cell experiments. MCF-7 cells were seeded in a 6-well plate at a cell concentration of 7.5×10^5 cells/mL and incubated for 24 h. After supernatant was removed, DMEM and solution of SiNP loaded with Gd_3TCAS_2 were added to each well and incubated for 24 hr. After washing with PBS, the cells were detached from the well and transferred to tubes to be irradiated with thermal neutron.

RESULTS: The TEM images of SiNPs revealed the size of the particles were 61.6 ± 3.8 nm in diameter, which is compatible to the one (10-100 nm) for the EPR effect. The amount of Gd loaded in the SiNPs were determined by ICP-AES to be 55 ng/mg, which was 1.8-fold larger than one obtained without using APTES, suggesting that Gd_3TCAS_2 was successfully anchored to ammonium group of APTES in the SiNP.

Optical images of MCF-7 cells incubated in the presence of SiNP loaded with Tb_3TCAS_2 were obtained with bright field and fluorescence microscopes (Fig. 2). As can be seen, emission of green light from Tb(III) inside the cell was observed to show successful delivery of the SiNPs to the cells. This implies that the SiNP loaded with Gd_3TCAS_2 could be used as the carrier of Gd to tumor in NCT.

We then attempted cell viability study after irradiation of neutron for 0, 30, and 60 min to MCF-7 cells incubated with 0, 50, and 100 μM of Gd in the medium added as Gd_3TCAS_2 in the SiNP. The cell viability for samples incubated in the presence of 100 μM of Gd showed decrease from 117 to 65% as time elapsed from 0 to 60 min. But similar trend was observed for control without containing Gd. Thus, it was still unclear whether the Gd in the SiNP sufficiently emit γ ray or internal conversion electron and Auger electron. SiO_2 shell of SiNP may have hindered the emission of these electrons from the material. Hence, we will seek other carriers of Gd_3TCAS_2 which allows emission of those electrons.

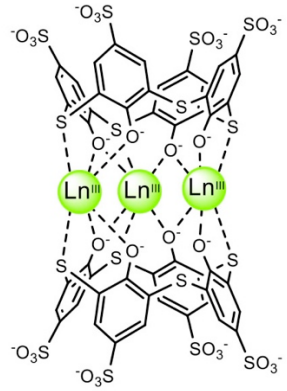

Fig. 1 Structure of Ln_3TCAS_2 complex.

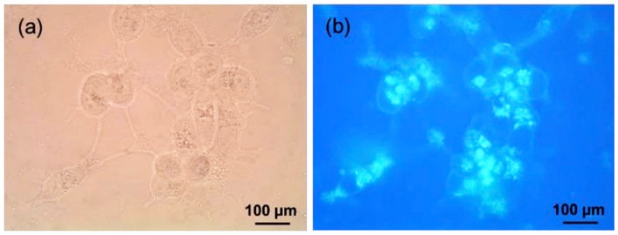

Fig. 2 Images of MCF-7 cells obtained with (a) bright field and (b) fluorescent microscopes.

REFERENCES:

[1] M. Takagaki *et al*., Future Application of Boron and Gadolinium Neutron Capture Thrapy, in *Boron Science*, Ed N. S. Hosmane (CRC Press) (2012) 243.

[2] N. Iki *et al.*, *Eur. J. Inorg. Chem.*, **2016** (2016) 5020-5027.

[3] R. Karashimada *et al.*, *Chem. Commun*. **52** (2016) 3139-3142.

[4] N. Iki *et al., Inorg. Chem.* **55** (2016) 4000-4005.

[5] W. Stöber *et al.*, J. *Colloid Interface Sci*., **26**, (1968) 62-69.

CO7-13 Development of New Gadrinium Neutron Capture Therepy Agent for Bone Cancer

T. Matsukawa[1], A. Kubota[1], M. Suzuki[2], H. Yanagie[3], A. Shinohara[1,4], T. Hirata[5], K. Yokoyama[1,6]
[1] *Juntendo University Faculty of Medicine*
[2] *Institute for Integrated Radiation and Nuclear Science, Kyoto University*
[3] *School of Engineering, The University of Tokyo*
[4] *Research Institute for Cultural Studies, Seisen University*
[5] *School of Science, The University of Tokyo*
[6] *International University of Health and Welfare*

INTRODUCTION

For developing the next generation cancer radiation therapy, we established a new method to evaluate tissue distribution of neutron capture therapy formulation containing gadolinium-157. Laser ablation inductively coupled plasma mass spectrometry (LA-ICP-MS) has been used for elemental imaging in the field of earth and planetary sciences. We applied this method to biological samples, enabled imaging intra-tissue distribution of gadolinium-157[1]. In this study, by using LA-ICP-MS, we revealed that EDTMP [ethylenediamine tetra (methylene phosphonic acid)] chelate of gadolinium (Gd-EDTMP) .

EXPERIMENTS

Female C3H/HeNJcl aged 7 weeks ware obtained from CLEA Japan, Inc (Tokyo, Japan). LM8 (RBRC-RCB1450) cells were purchased from Riken BRC Cell Bank (Ibaraki, Japan). Cultured LM8 cells were prepared for intratibial injection. The cells were injected (2×10^6 cells per mouse) into the right hind tibia of CH3 mice anesthetized with isoflurane, and mice were randomized into four groups (n=4 per group). At 4 days subsequent to the injection of cells, mice were injected Gd-EDTMP or saline.

Gd-EDTMP chelate solution was prepared from gadolinium chloride and EDTMP [1]. Gd-EDTMP was diluted with saline (1.0 mg-Gd/mL) and intraperitonealy administered to two groups of mice to 10.0 mg-Gd/kg, other eight mice were injected same volume of PBS as control. Twenty-four hours after injection, each one groups of mice which were injected Gd-EDTMP or saline were irradiated for 120 min with 8.0×10^{12} cm^{-2} thermal neutrons at the Kyoto University Reactor. Seven days after thermal neutron irradiation tibia samples were excised and analysed laser ablration inductively coupled plasma mass spectrometry (LA-ICP-MS). The size of the tumors are going to measure by photomicrograph of a hematoxylin-eosin stained section of tibia.

RESULTS

The distribution of ^{157}Gd in the tibia determined by LA-ICP-MS is shown in Fig. 1. Gd-EDTMP was concentrated to a bone at high concentration, that was 1500 times of muscle tissue. By limiting the application to bone tumors, Gd-EDTMP might be used sufficiently for neutron capture therapy by overwhelming tumor concentration effect. As for effect of neutron capture therapy, we would like to give it more consideration moving forward.

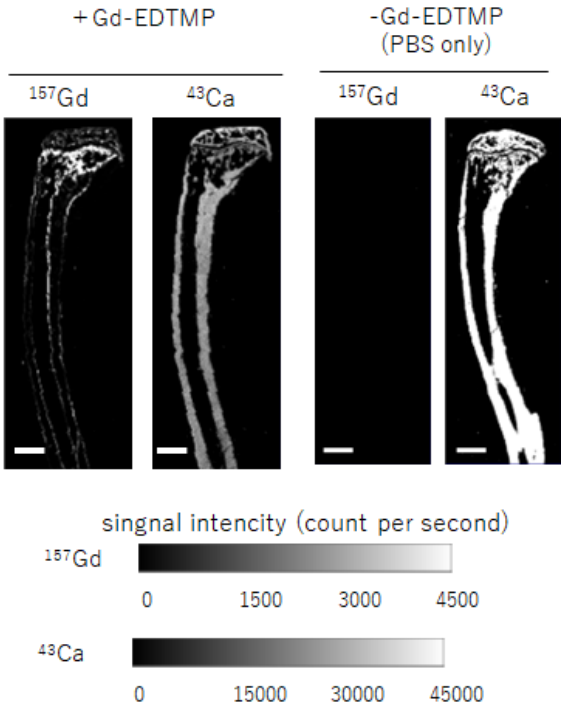

Fig. 1. Distribution of ^{157}Gd and ^{43}Ca in the mice tibia. Tibia section from Gd-EDTMP treated mice (left) and PBS treated mice as control (right) were analysed by LA-ICP-MS. Scale bar is 1mm.

REFERENCES:

[1] T. Matsukawa *et al.*, Jap. J. Hygene **74 Suppul.** (2019) S129.
[2] S. Arani *et al.*, Nucl. Electronic physician, **7** (2015) 977.

CO7-14 Enhanced neutron sensitivity by overexpression of *LAT1* in human cancer cells

K. Ohnishi[1], M. Misawa[2], N. Sikano[3] and M. Suzuki[4]
Departments of [1]Biology, [3]Radiological Science, Ibaraki Prefectural University of Health Sciences

[2]National Institute of Advanced Industrial Science and Technology

[4]KURNS, Kyoto University

INTRODUCTION: Outcome from BNCT largely depends on amount of intracellular accumulation of boron compound. L-type amino-acid transporter 1 (LAT1) [1], through which boronophenylalanine (BPA) is transported into cells, is predominantly expressed in various types of tumor cells including glioblastoma but not in normal cells [2]. We transfected *pCMV/LAT1-GFP* plasmids into a glioblastoma cell line, T98G, and selected several clones. Confocal laser microscopic observation confirmed that those clones stably overexpress LAT1 in cell membrane. Uptake of ^{14}C-BPA was measured by use of a RI tracer method in the LAT1-overexpressing T98G cells. The amount of intracellular ^{14}C-BPA was 1.5-5.0 times larger in several LAT1-overexpressing clones than that in a control clone. Cell growth rate was not affected by the LAT1 overexpression. We intend to examine the sensitivity to neutrons generated by KUR in stably LAT1-overexpressing T98G cells after ^{10}BPA treatment.

EXPERIMENTS: Stably LAT1-overexpressing T98G cells (T98G/K4 clone), control T98G cells (T98G/KC2 clone, transfected *LAT1*-empty plasmids) and transiently *pCMV/LAT1-GFP*-lipofected T98G/KC2 cells were plated on dishes. After overnight culturing, the cells were treated with ^{10}BPA (5 or 20 ppm) and 3 hours later the cells were trypsinized and irradiated with the beams (neutrons and γ-rays, 0.4 or 0.8 Gy in total dose) from KUR. The irradiated cells were plated on three replicate dishes for colony formation assay. The cells were fixed with ethanol and stained with crystal violet after cell culture for 10-14 days.

RESULTS: T98G/K4 cells showed slightly enhanced sensitivity to the beams compared with T98G/KC2 and the lipofected T98G/KC2 cells in the case of 5 ppm ^{10}BSA treatment (Fig. 1a). There is no significant difference in the sensitivity to the beams between T98G/KC2 and the transiently lipofected T98G/KC2 cells. In the case of 20 ppm ^{10}BSA treatment (Fig. 1b), T98G/K4 and the lipofected T98G/KC2 cells showed largely enhanced sensitivity to the beams compared with T98G/KC2 cells (ER=1.5). The sensitivity to the radiation flux depended on dose of ^{10}BSA.

CONCLUSION: Results obtained from this study showed that overexpression of LAT1 results in enhanced sensitivity to neutrons, depending on dose of ^{10}BPA, in human cancer cells.

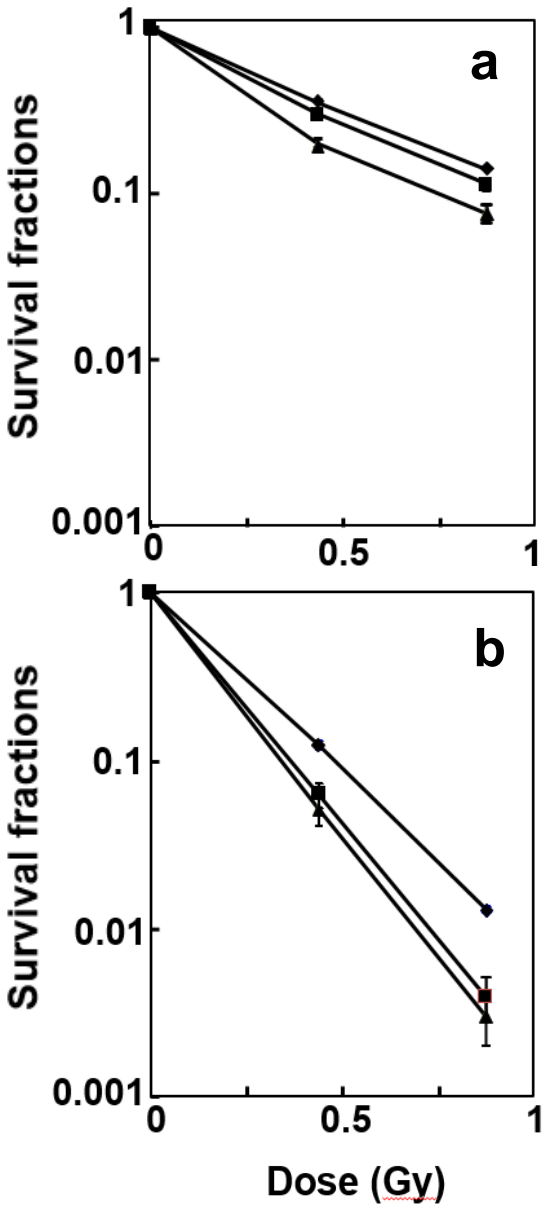

Fig. 1. Sensitivity to neutrons and γ-rays beams from KUR in T98G/K4 (▲), T98G/KC2 (♦) and transiently *pCMV/LAT1-GFP*-lipofected T98G/KC2 cells (■). Cells were treated with 5 (**a**) or 20 ppm ^{10}BPA (**b**) 3 hours before irradiation.

REFERENCES:

[1] Y. Kanai *et al.*, J. Biol. Chem., **273** (1998) 23629-23632.
[2] K. Kaira *et al.*, Br. J. Cancer, **107** (2012) 632-638.

30110

CO7-15 Clarify the Heterogeneity of Boron Distribution in BNCT

S. Takeno[1], T. Watanabe[2], H. Tanaka[2], Y. Tamari[2]
M. Suzuki[2]

[1.] *Graduate School of Science, Kyoto University*
[2.] *Institute for Integrated Radiation and Nuclear Science, Kyoto University*

INTRODUCTION:

Today, boronophenylalanine (BPA) is widely used as a boron compound for boron neutron capture therapy (BNCT). BPA is reported to be uptaken by SLC7A5 (LAT1), SLC7A8 (LAT2) and SLC6A14 (ATB^{0+}) which were identified as the transporters of BPA *in vitro* study [1]. However, relationship between BPA and these transporters *in vivo* has been unrevealed. The aim of this study is to investigate the relationship *in vivo* to clarify the mechanism of heterogeneity of BPA distribution.

EXPERIMENTS:

T3M4 (human pancreatic cancer cell line) was subcutaneously inoculated into the legs of BALC/c-nu/nu mice. BPA at the dose of 500mg/kg was injected subcutaneously and the tumor was removed two hours later. Frozen tumor sections (6-μm thickness) were made by cryostat and put them on CR-39 which are widely used as the solid state nuclear track detector. CR-39 plates were irradiated with thermal neutron using Tc-Pn in Kyoto Univesity Research Reactor (KUR). The thermal neutron fluence was approximately 8×10^{11} (n/cm^2). Two heavy particles (^4He and ^7Li) yielded by $^{10}B(n,\alpha)^7Li$ reaction made dots on the CR39 plate. The position of the dot correlated with that of BPA. Hematoxylin-Eosin (HE) staining of tumor sections were carried out followed by chemical etching process to enlarge the dot detectable by optical microscope. Before chemical etching, the image of HE-stained tumor sections were stored since the tumor sections were lost in the process of chemical etching.

To investigate the relationship between HE-stained tumor sections and dots images on CR 39, these images ware merged [2].

RESULTS:

Figures 1 and 2 show the images of boron distribution depicted as small black circles which were overlaid on the HE-stained image. The relationship between histological structure and BPA distribution was successfully imaged. Feasibility of the method for detecting BPA distribution on the tumor section image was confirmed. As the next experiment, we will investigate the identification of the transporters of BPA using the immunohistochemical staining.

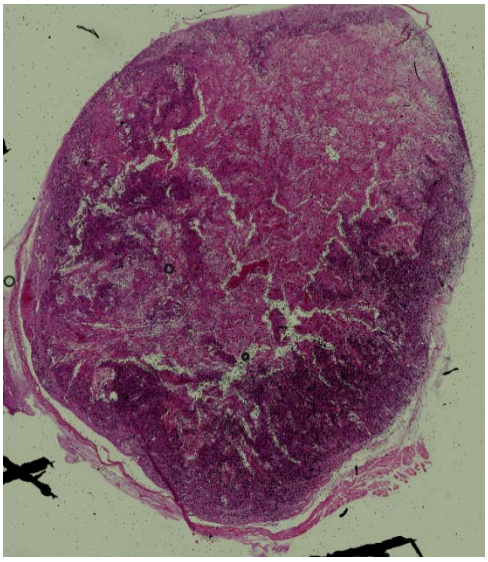

Fig.1 HE staining and boron distribution (x4)

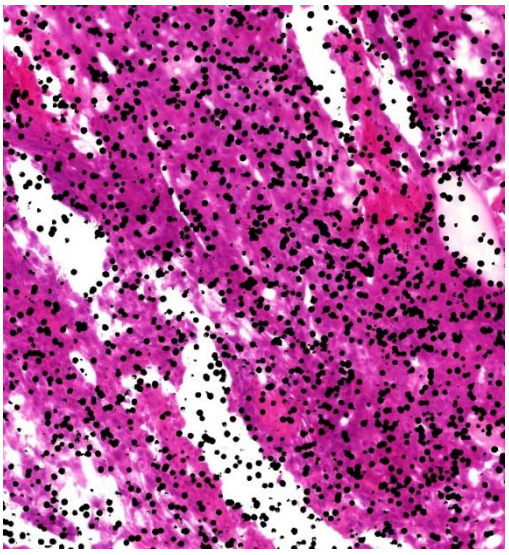

Fig.2 HE staining and boron distribution (x20)

REFERENCES:

[1] Wongthai, P., *et al.,* (2015). Cancer Sci 106(3): 279-286.
[2] Tanaka, H., *et al.,* (2014). J Radiat Res 55(2): 373-380.

CO7-16 The Effect of boron neutron capture therapy (BNCT) on normal lung in mice

M. Suzuki[1], Y.Tamari[1] and M. Fukahori[2]

[1.]Institute for Integrated Radiation and Nuclear Science, Kyoto University [2]. National Institutes for Quantum and Radiological Science and Technology

Introduction

Boron neutron capture therapy (BNCT) has been applied mainly for the treatment of locally recurrent malignant brain tumors or head and neck cancers in the irradiated region. The outcomes of the clinical BNCT studies on BNCT for both tumors have been reported to be promising in some studies.

Clinical trials using accelerator-based (AB)-BNCT system are currently in progress. Since the AB-BNCT system is much compact compared with a research reactor, the system can be installed in the existing medical institutes. The AB-BNCT system in the hospital is available to more patients suffering from malignant tumors compared with the BNCT system using research reactor. Lung cancer, breast cancer and hepatic tumors including hepatocellular carcinoma and multiple metastatic tumors are more common than malignant brain tumors and head and neck tumors.

In this study, for BNCT to apply more common cancer such as lung cancer, breast cancer and hepatic tumors, the effect of BNCT irradiation on normal was investigated. These normal lung are irradiated in the treatment of lung cancer, and breast cancer with BNCT. The research on the effect of BNCT on the normal lung is still ongoing. The preliminary results of the study on normal lung were reported.

Materials and methods

Experimental animals

Twelve- to thirteen-week-old female C3H/He mice were used for this study. All procedures for animal experiments were carried out in accordance with the regulations of Kyoto University Research Reactor Institute regarding animal care and handling.

Experimental protocols

In this study, the radiobiological effectiveness of high linear energy transfer (LET) irradiation by $^{10}B(n,\alpha)^{7}Li$ reaction on normal lung tissues is investigated in comparison to that of X-ray. The endpoint is occurrence of fatal radiation injuries.

Three types of irradiation carried out in this study ware as follows, X-ray irradiation, thermal neutron beam irradiation and BNCT-irradiation using p-boronophenylalanine –fructose complex (BPA-F). In each irradiation, the whole lung was irradiated with shielding other part of the body. In X-ray-irradiation, anesthetized mice were confined in 1mmPB box with 25x20 mm-sized window. The whole thoracic put within the window was irradiated with 150keV X-ray at 1.16 Gy min^{-1}. In thermal neutron beam irradiation, mice was held within a specially designed cage made with thick paper at the flux of 3.73E+10 $cm^{-2}\cdot min^{-1}$. LiF tiles (50-mm thick) were used to shield parts of the body other than the chest. Since all the mice treated with BNCT at the dose of 500 mg/kg have been alive in BNCT-irradiation groups, BPA-F was subcutaneously injected in each mouse at the dose of 1,000 mg/kg. Irradiation was started at two hours after the injection of BPA-F. Six- to nine mice were used for each data point.

At two or three days' intervals during one months from the irradiation and weekly intervals after two months, the mice were weighted and carefully observed.

Results

In X-ray treatment, mice were irradiated with a single dose (12 to 17 Gy). Fig.1 shows the survival curve for 12 months after the treatment day. Eight, seven and three mice died in 17 Gy, 16 Gy, and 15 Gy groups, respectively. One mouse in 13 Gy group died at 11 months after the treatment day. All the mice in no-treatment, 12 Gy and 14 Gy groups were alive for 12 months after the treatment day.

Fig. 1

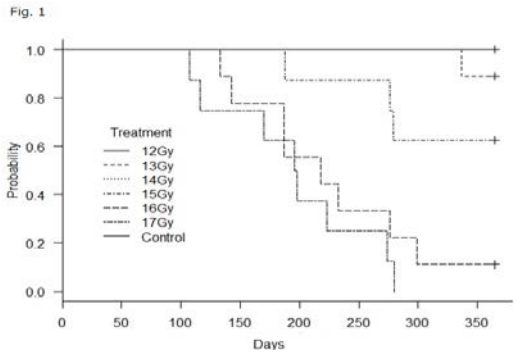

All the mice died in a week after the treatment day in thermal neutron irradiation experiments although two or three irradiation protocols at 5MW were tried. Since the course of death is thought to be acute radiation injury of intestine, optimization of irradiation time and adequate shield of abdomen will be needed.

The mice treated with BPA (1,000 mg/kg)-BNCT were sorted into three groups according to the irradiation time. Since all the mice irradiated with BPA-BNCT for 150 min died in a week, the mice in 60, 90, and 120 min-irradiation groups have been observed. All the mice are alive for 3 to 6 months after the treatment day.

CO7-17 Study of the influence on normal liver tissue by BNCT

Y. Tamari[1], M. Suzuki[1]

[1]*Institute for Integrated Radiation and Nuclear Science, Kyoto University*

INTRODUCTION: Pioneering clinical research aimed at expanding the application of BNCT is planed to be implemented as a joint use research adoption task at the Kyoto University Institute for Integrated Radiation and Nuclear Science. At the part of the study, a clinical study of BNCT for the hepatocellular carcinoma is planned.

The BNCT for liver tumor, which has been conducted up to the present, has used the compound effectiveness factor (CBE) determined by using genotoxicity for hepatocytes as an indicator, which has been clarified by Suzuki et al. But there is a problem whether it is appropriate as a real clinical endpoint. Fundamental researches of liver fibrosis that are the late effect of radiation therapy are necessary. It is necessary to do basic research that uses liver fibrosis, which is a late radiation injury to the liver, as an evaluation index.

A purpose of this study is to establish systematically and continuously technique that can analyze the harmful phenomenon in the normal liver tissue of BNCT.

EXPERIMENTS: Female C57BL6 mice at 6weeks of age were purchased from CLEA Japan Inc. BPA solution (500mg/kg or 1000mg/kg) was injected Subcutaneously 2 hours before neutron irradiation. The mice were irradiated for 60 minutes at the 1MW output. 1week after irradiation, mice were sacrificed and the livers were analyzed. It has been suggested that radiation of normal liver tissue cause steatosis leading to fiblosis [2]. HE staining and Triglyceride quantification were performed to investigate degree of the steatosis in the mouse normal liver tissue after BNCT.

RESULTS: As shown in Fig. 1, the result of HE staining demonstrated that the steatosis of the BNCT group was increased. Furthermore, quantification of triglyceride was performed to determine the degree of steatosis of normal mouse liver tissue after BNCT. Triglycerides in mouse normal liver tissue after BNCT tended to be increased compared to control (Fig.2). In the future, it is necessary to carry out verification of liver fibrosis and quantification of related proteins.

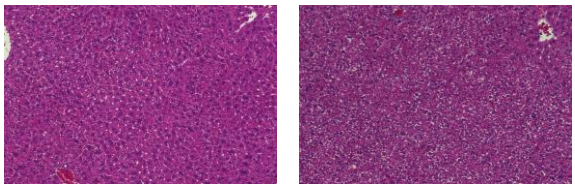

Control 1000mg/ml BPA + neutron

Fig.1. HE staining of mice liver tissue after BNCT. Left panel is control and right panel is 1000mg/ml BPA plus neutron irradiation.

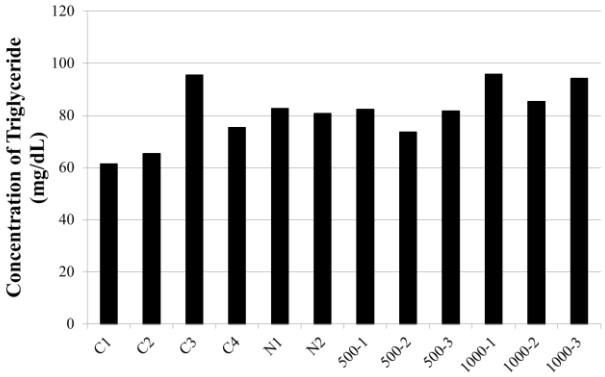

Fig.2. Triglyceride determination of mice normal liver tissue 1 week after BNCT. C: control, N: neutron alone, 500: 500mg/ml BPA + neutron, 1000: 1000mg/ml BPA + neutron.

REFERENCES:

[1] M. Suzuki *et al.*, Jpn. J. Cancer Res., **91** (2000) 1058-1064.

[2] S. Wang et al., Hepatol. Int., 7 (2013)1065-1074

30114

CO8-1

Mercury recovered from smeared solution by the organo-mercury lyase enzyme revealed and detected by an *in-cell* radioactive analysis

K. Takamiya and Y. Morimoto

Institute for Integrated Radiation and Nuclear Science, Kyoto University

INTRODUCTION: Methylmercury or organomercury are severe harmful compounds that cause neurological diseases represented by the Minamata disease. Some soil bacteria (such as *Desulfovibrio dusulfricans*) methylate inorganic mercury in seawater and pond freshwater, and then the food chain and body concentration are carried out to plankton, microorganisms and fish shellfish. In humans, in particular, since the binding mode between sulfur and mercury (Cys-S-Hg) of cysteine could not be distinguished from methionine at the methionine passage gate in the brain, it is impossible to block and avoid them into the brain. An accumulation of such toxic mercury causes nervous system poisoning. Therefore, purification of mercury-contaminated water and soil and mercury recovery has been desired since before. The most convenient method for purification and recovery against mercury contamination is a method as a chelated precipitate of EDTA, dimethyl captosuccinic acid (DMSA) or the others. However, this method merely aggregates and solidifies mercury compounds, and the inorganic mercurilization from them demands highly complicated chemical operation.

Recently, we succeeded in structural analysis of the mercury-bound form of an organomercury lyase B (MerB), in which one mercury was bound quantitatively per molecule even in additive of CH_3HgCl reagents (1). In other words, it has been shown that organic mercury molecules are incorporated into inorganic mercury and held in the enzyme in genetically modified E. coli over-expressing a large amount of the MerB. Therefore, it is thought that organic mercury in a cultivation medium could be recovered and mineralized into inorganic mercury by culturing the MerB-expression strain with high density (so called the bioremediation).

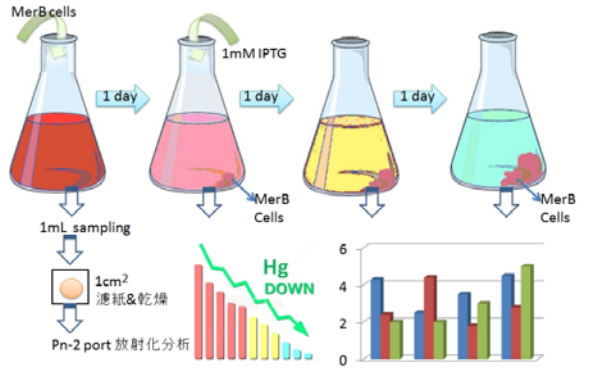

Fig.1 A schematic drawing of cultivation of the *E.coli* harboring MerB and medium sampling to radioactivation analysis

EXPERIMENTS: The enzyme was produced with an induction by isopropyl β-D-1-thiogalactopyranoside (IPTG) adding at the cell growth (OD 650 = 0.6). After this, MerB is accumulated in cells. During the sampling (Fig.1), 1 mL of medium is sampled, dried on filter paper, and used as a sample for neutron irradiation. Neutron irradiation and radioactive analysis at the irradiation port Pn-2 of the 5 MW research reactor (KUR) were carried out to which the applicant belongs. According to preliminary calculations, 500 ng Hg can be detected with 1 mL of filter paper dry-loaded with 1 mL of a medium containing mercury. The activation analysis is carried out by measuring γ-rays (279 keV) emitted with β-Decay of 203 Hg (T1 / 2 = 46.6 d) generated by 202 Hg (n, γ) 203 Hg. Specifically, neutron irradiation is performed for 1 hour with a standard sample using PUR-2 of KUR, and after attenuating short half-life nuclide generated from impurities over about one week, γ-ray using Ge semiconductor spectrometry. The production amount of 203 Hg is estimated to be about 15 Bq, which can be measured with a statistical error of several% in about one day measurement. The amount of mercury is determined by a comparison method estimated from the ratio of the counting rate of the standard sample and the actual sample.

RESULTS and DISCUSSION: At 50 mL culture scale, methylmercury chloride was added to a concentration of 5, 2.5 mM, and with the progress of culture, the medium solution and the amount of cells were sampled, dried on filter paper, and used as a radioactive analysis sample.

Since a large amount of MerB is biosynthesized in the transformed cells during culture, methylmercury in the culture medium at the end of culture or during culture is cleaved along with the production of the enzyme molecule, and it is decomposed into mercury atoms to be digested inside the enzyme molecule. As a result of quantification after 96 hours considering the half life sufficiently, when the IPTG is not added (normal expression amount), the amount of mercury in the intracellular / medium is captured about twice as strongly, but IPTG induced cells, the ratio was reversed or equal and no significant difference was found. It is considered that the growth itself would be unstable in the transformed strain in which the enzyme molecule was forcibly expressed.

Acknowledgement: This work was supported by the Sumitomo Foundation 2017 and Kyoto Univ. education and research grant.

REFFERENCES:

1) A study of preparation and structural analysis of the organomercury lyase for a neutron diffraction experiment. Y.Morimoto and A.Kita, Annual meeting of the KURRI 2017.

CO8-2 Neutron Phase Imaging with Talbot-Lau Interferometer at CN-3

Y. Seki, T. Shinohara, M. Hino[1], T. Oda[1], Y. Matsumoto[2], J.D. Parker[2], T. Samoto[3]

J-PARC Center, JAEA
[1]Institute for Integrated Radiation and Nuclear Science, Kyoto University
[2]Comprehensive Research Organization for Science and Society
[3]Institute of Multidisciplinary Research for Advanced Materials, Tohoku University

INTRODUCTION: Neutron phase imaging is an attractive method which can directly access the phase information of the neutron wave function, and investigate sensitively thinner or smaller structures of samples than by the conventional neutron radiography. We have been developing neutron phase imaging technique with the Talbot-Lau interferometer [1, 2], which consists of three gratings, at the Energy-Resolved Neutron Imaging System "RADEN" in J-PARC MLF.

One of the remarkable characteristics of the Talbot-Lau interferometer is attributed to the most upstream absorption grating (G0). G0 works as a multi-slit, and forms an array of spatially coherent line sources. Each source produces an interference pattern or a "moiré fringe" constructively through the middle phase grating (G1) and the most downstream absorption grating (G2). Therefore the Talbot-Lau interferometer is adaptable to even low-coherent and low-intensity beam of small- or middle-sized neutron sources.

For the spread of this method at such sources, we have developed a portable Talbot-Lau interferometry system and performed an imaging experiment at CN-3 beam line in Kyoto University Reactor (KUR). As the first step, typical visibility of moiré fringes and measurement precision at this beam line were studied by using a simple sample.

EXPERIMENTS: In the present experiment, we used a set of gratings which was fabricated for the RADEN beam line. The pitches of G0, G1, and G2 were 180 μm, 8.6 μm, and 9.0 μm, respectively. The distances from G0 to G1, and from G1 to G2 were 1534 mm and 76.5 mm, respectively. All the gratings were mounted on compact stage systems with pulsed-motors. As a neutron imager, the RPMT detector which consisted of a position-sensitive photomultiplier tube and a ZnS/^{6}LiF scintillator was employed behind G2.

The measurement was carried out by "phase-stepping method" as described below. First, a moiré fringe was scanned five times without the sample at the step of $2\pi/5$ rad by shifting the position of G2. From this measurement, the visibility of the moiré fringe was evaluated. Second, the same procedure was repeated with the sample. The measurement time was 40 min for each step, and totally $2 \times 5 \times 40 = 400$ min for one sample. By comparing the phase of two moiré fringes with and without the sample, a differential-phase contrast image was obtained.

RESULTS: Fig. 1 shows a visibility map of the moiré fringe. The average visibility was 19% in the grating region. The relatively low visibility was observed because G1 was designed for the central wavelength of 5 Å at the RADEN beam line which was quite different from the peak wavelength of 2.4 Å at CN-3 beam line. The visibility distribution should be derived from manly the thickness distribution of neutron absorber (gadolinium) on G2.

Fig. 2 shows a differential-phase contrast image of an aluminum rod with a diameter of 5 mm. The phase determination precision was about $2\pi \times 0.02$ rad with a pixel size of 0.22×0.22 mm^2. By fitting a theoretical curve to the profile of the observed image, the effective wavelength, which reproduced the literature value of the optical potential of aluminum, was evaluated to be 2.55 Å for differential-phase contrast imaging with this setup.

For more efficient measurement, we have a plan to fabricate new gratings in near future, which are optimized to the wavelength spectrum of CN-3 beam line.

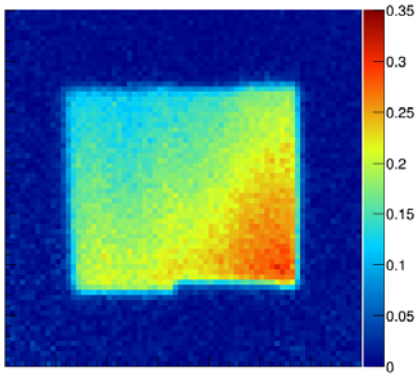

Fig. 1. Visibility map of moiré fringe.

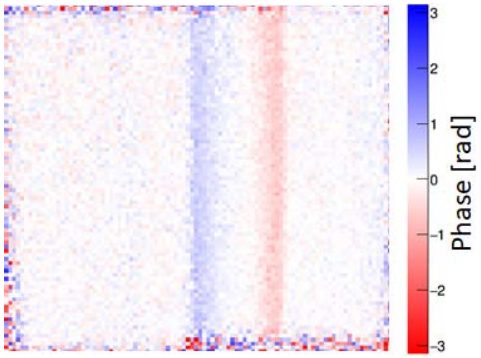

Fig. 2. Differential-phase contrast image of an aluminum rod.

REFERENCES:

[1] Y. Seki *et al.*, J. Phys. Soc. Jpn., **86** (2017) 044001.
[2] Y. Seki *et al.*, EPL, **123** (2018) 12002.

CO8-3 Test Result of Various Scintillator Sheet for Neutron Flat Panel Detector

T. Fujiwara[1] and M. Hino[2]

[1]*National Metrology Institute of Japan, National Institute of Advanced Industrial Science and Technology*

[2]*KURNS, Kyoto University*

INTRODUCTION: Neutron imaging is powerful tool for observing inside an object without destructing the object. Although neutron imaging (neutron radiography) is one of the most traditional uses of neutrons, still there are rooms for improvement. Here, we report on the progress of neutron imaging result at reactor with our new neutron imaging detector based on Thin-Film-Transistor (TFT) technology, the neutron Flat Panel Detector. Various type of scintillators were tested for nFPD at neutron beam port at KUR.

EXPERIMENTS: Experiments were held in CN-3 port at Kyoto University Reactor [1]. At this facility, approximately 20 × 100 mm^2 size cold neutron beam is available. Fig. 1 shows the outlook of the nFPD. The volume of the detector is remarkably compact and thin compared to the conventional neutron imagers. The size of this detector improves the flexibility for placing and it will be a great advantage for installation to various experiments. Meanwhile, nFPD only requires 5V (4W) single power supply, and simply connected to PC with USB cable. The detector has effective area with 512 × 512 pixels (200 mm pixel size).

In this experiment, we test 4 types of LiF/ZnS scintillators .

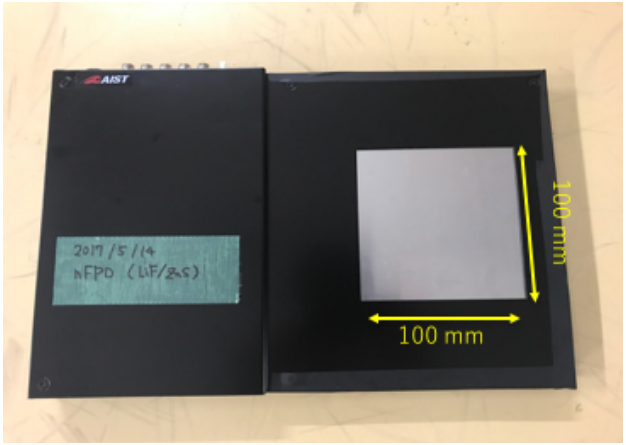

Fig. 1. Outlook of nFPD with 100 × 100 mm^2 effective area. For the neutron convertor, 320 mm thick LiF/ZnS(Ag) scintillator was used.

RESULTS: First, simple neutron imaging capability of nFPD was tested with Gd coated test chart developed at PSI [2]. As shown in Fig. 2, fine neutron radiograph was obtained. Fine structures less than 300 μm can be observed. From these results, it can be concluded as there are trade-off relationship between spatial resolution and the sensitivity of the scintillators.

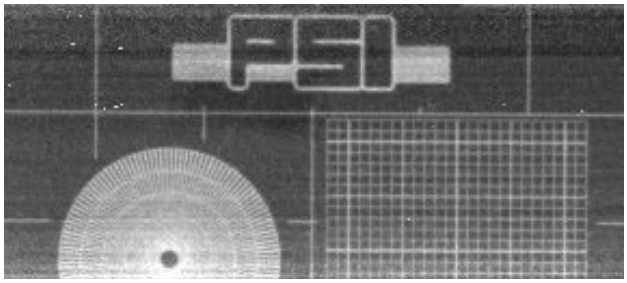

Fig. 2. Obtained neutron radiography of fine-structured Gd chart with nFPD. Integrating time was 5s at 1 MW operation. Fine patterns can be clearly observed.

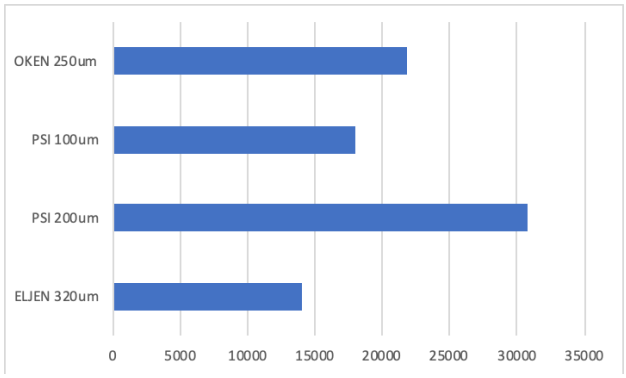

Fig. 3. Relative light output from various scintillators tested at CN-3.

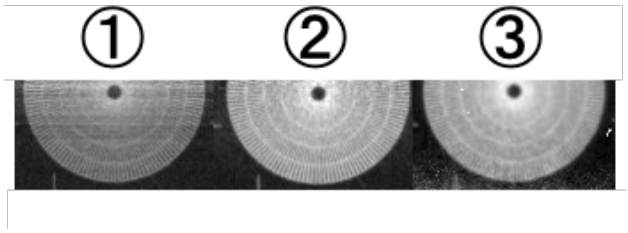

Fig. 4. Resolution comparison of various scintillators. (1) ELJEN Technologies EJ-426 320 μmt, (2) OKEN 250 μmt, (3) PSI 200 μmt.

REFERENCES:

[1] Y. Kawabata *et al.*, Physica B **311** (2002) 106.
[2] K.-U. Hess *et al.*, Geosphere **7** 6. (2011) 1294-130.

CO9-1 Investigation of coprecipitation with Sm hydroxide using KUR multitracer

Y. Kasamatsu, M. Nagase, Y. Shigekawa, N. Kondo, E. Watanabe, H. Ninomiya, K. Takamiya[1], and A. Shinohara

Graduate School of Science, Osaka University
[1]Institute for Integrated Radiation and Nuclear Science, Kyoto University

INTRODUCTION: Chemical researches on actinide and transactinide elements at the bottom of the periodic table are very important in inorganic chemistry. Owing to strong relativistic effect on the electronic shells of heavy elements, their chemical properties might be unique in the periodic table. It is, however, difficult to perform chemical experiment with heavy actinide and transactinide elements because these atoms must be produced at accelerators using heavy-ion induced nuclear reactions at low production rates. Furthermore, these nuclides have short half-lives. Thus, we need to establish new experimental methods with apparatuses specified for these elements. For such a purpose, it is important to perform fundament chemical experiments (with and without apparatuses) using the lighter elements whose chemical properties are known.

We previously proposed the coprecipitation method with Sm hydroxide as a new methodology for heavy elements [1]. Indeed, suitable experimental condition for element 104, Rf, was successfully determined through fundamental experiments using homologues of Rf: Zr, Hf, and Th [2]. Additionally, in the coprecipitation experiment of various elements [1], multitracer produced by spallation reaction of Ta in RIKEN was used to investigate the coprecipitation behaviors of elements belonging to various groups in the periodic table. In this study, coprecipitation behaviors of the elements contained in KUR multitracer were studied. The KUR multitracer was produced by neutron-induced fission reaction of ^{235}U. Thus, the product nuclides are different from those in RIKEN multitracer. We expect to obtain complementary data by this experiment.

EXPERIMENTS: The KUR multitracer sample was prepared by irradiating thermal neutrons on mixture powder sample ofUO_2 and RbCl using the reactor at Institute for Integrated Radiation and Nuclear Science, Kyoto University [3]. Fission products implanted in RbCl were dissolved in 0.01 M HCl and were separated from the undissolved UO_2 by a suction filtration. A portion of the sample was subjected to γ-ray measurement by a Ge detector, and count rates of γ-ray peaks and their time dependences were measured to identify the nuclides in the sample.

In the precipitation experiment, 20 μL (20 μg) of Sm standard solution (1 M HNO_3) was added into the multitracer solution. After mixing it, 2 mL of basic solution was added to generate hydroxide precipitate. In the present experiment, we used dilute NH_3 solution, concentrated NH_3 solution, 0.1, 1, 6, and 12 M NaOH solutions as the basic solutions to observe the dependence of the precipitation yield on the concentration of the basic solution. Subsequently, the solution was stirred for 10 s and was soon filtrated with a polypropylene membrane filter. To check the complete precipitation of the samples, precipitate samples with stirring for 10 min after adding the basic solution were also prepared. The samples were then dried on heater at 100 degree C and were assayed for γ-ray measurements. Supernatant solutions were evaporated to dryness and were also subjected to measurements. The coprecipitation yields were determined from the results of the γ-ray measurements.

RESULTS: The product nuclides were identified from the γ-ray energies and the half-lives. To obtain precipitation yields, we exclude the nuclides whose decays are affected by their parent or daughter nuclide from the analysis of the coprecipitation yield. The nuclides of Na, Zr, Mo, Ce, Ba, Te are elements observed in RIKEN multitracer although the mass numbers of the nuclides are different from those in RIKEN multitracer. ^{91}Sr, ^{103}Ru, ^{133}I, ^{151}Pm, ^{198m}Au, and ^{239}Np are newly observed elements in KUR multitracer. Especially, the ^{91}Sr and ^{151}Pm nuclides are of great importance for the establishment of the experimental method: Sr is comparative data for element 102, No, and Pm is near to Sm in the periodic table (Radioactive isotopes of Sm were not observed in both RIKEN and KUR multitracer). ^{133}I belongs to halogen and we had no data for halogen.

The coprecipitation yields were determined from the equation: A_{ppt} / A_{std}, where A represents the radioactivity of the nuclide, and ppt and std indicate the precipitate and standard, respectively. The yields of ^{143}Ce and ^{151}Pm (lanthanides) were approximately 100% under all the conditions studied. This result means that the yield of Sm is considered to be 100% under all conditions which is favorable in the experiment. For transition metal elements and alkali metal element: Na, consistent results with those obtained for RIKEN multitracer were obtained. The yields of Np were similar to those of transition metal elements and not to lanthanides. These results are basically consistent with the hydroxide precipitation properties of the corresponding elements. It suggests that the present coprecipitation method is suitable to investigate the precipitation behaviors of the elements whose properties are unknown (heavy elements).

REFERENCES:

[1] Y. Kasamatsu *et al.*, Appl. Radiat. Isot. **118** (2016) 105-116.
[2] Y. Kasamatsu *et al.*, J. Nucl. Radiochem. Sci. **14** (2014) 7-11.
[3] K. Takamiya *et al.*, J. Nucl. Radiochem. Sci., **1** (2000) 81-82.

CO9-2 Stability of Pyrrolidone Derivative against γ-Ray Irradiation in HCl

D. Nitta[1], R. Hamashiro[1], M. Nogami[1], and N. Sato[2]

[1]*Faculty of Science and Engineering, Kindai University*
[2]*Institute for Integrated Radiation and Nuclear Science, Kyoto University*

INTRODUCTION: Stability of pyrrolidone derivatives (NRPs) which are potential precipitants for uranium(VI) species in nitric acid media has been investigated. Irradiation to HNO_3 solutions up to 6 mol/dm^3 (= M) containing 2 M *N*-*n*-butyl-2-pyrrolidone (NBP : Fig. 1), one of NRPs has revealed that the residual ratios of NBP in the samples of HNO_3 up to 3 M decreased identically and linearly. On the other hand, the degradation of the samples irradiated in 6 M HNO_3 has been found more distinguished. It was proposed from the analyses of degraded compounds that the degradation of NBP in HNO_3 by γ-ray irradiation started from the cleavage of the pyrrolidone ring by the addition of oxygen atom originating from HNO_3, followed by the formation of chain compounds by the successive addition of oxygen, leading to the generation of oxalic acid and acetic acid. Some of the oxalic acid further decompose to CO_2[1]. In order to know more about the degradation mechanism of NRP, degradation property of NBP in hydrochloric acid media was investigated in the present study.

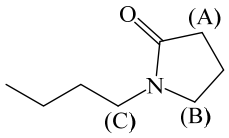

Fig. 1. Chemical structure of NBP.

EXPERIMENTS: 0.1, 3, and 6 M HCl solutions containing 0.5 M NBP, respectively, were prepared in Pyrex tubes for the samples for γ-ray irradiation. Irradiation was carried out by the ^{60}Co source up to 0.45 MGy at room temperature under ambient atmosphere, similarly to the earlier study[2]. Irradiated samples were analyzed by ^{1}H NMR. DMSO-d_6 containing a known weight of TMS which is a standard material was used as the NMR solvent. The residual ratio of NBP was calculated by the area ratio of each signal with that of TMS.

RESULTS: The sample solutions were found to turn yellow with increasing concentration of HCl and dose. In a ^{1}H NMR spectrum, neat NBP showed three signals; (A)2.3, (B)3.2, (C)3.3 ppm in Fig. 1, respectively. The calculated residual ratios of the sample vs. dose are shown in Fig. 2, together with the relationship between the position of hydrogen in the structure of NBP and that of the signal. The residual ratios calculated from the three signals show a nearly identical trend regardless of the concentration of HCl, where the residual ratios decrease linearly with an increase in dose, and the residual ratios are ca. 70 % at 0.3 MGy. The residual ratios for the of HNO_3 up to 3 M was ca. 90 %[1], indicating that the stability of NBP against γ-ray irradiation in HCl is lower than that in HNO_3 of lower concentrations. The reason why no dependence of degradation property on HCl concentration would result from the absence of oxygen atoms supplied for the above-mentioned HNO_3 system.

No new signals attributed to the decomposition products were observed for the ^{1}H NMR spectra in the irradiated samples, although some NBP was degraded. A possible degraded compound may be oxalic acid like the case for HNO_3 system, because the proton of oxalic acid is hardly detected in a ^{1}H NMR spectrum. What happened to NBP in the HCl system during irradiation remains unclear.

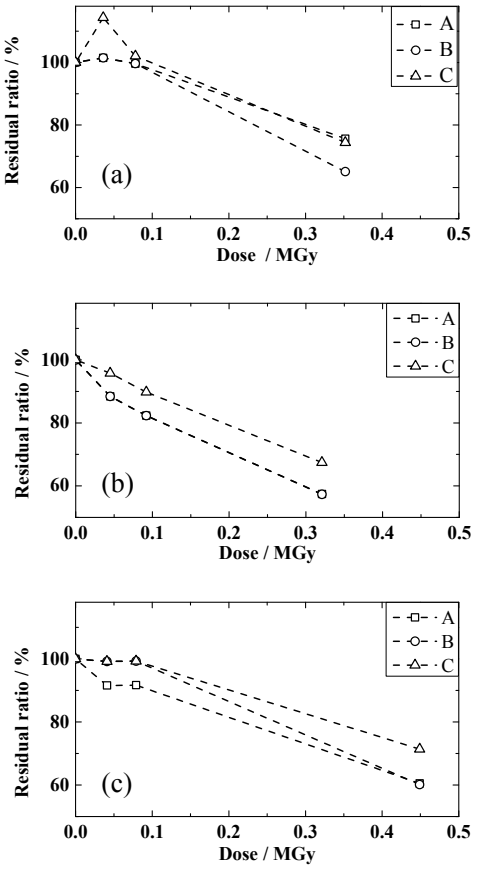

Fig.2. Dependence of residual ratio of NBP in (a) 0.1 M, (b) 3 M, (c) 6 M HCl on dose.

REFERENCES:

[1] M. Nogami, *et al.*, Sci. China Chem., **55** (2012) 1739-1745.
[2] T. Nishida, *et al.*, KURRI Progress Report 2013 (2014) 295.

CO10-1 Assessment of Internal doses from Environmental medias contaminated by the Fukushima Daiichi Nuclear Power Plant accident: Absorption fraction of Cs-137 from contaminated wild boars lived in Fukushima prefecture

S. Takahara, M.A. Pratama[1, 2], M. Ikegami[3]and S. Fukutani[3]

Nuclear Safety Research Center, Japan Atomic Energy Agency
[1]*Graduate School of Engineering, Kyoto University*
[2]*Faculty of Engineering, University of Indonesia*
[3]*Institute for Integrated Radiation and Nuclear Science*

INTRODUCTION: Fukushima Dai-ichi nuclear power plant (FDNPP) accident had released large amount of radioactive substances into the environment. Consequently, the living residents within the contaminated area were under threat of radiation exposure externally and internally. Ingestion of contaminated foodstuffs is one potential internal exposure pathways. From the experiences of the FDNPP accident, it is indicated that though the ingestion exposure was not sufficiently high compared to the contribution from external exposures, it still poses a long-term radiological risk and social impacts so that the evaluation of internal dosimetry needs to be addressed appropriately.

Internal dose form ingestion pathway is evaluated by using the committed effective dose coefficient, which is recommended by the International Commission on Radiological Protection (ICRP). The coefficients depend on body and organ masses, excretion rates from the urinary bladder and absorption fraction of ingested radionuclide from the gastrointestinal system. In particular, The ICRP adopted the absorption fraction is set to be 1 under an assumption that the all the Cs would be absorbed. However, this assumption is valid only to soluble form. If the absorption faction varied, this variability results in large uncertainties in the calculations of the coefficient (Pratama et al., 2017; 2018).

In the light of this background, to explore the insight on the absorption fraction of radionuclides in gastrointestinal, we are carrying out *in-vitro* digestion (IVD) tests for the environmental samples contaminated by Cs-137 from the FDNPP accident. As the first step of our project, we performed the in-vitro digestion test for the contaminated soils so far (Takahara et al., 2017). In this study, we focused on the absorption fraction of Cs-137 in foodstuffs contaminated by the FDNPP accident.

EXPERIMENTS: A boar living in difficult-to-return zone was obtained from a local hunter in November 2017. Thereafter, the boar meat was divided into three parts which are loin, belly and ham (n = 3). Each part were then split into 1 kg size meat and stored at -20 °C until the time of experiments in January 2019. The meats were minced by using a grounder. 5 g of each part of grounded meat were taken to be used for the IVD test.

In-vitro digestion test

The IVD test was adapted from standardized in vitro digestion method "INFOGEST" proposed by an international consensus in 2014 (Minekus et al., 2014). According to this method, we simulated oral phase, gastric phase, and intestinal phase.

Radioactivity measurement

Before the IVD test, the radioactivities in the meat samples were measured. The measurements were performed with an error of several percent using a high-purity germanium detector (ORTEC, GMX-30190). After the IVD test, we also measured the radioacvities in the liquid samples extracted with the IVD test.

RESULTS: As shown in Table 1, the radioactivities of loin, belly and ham is 1,863 Bq kg^{-1}, 1,810 Bq kg^{-1} and 1,652 Bq kg^{-1}, respectively. In addition, the absorption fractions were evaluated for each sample as the ratio of radioactivity in row meat to those in extraction. As the consequently, the absorption fraction of Cs-137 was evaluated in the range of 87%–93%. In our experiment, any differences of the concentration and the absorption fraction of Cs-137 in the meat samples of wild boar among the parts were not observed.

The absorption fraction of Cs in dietary sources been reported in the previous studies. It is generally accepted that Cs ingested as soluble Cs is well absorbed in the gastrointestinal tracts of humans and animals. Furthermore, radioactive Cs in foodstuffs is almost equally available for absorption in humans and animals (i.e. A result of literature review is described in Takahara et al. (2017)). As compared to these results, the absorption fraction from our experiment is not in contradiction to the previous ones. This result indicates that the dose coefficients of the ICRP recommended is reasonable for the dose assessment of the Fukushima case.

Table 1 Results of radioactivity measurement

Sample	Radioactivity (Bq kg^{-1})		Absorption fraction in Small intestinal
	Row meat	Extraction	
Loin	1,863	1,592	87%
Belly	1,810	1,596	88%
Ham	1,652	1,537	93%

REFERENCES:

[1] M.A. Pratama *et al.*, Jpn. J. Health Phys, **52** (2017) 200-209.
[2] M.A. Pratama *et al.*, Environ. Int., **115** (2018) 196-204.
[3] S Takahara *et al.*, Risk Anal., **37** (2017) 1256–1267.
[4] M. Minekus *et al.*, Food and Function, **5** (2014) 1113–1124.

CO10-2 Transfer of Cesium and Potassium to Lettuce (*Lactuca sativa var. crispa*) in Hydroponic Culture

T. Kubota, S. Fukutani and Y. Shibahara

Institute for Integrated Radiation and Nuclear Science, Kyoto University

INTRODUCTION: A large amount of radioactive materials was released into the environment by the Fukushima accident. Among them, Cs-137 is considered as one of critical radionuclides increasing public exposure. The evaluation of exposure requires, in general, environmental parameters, such as transfer factor (TF) and translocation ratio (TR), and it is desirable that they are obtained by using carrier-free radionuclide for convenience of experiment. Based on the knowledge that the behavior of cesium in biota is similar to that of potassium due to chemical analogy, carrier-free tracer of Cs-136 and K-43 was produced and the TF and TR values of both nuclides to lettuce in hydroponic culture were investigated.

EXPERIMENTS: Cs-136 and K-43 were produced from a barium and calcium target through a photonuclear reaction, respectively. The powder of $BaCl_2$ and $CaCl_2$ in each quartz test tube was heated at 350 ^{o}C for 5 hrs and then the dehydrated powder was encapsulated under a vacuum. The quartz tube inserted into an aluminum folder was irradiated with photons, which was generated by bombardment of platinum sheet (2 mm) with electrons of 30 MeV, for 12 hrs at the KURNS-LINAC [1].

Cesium and potassium was purified by removal of barium and calcium, respectively, as carbonate and then by cation exchange chromatography. Irradiated samples were dissolved with H_2O and added with ammonium carbonate solution to precipitate $BaCO_3$ and $CaCO_3$. After centrifugation the supernatant was heated to remove ammonium chloride. The residual was dissolved with HCl and diluted to 0.1 M HCl. The resulting solution was load onto cation exchange resin. The resin was washed with 1 M HCl to elute cesium or potassium.

The transfer of both elements to Lettuce (*Lactuca sativa var. crispa*) [2] was determined. Seedlings obtained commercially were grown in a nutrient solution [3] for several days and then exposed in a fresh solution containing Cs-136 and K-43 (Fig. 1). After one or three days exposure, seedlings harvested were divided into roots and leaves. The radioactivity of both parts and the nutrient solution was determined by γ-spectrometry. These results yielded the TF value from solution to lettuce and the TR value from root to leaf where TF and TR were defined as the ratio of the specific activity in root or leaf to that in nutrient solution in unit of Lkg^{-1} and the specific activity ratio of leaf to root in unit-less, respectively.

RESULTS: The induced radioactivity of Cs-136 and K-43 was 100 and 50 kBq, respectively. The purification results in the radio activity of barium and calcium under detection limit, which showing that each tracer of Cs-136 and K-43 was high purity and high specific activity. However, the cesium tracer purified contained Cs-129 produced simultaneously, which derives many photo-peaks on a gamma spectrum. It is desired to use this tracer after this nuclide decays. Each purification method, namely precipitation or chromatography, can decrease the radio activity of barium and calcium to a lower detection limit whereas the residue of their salts was slightly observed. In this study both methods were combined to obtain high-purity tracers.

The values of TF and TR are listed in Table 1. After three days of cultivating the TF values of both elements significantly increased, suggesting they totally transferred to lettuce. In contrast to TF, the values of TR showed some difference between two elements and that lower value of cesium would be caused by some plant physiology. Even though further investigations are required for the migration mechanism of these elements in plants, in this study, we prepared carrier-free radioactive tracers suitable for the investigations.

Fig. 1 Hydroponic cultivation of lettuce in a growth chamber

Table 1 Transfer factor and translocation ratio of potassium and cesium to lettuce

Element	Potassium		Cesium	
Exposure time	1d	3d	1d	3d
TF (root)	27	6700	26	16000
TF (leaf)	11	7000	5.3	2100
TR (leaf/root)	0.40	1.04	0.21	0.13

REFERENCES:

[1] T. Kubota *et al.,* KURRI Progress Report 2017 (2018) 209.

[2] K. Iwata *et al*., Proceeding of the 18th Workshop on Environmental Radioactivity (2017) 163 – 166.

[3] K. Fujiwara *et al*., Jpn. J. Health Phys., **50** (2015) 189 – 193.

CO10-3 Analysis of Radiocesium Interception Potential of Coniferous and Deciduous Forest-Floor Soil

H.A. Pratama[1], M. Yoneda[1], Y. Shimada[1], S. Fukutani[2], and M. Ikegami[2]

[1]*Faculty of Engineering, Kyoto University*
[2]*Institute for Integrated Radiation and Nuclear Science, Kyoto University*

INTRODUCTION: Radioactive cesium from nuclear accident is known retained strongly in the soil surface for a long time. Study of vertical distribution of radiocesium shows that it was strongly adsorbed by clay minerals in soils and most of deposited radiocesium remains in the surface soil. Understanding the adsorption characteristic of radioactive cesium in soil is a key to minimize the radiation exposure to local population. We collected top-soil samples from Takizawa Research Forest of Iwate University. They were from different type of forest vegetation which are coniferous and deciduous forest. Here, we measured their radiocesium interception potential (RIP) as an index of their radiocesium retention ability.

MATERIALS AND METHODS: The study site was located about 250 km far from Fukushima Daiichi NPP. The soil type is Andosol or Kuroboku soil according to the Japan soil classification. The soil samples used in the experiment were collected from the top-soil (0-10 cm). Four areas of field sampling were selected in two groups of coniferous forest floor and two groups of deciduous forest floor. In coniferous forest floor, the point sampling location were chosen based on their major vegetation type, such as the evergreen Sugi trees (Cryptomeria japonica) and Karamatsu trees (Larix kaempferi). The major vegetation type in around deciduous forest is other broadleaf forest and Japanese Oak trees such as Konara trees (Quercus serrata). Therefore, soil sample that used in this research were named as C1 and C2 respectively for soil sample from coniferous forest area, D1 and D2 respectively for soil sample from deciduous forest area. Soil samples were air-dried at 50 ^{o}C for 6 days and sieved through 2mm sieve. About 1.0 g of soil samples was put into a dialysis bag (Visking tube dialysis membrane, size 19.1 mm, As One) along with 5 mL of equilibration solution (0.1 mol/L $CaCl_2$ and 0.5 mmol/L KCl solution), and then transferred to 250 mL plastic bottle containing 200 mL of equilibration solution as outer solution. The solution was shaken for 2 h twice a day during 5 days dialysis using magnetic stirrer. Before shaking the solution, the outer solution was renewed each time to maintain the desired condition. After first step of dialysis, the bag was put into a new 50 mL plastic bottle containing the outer solution and each bottle was added with same mass amount of Cs concentration. In this study, radioactive tracer of 10 kBq of carrier ^{134}Cs and 2.5μg of stable ^{133}Cs were added respecricely. In the second step of dialysis also each bottle was shaken continuously during 5 d. After diluted, the outer solution was filtered using a membrane filter with a pore size of 0.45μm. The remained of Cs concentration then analysed using HPGe detector for radioactive tracer addition and ICP MS for stable Cs addition. The RIP value can be obtained as the product of distribution coefficient value of Cs and the concentration of K^+ in equilibration solution.

RESULTS AND DISCUSSION: In this study we compared RIP value of soils that used radioactive Cesium carrier ^{134}Cs and stable Cesium ^{133}Cs. The RIP values of coniferous soils were varied from 109.44 to 225.96 mmol kg^{-1}, and RIP of deciduous soils varied from 155.21 to 199.68 mmol kg^{-1}. The range of RIP values are in similar range between both of them and it was within the range reported for andosol soils collected worldwide (94 – 1320 mmol kg^{-1}) by Vandebroek et. al. Comparison of RIP values between coniferous and deciduous soil is presented in Figure 4. It shows that RIP measurement using stable Cs is not so different from radiocesium and the measurement using stable Cs is also possible.

Figure 1. Comparison of RIP values.

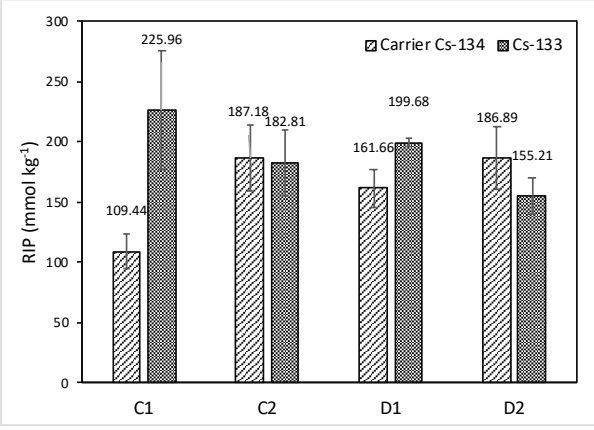

30081

CO12-1 Research and Development of a High Counting Rate ^{3}He Position Sensitive Detector System

S. Satoh, K. Mori[1], Y. Yoshino[1], T. Seya, T. Otomo, H. Oshita, K. Okawa[2], N. Hikida[2], K. Ishizawa[2], A. Yamaguchi[3], M. Matsuura[3]

High Energy Accelerator Laboratory, KEK
[1] Institute for Integrated Radiation and Nuclear Science, Kyoto University
[2] Canon Electron Tubes & Devices Co., Ltd
[3] Clear-Pulse Co., Ltd

INTRODUCTION: Neutron scattering experiments are indispensable in the structural analysis of various forms of condensed matter and in the development of advanced materials. A ^{3}He gas detector [1], which is the most frequently used apparatus in the neutron experiments, is the best neutron detector available; however, the ^{3}He gas detector is low counting rate, less than 20 k cps (count per second).

In this research, we are developing to increase the counting rate of a ^{3}He gas position sensitive detector (PSD), and a maximum counting rate of 535 k cps has been obtained. Even if the usage range is approximately 200 k cps, the PSD with a high counting rate of 10 times that of an ordinary one has been completed.

EXPERIMENTS: At the B3 beam port in KUR at 5 MW operation on August 23, 2018, the counting rate of 535 k cps has been obtained. Since the neutron did not come out with uniform beam density, the counting rate was compared with a monitor counter.

RESULTS: Figure 1 shows the counting rate of the fast PSD versus the counting rate of the monitor counter. These data were obtained with the same condition. The usage range of the PSD is approximately 200 k cps, although the maximum counting rate is 535 k cps.

As shown in Fig. 2(a), a usual slow PSD which has a slow charge amplifier with a band-pass filter time constant 0.5 us generates the wide pulse width approximately 2 us. As shown in (b), a fast PSD which has a fast charge amplifier with a time constant of 0.05 us generates the narrow pulse width approximately 200 ns. If you use the slow PSD and the fast time constant amplifier, the PSD generates charge exceeding the time constant. Since the charge is differentiated before being sufficiently integrated, it becomes a low pulse height with wide pulse width. It has a risk of double counts or triple counts because of a charge fluctuation. Therefore, the fast circuit should not be used for the slow PSD.

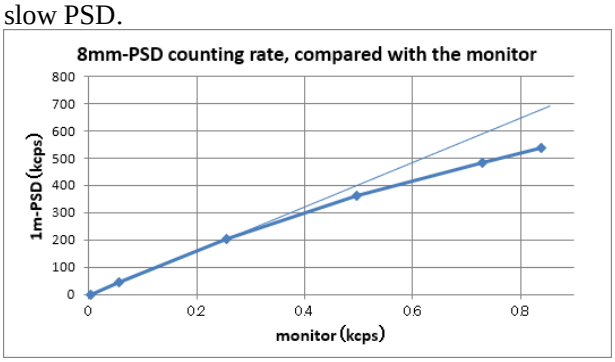

Fig. 1. Counting rate of the fast PSD, compared with the monitor counter.

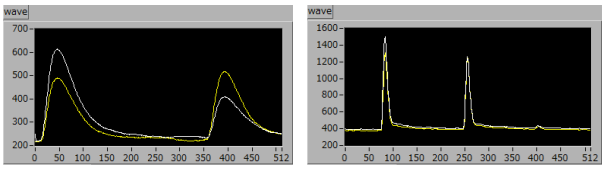

Fig. 2. (a) 0.5us amplifier for a slow PSD, (b) 0.05us amplifier for a fast PSD.

IMPROVEMENT: Since an ordinary PSD readout circuit is made to process the conventional slow PSDs, it is not suited for high counting rate. The following improvements have been added to the ordinary readout circuit to accommodate a high counting rate.

1- A fast time constant of charge amplifier has been developed for the fast PSD.

2- Data transmit way has been changed from bi-directional to uni-directional. G-bit network is also able to use and the maximum counting rate is able to be up to 300 k cps par PSD.

3- The fast PSD and slow PSD are able to be clearly distinguished by a pulse width measuring function that is installed in this version.

4- It is possible not to choose functions that inhibit the high counting rate.

REFERENCES:

[1] S. Satoh, S. Muto, N. Kaneko, T. Uchida, M. Tanaka, Y. Yasu, K. Nakayoshi, E. Inoue, H. Sendai, T. Nakatani, T. Otomo, Development of a readout system employing high-speed network for J-PARC, IPS08 Proc. Int. Symp. Pulsed Neutron Muon Sci. at J-PARC 2008, DOI:10.1016/j.nima.2008.11.054.

CO12-2 Dependency of Coherent Cherenkov Radiation Matched to the Circular Plane on Apex Angles of a Hollow Conical Dielectric

N. Sei and T. Takahashi[1]

Research Institute for Measurement and Analytical Instrumentation, National Institute of Advanced Industrial Science and Technology

[1]*Institute for Integrated Radiation and Nuclear Science, Kyoto University*

INTRODUCTION: To obtain intense terahertz (THz) waves, we proposed a principle of coherent Cherenkov radiation matched to the circular plane (CCR-MCP) [1]. We observed intense THz-wave radiation by using scheme of the CCR-MCP with an L-band linac at Kyoto University Institute for Integrated Radiation and Nuclear Science [2,3]. The radiation had the characteristics of the CCR-MCP, that is, the power of the radiation was proportional to the height of the hollow conical dielectric and a delay corresponding to the refractive index of the hollow conical dielectric was observed. To identify this radiation as the CCR-MCP, it was necessary to indicate that phase matching condition on the base of the hollow conical was satisfied when the apex angle of the hollow conical is half of the Cherenkov angle. Therefore, we investigated the dependency of the CCR-MCP on the apex angle.

EXPERIMENTS: High-density polyethylene (HDPE) was used as a material for the hollow conical dielectric. To prevent the electron beam from colliding with the hollow conical dielectric, the inner diameter of the hollow conical dielectric was set to be 16 mm. An aluminum collimator with an aperture diameter of 12 mm was installed in front of the hollow conical dielectric. Because the refractive index of the HDPE was 1.53 in the terahertz (THz) region, theoretical value of the apex angle satisfying the phase matching condition on the basal plane of the hollow conical dielectric was 24.6 degree. CCR beam generated in a hollow conical dielectric which did not satisfied the phase matching condition spread on a conical surface. It was difficult to transport the CCR beam without losing the power. Then, we have prepared hollow conical dielectrics with apex angles of 20 and 30 degrees in addition to the apex angle of 24.6 degree. Matching the effective length, at which the electron beam generated the CCR extracted on the basal plane, for each hollow conical dielectric, the heights of the hollow coni-cal dielectric were 60.4, 55, and 50 mm for the apex an-gles of 20, 24.6, and 30 degrees, respectively.

In the experiments, the electron energy was set to be 40 MeV and the electron-beam current was approxi-mately 0.18 mA. The duration and the repetition fre-quency were 22 ns and 30 Hz, respectively. The CCR was detected by a silicon bolometer and a Martin-Puplett in-terferometer with a step interval of 100 μm.

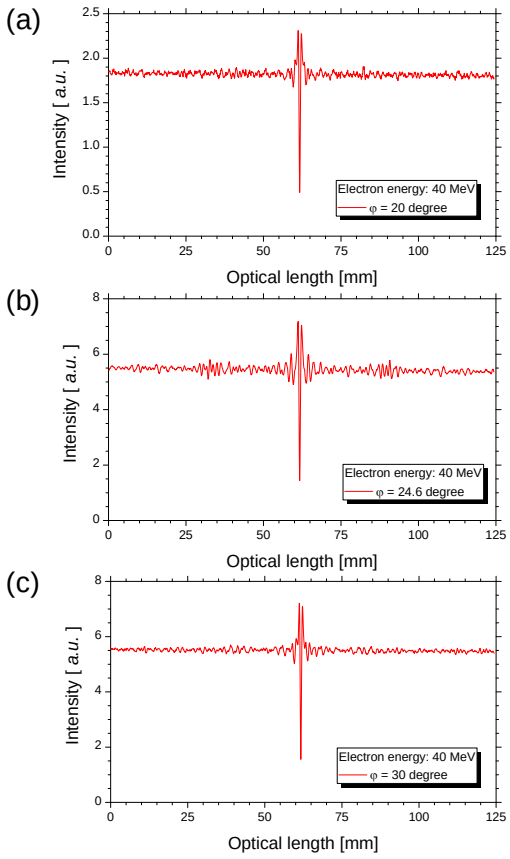

Fig. 1 Measured interferograms for the apex angles of (a) 20, (b) 24.6, and (c) 30 degrees.

RESULTS: Because the CCR passes through the dielectric, it delays the time to reach the detector compared to coherent diffraction radiation (CDR) generated at the exit of the aluminum collimator. As Fig. 1 shows, interference waveforms by the CCR and the CDR appeared at positions away from the center burst in the interferogram only when the apex angle was 24.6 mm. The distance between the interference waveform and the center burst is equal to the optical path difference between the CCR-MCP and the CDR considering the diffractive index of the HDPE. These experimental results demonstrate that the CCR-MCP can be observed only when the apex angle satisfies the phase matching condition. A series of experiments have shown that the theory of the CCR-MCP can describe the characteristics of the observed THz-waves. We plan to develop a high-power THz-wave source based on the principle of the CCR-MCP using high-quality electron beams in an advanced accelerator facility in the future.

REFERENCES:

[1] N. Sei *et al*., Phys. Lett. A **379** (2015) 2399.
[2] T. Takahashi *et al*., Phys. Rev. E **62** (2000) 8606.
[3] N. Sei and T. Takahashi, Sci. Rep. **7** (2017) 17440.

CO12-3 Neutron Activation Analysis for the stability monitoring of reference materials

T. Takatsuka, K. Hirata, Y. Iinuma[1], R. Okumura[1], and K. Takamiya[1]

National Metrology Institute of Japan, National Institute of Advanced Industrial Science and Technology
[1]Institute for Integrated Radiation and Nuclear Science, Kyoto University

INTRODUCTION: For high-performance silicon semiconductor devices, dopants are ion–implanted at lower energy to make shallower electric junctions. Dopant concentration should be controlled in 2 % as indicated in the international technology roadmap for semiconductors (ITRS) 2013 [1]. Several techniques, such as secondary ion mass spectrometry (SIMS) and Rutherford backscattering spectrometry (RBS), are widely used for characterizing the depth profiles of dopant concentration. In order to quantify the dopant concentration by these techniques, reference materials are required for calibration. Thus, certified reference materials (CRMs) of shallow arsenic implants in silicon were developed at the National Metrology Institute of Japan (NMIJ) [2].

This study aims to monitor arsenic quantity in the CRM by neutron activation analysis (NAA), and to confirm the reliability of the CRM.

EXPERIMENTS: For the fabrication of CRM, arsenic ions were implanted into Si(001) wafers at an energy of 10 keV and the nominal dose of 3×10^{15} /cm^2. The wafers were diced into 15 × 15 mm squares pieces by dicing saw. Several specimens were picked-up randomly at each time of the monitoring.

Arsenic amounts were evaluated by NAA with an internal standard method. For the production of standards to calibrate arsenic amounts, a working standard solution was prepared by diluting SRM 3103 (commercially available from NIST) gravimetrically. In addition, a standard solution for internal standard was prepared by diluting gold standard solution (SRM 3121) gravimetrically. A portion of the gold solution was dropped from a polyethylene pipette onto a cleaned filter paper on the CRM specimen. Portions of mixed solution (arsenic and gold standards) were dropped onto cleaned filter papers for the standards. All specimens and standards were heat-sealed in individual clean poly-ethylene envelopes and stacked in a poly-ethylene irradiation container. The neutron irradiation was performed for two hours with a 5.5×10^{12} cm^{-2}·s^{-1} thermal neutron fluence rate at Pn-2 in research reactor KUR of Institute for Integrated Radiation and Nuclear Science, Kyoto University. Gamma-ray activity of each specimen and standard was measured by a high-purity germanium detector (CANBERRA).

RESULTS: Figure 1 shows a gamma-ray spectrum obtained from the CRM specimen with gold internal standard solution. The peaks at around 559 keV from ^{76}As and 412 keV from ^{198}Au were focused to determine arsenic amount in the specimens. The counts in each peak were integrated for every specimen and standard, and then the intensities after the decay correction [3] were used to calculate relative intensities (^{76}As cps) / (^{198}Au cps/ ng). The arsenic content in the specimen is estimated from the calibration curve.

The monitoring results of arsenic area density are summarized in Fig. 2. The quantified values agree with each other on certification (●) and on monitoring (■), considering the uncertainties indicated with error bars. This shows the stability of the CRM for at least 8 years.

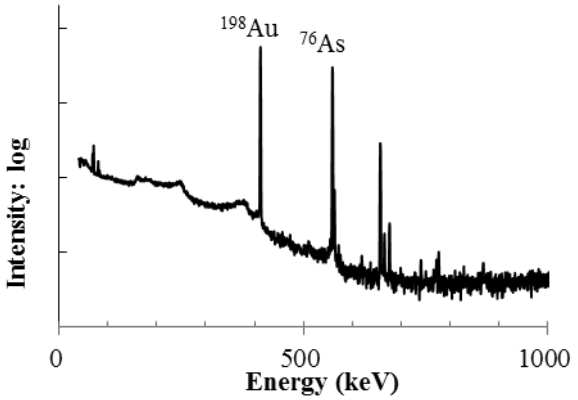

Fig. 1. Gamma-ray spectrum of the specimen with gold standard solution.

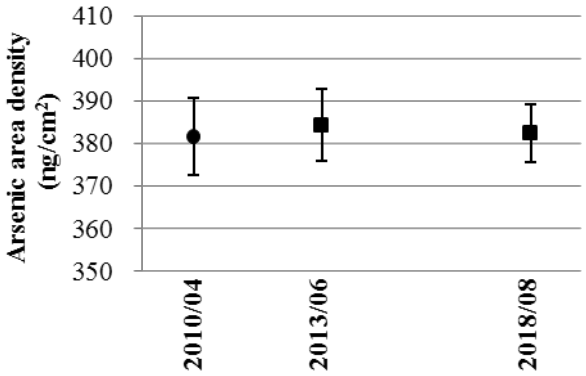

Fig. 2. The monitoring results of arsenic area density.

REFERENCES:

[1] International Technology Roadmap for Semiconductors 2013.
[2] Certificate of NMIJ-CRM 5603-a: Low energy arsenic implanted silicon, NMIJ / AIST.
[3] G.Gilmore and J. D. Hemingway, Practical gamma-ray spectrometry (John Wiley & Sons, Chichester, 1995.

CO12-4

Friction Reduction by the Combination Use of MoDTC and Organic Friction Modifier

T. Hirayama, N. Kikuchi[1], Y. Sasaki[1], M. Hino[2]

Dept. of Mechanical Eng., Doshisha University
[1]Dept. of Mechanical Eng., Graduate School of Doshisha University
[2]Institute for Integrated Radiation and Nuclear Science, Kyoto University

INTRODUCTION: Engine oil is a blend of base oil such as mineral oil and synthetic oil with additives, and it contributes to saving fuel by reducing the friction loss of the engine. Therefore, among various additives, those having a friction reducing effect under boundary lubricated conditions are blended in the engine oil, of which molybdenum dithiocarbamate (MoDTC) is particularly effective. MoDTC is known to produce a boundary lubrication layer containing molybdenum disulfide (MoS_2), which is effective for reducing friction. In addition, it is recently expected that a system using a combination organic friction modifier (OFM) that has no phosphorus in its molecule and MoDTC will alleviate environmental problems and obtain a sufficient friction reducing effect. The lubrication properties under boundary lubricated conditions are greatly influenced by the interfacial structure of the boundary lubrication layer formed by additives. Therefore, the interfacial structure formed by the combination use of MoDTC and OFM and its nanotribological properties were investigated in this study.

EXPERIMENTS: In this study, the oil in which MoDTC (0.3 mass%) and OFM is added to the base oil was used as the lubricating oil model. Hexadecane and palmitic acid (0.1 mass%) were used as models for the base oil and OFM. For neutron reflectometry (NR), deuterated palmitic acid, was used for the purpose of facilitating the analysis since a clear difference occurs in the reflectivity profile between hydrogen and deuterium.

We used the time-of-flight (TOF) type neutron reflectometer SOFIA installed at the J-PARC in Tokai, Ibaraki. In order to grasp the film thickness and density of the boundary lubrication layer formed on the Cu surface under each system added alone or in combination, experiments were conducted to obtain the reflectivity profile under each case.

RESULTS: First, we conducted the NR experiment to investigate the boundary layer structure formed by *d*-palmitic acid. When *d*-palmitic acid was added, the fringe interval became short; as a result of the analysis, it was found that an adsorption layer having a thickness of about 2.1 nm was formed on the copper surface immediately after the addition of *d*-palmitic acid. The SLD value of *d*-palmitic acid at the bulk state was 6.7×10^{-6} Å^{-2}, whereas the analysis value was 2.1×10^{-6} Å^{-2}. From this, the density of the adsorption layer was approximately 30% with respect to the bulk density. From 0h to 2h, the fringe interval did not change; it indicated that the film thickness and the density of the adsorption layer by *d*-palmitic acid barely change with time.

For the combined system being used, measurements were carried out under the three cases described below. [Case 1]: Measurement was carried out for four hours after placing hexadecane+*d*-palmitic acid (0.1 mass%) + MoDTC (0.3 mass%) into the sample holder. [Case 2]: Measurement was carried out for two hours after hexadecane+*d*-palmitic acid (0.1 mass%) was placed in the sample holder. After the measurement, the sample holder was rinsed with hexadecane, and hexadecane+ MoDTC (0.3 mass%) was added, and then the measurement was carried out for four hours. [Case 3]: Measurement was carried out for four hours after hexadecane+MoDTC (0.3 mass%) was placed in the sample holder. After the measurement, the sample holder was rinsed with hexadecane, and hexadecane+*d*-palmitic acid (0.1 mass%) was added, and then the measurement was carried out for two hours.

As a result of analysis of [Case 1], it was found that an adsorption layer with a thickness of about 2 nm and a density of approximately 30% with respect to the bulk density was formed immediately after *d*-palmitic acid was added. Although the film thickness did not change with time, the density increased to about 60% in four hours. When MoDTC is added first, film thickness and density cannot be detected since MoDTC was not deuterated. However, from the NR experiment of [Case 3], it can be seen that immediately after the addition of *d*-palmitic acid, an adsorption layer having the 2-nm film thickness and the approximately 30% density with respect to the bulk density is formed. While no change in film thickness with time was observed, the density increased from about 30% to about 45% in 2 hours. This result is shows the same tendency with as [Case 1]. In addition, it is interesting to note that the nanotribological property measured by SiO_2 colloidal probe was better when we used MoDTC and palmitic acid in combination than that when we used only MoDTC or palmitic acid each. It indicated that the combination use of MoDTC and OFM is effective for friction reduction by forming thicker boundary lubrication layer.

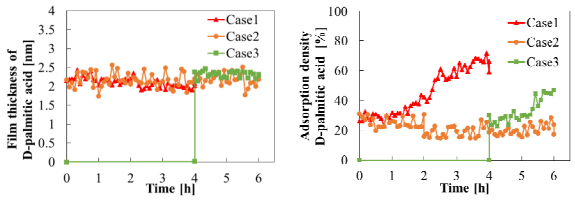

Fig. 1. Estimated film thickness and density of palmitic acid by neutron reflectometry for the three cases.

CO12-5 Strutctural studies of water-solubule menaquinone-7 from *Bacillus subtilis natto*

T. Chatake, T. Saito, K. Morishima, R. Inoue, M. Sugiyama, T. Kikkou[1], O. Matsumoto[1], R.Takayama[1], Y. Yanagisawa[1]
Institute for Integrated Radiation and Nuclear Science, Kyoto University
[1]Faculty of Pharmacy, Chiba Institute of Science.

INTRODUCTION: Natto is a popular fermented food in Japan. In manufacturing process of natto, *Bacillus subtilis natto* (BSN) produces various biologically active substances, which contribute to health. Especially, this bacterium produces a large quantity of menaquinone-7 (MK-7), which is a kind of vitamin K that contribute to osteogenesis [1] and blood coagulation [2]. While MK-7 is a fat-soluble compound, BSN produces a water-soluble complex of MK-7 (*natto*-MK-7) [3,4]. This property is the attractive point in application uses of *natto*-MK-7. Previously, it was reported that the size of *natto*-MK-7 was estimated to be ~100 kDa by size-exclusion chromatography [3,4], and that small peptides with the size of ~3 kDa (called K-binding factor in [4]) in *natto*-MK-7 contribute to water solubilization of MK-7 [4]. However, the further structural information had not been reported after reports of Ikeda and Doi [4]. The aim of our study is to reveal the structural mechanism of the water solubilization of *natto*-MK-7. Last year, we reported the established protocol of the purification and preliminary structural analysis *natto*-MK-7 [5]. In the present study, we further refined the purification protocol of *natto*-MK-7 and performed various analyses using highly purified *natto*-MK-7.

EXPERIMENTS: *Bacillus subtilis natto* (miyagino strain) was cultured in liquid medium, and the cultured medium was concentrated to 24 mL. 21 mL of the 24 mL was used for purification. Purification was carried out by a series of fast protein liquid chromatography (FPLC). The first FPLC was an ion exchange chromatography using the couple of DEAE sepharose FF with the column volume (CV) of 5 mL. The coupled columns (CV = 10 mL) were equilibrated by 20 mM Tris-HCl and 0.3 M NaCl buffer. Prior to injection, the salt concentration of the sample solution was adjusted by adding 9 mL of 1 M NaCl buffer solution (20 mM Tris-HCl (pH7.6)), then the sample solution was directly injected to the coupled column to avoid any damage on FPLC system. After the injection, the column was connected to the FPLC system. After 5 CV wash by 20 mM Tris-HCl and 0.3 M NaCl buffer, *natto*-MK-7 was eluted from the column by the gradient elution method, where NaCl concentration was gradually increased from 0.3 M to 1.0M during 10 CV. The second and third chromatography were carried out using another couple of DEAE sepharose FF columns. Before each injection, the NaCl concentration of the *natto*-MK-7 solution was adjusted to be below 0.3 M by adding the same volume of 20 mM Tris-HCl buffer (pH7.5). Wash and gradient protocols were same as the first chromatography. The final purification was performed by size-exclusion chromatography using GE Hiprep 16/60 sephacryl S-300. 2.5 mL of the eluted natto-MK-7 solution was injected to the column, and the chromatography was carried out with the rate of 0.4 mL/min using 20 mM Tris-HCl buffer (pH7.6) containing 0.1 M NaCl. Confirmation of the presence of *natto*-MK-7 was done by measuring MK-7 activity of each fraction eluted from the size-exclusion chromatography. The fraction was processed with hexane and analyzed by the high-performance liquid chromatography as reported previously [3,6].

RESULTS: In chromatography charts in the first and second FPLC, the elution curves of natto-MK-7 were not symmetrical, and MK-7 activities were observed in the fractions of the wash process while the activity was hardly observed in the second and third wash process. These results suggested the presence of the other structural type of *natto*-MK-7 than the purified *natto*-MK-7 in this experiment, although the present purified *natto*-MK-7 is the main product of *Bacillus subtilis natto*. ~11% of highly-purified *natto*-MK-7 could be obtained from the concentrated cultured medium by three times ion-exchange chromatography. Moreover, the *natto*-MK-7 has different sizes. In the final purification step by the size exclusion chromatography, large particles were observed as shown in Fig. 1. The activity of MK-7 were also confirmed in them, suggesting that the *natto*-MK-7 naturally aggregate. These structures were investigated by dynamic light scattering (DLS), analytical centrifugation (AUC) in IRNS, and atomic force microscopy (AFM) in Chiba institute of science. The further discussion is in progress.

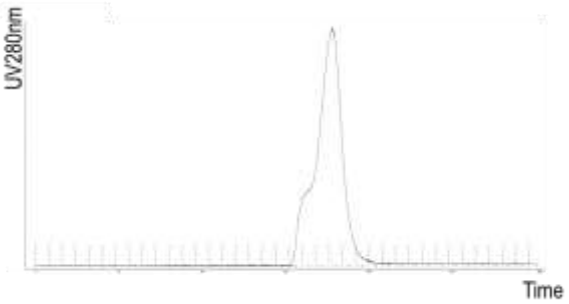

Fig. 1. The chart of the size-exclusion chromatography

REFERENCES:

[1] P.V. Hauschka, J.B. Lian, P. M. Gallop, Proc. Nat. Acad. Sci. USA **72** (1975) 3925–3929.
[2] H. Dam, Biochem. J. **29** (1935) 1273–1285.
[3] H. Sumi et *al.*, Clinical Pharmacology and Therapy **18** (2008) 297–305.
[4] H. Ikeda, Y. Doi, Y. Eur. J. Biochem. **192** (1990) 219–224.
[5] T. Chatake *et al.*, J. Food. Biochem. **42** (2018) e12630.
[6] Y. Yanagisawa, H. Sumi, H. J. Food. Biochem. **29** (2005) 267–277.

CO12-6 Neutron Activation Analysis of Cultivated Oysters in Miyagi Prefecture

M. Fukushima[1], A. Chatt[2], Y. Iinuma[3] and T. Maeda[1]

[1]*Department of Food and Environment, Ishinomaki Senshu University*

[2]*Department of Chemistry, Dalhousie University*
[3]*KURNS, Kyoto University*

INTRODUCTION: Miyagi Prefecture is the second largest producer of cultivated oysters in Japan, and most of the cultivated bays are located in northern part of Miyagi. Mating season of oysters in Miyagi Pref. is July-August due to preferred sea water temperature. Weight of soft tissues of oysters changes drastically before and after the mating season. No data are available on the element levels of oysters before and after the mating season. Selected trace element levels of soft tissues before and after the mating season were analyzed using neutron activation analysis (NAA). Bioaccesible fraction of trace elements in soft tissues of oysters was also estimated to investigate any seasonal variation. We have collected cultivated oysters from seven different bays in Dec. 2003 – Oct. 2005 and analyzed trace elements. Geological and marine environment in Pacific side of Tohoku district have drastically changed by earthquake and tsunami in 3.11, 2011. We have collected cultivated oysters from seven different bays in Miyagi, and analyzed trace elements to compare the effect of earthquake and tsunami.

EXPERIMENTS: 1) Samples: Oysters, estimated birth month were July 2012 and 2013, were collected from Higashimatsushima, Miyagi every month between April to September in 2014. Soft tissues of each 5 oysters were separated from their shells, separated to hepatopancreas, muscle, gill, and mantle, freeze dried, and pulverized. Another group of oysters were collected from Tanoura, Shizugawa, Nagatsurahama, Ogatsu, Ohishihama, Obuchi, and Higashimatsushima in Miyagi in May 2015. Soft tissues were treated same way as written above.
2) Analysis of Bioaccesible Levels of Elements in Oyster Tissue: One gram of soft tissue (dried powder) was incubated for 15 min at 95℃ with 0.10 ml of α-Amilase, 30 min at 60℃ with 0.10 ml of 50 mg/ml Protease, then 30 min at 60℃ with 0.10 ml of Amyloglucosidate. Precipitate was filtered after adding ethyl alcohol, freeze dried, and pulverized.
3) NAA: Samples were irradiated in KUR for 1 min in TcPn, and measured gamma spectra for 5 min after 1.5 min decay, or 1 hr in Pn and measured for 30 min after 1 month decay.

RESULTS: 1) Sample weight: Average weight of soft tissues were 2.8, 6.2, 6.8, 2.6, 3.5, 6.0, 15.2, 26.4, 42.2, 6.8, 25.1, and 33.3 g (wet weight) for 10-15 and 21-26 months after the birth, respectively. Both of 2.6 g and 6.8 g were obtained for oysters collected July 2014 and the reason of the decrease might be the mating season.
2) Seasonal variation of elements: Zn, Fe, Ag, Se, and Sc showed peak in July for the seasonal variations of elemental levels in hepatopancreas of oysters. Example for Zn is shown in Fig. 1. Zn level showed peak in July, but the mass showed peak in June and it decreased in July.
3) Bioaccesible fraction of elements: Bioaccesible levels of Zn, Fe, Ag, and Sc were almost proportional to total levels in soft tissues. Example for Zn is shown in Fig. 2. Both of 12 and 25 months were July, and both of total and bioaccesible levels showed peaks in 12 and 25 months.
4) Locational Variation of element levels in oysters: When we have analyzed oysters collected in 2003-2005, all the elements analyzed showed lowest levels in hepatopancreas, mantle, gill, and muscle from Nagatsurahama. In this work, all the element levels in organs from Nagatsurahama showed same levels as other 6 bays. In seven bays, geological condition of Nagatsurahama has changed most compared other six bays.

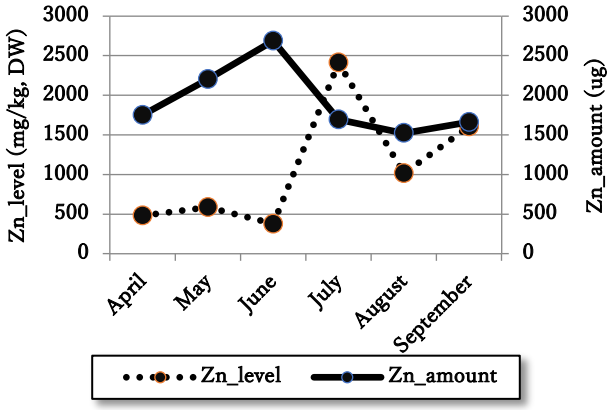

Fig. 1 Relation ships between Zn level and amount in hepatopancreas of seasonal variation.

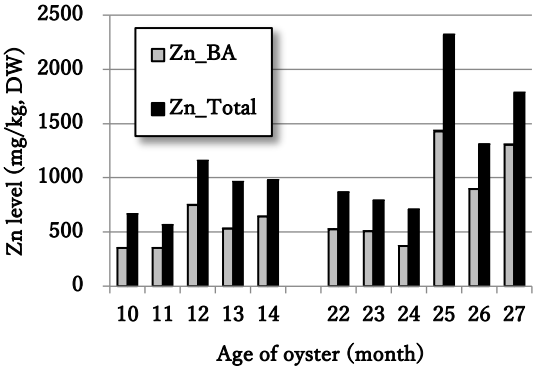

Fig. 2 Seasonal variations of total and bioaccesible levels in soft tissues.

Acknowledgement: We thank to Mr. Watanabes and Marine Technology Center of Miyagi Prefecture for supplying oyster samples for us. We also thank to Dr. Takeshige Matsutani in Ishinomaki Senshu University for discussion with us.

CO12-7 **Monuments of contaminated objects and memories**
Nagadoro Area, Iitate Village, Fukushima

M. Takagaki
Neurosurgery, Louis Pasteur Center for Medical Research
Graduate School of Human and Environmental Study, Kyoto University

I participated in a field research of a media that covers temporary returning home of villagers in Iidate Village, Fukushima, which is still a restricted area for their highly radioactive area (photo. 1). Mr. and Mrs. K. have engaged in cutting out the abundant granite in the area, and took over the business of forming tombstones, etc. until the time of the earthquake after their marriage. Their daily living have been still forced to a refuge because of highly contaminated radioactive areas, but even the aging population, the intention to return to the village has been fading out. In this time, I will report my joint research with the media in victim's temporary returning home.


Photo 1

It was as if time had stopped in the house after the earthquake. Calendar shows March 2011. The radioactivity in front of the home entrance exceed 30 μSv / hr.

Mrs. K's narrative:

Mrs. K, do you still have a mind to come home to live here?

"No, I'm not ready to go home because I came to my daughter-in-law to this home and I don't stick to my home. It's already difficult to put in the artificial joints of my knee last month, and it's already past a year."

"Hmm, this is my room, I want to know the current radiation activity here." (Mrs. K does not get out from her room to join the media group, she does not move away from her own room.)
Mrs. K's room faces the back yard mountain and the radiation is relatively high even in the room.

"I eager to know about the radioactivity of my photos and Kimonos that is a memory of my young era."

"OK. I'll tell the media to come to measure their radiation activity. And they immediately said to Mrs. K that your items did not polluted."

"Oh-good, the photos is not radioactive, you can bring them back to your home"

"Congratulations!"

"Kimono is also good?, ... (while showing a picture of Japanese dance in a kimono, ...)"

It's also good!

"Oh, I feel bliss."


Photo 2

After that, Mrs. K always carried the photo album with her during stay in the field (Photo 2).

Although we can give up on things, the monuments of memory cannot be erased. Mrs. K must have realized a disaster recovery by recovering her album. The figures measured in the field were not just physical quantities, but, for Mrs. K, the figures themselves must have been her recovered memories themselves that were not polluted. Disaster recovery may be to arrange memory on the line to the future and recover one's life by means of material recovery from the dark spots.

To see a world in a grain of sand.
And a heaven in a wild flower, Hold infinity
in the palm of your hand.
And eternity in an hour. *By William Blake*

Acknowledgment: This study has been financially supported by National Research Fund No. 17Ki8536 2017-19 from the Ministry of Education, Culture, Sports, Science and Technology, Japan.

30045

CO12-8 Development of neutron imager based on hole-type MPGD with glass capillary plate

F. Tokanai[1], R. Itoh[2], T. Moriya[1], T. Sumiyoshi[3], H. Kondo[4], H. Sugiyama[4], M. Hayashi[4], T. Okada[4], M. Hino[5]

[1]*Faculty of Science, Yamagata University*
[2]*Graduate School of Science and Engineering, Yamagata University*
[3]*Graduate School of Science, Tokyo Metropolitan University*
[4]*Electron Tube Division, Hamamatsu Photonics K. K.*
[5] *Institute for Integrated Radiation and Nuclear Science, Kyoto University*

INTRODUCTION: Neutron imaging is useful for light elements in the sample such as hydrogen, lithium, boron, carbon, and nitrogen. Owing to their unique ability to probe inside samples, neutrons have been widely utilized for neutron radiography in various fields, including fundamental science, archaeology, and industry.

High position resolution with a moderate effective area is required in practical applications of neutron imaging. We have been developing a high-spatial-resolution neutron gas scintillation imager (n-GSI) with a capillary plate gas detector (CPGD) [1]. Fig. 1 shows the operating principle of the CPGD. The detector consists of a conversion layer containing ^{10}B and a CP placed in a vessel. The vessel is filled with neon or argon gas mixtures. A ^{10}B converter is directly mounted on the inlet surface of the CP. Charged particles (α-rays and ^{7}Li nuclei) are generated by a nuclear reaction between incident neutrons and the ^{10}B. Since the ^{10}B converter is directly mounted on the inlet surface of the CP, the track length of the charged particles is restricted to within the capillary. Thus, the spatial resolution of incident neutrons is expected to be close to the capillary diameter.

The performance of the n-GSI was investigated using the cold neutron beam line CN-3 installed to the Kyoto University Reactor (KUR).

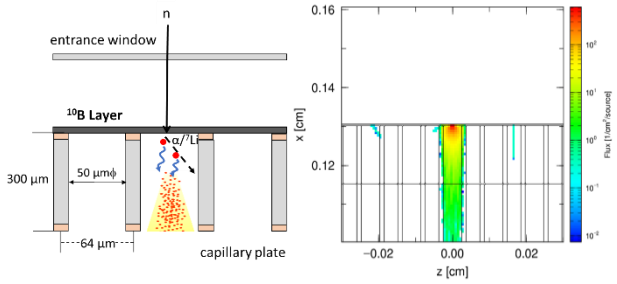

Fig. 1. Principle of the n-GSI and result of simulation using PHITS code [2].

EXPERIMENTS: Fig. 2 shows the experimental setup of the n-GSI. It consists of a CPGD filled with Ne (90%) and CF_4 (10%) gas mixture at 1 atm, mirror and lens optics, an image amplifier unit, and a cooled CMOS camera system. The CPGD consists of a converter layer and a CP in a sealed-type vessel [3]. The converter consists of a 2-μm-thick B_4C layer on a silicon substrate [4]. The converter is directly mounted on the CP. The CP has an effective diameter of 27 mm and a thickness, individual hole diameter, and pitch of 300 μm, 50 μm, and 64 μm, respectively. The neutron wavelength giving the maximum intensity and the total flux of the CN-3 guide tube were 2 Å and 3.8 × 10^6 neutron cm^{-2} s^{-1}, respectively. The n-GSI system was placed 300 mm from the downstream exit of the neutron guide. The neutrons were irradiated into a sample.

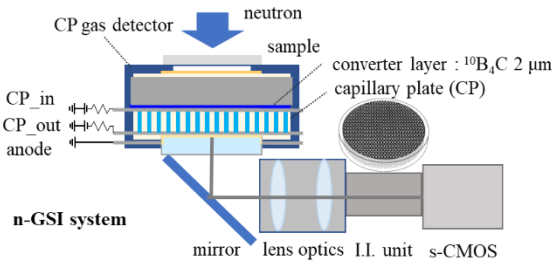

Fig. 2. Schematic view of n-GSI and experimental arrangement for evaluating performance using neutron beams from KUR.

RESULTS: Fig. 3 shows a neutron transmission image of a photomultiplier tube (PMT; Hamamatsu R9875) obtained using the n-GSI system [5]. The exposure time was 300 s. The structure of the dynode in the PMT is clearly seen in this image. Moreover, it is recognized that the neutrons are highly absorbed in the borosilicate glass compared with synthetic silica. This is because the borosilicate glass contains a large amount of boron, and hence the isotope of ^{10}B, as the main glass constituent.

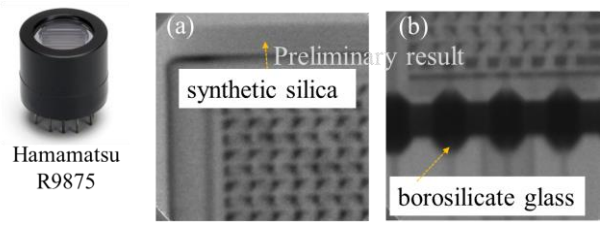

Fig. 3. Neutron transmission image of a photomultiplier tube (Hamamatsu R9875) obtained using the n-GSI system.

REFERENCES:

[1] T. Sumiyoshi *et al.,* Hamon 27 (1) (2017) 16-19.
[2] T. Sato *et al.,* J. Nucl. Sci. Technol. 55 (2018) 684.
[3] H. Kondo *et al.,* Plasma Fusion Res. 13 (2018) 2406018.
[4] M. Hino *et al.,* Nucl. Instrum. and Methods. A 797 (2015) 265.
[5] H. Kondo *et al.,* VCI 2019 conference.

CO12-9 Radius of Gyration of Polymer for Viscosity Index Improver at Various Temperatures Evaluated by Small-Angle X-Ray Scattering

T. Hirayama, R. Takahashi[1], K. Tamura[2], N. Sato[3], M. Sugiyama[3], M. Hino[3], Y. Oba[4]

Dept. of Mechanical Eng., Doshisha University
[1]Dept. of Mechanical Eng., Graduate School of Doshisha University
[2] Idemitsu Kosan Co., Ltd.
[3]Institute for Integrated Radiation and Nuclear Science, Kyoto University
[4]Japan Atomic Energy Agency

INTRODUCTION: Lubricating oils are necessary for friction reduction and high wear durability of sliding surfaces in machine components, and the development of the best oils is strongly required from industry. Viscosity index improver (VII) is a kind of additives for relieving the reduction of viscosity of lubricating oil due to temperature rise. Classical textbooks say that the VII molecules work with changing their equivalent radius in base oil in accordance with oil temperature. However, there are only few papers investigating the equivalent radius of VII molecules by small-angle X-ray scattering (SAXS) and/or small-angle neutron scattering (SANS)[1], and there is still room for discussion of the behavior and working mechanism of VII molecules in oil. This study tried to investigate the radius of gyration of several kinds of VII polymers in base oil at various temperatures by SAXS, and the behavior of polymers was investigated and discussed.

EXPERIMENT: To investigate the radius of gyration of VII polymer, we used a SAXS instrument (NANOPIX, Rigaku) with a Cu-target X-ray source emitting X-ray with a wavelength of 1.54 Å, a characteristic line of Cu-Kα. The 1.2 mm-thick aluminum cell having optical windows made of 20-μm thermally-resistant engineering plastic film (Superio-UT, Mitsubishi chemical) was used for the measurement. The cell temperature increased to be 25, 40, 60, 80 and 100ºC in turn, and the last measurement was carried out at 25ºC again after cooling for checking if the VII molecule degenerated or not by heat. Poly(methyl acrylate) (PMA) type VII, as shown in Fig. 1, was prepared as a typical one used in engine oil in the study. Squalane was used as a model base oil, and the concentrations of PMA into squalane were 0.5, 1.0 and 2.0 mass%.

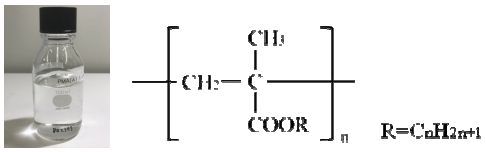

Fig. 1. Chemical structure of PMA type VII.

RESULTS AND DISCUSSION: The SAXS intensity profiles versus scattering vector q from squalane with 0.5 mass%-PMA type VII at each temperature were shown in Fig. 1, for example. The profiles were obtained by subtracting the intensity profiles from pure squalane at each temperature previously measured with the same liquid cell. The radius of gyration R_g and absolute intensity at the origin I_0 estimated from the Guinier plot are shown in Fig. 2. We can see that the intensity profiles had little change even if the temperature changed, and therefore the estimated R_g was almost constant in the observed range regardless of temperature rise. This result contradicts the fact that the PMA effectively work as VII. Meanwhile, it is interesting to note that I_0 gradually decreased in accordance with temperature rise. These facts indicate that the side chains of PMA molecules swell and expand in the squalane when the temperature rises, and then the core size of molecules estimated as R_g are almost constant while the I_0 decreased because the apparent atomic density for X-ray scattering decreased because of the side chain swelling in squalane. SANS will be tried to confirm the validity of this prediction as a next step.

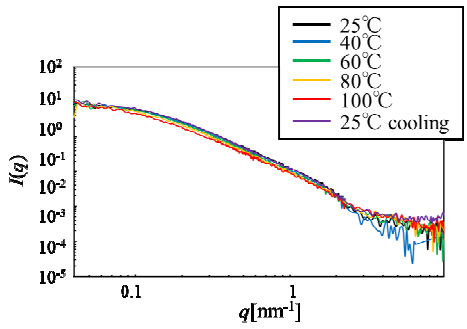

Fig. 1. SAXS profiles from squalane with 0.5 mass%-PMA type VII at various temperatures.

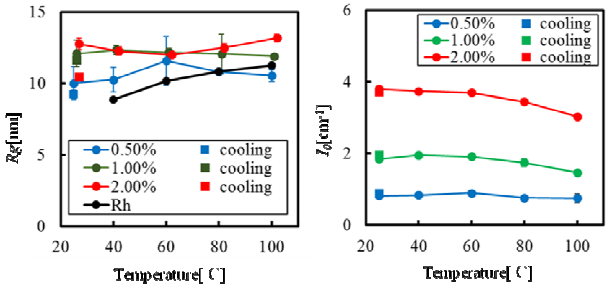

Fig. 2. Estimated Rg and I0 from Guinier plot of squalane with PMA type VII with various concentrations.

REFERENCES:

[1] M. J. Covitch, K. J. Trickett, How Polymers Behave as Viscosity Index Improvers in Lubricating Oils, Adv. Chem. Eng. Sci., 5 (2015) 134.

CO12-10 Study of Isotope Separation via Chemical Exchange Reaction

R. Hazama, T. Yoshimoto, Y. Sakuma[1], T. Fujii[2], T. Fukutani[3], Y. Shibahara[3]

Graduate School of Human Environment, Osaka Sangyo University
[1]Laboratory for Advanced Nuclear Energy, Tokyo Institute of Technology,
[2]Graduate School of Engineering, Osaka University
[3]Institute for Integrated Radiation and Nuclear Science, Kyoto University

INTRODUCTION: A liquid microspace formed by simple introduction of organic and aqueous phases into microchannel provides unique features of short molecular diffusion distance (T) and large specific interfacial area (S/V), which gives a fast and high conversion than that given by strong stirring and the other conditions for any macroscale reactions: S/V=200 & T=0.1s for 100μm [1].

EXPERIMENTS: Isotopic enrichment occurs according to the following chemical exchange reaction:

$$^{40}Ca^{2+}_{(aq)} + {}^{48}CaL^{2+}_{(org)} \rightarrow {}^{48}Ca^{2+}_{(aq)} + {}^{40}CaL^{2+}_{(org)} \quad (1)$$

where L represents macrocyclic polyether(18-crown-6). An aqueous solution (3M $CaCl_2$) and organic solution (0.7M DC18C6 in chloroform) were stirred by a single Y type microchip with 40 mm junction length (Fig. 2) at room temperature and separated. A stable liquid-liquid interface (Fig. 3) was formed by the introduction through two inlets of the microchip by microfluidic flow controller (Fig. 1). The output volume of one mL can be obtained by 30μl/min flow-rate for about 30 min.

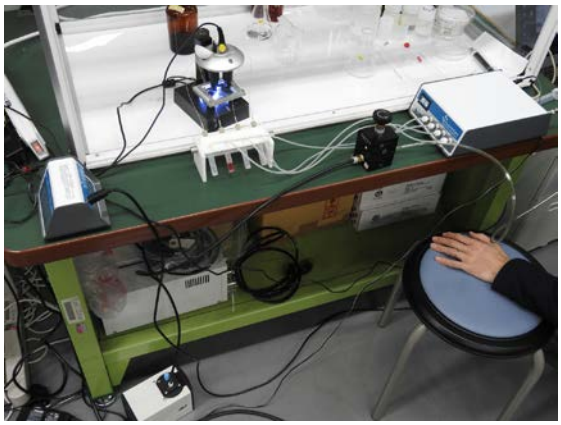

Fig 1. Photographs showing fast and high conversion phase-transfer tabletop system exploiting the liquid-liquid interface formed in a glass microchannel chip on microscope, microfluidic flow controller (MFCS-EZ), flow-rate sensors and air compressor of 0.7MPa.

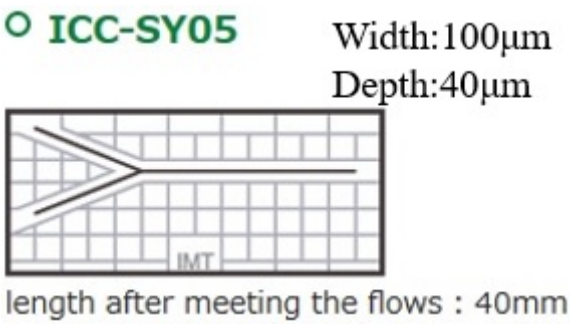

Fig 2. Single Y type microchip (ICC-SY05) with microchannel 100 μm wide, 40 μm deep and 4 cm length provided by IMT(Institute of Microchemical Technology Co., Ltd), which is made of borosilicate glass.

Fig 3. Laminar flow was formed by two solvents of aqueous(Right)-organic(Left) multiphase flow.

RESULTS: The Ca concentration in aqueous and organic phase for the laminar-flow was measured by ICP-MS. We obtained a similar value of about 20 % partition factor with the batch LLE process [2] and its Ca transfer between two phases without any stirring for only 0.3 sec (6000 times faster than [2]) on a chip, shown in Fig. 4.

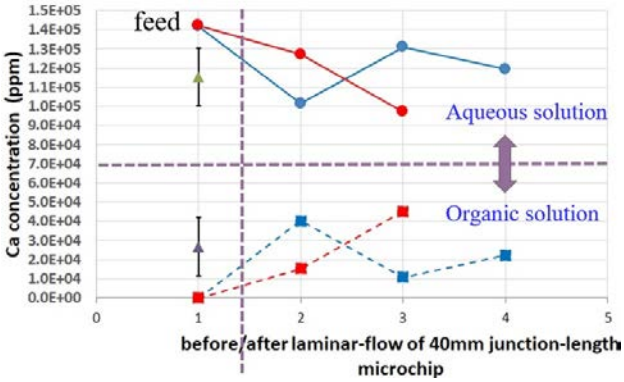

Fig 4. Ca concentration in aqueous phase (circle) and organic phase (square) for the laminar-flow of 4cm junction-length microchip. Triangle with error bar is the average of 2 – 4 after the reaction, 1 is feed solution for $CaCl_2$ aqueous and crown-ether organic ($CHCl_3$) phase.

REFERENCES:

[1]H. Hisamoto *et al.*, Chem. Commun. (2001) 2662.
[2]R. Hazama *et al.*, KURRI Progress Report 2017, 104.

CO12-11 Instrumental Neutron Activation Analysis of Iridium in a Chemical Reagent

T. Miura[1], R. Okumura[2], Y. Iinuma[2], S. Sekimoto[2], K. Takamiya[2]

[1]*National Metrology Institute of Japan, AIST*
[2] *Institute for Integrated Radiation and Nuclear Science, Kyoto University*

INTRODUCTION: National Metrology Institute of Japan (NMIJ) is responsible for developing certified reference materials and for establishing the traceability of SI (The International System of Units) on chemical metrology in Japan. To establish SI traceability, the primary method of measurements should be applied to the characterization of the certified reference materials. Recently, neutron activation analysis using comparator standard is recognized as a potential primary ratio method [1]. Despite the potential of neutron activation analysis as primary ratio method, the evaluation of the measurement uncertainty is required in any analysis. In general, there are three main components of uncertainty in neutron activation analysis, that is, sample preparation uncertainty, neutron flux homogeneity, and gamma ray measurement uncertainty. Usually, flux monitor is used to correct the neutron flux in-homogeneity. However, although the flux monitor can correct the neutron flux variation using the count rate of the known amount of the monitor nuclide, it does not reflect the neutron flux of the actual sample. The most practical method to eliminate neutron flux in-homogeneity and to improve gamma ray measurement uncertainty is an internal standard method [2-4]. For the development of primary inorganic standard solution as national standard, the purity of starting material has to be determined. The purity of starting material has to be determined for the development of primary inorganic standard solution as national primary standard. Recently, the needs of development the primary standard solution of precious metal including Rh, Pd, Ir, Os and Pt is increased from Japanese industry. However, it is well known that dissolution of high purity Iridium metal as most difficult case. And so, the purity of Iridium reagent an easy dissolution form was verified using instrumental neutron activation analysis. In this study, we presented that capability of instrumental neutron activation analysis for determination of Ir in high purity Iridium(IV) Bromide ($IrBr_4$).

EXPERIMENTS: The high purity $IrBr_4$ was purchased from Alfa Aesar. The informative purity value of the $IrBr_4$ was 99.99 % (metal basis). The comparator standard of Ir prepared from High purity Ir metal (Alpha Aesar, powder form, informative purity value was 99.99 % as metal basis). The Au solution for the internal standard was prepared from a high purity metal. The mass fraction of Au solution was 35 mg g^{-1}.

Few mill grams of $IrBr_4$ were weighed using Mettler Toledo XP26 micro balance. After adding the Au solution as internal standard, the samples of $IrBr_4$ in the polyethylene bags were heat sealed. The neutron irradiation was performed using KUR TCPn (thermal neutron flux: 8.0×10^{10} cm^{-2} s^{-1}) for 10min. The irradiated samples were cooled at 3 hours. The gamma rays from irradiated samples were measured using Canberra GC4070-7500 Ge detector with Laboratory Equipment Corporation MCA600. The measured radioactive isotopes were ^{192}Ir (γ ray energy; 316 keV and 468 keV, half-life; 73.829 day), ^{194}Ir (γ ray energy; 328 keV, half-life; 19.28 h) and ^{198}Au (γ ray energy; 412 keV, half-life; 2.6941 day) as internal standard).

RESULTS: In this study, Iridium in the high purity $IrBr_4$ sample could be precisely determined by instrumental neutron activation analysis with internal standard. The analytical results were shown in the Table 1. The improvement of linearity of calibration curves and measurement repeatability was successfully demonstrated by using the internal standard.

Table 1 Analytical results of Ir in $IrBr_4$

Nuclide	Measured γ ray	Mass fraction of Ir
^{192}Ir	316 keV	37.32 %
^{192}Ir	468 keV	37.47 %
^{194}Ir	328 keV	37.52 %
Mean ± RSD*		37.4 %±0.28 %

*relative standard deviation

Additionally, it was found that the element having large neutron capture cross section such as Ir, can be precisely measured.

REFERENCES:

[1] R.Greenberg, P. Bode, E. De Nardi Fernandes, Spectrochim. Acta B, 66 (2011) 193-241.
[2] T. Miura, K.Chiba, T. Kuroiwa, T. Narukawa, A.Hioki,Matsue, Talanta, 82 (2010) 1143-1148.
[3] T. Miura, H. Matsue, T. Kuroiwa, J. Radioanal. Nucl. Chem., 282, 49-52, 2009.
[4] T. Miura, R. Okumura, Y. Iinuma, S. Sekimoto, K. Takamiya, M. Ohata, A.Hioki, J. Radioanal. Nucl. Chem., 303, 1417-1420, 2015.

CO12-12 Neutron Activation Analysis of Household Al foils in Chemical Experimental Class for Undergraduate Students

Y. Oura and N. Shirai

Graduate School of Science, Tokyo Metropolitan University

INTRODUCTION: Chemical experimental class is very important for undergraduate students in every department of chemistry in university. Third-year undergraduate students in department of chemistry, Tokyo Metropolitan University (TMU), perform instrumental analysis as well as traditional and fundamental gravitational analysis, volumetric analysis, and colorimetric analysis in the experimental class for analytical chemistry. And they determine Fe concentration in a household Al foil by three different analytical methods; colorimetric analysis, ICP atomic emission analysis (ICP-AES) and instrumental neutron activation analysis (INAA). After Fukushima accident in 2011, INAA have not been performed because of nonoperation of JRR-3, Japan Atomic Energy Agency. In 2018 INAA experiment have been opened again using Kyoto University Reactor (KUR).

EXPERIMENTS: Al foils in double polyethylene bags were irradiated together with known amount of Fe and Sc standard samples by neutrons for 2 hours in Pn-2 at KUR. Gamma-rays were measured for about 3 hours at the RI research facility, TMU.

A pair of students prepared an Al foil sample (about 12 mg) to be irradiated, then we performed neutron irradiation and gamma-ray measurement. Count values at channels around interested peaks and net peak areas calculated by Hypermet-PC software for Fe and Sc standard samples were given to students. We gave them a lecture about a gamma-ray spectrum and a way to calculate manually a peak area from the channel - count numerical data. They plotted gamma-ray spectra, fixed channel regions for background and gamma-ray peak, and calculated Fe and Sc concentrations in Al foil using 2 different gamma-ray each (1099 keV and 1292 keV for Fe (^{59}Fe), and 889 keV and 1112 keV for Sc (^{46}Sc)).

RESULTS: 24 Al samples of different 16 products were totally analyzed. Determined concentration values of Fe using 1099 keV and 1192 keV gamma-ray were varied from 0.52 % to 1.2 % and from 0.50 % to 1.3 %, respectively. All students obtained consistent Fe concentrations for two different gamma-rays. For Sc, two determination values using 889 keV and 1121 keV gamma-ray were varied from 0.013 ppm to 0.096 ppm and 0.020 ppm to 0.078 ppm, respectively. Because of a smaller count (about 100 counts) consistency between two determination values for Sc was poorer than for Fe. Since 1115 keV gamma-ray of ^{65}Zn was appeared near 1121 keV gamma-ray of ^{46}Sc, some students calculated Sc concentration using gamma-ray of ^{65}Zn instead of ^{46}Sc or a background region included gamma-ray of ^{65}Zn for calculating a net area of 1121 keV gamma-ray. They reported different Sc concentrations between two gamma-rays, although we talked in the class that concentrations using each gamma-rays should be almost same.

Fe in Al foil was also determined by colorimetric analysis and ICP-AES in the class. About 200 mg of Al foil was dissolved in HCl then this solution was used for both analytical methods. Determination values by colorimetric analysis tend to be systematically smaller than ones by ICP-AES for many students. And determination values by ICP-AES were systematically larger than ones by INAA in 2018. We have no idea for a reason of this systematic higher Fe concentration by ICP-AES at present. One possible reason is inaccuracy of concentrations of Fe standard solutions used for three analytical methods, which were prepared for each method. Comparison between determination values by INAA and ICP-AES is shown in Fig.1 A variation of values by INAA is obviously smaller than by ICP-AES, though values by INAA are systematically smaller. It means generally that even beginners determine easily and appropriately by non-destructive INAA, which does not need chemical processes. In ICP-AES, quite a lot of nonlinear standard addition calibration curves were reported because of assumable inaccurate pipetting for adding standard solution.

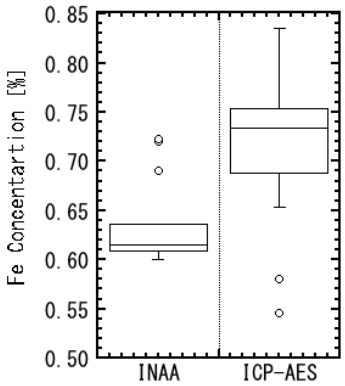

Fig. 1. Fe concentrations in Al foils of a manufacture determined by INAA and ICP-AES.

Concerned matter for INAA as an experimental class is that if KUR operates during when a class is open. In 2018 KUR started running after normal period of the class. We were anxious about the time schedule. This is an impenetrable difficulty.

CO12-13 Neutron induced prompt gamma ray measurement for nuclear power monitoring

K. Okada, A. Fushimi, S. Sekimoto[1] and T. Ohtsuki[1]

Center for Technology Innovation – Energy, Research and Development Group, Hitachi, Ltd.

[1] *Institute for Integrated Radiation and Nuclear Science, Kyoto University*

INTRODUCTION: Nuclear reactor power is monitored using neutron detectors in boiling water reactors (BWRs). Conventionally, fission chambers are adopted as the neutron detectors. Four fission chambers are installed as a single instrumentation tube and measure the local power at specific positions in the tube. As the fission chambers are located inside the reactor core of a reactor pressure vessel (RPV), maintenance of the chambers is difficult because the radiation dose rate of the area is high even during periodical inspection.

We considered a method in which the detector is located outside the RPV by converting neutrons into prompt gamma rays by a neutron capture reaction. Four kinds of metal boards are placed in neutron flux monitoring positions inside an instrumentation tube. Prompt gamma rays are emitted by neutron capture reactions between the metals and the neutrons. The gamma rays are measured by a gamma ray spectrometer located outside the RPV. The energy distribution of the gamma rays is specific for each metal, and their intensity is proportional to the thermal neutron flux at the position of each metal board. Therefore, the thermal neutron flux at each board position can be monitored by measuring the prompt gamma rays as the count rate of each gamma ray emission. By using this method, no detectors need to be installed in the reactor core.

In this study, we considered the identification of the peaks in an assumed situation where prompt gamma rays were emitted from four different metals at the same time. We confirmed that at least one peak for each of the four candidate metals was able to be separated from the peaks derived from the other candidate metals.

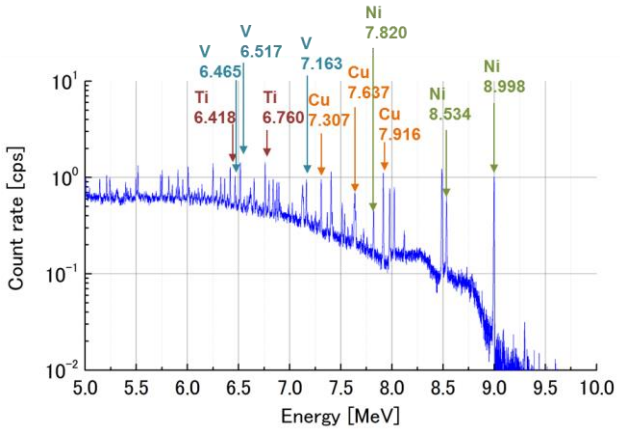

Figure 1: Energy spectrum which was obtained by superposing four energy spectra of the candidate metals

EXPERIMENTS: We limited the measurement energy to be above 5 MeV. Environmental gamma rays including decay gamma rays from radiated materials and scattered gamma rays mainly have an energy less than 3 MeV. When a high energy gamma ray is detected, a double escape peak is seen in the energy spectrum. The double escape peak is a peak having an energy 1.022 MeV lower than the energy of the gamma ray entering the detector. Thus, the lower energy limit of 6 MeV for the emitted prompt gamma ray was determined for separation of prompt gamma rays from environmental gamma rays in the energy spectrum. We chose Ti, V, Ni, and Cu as candidate metals by evaluating the prompt gamma ray emission rates estimated using nuclear data [1, 2].

We conducted a thermal neutron irradiation experiment for the candidate metals in the B4 port of the Kyoto University Research Reactor. The irradiation neutron flux to the candidate metals was 10^7 $cm^{-2}s^{-1}$. The thermal neutron beam size was 1 cm in width and 7 cm in height. The detector was a HPGe detector with relative efficiency of 33.4%. The surface of each piece of the target metals was larger than that of the thermal neutron beam.

RESULTS: We obtained four energy spectra above 5 MeV for the candidate metals. Figure 1 shows the energy spectrum which was obtained by superposing the four energy spectra. Labeled energies are full energy peaks separated from the peaks derived from the other candidate metals. The peaks which are not labeled were mainly escape peaks.

More than two peaks for each of the four candidate metals were identified. Thus, we confirmed that at least one peak for each of the four candidate metals was able to be separated from the peaks derived from the other candidate metals by using the HPGe detector.

REFERENCES:

[1] H. D. Choi, R. B. Lindstrom, G. L. Molnár Molnár, S. F. Mughabghab, R. Paviotti-Corcuera, Z. Révay, A. Trkov, V. Zerkin and C. Zhou, International Atomic Energy Agency, STI/PUB/1263 (2007) 87-194.

[2] Z. Révay, R. B. Firestone, T. Belgya and G. L. Molnár, G. L. Molnár (ed), Kluwer Academic Publishers, Dordrecht/Boston/New York (2004) 173-364.

CO12-14 **Beam Test of a micro-cell MWPC for a muon-electron conversion search experiment, DeeMe**

M. Aoki, N. Abe[1], M. Adachi[2], T. Hori, D. Nagao, H. Natori[3], T.M. Nguyen[4], R. Nishikawa, Y. Seiya[2], T. Takahashi[1], T. Takahashi[2], N. Teshima[2], K. Yamamoto[2] and H. Yoshinaka[2]

School of Science, Osaka University

[1] *KURN, Kyoto University*
[2] *Faculty of Science, Osaka City University*
[3] *Institute for Basic Science, Korea*
[4] *University of Science and Technology Da Nang City*

INTRODUCTION: There has been no observations related to a charged-lepton flavor violation (CLFV) process such as $\mu \to e\gamma$, μ-e conversion, τ-CLFV decays and so on. Based on this fact, the charged-lepton flavor is assumed to be conserved a priori in the Standard Model of particle physics (SM). However, it is rather natural not to be conserved in most of the models beyond SM (BSM). Any discoveries or improvements of the upper limit on the branching ratio of CLFV processes provide very important information to BSM. DeeMe is one of experiments that aim to search for CLFV with μ-e conversion in nuclear field [1]. It uses high-power high-purity pulsed proton beam from J-PARC RCS. The detector of DeeMe should be operational after $\mathcal{O}(\mu s)$ from a burst of particles (100 GHz/mm^2). We successfully developed such a detector with high-voltage switching technique [2]. It is very important to evaluate the performance of the detector before we start the physics data taking at J-PARC MLF.

EXPERIMENTS: The experiments were performed in 2 steps. In the 1st measurement, a gas mixture of the detector (Multi-Wire Proportional Chamber, MWPC) was optimized so that the delayed false pulses were suppressed while the gas gain was retained. A prototype MWPC was placed at the end of the beam line in the target room of the electron LINAC facility, and the waveforms from the readout strips were recorded with several different gas mixtures by using a special FADC system [3]. The several different sets of gas mixtures with small amount of SF_6 (0.05%, 0.1% and 0.15%) resulted in substantial drops of the detection efficiency. The gas mixture with 6% of R134a showed good efficiency and suppression on the delayed false pulses.

In the 2nd measurement, three MWPCs were sequentially placed so that the beam electrons hit through all three of them. The gas mixture was the one with R134a that provided less delayed false pulses.

At first, the low rate electron beam was used and the difference between the hit position at the 2nd MWPC from the expected hit position calculated with the 1st and 3rd MWPCs was evaluated. Figure 1 shows the typical distribution of the position difference. The obtained positional resolution is good enough for the μ-e conversion measurement. Please note that it was under the influence of the multiple-scattering and the further analysis is necessary to derive the intrinsic MWPC resolution.

Secondly, the high rate burst beam was injected to the MWPCs, and the off-timing field-emission electrons were used to derive hit efficiency and the random coincidence from the false pulses after the burst. The analysis is still ongoing.

RESULTS: The mixture of SF_6 does not improve the MWPC total performance. The mixture of R134a suppresses the delayed false pulses without apparent efficiency drop, thus it is very promising. The optimal gas mixture shall be 74% Ar, 20% i-C4H10 and 6% R134a. Another quench gas such as Methylal instead of R134a will be tested in 2019.

The positional resolution of MWPC is good enough for the μ-e conversion measurement. The detailed analysis is ongoing.

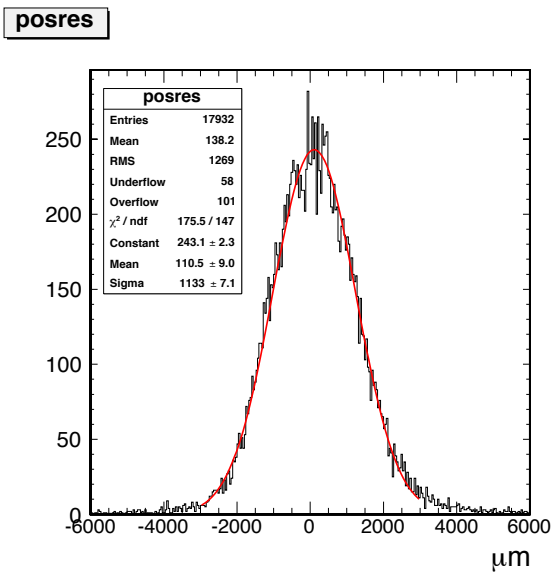

Fig. 1 A difference between the hit position of the 2nd MWPC from the expected hit position with the 1st and 3rd MWPCs.

REFERENCES:

[1] N. Teshima on behalf of the DeeMe Collaboration, "DeeMe experiment to search for muon to electron conversion at J-PARC MLF", in proceedings of NUFACT conference PoS (NuFact2017) 109 (2018).
[2] H. Natori, *et al*., "A fast high-voltage switching multi-wire proportional chamber", Prog. Theor. Exp. Phys. 2017(2) 023C01 (2017).
[3] N.M. Truong, *et al*., "Real-Time Lossless Compression of Waveforms Using an FPGA", IEEE Trans. Nucl. Sci. 65 2650 (2018).

CO12-15 Research on activation assessment of a reactor structural materials for decommissioning

M. Seki, K. Ishikawa, H. Nagata, K. Ohtsuka, T. Ohmori, H. Hanakawa, H. Ide, K. Tsuchiya, T. Sano[1], Y. Fujihara[1], J. Zhang[1] and J. Hori[1]

Department of JMTR, Japan Atomic Energy Agency [1]KURNS, Kyoto University

INTRODUCTION: JMTR (Japan Materials Testing Reactor) was decided as a decommissioning facility in the medium- and long-term plan of JAEA published in April 2017. Radioactive wastes are stored in drums and filled with concrete. However, since metal aluminum reacts with an alkaline substance such as concrete to generate hydrogen gas, there is a possibility that the manufactured waste packages may be damaged. Therefore, the treatment technology for radioactive aluminum waste has not been established, and it is stored in the plant.

The process of forming aluminum hydroxide ($Al(OH)_3$) via aluminate when metal aluminum is dis-solved with a strong base is known[1],[2]. It is converted to stable aluminum oxide (Al_2O_3) using this reaction. In cold tests, impurities were understood that it was in-dissolubility in sodium hydroxide (NaOH) in A6061 of Al-Mg-Si based materials but it was unknown to a de-tailed element.

This report was intended to recognize the behavior of impurities included within the aluminum alloy from an activation analysis.

EXPERIMENTS: The aluminum samples were ir-radiated in Pn-2 of KUR and cooled for 4 days. Table 1 shows the irradiation conditions of test samples in Pn-2 and Table 2 shows the chemical compositions of test samples. After irradiation, each sample was dissolved in a NaOH solution to form sodium aluminate ($Na[Al(OH)_4]$). A hydrochloric acid solution was added to the $Na[Al(OH)_4]$ solution for neutralization to pre-cipitate and to recover as $Al(OH)_3$ by the reaction of Equations (1) and (2). The radioactivity of the obtained materials in each process was measured using the gamma ray spectrometer.

$$2Al + 2NaOH + 6H_2O \rightarrow 2Na[Al(OH)_4] + 3H_2 \quad (1)$$

$$Na[Al(OH)_4] + HCl \rightarrow Al(OH)_3 + NaCl + H_2O \quad (2)$$

RESULTS and DISCUSSIONS: Table 3 shows the results of radioactivity measurement of aluminum samples, solids recovered in the filter and solutions after the filtration. The impurities such as ^{51}Cr and ^{59}Fe contained in each aluminum sample were not dis-solved in NaOH and remained as residuals, so they were separated by filtration.

^{24}Na was detected in the solution after filtration and was not recovered as the solid in the filter. ^{24}Na is generated by the reaction of fast neutrons ($^{27}Al(n, \alpha)\ ^{24}Na$). Thus, it is assumed that $^{24}Na[Al(OH)_4]$ has the same chemical behavior as Na^+ ion (see Eq.(1)).

$^{24}NaCl$ will be produced by the neutralization and collected with $Al(OH)_3$ (see Eq.(2)). Actually, it has been found that NaCl is contained in the gel of $Al(OH)_3$ in the test with the un-irradiated aluminum samples. It seems that $^{24}NaCl$ is able to be removed from the re-covered $Al(OH)_3$ by the washing with water after dry-ing and grinding if it is necessary to reduce the radio-activity of the wastes after treatment.

Table 1 Irradiation conditions of test samples in Pn-2.

Items	Values
Thermal power Thermal	5 MW
neutron flux Epithermal	2.8×10^{17} $m^{-2}s^{-1}$
neutron flux Fast neutron	1.1×10^{16} $m^{-2}s^{-1}$
flux Irradiation time	6.0×10^{16} $m^{-2}s^{-1}$
Cooling time	20 min.
Sample	4 days
	0.5 g

Table 2 Chemical Compositions of test samples

Element	A1050	A6061
Si	0.07	0.61
Fe	0.34	0.42
Cu	0.01	0.28
Mn	0.00	0.02
Mg	0.00	0.99
Cr	-	0.24
Zn	0.00	0.01
Ti	0.02	0.04
V	0.01	-0.01
other	0.00	
Al	99.54	97.92

Table 3 Main radioactive elements in each process

	Aluminum sample [Bq]	Recovered solid [Bq]	Solution after filtra-tion [Bq]
A1050			
^{54}Mn	2.81×10^{3}	7.66	1.78×10^{2}
^{59}Fe	1.74×10^{2}	1.64×10^{2}	-
^{24}Na	3.69×10^{5}	-	2.90×10^{5}
A6061			
^{51}Cr	3.64×10^{4}	3.77×10^{4}	3.80×10^{2}
^{54}Mn	1.91×10^{3}	1.63×10^{1}	4.22×10^{1}
^{59}Fe	2.25×10^{2}	1.95×10^{2}	-
^{24}Na	3.39×10^{5}	-	2.57×10^{5}

Remarks) No correction of measured values by the sample shapes in this test.

CONCLUSION: The preliminary test for the stable treatment of radioactive aluminum was performed by the wet process. The radioactive elements such as ^{51}Cr and ^{59}Fe in the aluminum alloys are able to be removed by this treatment and ^{24}Na will be reduced in the treatment process. In future, the optimization tests will be carried out for the production of the stable Al_2O_3.

REFERENCES:

[1] Taichi Sato, Journal of the Mineralogical Society of Japan, 19(1), 1989, pp.21-41.

[2] Gitzen, W.H. (ed.), *Alumina as a ceramic material*., American Ceramic Society, 1970.

III. PUBLICATION LIST
(APRIL 2018 – MARCH 2019)

1. Slow Neutron Physics and Neutron Scattering

Papers

Rheo-SANS study on relationship between micellar structures and rheological behavior of cationic gemini surfactants in solution
H. Iwase, R. Kawai, K. Morishima, S. Takata, T. Yoshimura and M. Shibayama
Journal of Colloid and Interface Science **538** (2019) 357-366.

Growth of adsorbed additive layer for further friction reduction
T. Hirayama, M. Maeda, Y. Sasaki, T. Matsuoka, H. Komiya and M. Hino
Lubrication Science **25** (2018) 1-8.

Phase transition and hydrogenation properties of Ce_2Ni_7-type Pr_2Co_7 during the hydrogen absorption process
K. Iwase, K. Mori, S. Tashiro and T. Suzuki
International Journal of Hydrogen Energy **43** (2018) 11100-11108.

Direct Evidence for the Effect of Glycerol on Protein Hydration and Thermal Structural Transition
M. Hirai, S. Ajito, M. Sugiyama, H. Iwase, S. Takata, N. Shimizu, N. Igarashi, A. Martel and L. Porcar
Biophysical Journal **112(2)** (2018) 313-327.

Imaging measurement of neutron attenuation by small-angle neutron scattering using soller collimator
Y. Oba, T. Shinohara, H. Sato, Y. Onodera, K. Hiroi, Y. Su and M. Sugiyama
Journal of the Physical Society of Japan **87** (2018) 094004-1-094004-5.

Small-angle scattering study of tetra-poly(acrylic acid) gels
K. Morishima, X.Li, K. Oshima, Y. Mitsukami and M. Shibayama
The Journal of Chemical Physics **149(16)** (2018) 163301.

A cold/ultracold neutron detector using fine-grained nuclear emulsion with spatial resolution less than 100 nm
N. Naganawa, T. Ariga, S. Awano, M. Hino, K. Hirota, H. Kawahara, M. Kitaguchi, K. Mishima, H.M. Shimizu , S. Tada, S. Tasaki and A. Umemoto
The European Physical Journal **C78(11)** (2018) 959.

Macromolecular crowding effect on protein structure and hydration clarified by using X-ray and neutron scattering
H. Mitsuhiro, S. Ajito, M. Sugiyama, H. Iwase, S. Takata, N. Shimizu, N. Igarashi, A. Martel and L. Porcar
Physica B: Condensed Matter **551** (2018) 212.

Proceedings

X 線・中性子反射率法による潤滑界面の平均構造評価の試み II /
A trial for structural evaluation of lubrication interface by X-ray and neutron reflectometry II
M. Hino, N. Adachi, Y. Todaka, Y. Oba and T. Hirayama
Proceedings of the 53rd KURNS Scientific Meeting Kumatori, Japan (Feb. 5-6, 2019) 15. (in Japanese)

J-PARC MLF BL06 MIEZE 型スピンエコー分光器の現状 /
Current status of the MIEZE-type neutron spin echo spectrometer at J-PARC MLF BL06
T. Oda, M. Hino, Y. Kawabata and H. Endo
Proceedings of the 53rd KURNS Scientific Meeting Kumatori, Japan (Feb.5-6, 2019) 34. (in Japanese)

A study of TOF-MIEZE reflectometry for nanomagnetic dynamics Polarized Neutron for Condensed Matter Investigation
M. Hino, T. Oda, H. Endo, N.L. Yamada, H. Seto, H. Ohshita and Y. Kawabata
(PNCMI2018) Abington, UK (July 3-6, 2018).

Experimental test of 3He neutron-spin filter in MIEZE spectrometer Polarized Neutron for Condensed Matter Investigation
H. Hayashida, M. Hino, H. Endo, T. Oku, T. Okudaira, K. Sakai and T. Oda
(PNCMI2018) Abington, UK (July 3-6, 2018).

2. Nuclear Physics and Nuclear Data

Papers

Delayed neutron effect in time-domain fluctuation analyses of neutron detector current signals
Y. Kitamura and T. Misawa
Annals of Nuclear Energy **123** (2019) 119-134.

Resonance analysis of ^{151,153}Eu from neutron capture cross section measurements in the energy range from 1 to 20 eV
L. Jaehong, J. Hori, T.Sano and K. Nakajima
Journal of Nuclear Science and Technology **55(8)** (2018) 900-910.

Neutron energy spectrum measurement using an NE213 scintillator at CHARM
T. Kajimoto, T. Sanami, N. Nakao, R. Froeschl, S. Roesler, E. Iliopoulou, A. Infantino, M. Brugger, E.J. Lee, N. Shigyo, M. Hagiwara, H. Yashima, H. Yamazaki, K. Tanaka and S. Endo
Nuclear Instruments and Methods in Physics Research Section B: Beam Interactions with Materials and Atoms **429 (2018)** 27-33.

Measurements of Neutron Total and Capture Cross Sections of Am-241 with ANNRI at J-PARC
K. Terada, T. Nakao, A. Kimura, S. Nakamura, K. Mizuyama, N. Iwamoto, O. Iwamoto, H. Harada, T. Katabuchi, M. Igashira, T. Sano, Y. Takahashi, C. H. Pyeon, S. Fukutani, T. Fujii, T. Yagi, K. Takamiya and J. Hori
Journal of Nuclear Science and Technology **55** (2018) 1198-1211.

Measurement and calculation of thermal neutrons induced by the 24 GeV/c proton bombardment of a thick copper target
T. Oyama, M. Hagiwara, T. Sanami, H. Yashima, N. Nakao, E.J. Lee, E. Iliopoulou, R. Froeschl, A. Infantino and S. Roesler
Nuclear Instruments and Methods in Physics Research Section B: Beam Interactions with Materials and Atoms **434(1)** (2018) 29-36.

Development of a neutron source for imaging at the electron linac facility in Kyoto University Research Reactor Institute
Y. Takahashi, Y. Kiyanagi, K. Watanabe, A. Uritani, T. Sano, J. Hori and K. Nakajima
Physica B: Condensed Matter **551** (2018) 488-491.

Proceedings

KUCA における DT 加速器開発の現状 /
Development Status of DT Accelerator at KUCA
Y. Kuriyama, Y. Tanaka, N. Kobayashi, T. Takeshita, T. Ueda, H. Yoshino, Y. Iinuma, C.H. Pyeon, Y. Takahashi, M. Yamanaka and Y. Fuwa
Proceedings of the 53rd KURNS Scientific Meeting Kumatori, Japan (Feb.5- 6, 2019) 37. (in Japanese)

Development of a Neutron Spin Filter for a T Violation Search in Compound Nuclei
T. Yamamoto, H.M. Shimizu, M. Kitaguchi, K. Hirota, T. Okudaira, C.C. Haddock, N. Oi, I. Ito, S. Endo, S. Takada, J. Koga, T. Yoshioka, T. Ino, K. Asahi, T. Momose, T. Iwata, K. Sakai, T. Oku, A. Kimura, M. Hino, T. Shima and Y. Yamagata
Proceedings of the International Conference on Neutron Optics (NOP2017) Nara, Japan (July 5-8, 2017) 11018.
(in Japanese)

ブーストトラップ法を活用した Feynman-α法の測定共分散評価/
Estimation od experimantal covariance in the Feyman- α metod using the bootstrap method
T. Endo
Proceedings of 7th Reactor Physics Workshop (RPW 2018) Kumatori, Japan (Nov. 26-27, 2018) 81-91.
(in Japanese)

Adaptive smooth-lasso を用いた感度系数評価に関する検討/
A study of the estimation of the sensitivity coefficients using adaptive smmoth-lasso
R. Katano
Proceedings of 7th Reactor Physics Workshop (RPW 2018) Kumatori, Japan (Nov. 26-27, 2018) 1-21.
(in Japanese)

KUCA 固体減速架台の数値計算ベンチマーク問題/
Benchmark problems for neutron transport calculations about KUCA solid-moderated cores
G. Chiba and T. Endo
Proceedings of 7th Reactor Physics Workshop (RPW 2018) Kumatori, Japan (Nov. 26-27, 2018) 30-48.
(in Japanese)

軽水炉における水の熱中性子散乱則データの違いによる核計算結果への影響評価/
Stdy on Impact of thermal Scattering Law Data Improvements on Nuclear Caliculation for right Water Reactor
S. Takeda, M. Muta, H. Yamaguchi, T. Kitada, Y. Ohoka, S. Matsuoka and H. Nagano
Proceedings of 7th Reactor Physics Workshop (RPW 2018) Kumatori, Japan (Nov. 26-27, 2018) 21-29.
(in Japanese)

Effect of Differences Fuel Material in Neutronic Parameters in Kartini Researc Reactor
A.S. Wicaksono, T. KItada and S. Takeda
Proceedings of 7th Reactor Physics Workshop (RPW 2018) Kumatori, Japan (Nov. 26-27, 2018) 49-56.

様々な各種の崩壊や生成などを考慮した福島第一原子力発電所内部の放射能インベントリ解析/
Radioactivity inventory analysis in the Fukushima Daiichi NPP considering such as various nuclides generation and decay
A. Ishi and G. Chiba
Proceedings of 7th Reactor Physics Workshop (RPW 2018) Kumatori, Japan (Nov. 26-27, 2018) 57-69.
(in Japanese)

Supercritical transient analysis using Multi-resion Integral Kinetic code: Basics and applications
D. Tuya and T. Obara
Proceedings of 7th Reactor Physics Workshop (RPW 2018) Kumatori, Japan (Nov. 26-27, 2018) 70-80.

粒子フィルタ法を用いた未臨界度と中性子生成時間の推定/
Estimation of subcriticality and neutron generation time using particle filter method
T. Ikeda, T. Endo and A. Yamamoto
Proceedings of 7th Reactor Physics Workshop (RPW 2018) Kumatori, Japan (Nov. 26-27, 2018) 92-104.
(in Japanese)

核破砕中性子源によるウラン-鉛ゾーン炉心 ADS 体系における放射化反応率への中性子スペクトルの影響/
Effect of neutron spectrom on reaction rate in ADS experiment with U-Pb zoned core and spallation neutron source
N. Aizawa, M. Yamanaka and C.H. Pyeon
Proceedings of 7th Reactor Physics Workshop (RPW 2018) Kumatori, Japan (Nov. 26-27, 2018) 105-114.
(in Japanese)

Neutron Capture Reaction Data Measurement of Minor Actinides in Fast Neutron Energy Region for Study on Nuclear Transmutation System
T. Katabuchi, O. Iwamoto, J. Hori, N. Iwamoto, A. Kimura, S. Nakamura, Y. Shibahara and K. Terada
Proceedings of the 2018 Symposium on Nuclear Data Tokyo, Japan (Nov. 29-30, 2018).

Reviews

Review of the performance of a ca-bourne survey system, KURAMA-II, used to measure the dose rate after the Fukushima Dai-ichi Nuclear Power Plant accident
S. Tsuda, M. Tanigaki, T. Yoshida and K. Saito
放射線 **44** (2018) 109-118.

放射光で探るレーザー光による超精密原子核制御の可能性:^{229}Th 極低核励起準位
吉見彰洋, 笠松良崇, 北尾真司, 瀬戸 誠, 増田孝彦, 山口敦史, 依田芳卓, 吉村浩司
放射光(放射光学会誌) **31** (2018) 305-314. (in Japanese)

Other

事故耐性の高い軽水炉用制御棒の開発(3) 新型中性子吸収材の反応度測定/
Development of accident tolerant control rod (3) Reactivity measurement of candidate neutron absorbing materials
太田宏一, 名内泰志, 中村勤也, 佐野忠史/
H. Ohta, Y. Nauchi, K. Nakamura and T. Sano
日本原子力学会 2018 春の年会予稿集/
Annual meeting of the Atomic Energy Society of Japa, Spring 2018 (2018) 2F16. (in Japanese)

3. Reactor Physics and Reactor Engineering

Papers

Comparison of theoretical formulae and bootstrap method for statistical error estimation of Feynman-α method
T. Endo and A.Yamamoto
Annals of Nuclear Energy **124** (2019) 606-615.

Application of Advanced Rossi-alpha Technique to Reactivity Measurements at Kyoto University Critical Assembly
C. D. Kong, J. W. Choe, S. P. Yum, J. R. Jang, W. H. Lee, H. J. Kim, W. K Kim, N. H. N. Khang, N. D. C. Tung, V. Dos, D. J. Lee, H. C. Shin, M. Yamanaka and C. H. Pyeon
Annals of Nuclear Energy **118** (2018) 92-98.

Experimental Analysis and Uncertainty Quantification using Random Sampling Technique for ADS Experiments at KUCA
T. Endo, G. Chiba, W. F. G. van Rooijen, M. Yamanaka and C. H. Pyeon
Journal of Nuclear Science and Technology **55** (2018) 450-459.

Implementation of a frequency-domain neutron noise analysis method in a production-level continuous energy Monte Carlo code: Verification and application in a BWR
T. Yamamoto
Annals of Nuclear Energy **115** (2018) 494-501.

Uncertainty Quantification of Criticality in Solid-Moderated and -Reflected Cores at Kyoto University Critical Assembly
C. H. Pyeon, M. Yamanaka, M. Ito, G. Chiba, T. Endo, S. H. Kim and W. F. G. van Rooijen
Journal of Nuclear Science and Technology **55** (2018) 812-821.

Some characteristics of gas-liquid two-phase flow in vertical large-diameter channels
X. Shen, J.P. Schlegel, T. Takashi and H. Nakamura
Nuclear Engineering and Design **333** (2018) 87-98.

Improvement of Fission Source Distribution by Correlation Sampling Method in Monte Carlo Perturbation Calculations
S. H. Kim. M. Yamanaka and C. H. Pyeon
Journal of Nuclear Science and Technology **55 (**2018) 945-954.

Estimation of porosity and void fraction profiles in a packed bed of spheres using X-ray radiography
D. Ito, K. Ito, Y. Saito, M. Aoyagi, K. Mastsuba and K. Kamiyama
Nuclear Engineering and Design **334** (2018) 90-95.

Monte Carlo perturbation methods using “virtual density” theory for calculating reactivity due to geometry change
T. Yamamoto and H. Sakamoto
Annals of Nuclear Energy **119** (2018) 362-373.

Effect of higher harmonics in the area-ratio pulsed neutron source technique
T. Yamamoto and H. Sakamoto
Progress in Nuclear Energy **108** (2018) 286-294.

Determination of prompt neutron decay constant by time-domain fluctuation analyses of detector current signals
Y. Kitamura, P. Imre and T. Misawa
Annals of Nuclear Energy **120** (2018) 691-706.

Significant spatial dependence observed in inverse kinetics analysis for a loosely coupled-core system of the Kyoto University Critical Assembly
T. Sano, K. Hashimoto, H. Taninaka and H. Unesaki
Journal of Nuclear Science and Technology **56** (2018) 1355-1361.

Experimental Analyses of Bismuth Sample Reactivity Worth at Kyoto University Critical Assembly
C. H. Pyeon, M. Yamanaka, A. Oizumi, M. Fukushima and K. Tsujimoto
Journal of Nuclear Science and Technology **55** (2018) 1324-1335.

Monte Carlo method for solving a B1 equation with complex-valued buckling in asymmetric geometries and generation of directional diffusion coefficients
T. Yamamoto and H.Sakamoto
Annals of Nuclear Energy **122** (2018) 37-46.

Constitutive equations for vertical upward two-phase flow in rod bundle
T. Hibiki, T. Ozaki, X. Shen, S. Miwa, I. Kinoshita, T. Hazuku and S. Rassame
International Journal of Heat and Mass Transfer **127** (2018) 1252-1266.

Bubble coalescence and breakup model evaluation and development for two-phase bubbly flows
X. Shen and T. Hibiki
International Journal of Multiphase Flow **109** (2018) 131-149.

Undersize solute element effects on defect structure development in copper under electron irradiation
Y. Satoh, T. Yoshiie and S. Arai
Philosophical Magazine **8** (2018) 646-672.

Proceedings

京都大学臨界集合体実験装置における加速器駆動システム実験 /
Accelerator-Driven System Experiment at Kyoto University Critical Assembly
M. Yamanaka
Proceedings of the 53rd KURNS Scientific Meeting Kumatori, Japan (Feb.5-6, 2019) 1. (in Japanese)

垂直ロッドバンドル流路内における局所界面積濃度の特性に関する研究 /
Experimental study on interfacial area concentration in gas-liquid two-phase flows in a rod bundle flow channel
X. Shen, S. Miwa, Y. Xiao, H. Sun and T. Hibiki
Proceedings of the 53rd KURNS Scientific Meeting Kumatori, Japan (Feb.5-6, 2019) 38. (in Japanese)

大口径流路内多次元気液二相流の流動機構解明に関する研究 /
Study on flow mechanism of multi-dimensional gas-liquid two-phase flow in large-diameter channels
X. Shen, T. Hibiki and H. Nakamura
Proceedings of the 53rd KURNS Scientific Meeting Kumatori, Japan (Feb.5-6, 2019) 52-54. (in Japanese)

Evaluation of Feedback Reactivity Coefficients by Inverse Kinetics in Monju
A. Kitano and K. Nakajima
2018 International Congress on Advances in Nuclear Power Plants (ICAPP 2018) Charlotte, NC, USA (Apr.8-11, 2018).

Sensitivity Coefficient Analysis of Omega-Eigenvalue based on First-Order Perturbation Theory
T. Endo and A. Yamamoto
PHYSOR2018 Cancun, Mexico (Apr.22-26, 2018) 1240-1253.

Dead-Time and Spatial Corrections for the KUCA Subcritical Assembly Experiments
A. Talamo, Y. Gohar, M. Yamanaka and C. H. Pyeon
Proc. Int. Conf. on the Reactor Physics (PHYSOR2018) Cancun, Mexico (Apr.22-26, 2018) 1-8.

Uncertainty by Nuclear Data and Highly-Enriched Uranium in keff Evaluation at Kyoto University Critical Assembly
M. Yamanaka and C. H. Pyeon
Proc. Int. Conf. on the Reactor Physics (PHYSOR2018) Cancun, Mexico (Apr.22-26, 2018) 1-8.

Feynman-α Analysis for a Subcritical Reactor System Driven by an Unstable Spallation Neutron Source in the Kyoto University Critical Assembly
K. Nakajima, A. Sakon, S. Hohara, K. Hashimoto, M. Yamanaka, T. Sano and C.H. Pyeon
PHYTRA4 – The Fourth International Conference on Physics and Technology of Reactors and Applications
Marrakech, Morocco (Sept.17-19, 2018).

Research of Measurement Condition for a Reactor Noise Measurement in the Power Operation of Kyoto University Reactor, KUR
S. Hohara, K. Nakajima, A. Sakon, K. Hashimoto and T. Sano
The Fourth International Conference on Physics and Technology of Reactors and Applications
Marrakech, Morocco (Sept.17-19, 2018).

An evaluation of one-group interfacial area transport equation with its constitutive bubble coalescence and breakup models in bubbly two-phase flows (Paper No.: 568)
X. Shen and T. Hibiki
Proceeding of the 12th International Topical Meeting on Nuclear Reactor Thermal-Hydraulics, Operation and Safety (NUTHOS-12) Qingdao, China (Oct.14-18, 2018).

Reactivity and Activation Measurements of Novel Neutron-Absorbing Materials for Accident-Tolerant Control Rod
H. Ohta, Y. Nauchi, K. Nakamura and T. Sano
ANS winter meeting Washington DC, USA (Nov.11-15, 2018).

Development of portable SNMs detection system with D-D neutron source based on combination of noise analysis and threshold energy neutron analysis method
T. Misawa, Y. Kitamura, Y. Takahashi, K. Masuda and B.A. Mahmoud
IEEE 2018 Nuclear Science Symposium and Medical Imaging Conference
Sydney, Australia (Nov.10-17, 2018).

Effect of porosity distribution on two-phase pressure drop in a packed bed
T. Kurisaki, D. Ito, K. Ito, Y. Saito, Y. Imaizumi, K. Matsuba and K. Kamiyama
Proceedings of 11th Korea-Japan Symposium on Nuclear Thermal Hydraulics and Safety (NTHAS-11)
Busan, Korea (Nov.18-21, 2018).

Measurements of liquid velocity and void fraction in vertical upward LBE two-phase flow under poor wettability conditions
G. Ariyoshi, D. Ito, K. Ito and Y. Saito
Proceedings of 11th Korea-Japan Symposium on Nuclear Thermal Hydraulics and Safety (NTHAS-11)
Busan, Korea (Nov.18-21, 2018).

Measurement and analysis of one-dimensional solidification process in lead-bismuth eutectic
D. Ito, K. Ito and Y. Saito
Proceedings of 11th Korea-Japan Symposium on Nuclear Thermal Hydraulics and Safety (NTHAS-11)
Busan, Korea (Nov.18-21, 2018).

Modeling of bathtub vortex in consideration of realistic axial velocity distribution
K. Ito, D. Ito, Y. Saito, T. Ezure and M. Tanaka
Proceedings of ANS Winter Meeting & Expo 2018, Embedded Topical Meeting: Advances in Thermal Hydraulics (ATH 2018) Orlando, FL, USA (Nov.11-15, 2018) 1120-1132.

Reviews

京都大学研究炉の運転再開について
中島 健, 三澤 毅
日本原子力学会・炉物理部会　会報「炉物理の研究」**70** (2018). (in Japanese)

研究用原子炉 KUR の新規制基準への対応
中島健
Isotope News **757** (2018) 48-51. (in Japanese)

4. Material Science and Radiation Effects

Papers

Combined effect of laser thermal shock and helium ion irradiation on W-Y_2O_3 composites
Y.X. Zhang, X.Y. Tan, L.M. Luo, Y. Xu, X. Zan, Q. Xu, Tokunaga Kazutoshi, X.Y. Zhu and Y.C. Wu
Fusion Engineering and Design **140** (2019) 102-106.

Preparation of ultrafine-grained/nanostructured tungsten materials: An overview
Y. C Wu, Q.Q Hou, L.M. Luo, X. Zan, X.Y. Zhu, Li Ping, Q. Xu, J.G. Cheng, G.N. Luo and J.L. Chen
Journal of Alloys and Compounds **779** (2019) 926-941.

Superconducting transition temperatures in the electronic and magnetic phase diagrams of $Sr_2VFeAsO_{3-\delta}$, a superconductor
Y. Tojo, T. Shibuya, T. Nakamura, K. Shoji, H. Fujioka, M. Matoba, S. Yasui, M. Itoh, S. Iimura, H. Hiramatsu, H. Hosono, S. Hirai, W. Mao, S. Kitao, M. Seto and Y. Kamihara
Journal of Physics: Condensed Matter **31** (2019) 115801.

Chiral crystal-like droplets displaying unidirectional rotational sliding
T. Kajitani, K. Motokawa, A. Kosaka, Y. Shoji, R. Haruki, D. Hashizume, T. Hikima, M. Takata, K. Yazawa, K. Morishima, M. Shibayama and T. Fukushima
Nature Materials **3** (2019) 266-272.

TEM studies of 1 MeV Fe^+ ion-irradiated W alloys by wet chemical method: high-temperature annealing and deuterium retention
X.Y. Ding, J.Q. Liu, L.M. Luo, Q. Xu, X. Gao, J.J. Huang, B. Yu, J.G. Li and Y.C. Wu
Nuclear Fusion **59** (2019) 016008.

Gamma-ray irradiation effect on ZnO bulk single crystal: Origin of low resistivity
J. Tashiro, Y. Torita, T. Nishimura, K. Kuriyama, K. Kushida, Q. Xu and A. Kinomura
Solid State Communications **292** (2019) 24-26.

Surface damage evolution during transient thermal shock of W-2%vol Y_2O_3 composite material in different surfaces
G. Yao, Z.Y. Tan, L.M. Luo, K.J. Hong, X. Zan, Q. Xu, X.Y. Zhuao, Y.Y. Lian, X. Liu and Y.C. Wu
Fusion Engineering and Design **139** (2019) 86-95.

Densification and microstructure evolution of W-TiC-Y_2O_3 during spark plasma sintering
Y.F. Zhou, Z.Y. Zhao, X.Y. Tan, L.M. Luo, Y. Xu, X. Zan, Q. Xu, K. Tokunaga, X.Y. Zhu and Y. C. Wu
International Journal of Refractory Metals and Hard Materials **79** (2019) 95-101.

Depth synergistic effect of irradiation damage on tungsten irradiated by He-ions with various energies
Y.L. Liu, E.Y. Lu, L.G. Song, R.Y. Bai, Q. Xu, S.X. Jin, T. Zhu, X.Z. Cao, Q.L. Zhang, D.Q. Yuan, B.Y. Wang and L.Q. Ge
Journal of Nuclear Materials **517** (2019) 192-200.

Evolution of Superconductivity with Sr-Deficiency in Antiperovskite Oxide $Sr_{3-x}SnO$
M. Oudah, J.N. Hausmann, S. Kitao, A. Ikeda, S. Yonezawa, M. Seto and Y. Maeno
Scientific Reports **9** (2019) 1831.

Development of a novel red-emitting cesium hafnium iodide scintillator
S. Kodama, S. Kurosawa, M. Ohno, A. Yamaji, M. Yoshino, J. Pejchal, R. Král, Y. Ohashi, K. Kamada, Y. Yokota, M. Nikl and A. Yoshikawa
Radiation Measurements **124** (2019) 54-58.

Influence of Nb Content on the Microstructure and Deuterium Retention of W-Nb Alloys
L.M. Luo, J.B. Chen, J.S. Lin, X. Zan, X.Y. Zhu, Q. Xu and Y.C. Wu
Fusion Engineering and Design **129** (2018) 120-129.

Characterization of Helium-Vacancy Complexes in He-Ions Implanted Fe9Cr by Using Positron Annihilation Spectroscopy
T. Zhu, S.X. Jin, P. Zhang, L.G. Song, X.Y. Lian, P. Fan, Q.L. Zhang, D.Q. Yuan, H.B. Wu, R.S. Yu, X.Z. Cao, Q. Xu and B.Y. Wang
Journal of Nuclear Materials **505** (2018) 69-72.

Nuclear spin relaxation of ^{111}Cd at the A site in spinel oxides, $CdFe_2O_4$ and $CdIn_2O_4$
W. Sato, S. Komatsuda and Y. Ohkubo
Journal of Radioanalytical and Nuclear Chemistry **316(3)** (2018) 1289-1293.

Thermal stability of irradiation-induced metastable lattice structures in NiTi intermetallic compound
M. Ochi, H. Kojima, K. Fukuda, Y. Kaneno, S. Semboshi, F. Hori, Y. Saitoh and A. Iwase
Transactions of the Materials Research Society of Japan **43(2)** (2018) 53-56.

(Ar-CO-C[triple bond, length as m-dash]C)(PEt_3)Au and (Ar-C[triple bond, length as m-dash]C)(PEt_3)Au complexes bearing pyrenyl and ferrocenyl groups: synthesis, structure, and luminescence properties
M. Głodek, A. Makal, P. Paluch, G.M. Kadziołka, Y. Kobayashi, J. Zakrzewski and D. Plażuk
Dalton Transactions **47(19)** (2018) 6702-6712.

Helium Irradiation Behavior of Tungsten-Niobium Alloys under Different Ion Energies
M.Y. Xu, L.M. Luo, Y.F. Zhou, X. Zan, Y. Xu, Q. Xu, K. Tokunaga, X.Y. Zhu and Y.C. Wu
Fusion Engineering and Design **132** (2018) 7-12.

Versatile Mechanical Properties of Novel g-SiCx Monolayers from Graphene to Silicene: A First-Principles Study
X.K. Lu, T.Y. Xin, Q. Zhang, Q. Xu, T.H. Wei and Y.X. Wang
Nanotechnology **29** (2018) 315701.

Effect of Ti addition on microstructural evolution of V-Cr-Ti alloys to balance irradiation hardening with swelling suppression
K. Fukumoto, K. Tone, T. Onitsuka and T. Ishigami
Nuclear Materials and Energy **15** (2018) 122-127.

Spin order in FeV_2O_4 determined by single crystal Mössbauer spectroscopy in applied magnetic field
S. Nakamura, Y. Kobayashi, S. Kitao and M. Seto
Physica B: Condensed Matter **536** (2018) 620-624.

Valence fluctuating compound α-$YbAlB_4$ studied by ^{174}Yb Mössbauer spectroscopy and X-ray diffraction using synchrotron radiation
M. Oura, S. Ikeda, R. Masuda, Y. Kobayashi, M. Seto, Y. Yoda, N. Hirao, S.I. Kawaguchi, Y. Ohishi, S. Suzuki, K. Kuga, S. Nakatsuji and H. Kobayashi
Physica B: Condensed Matter **536(1) (**2018) 162-164.

An Overview of Oxidation-Resistant Tungsten Alloys for Nuclear Fusion
D.G. Liu, L. Zheng, L.M. Luo, X. Zan, J.P. Song, Q. Xu, X.Y. Zhu and Y.C. Wu
Journal of Alloys and Compounds **765** (2018) 299-312.

Positron Lifetime Calculation of Vacancy Clusters in Tantalum Containing Hydrogen and Helium
Q. Xu, E. Popov, T. Troev, J. Zhang and Y. Dai
Journal of Nuclear Materials **506** (2018) 71-75.

Effect of laser beam thermal shock on the helium ion irradiation damage behavior of W-TiC-Y_2O_3 composites
M.Y. Xu, L.M. Luo, Y. Xu, X. Zan, Q. Xu, K. Tokunaga, X.Y. Zhu and Y.C. Wu
Journal of Nuclear Materials **509** (2018) 198-203.

Factors Driving Stable Growth of He Clusters in W: First-Principles Study
Y.J. Feng, T.Y. Xin, Q. Xu and Y.X. Wang
Nuclear Fusion **58** (2018) 076024.

Thermal Stability and Evolution of Microstructures Induced by He Irradiation in W-TiC Alloys
Q. Xu, X.Y. Ding, L.M. Luo, M. Miyamoto, M. Tokitani, J. Zhang and Y.C. Wu
Nuclear Materials and Energy **15** (2018) 76-79.

Detection of Phase Separation of Nuetron-Irradiated Fe-Cr Binary Alloys using Positron Annihilation Spectroscopy
Y. Noshita, K. Sato, H. Yamashita, R. Kasada, Q. Xu, M. Hatakeyama and S. Sunada
Nuclear Materials and Energy **15** (2018) 175-179.

Vibrations and chemical states of iron ions in soda-lime glasses determined by element-specific X-ray analyses
K. Okada, Y. Nagashima, K. Shiraki, H. Kageyama, H. Ofuchi, Y. Yoda, Y. Kobayashi, N. Umesaki and Y. Sakurai
X-Ray Spectrometry **47(5)** (2018) 359-371.

Microstructure and transient laser thermal shock behavior of W–TiC–Y_2O_3 composites prepared by wet chemical method
M.Y. Xu, L.M. Luo, J.S. Lin, Y. Xu, X. Zan, Q. Xu, K. Tokunaga, X.Y. Zhu and Y.C. Wu
Journal of Alloys and Compounds **766** (2018) 784-790.

Contribution of irradiation-induced defects to hardening of a low-copper reactor pressure vessel steel
M. Shimodaira, T. Toyama, K. Yoshida, K. Inoue, N. Ebisawa, K. Tomura, T. Yoshiie, M.J. Konstantinović, G. Robert and Y. Nagai
Acta Materialia **155(15)** (2018) 402-409.

Radiophotoluminescence phenomenon in copper-doped aluminoborosilicate glass
R. Hashikawa, Y. Fujii, A. Kinomura, T. Saito, A. Okada, T. Wakasugi and K. Kadono
Journal of the American Ceramic Society **102(4)** (2018) 1642-1651.

Investigation of mechanical properties of stress-relieved and electron-irradiated tungsten after hydrogen charging
K. Sato, H. Yamashita, A. Hirosako, S. Komazaki, Q. Xu, M. Onoue, R. Kasada, K. Yabuuchi and A. Kimura
Nuclear Materials and Energy **17** (2018) 29-33.

Thermal behavior of In impurities in ZnO
W. Sato, H. Shimizu, S. Komatsuda and Y. Ohkubo
Journal of Applied Physics **124(10)** (2018) 105101-7.

Measurement of displacement cross sections of aluminum and copper at 5 K by using 200 MeV protons
Y. Iwamoto, M. Yoshida, T. Yoshiie, D. Satoh, H. Yashima, H. Matsuda, S. Meigo and T. Shima
Journal of Nuclear Materials **508** (2018) 195-202.

Gamma-ray irradiation impact of humic substances on apparent formation constants with Cu(II)
T. Sasaki, R. Goto, T. Saito, T. Kobayashi, T. Ikuji and Y. Sugiyama
Journal of Nuclear Science and Technology **55** (2018) 1299-1308.

Variable-bandwidth ^{57}Fe Synchrotron Mössbauer Source
T. Mitsui, R. Masuda, M. Seto and N. Hirao
Journal of the Physical Society of Japan **87(9) (**2018) 093001.

Isotropic thermal conductivity in rolled large-sized W-Y_2O_3 bulk material prepared by powder metallurgy route and rolling deformation technology
G. Yao, X.Y. Tan, M.Q. Fu, L.M. Luo, X. Zan, Q. Xu, J.Q. Liu, X.Y. Zhu, J.G Cheng and Y.C. Wu
Fusion Engineering and Design **137** (2018) 325-330.

Effect of temperature and dose on vacancy-defect evolution in 304Lstainless steel irradiated by triple ion beam
T. Zhu, B. Wang, D. Yuan, S. Jin, P. Zhang, E. Lu, L. Song, Y. Liu, H. Ma, Q. Zhang, P. Fan, X. Cao and Q. Xu
Journal of Nuclear Materials **512** (2018) 94-99.

Measurement of the excitation function of ^{96}Zr(α,n)^{99}Mo for an alternative production source of medical radioisotopes
M. Hagiwara, H. Yashima, T. Sanami and S. Yonai
Journal of Radioanalytical and Nuclear Chemistry **318(1)** (2018) 569-573.

Nuclear Bragg reflection of $^{57}FeBO_3$ in radio-frequency magnetic field observed with Si-APD linear array detector
S. Kishimoto, R. Haruki, R. Masuda, M.M .Tanaka and T. Mitsui
Japanese Journal of Applied Physics **58(1)** (2018) 016501.

Structure, microscopic ordering, and viscous properties of amorphous poly(n-alkylsilsesquioxane) liquids and solids synthesized by cosolvent-free hydrolytic polycondensation of n-alkyltrimethoxysilanes
K. Kajihara, R. Setp, K. Kanamura, Y. Onodera and S. Kohara
Physica Status Solidi A **216** (2018) 1800475-1-1800475-8.

Six tris(bipyridyl)iron(II) complexes with 2-substituted 1,1,3,3-tetracyanopropenide, perchlorate and tetrafluoridoborate anions; order versus disorder, hydrogen bonding and C-N...π interactions
A. Addala, Z. Setifi, Y. Morimoto, B. Artetxe, T. Matsumoto, J. Gutiérrez-Zorrilla M.and C. Glidewell
Acta Crystallographica Section E Crystallographic Communications **74(12)** (2018) 1717-1726.

Electronic properties and compressional behavior of Fe-Si alloys at high pressure
S. Kamada, N. Suzuki, F. Maeda, N. Hirao, M. Hamada, E. Ohtani, R. Masuda, T. Mitsui, Y. Ohishi and S. Nakano
American Mineralogist **103(12)** (2018) 1959-1965.

A Nuclear Resonance Vibrational Spectroscopic Study of Oxy Myoglobins Reconstituted with Chemically Modified Heme Cofactors: Insights into the Fe-O_2 Bonding and Internal Dynamics of the Protein
T. Ohta, T. Shibata, Y. Kobayashi, Y. Yoda, T. Ogura, S. Neya, A. Suzuki, M. Seto and Y. Yamamoto
Biochemistry **57(48)** (2018) 6649-6652.

Viscoelastic change of block copolymer ion gels in a photo-switchable azobenzene ionic liquid triggered by light
C. Wang, K. Hashimoto, R. Tamate, H. Kokubo, K. Morishima, X. Li, M. Shibayama, F. Lu, T. Nakanishi and M. Watanabe
Chemical Communications **12** (2018) 1710-1713.

Precise determination of hyperfine interactions and second-order doppler shift in ^{149}Sm Mössbauer transition
S. Tsutsui, R. Masuda, Y. Yoda and M. Seto
Hyperfine Interactions **239** (2018) 50.

Correlation between mechanical properties and Cu precipitates induced by neutron irradiation of Fe Cu alloys
X. Qiu, T. Yokotani, T. Onitsuka and K. Sato
Journal of Nuclear Materials **512** (2018) 314-319.

Nuclear Resonance Vibrational Spectroscopy Definition of O_2 Intermediates in an Extradiol Dioxygenase: Correlation to Crystallography and Reactivity
K.D. Sutherlin, Y. Wasada-Tsutsui, M. Mbughuni Michael, S. Rogers Melanie, K. Park, L.V. Liu, Y. Kwak, M. Srnec, L.H. Böttger, M. Frenette, Y. Yoda, Y. Kobayashi, M. Kurokuzu, M. Saito, M. Seto, H. Michael, J. Zhao, E. A. Ercan, J.D. Lipscomb and E.I. Solomon
Journal of the American Chemical Society **140(48)** (2018) 16495-16513.

Thermal evolution of irradiation defects in ferritic/martensitic steel during isochronal annealing
Z. Te, C. Xingzhong, J. Shuoxue, Z. Peng, L. Eryang, K. Peng, G. Yihao, G. Liping, X. Qiu and W. Baoyi
Nuclear Instruments and Methods in Physics Research Section B: Beam Interactions with Materials and Atoms **436** (2018) 35-39.

Charge disproportionation of Mn*3d* and O*2p* electronic states depending on strength of *p-d* hybridization in $(LaMnO_3)_2(SrMnO_3)_2$ superlattices
H. Nakao,C. Tabata, Y. Murakami, Y. Yamasaki, H. Yamada, S. Ishihara and M. Kawasaki
Physical Review B **98（24）** (2018) 245146.

Proceedings

Nuclear resonant small-angle scattering for investigation of microstructures in electronic states
S. Kitao, M. Kurokuzu, Y. Kobayashi, M. Seto, Y. Yoda and S. Kishimoto
International Conference on Synchrotron Radiation Instrumentation (SRI2018) / AIP Conf. Proc. 2054(2019)
Taipei, Taiwan (June10-15, 2019) 50013.

X 線小角散乱法による鉄鋼材料中のミクロ組織の解析 /
Characterization of microstructures in steels using small-angle X-ray scattering
Proceedings of the 53rd KURNS Scientific Meeting Kumatori, Japan (Feb.5-6, 2019) 13. (in Japanese)

フッ化物イオン電池用 $Ce_{0.95}Sr_{0.05}F_{2.95}$ 固体電解質の構造および電気化学特性/
Structural and electrochemical properties of $Ce_{0.95}Sr_{0.05}F_{2.95}$ solid electrolyte for Fluoride Ion Batteries
A. Okumura, K. Mori, F. Fujisaki, M. Yonemura and Y. Ishikawa
Proceedings of the 53rd KURNS Scientific Meeting Kumatori, Japan (Feb.5-6, 2019) 20. (in Japanese)

原子炉および電子加速器を用いた種々のメスバウアー線源の作成 /
Various Mössbauer source preparation using reactor and electron accelerator
S. Kitao, Y. Kobayashi, T. Kubota, M. Saito, R. Masuda, M. Kurokuzu, S. Hosokawa, H. Tajima, S. Yazaki and M. Seto
Proceedings of the 53rd KURNS Scientific Meeting Kumatori, Japan (Feb.5-6, 2019) 28. (in Japanese)

金属間化合物合金に対する量子線照射効果による微細構造変化 /
Microstructural change of intermetallic compounds irradiated with particle beam
A. Takano, Y. Sumikura, K. Sugita, K. Osawa, G. jo and H. Hori
Proceedings of the 53rd KURNS Scientific Meeting Kumatori, Japan (Feb.5-6, 2019) 33. (in Japanese)

照射還元法により合成した Cu 合金ナノ粒子の安定性と微細構造 /
Synthesis of Cu nanoparticles stabilized by alloying under gamma-ray irradiation field.
Y. Uchimura, S. Toda, M. Tanaka, Y. Mizukoshi, N. Taguchi, S. Tanaka, T. Matsui, X. Qiu and F. Hori
Proceedings of the 53rd KURNS Scientific Meeting Kumatori, Japan (Feb.5-6, 2019) 35. (in Japanese)

高純度タングステンにおける電子線照射誘起空孔の回復挙動 /
Irradiation-Induced Vacancy Defects and Its Recovery Behavior in High-Purity Tungsten
M. Tanaka, A. Yabuuchi and A. Kinomura
Proceedings of the 53rd KURNS Scientific Meeting Kumatori, Japan (Feb.5-6, 2019) 36. (in Japanese)

Analysis of irradiated materials by intense slow positron beams
A. Kinomura
Proceedings of the 37th Symposium on Materials Science and Engineering, Research Center of Ion Beam Technology Koganei, Tokyo (Dec.5, 2019) 3-6.

Radiation Damage Calculation in Phits and Benchmarking Experiment for Cryogenic-Sample High-Energy Proton Irradiation
Y. Iwamoto, H. Matsuda, S. Meigo, D. Satoh, Tokai, T. Nakamoto, M. Yoshida, Y. Ishi, Y. Kuriyama, T. Uesugi, H. Yashima, T. Yoshiie, T. Shima and R. M. Ronningen
61st ICFA ABDW on High-Intensity and High-Brightness Hadron Beams HB2018 Daejeon (June18-22, 2018) 116-121.

Operation of field emitter arrays under high dose rate gamma-ray irradiation
T. Morito, Y. Handa, Y. Gotoh, N. Sato, I. Takagi, M. Nagao, M. Akiyoshi and T. Okamoto
31st International Vacuum Nanoelectronics Conference, IVNC 2018 Kyoto, Japan (July9-13, 2018) 8520096.

Gamma-Ray Irradiation Effects of CdS/CdTe Photodiode for Radiation Tolerant FEA Image Sensor
T. Okamoto, T. Igari, T. Fukui, Y. Gotoh, N. Sato, M. Akiyoshi and I. Takagi
31st International Vacuum Nanoelectronics Conference, IVNC 2018 Kyoto, Japan (July9-13, 2018) 8520196.

Radiation tolerance of a compact image sensor made of CdTe based photoconductive film and field emitter array
T. Masuzawa, Y. Neo, H. Mimura, T. Okamoto, M. Nagao, M. Akiyoshi, N. Sato, I. Takagi and Y. Gotoh
10th Japan-Korea Nanoelectronics Symposium Hachinohe, Japan (Oct.12-14, 2018).

Recent progress in development of radiation tolerant image sensor with field emitter array
T. Masuzawa, Y. Neo, H. Mimura, M. Nagao, M. Akiyoshi, I. Takagi, Y. Gotoh, T. Okamoto, T. Igari and N. Sato
31st International Vacuum Nanoelectronics Conference, IVNC 2018 Kyoto, Japan (July9-13, 2018) 8520056.

Reviews

An overview of oxidation-resistant tungsten alloys for nuclear fusion
L. D. Guang, Z. Liang, L.L. Ma, Z. Xiang, S.J. Peng, X. Qiu, Z.X. Yong and W.Y. Cheng
Journal of Alloys and Compounds **765** (2018) 299-312.

Evolution of Nuclear Resonant Scattering Research at SPring-8
M. Seto
SPring-8/SACLA Research Frontiers 2017 (2018) 12-15.

ガンマ線をもちいたナノ-マイクロ秒の原子・分子のミクロな運動性の研究
齋藤真器名
自動車技術 **72** (2018) 120-121. (in Japanese)

多色 γ 線を用いた原子・分子運動の観察
齋藤真器名
Isotope news **758** (2018) 21-24. (in Japanese)

陽電子寿命測定と第一原理計算から視えてきたハイエントロピー合金 CoCrFeMnNi 中の空孔形成と移動のエンタルピー/
Evaluation of Vacancy Formation and Migration Enthalpies in CoCrFeMnNi High-entropy Alloy using Positron Lifetime Measurements and Firstprinciples Calculations
杉田一樹, 水野正隆, 荒木秀樹, 白井泰治/
K. Sugita, M. Mizuno, H. Araki and Y. Shirai
まてりあ **57** (2018) 323-327. (in Japanese)

量子ビーム実験と構造モデリングによる亜鉛リン酸塩ガラスの熱膨張係数異常の起源の解明
小野寺陽平, 小原真司, 正井博和
放射光 **32** (2019) 67-74. (in Japanese)

5. Geochemistry and Environmental Science

Papers

Ultrahigh-pressure form of SiO2 glass with dense pyrite-type crystalline homology
M. Murakami, S. Kohara, N. Kitamura, J. Akola, H. Inoue, A. Hirata, Y. Hiraoka, Y. Onodera, I. Obayashi, J. Kalikka, N. Hirao, T. Musso, A. S. Foster, Y. Idemoto, O. Sakata and Y. Ohishi
Physical Review B **99** (2019) 045153-1-045153-12.

Deposition and Dispersion of Radio-Cesium Released Due to the Fukushima Nuclear Accident: Sensitivity to Meteorological Models and Physical Modules
M. Kajino, T.T. Sekiyama, Y. Igarashi, G. Katata, M. Sawada, K. Adachi, Y. Zaizen, H. Tsuruta and T. Nakajima
Journal of Geophysical Research: Atmospheres **124(3)** (2019) 1823-1845.

Analysis on the influence of forest soil characteristics on radioactive Cs infiltration and evaluation of residual radioactive Cs on surfaces
Y. Mori, M. Yoneda, Y. Shimada, S. Fukutani, M. Ikegami and R. Shimomura
Environmental Monitoring and Assessment **190(4)** (2018) 256.

Distribution and Chemical Speciation of Molybdenum in River and Pond Sediments Affected by Mining Activity in Erdenet City, Mongolia
T. Solongo, K. Fukushi, O. Altansukh, Y. Takahashi, A. Akehi, G. Baasansuren, Y. Ariuntungalag, O. Enkhjin, B. Davaajargal, D. Davaadorj and N. Hasebe
Minerals **8(7)** (2018) 288.

Laser step−heating $^{40}Ar/^{39}Ar$ analyses of biotites from meta−granites in the UHP Brossasco−Isasca Unit of Dora−Maira Massif, Italy
T. Itaya, H. Hyodo, T. Imayama and C. Groppo
Journal of Mineralogical and Petrological Sciences **4** (2018) 171-180.

Cooling history and exhumation of the Nepheline Syenites, NW Iran: Constraints from Apatite fission track
N. Ashraf, N. Hasebe and J. Ahmad
Iranian Journal of Earth Sciences **10(2)** (2018) 109-120.

Petrology, geochemistry and geodynamic setting of Eocene-Oligocene alkaline intrusions from the Alborz-Azerbaijan magmatic belt, NW Iran
N. Ashrafi, A. Jahangiri, N. Hasebe, .N. Eby and G. Nelson
Geochemistry **78(4)** (2018) 432- 461.

Proceedings

廃水中トリチウムの処理に向けた試み /
New Approach for Tritium Separation from Water
S. Fukutani
Proceedings of the 53rd KURNS Scientific Meeting Kumatori, Japan (Feb.5-6, 2019) 6. (in Japanese)

福島原発事故で放出された放射性エアロゾルの生成メカニズムの解明 /
Production mechanism of radioactive aerosols released from Fukushima Daiichi Nuclear Power Plant
K. Takamiya, T. Tanaka, S. Nitta, Y. Nishiyama, Y. Nishizawa, F. Futagami, Y. Takeuchi, Y. Oki, N. Osada, Y. Ishi, T. Uesugi, Y. Kuriyama, M. Sakamoto, A. Kirishima, M. Onodera, N. Sato, S. Sekimoto and T. Ohtsuki
Proceedings of the 53rd KURNS Scientific Meeting Kumatori, Japan (Feb.5-6, 2019) 7-10. (in Japanese)

Measurement of ^{134}Cs / ^{137}Cs activity ratio of cesium micro-particles and contaminated soil particles using well-type germanium detector.
M. Soliman. F. Futagami, K. Takamiya, S. Sekimoto, T. Oki and T. Ohtsuki
Proceedings of the 53rd KURNS Scientific Meeting Kumatori, Japan (Feb.5-6, 2019) 14.

海塩粒子の塩素及び臭素損失 /
Depletion of Cl, Br in the sea salt aerosol.
N. Ito, A. Mizohata, Y. Iinuma and R. Okumura
Proceedings of the 53rd KURNS Scientific Meeting Kumatori, Japan (Feb.5-6, 2019) 21. (in Japanese)

Eu:LiCAF を用いた加速器 BNCT における中性子測定技術開発 /
Development of neutron detection technology using Eu:LiCAF scintillator
D. Nio, K. Sakasai, H. Nakashima, S. Tanaka, H. Kumada and K. Takamiya
Proceedings of the 53rd KURNS Scientific Meeting Kumatori, Japan (Feb.5-6, 2019) 22. (in Japanese)

東京電力(株)福島第一原子力発電所事故における線量評価 /
Dose assessment of radiation exposure due to the Fukushima-Daiichi nuclear power plant accident
T. Takahashi
Proceedings of the 53rd KURNS Scientific Meeting Kumatori, Japan (Feb.5-6, 2019) 44-46. (in Japanese)

福島第一原発周辺土壌に沈着した FP の深部移行挙動 /
Vertical migration behavior of FP deposited on soil around Fukushima Daiichi Nuclear Power Plant
D. Matoba, T. Sasaki and T. Kobayashi
Proceedings of the 53rd KURNS Scientific Meeting Kumatori, Japan (Feb.5-6, 2019) 32. (in Japanese)

Tectonic setting leading to subduction initiation of Izu-Bonin-Mariana arc -new implications from the Philippine Sea basins-
O. Ishizuka, K. Tani, Y. Harigane, G. Shimoda, T. Sato, S. Umino, I. Sakamoto, Y. Ohara, Y. Yokoyama, A. Perez, C. Conway and S. Sekimoto
American Geophysical Union Fall meeting Washington DC, USA (Dec.10-14, 2018).

Sustainable way of treating groundwater polluted with arsenic, iron and ammonium by a combination of biological filtration and one-stage nitritation - anammox process 10-03-O (Theme3)
Y. Fujikawa Y., Ph. D. Hung, D. Hira, M. Sugahara and K. Furukawa
structures in Electronic States Tokyo, Japan (Dec.5, 2018) 18.

Reviews

環境の分析技術　無機機器分析(1)
藤川陽子
環境技術 **47** (2018) 221-225. (in Japanese)

環境の分析技術　無機機器分析(2)
藤川陽子
環境技術 **47** (2018) 287-291. (in Japanese)

沈み込み帯の火山岩中かんらん石斑晶とマントルかんらん岩のハロゲン・希ガスからみた水の沈み込み過程
角野浩史, 小林真大
月刊 地球/ The earth monthly **40** (2018) 260-271. (in Japanese)

日本のエネルギーの現状
藤川陽子
環境技術 **47** (2018) 236-238. (in Japanese)

Others

フィリピンパラワン島における炭酸塩の熱ルミネッセンス年代測定/
Thermoluminescence dating of carbonates from Palawan island of the Philippines
河原弘樹, 長谷部徳子, 小形 学,福士圭介, 田村明弘, 藤井直樹, 山川 稔/
H. Kawahara, N. Hasebe, M. Ogata, K. Fukushi, A. Tamura, N. Fuji and M. Yamakawa
フィッション, トラックニュースレター = Fission track news letter **31** (2018) 23-25. (in Japanese)

原子間力顕微鏡を用いたジルコンのαリコイルトラック年代測定/
Alpha recoil track dating on zircon by using atomic force microscope
早坂　怜, 長谷部徳子, 松木 篤, 福間剛士, 田村明弘/
R. Hayasaka, N. Hasebe, A. Matsuki, T. Fukuma and A. Tamura
フィッション, トラックニュースレター = Fission track news letter **31** (2018) 20-22. (in Japanese)

U-Pb 法を用いた東南極北東部の年代測定/
The dating of Northeast Antarctica by zircon U-Pb Method
西野紗也子, 長谷部徳子, 田村明弘, 石川尚人/
S. Nishino, N. Hasebe, A. Tamura and N. Ishikawa
フィッション, トラックニュースレター = Fission track news letter **31** (2018) 17-19. (in Japanese)

アパタイト FT 法に基づいた東北日本弧における隆起,削剥史の推定：島弧山地形成過程の解明を目指して
/Estimation of uplift/denudation history of NE Japan Arc based on the apatite fission-track (AFT) method:
Toward understanding of the mountain building process in an island arc
福田将眞, 末岡 茂, 長谷部徳子, 田村明弘, 荒井章司, 田上高広/
S. Fukuda, S. Sueoka, N. Hasebe, A. Tamura, S. Arai and T. Tagami
フィッション,トラックニュースレター = Fission track news letter **31** (2018) 13-16. (in Japanese)

茂住祐延断層のジルコン FT 熱年代解析：熱史モデルによる再検討/
Thermal analysis along the Mozumi-Sukenobu fault, central Japan, based on zircon
fission-track thermochronometry: Reexamination by using thermal history modeling
末岡　茂, 郁芳随徹, 長谷部徳子, 田上高広/
S. Sueoka, Z. Ikuho, N. Haesbe and T. Tagami
フィッション, トラックニュースレター = Fission track news letter **31** (2018) 9-12. (in Japanese)

6. Life Science and Medical Science

Papers

Formation of Clusters in Whiskies During the Maturation Process
K. Morishima, N. Nakamura, K. Matsui,Y. Tanaka, H. Masunaga, S. Mori, T. Iwashita, X. li and M. Shibayama
Journal of Food Science **84(1)** (2019) 59-64.

Highly active copper(i) complexes of aroylthiourea ligands against cancer cells – synthetic and biological studies
K. Jeyalakshmi, J. Haribabu, C. Balachandran, E. Narmatha, S.P.B. Nattamai, S. Aoki, S. Awale and R. Karvembu
New Journal of Chemistry **43(7)** (2019) 3188-3198.

Negative charge at aspartate 151 is important for human lens αA-crystallin stability and chaperone function
T. Takata, T. Matsubara, H.T. Nakamura and N. Fujii
Experimental Eye Research **182** (2019) 10-18.

Stereoselective aldol reactions of dihydroxyacetone derivatives catalyzed by chiral Zn^{2+} complexes
M. Yasuda, Y. Saga, T. Tokunaga, S. Itoh and S. Aoki
Tetrahedron **75(6)** (2019) 757-777.

Simple and Convenient Method for the Isolation, Culture, and Re-collection of Cancer Cells from Blood by Using Glass-Bead Filters
B. Shashni, H. Matsuura, R. Saito, T. Hirata, S. Ariyasu, K. Nomura, H. Takemura, K. Akimoto, N. Aikawa, A. Yasumori and S. Aoki
ACS Biomaterials Science & Engineering **2** (2019) 438-452.

Stereospecific Synthesis of Tris-heteroleptic Tris-cyclometalated Iridium (III) Complexes via Different Heteroleptic Halogen-Bridged Iridium(III) Dimers and Their Photophysical Properties
Y. Tamura, Y. Hisamatsu, A. Kazama, K. Yoza, K. Sato, R. Kuroda and S. Aoki
Inorganic Chemistry **57(8)** (2018) 4571-4589.

NRVS Studies of the Peroxide Shunt Intermediate in a Rieske Dioxygenase and Its Relation to the Native Fe^{II} O_2 Reaction
K.D. Sutherlin, B.S. Rivard, L.H. Böttger, L.V. Liu, M.S. Rogers, M. Srnec, K. Park, Y. Yoda, S. Kitao, Y. Kobayashi, M. Saito, M. Seto, M. Hu, J. Zhao, J.D. Lipscomb and E.I. Solomon
Journal of the American Chemical Society **140** (2018) 5544-5559.

Not Oligomers but Amyloids are Cytotoxic in the Membrane-Mediated Amyloidogenesis of Amyloid-β Peptides
N. Itoh, E. Takada, K. Okubo, Y. Yano, M. Hoshino, A. Sasaki, M. Kinjo and K. Matsuzaki
ChemBioChem **19(5)** (2018) 430-433.

Oxytocin Inhibits Corticosterone-induced Apoptosis in Primary Hippocampal Neurons
H.M. Latt, H. Matsushita, M. Morino, Y. Koga, H. Michiue, T. Nishiki, K. Tomizawa and H. Matsui
Neuroscience **379** (2018) 383-389.

Asp 58 modulates lens αA-crystallin oligomer formation and chaperone function
T. Takata, H.T. Nakamura, R. Inoue, K. Morishima, N. Sato, M. Sugiyama and N. Fujii
The FEBS Journal **285(12)** (2018) 2263-2277.

Identification of Isomeric Aspartate residues in βB2-crystallin from Aged Human Lens
T. Takata, K. Murakami, A. Toyama and N. Fujii
Biochimica et Biophysica Acta (BBA) - Proteins and Proteomics **7** (2018) 767-774.

D-Amino acids in protein: The mirror of life as a molecular index of aging
N. Fujii, T. Takata, N. Fujii, K. Aki and H. Sakaue
Biochimica et Biophysica Acta (BBA) - Proteins and Proteomics **1866(7)** (2018) 840-847.

Regioselective O-Glycosylation of Nucleosides via the Temporary 2
H. Someya, T. Itoh, M. Kato and S. Aoki
Journal of Visualized Experiments **137** (2018) e57897.

Mutagenic potential of 8-oxo-7,8-dihydroguanine (8-oxoG) is influenced by nearby clustered lesions"
N. Shikazono and K. Akamatsu
Mutation Research/Fundamental and Molecular Mechanisms of Mutagenesis **810** (2018) 6-12.

Cryoprotectant-free high-pressure cooling and dynamic nuclear polarization for more sensitive detection of hydrogen in neutron protein crystallography
I. Tanaka, N. Komatsuzaki, W.X. Yue, T. Chatake, K. Kusaka, N. Niimura, D. Miura, T. Iwata, Y. Miyachi, G. Nukazuka and H. Matsuda
Acta Crystallographica Section D Structural Biology **74(8)** (2018) 787-791.

Luminescent Iridium Complex-Peptide Hybrids (IPHs) for Therapeutics of Cancer: Design and Synthesis of IPHs for Detection of Cancer Cells and Induction of Their Necrosis-Type Cell Death
A.A. Masum, Y. Hisamatsu, K. Yokoi and S. Aoki
Bioinorganic Chemistry and Applications **7578965** (2018)1-18.

Purification and structural characterization of water-soluble menaquinone-7 produced by *Bacillus subtilis natto*
T. Chatake, Y. Yanagisawa, R. Inoue, M. Sugiyama, T. Matsuo, S. Fujiwara, T. Ohsugi and H. Sumi
Journal of Food Biochemistry **e12630** (2018) 1-7.

Design and synthesis of a luminescent iridium complex-peptide hybrid (IPH) that detects cancer cells and induces their apoptosis
A.A. Masum, K. Yokoi, Y. Hisamatsu, K. Naito, B. Shashni and S. Aoki
Bioorganic & Medicinal Chemistry **26(17)** (2018) 4804-4816.

Use of a Compact Tripodal Tris(bipyridine) Ligand to Stabilize a Single-Metal-Centered Chirality: Stereoselective Coordination of Iron(II) and Ruthenium(II) on a Semirigid Hexapeptide Macrocycle
Y. Kobayashi, M. Hoshino, T. Kameda, K. Kobayashi, K. Akaji, S. Inuki, H. Ohno and S. Oishi
Inorganic Chemistry **9** (2018) 5475-5485.

Structural Basis for Selective Binding of Export Cargoes by Exportin-5
R. Yamazawa, C. Jiko, S. Choi, I.Y. Park, A. Nakagawa, E. Yamashita and S.J. Lee
Structure **26(10)** (2018) 1393-1398.

The Effect of *p53* Status on Radio-Sensitivity of Quiescent Tumor Cell Population Irradiated With γ-Rays at Various Dose Rates
S. Masunaga, J. Kobayashi, K. Tano, Y. Sanada, M. Suzuki and K. Ono
Journal of Clinical Medicine Research **10(11)** (2018) 815-821.

Protein assemblies ejected directly from native membranes yield complexes for mass spectrometry
D.S. Chorev, L.A Baker, D. Wu, Beilsten-Edmands Victoria,Rouse Sarah L.,Zeev-Ben-Mordehai Tzviya, C. Jiko, F. Samsudin, C. Gerle, S. Khalid, A.G. Stewart, S.J. Matthews, K. Grünewald and C.V. Robinson
Science **6416** (2018) 829-834.

Design and synthesis of boron containing monosaccharides by the hydroboration of d-glucal for use in boron neutron capture therapy (BNCT)
T. Itoh, K. Tamura, H. Ueda, T. Tanaka, K. Sato, R. Kuroda and S. Aoki
Bioorganic & Medicinal Chemistry **26(22)** (2018) 5922-5933.

Concentrations and biological half-life of radioactive cesium in epigeic earthworms after the Fukushima Dai-ichi Nuclear Power Plant accident
S. Tanaka, T. Adati, T. Takahashi, K. Fujiwara and S. Takahashi
Journal of Environmental Radioactivity **192** (2018) 227-232.

Proceedings

マルチドメイン蛋白質の階層的な動的構造と機能発現との関係性に関する研究 /
Solution structure of multi-domain protein
H. Nakagawa, T. Saio, M. Sugiyama and R. Inoue
Proceedings of the 53rd KURNS Scientific Meeting Kumatori, Japan (Feb.5-6, 2019) 11. (in Japanese)

フィブリノーゲンによるインスリン B 鎖アミロイド線維の形成阻害 /
Inhibition of amyloid fibril formation of insulin B chain by fibrinogen
E. Chatani, N. Yamamoto, T. Akai, R. Inoue, M. Sugiyama and A. Tamura
Proceedings of the 53rd KURNS Scientific Meeting Kumatori, Japan (Feb.5-6, 2019) 12. (in Japanese)

ヒト水晶体内 αA-クリスタリン中における Asp58 部位の重要性と白内障との関係 /
Asp Isomerizations Caused Lens Protein Insolubilization
T. Takata, K. Morishima, R. Inoue, N. Sato, M. Sugiyama and N. Fujii
Proceedings of the 53rd KURNS Scientific Meeting Kumatori, Japan (Feb.5-6, 2019) 16. (in Japanese)

クライオ電顕のための牛心筋 FoF1ATP 合成酵素の試料調整 /
Preparation of bovine FoF1ATPsynthase for cryo-EM structural analysis
C. Jiko, C. Gerle and Y. Morimoto
Proceedings of the 53rd KURNS Scientific Meeting Kumatori, Japan (Feb.5-6, 2019) 24. (in Japanese)

超遠心分析と X 線小角散乱を用いたタンパク質溶液の相補的構造解析 /
Structural analysis of a protein solution by complementary use of analytical ultracentrifugation and small angle X-ray scattering
K. Morishima, N. Sato, R. Inoue and M. Sugiyama
Proceedings of the 53rd KURNS Scientific Meeting Kumatori, Japan (Feb.5-6, 2019) 26. (in Japanese)

アミロイド *β*タンパク質産生量を減少させるタンパク質 ILEI の物理化学的解析/
Physicochemical study on ILEI suppressing amyloid-β generation
E. Hibino, K. Morishima, R. Inoue, M. Sugiyama, M. Nakano, N. Watanabe, T. Sugi and M. Nishimura
Proceedings of the 53rd KURNS Scientific Meeting Kumatori, Japan (Feb.5-6, 2019) 27. (in Japanese)

重水素化支援小角中性子散乱中性子散乱及び分析超遠心法による α-クリスタリンのサブユニット交換の機構解明 /
Clarification of mechanism of subunit dynamics of α-crsytallin through deuteration assisted small-angle neutron scattering and analytical ultra-centrifuge
R. Inoue, K. Morishima, T. Takata, N. Sato, K. Wood, R. Urade, N. Fujii and M. Sugiyama
Proceedings of the 53rd KURNS Scientific Meeting Kumatori, Japan (Feb.5-6, 2019) 49-51. (in Japanese)

小麦タンパク質グリアジンの凝集体構造の SAXS による解析 /
SAXS analysis of nanostructures of hydreated wheat gliadins
R. Urade, N. Sato, M. Sugiyama, Y. Higashino, R. Inoue and K. Morishima
Proceedings of the 53rd KURNS Scientific Meeting Kumatori, Japan (Feb.5-6, 2019) 19. (in Japanese)

重水素化を利用したタンパク質の変性に関する研究 /
Elucidation of denatured protein using deuteration
A. Kita
Proceedings of the 53rd KURNS Scientific Meeting Kumatori, Japan (Feb.5-6, 2019) 47-48. (in Japanese)

Adhesion-free Separation of Particles/Cells Using Three Dimensional Negative Dielectrophoretic Force
M. Mizoguchi, K. Yamamoto, B. Shashni, S. Aoki and M. Motosuke
Proceedings of 9th Asia-Pacific Conference of Transducers and Micro-Nano Technology (APCOT 2018)
Hong Kong, China (June24-27, 2018).

Book

タンパク質のアモルファス凝集と溶解性—基礎研究からバイオ産業・創薬研究への応用まで—
第Ⅱ編 第 4 章　小角散乱法
黒田　裕, 有坂文雄, 白木賢太郎, 岩下和輝, 三村真大, 宗　正智, 後藤祐児, 今村比呂志, 渡邊秀樹, 千賀由佳子, 本田真也, 太田里子, 杉山正明, 城所俊一, 若山諒大, 内山　進, デミエン ホール, 廣田奈美, 五島直樹, 河村義史, 廣瀬修一, 野口　保, 丹羽達也, 田口英樹, 伊豆津健一, 津本浩平, 伊倉貞吉, 池口雅道, 荒川　力, 江島大輔, 浅野竜太郎, 赤澤陽子, 萩原義久, 小澤大作, 武内敏秀, 永井義隆, 安藤昭一朗, 石原智彦, 小野寺　理, 加藤昌人, 米田早紀, 鳥巣哲生, 黒谷篤之, 柴田寛子, 石井明子
黒田 裕, 有坂文雄
(株)シーエムシー出版 (in Japanese)

Reviews

4 液混合液体クロマトグラフィーポンプを用いた各種濃度溶液の作成
森本幸生
Jasco Report **60(1)** (2018) 1-4. (in Japanese)

Gliadins from wheat grain: an overview、from primary structure to nanostructures of aggregates
R. Urade, N. Sato and M. Sugiyama
Biophysical Reviews **10(2)** (2018) 435-443.

がん診断・治療のための異分野連携
-血中循環がん細胞の検出、補捉法の開発-
青木 伸
理大科学フォーラム **404** (2018) 10-13. (in Japanese)

ナットウキナーゼによる血栓溶解ならびに疾病予防 (特集 つまらない,もれない血管力)
須見洋行，矢田貝智恵子，茶竹俊行，森本幸生，柳澤泰任，満尾　正，井上浩義，丸山眞杉
Food style 21 **22** (2018) 43-47. (in Japanese)
水晶体構成蛋白質中におけるアミノ酸の自発的化学修飾が引き起こす白内障発症機構に関する研究
高田 匠
日本白内障学会誌 **30** (2018) 7-12. (in Japanese)

生物物理学的手法を用いた納豆菌の研究 : 納豆菌が生産する生理活性物質と納豆菌の放射線耐性/
Biophysical study of Bacillus subtilis natto: Physiologically active substances produced by Bacillus subtilis natto, and radioresistance of Bacillus subtilis natto
茶竹俊行, 齊藤 剛, 柳澤泰任
放射線生物研究/Radiation biology research communications **53** (2018) 280-290. (in Japanese)

蛋白質中の D-アミノ酸と老化
藤井紀子, 高田 匠, 金 仁求
臨床免疫・アレルギー科 **70** (2018) 467-474. (in Japanese)

老化による蛋白質中の D-アミノ酸生成と加齢性疾患
藤井紀子
海洋化学研究 / Transactions of the Research Institute of Oceanochemistry **31(2)** (2018) 84-90. (in Japanese)

Other

有機水銀分解酵素・重原子結合型の高分解能結晶構造解析/
Crystal structure analysis of organomercurial lyase and its heavy atom derivatives
森本幸生, 喜田昭子
Photon Factory Activity Report 2017 **35** (2018) 19. (in Japanese)

7. Neutron Capture Therapy

Papers

Effect of a change in reactor power on response of murine solid tumors in vivo, referring to impact on quiescent tumor cell population
S. Masunaga, Y. Sakurai, H. Tanaka, T. Takata, M. Suzuki, Y. Sanada, K. Tano, A. Maruhashi and K. Ono
International Journal of Radiation Biology (2019) 1-11.

Proposal for determining absolute biological effectiveness of boron neutron capture therapy—the effect of $^{10}B(n,\alpha)^{7}Li$ dose can be predicted from the nucleocytoplasmic ratio or the cell size
K. Ono, H. Tanaka, Y. Tamari, T. Watanabe, M. Suzuki and S. Masunaga
Journal of Radiation Research **60(1)** (2019) 29-36.

Radiological diagnosis of brain radiation necrosis after cranial irradiation for brain tumor: a systematic review
M. Furuse, N. Nonoguchi, K. Yamada, T. Shiga, J.D. Combes, N. Ikeda, S. Kawabata, T. Kuroiwa and S. Miyatake
Radiation Oncology **14(1)** (2019) 28.

Folate receptor-targeted novel boron compound for boron neutron capture therapy on F98 glioma-bearing rats
T. Kanemitsu, S. Kawabata, M. Fukumura, G. Futamura, R. Hiramatsu, N. Nonoguchi, F. Nakagawa, T. Takata, H. Tanaka, M. Suzuki, S. Masunaga, K. Ono, S. Miyatake, H. Nakamura and T. Kuroiwa
Radiation and Environmental Biophysics **58(1)** (2019) 59-67.

Boron neutron capture therapy for vulvar melanoma and genital extramammary Paget's disease with curative responses
J. Hiratsuka, N. Kamitani, R. Tanaka, E. Yoden, R. Tokiya, M. Suzuki, R.F. Barth and K. Ono
Cancer Communications **1** (2018) 38.

Modeling the detection efficiency of an HP-Ge detector for use in boron neutron capture therapy
S. Nakamura, A. Wakita, M. Ito, H. Okamoto, S. Nishioka, K. Iijima, K. Kobayashi, T. Nishio, H. Igaki and J. Itami
Applied Radiation and Isotopes **125** (2018) 80-85.

Boron Neutron Capture Therapy of Malignant Gliomas
S. Miyatake, S. Kawabata, R. Hiramatsu, T. Kuroiwa, M. Suzuki and K. Ono
Progress in Neurological Surgery **32** (2018) 48-56.

Preliminary design study of a simple neutron energy spectrometer using a CsI self-activation method for daily QA of accelerator-based BNCT
R. Kurihara, A. Nohtomi, G. Wakabayashi, Y. Sakurai and H. Tanaka
Journal of Nuclear Science and Technology **56(1)** (2018) 70-77.

Feasibility study on the use of 3D silicon microdosimeter detectors for microdosimetric analysis in boron neutron capture therapy
N. Hu, R. Uchida, L.T. Tran, A. Rosenfeld and Y. Sakurai
Applied Radiation and Isotopes **140** (2018) 109-114.

Boron Neutron Capture Therapy for High-Grade Skull-Base Meningioma
K. Takeuchi, R. Hiramatsu, Y. Matsushita, H. Tanaka, Y. Sakurai, M. Suzuki, K. Ono, S. Miyatake, T. Kuroiwa and S. Kawabata
Journal of Neurological Surgery Part B: Skull Base Suppl **4** (2018) S322-S327.

Development of real-time thermal neutron monitor array for boron neutron capture therapy
H. Tanaka, T. Takata, Y. Sakurai, S. Kawabata, M. Suzuki, S. Masunaga and K. Ono
Therapeutic Radiology and Oncology (2018) 2-51.

Preliminary feasibility study on differential diagnosis between radiation-induced cerebral necrosis and recurrent brain tumor by means of [18F]fluoro-borono-phenylalanine PET/CT
R. Beshr, K. Isohashi, T. Watabe, S. Naka, G. Horitsugi, V. Romanov, H. Kato, S. Miyatake, E. Shimosegawa and J. Hatazawa
Annals of Nuclear Medicine **32(10) (**2018) 702-708.

Boron Neutron Capture Therapy Combined with Early Successive Bevacizumab Treatments for Recurrent Malignant Gliomas – A Pilot Study
H. Shiba, K. Takeuchi, R. Hiramatsu, M. Furuse, N. Nonoguchi, S. Kawabata, T. Kuroiwa, N. Kondo, Y. Sakurai, M. Suzuki, K. Ono, S. Oue, E. Ishikawa, H. Michiue and S. Miyatake
Neurologia medico-chirurgica **58(12)** (2018) 487-494.

Influence of field-of-view and section thickness of diagnostic imaging on thermal neutron flux estimation in dose-planning for boron neutron capture therapy
H. Sato, T. Takata and Y. Sakurai
Radiological Physics and Technology **12(1) (**2018) 76-85.

Proceedings

Enhanced tumor-targeted delivery of p-boronophenylalanine using fructose-functionalized polymers for boron neutron capture therapy
Y. Yao, T. Nomoto, Y. Inoue, M. Suzuki, M. Matsui, H. Takemoto, K. Tomoda and N. Nishiyama
18th International Congress on Neutron Capture Therapy (ICNCT-18) Taipei, Taiwan (Oct.28-Nov.2, 2018).

Metabolism-controlled boron delivery systems composed of p-boronophenylalanine and poly(vinyl alcohol)
T. Nomoto, Y. Inoue, Y. Yao, M. Suzuki, H. Takemoto, M. Matsui, K. Tomoda and N. Nishiyama
18th International Congress on Neutron Capture Therapy (ICNCT-18) Taipei, Taiwan (Oct.28-Nov.2, 2018).

Boron Tracedrugs: Drug-Design Challenge for Neutron Dynamic Therapy
H. Hori, T. Sugihara, T. Tashiro, H. Terada, R.Takeuchi, N. Kamegawa and Y. Morimoto
18th International Congress on Neutron Capture Therapy (ICNCT-18) Taipei, Taiwan (Oct.28-Nov.2, 2018).

Effect of the Change in a Reactor Power on the Response of Murine Solid Tumors in Vivo, Referring to that in Intratumor Quiescent Cells and Its Clinical Significance in Boron Neutron Capture Therapy (BNCT)
S. Masunaga, Y. Sakurai, H. Tanaka, T. Takata, K. Tano, Y. Sanada, M. Suzuki, A. Maruhashi and K. Ono
104th Scientific Assembry and Annual Meeting, Radiological Society of North America Chicago, USA (Oct.28-Nov.2, 2018).

Disruption of Hif-1a enhances the sensitivity to BNCT in murine squamous cell carcinoma
Y. Sanada, T. Takata, Y. Sakurai, H. Tanaka, K. Tano and S. Masunaga
18th International Congress on Neutron Capture Therapy (ICNCT-18) Taipei, Taiwan (Oct.28-Nov.2, 2018).

Functional evaluation of kojic acid-modified carborane developed as a boron drug for melanoma BNCT
S. Dowaki, K. Matsuura, R. Kawasaki, Y. Hattori, Y. Sakurai, S. Masunaga, M. Kirihata and T. Nagasaki
18th International Congress on Neutron Capture Therapy (ICNCT-18) Taipei, Taiwan (Oct.28-Nov.2, 2018).

Effect of the change in reactor power on the response of murine solid tumors in vivo, also referring to that in quiescent tumor cells, and its clinical significance in boron neutron capture therapy (BNCT)
S. Masunaga
18th International Congress on Neutron Capture Therapy (ICNCT-18) Taipei, Taiwan (Oct.28-Nov.2, 2018).

The role of GM-CSF during early cellular responses after BNCR and gamma irradiation
L. Chen, S. Imamichi, S. Masunaga, T. Onodera, Y. Sasaki and M. Masutani
18th International Congress on Neutron Capture Therapy (ICNCT-18) Taipei, Taiwan (Oct.28-Nov.2, 2018).

Pilot study of gadolinium accumulation in tumour with intra-arterial administration of gadoteridol-entrapped water-in-oil-in-water emulsion in VX-2 rabbit hepatic cancer model for neutron capture therapy
M. Yanagawa, H. Yanagie, T. Fujino, T. Matsukawa, A. Kubota, Y. Morishita, Y. Sakurai, K. Mouri, M. Fujihara, R. Mizumachi, Y. Murata, Y. Nonaka, D. Novraina, T. Hirata, A. Shinohara, K. Yokoyama, T. Sugihara, M. Suzuki, S. Masunaga, Y. Sakurai, H. Tanaka, K. Ono, R. Nishimura, M. Ono, J. Nakajima and H. Takahashi
18th International Congress on Neutron Capture Therapy (ICNCT-18) Taipei, Taiwan (Oct.28-Nov.2, 2018).

The combination effect of neutron irradiation and exposure to DNA-alkilating agent on glioblastoma cell lines with different MGMT and p53 status
Y. Kinashi, T. Ikawa and S. Takahashi
18th International Congress on Neutron Capture Therapy (ICNCT-18) Taipei, Taiwan (Oct.28-Nov.2, 2018) 228-229.

Boron neutron capture therapy for makignant pleural mesothelioma: Acase report
M. Suzuki, N. Kondo, Y. Tamari, E. Shibata, T. Kijima, Y. Kinashi, S. Masunaga, T. Takata, H. Tanaka and Y. Sakurai
18th International Congress on Neutron Capture Therapy (ICNCT-18) Taipei, Taiwan (Oct.28-Nov.2, 2018).

Study on application of BNCT to synovial sarcoma
T. Fujimoto, M. Suzuki, S. Kuratsu, T. Sudo, T. Sakuma, Y. Sakurai, T. Takata, Y. Tamari, H. Tanaka, S. Masunaga, Y. Kinashi, N. Kondo, H. Igaki, I. Fujita, T. Andoh, M. Morishita, S. Yahiro, R. Shigemoto, T. Kawamoto, T. Akisue, H. Ichikawa, R. Kuroda and T. Hirose
18th International Congress on Neutron Capture Therapy (ICNCT-18) Taipei, Taiwan (Oct.28-Nov.2, 2018).

Treatment of major cervical invasion of head and neck cancer with boron neutron capture therapy
M. Ohmae, I. Kato, Y. Fujita, M. Suzuki, S. Masunaga, K. Ono, Y. Sakurai, M. Nakazawa and N.Uzawa
18th International Congress on Neutron Capture Therapy (ICNCT-18) Taipei, Taiwan (Oct.28-Nov.2, 2018).

Books

Handbook of Boron Science With Applications in Organometallics, Catalysis, Materials and Medicine
Volume 4: Boron in Medicine
An Overview of Clinical and Biological Aspects of Current Boron Neutron Capture Therapy (BNCT) for Cancer Treatment
M. Takagaki, K. Uno and N. S Hosmane
WORLD SCIENTIFIC (EUROPE) (2018).

「BNCT 基礎から臨床応用まで」—BNCT を用いて治療にかかわる人のためのテキスト— 増刷版
中性子捕捉療法を理解するための生物学の基礎 "
増永慎一郎
日本中性子捕捉療法学会 (著)
大阪公立大学共同出版会 (2018). (in Japanese)

「BNCT 基礎から臨床応用まで」—BNCT を用いて治療にかかわる人のためのテキスト— 増刷版
中性子捕捉療法による抗腫瘍効果
増永慎一郎
日本中性子捕捉療法学会 (著)
大阪公立大学共同出版会 (2018). (in Japanese)

Reviews

Design of drug delivery systems for physical energy-induced chemical surgery
T. Nomoto and N. Nishiyama
Biomaterials **178** (2018) 583-596.

悪性骨・軟部腫瘍,多発肺転移に対するホウ素中性子捕捉療法適応に向けての戦略
鈴木 実, 藤本卓也, 安藤 徹
日本整形外科雑誌 **92** (2018) 757-764. (in Japanese)

国内の BNCT 施設の現状
櫻井良憲
放射線化学会誌 **105** (2018) 41-46. (in Japanese)

最近報告されたがんの統計と疫学的解析結果報告について
増永慎一郎
日本ハイパーサーミア学会誌 **34** (2018) 138-140. (in Japanese)

質疑応答,臨床一般/ホウ素原子と中性子線によるがん治療は可能か？
増永慎一郎
日本医事新報 **4903** (2018) 61-62. (in Japanese)

8. Neutron Radiography and Radiation Application

Papers

Synthesis of the reported structure of homocereulide and its vacuolation assay
T. Naka, Y. Hattori, H. Takenaka, Y. Ohta, M. Kirihata and S. Tanimori
Bioorganic & Medicinal Chemistry Letters **29(5)** (2019) 734-739.

Flow visualization of heavy oil in a packed bed using real-time neutron radiography
E. Shoji, K. Yamagiwa, M. Kubo, T. Tsukada, S. Takami, K. Sugimoto, D. Ito, Y. Saito and S. Teratani
Chemical Engineering Science **196** (2019) 425-432.

Cellular uptake evaluation of pentagamaboronon-0 (PGB-0) for boron neutron capture therapy (BNCT) against breast cancer cells
A. Hermawan, R.A. Susidarti, R. D. Ramadani, L. Qodria, R.Y. Utomo, M. Ishimura, Y. Hattori, Y. Ohta, M. Kirihata and E. Meiyanto
Investigational New Drugs 2019 1-8.

Local void fraction and heat transfer characteristics around tubes in two-phase flows across horizontal in-line and staggered tube bundles
H. Murakawa, M. Baba, T. Miyazaki, K. Sugimoto, H. Asano and D. Ito
Nuclear Engineering and Design **334** (2018) 66-74.

A new detector system for the measurement of high-energy prompt γ-rays for low-energy neutron induced fission
H. Makii, K. Nishio, K. Hirose, R. Orlandi, R. Léguillon, T. Ogawa, T. Soldner, F.-J. Hambsch, M. Aïche, A. Astier, S. Czajkowski, R. Frost, S. Guo, U. Köster, L. Mathieu, T. Ohtsuki, C.M. Petrache, A. Pollitt, S. Sekimoto, K. Takamiya and I. Tsekhanovich
Nuclear Instruments and Methods in Physics Research Section A: Accelerators, Spectrometers, Detectors and Associated Equipment **906** (2018) 88-96.

Generation of $^{4}He^{*}_{2}$ Clusters via Neutron-^{3}He Absorption Reaction Toward Visualization of Full Velocity Field in Quantum Turbulence
T. Matsushita, V. Sonnenschein, W. Guo, H. Hayashida, K. Hiroi, K. Hirota, T. Iguchi, D. Ito, M. Kitaguchi, Y. Kiyanagi, S. Kokuryu, W. Kubo, Y. Saito, H.M. Shimizu, T. Shinohara, S. Suzuki, H. Tomita, Y. Tsuji and N. Wada
Journal of Low Temperature Physics none 2018 1-8.

Proceedings

Identification and Quantification of Nuclear Nuclides Using a Pulsed Neutron Imaging Technique
D. Ito, Y. Takahashi, T. Sano, J. Hori and K. Nakajima
JPS Conference Proceedings Vol. 24, Proceedings of the Second International Symposium on Radiation Detectors and Their Uses (ISRD2018) Tsukuba, Japan (Jan.23-26, 2018).

4π Compton Gamma Imaging toward Determination of Radioactivity
K. Uema, H. Tomita, K. Kanamori, T. Takahashi, T. Iguchi, J. Hori, T. Matsumoto, T. Shimoyama and J. Kawarabayashi
JPS Conference Proceedings Vol. 24, Proceedings of the Second International Symposium on Radiation Detectors and Their Uses (ISRD2018) Tsukuba, Japan (Jan.23-26, 2018).

高速度中性子イメージングにおける時間分解能の向上 /
Improvement of temporal resolution in high speed neutron imaging
D. Ito, K. Ito and Y. Saito
Proceedings of the 53rd KURNS Scientific Meeting Kumatori, Japan (Feb5-6, 2019) 40. (in Japanese)

鉛ビスマス-窒素二相流の分布特性に関する研究 /
Distribution characteristics in LBE/nitrogen gas two-phase flow
G. Ariyoshi, D. Ito, K. Ito and Y. Saito
Proceedings of the 53rd KURNS Scientific Meeting Kumatori, Japan (Feb5-6, 2019) 41. (in Japanese)

多点センサを用いた静電容量式液膜厚さ計測手法の高度化 /
Development of electrical capacitance method for liquid film thickness measurement by use of multipoint liquid film sensor
T. Matsushita, D. Ito, K. Ito and Y. Saito
Proceedings of the 53rd KURNS Scientific Meeting Kumatori, Japan (Feb5-6, 2019) 42. (in Japanese)

多孔質内における気液二相流圧力損失に及ぼす偏流の影響 /
Effect of drift on a gas-liquid two-phase pressure drop in porous media
T. Kurisaki, D. Ito, K. Ito and Y. Saito
Proceedings of the 53rd KURNS Scientific Meeting Kumatori, Japan (Feb5-6, 2019) 43. (in Japanese)

中性子イメージングの高度化 /
Development on Neutron Imaging Application
Y. Saito, D. Ito, H. Asano, H. Murakawa, K. Sugimoto, T. Tsukada, E. Shoji, M. Kubo, H. Umekawa, R. Matsumoto, T. Ami, Y. Yamagata, S. Morita, U. Matsushima, T. Numao, T. Harada, T. Sakai, M. Matsubayashi, M. Kanematsu, K. Mizuta, M. Tamaki, Y. Tsuji and S. Takami
Proceedings of the 53rd KURNS Scientific Meeting Kumatori, Japan (Feb5-6, 2019) 55-59. (in Japanese)

高エネルギー粒子照射研究における評価手法の高度化 /
Advancement of Characterization Techniques in High-Energy-Particle Irradiation Studies
A. Kinomura, K. Inoue, K. Sato, T. Nishimura, M. Akiyoshi, T. Onitsuka, K. Kanda and S. Nakao
Proceedings of the 53rd KURNS Scientific Meeting Kumatori, Japan (Feb5-6, 2019) 60-63. (in Japanese)

Estimation of Frost Formation on the Plate Fin-tube Heat Exchanger by Using 3D Neutron Computed Tomography
Y. Nagasawa, R. Matsumoto, T. Uechi, D. Ito and Y. Saito
ACRA 2018 - 9th Asian Conference on Refrigeration and Air-Conditioning Sapporo, Japan (Jun.10-13, 2018) 6-13, ACRA2018-B224.

Frost density profile measured by using X-ray radiography
Y. Nagasawa, R. Matsumoto, T. Uechi, D. Ito and Y. Saito
Proceedings of the 16th International Heat Transfer Conference, IHTC-16 Beijing, China (Aug.10-18, 2018) 6369-6374.

Imaging of Actinide Nuclides using Neutron Resonance Absorption
T. Sano, D. Ito, J. Hori, Y. Takahashi, J. Lee, N. Abe and K. Nakajima
2018 IEEE NSS-MIC Sydney, Australia (Oct.10-17, 2018).

Development of Medium-Chain Alkyl Sulfoniododecaborate Containing L-Amino Acids for Boron Neutron Capture Therapy
Y. Hattori, A. Nagasawa, M. Ishimura, J.K. H. Chen, Y. Ohta, H. Takenaka, K. Matsumoto, K. Uehara, T. Asano and M. Kirihata
Peptide Science 2018(10th International Peptide Symposium) Kyoto, Japan (Dec.3-7, 2018).

Other

X 線ラジオグラフィを用いた除霜時の融解水挙動の評価/
Evaluation of Melted Water Behavior During Defrosting by Using X-ray Radiography
塩川貴大，松本亮介，長澤 佳輝，西浦 雄人，齊藤 泰司，伊藤 大介/
T. Shiokawa, R. Matsumoto, Y. Nagasawa, Y. Nishimura, Y. Saito and D. Ito
2018 年度日本冷凍空調学会年次大会講演論文集（2018.9.4-7，郡山）
JSRAE annual conference 2018 (2018) B333-1-B333-6. (in Japanese)

9. TRU and Nuclear Chemistry

Papers

Wet chemical processing for nuclear waste glass to retrieve radionuclides
K. Takao, T. Mori, M. Kubo, A. Uehara and Y. Ikeda
Journal of Hazardous Materials **362** (2019) 368-374.

Enhancement of superconductivity by pressure-induced critical ferromagnetic fluctuations in UCoGe
M. Manago, S. Kitagawa, K. Ishida, K. Deguchi, N.K.Sato and T. Yamamura
Physical Review B **99 (**2019) 020506.

Adsorption study of U and Th by N,O-hybrid donor ligand-immobilized hydrogels
M. Nakase, T. Yamamura, K. Shirasaki, M. Nagai and K. Takeshita
Separation Science and Technology (2019) 1-8.

Study on the leaching behavior of actinides from nuclear fuel debris
A. Kirishima, M. Hirano, D. Akiyama, T. Sasaki and N. Sato
Journal of Nuclear Materials **502** (2018) 169-176.

Solubilities and solubility products of thorium hydroxide under moderate temperature conditions
S. Nishikawa, T. Kobayashi, T. Sasaki and I. Takagi
Radiochimica Acta **106(8)** (2018) 655-667.

Actinide molecular ion formation in collision/reaction cell of triple quadrupole ICP-MS/MS and its application to quantitative actinide analysis
T. Suzuki, T. Yamamura, C. Abe, K. Konashi and Y. Shikamori
Journal of Radioanalytical and Nuclear Chemistry **318(1)** (2018) 221-225.

Measurements of gamma-ray emission probabilities in the decay of americium-244g
S. Nakamura, K. Terada, A. Kimura, T. Nakao, O. Iwamoto, H. Harada, A. Uehara, K. Takamiya and T. Fujii
Journal of Nuclear Science and Technology **56(1)** (2018) 123-129.

Development of new methods for aqueous chemistry on element 104, rutherfordium: Batchtype solid-liquid extraction and coprecipitation
Y. Kasamatsu
Journal of Nuclear and Radiochemical Sciences **18** (2018) 24-31.

Cation-cation interaction between $Np^{V}O^{2+}$ and Li^{+} in a concentrated LiCl solution
T. Fujii, Y. Shibahara, C. Kato and A. Uehara.
Progress in Nuclear Science and Technology **5** (2018) 41-43.

Proceedings

アクチノイド物性化学分野における課題と研究計画 /
Subjects and research programs in the division of Condensed-matter Chemistry in Actinides
T. Yamamura
Proceedings of the 53rd KURNS Scientific Meeting Kumatori, Japan (Feb5-6, 2019) 2. (in Japanese)

ウランの金属酸化物への収着反応に関する分光学的評価 /
Spectroscopic evaluation on sorption reaction of uranium to metal oxide
D. Harumoto, T. Kobayashi and T. Sasaki
Proceedings of the 53rd KURNS Scientific Meeting Kumatori, Japan (Feb5-6, 2019) 31. (in Japanese)

化学交換法による同位体分別研究 /
Study of Isotope Separation via Chemical Exchange Reaction
R. Hazama, T. Yoshimoto, Y. Sakuma, T. Fujii, S. Fukutani and Y. Shibahara
Proceedings of the 53rd KURNS Scientific Meeting Kumatori, Japan (Feb5-6, 2019) 39. (in Japanese)

Investigation of Direct Observation System for Crossover in Vanadium Redox-Folw Battery by Using Radioactive V-48
K. Shirasaki and T. Yamamura
ECS Meeting (ElectroChemical Society) Yonezawa, Japan (Aug.27-29, 2018).

Review

^{229m}Th と ^{235m}U の核壊変の化学状態依存性/
Chemical effect on the nuclear decays of ^{229m} Th and ^{235m}U
笠松良崇，菊永英寿
DIOISOTOPES **67(10)** (2018) 471-482. (in Japanese)

10. Health Physics and Waste Management

Papers

Using Experimental Transfer Factors to Estimate the Ratio between the Committed Effective Dose from Ingestion of Radio-tellurium to that of Radio-cesium Released by the Fukushima Daiichi Nuclear Power Plant Accident
T. Takahashi, K. Fujiwara, T. Kinouchi, S. Fukutani and S. Takahashi
Japanese Journal of Health Physics **53(1) (**2018) 12-16.

Estimation of the radiation dose of ^{107}Pd in palladium products and preliminary proposal of appropriate clearance level
S. Takahashi, M. Ikeda, K. Iwata, S. Tanaka, R. Akayama and T. Takahashi
Journal of Nuclear Science and Technology **55(12)** (2018) 1490-1495.

Tritium separation from parts-per-trillion-level water by a membrane with protonated manganese dioxide
H. Koyanaka and S. Fukutani
Journal of Radioanalytical and Nuclear Chemistry **318** (2018) 175-182.

Estimation of the Release Time of Radio-Tellurium During the Fukushima Daiichi Nuclear Power Plant Accident and Its Relationship to Individual Plant Events
S. Takahashi, S. Kawashima, A. Hidaka, S. Tanaka and T. Takahashi
Nuclear Technology **5** (2018) 646-654.

Proceedings

燃料デブリのガラス固化に関する実験的研究 /
Vitrification of simulated MCCI debris and dissolution behavior of nuclides
Y. Kodama, T. Sasaki, N. Sato, A. Kirishima, D. Akiyama, S. Sekimoto, R. Okumura and T. Kobayashi
Proceedings of the 53rd KURNS Scientific Meeting Kumatori, Japan (Feb.5-6, 2019) 17. (in Japanese)

原子炉中性子によって生じる DNA 損傷の分析 /
DNA damage with the neutrons from reactor
H. Terato, Y. Tokuyama, K. Mori, N. Osada, H. Tanaka and T. Saito
Proceedings of the 53rd KURNS Scientific Meeting Kumatori, Japan (Feb.5-6, 2019) 23. (in Japanese)

溶液中のトリチウムに対する水酸化物のプロトン交換反応 /
Exchange reaction of proton in hydroxide with tritium in aqueous solution
H. Hashizume, A. Uehara, S. Fukutani, K. Fujii and T. Ando
Proceedings of the 53rd KURNS Scientific Meeting Kumatori, Japan (Feb.5-6, 2019) 30. (in Japanese)

耐放射線小型軽量撮像素子の開発－構成要素のガンマ線照射下における挙動 /
Development of radiation tolerant compact image sensor − characteristics of components under gamma-ray irradiation.
Y. Gotoh, T. Morito, Y. Handa, M. Nagao, T. Okamoto, T. Igari, T. Fukui,T. Masuzawa, Y. Neo, H. Mimura, N. Sato, M. Akiyoshi and I. Takagi
Proceedings of the 53rd KURNS Scientific Meeting Kumatori, Japan (Feb.5-6, 2019) 29. (in Japanese)

11. Accelerator Physics

Proceedings

FFAG 加速器これまでの歩みと今後の展開 /
Research and Development and Future Plans of FFAG accelerators at KURNS
Y. Ishi
Proceedings of the 53rd KURNS Scientific Meeting Kumatori, Japan (Feb.5-6, 2019) 3-5. (in Japanese)

1.5 MW 大強度高繰り返しシンクロトロンにおけるビーム挙動の解析 /
Analysis of Beam Dynamics in a 1.5 MW High-Intensity Rapid Cycle Synchrotron
Y. Fuwa, Y. Ishi, T. Uesugi and Y. Kuriyama
Proceedings of the 53rd KURNS Scientific Meeting Kumatori, Japan (Feb.5-6, 2019) 25. (in Japanese)

Design of Multi-MW Rapid Cycling Synchrotron for Accelerator Driven Transmutation System
Y. Fuwa, N. Amemiya, Y. Ishi, Y. Kuriyama and T. Uesugi
Proceedings of 9th Internatianal Particle Accelerator Conference Vancouver, Canada (Apr.29-May5, 2018) 1057-1059.

Improvement of RF Capture with Multi-Turn H- Injection in KURRI FFAG Synchrotron
T. Uesugi, Y. Fuwa, Y. Ishi, Y. Kuriyama, Y. Mori and H. Okita
Proceedings of 9th Internatianal Particle Accelerator Conference Vancouver, Canada (Apr.29-May5, 2018) 1066-1066.

Practical betatron tune behavior during accelerationin scaling FFAG rings at KURNS
Y. Ishi, Y. Fuwa, Y. Kuriyama, H. Okita, T. Uesugi, Y. Mori and J-B. Lagrange
Proceedings of 9th Internatianal Particle Accelerator Conference Vancouver, Canada (Apr.29-May5, 2018) 3287-3289.

Control System Upgrade for the FFAG Accelerator Complex at KURNS
Y. Kuriyama, Y. Fuwa, Y. Ishi, Y. Mori, H. Okita and T. Uesugi
Proceedings of 12th PCaPAC, International Workshop on Emerging Technotogies and Scientific Facilities Control Hsinchu, Taiwan (Oct.16-19, 2018).

Review

タングステン繊維状ナノ構造を用いたミュオニウム生成
薮内 敦，大野哲靖，三宅康博，池戸 豊，下村浩一郎，西山樟生，小嶋健児，河村成肇，STRASSER Patrick，藤森 寛，牧村俊助，中村惇平，齊藤直人，三部 勉，大谷将士，神田聡太郎，西村昇一郎，北村 遼，長嶋泰之，鈴木卓爾，長友 傑
プラズマ・核融合学会誌 **94** (2018) 315-319. (in Japanese)

12. Others

Papers

Measurement of bunch length evolution in electron beam macropulse of S-band linac using coherent edge radiation
N. Sei, H. Zen and H. Ohgaki
Physics Letters A **383(5)** (2019) 389-395.

2018 年 6 月 18 日の大阪府北部の地震(MJMA6.1)で得られた箕面市とその周辺での強震動アレイ記録の特徴/Feature of the Strong-Motion Array Observation Records obtained at Minoh City and its neighboring Area during the Earthquake in Osaka-Fu Hokubu on 18 June 2018
上林宏敏 / H. Uebayashi
Journal of Japan Association for Earthquake Engineering **19(1)** (2019) 1_68-1_81. (in Japanese)

Development of Continuous Line Scanning System Prototype for Proton Beam Therapy
R. Kohno, K. Hotta, T. Dohmae, Y. Matsuzaki, T. Nishio, T. Akimoto, T. Tachikawa, T. Asaba, J. Inoue, T. Ochi, M. Yamada and H. Miyanaga
International Journal of Particle Therapy **3(4)** (2018) 429-438.

Aggregate of oligonucleotides bearing azobenzene unit as radiation-activated drug carrier.
T. Itagaki, R. Kurihara and K. Tanabe
Photomedicine and Photobiology **39** (2018) 27-28.

非線形性を考慮した不均質地盤の地震動空間変動特性と基礎地盤安定性/
Spatially Variation of Seismic Ground Motions and Foundation Ground Stability of Inhomogeneous Layered Ground Considering Nonlinearity
O. Uchida, K. Arai, H. Uebayashi and K. Kamae
Journal of Japan Association for Earthquake Engineering **18(2)** (2018) 2_166-2_183. (in Japanese)

Simple Evaluation Index for Structural Damage of High-Rise Reinforced Concrete Buildings due to Long-Period Strong Ground Motion
H. Uebayashi, M. Nagano, K. Kamae and H. Kawabe
Journal of Japan Association for Earthquake Engineering **18(3)** (2018) 3_75-3_90.

Real-Time Lossless Compression of Waveforms Using an FPGA
N.M. Truong, M. Aoki, Y. Igarashi, M. Saito, S. Ito, D. Nagao, Y. Nakatsugawa, H. Natori, Y. Seiya, N. Teshima and K. Yamamoto
IEEE Transactions on Nuclear Science **65(9)** (2018) 2650-2656.

Multi-Channel Fiber-Optic Temperature Sensor System using An Optical Time-Domain Reflectometer
H. J. Kim, H. Byun, Y. B. Song, S. H. Shin, S. Cho, C. H. Pyeon and B. Lee
Results in Physics **11** (2018) 743-748.

和歌山平野の 3 次元地下構造モデル構築と中央構造線断層帯による強震動予測/
Three-dimensional Subsurface Structure Model beneath the Wakayama Plain and Strong Ground Motion Prediction for the Median Tectonic Line
H. Uebayashi, M. Ohori, H. kawabe, K. Kamae, K. Yamada, K. Miyakoshi, T. Iwata, H. Sekiguchi and K. Asano
Journal of Japan Association for Earthquake Engineering **18(5)** (2018) 5_33-5_56. (in Japanese)

^{99m}Tc production via the (γ, n) reaction on natural Mo
T. Takeda, M. Fujiwara, M. Kurosawa, N. Takahashi, M. Tamura, T. Kawabata, Y. Fujikawa, K.N. Suzuki, N. Abe, T. Kubota and T. Takahashi
Journal of Radioanalytical and Nuclear Chemistry **318(2)** (2018) 811-821.

Efficient laser acceleration of deuteron ions through optimization of pre-plasma formation for neutron source development
A. Sunahara, T. Asahina, H. Nagatomo, R. Hanayama, K. Mima, H. Tanaka, Y. Kato and S. Nakai
Plasma Physics and Controlled Fusion **61(2)** (2018) 025002.

An institutional analysis of the Japanese energy transition
J.B. Kucharski and H. Unesaki
Environmental Innovation and Societal Transitions **29** (2018) 126-143.

マルチキャピラリーX 線レンズを用いた顕微メスバウアー分光/
Mössbauer microspectrometer with a multicapillary X-ray lens
篠田 圭司, 小林 康浩/ K. Shinoda and Y. Kobayashi
岩石鉱物科学/Japanese Magazine of Mineralogical and Petrological Sciences **47(4)** (2018) 163-167. (in Japanese)

Proceedings

B-3 小型多目的中性子回折計の進捗状況 2018 /
The current state for the compact versatile neutron diffractometer on the B−3 beam port, 2018
K. Mori, R. Okumura, H. Yoshino, M. Kanayama, S. Sato, H. Hiraka, K. Iwase, A. Okumura and F. Kobayashi
Proceedings of the 53rd KURNS Scientific Meeting Kumatori, Japan (Feb.5-6, 2019) 18. (in Japanese)

Coherent Edge Radiation Sources in Linac-Based Infrared Free-Electron Laser Facilities
N. Sei, K. Hayakawa, Y. Hayakawa, K. Nogami, H. Ogawa, H. Ohgaki, T. Sakai, Y. Sumitomo, T. Tanaka and H. Zen
Proceedings of Linear Accelerator Conference-LINAC Beijing, China (Sept.16-21, 2018) 154-156.

Books

原子力年鑑 2019
「Part V:原子力教育・人材育成」の「1.原子力教育」の「2. 特色ある教育の例」の「(4)京都大学」
中島 健
「原子力年鑑」編集委員会
日刊工業新聞社(2018). (in Japanese)

新版 X 線反射率法入門
9 章 1～4
日野正裕, 宮田 登
桜井健次 編
講談社 (2018). (in Japanese)

トラウマ研究 1
トラウマを生きる 第 10 章　トランスジェンダーとトラウマ
高垣雅緒
田中 雅一, 松嶋 健 編
京都大学学術出版会 (2018). (in Japanese)

Review

国内外の原子力教育事情(2)京都大学原子核工学専攻・原子核工学コース
高木郁二, 中島健
日本原子力学会誌（アトモス） **61** (2019) 143- 145. (in Japanese)

Other

88Zr from soil with artificial digestive juices
T. Kubota, K. Iwata, S. Fukutani, T. Takahashi, S. Yanou, S. Shibata, H. Haba and S. Takahashi
Desorption of RIKEN Accel. Procg. Rep. **51** (2018) 10-12.

KURNS Progress Report 2018

Issued in August 2019

Issued by the Institute for Integrated Radiation and Nuclear Science,
Kyoto University
Kumatori-cho, Sennan-gun, Osaka 590-0494, Japan

Tel. +81-72-451-2300
Fax. +81-72-451-2600

In case that corrections are made, an errata will be provided
in the following webpage:
https://www.rri.kyoto-u.ac.jp/PUB/report/PR/ProgRep2018/ProgRep2018.html

Publication Team

HASEGAWA, Kei
IINUMA, Yuto
INOUE, Rintaro (Subchief)
ITO, Kei
KINASHI, Yuko
MORI, Kazuhiro (Chief)
NAKAYAMA, Chiyoko
SAKURAI, Yoshinori (Subchief)
SANO, Hiroaki
TAKATA, Takushi
TSURUTA, Yachiyo
YOKOTA, Kaori